

The Early Generations of Rotating Massive Stars and the Origin of Carbon-Enhanced Metal-Poor Stars

THÈSE

présentée à la Faculté des sciences de l'Université de Genève
pour obtenir le grade de Docteur ès sciences,
mention Astronomie et Astrophysique

par

Arthur CHOPLIN

de

Gex (France)

Thèse N° 5269

GENÈVE
Observatoire de Genève
2018



**UNIVERSITÉ
DE GENÈVE**

FACULTÉ DES SCIENCES

**DOCTORAT ÈS SCIENCES
MENTION ASTRONOMIE ET ASTROPHYSIQUE**

Thèse de Monsieur Arthur CHOPLIN

intitulée :

**«The Early Generations of Rotating Massive Stars and
the Origin of Carbon-Enhanced Metal-Poor Stars»**

La Faculté des sciences, sur le préavis de Monsieur G. MEYNET, professeur ordinaire et directeur de thèse (Département d'astronomie), Madame S. EKSTRÖM, docteure et codirectrice de thèse (Département d'astronomie), Madame C. CHARBONNEL, professeure associée (Département d'astronomie), Monsieur A. MAEDER, professeur honoraire (Département d'astronomie), Madame M. LUGARO, docteure (Konkoly Observatory, Research Centre for Astronomy and Earth Sciences, Hungarian Academy of Sciences, Budapest, Hungary), Madame C. CHIAPPINI, docteure (Milky Way and the Local Volume Section, Leibniz-Institut für Astrophysik Postdam, Deutschland), autorise l'impression de la présente thèse, sans exprimer d'opinion sur les propositions qui y sont énoncées.

Genève, le 19 octobre 2018

Thèse - 5269 -

Le Doyen

N.B. - La thèse doit porter la déclaration précédente et remplir les conditions énumérées dans les "Informations relatives aux thèses de doctorat à l'Université de Genève".

Abstract

The study of the long-dead early generations of massive stars is crucial in order to obtain a complete picture of the chemical evolution of the Universe, hence the origin of the elements. The nature of these stars can be inferred indirectly by investigating the origin of low-mass metal-poor stars observed in our Galaxy, some of which are almost as old as the Universe. The peculiar extremely iron-poor Carbon-Enhanced Metal-Poor (CEMP) stars, whose precise origin is still debated, are thought to have formed with the material ejected by only one or very few previous massive stars, hereafter called the source stars. In this context, the source stars belong to the very first generations of massive stars.

The main aim of this thesis is to explore the physics and the nucleosynthesis of the early generations of massive stars. It is achieved by combining stellar evolution modeling including rotation and full nucleosynthesis with observations of CEMP stars. By fitting the abundances of CEMP stars with the ejecta of new massive source star models, characteristics of the massive source stars can be deduced.

The efficient rotational mixing operating in rotating source stars triggers exchanges of material between the helium burning core and the hydrogen burning shell, and leads to a very rich and varied nucleosynthesis. This interplay between rotation and nucleosynthesis in massive source stars is able to cover the abundance scatter of light elements (carbon to silicon) of the CEMP stars with $[\text{Fe}/\text{H}] < -3$. Some remaining discrepancies between models and observations can be alleviated if a late mixing process is included in the source star. It operates about 200 years before the end of the source star evolution, between the hydrogen burning shell and the helium burning shell. A detailed investigation of the abundances of light elements of 69 CEMP stars with $[\text{Fe}/\text{H}] < -3$ suggests that the best source stars are preferentially fast rotating $20 M_{\odot}$ stars which experienced the late mixing process and an ejection of only their outer layers.

The rotation-induced mixing also boosts the weak s-process in source stars, provided the initial metallicity is not strictly zero. The s-elements up to barium are strongly overproduced, especially if the initial rotation rate is high. The s-process boost induced by rotation was found to be significant for stars with initial masses below $60 M_{\odot}$. Above this threshold, the interplay between rotation and nucleosynthesis is weaker so that rotating and non-rotating models give similar results. The signature of the rotation-induced s-process boost in $20 - 25 M_{\odot}$ source stars was found to be consistent with the abundance pattern of several CEMP stars enriched in s-elements.

The examination of the origin of CEMP stars in light of new massive source star models suggests that rotation was a dominant effect in the early generations of massive stars. Strong mixing events between burning shells are also expected to be a common feature in these early massive stars. Finally, early massive stars should have lost only their envelope and experienced rather strong fallback.

Résumé

Les premières générations d'étoiles massives en rotation et l'origine des étoiles CEMP

Contexte

Les premières générations d'étoiles massives¹ sont des acteurs essentiels dans l'histoire de l'Univers. À la fin de leur évolution, ces étoiles à courte durée de vie ont explosé en supernovae – un évènement dont la luminosité peut atteindre 10 milliards de fois celle du Soleil – et ont, pour la première fois, enrichi l'Univers en métaux², dont nous-mêmes et notre Terre sommes constitués. La compréhension, encore méconnue aujourd'hui, de l'évolution de ces étoiles, est primordiale afin d'acquérir une connaissance globale de l'évolution de l'Univers, en particulier de son évolution chimique.

Bien qu'autour de nous, ces étoiles ne peuvent plus être observées, leur nature peut être étudiée indirectement grâce à l'observation, dans notre Galaxie, d'étoiles de faible masse et très pauvres en métaux. Certaines de ces étoiles – *Carbon-Enhanced Metal-Poor* ou *CEMP* – se sont probablement formées très tôt dans l'Univers, avec la matière éjectée d'une ou de quelques-unes des premières étoiles massives, appelées ci-après *étoiles sources*. La composition chimique particulière des étoiles CEMP, déterminée par spectroscopie, donne de précieuses informations sur la nucléosynthèse, et donc sur la nature de leur(s) étoile(s) source(s). Les étoiles CEMP pourraient être comparées à des "Pierre de Rosette": leur déchiffrement permet d'étudier une civilisation ancienne, aujourd'hui disparue.

Objectifs et méthodes

Le but principal de ce travail de thèse est d'obtenir de nouveaux indices sur la physique des premières générations d'étoiles massives en utilisant les contraintes liées à l'observation des étoiles CEMP. Une telle étude est possible en combinant des modèles numériques d'étoiles sources avec les observations d'étoiles CEMP disponibles dans la littérature. Le code d'évolution stellaire de Genève, principal outil utilisé durant cette thèse, permet de modéliser l'évolution des étoiles sources. Une des spécificités de ce code est d'inclure une modélisation sophistiquée de la rotation

¹Au moins $8 M_{\odot}$, i.e. 8 fois la masse du Soleil.

²Éléments plus lourds que l'hélium (par exemple l'oxygène).

différentielle. En outre, ce code permet le calcul de la nucléosynthèse complète, y compris le *processus s* (capture lente de neutron par des noyaux atomiques, permettant la production d'éléments lourds). Ce processus, intervenant dans les étoiles de masse intermédiaire – entre 1 et 8 M_{\odot} – et massives, est supposé être à l'origine d'environ 50 % des éléments plus lourds que le fer, tels que le strontium, baryum, tungstène ou plomb par exemple.

Résultats

Le mélange induit par la rotation dans l'étoile source déclenche des échanges successifs de matière entre la zone de combustion d'hélium et celle d'hydrogène. Il en résulte une nucléosynthèse riche et variée, permettant la création, en grande quantité, de carbone, azote, oxygène, fluor, néon, sodium, magnésium et aluminium. La composition chimique de cette matière, enrichie en éléments divers, et finalement éjectée par les vents stellaires et/ou lors de la supernova des modèles d'étoiles sources, est en accord global avec la composition chimique des étoiles CEMP les plus pauvres en fer.

Une comparaison plus détaillée entre ces étoiles CEMP et les modèles d'étoiles sources a mis en évidence certains écarts entre les modèles et les observations. Un mélange additionnel, survenant dans une zone spécifique de l'étoile source, quelques centaines d'années avant son explosion, permet de pallier ces désaccords. Une procédure automatique, déterminant, parmi environ 35000 possibilités, le meilleur modèle d'étoile source pour une étoile CEMP donnée, a été appliquée à un échantillon de 69 étoiles CEMP. Les résultats suggèrent que les étoiles sources sont préférentiellement des étoiles en rotation rapide, d'environ 20 M_{\odot} , qui ont subi le mélange additionnel et qui n'ont éjecté que leurs couches externes.

Le mélange rotationnel affecte également la synthèse d'éléments *s* dans l'étoile source, et ce, d'autant plus que la vitesse de rotation initiale est élevée. La modélisation d'une nouvelle grille d'étoiles massives – $10 < M_{\text{ini}} < 150 M_{\odot}$ –, incluant rotation et *processus s* montre que l'effet de la rotation sur le *processus s* intervient de manière significative uniquement si la masse initiale de l'étoile est inférieure à 60 M_{\odot} . Au-delà de ce seuil, l'interaction entre le mélange rotationnel et la nucléosynthèse est moindre. Par conséquent, les modèles d'étoiles sources en rotation donnent des résultats similaires aux modèles sans rotation. La signature chimique induite par la rotation sur la production d'éléments *s* dans des étoiles sources de 20 – 25 M_{\odot} a été identifiée dans plusieurs étoiles CEMP enrichies en éléments *s*.

Conclusion

L'étude de l'origine des étoiles CEMP à la lumière de nouveaux modèles d'étoiles sources vient corroborer l'idée selon laquelle la rotation a joué un rôle prépondérant dans l'Univers jeune. Par ailleurs, ce travail suggère que (1) les premières générations d'étoiles massives pourraient, pour la plupart, avoir une masse d'environ 20 M_{\odot} (2) de puissantes interactions entre différentes coquilles de combustion étaient à l'œuvre dans ces étoiles et (3) ces étoiles ont probablement éjecté uniquement leur enveloppe, tandis que les régions plus internes sont tombées sur l'objet compact central.

Remerciements

Tout d'abord, un immense merci à Georges. C'est une grande chance d'avoir eu un directeur si enthousiaste et compétent, doté d'une curiosité sans bornes, captivant en cours, conférence ou lors d'une fondue bien arrosée. Merci de m'avoir laissé si libre et autonome, tout en restant toujours immédiatement disponible pour discuter, pour me conseiller, me rassurer ou me remettre sur les rails quand je m'égarais un peu. Un grand merci à Sylvia, en particulier pour son aide précieuse dans les premiers mois. Il en va de même pour André, ses conseils avisés et encouragements furent très appréciés. Merci à Cyril, toujours disponible et prêt à m'aider quand je l'ai sollicité. Merci à Corinne pour m'avoir chaleureusement accueilli et pour sa bienveillance. Je tiens à souligner que ce fut un vrai régal de travailler au sein d'une telle équipe, accueillante, dynamique, drôle. Bref, l'ambiance est bonne. Un merci tout spécial à Patrick, pour sa bonne humeur et son indéfectible humour.

En dehors de Genève, je remercie Raphael, avec qui c'est un vrai plaisir de collaborer. Merci pour m'avoir initié au *processus s*, au golf et pour m'avoir gracieusement permis de stocker quelques téraoctets sur tes disques... Je remercie Cristina pour ses précieux conseils scientifiques et encouragements. Merci à Alain Coc, Keith A. Olive, Jean-Philippe Uzan et Elisabeth Vangioni, sans lesquels une partie de cette thèse n'aurait pas pu exister. Merci à Alison Laird pour sa contribution et son intérêt pour certains des travaux de cette thèse. Merci à Maria Lugaro pour ses commentaires bienveillants et constructifs sur mon travail. Merci à Tim Beers, aux organisateurs de *Gala of GALAH* et à Jinmi Yoon pour l'intérêt qu'ils ont porté à mon travail et pour la confiance qu'ils m'ont accordée. Une pensée aussi à mes anciens maîtres de stage de Grenoble, Jérôme, Véronique et Jean-Charles avec qui j'ai fait mes premiers pas dans le monde de la recherche.

De retour à Genève, je dis grazie à Giovanni pour m'avoir épaulé au démarrage, et aussi pour ses merveilleuses lasagnes. Merci à Mads pour nos premières soirées sans limites à Gex, Sauverny ou Genthod. Merci à Lionel pour son introduction musclée au marxisme-léninisme. Merci à Thibaut, un compagnon fort sympathique et enjoué pour cette fin de thèse. Merci à ceux qui excellent dans l'art d'égayer les pauses cafés, les parties de pétanque ou de ping-pong: Patrick bien sûr mais aussi Stéphane et Thierry. Merci à Song, qu'il me suffisait de croiser dans le couloir pour passer une bonne journée, tant sa joie et son affection sont grandes et communicatives. Merci à Koh et Yu, mes collègues éphémères, curieux de tout, au travail comme en dehors. Merci à Carlo pour sa visite à Genève et nos discussions sur ces beaux objets que sont les CEMP. Merci à Jose et Aline pour leur gentillesse et leur accueil bien amical au sein du groupe. Ce fut un vrai plaisir de les retrouver à Dublin pour un petit projet scientifique. Ce séjour irlandais n'aurait pu être aussi fructueux sans l'attention et la patience de Jose. En passant, merci aux collègues dublinois, en particulier Laura, Ioana et Eoin. Assez rapidement, on se sent bien parmi eux, au bureau comme au pub. Au risque d'en faire un peu trop, j'ai envie de remercier l'Observatoire en général, car l'atmosphère y est bien agréable... je pense à l'administration, la cafet', la mécanique (Robin pour la réparation du piano...), les footex du vendredi, les (not so) lazy runners et les grimpeurs. Un grand merci au groupe de musique de l'Obs. C'était une superbe parenthèse hebdomadaire que de

jouer avec vous dans ce bunker antiatomique. Je pense aussi à la belle fête de Noël 2016 de l'Obs organisée avec vous, inoubliable! Toujours dans la musique, merci à Lorenzo et Iris pour m'avoir fait connaître puis permis de jouer le jeudi soir dans ce chouette endroit qu'est *c'est ici l'endroit où*. Musique encore: merci à la team du Cully Jazz Festival, spécialement Barbara et l'incroyable Job (je te suis reconnaissant d'avoir gardé ton sang froid à la fourrière). Enfin, merci à Uriel pour m'avoir fait découvrir les joies du studio.

J'ai aussi des pensées affectueuses et non sans émotion pour tous ceux que j'ai rencontré voire rerencontré lors de mes escapades, parfois dans le cadre professionnel, parfois en dehors. Je pense déjà à Taygun, Panos, Matt, Sanjana, Jacqueline, Brent et tout ce chouette petit monde croisé à Niigata. Je pense à Taygun encore, Melisa, Mehmet et son chat à Istanbul. Je pense aussi à Gen, Tilman, Rick, Tim, Camilla et Marc-Antoine à Melbourne, à Rana à Notre-Dame. Je pense à ceux du Chili, où j'ai vécu une magnifique expérience d'observation sur Euler. Soyez salués sur l'heure Justyn, Simona, Chiara (membres du LSVB ou La Silla VolleyBall), James, Vincent, Sophie, Amélie, Max, Mikaela et Lila! Je pense aussi aux chamoniards et au refuge. Je pense à Solène, Klimt et Bill Viola. Je pense à Nicolas, Guillaume, Marco et autres très joyeux drilles de l'EJC 2016. Je pense à Simon, Damien et aux Genevois à Saas-Fee. Je pense enfin à Michael, Eric et les amis de l'Observatoire François-Xavier Bagnoud pour avoir partagé avec moi cette conférence, raclette et belle soirée à Saint-Luc.

Pendant cette thèse, si j'ai pu garder (je crois) les pieds sur Terre, c'est déjà en partie grâce aux volleyeurs de Prévessin, avec qui j'allais me défouler, boire des canettes et manger des 'zia' chez da Ettore. C'est sûrement aussi grâce à la sophrologie (quelle belle découverte...) chez Philippe et Dominique. C'est certainement aussi grâce à mes très chers amis Gessiens, Chenevessiens et Divonnais. Je vous salue chaleureusement Louis, Florian, Tim, Olja, William, Nico, Remy, Aline, Baptiste...! Allez... quelques doux mots-clés, au hasard de mes pensées: lingot, chess championship à l'huile de foie de morue, bière-pizza (Charly's), Salève, parcours de santé (10 tours), lactaire délicieux (1), bobsleigh, Krazy House... Une franche accolade à Louis, présent (mais disparaissant parfois après quelques pintes) aussi bien dans les moments un peu difficiles que moins difficiles. Si j'ai gardé la raison, c'est aussi grâce à Fanny, qui a compté, et à tous les chouettes moments passés avec la bande, à Grenoble, Gex, Paris ou au fin fond de l'Ardèche. C'est sans nul doute aussi grâce à mes tous proches et leur bienveillance, mes parents et grand-parents, ma sœur, Nathalie, Uli, Julia. Je remercie au passage les relecteurs pour vos corrections et suggestions en général fort pertinentes (mention spéciale à Laurent et Jacqueline). Avec certitude, si je n'ai pas débloqué, c'est aussi grâce à ma chère petite Perru***, arrivée sur le tard mais bien arrivée. Que dire? Comment dire? Merci pour ta pétillance, bonne humeur permanente, légèreté, humour, joie de vivre si communicative, pour avoir eu des paroles réconfortantes quand mon moral dégringolait. Merci surtout de m'avoir initié aux plantes vertes, à Dalida, aux Colocs, à la brasse coulée et j'en passe. En passant, justement, merci au reste de la famille Lap' pour votre accueil simple et chaleureux. Pour terminer, si je n'ai pas trop ondulé de la toiture pendant ces années, c'est peut être aussi grâce à mes amis de longue et très longue date. Je pense à Nathan, notre récent chavirement et notre future régata, à Rémi, au frelon disparu et aux micro trous noirs, à Bidou et au thème entêtant de Taxi Driver, à Dri, mutique ou chantant John Legend, à Verrier ainsi qu'à son lit à mémoire de forme, à Dupin, aux ménisques bien faits et aux GBF bien réglés, à Robin et Jeff Thirion, à Jouty et à nos frasques à la Machine du Moulin Rouge, à Fercot et au Rachais, à Antoine motocross et au robot de table, à Félix et au fameux jeu, à Manu et à l'inondation du 3ème étage, à Gorjup enfin, avec sa clochette et son poil soyeux.

Contents

Abstract	i
Résumé en français	iii
Remerciements	v
List of Figures	xii
List of Tables	xiii
1 Introduction	1
1.1 From the Big Bang to the first stars	1
1.1.1 Big Bang nucleosynthesis	1
1.1.2 The formation of the first stars	1
1.2 Origin of the elements	3
1.3 Stellar rotation	4
1.4 Observable signatures of the early generations of massive stars	6
1.5 Overview of this thesis	10
2 CEMP stars: observations and origins	11
2.1 Generalities on metal-poor stars	11
2.2 Observation and abundances of metal-poor stars	13
2.2.1 The observational steps	13
2.2.2 Abundances and uncertainties	18
2.3 CEMP stars as peculiar metal-poor stars	18
2.4 Internal mixing processes in CEMP stars	22
2.5 The origin of CEMP stars: external sources	25
2.5.1 CEMP-s stars	25
2.5.2 CEMP-r, -r+s, -r/s, -i stars	26
2.5.3 CEMP-no stars	27
2.6 Summary	32
3 Massive source stars: nucleosynthesis and models with rotation	35
3.1 Nucleosynthesis processes in massive stars	35
3.1.1 Stellar fusion	35
3.1.2 The weak s-process	37
3.1.3 Explosive nucleosynthesis	38
3.2 The s-process in AGB stars	38

3.3	Massive stellar models including rotation	40
3.3.1	Transport induced by rotation	41
3.3.2	Convection	44
3.3.3	Nuclear network	44
3.3.4	Initial composition and opacity tables	46
3.3.5	Mass loss	47
3.3.6	Chemical composition of the ejecta	48
3.4	Axions and their impact on Pop III stars	49
3.5	Summary	50
4	Mixing in CEMP-no source stars	51
4.1	The back-and-forth mixing process	51
4.2	Nucleosynthesis in a box	52
4.3	Massive source stars with rotation	58
4.3.1	Physical ingredients	58
4.3.2	Evolution with rotation	58
4.3.3	Composition of the ejecta	62
4.4	Comparison with CEMP-no stars	70
4.4.1	A global comparison	70
4.4.2	The C/N – $^{12}\text{C}/^{13}\text{C}$ puzzle	74
4.5	The late mixing process in the source star	76
4.5.1	General idea	77
4.5.2	Implementation in source star models	78
4.5.3	Comparison with CEMP-no stars	79
4.5.4	Physical origin	80
4.6	A systematic study of the CEMP-no source star population	81
4.7	Are CEMP-no stars helium-rich?	87
4.8	Other CEMP-no source star models	89
4.8.1	An energetic H-ingestion event in the source star	89
4.8.2	Other source star models in the C/N – $^{12}\text{C}/^{13}\text{C}$ diagram	90
4.9	Summary	93
5	The s-process in CEMP source stars	95
5.1	The weak s-process in a box	95
5.2	A new grid of massive stars with rotation and s-process	96
5.2.1	Nuclear network and reaction rates	97
5.2.2	The μ and Ω profiles	98
5.3	The origin of the single CEMP-s stars	116
5.3.1	Massive source stars	116
5.3.2	The AGB scenario	122
5.4	The weak s-process at lower metallicities	123
5.4.1	A rotating $25 M_{\odot}$ model with various initial metallicities	124
5.4.2	The origin of HE 1327-2326	124
5.5	Summary	126
6	Conclusions and perspectives	127
6.1	Conclusions	127
6.2	Perspectives	129
6.2.1	Linking the old and local with the old and distant Universe	131

A Numerical aspects	133
A.1 Axion cooling	133
A.2 Secular shear mixing	134
A.3 Mass loss recipes	136
A.4 Locally weighted scatterplot smoothing	136
A.5 S-process parameters	137
B Abundance fits	141
C Publications	147
References	189

List of Figures

1.1	Big Bang nucleosynthesis	2
1.2	Mass range of the first stars	3
1.3	Schematic view of the pre supernovae structure of a massive star	4
1.4	Neutron capture processes	5
1.5	Probability density of the rotation velocities for 496 observed OB stars	6
1.6	Schematic view of the chemical evolution of the Universe	9
2.1	Spectrum of stars with different metallicities	12
2.2	Schematic view of the architecture of the Galaxy	14
2.3	Spectrum of a metal-poor star: from low to high resolution	15
2.4	X/Fe ratios of the most iron-poor stars	19
2.5	Abundances of iron-poor stars	21
2.7	Schematic view of the binary scenario for CEMP-s stars	25
2.8	Schematic view of a possible formation channel for CEMP-no stars	28
2.9	Inner abundances of a Pop III 25 M_{\odot} after explosive nucleosynthesis	29
2.10	Schematic view of the mixing and fallback model	30
2.11	Post-supernova yields of a non rotating Pop III 40 M_{\odot} model	31
3.1	The CNO cycle	36
3.2	The Ne-Na and Mg-Al chains	37
3.3	Schematic view of the interior of a star during the AGB phase	39
3.4	Internal $U(r)$ profile in rotating 20 M_{\odot} models with various metallicities	42
3.5	HR diagram of rotating 20 M_{\odot} computed with different D_{shear} coefficients	44
3.6	Visualization of the large network used in the present work	45
3.7	Some important effects of rotation at low metallicity	49
4.1	Schematic view of the back-and-forth mixing process	52
4.2	Abundances profile of a 20 M_{\odot} with $v_{\text{ini}}/v_{\text{crit}} = 0.7$ at $Z = 10^{-5}$	53
4.3	A possible classification of CEMP-no stars	54
4.4	Nucleosynthesis in a one-zone model while injecting ^{12}C , ^{16}O , ^{22}Ne and ^{26}Mg	55
4.5	Masses of the cores as a function of initial velocity for 20 M_{\odot} model with $Z = 10^{-5}$	59
4.6	Internal abundance profiles of 20 M_{\odot} models at $Z = 10^{-5}$ with various initial rotations	60
4.7	Same as Fig. 4.6 for other isotopes	61
4.8	Wind composition of 20 M_{\odot} models at $Z = 10^{-5}$ with various initial rotations	62
4.9	Same as Fig. 4.8 but for the composition of all the H-rich material	63
4.10	Same as Fig. 4.9 but for the composition of all the H-rich + He-rich material	63
4.11	Abundances of the 20 M_{\odot} at $Z = 10^{-5}$ and $v_{\text{ini}}/v_{\text{crit}} = 0.4$ (pre-SN)	64

4.12	Ejecta composition of a $20 M_{\odot}$ model with $Z = 10^{-5}$ and $v_{\text{ini}}/v_{\text{crit}} = 0.4$ for various mass cuts	64
4.13	Impact of the dilution in the ejecta composition for a fast rotating $20 M_{\odot}$	66
4.14	Effect of varying the efficiency of rotational mixing (f_{energ}) on the yields	68
4.15	Ejecta composition of $Z = 10^{-5}$, $v_{\text{ini}}/v_{\text{crit}} = 0.4$ models with different initial masses	69
4.16	Ejecta composition of $20 M_{\odot}$, $v_{\text{ini}}/v_{\text{crit}} = 0.4$ models with different metallicities	69
4.17	C/N vs. $^{12}\text{C}/^{13}\text{C}$: CEMP-no stars and source star models	75
4.18	CNO equilibrium timescales as a function of the temperature	76
4.19	Schematic view of the late mixing process at work in the source star	77
4.20	Abundances of the $20 M_{\odot}$ with $v_{\text{ini}}/v_{\text{crit}} = 0.7$ with/without late mixing	79
4.21	C/N vs. $^{12}\text{C}/^{13}\text{C}$: CEMP-no stars and source star models including late mixing	79
4.22	Convective boundary regions of the C-burning shell of a $15 M_{\odot}$ model	81
4.23	Best fits of G77-61 and HE 1005-1439 with the source star models of Table 4.4	83
4.24	Characteristics of the best source star models	84
4.25	Occurrence of the four categories of the best source star models	85
4.26	Distribution of $f_{\text{H}} + f_{\text{He}} + f_{\text{CO}}$ for the best source star models	85
4.27	Same as Fig. 4.23 but for CS 29498-043	86
4.28	Distribution of the helium mass fraction in the ejecta of the best source star models	87
4.29	$\log g$ vs. $\log(T_{\text{eff}})$ for CEMP-no star models with various initial helium content	88
4.30	Ejecta composition of massive and AGB star models from various authors	90
4.31	Same as Fig. 4.30 but in the region where observations lie	91
5.1	Composition of a one-zone model with various ^{22}Ne content	96
5.2	Composition of a one-zone model with various ^{16}O content	97
5.3	Rate of the $^{17}\text{O}(\alpha, \gamma)^{21}\text{Ne}$ reaction	98
5.4	D_{shear} , ^{14}N and ^{22}Ne profiles in $25 M_{\odot}$ models	99
5.5	Composition of the ejecta of models computed with low and high resolution	99
5.6	Composition of AGB models and apparently single CEMP-s stars	122
5.7	Ejected mass of 4 isotopes as a function of metallicity for rotating $25 M_{\odot}$ models	123
5.8	Production factors of $25 M_{\odot}$ models with various initial rotation rates	124
5.9	Composition of HE 1327-2326 and of a $25 M_{\odot}$ source star models with s-process	125
6.1	Link between the old and local Universe with the old and distant Universe	130
6.2	Emergent spectra of massive non-rotating models	131
A.1	Locally weighted scatterplot smoothing	137
A.2	$\nabla\mu$ in a rotating $25 M_{\odot}$ model: the impact of smoothing	138
B.1	Best fits of 69 CEMP stars with 20 – 60 source star models	141
B.2	Fig. B.1, continued	142
B.3	Fig. B.1, continued	143
B.4	Fig. B.1, continued	144
B.5	Fig. B.1, continued	145

List of Tables

2.1	Nomenclature of iron-deficient stars.	13
2.2	Classification of CEMP stars.	20
4.1	Effect of dilution on the source star ejecta composition	66
4.2	Stars with $[\text{Fe}/\text{H}] < -3$ and $[\text{C}/\text{Fe}] > 1$ (recognized CEMP-s, -r/s and -r excluded) .	71
4.3	Initial and final surface $\log(^{12}\text{C}/^{13}\text{C})$ and $[\text{C}/\text{N}]$ ratios for $0.8 M_{\odot}$ models	75
4.4	Properties of the source star models	78
4.5	Parameters of the best source star models	82
5.1	Apparently single CEMP-s stars	117

Introduction

Stars are cosmic engines catching interstellar material, processing it and giving it back during their lives or when they die. Almost all the content in metal¹ in the Universe was synthesized in stars. Especially, the first metals in the Universe were synthesized by the first stars, that were predominantly massive² and that are long-dead now. The comprehension of the entire chemical evolution of the Universe requires to understand its chemical evolution at all the different epochs, from the first stars era to the present day Universe. The onset of the chemical evolution, triggered by the early generation of massive stars, is a crucial and still largely missing piece of the puzzle.

1.1 From the Big Bang to the first stars

1.1.1 Big Bang nucleosynthesis

During the first minutes following the Big Bang, as the temperature decreased from $\sim 10^{32}$ K to about 10^8 K, the first nucleosynthetic event in the Universe took place. The Big Bang nucleosynthesis (BBN) finished about 15 minutes after the Big Bang, when the density and temperature became too low for further nucleosynthesis to occur. At this time, for 100 g of Universe, about 24.8 g was in the form of ^4He and almost all the rest in the form of protons (Cyburt et al. 2003). As shown in the left panel of Fig. 1.1, a bit of ^2H , ^3H , ^3He and other light elements is also found. Metals up to oxygen could also be synthesized but in negligible amounts (generally below 10^{-15} in mass fraction, see Fig. 1.1, right panel, also Iocco et al. 2007; Coc et al. 2012, 2014).

380000 years after the BBN, the Universe became cool enough (about 3100 K), allowing protons and electrons to recombine and form neutral hydrogen atoms. From this point, the Universe entered the dark ages. It is transparent but no light-producing structures such as stars exist yet.

1.1.2 The formation of the first stars

The first stars (Population III or Pop III stars) formed ~ 200 Myr later, with almost exactly 25 % of Helium and 75 % of Hydrogen in mass. For a star to form, a gas cloud has to cool until its Jeans mass³ $M_J \propto T^{3/2} \rho^{-1/2}$ reaches the mass scale of individual stars. In metal-rich environments, the cooling of the molecular cloud is mainly controlled by heavy elements such as carbon or oxygen. On the other side, it was found by Saslaw & Zipoy (1967) that the cooling in a low-temperature and

¹Metals are elements heavier than helium.

²Stars are considered as massive when they go through all hydrostatic burning stages, ultimately leading to an iron-core. The lower mass limit is around $10 M_{\odot}$.

³The Jeans mass is the minimum mass of a gas cloud required in order the gravitational force to overcome the gas pressure. When M_J is reached, the cloud becomes unstable and collapses.

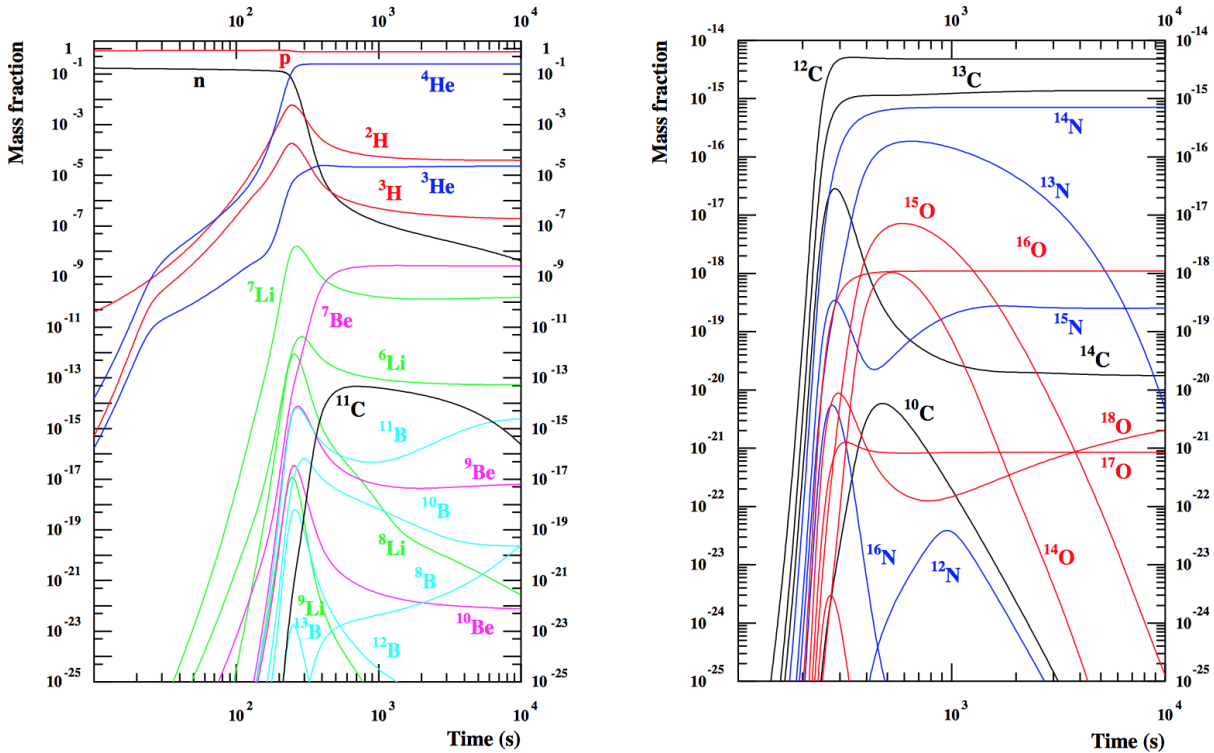


Figure 1.1: Big Bang nucleosynthesis (mass fraction as a function of time in seconds). Note the different vertical scales between the two panels (figure from Coc et al. 2012).

metal-free environment is achieved by molecular hydrogen H_2 . The cooling efficiency of H_2 being low, the primordial gas is able to cool down to about 200 K only (Abel et al. 2002; Bromm et al. 2002), against $\sim 10 - 20$ K at solar metallicity⁴. The higher temperature in primordial gas clouds implies a higher M_J and makes the collapse and fragmentation of these clouds more difficult. The fragments are consequently larger, suggesting that the first stars were more massive.

Various multidimensional cosmological simulations have shown that the first stars were predominantly massive (generally $\gtrsim 30 M_\odot$, e.g. Abel et al. 2002; Bromm et al. 2002). Some authors have refined this picture by suggesting the existence of two distinct star formation modes for Pop III, leading to two classes of Pop III stars: Pop III.1 and Pop III.2 (e.g. Johnson & Bromm 2006). Pop III.1 stars formed from metal-free $\sim 10^6 M_\odot$ dark matter minihalos. Pop III.2 stars formed from a metal-free gas cloud but which was significantly ionized by photons from already existing Pop III.1 stars. Such an ionization favors the creation of HD molecules in the star forming cloud, which increases the cooling efficiency and leads to lower initial stellar masses. The mass distribution of Pop III.2 stars, possibly peaking at $\sim 10 M_\odot$ (Hirano et al. 2014), is shifted towards lower values compared to Pop III.1 stars. However, if important turbulent motions were present in primordial gas clouds, the picture is reversed: Pop III.2 stars are on average more massive than Pop III.1 stars (Clark et al. 2011). Indeed, Clark et al. (2011) have shown that turbulence may be more vigorous in Pop III.1 clouds than in Pop III.2 clouds, hence facilitating the fragmentation of Pop III.1 clouds, and ultimately leading to less massive stars on average. The Pop III initial mass range predicted by the most recent simulations still varies a lot from a study to another (cf. Fig. 1.2). For instance, Stacy et al. (2016) predicts masses between 0.05 and $20 M_\odot$ while Hosokawa et al. (2016) between 15 and $600 M_\odot$. This could be due to differences in the adopted resolution, number of minihaloes followed during the simulation, time of the simulation or types of feedback

⁴The metallicity is the sum of the mass fraction of elements heavier than helium. The solar metallicity is $Z_\odot = 0.0134$ (Asplund et al. 2009).

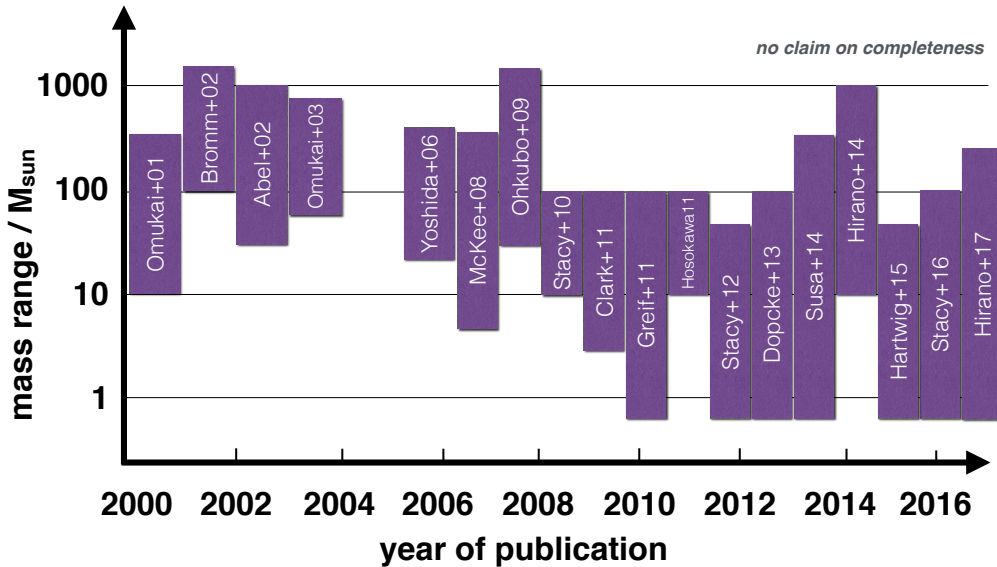


Figure 1.2: Predicted mass range of the first stars as a function of the year of publication. Courtesy of T. Hartwig (adapted from a plot by N. Yoshida). No distinction is made between Pop III.1 and Pop III.2 stars (see text for details).

implemented in the simulation (see Table 1 of Stacy et al. 2016, for an overview of the characteristics of some simulations of first star formation).

1.2 Origin of the elements

If gravity were the only force in stars, they would collapse in less than one hour (the free-fall timescale is about 30 minutes for the Sun). Stars have to produce energy to counteract their own gravity. The Kelvin-Helmholtz timescale τ_{KH} gives an estimate of how long a star would shine with its current luminosity if the only power source were the conversion of gravitational potential to heat. For the Sun, $\tau_{\text{KH}} = GM_{\odot}^2 / (R_{\odot} L_{\odot}) \simeq 30$ Myr. A lifetime of 30 Myr for the Sun is however too short in regards to geological and biological evidences that the Earth is billions of years old. Nuclear fusion provides another source of energy that sustains stars for a much longer time. Stars gain energy by fusion only up to iron because it is the most bound nucleus. Beyond iron, no fusion can occur. Massive stars with initial masses $M_{\text{ini}} > 8 M_{\odot}$ undergo successive shorter and shorter core burning stages, lasting from millions of years to fractions of days, and ultimately leading to the onion-like structure shown in Fig. 1.3. At the end of each core burning phase, the burning continues in a shell. As evolution proceeds, more and more burning regions are present in the massive star (Fig. 1.3). Nucleosynthesis in massive stars is discussed in more details in Sect. 3.1.

As mentioned, stellar fusion can synthesize elements up to iron. The main processes building elements beyond iron are neutron capture processes (Burbidge et al. 1957). Neutrons are captured by nuclei that can experience a β -decay reaction (a neutron is transformed into a proton) if they are unstable. Neutron capture processes are generally separated into two categories: slow and rapid (s- and r-processes), that are both expected to contribute to synthesize about 50 % of the nuclei beyond iron. For the r-process, neutron captures operate on much smaller timescales than for the s-process, giving the possibility to reach very neutron rich (unstable) isotopes that finally decay to the valley of stability (i.e. to stable isotopes, see Fig. 1.4). For the s-process, the neutron

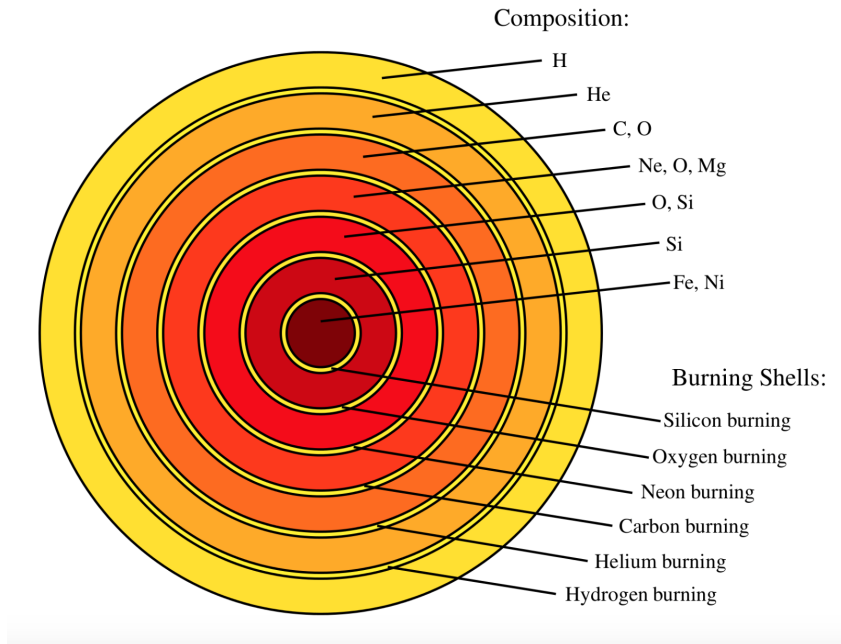


Figure 1.3: Schematic view of the stellar structure of a massive star before its death. The most abundant species in the different layers are indicated, as well as the different burning shells (figure from Frischknecht (2012) PhD thesis, originally from C. Winteler).

capture timescales τ_n are larger than the β -decay timescales τ_β of unstable isotopes. It means that unstable isotopes β -decay before another neutron is captured (with the exception of the branching points where $\tau_n \sim \tau_\beta$). Starting from Fe, the s-process runs mainly along the s-process path which stays close to the valley of stability (black path in Fig. 1.4). The small neutron cross sections of the magic nuclei around $A=88$, 140, and 208 are bottlenecks for the flow and create distinct peaks in the typical s-process abundance pattern. These peaks can be seen in the abundance pattern of the Sun (top left panel of Fig. 1.4). The s-process ends at ^{208}Pb , the last stable nucleus.

Some isotopes are called s-only (marked as *s* in Fig. 1.4) because they cannot be synthesized with the r-process. An example is ^{82}Kr . The very neutron-rich isotopes that β -decays to the valley of stability (following a diagonal in the (N, Z) plane) after r-process nucleosynthesis cannot reach ^{82}Kr . This isotope is shielded by the stable isotope ^{82}Se . Clayton et al. (1961) have shown that abundances of s-only isotopes in the Sun cannot be reproduced by a single neutron irradiation of an iron seed. In fact, the abundances of elements between $90 < A < 204$ can be reproduced by a *main* s-process component while for the elements below $A = 90$, a *weak* s-process component is required (Kappeler et al. 1989). The main component is associated to Thermally Pulsing (TP) Asymptotic Giant Branch (AGB) stars with $1 \lesssim M_{\text{ini}} \lesssim 8 M_\odot$. The weak component is associated to massive stars with $M_{\text{ini}} \gtrsim 8 M_\odot$. These two s-process components are discussed in Sect. 3.1 and 3.2.

1.3 Stellar rotation

During the star formation process, the initial molecular cloud shrinks by $\gtrsim 5$ orders of magnitudes. The local conservation of angular momentum ($\Omega r^2 = \text{constant}$) tells us that even if the initial gas cloud rotates very slowly, the newly formed star will rotate fast. A simple conservation of the angular momentum during star formation will however produce only very fast rotator. Since all stars are not very fast rotators, some processes able to dissipate angular momentum during the star formation process have to be invoked.

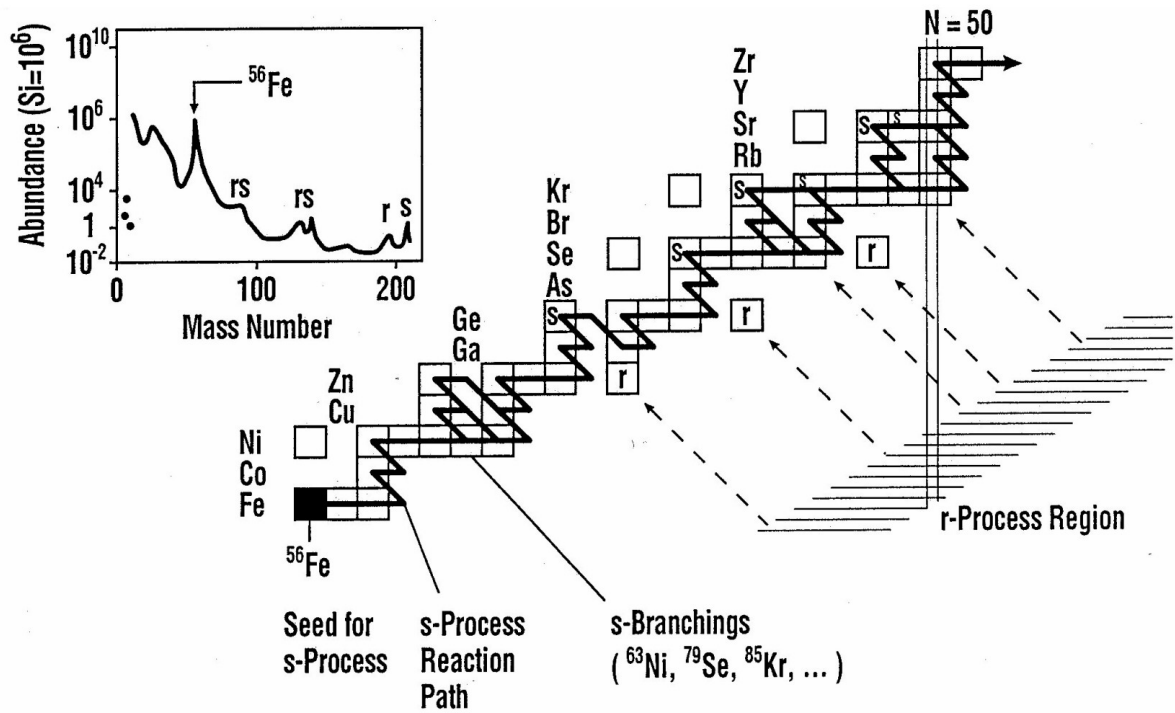


Figure 1.4: Illustration of the neutron capture processes responsible for the formation of the nuclei beyond iron. Only the stable nuclei between Fe and Zr are shown. The top left panel shows the solar system abundances with the abundance of silicon normalized to 10^6 (figure from Käppeler et al. 2011).

There are many observational evidences that stars rotate. Huang & Gies (2006) have reported the equatorial velocity distribution of 496 OB stars, whose velocity distribution peaks at 200 km s^{-1} (Fig. 1.5). Because of the centrifugal force exerted by rotation, fast rotating stars have an ellipsoid-like shape with a bigger equatorial than polar radius. Thanks to interferometric observations, Domiciano de Souza et al. (2003) have reconstructed the shape of the fast rotating massive star Achernar (about $10 M_{\odot}$). They reported an equatorial radius 1.56 ± 0.05 larger than the polar radius.

Rotation is expected to affect the stellar luminosity, stellar lifetimes, mass loss or the chemical composition of the stellar surface for instance (e.g. Meynet & Maeder 2000; Heger & Langer 2000). Especially, massive stellar models predict surface nitrogen enhancements because of the combined effect of the CNO cycle operating in the stellar interior and rotational mixing. Martins et al. (2015) reported the CNO surface abundances of 74 observed O-type stars with masses between about 20 and $50 M_{\odot}$. 80 % of their sample can be explained by single stellar models including rotation.

Rotation at low and zero metallicity

Low metallicity stars have less metals so that they are less opaques and more compact. As a consequence, for the same angular momentum content, low-metallicity stars rotate faster than solar metallicity stars. Low metallicity stars generally lose little mass through winds meaning that they keep more angular momentum than their solar counterpart. This also favors a faster rotation. Faster rotation at low metallicity is supported by different observations: Hunter et al. (2008) have shown that stars in the Small Magellanic Cloud rotate on average faster than Galactic stars (the latter having higher metallicities in general). Maeder et al. (1999) and Martayan et al.

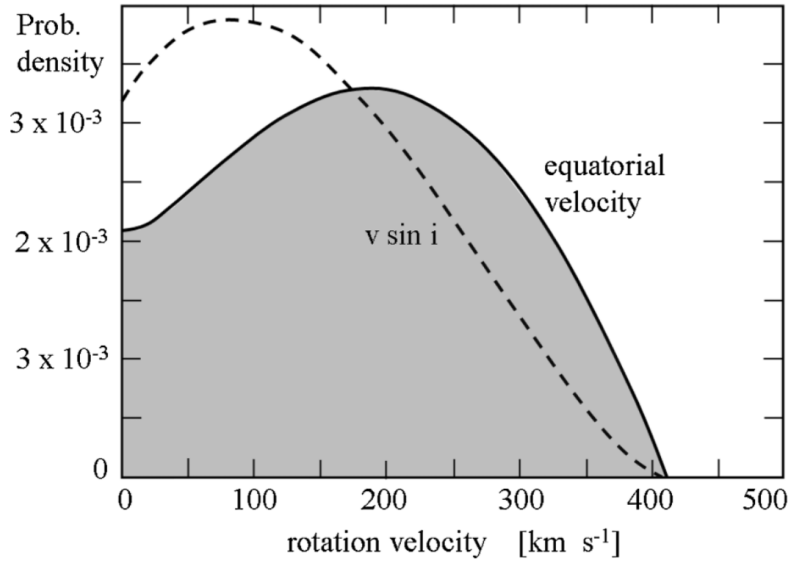


Figure 1.5: Probability density of the rotational velocities of 496 observed OB stars (masses between about 3 and 20 M_{\odot}). Figure from Maeder & Meynet (2012), originally from Huang & Gies (2006).

(2007) have shown that the fraction of Be-type stars, whose existence is possibly linked to fast rotation, increases with decreasing metallicity.

For Pop III stars, Stacy et al. (2011) estimated their rotation speed thanks to smoothed particle hydrodynamic simulations. They have recorded the angular momentum of the sink particles falling into the growing protostar. The large amount of angular momentum suggests initial velocities of 1000 km s^{-1} or higher for stars with $M_{\text{ini}} \geq 30 M_{\odot}$. A caveat in this study is that they estimated the total angular momentum accreted within a radius of 50 UA from the center of the star, meaning that they do not resolve stellar scales. This prevents to see whether some angular momentum removal processes (e.g. stellar winds, disk-locking or magnetic torques) occur in the inner region.

Recently, by studying the angular momentum transfer in primordial discs including magnetic fields, Hirano & Bromm (2018) suggested that the final rotational state of Pop III protostars should exhibit a net bimodality: either the protostar do not rotate at all, or it is a fast rotator, close to breakup speed. As mentioned in their paper, this study does not properly include MHD effects, which are likely required to self-consistently assess this possible bimodality.

Rotation and its effect in low metallicity massive stars is discussed in more details in the next chapters (especially in Sect. 2.5.3 and 3.3).

1.4 Observable signatures of the early generations of massive stars

We have many images of the Universe when it was older than a billion year. With the Cosmic Microwave Background, we also have a picture of the Universe when it was only 380000 years old. One big challenge today is to obtain pictures in between these two periods, when the primordial Universe started to evolve into the incredibly rich zoo of objects we see today. To cite Loeb (2010): “ the situation is similar to having a photo album of a person that begins with the first ultrasound image of him or her as an unborn baby and then skip to some additional photos of his or her years as teenager and adult ”.

The first generations of massive stars in the Universe have specific signatures that one can look for to reveal their nature. The present work focuses on one of these signatures (the metal-poor stars) but the list below includes also other observables, for completeness.

Integrated light of high redshift galaxies

Thousands of very distant galaxies with redshift $z > 5$ have been observed (e.g. Bouwens et al. 2007, 2009; Oesch et al. 2010; McLure et al. 2010). The most distant object observed today is a galaxy, GN-z11, with $z = 11.1_{+0.08}^{-0.12}$, possibly formed ~ 400 Myr after the Big Bang (Oesch et al. 2016). In the future, the James Webb Space Telescope (JWST) might be able to detect up to a thousand star-bursting galaxies with $z > 10$ (Pawlik et al. 2011). Their colors and spectra could be compared with predictions of the integrated light coming from such objects in order to interpret these observations in terms of stellar populations (e.g. Schaerer 2002; Salvaterra et al. 2011).

Abundance determination of high- z objects is challenging. Past and current observations managed to evaluate the abundances of a few elements (generally C, N, O, Si) of $z \lesssim 4$ objects. These objects are mostly damped Lyman α (DLA) systems with $2 < z < 3$ (e.g. Lehner et al. 2016). In general, the metallicity of such objects is estimated from considerations on the nebular emission lines formed in ionized gas at the sites of star formation (e.g. Pettini & Pagel 2004; Pettini 2008). To date, the most metal-poor DLA system is at $z = 3.076$ and has $[C/H] = -3.43 \pm 0.06$, $[O/H] = -3.05 \pm 0.05$, $[Si/H] = -3.21 \pm 0.05$ and $[Fe/H] \leq -2.81$ (Cooke et al. 2017).

One difficulty regarding high- z objects is that most of the metal lines are redshifted to the infrared range (by a factor of $1+z$), a regime where the sky background is high. In space, although the current telescopes cannot reach the far infrared region (the Hubble Space Telescope, HST, goes up to $\lambda = 2.5 \mu\text{m}$), JWST should reach $\lambda = 28 \mu\text{m}$, which may allow to detect the metal lines of very high- z objects.

Reionization

As the first stars formed and radiated energy, the Universe reverted from being neutral, to being ionized once again. At the epoch of reionization and before significant expansion had occurred, the free electron density in the Universe was high enough for Cosmic Microwave Background (CMB) photons to undergo significant Thomson scattering. This left a detectable imprint on the CMB anisotropy map. Inspection of the tiny fluctuations in the CMB polarization by the Wilkinson Microwave Anisotropy Probe (WMAP) first suggested that reionization occurred between $11 < z < 30$ (Kogut et al. 2003). Nine years of observations by WMAP have revised this result and suggested a reionization at $z \sim 10.4$ (Hinshaw et al. 2013). More recently, Planck Collaboration et al. (2016) found that the average redshift at which reionization occurred lies between $z = 7.8$ and 8.8 .

Photons from reionization also altered the excitation state of the 21-cm hyperfine line of neutral hydrogen (e.g. the reviews of Morales & Wyithe 2010; Pritchard & Loeb 2012). Models predict that the 21 cm cosmic hydrogen signal will show an absorption feature at $z \simeq 20$, coming from the Lyman- α radiation of the earliest stars. The 21-cm transition is forbidden but since hydrogen amounts to $\sim 75\%$ of the gas mass present in the intergalactic medium, the line intensity is enough to be detected. The line frequency is $\nu = \nu_0/(1+z)$ MHz with ν_0 the rest-frame frequency of 1420 MHz. For redshifts $6 < z < 50$ the corresponding frequencies are $30 < \nu < 200$ MHz. It corresponds to the radio frequency domain, making this line a prime target for present and future radio interferometers like the Murchison Widefield Array, the Low Frequency Array or the Experiment to Detect the Global Epoch of Reionization Signature (EDGES). Recently, Bowman et al. (2018) reported the detection (with EDGES) of such an absorption feature peaking at 78 MHz consistent with expectations for the 21-cm signal induced by stars having existed by 180 million years ($z \simeq 20$) after the Big Bang. Some discrepancies between this observation and models further

suggest that an unknown interaction between dark matter and baryons occurred at early times (Barkana 2018). It may provide new clues on the nature of dark matter.

Supernovae and Gamma-Ray Bursts in distant galaxies

Until now, the Swift Gamma-Ray Burst⁵ mission (Gehrels et al. 2004) has detected 8 Gamma-Ray Bursts (GRB) at $z > 6$ (reported in Table 1 of Salvaterra 2015). The [S/H] ratio of the host system of GRB 050904 ($z = 6.3$, Kawai et al. 2006) has been inferred to be $[S/H] = -1.6 \pm 0.3$ (Thöne et al. 2013), suggesting a sub-solar metallicity for this object. It remains nevertheless still far from the zero or extremely low metallicity Universe. The fact that the metallicity is likely already rather high at $z = 6$ somewhat supports the idea of a rapid enrichment in metals. The next generation of space and ground telescopes, such as JWST, the European Extremely-Large Telescope (E-ELT) or the Giant Magellan Telescope (GMT) may not be able to directly see individual first stars (Pawlik et al. 2011). Even if such stars are gravitationally lensed, their detection will remain extremely challenging (Rydberg et al. 2013). The explosion of the first massive stars, on the other hand, should be observable with the next generation of telescopes (Tanaka et al. 2013; Whalen et al. 2013a,b,c).

Gravitational waves

The first stars were likely top-heavy and retained a significant part of their mass because of weaker stellar winds. As a consequence, they could have produced massive black holes (BH) that released gravitational waves (GW) if two of them merged. Recent results suggested that the GW background coming from Pop III binary black holes mergers might be detectable by Advanced LIGO/VIRGO detectors (Kinugawa et al. 2014; Inayoshi et al. 2016).

GW150914 was the first direct detection of gravitational waves. The signal came from the coalescence of a binary BH merger whose components had masses of 36_{-4}^{+5} and $29_{-4}^{+4} M_{\odot}$ (Abbott et al. 2016). Cosmological simulations of Hartwig et al. (2016) show that there is a probability of $\gtrsim 1\%$ that GW150914 is of primordial origin. These simulations also suggest that Advanced LIGO could detect ~ 1 primordial BH-BH merger per year. The GW background from the explosion of the first massive stars might also be detectable but with the next-generation space GW detectors, like the Decihertz Interferometer Gravitational wave Observatory (DECIGO) and the Big Bang Observer (BBO, Sandick et al. 2006; Suwa et al. 2007; Marassi et al. 2009).

Pockets of primordial material

Pockets of primordial gas might be observable in the very distant Universe, but possibly also in the relatively local Universe if such pockets escaped metal pollution. Fumagalli et al. (2011) have observed two gas clouds at $z \sim 3$ with no discernible elements heavier than hydrogen. The derived upper limit for the metallicity is $Z < 10^{-4} Z_{\odot}$. Simcoe et al. (2012) have reported the discovery of another similar cloud at $z = 7$. Such gas clouds might be used as laboratories to probe the formation of metal-free stars. However, in such clouds, the stellar formation process may be different from the formation process of true Pop III stars, formed at the beginning of the Universe: in the early Universe, it is the mass of the cloud that triggers the collapse and the star formation process. In the more mature Universe, a cloud is believed to collapse because of one of several events (e.g. nearby supernovae, collision of molecular clouds...) that compress the cloud and initiate its gravitational collapse. The way the star formation process is triggered may change the initial stellar characteristics (e.g. initial mass).

⁵Gamma-Ray Bursts are sudden and powerful gamma-ray flashes observed in the Universe, lasting from 0.001 seconds to about 15 minutes.

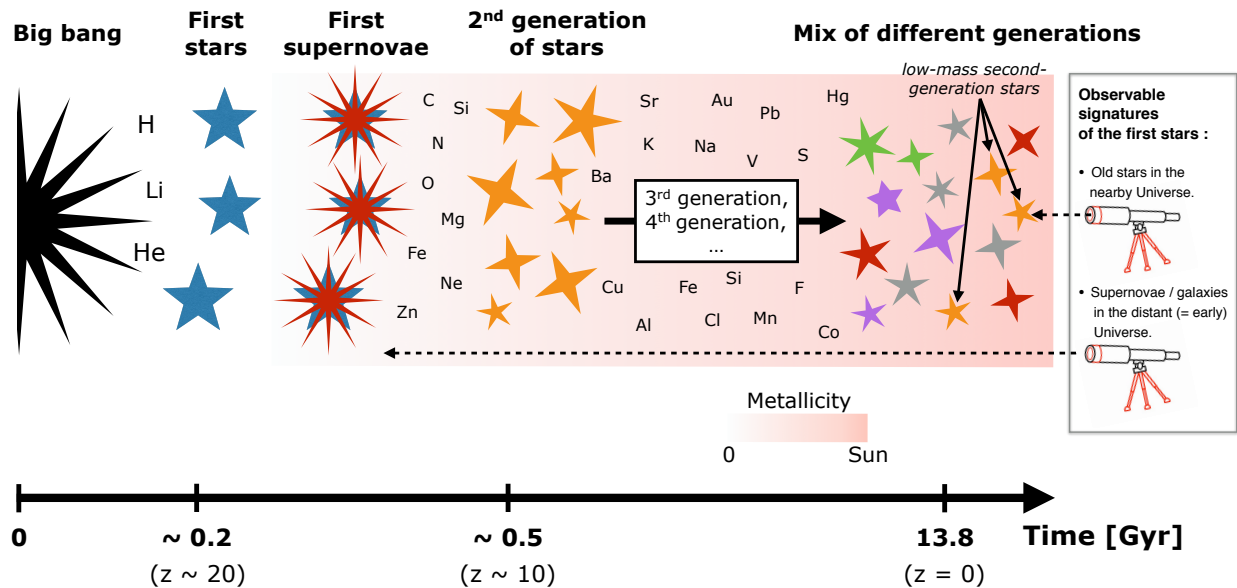


Figure 1.6: Schematic view of the chemical evolution of the Universe. Massive first stars (Pop III) formed with the products of Big Bang nucleosynthesis and released the first metals. Then, successive stellar generations formed with the ejecta of the previous generations and released new metals. The nature of the early massive stars can be inferred by observing old low-mass stars in the nearby Universe or by observing the extremely high redshift Universe.

Nucleosynthetic imprints in low-mass metal-poor stars

As discussed in Sect. 1.1.1, Big Bang nucleosynthesis formed almost only H and He. The first metals were created and released by the first stars. As time proceeded, successive generations of stars formed, evolved and exploded as supernovae, releasing more and more metals in the Universe (see Fig. 1.6 for a schematic view). A consequence is that the global metallicity in the Universe increases with time. It also implies that the metallicity of a star can be used as a proxy for its age. From this consideration follows the assumption that the most metal-poor stars are the oldest stars and then the best candidates to probe the beginning of the stellar era⁶. While massive metal-poor stars have short lifetimes and are then long dead, low-mass metal-poor stars that formed very early may still be alive around us, and hence observable. These low-mass and very metal-poor stars likely formed with the material ejected by the first short-lived massive stars. On the opposite, the Sun, which was born about 9 Gyr after the Big Bang, formed with a more metal rich material, processed by different generations of stars.

The quest for the most metal-deficient stars in our neighborhood, called stellar archaeology, has started with the HK-survey (Beers et al. 1985, 1992) and the Hamburg/ESO survey (Wisotzki et al. 1996). These surveys discovered a population of metal-poor stars in the Galactic halo. A significant fraction of these stars, especially the most iron-poor, are enriched in carbon (they are called Carbon-Enhanced Metal-Poor or CEMP stars, Beers & Christlieb 2005, see also Chapter 2). Nowadays, several thousands of metal-poor stars are known, some of them possibly having an age close to the age of the Universe (e.g. Sneden et al. 1996, 2008). This opened a new window on the first stars: the chemical composition of the most metal-poor stars delivers valuable clues on the first nucleosynthetic events that took place in the Universe, hence on the nature of early massive stars. Chapter 2 discusses metal-poor stars in more detail.

⁶This assumption is however challenged by recent works suggesting that more metal-rich stars (in the Galactic bulge) are better candidates (see the next point).

Nucleosynthetic imprints in the metal-poor stars of the Galactic bulge

The star formation rate is likely more intense in the bulge than in the other parts of the Milky Way. It implies that the metal content increased more rapidly so that there is a different metallicity-age relation in the bulge compared to the Galactic halo. A given metallicity likely corresponds to an earlier age in the bulge than in the halo. Using a chemodynamical model that mimics the formation of the Milky Way, Tumlinson (2010) suggested that of all the stars with very little metals (less than 1/1000 of the solar metallicity), those found in the central regions of the Galaxy were more likely to have formed earlier. It is however very challenging to find metal-poor stars in the bulge since this is the place in the Galaxy where the average metallicity is the highest (the most metal-rich stars known are in the bulge). Another difficulty is that the bulge is a crowded region with high extinction due to dust, making observations more difficult. Finally, the large distance to the bulge (around 8.5 kpc) precludes the observation of too faint stars, unless they are gravitationally microlensed (Bensby et al. 2013).

The globular cluster (GC) NGC 6522 (first observed by Baade 1946), is an interesting metal-poor object located in the bulge. The low metal content derived from the spectra of 8 stars in this GC (about 1 tenth of the solar metallicity, Barbuy et al. 2009) suggests that this GC is old. Images from HST were obtained for this cluster and compared to isochrones (Kerber et al. 2018). The derived age is $\sim 12.5 \pm 0.5$ Gyr. High abundances of s-element (Y and Sr) were also detected, possibly pointing towards a signature of massive rotating stars, that enriched the original gas from which the GC formed (Chiappini et al. 2011).

1.5 Overview of this thesis

The aim of the present work is to get clues on the nature of the early generations of massive stars. Informations on these short-lived hence long-dead massive stars are obtained by combining predictions from stellar evolution models including rotation with the observation of metal-poor low-mass stars observed in the halo of the Milky Way.

Chapter 2 reviews the observational steps to get abundances from metal-poor stars as well as the scenarios for the origin of the peculiar Carbon-Enhanced Metal-Poor (CEMP) stars. The mixing & fallback and spinstar scenarios are discussed in detail.

Chapter 3 discusses the theoretical and modeling aspects of massive stellar evolution that are relevant for this work. The specificities of low metallicity models are stressed. The physical ingredients used and/or implemented in the stellar evolution code are presented. A study on the effect of axions on Pop III stars is also included.

Chapter 4 and 5 are the main results of this thesis. The origin of the CEMP (mainly CEMP-no and CEMP-s) stars is investigated using predictions from new massive stellar models I have computed. Chapter 4 investigates the origin of the most iron-poor CEMP stars, generally not significantly enriched in s- and/or r-elements. A simplified nucleosynthesis model is first used and compared to observations. Then, massive source star models are computed, their physics (especially nucleosynthesis) is discussed before comparing the chemical composition of their ejecta to observations. Chapter 5 extends the investigation by following the s-process in massive source star models. New confrontations between source star models including extended nucleosynthesis and observations of CEMP stars enriched in s-elements are presented.

Chapter 6 summarizes the main results of this work, goes to the conclusions and considers the perspectives.

CEMP stars: observations and origins

This chapter reviews observational aspects and existing scenarios for the origin of CEMP stars. Metal-poor stars are first discussed before going into the special case of CEMP stars. What are the observational and modeling steps to obtain their abundances? What are the specificities of CEMP stars? Can these chemically peculiar stars be explained by internal mixing processes? If no, what kind of external sources should be invoked?

2.1 Generalities on metal-poor stars

Observing the oldest stars is a crucial task to better understand the early Universe. As a first step, it seems natural to wonder whether some stars born very early could live for long enough to be still alive today and around us. At first order, the lifetime of a star τ_* is equal to the mass of fuel available divided by the stellar luminosity. It yields

$$\tau_* \simeq 10 \left[\frac{M}{M_\odot} \right] \cdot \left[\frac{L_\odot}{L} \right] \simeq 10 \left[\frac{M}{M_\odot} \right]^{1-a} \text{ Gyr} \quad (2.1)$$

where the mass-luminosity (ML) relationship $L \sim M^a$ is used. Setting a standard value of $a = 3.5$ leads to lifetimes of 17.5 and 13 Gyr for 0.8 and 0.9 M_\odot stars, respectively. It means that nowadays, stars with mass $\lesssim 0.9 M_\odot$ that formed early in the Universe are still alive, hence possibly observable.

As discussed in Sect. 1.4, the metallicity of a star can be used as a proxy for its age. As a consequence, the oldest stars may be searched among the most metal-poor stars. However, determining the metallicity Z at the surface of a star would require to determine the abundance of all elements heavier than helium, which is not possible. Iron is often taken as an indicator of the metallicity of a star since it is one of the most abundant and easily measurable element in a stellar spectrum. It can be obtained from every observed star. The iron content at the surface of a star is given with the $[\text{Fe}/\text{H}]$ ratio. For two elements X and Y one has

$$[X/Y] = \log_{10}(N_X/N_Y)_* - \log_{10}(N_X/N_Y)_\odot \quad (2.2)$$

with N_X and N_Y the number density¹ of elements X and Y . For instance, $[\text{Fe}/\text{H}] = -4.0$ corresponds to an iron abundance of 1/10000 that of the Sun. This notation requires the abundances of the observed star and the ones of the Sun, taken as a reference. Chamberlain & Aller (1951) first reported a deficiency in iron for 2 stars: HD19445 and HD140283. They derived values of $[\text{Fe}/\text{H}] = -0.8$ and -1.0 . Nowadays, several hundreds of stars with $[\text{Fe}/\text{H}] < -3$ are known.

¹In the Sun, $N_{\text{H}}/N_{\text{Fe}} \simeq 32000$ (Asplund et al. 2009) meaning that for each iron atom there are 32000 hydrogen atoms.

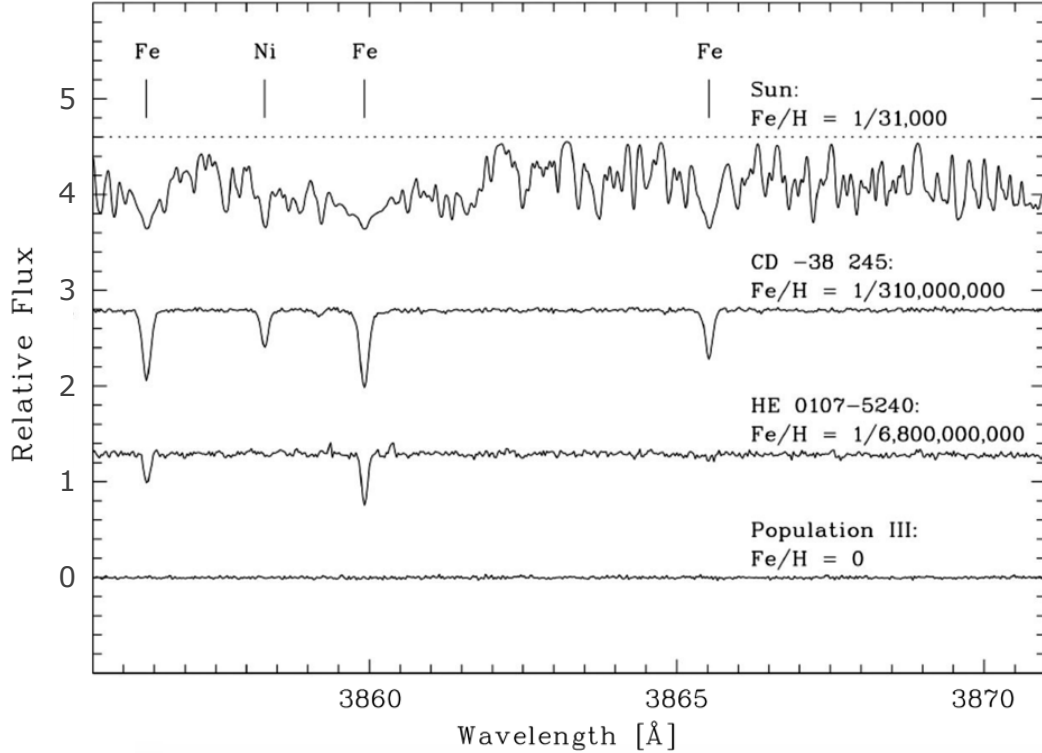


Figure 2.1: Spectrum of stars with different metallicities. The spectra are on the same scale and have been offset arbitrarily in the vertical direction (source: www.eso.org).

Eight stars with $[\text{Fe}/\text{H}] < -4.5$ were observed (listed in the Table 1 of Frebel & Norris 2015). The spectra of the Sun and 3 stars with decreasing $[\text{Fe}/\text{H}]$ ratios are shown in Fig. 2.1. We clearly see the decreasing line strength with decreasing metallicity. We also see that at very low metallicity, the iron line is the (or among the) strongest lines.

Beers & Christlieb (2005) first established a classification of metal-poor stars based on the $[\text{Fe}/\text{H}]$ ratio (Table 2.1). According to this terminology, iron-poor stars are classified as metal-poor stars. Rigorously, this association is correct as long as all the abundances (compared to the Sun) of a given iron-poor star scale down like iron, i.e. if a star having $[\text{Fe}/\text{H}] = -4$ has also $[\text{X}/\text{H}] = -4$ (where X are all metals). For instance, an iron-poor star with $[\text{Fe}/\text{H}] = -4$ and $[\text{X}/\text{H}] = 1$ (where X are all metals except iron) is iron-poor but not metal-poor. It will have a super-solar metallicity. However, observations of iron-poor stars show that, in general, other metals roughly scale down in proportion to iron. Notable exceptions, which are the object of this thesis, nevertheless exist: some iron-poor stars are strongly enhanced in other metals and then their chemical pattern is highly non-solar (cf. Sect. 2.3). But even in such extreme cases, the star very likely stays metal-poor. As an illustrative example, a star with $[\text{X}/\text{H}] = -4$ (X are all metals) has a total metallicity $Z = Z_{\odot}/10^4 \simeq 1.4 \cdot 10^{-6}$. Taking the same star but with $[\text{C}/\text{H}] = 0$ (equivalent to $[\text{C}/\text{Fe}] = +4$) gives $Z = 2.2 \cdot 10^{-3}$, which is ~ 6 times lower than Z_{\odot} . It shows that even if some metals are strongly enhanced in iron-poor stars, one can securely guess that the total metal content of an iron-poor star stays low (except in very rare cases²). This said, it is important to keep in mind that the most iron-poor stars are not necessarily the most metal-poor stars.

²Taking the same star as before but this time with $[\text{C}/\text{H}] = 1$ (equivalent to $[\text{C}/\text{Fe}] = +5$) will have $Z > Z_{\odot}$. Such kind of stars with very little iron but with $Z > Z_{\odot}$ are extremely rare. HE 1045-1434 (Beers et al. 2007) and SDSS J1245-0738 (Bonifacio et al. 2015), with respectively $[\text{Fe}/\text{H}] = 2.55$ and $[\text{C}/\text{Fe}] = 3.2$, and $[\text{Fe}/\text{H}] = -3.21$ and $[\text{C}/\text{Fe}] = 3.45$, may belong to this rare class of stars.

Table 2.1: Nomenclature for stars of different metallicities, as defined in Beers & Christlieb (2005). The last column is the number of Milky Way stars observed below the given $[\text{Fe}/\text{H}]$ ratio (numbers are from the SAGA database). For the MMP class, the recently discovered star J0023+0307, with $[\text{Fe}/\text{H}] < -6.6$ (Aguado et al. 2018), was added since not in SAGA yet.

$[\text{Fe}/\text{H}]$	Term	Acronym	N
< -1	Metal-poor	MP	> 500
< -2	Very Metal-poor	VMP	> 500
< -3	Extremely Metal-poor	EMP	499
< -4	Ultra Metal-poor	UMP	29
< -5	Hyper Metal-poor	HMP	5
< -6	Mega Metal-poor	MMP	2

As a final remark, let us mention that the direct association of the lack of metals with the stellar age is not straightforward. For instance, some metal-poor stars could have formed later in isolated pockets of interstellar material that remained metal-poor. Also, some more metal-rich stars could have formed early if the star formation rate (hence steepness of age-metallicity relation) was very high. Nevertheless, it is worth noting that the age of some very metal-poor stars was determined owing to the detection of radioactive elements like Th and U at their surface. ^{238}U and ^{232}Th have half lives of about 4.5 and 14 Gyr respectively. Assuming that Th and U were synthesized before the birth of the metal-poor star and supposing that the initial abundances of Th and U are known, one can compare the initial abundances of Th and U to the observed abundances to estimate the age of the star. Ages of about 13 – 14 Gyr were derived for several metal-poor stars with $[\text{Fe}/\text{H}] \sim -3$ (Hill et al. 2002; Sneden et al. 2003; Frebel et al. 2007a). It gives some support to the fundamental hypothesis of stellar archaeology stating that very metal-poor stars are very old stars. The uncertainties related to this dating method are however large (several Gyr). It is mainly because our understanding of the nuclear processes responsible for the formation of Th is still incomplete (especially the uncertainties in the nuclear data and unknown thermodynamic conditions in which the nuclear processes, able to form Th, take place, Goriely & Clerbaux 1999).

2.2 Observation and abundances of metal-poor stars

Metal-poor stars are very rare objects: in the solar neighborhood, only $\sim 1/10^5$ field star would have $[\text{Fe}/\text{H}] < -3.5$ (Frebel & Norris 2015, see also Table 2.1). How and where to find them in the Milky Way which contains billion of stars? As schematically shown in Fig. 2.2, our Galaxy contains four main components: a thick disk, a thin disk, a bulge and a spheroidal halo. The disk is about 30 kpc. Carollo et al. (2007) have shown that the halo can be divided into two broadly overlapping structural components: the inner (radius $\lesssim 15$ kpc) and outer halo (radius $\gtrsim 15$ kpc). These two components have different spatial density profiles, stellar orbits and stellar metallicities. The metallicity of the inner and outer halo peaks at $[\text{Fe}/\text{H}] \simeq -1.6$ and -2.2 , respectively. Surveys carried out over the past decades have shown that the most metal-poor stars are found in the halo of the Milky Way. It is reviewed below the observational steps required to efficiently spot the good metal-poor candidates among the field stars.

2.2.1 The observational steps

The process of getting the surface chemical composition of metal-poor stars is long. As discussed in the review of Beers & Christlieb (2005), there are 3 main observational steps to obtain accurate abundances of metal-poor stars:

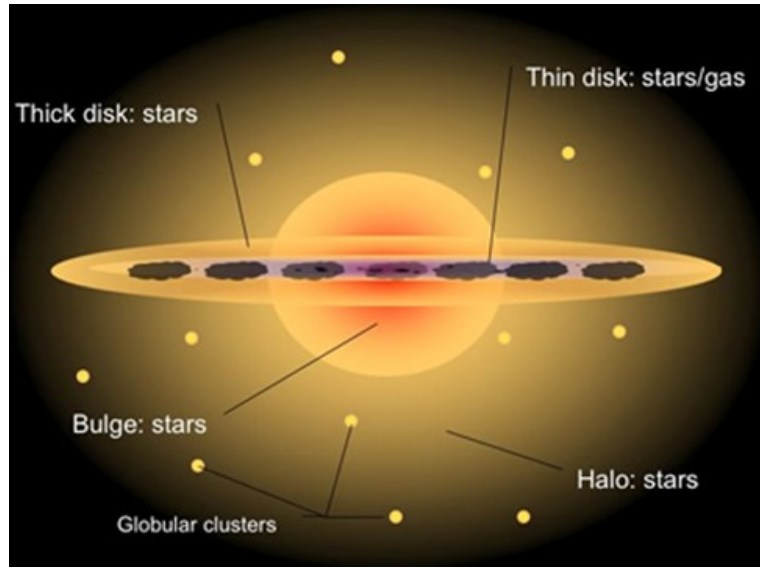


Figure 2.2: Schematic view of the architecture of the Galaxy (source : <http://www.cefns.nau.edu>).

- Step 1 : a wide-angle survey in order to select the metal-poor candidates.
- Step 2 : a moderate-resolution spectroscopic follow-up of the candidates to validate their lack of metals.
- Step 3 : a high-resolution spectroscopy of the most interesting candidates to accurately determine the abundances.

Typical spectra obtained from each of these three steps are shown in Fig. 2.3. The star is HE 1327-2326 (Frebel et al. 2005a,b, 2006a,b, 2008; Aoki et al. 2006), having $[\text{Fe}/\text{H}] = -5.6$. From step 1 to 3, the resolution $R = \lambda/\Delta\lambda$ increases from 400 to 60000. The high resolution spectroscopy (step 3) was performed with the High Dispersion Spectrograph (Noguchi et al. 2002) on the 8.2-meter optical-infrared SUBARU telescope in Hawaii. Below I give some details on these three observational steps.

Step 1 : wide-angle surveys

The first step, finding metal-poor candidates, can be achieved in different ways.

Proper-motion surveys A significant fraction of halo stars has high proper motion³ compared to Galactic disk stars. It arises because halo stars have elliptical orbits that are not in the Galactic plane (i.e. very different orbits than disk stars like the Sun) and because halo stars have typically larger space velocities than disk stars. This last point implies that a halo star will likely have a higher proper motion than a disc star at the same distance. Schwarzschild & Schwarzschild (1950) and Roman (1950) first suggested a possible correlation between the space velocity of stars and the weakness of their lines (attributed to the lack of metals in their atmosphere). These pioneering works motivated further studies that confirmed the connection between the kinematics of stars and their abundances: metal-poor stars are preferentially found among the stars with a high space velocity. For instance, the first star having $[\text{Fe}/\text{H}] < -3.0$ (G64-12) was discovered by Carney & Peterson (1981) as the result of its high space velocity. Ryan & Norris (1991) carried out a large

³The proper-motion of a star corresponds to its apparent angular motion across the sky with respect to more distant stars.

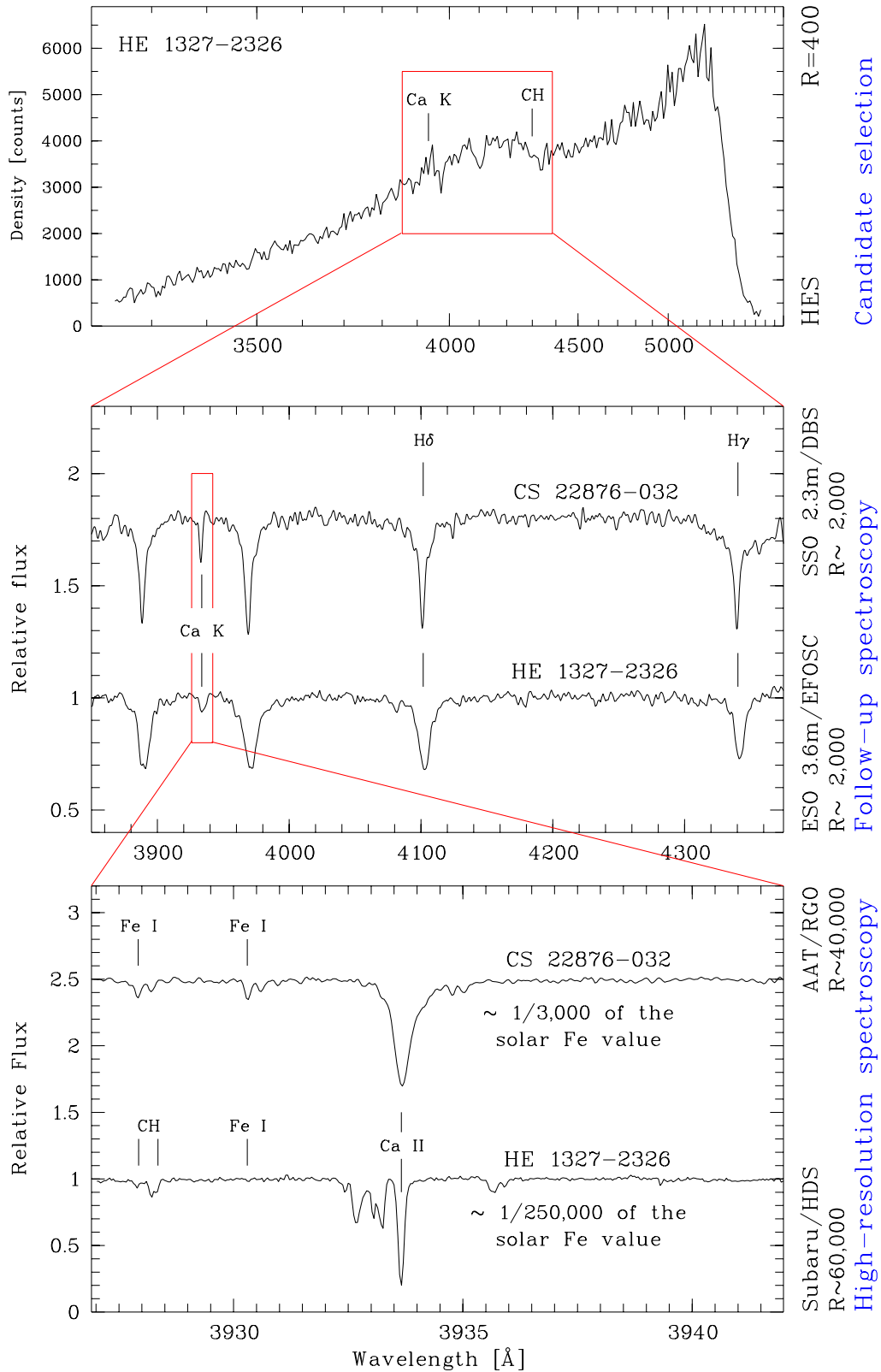


Figure 2.3: Spectrum of the metal-poor star HE 1327-2326 with $[\text{Fe}/\text{H}] = -5.6$, from low to high resolution. It shows the three steps required to obtain accurate abundances. CS 22876-032, with $[\text{Fe}/\text{H}] = -3.7$ (Norris et al. 2000) is shown for comparison (figure from Frebel et al. 2005a).

spectroscopic follow-up of a sample of stars with high proper-motion. About 10 % of the sample was found to have $[\text{Fe}/\text{H}] < -2.0$.

Among the first surveys measuring proper motion, which were based on photographic plates, one finds the Lick Northern Proper Motion survey (Klemola et al. 1987), the Southern Proper Motion survey (Girard et al. 1998) or the SuperCOSMOS Sky Survey (Hambly et al. 2001). More recent surveys are the Sloan Digital Sky Survey (SDSS, York et al. 2000, both photometry and spectroscopy) or the Gaia mission (e.g Perryman et al. 2001).

Colorimetric surveys The metals (particularly Fe) in the atmospheres of stars absorb preferentially the blue light so that metal-rich stars appear redder while metal-poor stars appear bluer. The color of a star and more specifically the ultraviolet excess $\delta(U - B)$ can be used as a metallicity indicator (e.g. the early works of Wallerstein & Carlson 1960; Wildey et al. 1962).

The SkyMapper Southern Sky Survey (SMSS, Keller et al. 2007) is a photometric program of the Southern Hemisphere started in 2008 and giving accurate estimates of atmospheric parameters of metal-poor stars (effective temperature, surface gravity and stellar metallicity). This survey led to the discovery of the most metal-poor star currently known: SM 0313-6708 with $[\text{Fe}/\text{H}] < -7.3$ (Keller et al. 2014).

The Pristine survey (Starkenburger et al. 2017) is a photometric survey using a narrow filter with a width of $\sim 100 \text{ \AA}$ that covers the wavelengths of the Ca doublet lines (at 3968.5 and 3933.7 \AA). A spectroscopic follow-up of promising metal-poor candidates selected by the Pristine survey has led to the discovery of numerous metal-poor stars with $[\text{Fe}/\text{H}] < -3$ (Youakim et al. 2017).

Objective-prism surveys Such surveys are wide-angle spectroscopic surveys with low-resolution ($R \simeq 400$). The idea is generally to examine the strength of the CaII K line so as to obtain a first estimate of the metal content of the star. Bond (1970) and Bidelman & MacConnell (1973) first carried out such surveys, aiming at identifying metal-poor stars based on spectroscopy only. The HK survey (Beers et al. 1985, 1992) and the Hamburg/ESO (HES) survey (Wisotzki et al. 1996) are other surveys of this type, that were prolific sources of metal-poor stars.

After a spectroscopic follow-up of metal-poor candidates selected from the HK survey, it appeared that 11 % of the candidates had $[\text{Fe}/\text{H}] < -2.0$ (Beers & Christlieb 2005). A drawback regarding the HK survey is that metal-deficient cool stars would likely be missed. Indeed, such stars have enhanced strengths of their Ca II K lines because of the lower temperature and therefore are considered as metal-rich stars. The HK-II survey (Rhee 2001) aimed at identifying the metal-poor red giant cool stars that may have been missed in the original analysis due to the temperature bias against cool stars. It allowed to raise the efficiency of the HK survey to detect metal-poor stars from 11 to 32 %.

The HES survey can observe fainter objects than the HK survey (about 2 magnitude deeper). Because of the broad wavelength range covered ($3200 < \lambda < 5200$ against $3875 < \lambda < 4025$ for the HK survey), the $U - V$ color of stars can be directly obtained from the spectra and combined to the spectroscopy to select metal-poor candidates with more security. A spectrum obtained from the HES survey is shown on the upper panel of Fig. 2.3. Spectroscopic follow-up of metal-poor candidates selected from the HES survey have shown that 50 – 60 % of the candidates have $[\text{Fe}/\text{H}] < -2.0$.

Step 2 : moderate-resolution spectroscopy

After step 1, a moderate-resolution spectroscopic follow-up of the candidates is required to validate the metal-poor stars among the sample. It also exists surveys targeting hundredth thousands of stars with a moderate-resolution and thus allowing to skip the step 1.

The SDSS survey do both photometry and medium resolution spectroscopy ($R \sim 2000$). SDSS has gone through 3 stages: SDSS-I (from 2000 to 2005), SDSS-II (from 2005 to 2008) and SDSS-III (from 2008 to 2014, Eisenstein et al. 2011). SDSS includes several individual surveys, among them the Sloan Extension for Galactic Understanding and Exploration (SEGUE) survey (Yanny et al. 2009). The two phases of SEGUE, SEGUE-1 and -2, obtained spectra for 240000 and 118151 stars, respectively, with typical errors in T_{eff} , $[\text{Fe}/\text{H}]$ and $\log g$ of 117 K, 0.22 and 0.26 dex, respectively. SDSS/SEGUE surveys were prolific sources of metal-poor stars (e.g. Fukugita et al. 1996; Adelman-McCarthy et al. 2008; Abazajian et al. 2009) and motivated numerous high-resolution observations (e.g. Aoki et al. 2013, where 137 metal-poor SDSS candidates were observed with the high dispersion spectrograph of the Subaru telescope.).

The Large Sky Area Multi-Object Fiber Spectroscopic Telescope (LAMOST) survey (Deng et al. 2012) started in 2008. It should provide spectra for 2.5 million stars. The resolution is about $R = 1800$. This survey also triggered high-resolution observations. Li et al. (2015) reported $R = 36000$ spectra for two stars with $[\text{Fe}/\text{H}] \sim -4$, selected in the LAMOST database.

From 2003 to 2013, the RADial Velocity Experiment (RAVE, Steinmetz 2003) targeted bright stars ($8 < m < 12$, it represents stellar distances up to ~ 3 kpc from the Sun). This survey delivered spectra for about 480000 stars with a resolution $R = 7000$. In a RAVE database of approximately 200000 stars belonging to the Galactic disk or halo, Fulbright et al. (2010) identified 631 stars with $[\text{Fe}/\text{H}] < -2$ ($\sim 0.3\%$). In the Galactic bulge, the ARGOS survey (Abundances and Radial velocity Galactic Origins Survey) revealed 16 stars with $[\text{Fe}/\text{H}] < -2$ within a sample of 14150 stars ($\sim 0.1\%$, Ness et al. 2013). In the frame of the EMBLA (Extremely Metal-poor BuLge stars with AAOmega) survey, Howes et al. (2014, 2015, 2016) reported the discovery of about 30 other bulge stars with $[\text{Fe}/\text{H}] < -2$ (among them a star with $[\text{Fe}/\text{H}] = -3.94 \pm 0.16$). No star with $[\text{Fe}/\text{H}] < -4$ was found in the bulge.

Step 3 : high-resolution spectroscopy

Once the promising candidates are identified, the next step consists in obtaining high-resolution ($R \geq 30000$), high S/N (signal-to-noise) spectra.

Numerous studies conducted high-resolution spectroscopic observations on metal-poor star candidates, originally selected from the HE, HK, SDSS or SEGUE surveys (e.g. McWilliam et al. 1995; Carretta et al. 2002; Cohen et al. 2004, 2008, 2013; Barklem et al. 2005; Aoki et al. 2007, 2013; Hollek et al. 2011; Caffau et al. 2011; Bonifacio et al. 2012; Norris et al. 2013; Yong et al. 2013; Roederer et al. 2014b; Hansen et al. 2014). There are at least three public database, grouping the abundances of metal-poor stars derived from high-resolution spectra:

- The SAGA database⁴ (Suda et al. 2008).
- The Frebel (2010) database⁵.
- The JINAbase⁶ (Abohalima & Frebel 2017).

Among the future high resolution surveys one finds 4MOST (e.g. Feltzing et al. 2017), WEAVE, a spectrograph that will offer two possible resolutions: 5000 and 20000 or GALAH (Galactic Archaeology with the HERMES spectrograph Martell 2016) which aims at collecting $R \sim 28000$ spectra for one million stars in the Milky Way.

⁴<http://sagadatabase.jp>.

⁵<http://www.metalpoorstars.com>.

⁶<http://jinabase.pythonanywhere.com>.

2.2.2 Abundances and uncertainties

Once a high-resolution spectrum is acquired from a star, the abundances in term of numbers have to be determined (e.g. $[X/Fe]$ ratios). This is a highly nontrivial task that required a realistic stellar atmosphere model. Stellar abundances are therefore not *observed* but deduced by *modeling* the spectral lines. The stellar abundances are generally determined by inspection of the equivalent width of spectral absorption lines. The observational uncertainty varies as $\sqrt{\text{FWHM}} / (S/N)$ where FWHM is the full width at half maximum of the line. A spectrograph with a high resolving power and a high S/N minimizes the uncertainties, allowing the detection of weaker features, which is primordial when observing stars with little metals, hence with weak lines.

A perfect atmosphere model would be a 3D model taking into account departures from local thermodynamic equilibrium (LTE) and where all the atomic and molecular physics (determining the absorption lines) is included. Such a model does not exist. Often, abundances are derived using a 1D LTE model.

Frebel et al. (2008), have estimated by how much the abundances are affected when deriving the abundances with either a 1D or a 3D model. They investigated the star HE 1327-2326 ($[Fe/H] = -5.7$). They found a 3D-1D correction for C, N and O of about -0.7 dex.

Ezzeddine et al. (2017) studied anew the stellar parameters of 20 stars with $[Fe/H] < -4$ using a 1D NLTE (non LTE) atmosphere model instead of a 1D LTE model. They derived $[Fe/H]$ corrections up to 1 dex compared to the 1D LTE case. These corrections are larger at lower $[Fe/H]$: at $[Fe/H] = -4$ and -7 , the corrections are about 0.5 and 1 dex respectively. Lind et al. (2012) reported a similar trend: they derived NLTE corrections of $\lesssim 0.1$ and $\lesssim 0.5$ dex at solar and low metallicity, respectively. Also, these corrections apply only for the derivation of Fe abundances from neutral lines (Fe I). The corrections are mostly insignificant if using Fe II lines. Determining the Fe abundance with accuracy is important since it is generally a prerequisite for the determination of the abundance of other elements.

2.3 CEMP stars as peculiar metal-poor stars

This section aims at describing the characteristics of CEMP stars. Their possible origin is discussed in the next section.

A natural guess could be that in metal-poor stars, all metals are scaled down compared to the Sun by roughly the same factor. However, observations progressively revealed that metal-poor stars generally have non-solar-like abundance patterns. In particular, the carbon to iron ratio is super-solar in many metal-poor stars. The first carbon stars were observed about 150 years ago by Angelo Secchi (Secchi 1868). At that time, he only reported a peculiar banding in the stellar spectra. These stars were later identified by Rufus (1916) as stars enriched in carbon. Since, many carbon-rich stars were discovered, particularly among the most iron-poor stars. Stars enriched in carbon and depleted in iron were called Carbon-Enhanced Metal-Poor (CEMP, Beers & Christlieb 2005). This name might seem somewhat contradictory since carbon is a metal. However, CEMP stars likely stay metal-poor compared to the Sun, even if they show overabundances in carbon or other metals (cf. discussion in Sect. 2.1). Beers & Christlieb (2005) proposed two criteria defining a CEMP star: $[Fe/H] < -1.0$ and $[C/Fe] > 1.0$. The criterium of $[C/Fe] > 0.7$ is also often used in the literature (first proposed by Aoki et al. 2007). For what follows, depending on the criterium used by the considered author, I use the names

- CEMP_{1.0} if the condition is $[C/Fe] > 1.0$.
- CEMP_{0.7} if the condition is $[C/Fe] > 0.7$.

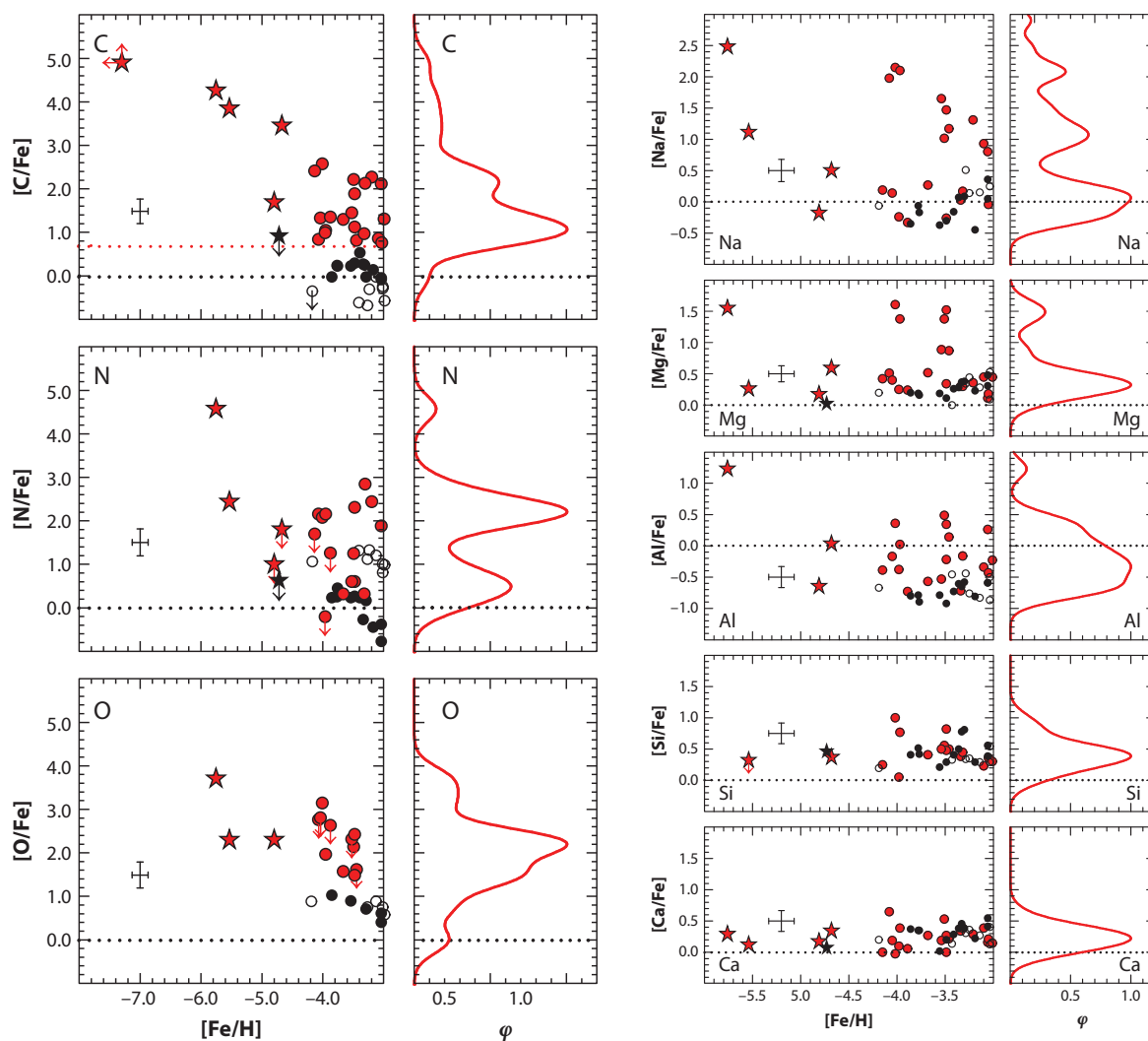


Figure 2.4: $[X/Fe]$ ratios of the most iron-poor stars. Red symbols show C-rich stars (CEMP-s, CEMP-r, and CEMP-r/s stars are excluded). Black symbols show C-normal stars. Stars show objects with $[Fe/H] < -4.5$. Histograms of the abundances are shown on the right. (figure adapted from Frebel & Norris 2015).

Are CEMP stars enriched in other elements?

CEMP stars have various lithium abundances, from⁷ $A(\text{Li}) \simeq 2$ (i.e. close to the Spite plateau of 2.05 ± 0.16 , Spite & Spite 1982) to $A(\text{Li}) < 0.62$ for HE 1327-2326 with $[Fe/H] = -5.7$ (Frebel et al. 2008). Some observational works have suggested a melt-down of the Spite plateau below $[Fe/H] \simeq -3$ (Aoki et al. 2009; Sbordone et al. 2010; Bonifacio et al. 2012). The melt-down has nevertheless to be further confirmed since some iron-poor stars could have experienced severe surface Li depletion episodes (especially those who are giants). Korn et al. (2009) have computed models of the star HE 1327-2326 including the effects of atomic diffusion. They predict a maximal Li depletion of 1.2 dex from the birth of the star to the present day. It gives a maximal initial Li abundance of about 1.8, which is much closer to the Spite plateau. Other scenarios in the same work predict a milder Li depletion, of the order of 0.2 dex, which would give an initial Li well below the Spite plateau. In any case, these initial Li abundances are not compatible with the WMAP-based primordial Li

⁷ $A(X) = \log \epsilon(X) = \log(N_X/N_H) + 12$, where X represents a given element.

Table 2.2: Classification of CEMP stars, as defined in Beers & Christlieb (2005).

Term	Conditions
CEMP	$[C/Fe] > 1.0$
CEMP-r	$[C/Fe] > 1.0$ $[Eu/Fe] > 1.0$
CEMP-s	$[C/Fe] > 1.0$ $[Ba/Fe] > 1.0$ $[Ba/Eu] > 0.5$
CEMP-r/s	$[C/Fe] > 1.0$ $0.0 < [Ba/Eu] < 0.5$
CEMP-no	$[C/Fe] > 1.0$ $[Ba/Fe] < 0$

abundance of 2.63 predicted from primordial nucleosynthesis (Spergel et al. 2007).

Many CEMP stars have high N/Fe, O/Fe, Na/Fe or Mg/Fe ratios. For stars with $[Fe/H] < -3$, the scatter of the $[X/Fe]$ ratios globally decreases from $X = C$ to Ca (Frebel & Norris 2015). For instance, the $[C/Fe]$, $[O/Fe]$, $[Na/Fe]$, $[Mg/Fe]$ and $[Ca/Fe]$ ratios span about 5, 4, 2.5, 1.5 and 0.5 dex, respectively (see Fig. 2.4).

A significant amount of CEMP stars are also enriched in elements heavier than iron. These elements are thought to be mostly synthesized through the slow and rapid neutron capture processes (also the intermediate process or i-process, see Sect. 2.5). Aoki et al. (2000) and Van Eck et al. (2001) discovered the first VMP stars enriched in Pb. Many other CEMP stars enriched in s- and/or r-elements were discovered, down to $[Fe/H] \sim -3$ (Burriss et al. 2000; Simmerer et al. 2004; Sivarani et al. 2004; Lai et al. 2007; Placco et al. 2013). Below this threshold, enhancements in s- and r- elements are generally very modest (see Fig. 2.5).

Beers & Christlieb (2005) established a classification of CEMP stars based on their heavy element abundances (see Table 2.2). One finds CEMP stars enriched in s-elements (CEMP-s), r-elements (CEMP-r), both r- and s-elements (CEMP-r/s) and without significant enhancement in s-/r-elements (CEMP-no). As they note, this classification should be viewed as a first approximation and used as a guideline for the future. Indeed, the location of the class boundaries are somewhat arbitrary and in some cases, it may exist a continuity between the classes rather than very distinct groups. Eu and Ba were chosen to define such classes because (1) they are generally readily measurable in a stellar spectrum and (2) they are expected to be produced in a different amount by the s- and r-process (Eu: mainly r-process, Ba: mainly s-process). It has been shown (especially Yoon et al. 2016) that CEMP-no stars are generally found on the *low carbon band* with $A(C) \leq 7.1$ and CEMP-s/rs on the *high carbon band* with $A(C) > 7.1$. It might be linked to the different formation channel for CEMP-no and CEMP-s/rs stars (Sect. 2.5). Interestingly, this separation into 2 bands, allows (with some level of confidence) to classify CEMP stars only based on their C abundance rather than on e.g. Ba, whose abundance determination requires much higher resolution spectra. Fig. 2.5 shows that CEMP-s stars mainly lie at $[Fe/H] > -3$ (green symbols). CEMP-no stars (blue symbols) are generally found at lower $[Fe/H]$. Some CEMP stars (magenta symbols) are still unclassified, according to the criteria of Table 2.2.

Are CEMP stars frequent?

Carbon et al. (1987) and Norris et al. (1997) first emitted the possibility of a higher frequency of C-rich stars with decreasing $[Fe/H]$. Marsteller et al. (2005) reported a possibly high fraction of about 50 % of CEMP_{1.0} stars⁸ among $[Fe/H] < -2$ stars selected in the HES survey. However, Cohen et al. (2005) showed that the $[Fe/H]$ ratio of some stars in the HES survey was overestimated by ~ 0.5 dex. Consequently, they derived a CEMP_{1.0} fraction of 14 ± 4 % (instead of 50 %) among the stars with $[Fe/H] < -2$. In 240 stars with $[Fe/H] \leq -2$, Lucatello et al. (2006) found a CEMP_{1.0} fraction of 21 ± 2 %. Lee et al. (2013) considered a sample from SDSS/SEGUE of about 247000 stars

⁸I remind here that CEMP_{1.0} means that the author used the condition $[C/Fe] > 1$ for a star to be CEMP. CEMP_{0.7} means that the author used the condition $[C/Fe] > 0.7$.

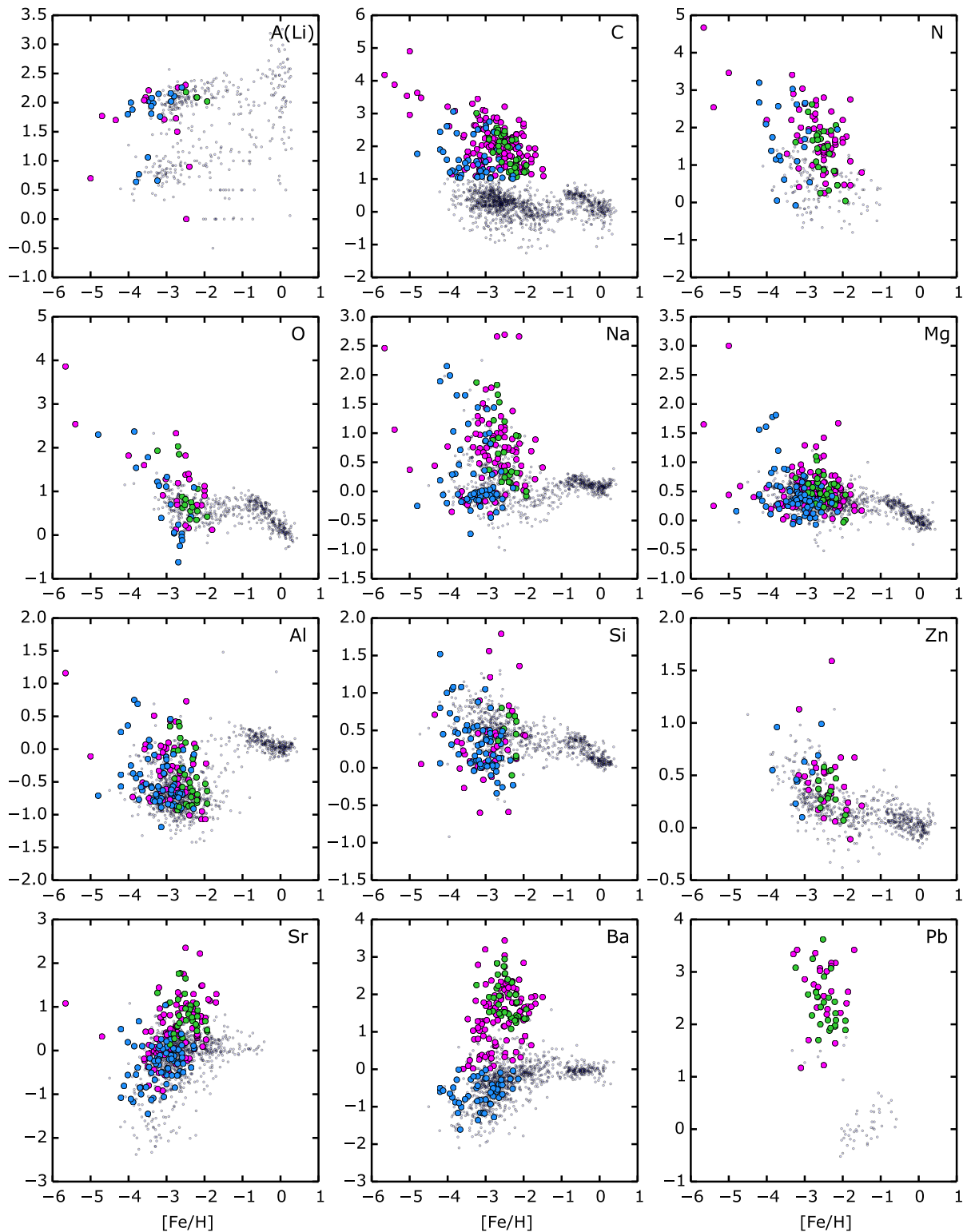


Figure 2.5: $A(\text{Li})$ (upper left) and $[X/\text{Fe}]$ as a function of $[\text{Fe}/\text{H}]$. Green symbols are CEMP-s, blue are CEMP-no, according to criteria of Table 2.2. Magenta symbols are unclassified CEMP because of missing abundances (Ba, Eu). Light grey dots show carbon normal stars. Abundances with upper limits are not plotted. The typical uncertainty is ± 0.3 dex. When abundances from different authors are available for one star, the most recent one is selected. The abundance data is taken from the SAGA database (Suda et al. 2008, last update on Sept. 2017).

and found that 12 % of $[\text{Fe}/\text{H}] < -2$ stars are CEMP_{0.7}.

One of the possible bias to these frequencies is that in giant stars, the first dredge-up has occurred. Amongst other, it changes the surface carbon abundance (cf. Sect. 2.4). For a sample of 505 stars with $[\text{Fe}/\text{H}] < -2$, Placco et al. (2014c) have estimated the effect of the first dredge-up on the surface carbon abundance. The recognized CEMP stars enriched in s- and/or r-elements were excluded from their analysis⁹. The stellar models they used predict that the correction on the $[\text{C}/\text{Fe}]$ ratio induced by the first dredge-up is generally about 0.5 dex for the evolved stars. They recovered the initial $[\text{C}/\text{Fe}]$ ratio of the 505 stars of their sample (the initial ratio is higher in case the star has experienced the first dredge-up). They finally found that 20, 43 and 81 % of stars with $[\text{Fe}/\text{H}] < -2$, < -3 and -4 are CEMP_{0.7}, respectively. The first dredge-up effect corrected, it likely gives the fraction of stars which were born as CEMP_{0.7}.

There is also a spatial variation of the CEMP frequency: Carollo et al. (2012) have shown that the CEMP_{0.7} frequency is increasing with the distance to the Galactic plane. Almost all CEMP_{0.7} stars belong to the halo and the fraction is higher in the outer than in the inner halo. Considering the most distant stars (more than 9 kpc from the Galactic plane, i.e. mainly in the outer halo), they derived a CEMP_{0.7} frequency of 20 %. Carollo et al. (2014) reported a fraction of CEMP-no stars of 43 and 70 % in the inner and outer halo respectively. For the CEMP-s stars, they found 57 and 30 % in the inner and outer halo respectively. It suggests that the dominant source of CEMP stars in the two halo components were different. A recent study suggested that the CEMP fraction (among the $[\text{Fe}/\text{H}] < -3$ stars and after excluding the likely CEMP-s and -r/s stars) in the Sculptor dwarf galaxy is $\sim 36 \pm 8$ % (Chiti et al. 2018), i.e. similar to the ~ 43 % of the Galactic halo (Placco et al. 2014c).

Are CEMP stars in binary systems?

Lucatello et al. (2005) and Starckenburg et al. (2014) showed that the whole sample of CEMP-s stars is consistent with the hypothesis of them all existing in binary systems. A careful monitoring of the radial velocity of 22 CEMP-s stars over several years has revealed a clear orbital motion for 18 stars (~ 82 %) while 4 stars appeared to be single (Hansen et al. 2016b). The probability of finding one face-on system in their sample is about 0.01 %, meaning that it is extremely unlikely that all the four apparently single CEMP-s stars are in fact binary systems that were seen face-on. Apparently single stars might nevertheless have a companion with a long orbital period (about $10^3 - 10^4$ days at minimum), which would prevent to detect radial motions of the CEMP-s stars. A similar study was carried out for CEMP-r and CEMP-no stars. The binary frequency was found to be 18 ± 6 % for CEMP-r (Hansen et al. 2015b) and 17 ± 9 % for CEMP-no stars (Hansen et al. 2016a), i.e. much lower than for CEMP-s stars. It suggests that the CEMP-r and CEMP-no stars are likely disconnected from a binary origin.

2.4 Internal mixing processes in CEMP stars

CEMP stars formed with the material ejected by previous stars (at least some of it). One may see the nucleosynthetic signature from these previous stellar generations in the CEMP star surface chemical composition. However, the CEMP star surface composition can be altered during the life of the CEMP star itself. If this alteration is important enough, it could erase the chemical imprint let by the previous star(s). Two different categories of processes can affect the surface abundances of CEMP stars: external and internal processes.

- External processes can be accretion of interstellar material or accretion of material from a binary companion. While accretion of interstellar material was found to not have a signif-

⁹Note that this does not mean that all stars they consider are CEMP-no. Some CEMP stars in the sample without a determined Ba abundance might appear to be CEMP-s, -r/s or -r in the future.

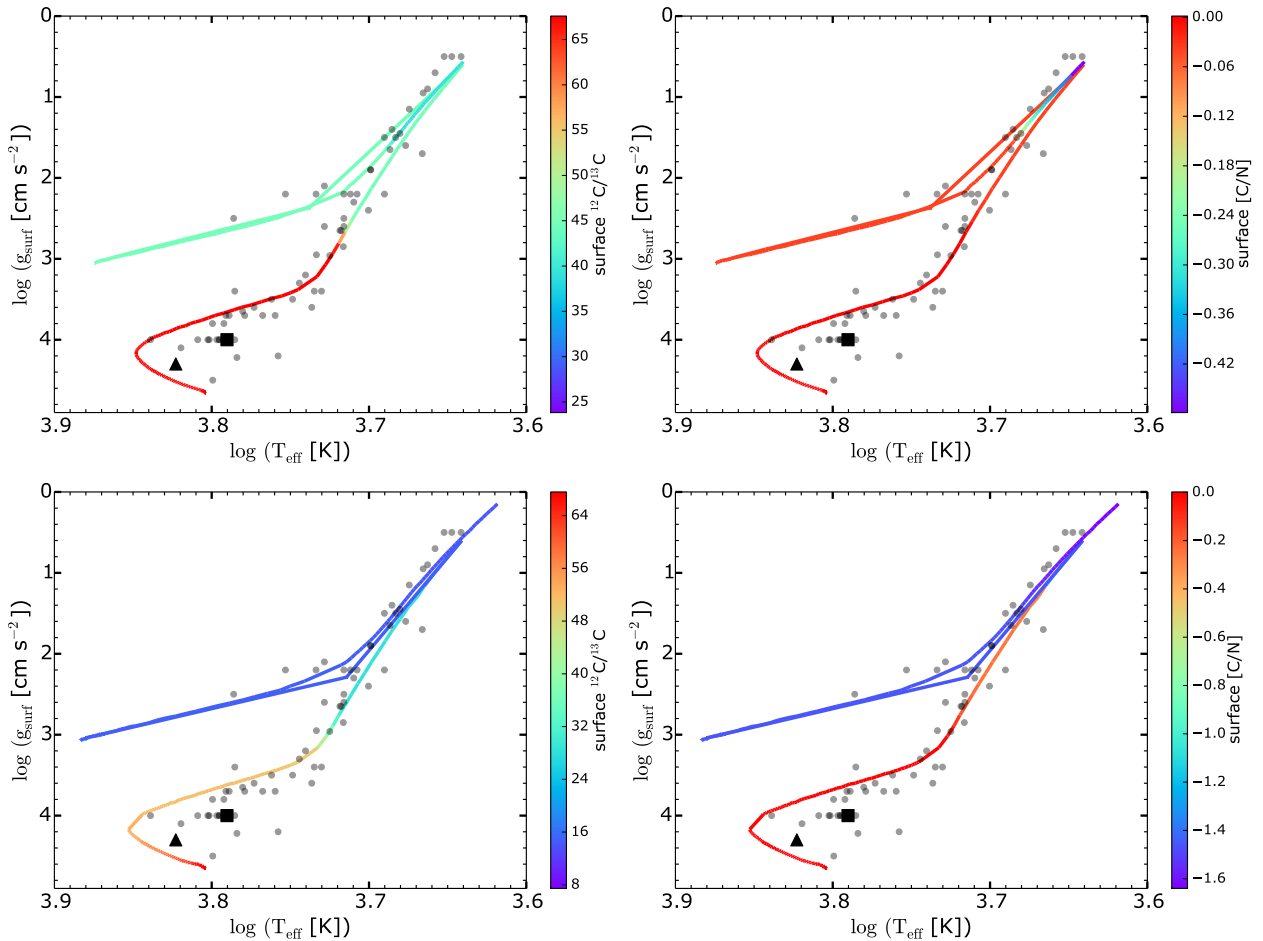


Figure 2.6: Evolutionary tracks of $0.85 M_{\odot}$ models at $Z = 0.0001$ without thermohaline and without rotation (top panels), with thermohaline and with rotation (bottom panels, models from Lagarde et al. 2012). The color shows the surface $^{12}\text{C}/^{13}\text{C}$ (left panels) and $[\text{C}/\text{N}]$ ratios (right panels). Symbols show CEMP stars with $[\text{C}/\text{Fe}] > 1$ and $[\text{Fe}/\text{H}] < -3$ (recognized CEMP-s, -r and -r/s are not plotted). The triangle shows HE 1029-0546 with $^{12}\text{C}/^{13}\text{C} = 9$ and $[\text{C}/\text{N}] = -0.26$. The square shows CS 29528-041 with $[\text{C}/\text{N}] = -1.47$ ($^{12}\text{C}/^{13}\text{C}$ is unknown).

icant effect on metal-poor stars (Frebel et al. 2009; Johnson & Khochfar 2011), the accretion of material ejected by a companion is certainly an important process, especially for CEMP-s stars (cf. Sect. 2.5.1).

- Internal processes happen in the CEMP star itself. There are for instance the first dredge-up or thermohaline mixing.

Below it is discussed the main (known) internal mixing processes that can happen in CEMP stars and possibly alter their surface composition. A sample of CEMP stars is considered and compared with low-mass stellar models. The sample comprises the CEMP stars with $[\text{C}/\text{Fe}] > 1$ and $[\text{Fe}/\text{H}] < -3$. The CEMP stars enriched in s- and/or r-elements are excluded¹⁰.

The first dredge-up. Stellar models predict that as a low-mass star runs out of hydrogen, its envelope expands, the surface temperature decreases, making the star evolving to the red giant

¹⁰This likely excludes most of the CEMP stars whose surface abundances were modified because of the accretion of material from a companion (especially the CEMP-s stars, see Sect. 2.5.1).

branch (RGB). During that stage, the outer convective envelope expands inward and penetrates hotter regions, where the CN-cycle is active. Some CN-processed material is consequently brought to the surface and alters the star's surface light element abundances. This mixing episode is called the first dredge-up (Iben 1964). Since the CN-cycle mainly transforms ^{12}C into ^{14}N and to a lesser extent into ^{13}C , the effect of the first dredge-up is to decrease the surface C/N and $^{12}\text{C}/^{13}\text{C}$ ratios. Charbonnel (1994) has shown that if starting with $^{12}\text{C}/^{13}\text{C} \simeq 65$ and $^{12}\text{C}/^{14}\text{N} \simeq 3.7$ (equivalent to $[\text{C}/\text{N} = 0]$) in a $1 M_{\odot}$ model at $Z = 10^{-3}$, the first dredge-up decreases $^{12}\text{C}/^{13}\text{C}$ and $^{12}\text{C}/^{14}\text{N}$ to about 25 and 2 (equivalent to $[\text{C}/\text{N}] \sim -0.3$) respectively. In the top panels of Fig. 2.6 the surface $^{12}\text{C}/^{13}\text{C}$ and $[\text{C}/\text{N}]$ ratios along the evolution of a standard low metallicity $0.85 M_{\odot}$ model are shown. The first dredge-up occurs at $\log(T_{\text{eff}}) \sim 3.7$ and $\log g \sim 3$ and decreases the surface $^{12}\text{C}/^{13}\text{C}$ from about 70 to 45. The $[\text{C}/\text{N}]$ ratio is barely affected by the first dredge-up (top right panel). Dredge-up events generally cannot explain CEMP stars since (1) they tend to deplete the carbon while we look for the opposite and (2) some CEMP stars are still unevolved (Fig. 2.6) meaning that they did not experienced any dredge-up episode. Quantifying this process for each CEMP star is nevertheless important in order to correct the surface abundances of evolved stars and recover their initial surface abundances, that reflect more directly the abundances in their natal cloud. This was done in Placco et al. (2014c) for the carbon abundance. Their CEMP stellar models suggest that the first dredge-up correction on the surface C abundance is about 0.5 dex (0.8 dex in the most extreme case).

Thermohaline mixing and rotation. Thermohaline mixing occurs after the first dredge-up so that unevolved CEMP stars are not affected by this process (provided they do not accrete heavy material from a companion, cf. Sect. 2.5.1). Thermohaline mixing can occur in giant stars because of an inversion of the molecular weight around the top of the H-burning shell, just below the convective envelope. The negative ∇_{μ} (μ , the mean molecular weight, is growing outward) results in a mixing event, following the first dredge-up, and decreasing again the C/N and $^{12}\text{C}/^{13}\text{C}$ ratios (e.g. Charbonnel & Zahn 2007; Eggleton et al. 2008). Rotation transports the H-burning products outwards. It likely adds another mechanism to decrease the surface C/N and $^{12}\text{C}/^{13}\text{C}$ ratios. The bottom panels of Fig. 2.6 show the surface $^{12}\text{C}/^{13}\text{C}$ and $[\text{C}/\text{N}]$ ratios during the evolution of a low metallicity $0.85 M_{\odot}$ model including thermohaline mixing and rotation. In this case, the surface ratios are significantly reduced, particularly near the end of the evolution, where $^{12}\text{C}/^{13}\text{C} \sim 8$ and $[\text{C}/\text{N}] \sim -1.6$. According to these models, some of the evolved CEMP stars shown in Fig. 2.6 may have experienced an important modification of their surface C and N abundances (cf. also the work of Stancliffe et al. 2009). Among the unevolved CEMP stars, some have low $^{12}\text{C}/^{13}\text{C}$ ratios, like HE 1029-0546 with $^{12}\text{C}/^{13}\text{C} = 9$ (triangle in Fig. 2.6, Hansen et al. 2015a). Some other unevolved stars have low $[\text{C}/\text{N}]$ ratios like CS 29528-041 with $[\text{C}/\text{N}] = -1.47$ (square in Fig. 2.6, Sivarani et al. 2006). These low ratios likely cannot be explained by internal processes. Such ratios probably reflect some processes at work in external sources (e.g. previous massive stars).

Atomic diffusion. Such a process has the effect of separating the elements. It groups together the effects of gravitational settling, thermal diffusion and radiative acceleration (Michaud et al. 2015). Richard et al. (2002) predicted that atomic diffusion can alter the surface composition of metal-poor stars by $\sim 0.1 - 1$ dex. It depends on the chemical species considered, effective temperature and the evolutionary stage. For C, O, Na, Mg, Al and Si, the alteration does not exceed 0.5 dex, except in some hot models ($T_{\text{eff}} \gtrsim 6300$ K). Richard et al. (2002) have also shown that the impact of atomic diffusion becomes very small (about ~ 0.1 dex) if including an additional turbulence effect that is required to account for the chemical anomalies of some stars (the AmFm stars, Richer et al. 2000).

Overall, although internal processes in CEMP stars can modify their surface abundances, these processes likely cannot account for the unevolved or relatively unevolved CEMP stars. For the

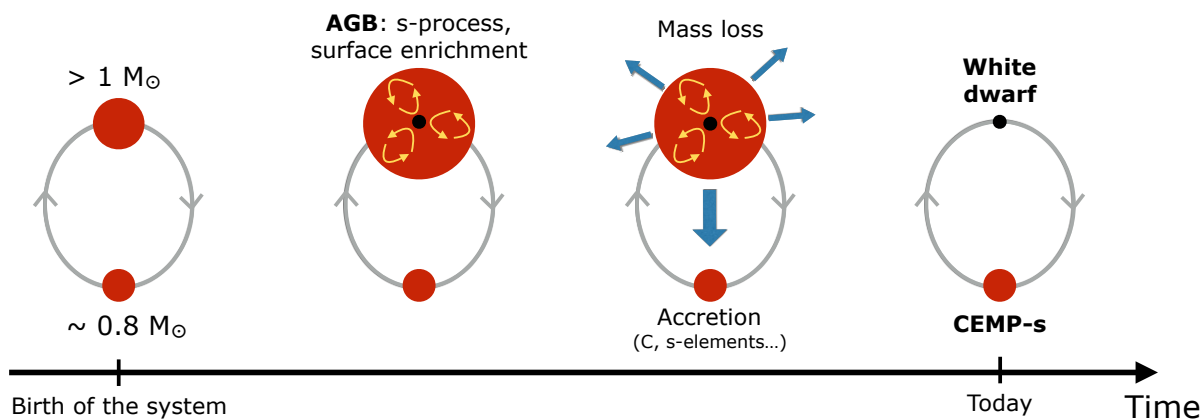


Figure 2.7: Schematic view of the binary scenario to explain the peculiar abundance pattern of CEMP-s stars. In a binary system composed of a $0.8 M_{\odot}$ and a $> 1 M_{\odot}$ stars, the more massive star goes through the Asymptotic Giant Branch (AGB) phase and loses mass. This lost material is enriched, among other, in carbon and s-elements. Some of this material is accreted by the secondary, that becomes a CEMP-s star. The primary ends its life as a white dwarf (see text for more details).

most evolved CEMP stars, internal mixing processes might have erased the initial surface chemical composition (hence the signature of previous stellar generations) for some elements like C or N. An important work would be to compute a grid of CEMP stellar models including various mixing processes in order to quantify the degree of mixing experienced by each observed evolved CEMP star. The aim would be to recover the initial surface abundances of all elements. Such a correction would give the chemical composition of the CEMP natal cloud. It will establish a more direct link between the evolved CEMP stars and the ejecta of the previous generation of stars.

2.5 The origin of CEMP stars: external sources

The origin of the CEMP stars is closely linked to the origin of the elements. When investigating the origin of CEMP stars, the aim is generally to find what is the astrophysical source able to provide the carbon, nitrogen, s-, r-elements...

It really seems that external sources are needed to explain the peculiarities of CEMP stars. The external sources can be objects that lived before and enriched the cloud in which the CEMP star formed and/or companions stars that transferred material to the (future) CEMP star. In this global frame, the existing scenarios for the origin of the different classes of CEMP stars are discussed below.

2.5.1 CEMP-s stars

Near the end of their lives, stars with initial masses between about 1 and $8 M_{\odot}$ evolve to the Asymptotic Giant Branch (AGB). AGB stars are known to be at the origin of the *main* s-process component (cf. Sect. 3.2) and also to produce light elements such as carbon. Are CEMP-s AGB stars? Actually no: many CEMP-s stars are still rather unevolved and therefore do not have gone through the AGB phase, where s-elements can be produced. The main scenario (see Fig. 2.7 for a schematic view) considers that CEMP-s were born as $\sim 0.8 M_{\odot}$ normal stars (i.e. not C-rich, not s-rich) in a binary system with a more massive companion (e.g. $1.5 M_{\odot}$). During its AGB stage, the companion produces and ejects through winds a material enriched in light and s-elements. Some of the wind material is accreted by the companion, that becomes a CEMP-s star. The AGB star

ends its life as a white dwarf.

In the scenario described above, the mechanism for the transfer of mass is wind mass transfer. The transfer of mass may indeed preferentially occur through wind accretion rather than through Roche-lobe¹¹ overflow because when the donor is an AGB star, Roche-lobe overflow may be unstable (Paczynski 1965) and brings the system to the common envelope phase. In this phase, 3D hydrodynamic simulations suggest that accretion is very inefficient (Ricker & Taam 2008), meaning that the formation of CEMP-s stars might not happen. By investigating the origin of 15 CEMP-s stars with known orbital periods, Abate et al. (2015b) have shown that the wind mass transfer model generally agrees well with observations but in most of the cases, the wind accretion rate should be enhanced by a factor of 5 – 10 to account for the observations.

Atomic diffusion and thermohaline mixing on CEMP-s stars are important ingredients that may induce important surface composition changes (e.g. Stancliffe et al. 2007). The accreting CEMP-s star undergoes thermohaline mixing because the material coming from the AGB companion has a larger mean molecular weight than the material at the surface of the accreting future CEMP-s star¹². After the accretion, thermohaline can reduce the surface carbon abundance in the CEMP-s by ~ 1 dex (Stancliffe et al. 2007). A too strong thermohaline would make the s-elements sink and disappear from the stellar surface. However, if CEMP-s stars rotate, the horizontal turbulence induced by rotation may reduce or even kill the thermohaline mixing (Denissenkov & Pinsonneault 2008; Maeder et al. 2013). Models of rotating CEMP-s stars computed by Matrozis & Stancliffe (2017) supports this view by showing that even a mild rotational mixing severely inhibits thermohaline mixing (also atomic diffusion is inhibited).

Worth to mention is also that if a substantial amount of material (hence angular momentum) is accreted from the AGB companion, the CEMP-s star should spin up significantly. Matrozis et al. (2017) have shown that $\sim 0.05 M_{\odot}$ can be accreted before the CEMP-s reaches critical rotation and therefore stops accreting more material. However, more than $0.1 M_{\odot}$ is often needed to reproduce the chemical composition of observed CEMP-s stars (e.g. Abate et al. 2015a,b). This said, a generally good agreement is found between the yields of AGB stars and chemical composition of CEMP-s stars (with nevertheless several persisting discrepancies, especially for C, N, F, Na, and $^{12}\text{C}/^{13}\text{C}$, Lau et al. 2009; Stancliffe 2010; Bisterzo et al. 2011, 2012; Lugaro et al. 2012).

The AGB binary scenario is also well supported by the fact that a large fraction of CEMP-s stars is in a binary system (cf. Sect. 2.3). The apparently single CEMP-s stars nevertheless challenge this scenario, even if one can imagine that the single CEMP-s stars have lost their AGB companion or that they are in a binary system with a very long period, explaining the non-detection of radial velocity variation.

In general, even if CEMP-s stars are explained with the AGB scenario, it does not mean that the previous generations of massive stars did not contribute. Likely, it means that the nucleosynthetic signature let by the AGB companion on the CEMP-s star is the dominant one and has blurred the nucleosynthetic signature let by the previous generation of stars. In Chapter 5, I investigate whether the nucleosynthetic imprint of previous massive stars can be identified in CEMP stars enriched in s-elements.

2.5.2 CEMP-r, -r+s, -r/s, -i stars

The origin of CEMP-r stars is tightly linked to the astrophysical site for the r-process, which is still unknown. The two main possible r-process sites are magnetorotationally driven supernovae (MRSNe, e.g. Thielemann et al. 2011; Winteler et al. 2012; Nishimura et al. 2015) and neutron star (NS) merger (e.g. Symbalisty & Schramm 1982; Freiburghaus et al. 1999; Thielemann et al. 2011,

¹¹The Roche-lobe is a distinctively shaped region that surrounds a star in a binary system. In this region, the material is gravitationally bound to the star. If the primary exceeds the Roche-lobe radius, some material can flow towards the secondary.

¹²In this case, thermohaline mixing can occur during the main sequence.

2017; Wanajo et al. 2014). Recently, LIGO detected GW170817, the first observed binary neutron star inspiral (Abbott et al. 2017). The light curve of the electromagnetic counterpart was found to be compatible with a NS merging event producing r-elements (Smartt et al. 2017; Pian et al. 2017).

NS mergers alone may nevertheless face difficulties to explain the most iron-poor CEMP-r stars (e.g. SM 0248–6843 with $[\text{Fe}/\text{H}] = -3.71$ and $[\text{Eu}/\text{Fe}] = 1$, Jacobson et al. 2015), as shown by inhomogeneous chemical evolution models (Argast et al. 2004; Wehmeyer et al. 2015). As summarized in the review of Thielemann et al. (2017), one important reason is that the merging of two NS requires two prior supernova events, that can already lead to a substantial floor of Fe. This floor may be too high compared to the CEMP-r stars with the lowest $[\text{Fe}/\text{H}]$ ratios. This issue may nevertheless be solved if the two NS have undergone kicks at the time of the supernova (SN) explosion: in this case, they were removed from the SN debris and moved into a medium with low Fe pollution. With chemical evolution models, Wehmeyer et al. (2015) have also shown that if the NS-NS system takes too long to coalesce, further nucleosynthesis events can occur and enrich the interstellar medium (ISM) in Fe. When the NS-NS system finally merges, the surrounding ISM has a higher $[\text{Fe}/\text{H}]$ than at the birth of the NS-NS system. In particular, they show that considering NS merger alone in their models cannot explain the $[\text{Eu}/\text{Fe}]$ ratios at $[\text{Fe}/\text{H}] < -2.5$. Considering also MRSNe as sources of r-elements can provide a solution to account for the enrichment in Eu at $[\text{Fe}/\text{H}] < -2.5$ (Cescutti & Chiappini 2014; Wehmeyer et al. 2015).

Some other stars have abundance patterns that neither a s-process pattern, nor a r-process pattern and nor a combination of both can fit the abundances. In such cases, an intermediate neutron capture process (i-process, first named by Cowan & Rose 1977), operating at neutron densities in between the s- and r-process may be the solution (e.g. Lugaro et al. 2012; Roederer et al. 2016; Hampel et al. 2016). The astrophysical sites for the i-process are unknown. Such a process may operate in AGB or super-AGB stars (Herwig et al. 2011; Jones et al. 2016), in accreting white dwarfs in close binary systems (Denissenkov et al. 2017) or in the He burning shell of Pop III massive stars (Clarkson et al. 2018). The s-process boost induced by rotation in the massive stars models of the present work (cf. Chapter 5) does not meet the required conditions (especially neutron density) for the i-process to occur.

Finally, some other stars seems to show an r+s pattern (Jonsell et al. 2006; Gull et al. 2018). Gull et al. (2018) reported the discovery of a CEMP star with $[\text{Fe}/\text{H}] = -2.2$ whose best fit is achieved by a combination of s- and r-process pattern. In this case, the CEMP star would have formed from at least two sources, one experiencing the s-process, the other experiencing the r-process.

2.5.3 CEMP-no stars

At the present day, no CEMP-s, -r, -r/s stars were found below $[\text{Fe}/\text{H}] \lesssim -3.5$. Below this threshold, all the CEMP stars are either CEMP-no or just CEMP in case no Ba (and Eu) abundance is available to classify them. For convenience, I use the term CEMP-no also for the most iron-poor stars whose rigorous classification is just CEMP.

While interesting in the case of CEMP-s stars, the AGB binary scenario applied to CEMP-no stars (Suda et al. 2004; Suda & Fujimoto 2010; Campbell et al. 2010) faces difficulties to account for the observables. One reason is that most CEMP-no stars appear to be single stars (Hansen et al. 2016a). The self-enrichment scenario (Fujimoto et al. 2000) seems unlikely, especially to explain the unevolved stars (cf. Sect. 2.4). Venn & Lambert (2008) proposed that the high C and low Fe may be explained by the separation of gas and dust beyond the CEMP star surface, followed by the accretion of dust-depleted gas. In this case, a dusty disk should exist around CEMP stars, whose presence would be betrayed by a mid infrared excess. Later, Venn et al. (2014) have shown that no mid infrared excess was found for six out of the seven stars they examined (the exception is for HE 0107-5240, that shows a small excess). Also, this dust-gas separation process should affect in a similar way the different isotopes of a given element. The carbon isotopic ratio for instance, will not be modified by this process. The very low $^{12}\text{C}/^{13}\text{C}$ ratios on some CEMP-no stars need to be

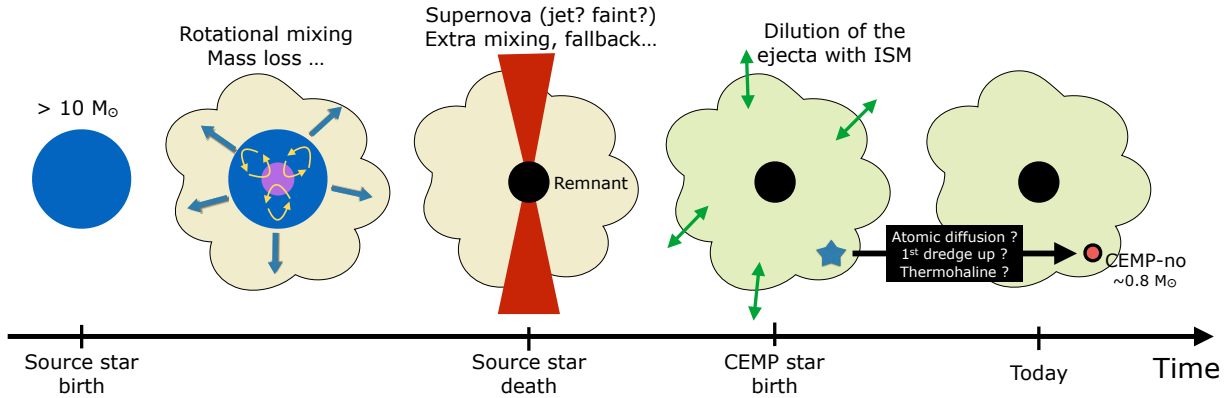


Figure 2.8: Schematic view of a possible formation channel for CEMP-no stars. What is shown are more some of the interesting ingredients to explain CEMP-no stars rather than an exact scenario. A previous massive source star (Pop III or low metallicity) is at the origin of the material used to form the CEMP-no star (a combination of more than one source is also possible). The massive star can experience rotational mixing, mass loss and a supernova (that might be asymmetric because of the fast rotation of the core). The material ejected through winds and/or supernova can be diluted with the ISM and finally be used to form a CEMP-no star. From its birth to now, the CEMP-no star may have experienced internal mixing processes, blurring the nucleosynthetic signature of the previous massive star (cf. text for more details).

explained by another process.

In the end, this let us with the interesting possibility that CEMP-no stars are the rather direct daughters of a previous generation of stars. These previous stars should be massive since at the very low metallicity considered here, low or intermediate mass stars may not had time to contribute to the chemical enrichment yet. Also, these previous massive stars should have contributed little in iron.

The fact that the CEMP-no class of star shows very large abundances scatter suggests that they formed with the ejecta of only one or a few previous stars. If they were formed from a well mixed reservoir of many previous stars, the scatter should be much smaller, as is it observed at higher metallicities or in normal metal-poor stars. Over the past ~ 15 years, multiple scenarios, aiming at characterizing the nature of the CEMP-no source stars, emerged:

- Mixing and fallback + faint SN (Umeda & Nomoto 2002, 2003, 2005; Iwamoto et al. 2005; Tominaga et al. 2007; Heger & Woosley 2010; Tominaga et al. 2014; Ishigaki et al. 2014).
- Very low metallicity stars experiencing fast rotation (spinstars, Meynet et al. 2005, 2006, 2010; Hirschi & Maeder 2010; Maeder et al. 2015; Maeder & Meynet 2015; Choplin et al. 2016, 2017b).
- Normal SN from $15 M_{\odot}$ + faint SN with strong fallback from $35 M_{\odot}$ (Limongi et al. 2003).
- Jet-induced SN from $25 - 40 M_{\odot}$ Pop III stars (Maeda & Nomoto 2003; Tominaga 2009).
- Rotation + faint SN (no fallback, Takahashi et al. 2014).
- $15 - 40 M_{\odot}$ rotating Pop III stars with mixing and fallback (Joggerst et al. 2010).
- H-ingestion event in the He burning shell of a $45 M_{\odot}$ Pop III star (Clarkson et al. 2018).

This is a tentative list. Some scenario of the list above may be grouped together. Also, for a given scenario, some works occasionally consider slightly different methods or physical ingredients, so that they may be considered as separated scenarios.

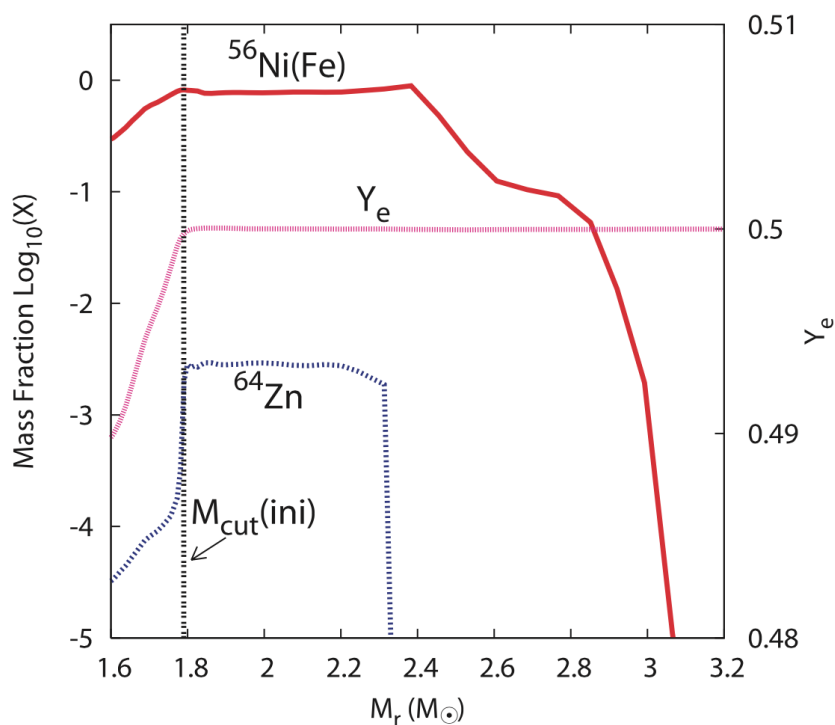


Figure 2.9: Inner abundances of a Pop III $25 M_{\odot}$ after explosive nucleosynthesis. Y_e is the electron fraction (figure from Tominaga et al. 2007)

Some works suggest that more than one class of source star is required to explain the CEMP-no stars. For instance, the $A(C) - [Fe/H]$ diagram (where $A(C) = \log(N_C/N_H) + 12$) suggests that the $[Fe/H] \lesssim -4$ stars separate in at least two groups (Yoon et al. 2016), so that at least two different classes of progenitor might be needed. Also, comparisons of the chemical composition of CEMP-no stars with ejecta of massive source stars often show that only one class of progenitor faces difficulty to reproduce large sample of CEMP-no stars. Placco et al. (2016) have used the yields of non-rotating Pop III stars of Heger & Woosley (2010) and shown that 5 out of the 12 investigated CEMP-no stars can be reproduced by the predicted source star yields while 7 stars are left without an acceptable source star.

The scenarios listed above all consider that (1) the surface abundances of CEMP-no stars reflect rather directly the abundances in their natal clouds and (2) the natal cloud was polluted by one or very few zero or very low metallicity massive source star (schematic view in Fig. 2.8). Each scenario has nevertheless its own specificity. Among the quoted works in the list above, frequent ingredients considered in source star models are rotation, extra mixing events (in the sense of Umeda & Nomoto 2002, see details below) and strong fallback. Occasionally, both are considered. Occasionally, refinements or additional ingredients were proposed. Below are discussed two scenarios in more detail: mixing & fallback and fast rotating massive stars.

Mixing and fallback

Mixing. The $[Zn/Fe]$ ratio of normal metal-poor stars was found to rise with decreasing $[Fe/H]$ (Cayrel et al. 2004, their figure 12). Models of massive stars including explosive nucleosynthesis show that at the end of the evolution, Zn is located in deeper regions than Fe (Fig. 2.9). Consequently, if some Zn is ejected from the massive star (through a supernova event), also a large amount of Fe is ejected and the trend of $[Zn/Fe]$ observed at low $[Fe/H]$ cannot be explained. In order to expel some Zn without expelling too much Fe, Umeda & Nomoto (2002) have included an

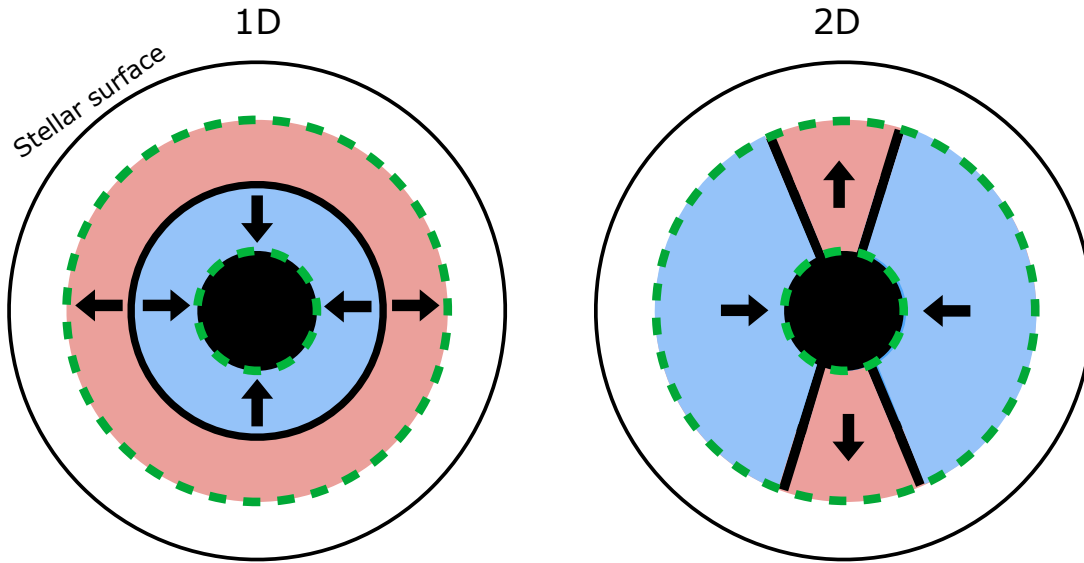


Figure 2.10: Schematic view of the 1D mixing and fallback model (left) that mimics the 2D jet SN model (right). At the end of the massive star evolution, a region, delimited here by the 2 green dashed circles, is mixed. A part of this region is expelled (red), the other part (blue) falls onto the central remnant. In the 2D jet model, the material is ejected along the jet axis (figure adapted from Tominaga et al. 2007).

extra mixing event in the source star models. The mixing event occurs at the time of the massive star explosion and brings material from inner layers closer to the surface. This allows to bring some Zn upward, without having too much Fe. When considering such a mixing, the supernova yields can reproduce the observed $[\text{Zn}/\text{Fe}]$ ratios at low $[\text{Fe}/\text{H}]$.

Fallback. For stars having a large $[\text{C}/\text{Fe}]$ and low $[\text{Fe}/\text{H}]$ (CEMP stars), the concept of faint supernova with strong fallback was also introduced (Nomoto et al. 2003; Umeda & Nomoto 2003). The idea of a strong fallback comes from the fact that in the massive source star, carbon is located closer to the surface than iron. Therefore, in order to have a large $[\text{C}/\text{Fe}]$ ratio in the ejecta, not too deep layers should be expelled so as to eject mostly carbon and little iron. The supernova is faint because very little ^{56}Ni (whose decay into ^{56}Fe is mainly responsible for the luminosity of the supernova) is ejected. If too much ^{56}Ni is ejected, one will ultimately get too much ^{56}Fe compared to the low $[\text{Fe}/\text{H}]$ ratios of the most iron poor stars. The concept of strong fallback and faint supernova for the source star is somewhat consistent with the fact that low-metallicity stars are more compact and hence might explode less easily.

The mixing & fallback scenario is a combination of both events. To fit the observations with a massive source star experiencing mixing and fallback, a massive source star model is evolved until the end of its evolution. Then a region inside the model, between two limiting shells (the two green dashed circles in Fig. 2.10), is considered to be fully mixed at the time of the supernova explosion. A part of the mixed region is ejected (red part in Fig. 2.10), a part is kept into the remnant (blue part). The extension of the mixed region and the fraction of this region which is expelled are chosen so as to reproduce the abundances of observed metal-poor stars.

Although the source star models with mixing and fallback are generally 1D models, Tominaga (2009) has shown that for a Pop III stellar model of $40 M_{\odot}$, the 1D mixing and fallback model

gives similar chemical yields than a 2D jet-induced explosion with fallback (Fig. 2.11). It can be roughly understood by the fact that the mixed region is ejected differently in 1D (spherically) and 2D (along the jet axis) but has a similar chemical composition. Nevertheless, some chemical species are overproduced in the 2D jet SN model (e.g. Sc, see Fig. 2.11). This is due to the higher energy concentration in the jet-induced explosion, that leads to a bit different explosive nucleosynthesis. Overall, it suggests that the spherical mixing and fallback model is rather well mimicking a 2D jet-induced explosion.

The mixing and fallback scenario for CEMP-no stars has the advantage to well explain the iron-peak elements like Zn or Fe. One caveat is that it faces difficulties in reproducing the high N abundance of some metal-poor stars (Tominaga et al. 2007) except if additional mixing is considered between the He-convective shell and the H-rich envelope just before the supernova (Iwamoto et al. 2005; Tominaga et al. 2014).

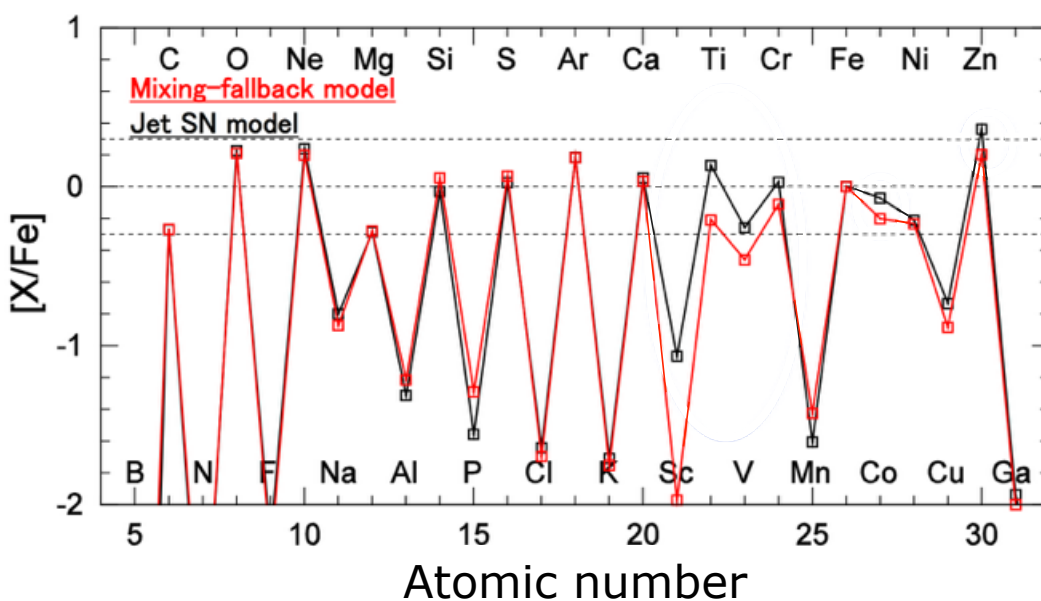


Figure 2.11: Post-supernova yields of a non rotating Pop III $40 M_{\odot}$ model. The red pattern stands for the 1D mixing and fallback model, the black pattern results from a 2D jet-SN model. Figure adapted from a slide of K. Nomoto (http://www.astro.rug.nl/archeocomic/PDF_TALKS/Nomoto.pdf). See also the Fig. 6 of Tominaga (2009).

Fast rotating massive stars

In a broad context, the fast rotating massive star scenario or spinstar¹³ scenario proposes that fast rotation at low metallicity is a dominant process that largely impacts the outputs of massive stars (especially the stellar yields). It is motivated by several aspects (see also Sect. 1.3 and 3.3). One of the aspect, further discussed in Sect. 3.3.1, is that the efficiency of the rotational mixing operating inside the star is expected to increase with decreasing metallicity. This effect arises naturally, as a result of the physics of rotation in stars (discussed in Sect. 3.3). As a consequence of this efficient rotational mixing, the yields of some elements like C, N, O (e.g. Meynet & Maeder 2002) or s-elements (e.g. Pignatari et al. 2008; Frischknecht et al. 2016) are impacted a lot by rotation in low metallicity massive stellar models. The spinstar scenario tells us that the low-mass stars that formed early in the Universe should contain mostly (but possibly among others) the nucleosynthetic signatures of previous fast rotating massive stars.

¹³The present work focuses on massive stars but, originally, the term spinstar also designates intermediate mass stars.

Thanks to Galactic chemical evolution models, it was shown that the N/O, C/O, $^{12}\text{C}/^{13}\text{C}$ and Sr/Ba ratios of very metal-poor (mostly normal, i.e. not carbon-enhanced) halo stars are better reproduced if including the yields of fast rotating massive stars (Chiappini et al. 2006, 2008; Cescutti et al. 2013). The spinstar scenario has also been proposed to explain the abundance anomalies (particularly the Mg-Al anticorrelation) in Globular Clusters (Decressin et al. 2007).

When applied to CEMP stars, the spinstar scenario proposes that most CEMP stars have formed from the material ejected through winds and/or supernova by a previous fast rotating massive source star. Meynet et al. (2006) have shown that the [C/Fe], [N/Fe] and [O/Fe] ratios in the ejecta (wind + supernova) of a very low-metallicity fast rotating $60 M_{\odot}$ are similar to the surface ratios of the unevolved CEMP stars G77-61 and HE 1327-2326 (with [Fe/H] < -4). In the same line, Hirschi (2007) has shown that the CNO abundances of HE 1327-2326 can be explained by the wind of a low metallicity fast rotating $40 M_{\odot}$ model, whose ejecta was diluted 600 times with ISM (i.e. 600 times more ISM material than stellar ejecta). Meynet et al. (2010) have predicted that CEMP stars formed from a fast rotating massive source star should be helium rich, provided the ejecta was little diluted with pristine ISM. Maeder et al. (2015) and Maeder & Meynet (2015) proposed that the back-and-forth, partial mixing at work between the He- and H-regions of the rotating source star may account for the wide variety of CEMP-no stars abundances (more details in Sect. 4.1).

It is important to make the difference between the two different kinds of mixing at work in the spinstar and mixing & fallback scenarios:

- Spinstar: the mixing is induced by rotation and occurs progressively during the evolution of the star.
- Mixing & fallback: the mixing arises only at the time of the supernova.

Contrary to the mixing & fallback process, the process of rotation, which is at the heart of the spinstar scenario, was not introduced in stellar models so as to explain the abundances of MP or CEMP stars. As mentioned, spinstars are expected to exist at very low metallicity, as a result of the physics of rotation (more details in Sect. 3.3). One strength of the spinstar scenario is that it provides a natural physical process to explain the abundances of most elements in CEMP stars. Another strength is that spinstars can account for other observables like the abundances of normal halo stars (cf. previous discussion). Rotation may also be a key process to explain the variation of surface abundances observed in solar metallicity, nearby massive stars (e.g. Martins et al. 2015). Rotation is linked to different observables, one of which could be CEMP stars.

The spinstar scenario alone does not offer a solution to explain the little enrichment in iron-peak elements of CEMP stars (e.g. Fe, Zn). For instance, in the material ejected by the stellar winds of a rotating Pop III star, no iron is ejected so that [Fe/H] = 0. Iron, zinc, ... can be explained by the mixing process in the sense of Umeda & Nomoto (2002) or they can come from another source. Overall, the spinstar scenario proposes that rotation in massive stars played a major role in the chemical enrichment of the early Universe. It does not exclude other ingredients like mixing & fallback. As noted in Maeder et al. (2015), spinstar and mixing & fallback scenarios are more complementary than contradictory: one can imagine a rotating star experiencing an additional mixing event at the end of its evolution.

2.6 Summary

Carbon-Enhanced Metal-Poor (CEMP) stars are peculiar MP stars observed in the halo of the Galaxy and showing overabundances in light and sometimes heavy s- and/or r- elements. CEMP stars are more frequent at low [Fe/H]: about 80 % of stars with [Fe/H] < -4 are CEMP. The most iron-poor stars are generally weakly enriched in s- and/or s-elements (CEMP-no). They can be used to constrain the very early chemical evolution of the Universe.

Evolved CEMP stars probably underwent internal mixing processes (especially the first dredge-up and thermohaline mixing), altering their surface abundances. Although important, these processes are likely not able to explain the peculiar abundances of this class of stars (especially the unevolved stars). The abundances of CEMP-s stars may be explained by an accretion episode from the material (enriched in carbon and s-elements) ejected from an AGB companion. The fact that many CEMP-s stars are in a binary system supports this scenario. CEMP-no stars are generally single stars so that another scenario should be invoked. CEMP-no stars (and generally the most iron-poor stars) are thought to have kept the nucleosynthetic imprint of only one or very few previous massive source stars. In some cases however, this imprint may have been blurred by internal mixing processes in the CEMP-no star itself. Rotation, pre supernova mixing and strong fallback are among the interesting characteristics the source stars should have to account for the abundances of observed CEMP-no stars.

Massive source stars: nucleosynthesis and models with rotation

This chapter first discusses the nucleosynthesis in massive stars. A section is dedicated to the s-process in AGB stars for completeness. The theoretical and modeling aspects of massive stellar evolution that are relevant for this work are then presented. Emphasis is placed on the specificities of stellar evolution at low metallicity.

3.1 Nucleosynthesis processes in massive stars

3.1.1 Stellar fusion

Core hydrogen burning. The first burning stage, lasting for ~ 1 Myr to several tens of Myr, is the fusion of hydrogen to helium. The pp-chains and the CNO-cycle both contribute to transform H into He. Above 17 MK (corresponding the H-burning temperatures of a $\sim 1.2 M_{\odot}$ star), the CNO cycle becomes more efficient than the pp-chain. Provided a little bit of CNO elements are available, this is the CNO-cycle that dominates the production of energy during the H-burning stage of massive stars. The main CNO loop (CNOI) is shown by the colored loop in Fig. 3.1. One loop transforms four protons into one ${}^4\text{He}$. As shown by the colors of the arrows, ${}^{14}\text{N}(p, \gamma)$ is the slowest reaction, followed by ${}^{12}\text{C}(p, \gamma)$ and ${}^{13}\text{C}(p, \gamma)$. After a timescale determined by ${}^{14}\text{N}(p, \gamma)$ (the slowest reaction) the CNOI cycle reaches an equilibrium where ${}^{12}\text{C}/{}^{14}\text{N} = 0.025$ and ${}^{12}\text{C}/{}^{13}\text{C} = 3.3$. Because ${}^{14}\text{N}(p, \gamma)$ is the bottleneck reaction, the main effect of CNOI is to transform the initial C nuclei into ${}^{14}\text{N}$. The branching point at ${}^{15}\text{N}$ is the starting point of other CNO loops that take place at higher temperatures and that allow the synthesis of other isotopes, particularly ${}^{16}\text{O}$.

During this first stage, the Ne-Na and Mg-Al chains (Fig. 3.2) can also be activated for temperatures higher than ~ 35 MK for Ne-Na and ~ 50 MK for Mg-Al. The rates of the reactions at work in these chains are more uncertain than the reactions rates of the CNO-cycle. At the branching point ${}^{23}\text{Na}$, the ${}^{23}\text{Na}(p, \alpha)/{}^{23}\text{Na}(p, \gamma)$ ratio equals 159 and 7 at 40 and 70 MK respectively according to Iliadis et al. (2010). For the rates of Cyburt et al. (2010), these ratios are 0.3 and 0.6 (still at 40 and 70 MK). We see that depending on the literature source used and of the temperature, the Ne-Na and Mg-Al chains can either be considered as closed loops or not. They are closed loops if the ${}^{23}\text{Na}(p, \alpha)/{}^{23}\text{Na}(p, \gamma)$ ratio is high.

Generally, the production of Ne, Na, Mg and Al in massive stars can be significantly affected if considering nuclear reaction rates from different sources. Decressin et al. (2007) have shown that multiplying the rate of ${}^{24}\text{Mg}(p, \gamma)$ by 10^3 around 50 MK changes the production of Mg-Al isotopes during the main sequence of low metallicity massive stars by 0.5 – 1 dex.

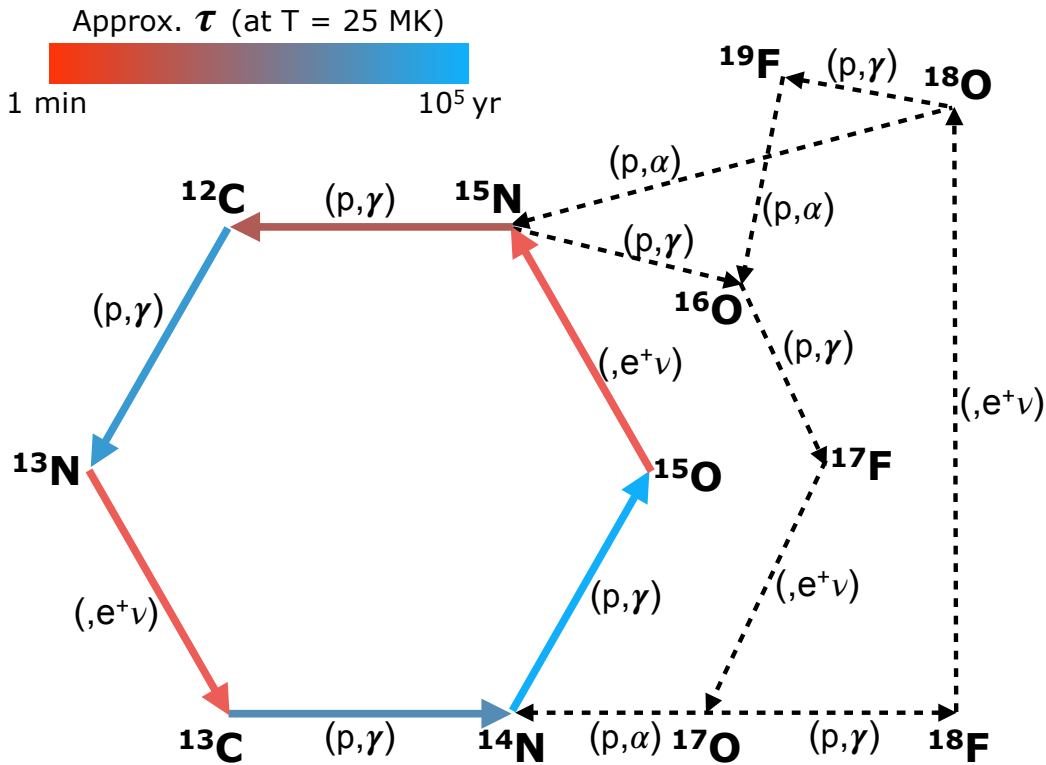


Figure 3.1: Illustration of the CNO cycle. The colored hexagon shows the main loop (CNOI). The other loops are shown by dashed lines. The colored arrows show the approximate timescales for the associated reactions (adapted from Maeder 2009).

Core helium burning. When running out of hydrogen, the core contracts until the central temperature is hot enough (about 100 MK) for the 3α process to start. The second burning stage is the core helium burning phase. It lasts for $\sim 0.1 - 1$ Myr, which is about 1/10 of the core hydrogen burning phase. At the beginning of core He-burning, the ^{14}N synthesized during core H-burning through the CNO cycle (cf. previous discussion) is quickly transformed into ^{22}Ne via the chain $^{14}\text{N}(\alpha, \gamma)^{18}\text{F}(e^+\nu_e)^{18}\text{O}(\alpha, \gamma)^{22}\text{Ne}$. The $^{22}\text{Ne}(\alpha, n)^{25}\text{Mg}$ reaction, activated at $T \sim 220$ MK releases free neutrons that can be captured by seeds like iron and heavier elements. This is the slow neutron capture process (s-process) which is discussed below in Sect. 3.1.2.

During core He-burning, a hydrogen shell burns above the helium core. The H-shell burns at a slightly higher temperature than the H-core. It induces a somewhat different nucleosynthesis in the H-shell. For instance, the Ne-Na and Mg-Al cycles are more active in the H-shell. Rotational mixing can transport elements from the He-burning core to the H-burning shell (and vice-versa) and trigger a rich and varied nucleosynthesis (Sect. 4.1).

Advanced burning stages. At the end of the core He-burning stage, the most abundant species in the core are ^{12}C and ^{16}O . Since the $^{12}\text{C} + ^{12}\text{C}$ reaction has the lowest coulomb barrier, the next burning stage is core carbon burning. After carbon burning comes neon photodisintegration, oxygen and then silicon burning. The advanced stages last for 10–1000 yr (C), 0.1–1 yr (Ne), 0.1–1 yr (O) and 0.1–10 days (Si, e.g. Heger et al. 2000; Hirschi et al. 2004). During these stages, most of the energy goes out from the star in the form of neutrinos. To compensate for this strong energy loss, the rates of nuclear reactions increase. This leads to a quick burning of chemical species, explaining the short duration of the advanced stages. During these stages, the core is decoupled from the

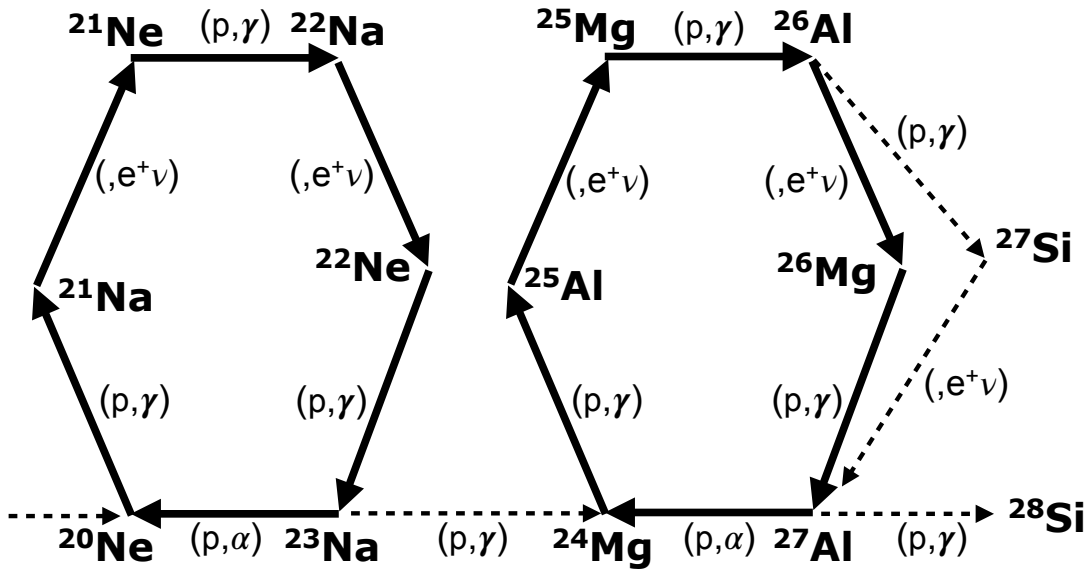


Figure 3.2: Ne-Na and Mg-Al chains (or cycles) (adapted from Maeder 2009).

rest of the star. It implies that the star does not move anymore in the Hertzsprung-Russell (HR) diagram. The main products of C-burning are ^{20}Ne , ^{23}Na and ^{24}Mg . Neon photodisintegration produces mainly ^{16}O , ^{24}Mg and ^{28}Si , oxygen burning mostly ^{28}Si and ^{32}S and silicon burning ^{56}Ni (cf. Woosley & Weaver 1995, especially their Table 19). At the end of each core burning phase, the burning continues in a shell. As evolution proceeds, more and more different burning regions are present in the massive star.

3.1.2 The weak s-process

Massive stars are generally associated to the *weak* s-process, mainly responsible for the elements with $A < 90$. Cameron (1960) identified that at the beginning of the core He-burning phase of massive stars, the secondary¹ ^{14}N (synthesized during the main sequence thanks to the CNO-cycle) is converted into ^{22}Ne by successive α -captures and can provide a source of neutrons with the $^{22}\text{Ne}(\alpha, n)$ reaction. This reaction is efficiently activated at $T > 220$ MK. It was later recognized that the s-process in massive stars occurs principally in the He-burning core of massive stars (Peters 1968; Couch et al. 1974; Lamb et al. 1977; Langer et al. 1989; Prantzos et al. 1990; Raiteri et al. 1991a). In solar metallicity stars with $M_{\text{ini}} \gtrsim 30 M_{\odot}$, some ^{22}Ne is left at the end of core He-burning phase so that s-process can occur during later stages (Couch et al. 1974). The carbon shell burning is the second efficient s-process production site inside massive stars (it contributes to $\sim 20\%$ at solar metallicity, Raiteri et al. 1991b; The et al. 2007). Neutrons are released by $^{22}\text{Ne}(\alpha, n)$ with the α particles provided by the $^{12}\text{C}(^{12}\text{C}, \alpha)^{20}\text{Ne}$ reaction. The neutron density is typically $\sim 10^{11} \text{ cm}^{-3}$, which is ~ 4 dex higher than in the He-burning core. He-burning shell and C-burning core do not contribute significantly in producing s-elements (Arcoragi et al. 1991). At low metallicity, the $^{13}\text{C}(\alpha, n)^{16}\text{O}$ reaction provides a small burst of neutrons at the very beginning of the core He-burning phase that can synthesize some light s-elements ($A \lesssim 85$, Baraffe et al. 1992).

¹An isotope is synthesized through the *secondary* channel if it comes from the initial metal content of the star. It is formed through the *primary* channel if produced from the initial hydrogen and helium content of the star.

The synthesis of s-elements (Sr, Ba...) is due to neutron capture on heavy seeds (e.g. Fe). However, neutrons are also captured by light elements. ^{12}C and ^{16}O are abundant in the He-core and are important poisons for the s-process. ^{16}O captures neutrons via $^{16}\text{O}(n, \gamma)$. Then, either the neutron is recycled with $^{17}\text{O}(\alpha, n)$ or it is definitely lost with $^{17}\text{O}(\alpha, \gamma)$. The ratio of these two reaction rates plays an important role on the efficiency of the s-process. At low metallicity, the poisoning effect of ^{16}O is stronger because the ratio of ^{16}O to s-process seeds (e.g. iron) is higher (Prantzos et al. 1990; Rayet & Hashimoto 2000). During the shell carbon burning phase, important additional neutron poisons (^{20}Ne and ^{24}Mg) limit the efficiency of the s-process.

Meynet et al. (2006) and Hirschi (2007) have shown that extra ^{22}Ne can be synthesized during the core He-burning phase of massive rotating stars (the interplay between rotation and nucleosynthesis in low-metallicity massive stars is discussed in Sect. 4.1). Compared to non-rotating models, rotation gives more neutrons (source) with the same amount of seed. A higher source over seed ratio shifts the production of s-elements towards higher atomic masses (Gallino et al. 1998). Pignatari et al. (2008) have shown that rotational mixing would allow the production of s-elements up to $A \simeq 140$. Frischknecht et al. (2012, 2016) started to explore the s-process in rotating massive stars, by computing models (about 30 models in total) of different masses ($15 < M_{\text{ini}} < 40 M_{\odot}$) and metallicities ($10^{-7} < Z < Z_{\odot}$) while following the complete s-process during the evolution. The Chapter 5 of this thesis aims at extending this work by computing a new grid of models and compare the yields to low mass metal-poor stars enriched in s-elements.

3.1.3 Explosive nucleosynthesis

The chemical composition of the massive star can be further modified by explosive nucleosynthesis (e.g. Thielemann et al. 1996). It is activated by a shock wave that heats the material, processes it and finally ejects the envelope of the star while the central part will form a neutron star or a black hole. The innermost layers, from the center to the C-shell can burn explosively. The outer stellar layers are mostly unprocessed by explosive nucleosynthesis. Thielemann et al. (1990) reported that above the mass coordinate $\sim 2 M_{\odot}$ of a $20 M_{\odot}$ model (corresponding roughly to the location of the O-burning shell), the material is not significantly altered by explosive nucleosynthesis. In the region affected by explosive nucleosynthesis, the abundances of elements lighter than neon and heavier than zinc are marginally modified. By contrast, the iron-peak elements are the most affected (Woosley & Weaver 1995; Thielemann et al. 1996; Woosley et al. 2002; Chieffi & Limongi 2003; Limongi et al. 2003; Nomoto et al. 2006). The s-elements produced during the evolution (cf. Sect. 3.1.2) are not expected to be strongly affected by the explosion (Rauscher et al. 2002; Tur et al. 2009). The shock of the explosion may nevertheless affect the isotopic distribution of heavy nuclei in the He-shell of the progenitor (Meyer et al. 2000; Pignatari et al. 2013). In some cases, massive stars may also experience magneto-rotational supernovae, which is a possible site for the r-process (Winteler et al. 2012).

In this work, the explosive nucleosynthesis is not calculated. Pre-supernova models provide nevertheless a good estimation for the many species that are not much affected by the explosion. Likely, pre-supernova models also provide a good estimate of the nucleosynthesis of all elements above the carbon or oxygen burning shell, where explosive burning may not operate significantly.

3.2 The s-process in AGB stars

The present work focuses on massive stars but the s-process in AGB stars is also discussed for completeness. Thermally pulsing AGB stars are associated to the *main* s-process component, responsible for the elements with $90 < A < 209$. The AGB corresponds to the last stage of the life of stars having initial masses between about 1 and $8 M_{\odot}$ (e.g. the reviews of Iben & Renzini 1983; Busso et al. 1999; Herwig 2005; Karakas & Lattanzio 2014). At this phase, the star becomes

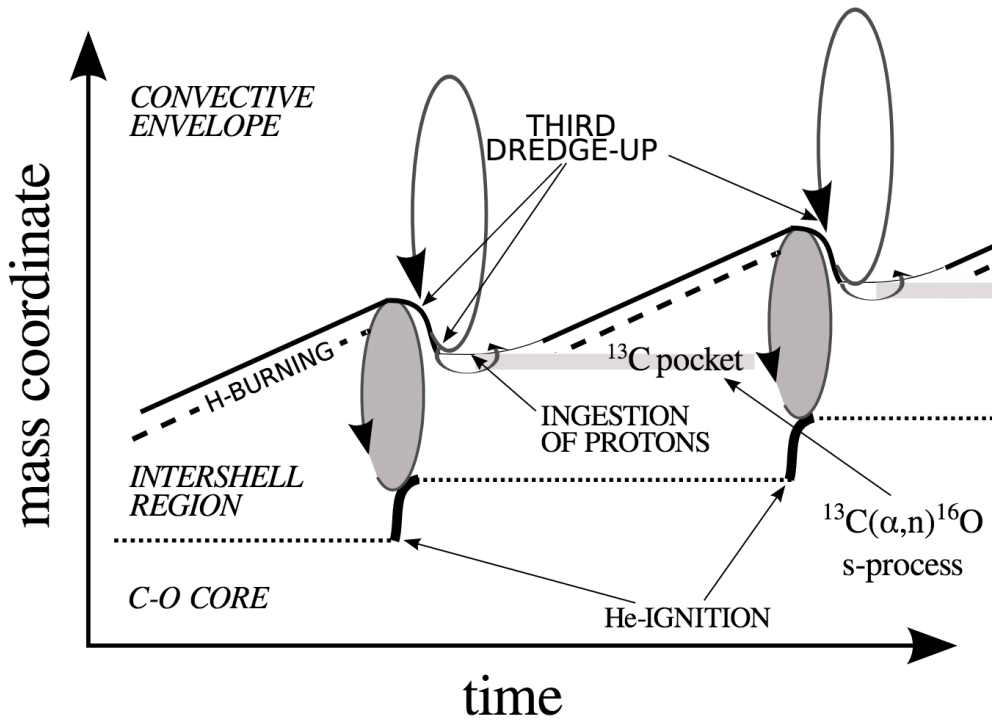


Figure 3.3: Schematic view of the interior of a star during the AGB phase. The horizontal grey bars represents the zone where protons are assumed to be ingested by ^{12}C to make ^{13}C (see text for explanation, from C. Abate, PhD thesis, adapted from Busso et al. 1999).

larger and more luminous and strong mass loss episodes may occur (up to $10^{-4} M_{\odot} \text{ yr}^{-1}$). AGB stars have a degenerate carbon-oxygen core. The core is surrounded by the helium and hydrogen shells, separated by the intershell region. Above is a convective envelope. The energy production is dominated by the H-burning shell. The He shell stays quiet most of the time. As H is burning in its shell, helium is synthesized, making the intershell region growing in mass (Fig. 3.3). When a critical value is reached, He-burning is suddenly ignited and a thermal pulse occurs. The energy produced drives convection so that the products of He-burning are brought upward, to the intershell region. The energy produced also expands the outer layers of the star. It has the effect of moving the H-burning shell outward and therefore stopping the burning in the H shell. It also makes the inner boundary of the convective envelope moving inward and eventually reaching the intershell region. Then, products of internal nucleosynthesis are brought up to the surface (this episode is called third dredge-up or TDU, Fig. 3.3). The process described above occurs cyclically (~ 50000 yrs between 2 thermal pulses) until the convective envelope is entirely removed through winds.

During the TDU, protons are mixed down to the intershell region and they are directly captured by the abundant ^{12}C to form ^{13}C through the chain $^{12}\text{C}(p, \gamma)^{13}\text{N}(\beta^+)^{13}\text{C}$. It forms a ^{13}C pocket. During the next thermal pulse, the reaction $^{13}\text{C}(\alpha, n)^{16}\text{O}$ occurs, providing neutrons and thus triggering the s-process. If too many protons are mixed in the intershell region, ^{14}N is also significantly formed from ^{12}C (thanks to the CNO cycle) and suppresses the s-process by capturing the neutrons via $^{14}\text{N}(n, p)^{14}\text{C}$.

The $^{22}\text{Ne}(\alpha, n)^{25}\text{Mg}$ reaction is not expected to contribute much in producing the main s-process component in AGB stars. One reason is that this reaction is activated in AGB stars with initial masses $M_{\text{ini}} \gtrsim 3 M_{\odot}$ (Truran & Iben 1977) while the solar s-only abundances are best reproduced by $1.5 - 3 M_{\odot}$ AGB models (e.g. Gallino et al. 1988; Hollowell & Iben 1988). This said, a contribution of $^{22}\text{Ne}(\alpha, n)$ is nevertheless expected to occur in low mass AGB stars (e.g. Straniero

et al. 1995), and particularly in the low metallicity regime, for initial masses above about $2 M_{\odot}$ (Lugaro et al. 2012).

With time, more and more sophisticated AGB stellar models with different initial masses, metallicities, reaction networks, etc... were computed (e.g. Renzini & Voli 1981; Gallino et al. 1998; Herwig 2004; Karakas 2010; Cristallo et al. 2011; Lugaro et al. 2012; Doherty et al. 2014; Cristallo et al. 2015). Several important uncertainties remain like for instance the formation mechanism of the ^{13}C pocket² which is a critical ingredient and is not fully understood yet (e.g. Lattanzio & Lugaro 2005), the third dredge-up (more generally the convection) or the mass loss (cf. Sect. 4 of Karakas & Lattanzio 2014, for an extensive discussion about uncertainties in AGB models).

Despite these uncertainties, the detection of CNO and s-elements at the surface of observed AGB stars provides evidences of the ongoing nucleosynthesis in such stars (e.g. Smith & Lambert 1990). The best evidence is probably the detection of the unstable element Tc at the surface of AGB stars (Merrill 1952; Smith & Wallerstein 1983): the longest-lived Tc isotope (^{99}Tc) has a mean life of about 1/10 of the duration of the AGB phase, meaning that it has to be synthesized by the AGB star itself.

3.3 Massive stellar models including rotation

To study the nucleosynthetic processes mentioned in the previous section, and more generally the evolution of stars, stellar models are required. Although stars are 3D objects, following their entire life and structure using multi dimensional codes is computationally too expensive. At the present day, only specific stages/zones of a star can be followed using multi dimensional codes (e.g. Herwig et al. 2014; Cristini et al. 2017). In stellar evolution models, a star is often considered as a spherically symmetric object. This greatly simplifies the modeling since reducing the problem to one dimension. Compared to multi dimensional codes, 1D codes have the advantage to be able to model the entire life of stars and to explore a large parameter space. They have the disadvantage to use a parametrized physics to describe the multi dimensional processes (e.g. turbulence).

Interestingly, rotating stars can also be modeled with 1D codes, following the theory of shellular rotation (Zahn 1992). The fundamental assumption of this theory is that in rotating stars, the horizontal turbulence (on an isobaric surface, i.e. surface of same pressure) is much stronger than the vertical one. This is motivated by the stable density stratification in the vertical direction, opposing a strong force to vertical fluid motions. In this theoretical frame, internal rotation depends essentially on the distance to the stellar center and little on latitude. The generalized 1D equations of hydrostatic equilibrium, mass conservation, energy conservation and energy transport, describing a star in shellular rotation are (Meynet & Maeder 1997):

$$\frac{dP}{dM_P} = -\frac{GM_P}{4\pi r_P^4} f_P \quad (3.1)$$

$$\frac{dr_P}{dM_P} = \frac{1}{4\pi r_P^2 \bar{\rho}} \quad (3.2)$$

$$\frac{dL_P}{dM_P} = \epsilon_{\text{nucl}} - \epsilon_{\nu} + \epsilon_{\text{grav}} \quad (3.3)$$

²In AGB models, a partial mixing zone is added artificially in a post-processing algorithm in order to mix protons with ^{12}C into the intershell region (Lugaro et al. 2004). It forms the ^{13}C -pocket which is needed to produce the neutrons required for the s-process.

$$\frac{d \ln T}{dM_P} = -\frac{GM_P}{4\pi r_P^4} f_P \min \left[\nabla_{\text{ad}}, \nabla_{\text{rad}} \frac{f_T}{f_P} \right] \quad (3.4)$$

with

$$f_P = \frac{4\pi r_P^4}{GM_P S_P} \frac{1}{\langle g_{\text{eff}}^{-1} \rangle} \quad \text{and} \quad f_T = \left(\frac{4\pi r_P^2}{S_P} \right)^2 \frac{1}{\langle g_{\text{eff}} \rangle \langle g_{\text{eff}}^{-1} \rangle}$$

and M_P the mass enclosed by the sphere of radius r_P , g_{eff} the effective gravity (resulting from both gravitational and centrifugal acceleration), ∇_{rad} and ∇_{ad} the radiative and adiabatic temperature gradients, $\bar{\rho}$ the average density between two isobars, ϵ_{nucl} , ϵ_{ν} , ϵ_{grav} the rates of nuclear energy production, neutrino losses, and gravitational energy (energy released/absorbed by contraction/expansion of the star). The quantities in brackets are averaged over an isobar according to

$$\langle X \rangle = \frac{1}{S_P} \oint_{\text{isobar}} X(r, \theta) d\sigma \quad (3.5)$$

where S_P is the surface of the isobar, defined by $S_P = 4\pi r_P^2$ with r_P the radius of the equivalent sphere, having the same volume than the oblate isobar. $d\sigma$ is a small surface element on the isobar.

In this work, the Geneva stellar evolution code GENEC (Eggenberger et al. 2008) is used. It was mainly developed and used for the computation of massive stellar models (e.g. Maeder 1987, 1992) with a sophisticated treatment of rotation (Meynet & Maeder 1997). The physical and modeling ingredients relevant for this work are discussed in the following sections.

3.3.1 Transport induced by rotation

In a differentially rotating star, the equipotentials are differently spaced as a function of the colatitude θ because the star is distorted by the centrifugal effect. The centrifugal force makes the equatorial radius larger than the polar radius so that the equipotentials are closer to each other at the poles and more spaced at the equator. Consequently, the effective gravity is larger at the poles. The radiative flux is proportional to the local effective gravity (von Zeipel 1924) meaning that there is an excess of flux along the polar axis and a deficiency close to the equatorial plane. This imbalance triggers global circulation motions called meridional circulation. Such currents, which are advective, contribute to the transport of angular momentum and chemical elements in rotating stars. In differentially rotating stars, because the stellar layers have different angular velocities, shear instabilities arise and also contribute (in a diffusive way) to the transport of angular momentum and chemical elements.

Transport of angular momentum

In the radial direction, the transport of angular momentum obeys the advective-diffusive equation (Chaboyer & Zahn 1992)

$$\rho \frac{d}{dt} (r^2 \bar{\Omega})_{M_r} = \underbrace{\frac{1}{5r^2} \frac{\partial}{\partial r} (\rho r^2 U(r) \bar{\Omega})}_{\text{advection}} + \underbrace{\frac{1}{r^2} \frac{\partial}{\partial r} \left(\rho r^4 D \frac{\partial \bar{\Omega}}{\partial r} \right)}_{\text{diffusion}} \quad (3.6)$$

where $\bar{\Omega}$ is the angular velocity of a shell, ρ the density, D the total diffusion coefficient, taking into account the various instabilities transporting angular momentum (especially convection and shear turbulence) and $U(r)$ the amplitude of the radial component of the meridional velocity (Maeder & Zahn 1998). A large³ $|U(r)|$ implies an efficient transport of angular momentum in the radial

³ $U(r)$ can be positive or negative. Here the absolute value is considered.

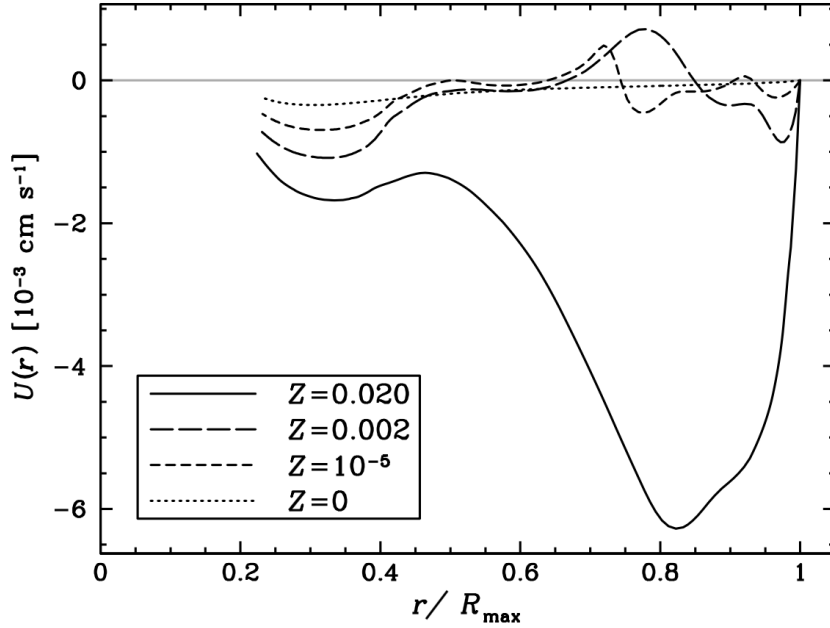


Figure 3.4: Internal profile of the amplitude of the radial component of the meridional velocity $U(r)$ in rotating $20 M_{\odot}$ models with various metallicities. The radius is normalized to the total radius R_{\max} . For all the models, the central H mass fraction is about 0.40 (figure from Ekström et al. 2008).

direction. $U(r)$ scales with E_{Ω} , a term of particular importance in the expression of $U(r)$ and that can be approximated by

$$E_{\Omega} \simeq \frac{8}{3} \left[1 - \frac{\Omega^2}{2\pi G \bar{\rho}} \right] \left(\frac{\Omega^2 r^3}{GM_r} \right). \quad (3.7)$$

The second term in brackets is the Gratton-Öpik term. In the outer layers of stars, the density $\bar{\rho}$ is small so that E_{Ω} , hence $U(r)$, can become largely negative (see solid line in Fig. 3.4). It contributes to redistribute efficiently the angular momentum and therefore smooth the Ω -profile.

Low metallicity stars contain less metals so they are less opaque and therefore more compact. Consequently, $\bar{\rho}$ is larger so that the Gratton-Öpik term is generally smaller. This reduces $U(r)$ (see Fig. 3.4), meaning that the angular momentum is less redistributed inside the star. It leads to steeper internal Ω -profiles. This tends to produce larger Ω -gradients which lead to stronger shear instabilities and then to a more efficient shear mixing.

Transport of chemical elements

Chaboyer & Zahn (1992) have shown that for chemical elements, the combination of meridional circulation and horizontal turbulence can be described by a pure diffusive process. The associated diffusion coefficient is

$$D_{\text{eff}} = \frac{1}{30} \frac{|rU(r)|^2}{D_h} \quad (3.8)$$

with D_h the horizontal (i.e. on an isobaric surface) shear diffusion coefficient from Zahn (1992). It is written as $D_h = c_h^{-1} r |2V - \alpha U(r)|$ with $\alpha = \frac{1}{2} \frac{d \ln(r^2 \Omega)}{d \ln r}$ and $c_h = 1$. As a consequence, in contrast with the angular momentum transport equation (Eq. 3.6), the equation for the change of abundance of a given chemical element i in a given shell at coordinate r is a pure diffusive equation:

$$\rho \frac{dX_i}{dt} = \frac{1}{r^2} \frac{\partial}{\partial r} \left[\rho r^2 (D + D_{\text{eff}}) \frac{\partial X_i}{\partial r} \right] + \left(\frac{dX_i}{dt} \right)_{\text{nucl}}. \quad (3.9)$$

The last term accounts for the changes due to the nuclear reactions (cf. Sect. 3.3.3). In radiative zones, $D = D_{\text{shear}}$ with D_{shear} the diffusion coefficient accounting for the shear instabilities. Several prescriptions exist in the literature (Maeder 1997; Talon & Zahn 1997; Maeder et al. 2013). The one used in this work is from Talon & Zahn (1997). It can be expressed as

$$D_{\text{shear}}^{\text{TZ97}} = f_{\text{energ}} \frac{H_p}{g\delta} \frac{K + D_h}{(\nabla_{\text{ad}} - \nabla) + \frac{\epsilon}{\delta} \nabla_{\mu} \left(\frac{K}{D_h} + 1 \right)} \left(\frac{9\pi}{32} \Omega \frac{d \ln \Omega}{d \ln r} \right)^2 \quad (3.10)$$

where K is the thermal diffusivity, and $f_{\text{energ}} = 2Ri_c$ with Ri_c the critical Richardson number below which the medium becomes dynamically unstable and turbulent. Although the canonical value for Ri_c is 1/4 some works have shown that turbulence may happen for larger Richardson number. Canuto (2002) has shown that turbulence may arise for $Ri \leq Ri_c \sim 1$. Brüggem & Hillebrandt (2001) have done numerical simulations suggesting that shear mixing occurs already at $Ri \sim 1.5$. The physical range of values may be around $0.25 < Ri_c < 2$, corresponding to $0.5 < f_{\text{energ}} < 4$.

I computed two $15 M_{\odot}$ models at solar metallicity with $v_{\text{ini}} = 300 \text{ km s}^{-1}$ and with $f_{\text{energ}} = 1$ and 4. At core H depletion, the surface N/H ratios are enhanced by a factor of 2 ($f_{\text{energ}} = 1$) and 3 ($f_{\text{energ}} = 4$) compared to the initial surface N/H ratio. Such surface enrichments qualitatively agree with observation of $10-20 M_{\odot}$ rotating stars (e.g. Gies & Lambert 1992; Villamariz & Herrero 2005; Hunter et al. 2009). In this work, except stated explicitly, $f_{\text{energ}} = 4$. The effect of f_{energ} on the internal mixing of low metallicity massive stars is investigated in Sect. 4.3.3.

A comparison of 3 different prescriptions for the shear mixing

Although not used in the present work, I have included in GENEC the global diffusion coefficient proposed by Maeder et al. (2013), taking into account different instabilities together and their possible interaction (see Appendix A.2 for calculation details).

Fig. 3.5 shows the tracks of $20 M_{\odot}$ models with $v_{\text{ini}}/v_{\text{crit}} = 0.4$, $Z = 10^{-5}$ and computed with various D_{shear} coefficients: from Maeder (1997), from Talon & Zahn (1997) and the global coefficient from Maeder et al. (2013). The new coefficient $D_{\text{global}}^{\text{M13}}$ combining the different instabilities leads to a bluer and more luminous evolution, characteristic of stars experiencing a high degree of mixing. The surface ${}^4\text{He}$ mass fraction at the end of the main sequence is the highest in the $D_{\text{global}}^{\text{M13}}$ model (0.56 against 0.25 and 0.31 for the $D_{\text{shear}}^{\text{TZ97}}$ and $D_{\text{shear}}^{\text{M97}}$ models, respectively), which is also a signature of an efficient rotational mixing. An estimation of the mixing efficiency in the deep stellar interior can be obtained with the amount of central ${}^{22}\text{Ne}$ after the main sequence (more details in Sect. 4.1). ${}^{22}\text{Ne}$ in the center reaches a much higher mass fraction in the $D_{\text{shear}}^{\text{TZ97}}$ and $D_{\text{global}}^{\text{M13}}$ models. It suggests that, after the main sequence, a more efficient mixing in the deep interior is at work in these two models compared to the $D_{\text{shear}}^{\text{M97}}$ model. The efficiency of the s-process in massive stars is impacted by the amount of ${}^{22}\text{Ne}$ (main neutron source, cf. Sect. 3.1.2). From Fig. 3.5, we see that the s-process should operate similarly in the $D_{\text{shear}}^{\text{TZ97}}$ and $D_{\text{global}}^{\text{M13}}$ because of the similar ${}^{22}\text{Ne}$ content. On the opposite, the $D_{\text{shear}}^{\text{M97}}$ model predicts a less efficient operation of the s-process.

The dashed track in Fig. 3.5 shows the main sequence of the $D_{\text{shear}}^{\text{TZ97}}$ model but with $f_{\text{energ}} = 40$ instead of 4. In this case, the track is rather close to the track of the model with the global diffusion coefficient. A higher f_{energ} value for the $D_{\text{shear}}^{\text{TZ97}}$ model may mimic the more complex physics contained in the $D_{\text{global}}^{\text{M13}}$ coefficient. It shows that finally, even if $f_{\text{energ}} = 4$ was proposed as a possible upper limit for the D_{shear} of Talon & Zahn (1997), a higher f_{energ} (i.e. higher mixing efficiency) probably cannot be excluded.

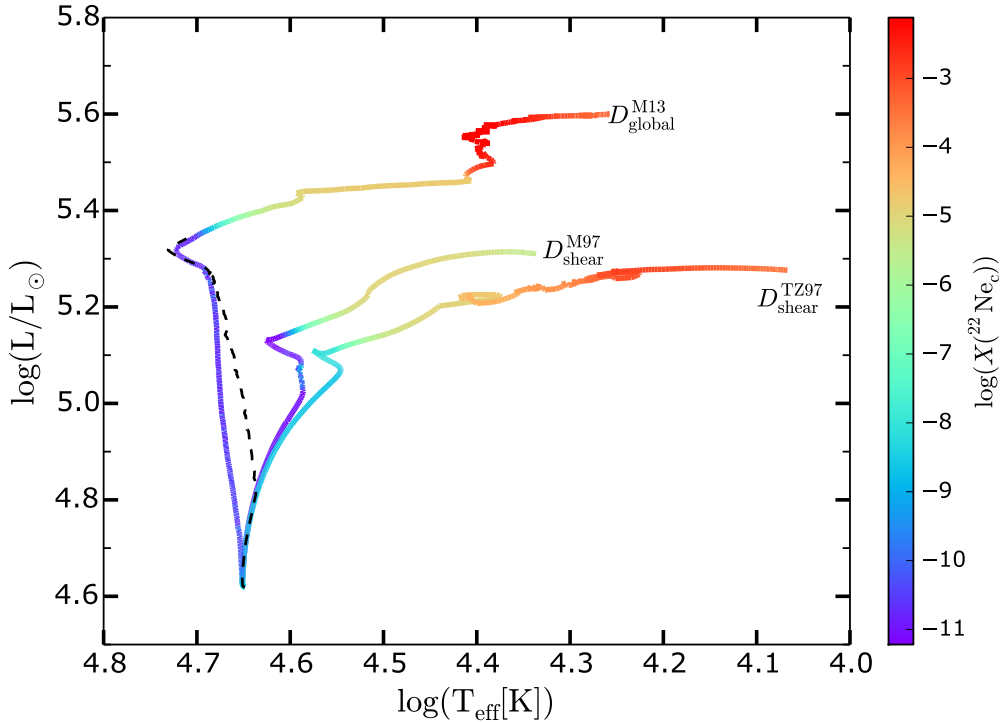


Figure 3.5: Hertzsprung-Russell (HR) diagram of a $20 M_{\odot}$ model with $Z = 10^{-5}$ and $v_{\text{ini}}/v_{\text{crit}} = 0.4$ with different D_{shear} coefficients. The color shows the central mass fraction of ^{22}Ne . The dashed black track is computed with the same physics as the $D_{\text{shear}}^{\text{TZ97}}$ model but with the D_{shear} coefficient multiplied by 10. The 3 colored models are computed until the end of the core helium burning phase. The dashed model is computed until the end of the main sequence.

3.3.2 Convection

In a star, a heat excess with respect to what radiation can transfer drives turbulent convective motions. It provides an additional and efficient way of transporting the energy. In this work, the Schwarzschild criterion is used to determine the stability of a given stellar layer.

In the interior of the Sun, the turnover timescale t_{turn} (timescale for an element of material to complete a loop in a convective cell) can be estimated using the mixing-length theory. It is about 0.5 yr (Maeder 2009), suggesting that chemical homogeneity is quickly reached in a convective zone. Since the lifetime of a star is much longer than the turnover timescale, the convective mixing can be considered as instantaneous during most of the stellar life. The last stages of massive stars (after central carbon burning) are however very short (less than 1 yr, e.g. Hirschi et al. 2004) so that the approximation of instantaneous convective mixing is no more valid. In this case, the convection is treated as a diffusive process.

During the H- and He-burning phases of the models computed in the present work, overshoot is considered: the size of the convective core is extended by $d_{\text{over}} = \alpha H_{\text{P}}$ where H_{P} is the pressure scale height and $\alpha = 0.1$ for initial masses above $1.7 M_{\odot}$. α was calibrated so as to reproduce the observed main-sequence width of stars with $1.35 < M < 9 M_{\odot}$ (Ekström et al. 2012).

3.3.3 Nuclear network

In a stellar evolution code, to follow the abundance changes due to nuclear reactions, one has to express the nuclear term in Eq. 3.9 (last term). It is written as

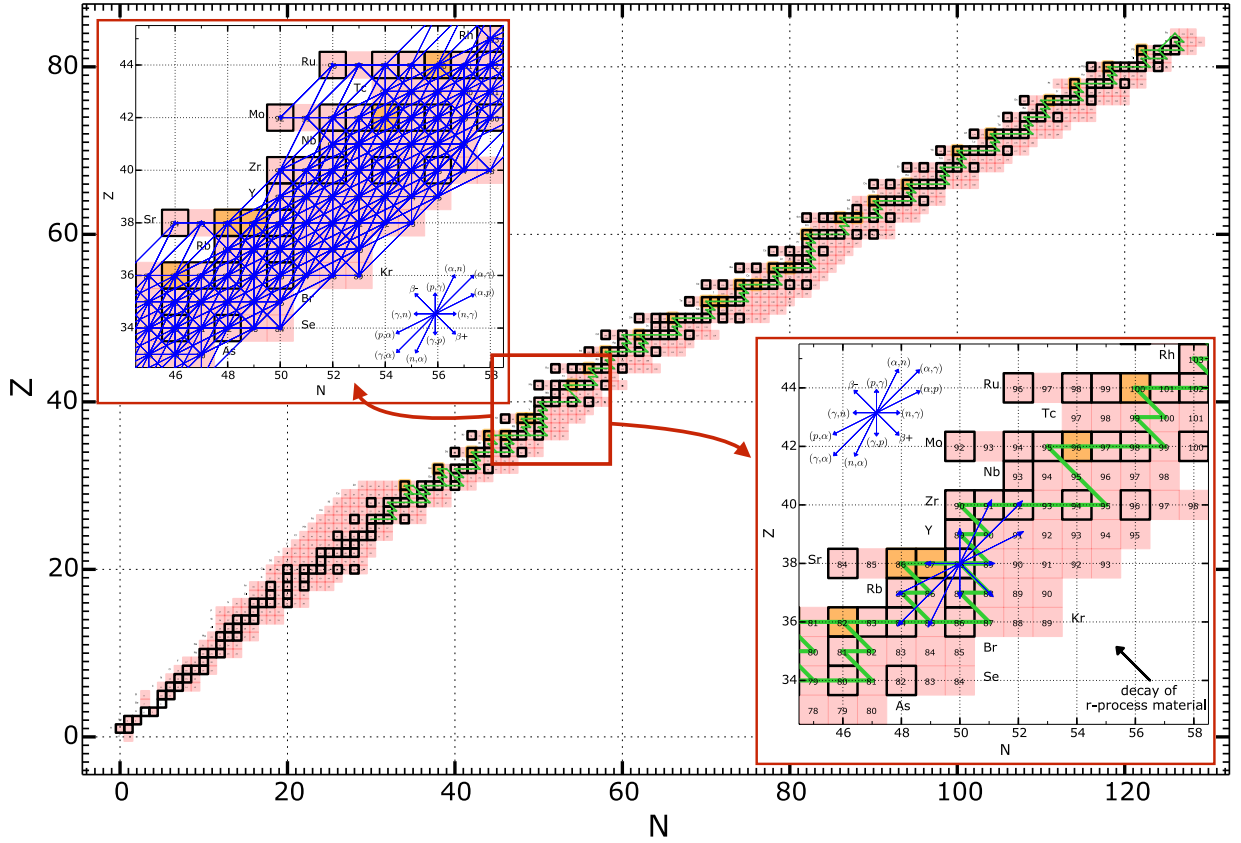


Figure 3.6: The red shaded squares show the 737 isotopes considered in the extended network used in this work (Chapter 5). The black squares show the stable isotopes. The green path shows the principal s-process path. *Lower right panel:* zoom on a specific region. Blue arrows show the nuclear reactions starting from ^{88}Sr . Orange squares denote stable isotopes that can be synthesized by the s-process (also by p-process, possibly) but not by the r-process. *Upper left panel:* blue segments show all reactions included in the extended network, from ^{78}As to ^{103}Rh .

$$\begin{aligned}
 \left(\frac{dX_i}{dt}\right)_{\text{nucl}} &= \underbrace{A_i \sum_j N_j^i \lambda_j \frac{X_j}{A_j}}_{\text{1-body reactions}} + \underbrace{A_i \sum_{j,k} \frac{1}{1 + \delta_{jk}} N_{j,k}^i \rho N_A \langle \sigma v \rangle_{j;k} f_{j;k}}_{\text{2-body reactions}} \frac{X_j X_k}{A_j A_k} \\
 &+ \underbrace{A_i \sum_{j,k,l} \frac{1}{1 + \Delta_{ijk}} N_{j,k,l}^i \rho^2 N_A^2 \langle \sigma v \rangle_{j;k;l} f_{j;k;l}}_{\text{3-body reactions}} \frac{X_j X_k X_l}{A_j A_k A_l}
 \end{aligned} \tag{3.11}$$

where A_i , A_j , A_k and A_l are the mass number of isotopes i , j , k and l , N_j^i , $N_{j,k}^i$ and $N_{j,k,l}^i$ are the number of particles of isotope i destroyed < 0 or produced > 0 in a particular reaction, $f_{j;k}$ and $f_{j;k;l}$ the screening factors, $\Delta_{ijk} = \delta_{jk} + \delta_{jl} + \delta_{kl} + 2\delta_{jkl}$ and δ 's are factors preventing double counting. 1-body reactions refer to photo-disintegrations, β -decays, ν^- , e^- and e^+ captures. λ_j , $\langle \sigma v \rangle_{j;k}$ and $\langle \sigma v \rangle_{j;k;l}$ are the nuclear reaction rates. These rates are estimated experimentally (e.g. Caughlan & Fowler 1988) or theoretically (e.g. Rauscher & Thielemann 2000) and tabulated over a certain range of temperature.

The set of differential equation 3.11 is called *stiff* because of the strong variety of reaction

timescales, ranging from fraction of seconds to Gyr. An explicit method is not possible to solve these equations because it would require extremely small timesteps in order to follow the fastest reactions. In the new version of GENEC, these equations are solved in a implicit manner by the backward Euler method⁴.

In Chapter 4 of this work, I rely on models computed with a small nuclear network, that follows 31 species in total: n , ^1H , $^3,^4\text{He}$, $^{12,13,14}\text{C}$, $^{14,15}\text{N}$, $^{16,17,18}\text{O}$, $^{18,19}\text{F}$, $^{20,21,22}\text{Ne}$, ^{23}Na , $^{24,25,26}\text{Mg}$, $^{26,27}\text{Al}$, ^{28}Si , ^{32}S , ^{36}Ar , ^{40}Ca , ^{44}Ti , ^{48}Cr , ^{52}Fe and ^{56}Ni . It allows to track the reactions that contribute significantly to generate nuclear energy. This network is also enough to follow the nucleosynthesis of the main species beyond Fe until the ultimate stages of evolution. Finally, this network is well suited for investigating the origin of CEMP-no stars since such stars do not show strong overabundances in heavy elements. In Chapter 5 instead, a network of 737 isotopes is considered, from ^1H to ^{212}Po (Fig. 3.6), that allows to follow the full s-process nucleosynthesis. Some of the reactions linking the isotopes are shown by the blue segment in Fig. 3.6. The nucleosynthesis is followed thanks to the BasNet code (Basel Network, Arnett & Thielemann 1985; Thielemann & Arnett 1985) which is coupled to GENEC⁵. It allows to follow consistently all the nucleosynthesis during the entire evolution.

3.3.4 Initial composition and opacity tables

In this work, the initial composition of the low metallicity massive source stars is taken α -enhanced. Details are given below. In GENEC, the initial abundances are in mass fraction. The solar mass fraction $X_{i,\odot}$ of an isotope i , associated to an element e can be written as

$$X_{i,\odot} = 10^{\log \epsilon_{e,\odot} - 12} f_i A_i X_{\text{H},\odot} \quad (3.12)$$

where $\log \epsilon_{e,\odot}$ is the solar abundance of element e taken from Asplund et al. (2005), except for Ne, which is from Cunha et al. (2006). f_i is the isotopic fraction in the solar system (Lodders 2003). A_i is the mass number of isotope i and $X_{\text{H},\odot} = 0.7399$ is the solar hydrogen mass fraction, at the present day and corresponding to the Asplund+Cunha mixture. As a remark, since the Sun is 4.57 Gyr old, it has likely experienced atomic diffusion since its birth. Atomic diffusion progressively decreases the surface helium and increases the surface hydrogen. Then, the initial solar abundances are different than the present-day abundances. Ekström et al. (2012) have calibrated a $1 M_\odot$ model including atomic diffusion to reproduce the solar radius, luminosity and surface chemical composition at the age of the Sun. It gives an initial hydrogen and helium mass fraction of 0.720 and 0.266 respectively. The associated initial solar metallicity is $Z_\odot = 0.014$.

In case the initial metallicity Z of the model is not solar, X_{He} is calculated according to the relation $X_{\text{He}} = X_{\text{He,p}} + \Delta X_{\text{He}}/\Delta Z \times Z$ where $X_{\text{He,p}}$ is the primordial helium abundance and $\Delta X_{\text{He}}/\Delta Z = (X_{\text{He},\odot} - X_{\text{He,p}})/Z_\odot$ the average slope of the helium-to-metal enrichment law. I set $X_{\text{He,p}} = 0.2484$ (Cyburt et al. 2003). Once the helium mass fraction is calculated, the initial hydrogen mass fraction is deduced from $X_{\text{H}} = 1 - X_{\text{He}} - Z$.

When Z is not solar, if the mixture of metal remains solar-like, the mass fractions of metals are just multiplied by Z/Z_\odot i.e. $X_i = X_{i,\odot} Z/Z_\odot$ with $X_{i,\odot}$ from Eq. 3.12. This leads to a solar-scaled mixture, meaning that $[X/\text{Fe}] = 0$. However, at $[\text{Fe}/\text{H}] < 0$, it appears that $[\alpha/\text{Fe}] > 0$ where α represent the α -elements (e.g. Reddy et al. 2006). In GENEC, for $-1 < [\text{Fe}/\text{H}] < 0$, $[\alpha/\text{Fe}] = -B_\alpha [\text{Fe}/\text{H}]$ with $B_\alpha = 0.562, 0.886, 0.500, 0.411, 0.307, 0.435, 0.300, 0.222$ and 0.251 for the α -elements ^{12}C , ^{16}O , ^{20}Ne , ^{24}Mg , ^{28}Si , ^{32}S , ^{36}Ar , ^{40}Ca and ^{48}Ti respectively. These numbers were derived by fitting the abundance trends $[\alpha/\text{Fe}]$ versus $[\text{Fe}/\text{H}]$ from halo and thick disc F- and G-dwarfs stars with $-1 \lesssim [\text{Fe}/\text{H}] \lesssim 0$ (Reddy et al. 2006). At $[\text{Fe}/\text{H}] < -1$, $[\alpha/\text{Fe}] = B_\alpha$ is set (i.e.

⁴Details can be found in the Sect. 3.5 of Frischknecht, PhD thesis (2012, <https://edoc.unibas.ch/21287/>).

⁵Details can be found in the Sect. 3.7 of Frischknecht, PhD thesis (2012, <https://edoc.unibas.ch/21287/>).

no dependance on metallicity). The mass fractions of the α -isotopes are calculated according to

$$X_{i,\alpha} = X_{i,\odot} \frac{X_{\text{Fe}}}{X_{\text{Fe},\odot}} 10^{B_\alpha} f_i A_i \quad (3.13)$$

where X_{Fe} is the sum of the mass fractions of all Fe isotopes. The mass fraction of the non α -isotopes are calculated with the same equation but with $B_\alpha = 0$. Accordingly to this α -enhanced mixture, the opacity tables were computed with the OPAL tool⁶. They are complemented at low temperatures by the opacities from Ferguson et al. (2005).

In general, at low metallicity, the initial mixture is poorly known and other initial mixtures cannot be excluded. An α -enhanced mixture may be the most natural choice. However, it is worth noting that for most of the elements and low-metallicity models considered in this work, the abundances in the ejecta of the massive star models are very different from the initial ones. It implies that the dependance of the chemical yields on the initial composition is weak.

Also worth to mention is that with Galactic chemical evolution models, Chiappini et al. (2008) have shown that if massive fast rotators were common in the early Universe, $^{12}\text{C}/^{13}\text{C}$ would be between about 30 and 300 in the (almost) primordial ISM. Without fast rotators, $^{12}\text{C}/^{13}\text{C}$ would be between about 4500 and 31000. Here I take $^{12}\text{C}/^{13}\text{C} = 300$. Lower or higher values cannot be excluded. This is discussed in the next chapters.

3.3.5 Mass loss

AGB and massive stars show spectroscopic evidences of stellar winds (Kudritzki & Puls 2000, for a review). Stellar winds are mainly driven by the absorption of UV-photons by metal lines. Winds are consequently stronger in hot metal-rich stars. The radiation pressure expels stellar material. It can make a $120 M_\odot$ solar metallicity star losing more than 70 % of its initial mass (Ekström et al. 2012). At low metallicity, radiative winds are weaker because of the smaller content in metals. Radiative mass loss rates follow a scaling relation with metallicity Z :

$$\dot{M}(Z) = \left(\frac{Z}{Z_\odot} \right)^a \dot{M}(Z_\odot) \quad (3.14)$$

where $\dot{M}(Z_\odot)$ is the solar metallicity mass loss rate and $0.5 < a < 0.85$ (Vink et al. 2001). In this work, radiative mass-loss rates are from Vink et al. (2001) when $\log(T_{\text{eff}}) \geq 3.95$ and from de Jager et al. (1988) when $\log(T_{\text{eff}}) < 3.95$. For the models of Sect. 4.5.2 however, the prescription of Kudritzki & Puls (2000) is used instead of Vink et al. (2001). Radiative winds at low metallicity are generally small so that no big impact is expected. Also, for $\log(T_{\text{eff}}) < 3.95$, de Jager et al. (1988) is used in any case.

The stellar surface can also reach the Eddington luminosity L_{EDD} (luminosity when the radiative force balances the gravitational force) which triggers additional mass loss. In GENE, the mass-loss rate is increased by a factor of 3 when the luminosity of any layer in the stellar envelope becomes higher than five times the Eddington luminosity (Ekström et al. 2012).

Another recent mass loss mechanism was proposed for metal-free stars with $M_{\text{ini}} \geq 150 M_\odot$ (Moriya & Langer 2015): if $\log(T_{\text{eff}}) < 3.7$ the envelope of such stars may become pulsationally unstable near the end of their evolution and undergo extreme mass-loss events, of the order of $10^{-4} - 10^{-2} M_\odot \text{ yr}^{-1}$. Although not used in the models of this work, I have added this prescription in GENE (details in Appendix A.3).

Effect of rotation on mass loss

Rotation is expected to affect the mass loss of stars. First, it makes the stellar winds anisotropic by favoring an ejection of matter through both the poles and the equator (Maeder 1999). The

⁶<http://opalopacity.llnl.gov>.

reason is that the polar regions are hotter than the equatorial regions (cf. Sect. 3.3.1) so that the radiation pressure, hence the mass loss rate is stronger at the poles. Also, for stars with equatorial temperatures $T \lesssim 23000$ K (rotation tends to reduce the temperature at the equator), the high opacity around the equator triggers enhanced radiative winds that push the matter outward and produce an equatorial ring.

When the stellar surface reaches the critical velocity, the outer layers are no longer bound and some mass is removed mechanically. In rotating stars having an Eddington factor $\Gamma = L/L_{\text{EDD}} > 0.639$, because of the interplay between radiation and rotation, the critical velocity is reduced (Maeder & Meynet 2000). The consequence is that mechanical mass loss occurs more easily (i.e. at a smaller rotation rate). Mechanical mass losses on the rotating massive Pop III models of Ekström (2008) removes < 10 % of the total stellar mass.

More generally, if considering 2 stars of same mass M , one rotating at Ω and one non-rotating, at about the same location in the HR diagram, the mass loss ratio $\dot{M}(\Omega)/\dot{M}(0)$ is greater than one and depends, among other, on Ω and Γ (Maeder & Meynet 2000). Models including rotation are corrected by this factor, that becomes very high for large Γ factors.

Also, by changing the distribution of the chemical species in the stellar interior, rotation modifies the tracks in the HR diagram. Since radiative mass loss rates depend on L and T_{eff} , the mass loss experienced by the star is changed. For instance, rotation tends to produce bigger cores, increasing the luminosity L of the star hence increasing the mass loss rate \dot{M} , that varies as $L^{2.2}$ (Vink et al. 2001).

Fast rotation may also induce extreme radiative winds during the core He-burning stage of very low massive metallicity stars. It occurs if a large amount of metals from the stellar interior is brought up to the surface. In this case, the surface metallicity increases dramatically so that strong radiative winds are triggered (Eq. 3.14). It can make a very low metallicity ($Z = 10^{-8}$) massive star to lose about 70 % of its mass (Hirschi 2007). Such strong mass loss episodes are however not happening in all low/zero metallicity rotating models (Hirschi 2007; Ekström et al. 2008) and are sensitive to different parameters (see Sect. 4.8 for additional discussions).

3.3.6 Chemical composition of the ejecta

For a stellar model, the ejected mass m_i^{ej} in M_{\odot} under the form of an isotope i is given by

$$m_i^{\text{ej}} = \underbrace{\int_0^{\tau} \dot{M}(t) X_{i,s}(t) dt}_{\text{wind contribution}} + \underbrace{\int_{M_{\text{cut}}}^{M_{\text{fin}}} X_i(M_r) dM_r}_{\text{supernova contribution}}, \quad (3.15)$$

where the bounds τ , M_{fin} , and M_{cut} are the total lifetime, mass at the end of the evolution and mass cut⁷ of the model, respectively. $X_{i,s}(t)$ and $\dot{M}(t)$ are the surface mass fraction and the mass loss rate at time t respectively. $X_i(M_r)$ is the mass fraction of the isotope i at coordinate M_r , at the end of the evolution. From Eq. 3.15 and knowing the solar composition, the $[X/Y]$ ratios in the ejected material can be computed⁸.

The stellar yield of an isotope i is expressed as

$$m_i = \underbrace{\int_0^{\tau} \dot{M}(t) (X_{i,s}(t) - X_{i,0}) dt}_{\text{wind contribution}} + \underbrace{\int_{M_{\text{cut}}}^{M_{\text{fin}}} (X_i(M_r) - X_{i,0}) dM_r}_{\text{supernova contribution}}, \quad (3.16)$$

⁷At the end of the evolution, the mass cut is the mass coordinate that delimitates the part of the star which is expelled from the part which is kept into the remnant.

⁸In the bracket notation, X and Y are in number so that the mass ejected m_i^{ej} of an isotope i has to be divided by its atomic mass A_i . For instance, $[C/H] = \log \left(\frac{m_{12C}^{\text{ej}}/12 + m_{13C}^{\text{ej}}/13}{m_{1H}^{\text{ej}}} \right) - \log \left(\frac{C}{H} \right)_{\odot}$.

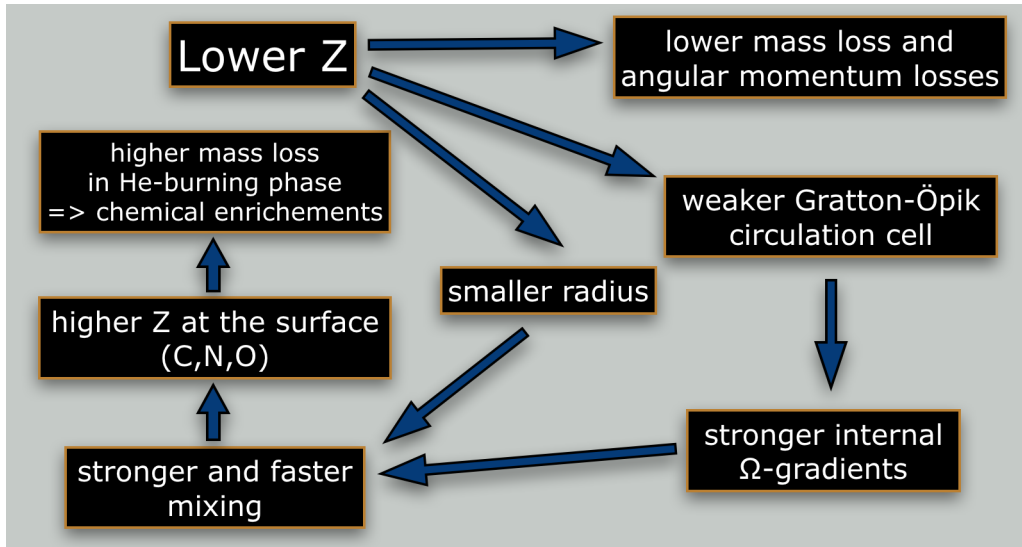


Figure 3.7: Some important effects of rotation at low metallicity (adapted from Maeder 2009).

with $X_{i,0}$ the initial mass fraction of isotope i . The only difference with Eq. 3.15 is that the mass under the form of the isotope i that was initially present in the star is deduced. Hence, m_i can be either positive or negative.

Finally, for an isotope i , the production factor f_i is defined as

$$f_i = \frac{M_{ej} X_{i,ej}}{M_{ini} X_{i,0}}, \quad (3.17)$$

with M_{ej} the total mass ejected by the star, M_{ini} the initial mass and $X_{i,ej}$ the mass fraction of isotope i in the ejecta. It expresses, for a given isotope, the ratio of what is given back by the star divided by what was present initially in the whole star.

3.4 Axions and their impact on Pop III stars

This section presents a side project of the thesis, related to the evolution of metal-free massive stars including axion cooling. Axions are hypothetical elementary particles that are of interest as possible components of cold dark matter (Preskill et al. 1983; Abbott & Sikivie 1983; Dine & Fischler 1983). They interact weakly with matter. In stars, they can be considered as an energy sink, taking away the energy, like neutrinos. An axion loss rate as a function of the stellar temperature and density can be derived and introduced in stellar evolution codes in order to see how such losses affect the life of stars. Friedland et al. (2013) found that axion losses can shorten and eliminate the blue loop phase of solar metallicity $8 - 12 M_{\odot}$ stars.

In collaboration with Alain Coc (Centre de Sciences Nucléaires et de Sciences de la Matière (CSNSM), France), Keith A. Olive (William I. Fine Theoretical Physics Institute, School of Physics and Astronomy, University of Minnesota, USA), Jean-Philippe Uzan and Elisabeth Vangioni (Institut d’Astrophysique de Paris (IAP), France), I have studied the effects of axions on Pop III stars in the article (the full paper can be found page 149 of this thesis):

Effects of axions on Population III stars

A. Choplin, A. Coc, G. Meynet, K. A. Olive, J.-P. Uzan & E. Vangioni, 2017 *A&A* **605**, 106

First, I introduced the axion losses ϵ_{ax} in GENEC. The derivatives of ϵ_{ax} as a function of the pressure P and temperature T were also introduced in GENEC so as to help for convergence when

solving the structure equations (see Appendix A.1 for more details and calculations). Then, I computed a grid of non-rotating Pop III massive stars with initial masses of 20, 25, 32, 40, 60, 85, 120 and 150 M_{\odot} , with and without axion losses, until the end of the core C-burning phase.

During the main sequence, the energy is mainly transported by radiation and convection. Axion losses have a modest effect: the main sequence lifetime is shortened by less than 3 % in models including axions. Although still modest, axion losses are stronger during the core He-burning stage, because of higher temperature. Consequently, the core He-burning lifetime is reduced by 7 – 10 %. The phase from core He depletion to core C-burning ignition lasts for $10^3 - 10^4$ yr. During this phase, the carbon-oxygen core contracts so that the central temperature increases and axion losses become important. Neutrino losses are not strong yet. This is during this short axion-dominated phase that axions are likely inducing the most significant changes in the evolution. From core C-burning ignition to the end of the evolution, axion losses become negligible compared to neutrino losses so that stellar evolution is no more altered.

We found that globally, the effects of axions on stellar evolution are very modest and will be very hardly observable. The strongest effect of axions arises in the 85 and 120 M_{\odot} models. Differences in central temperature, density and chemical composition appear after core He depletion, for a short period of time, as a transitory reaction of the model to the increased loss of energy in the central regions (cf. previous discussion). Such differences might prevent the 85 and 120 M_{\odot} models with axion losses to experience a pulsational pair-instability supernova (PPISN), as it may be expected for stars with initial masses between 70 and 140 M_{\odot} (Woosley 2017). If so, such stars with axions could produce black holes in a mass range where standard stellar models do not predict them. It might induce a potential signature in gravitational waves. As discussed in the paper, however, the uncertainties of different stellar model parameters produce effects at least as strong as axions on the structure of the star, particularly during the late evolution stages. We are therefore still far from a situation where Pop III stellar models can be used as a physics laboratory to verify the presence of axions or constrain their properties.

3.5 Summary

A quick summary of nucleosynthesis, modeling and theoretical aspects important for what follows is given. In the H-burning region of massive stars, the operation of the CNO cycle, Ne-Na and Mg-Al-Si chains can synthesize elements from C to Si. The ^{14}N transformed in ^{22}Ne at the core He-burning ignition will later (when the central temperature $T > 220$ MK) provides free neutrons. It leads to the principal component of the *weak* s-process in massive stars (the other and smaller component comes from the C-burning shell), able to synthesize elements with $A < 90$. Rotation-induced mixing provides additional ^{22}Ne , which can shift the s-process pattern towards heavier elements. Among others light elements, ^{16}O , which is abundant in the He-burning core, can poison the s-process by capturing neutrons. The *main* s-process, responsible for elements with $90 < A < 209$ is associated with thermally pulsing AGB stars, having initial masses between about 1 and 8 M_{\odot} .

Some important physical ingredients were presented in Sect. 3.3 for the modeling of massive stars including rotation. At low metallicity, a natural effect of the physics of rotation in stars is that the rotation-induced mixing of chemical elements is more efficient. One reason is due to the less efficient redistribution of the angular momentum by meridional currents. Rotation enhances the mass loss in different ways, particularly because of the interplay of radiation and rotation. The mass loss is generally reduced at low metallicity but extreme mass loss events can nevertheless happen in fast rotating massive models (Fig. 3.7 for a schematic view). The nuclear network considered in this work comprises either 31 isotopes (Chapter 4) or 737, from ^1H to ^{212}Po (Chapter 5). While the small network is suitable for the study of CEMP-no stars, the second is required to study CEMP stars enriched in heavier elements like strontium or barium.

Mixing in CEMP-no source stars

In this chapter, the origin of the CEMP stars with $[\text{Fe}/\text{H}] < -3$ is investigated. The recognized CEMP-s, -r/s and -r stars are not considered. For convenience, the stars considered here are referred to as CEMP-no stars, even if strictly speaking, some of them are just CEMP (because of missing abundance data to classify them). Sections 4.2 and 4.5 include the results published in the first and second articles mentioned below, respectively (the full papers can be found page 159 and 176 of this thesis).

Constraints on CEMP-no progenitors from nuclear astrophysics

A. Choplin, A. Maeder, G. Meynet, & C. Chiappini, 2016 *A&A* **593**, 36

Pre-supernova mixing in CEMP-no source stars

A. Choplin, S. Ekström, G. Meynet, A. Maeder, C. Georgy, & R. Hirschi, 2017 *A&A* **605**, 63

4.1 The back-and-forth mixing process

In the previous chapter, some aspects regarding the nucleosynthesis and the physics of rotation were discussed. The interplay between rotation and nucleosynthesis in rotating massive stars is now discussed.

During the core H-burning and He-burning phase, the mixing induced by rotation changes the distribution of the chemical elements inside the star. In advanced stages (C-burning and after), the burning timescale becomes small compared to the rotational mixing timescale so that rotation barely affects the distribution of chemical elements. During the core He-burning phase, two different burning regions exist in the star (He-burning core and H-burning shell). The rotational mixing triggers exchanges of material between the convective He-burning core and the convective H-burning shell: He-burning products are transported to the H-burning shell, processed by H-burning, transported back to the He-burning core, etc... The main steps of this mixing process are (see Fig. 4.1 for a schematic view):

1. In the He-burning core, the triple alpha process synthesizes ^{12}C . ^{16}O is formed by $^{12}\text{C}(\alpha, \gamma)^{16}\text{O}$.
2. ^{12}C and ^{16}O are mixed into the H-burning shell. It boosts the CNO cycle and creates primary CNO elements, especially ^{14}N (and ^{13}C to a smaller extent).
3. The products of the H-burning shell (among them primary ^{13}C and ^{14}N) are mixed back into the He-core. From the primary ^{14}N , the reaction chain $^{14}\text{N}(\alpha, \gamma)^{18}\text{F}(e^+ \nu_e)^{18}\text{O}(\alpha, \gamma)^{22}\text{Ne}$ allows the synthesis of primary ^{22}Ne . The reactions $^{22}\text{Ne}(\alpha, n)$ and $^{22}\text{Ne}(\alpha, \gamma)$ make ^{25}Mg and

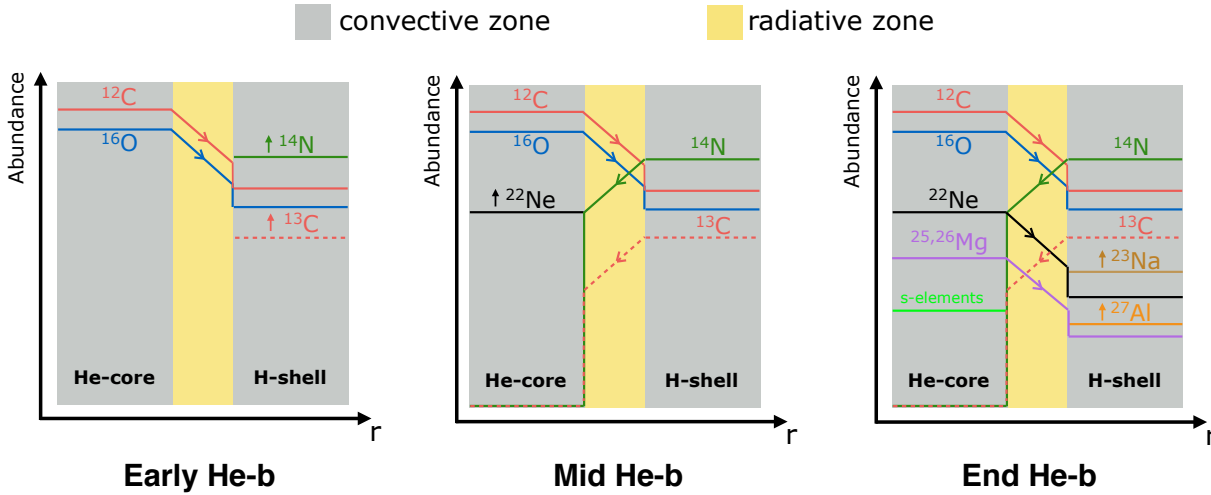


Figure 4.1: Schematic view of the back-and-forth mixing process at work in a fast rotating massive star (for clarity, only some chemical species are represented). The small vertical arrows denote some of the elements whose abundance is increased by the arrival of the products of the other burning zone.

^{26}Mg respectively. The neutrons released by the $^{22}\text{Ne}(\alpha, n)$ reaction produce ^{19}F , ^{23}Na , ^{24}Mg and ^{27}Al by $^{14}\text{N}(n, \gamma)^{15}\text{N}(\alpha, \gamma)^{19}\text{F}$, $^{22}\text{Ne}(n, \gamma)^{23}\text{Ne}(e^- \bar{\nu}_e)^{23}\text{Na}$, $^{23}\text{Na}(n, \gamma)^{24}\text{Na}(e^- \bar{\nu}_e)^{24}\text{Mg}$ and $^{26}\text{Mg}(n, \gamma)^{27}\text{Mg}(e^- \bar{\nu}_e)^{27}\text{Al}$, respectively. Free neutrons can also be captured by heavier seeds like ^{56}Fe and boost the s-process (cf. Sect. 3.1.2). This point is investigated in details in Chapter 5.

4. The newly formed elements in the He-burning core can be mixed again into the H-burning shell. It boosts the Ne-Na and Mg-Al chains: additional Na and Al are produced.

A very fast rotator will go through all the steps while a slow rotator only through the first one. An important effect (not shown in Fig. 4.1) is the growth of the convective He-burning core that helps reaching layers that had been previously enriched in H-burning products (e.g. ^{13}C , ^{14}N). Both the growing of the convective He core and the backward diffusion of chemical elements impact the nucleosynthesis in the He-burning core of rotating models.

Fig. 4.2 shows the results of this mixing process in a $20 M_{\odot}$ stellar model, when the central ^4He mass fraction is about 0.2. The ^{14}N and ^{13}C peaks can be seen and to a smaller extent, the ^{23}Na peak (at $M_r \sim 8 M_{\odot}$). In the He-core, ^{22}Ne has been enhanced because of the ingestion of the extra ^{14}N . Complete stellar models are discussed in more details in Sect. 4.3.

4.2 Nucleosynthesis in a box

Maeder et al. (2015) suggested that the wide range of abundances covered by CEMP-no stars could come from a material ejected by massive source stars having experienced various degree of rotational mixing. In this scenario, the variety of CEMP-no star abundances are mainly explained by the interplay between rotation and nucleosynthesis at work during the core He-burning phase of the massive source star (described in Sect. 4.1). Maeder & Meynet (2015) built a new classification scheme for CEMP-no stars by considering the successive steps in the back-and-forth mixing process. Five classes were proposed, the first one showing a complete absence of mixing and the fifth one a high degree of mixing (see Fig. 4.3). For instance, HE 1327-2326, with $[\text{Fe}/\text{H}] = -5.7$ (Frebel et al. 2008) and showing strong overabundances in light elements (e.g. CNO) as well as in

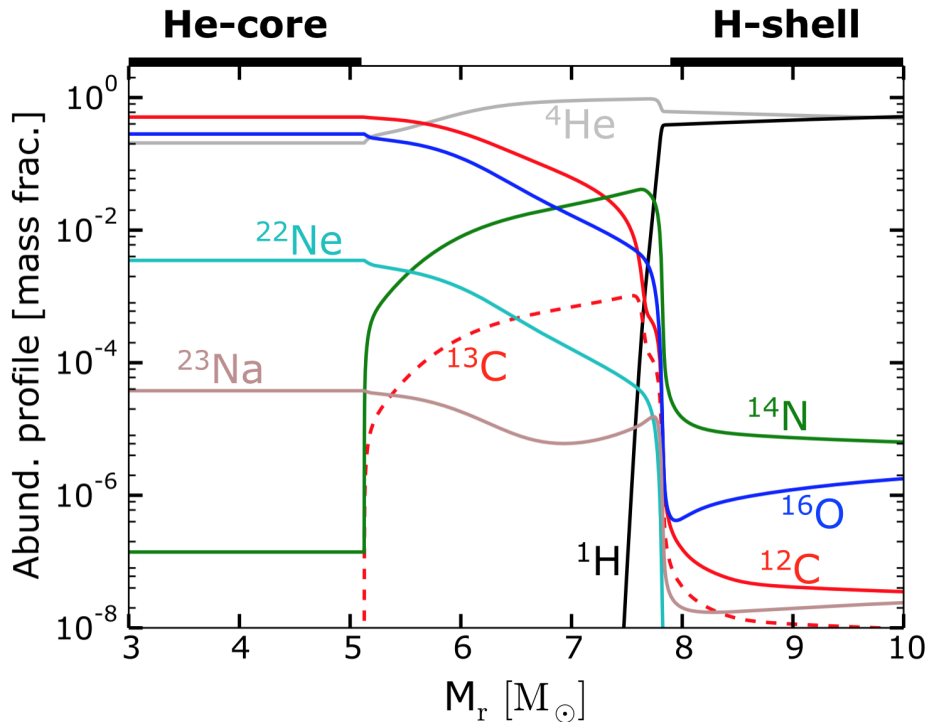


Figure 4.2: Abundance profile of a fast rotating $20 M_{\odot}$ model with $v_{\text{ini}}/v_{\text{crit}} = 0.7$ at $Z = 10^{-5}$. The model is near the end of the core He-burning stage. The thick black lines on the top labelled He-core and H-shell show the location of the convective He-burning core and H-burning shell respectively.

strontium, is belonging to class 4. In Maeder & Meynet (2015), they considered 46 stars, 4 appeared to be of class 2, 17 of class 3, 9 of class 4 and 16 unclassified because of missing abundance data. No star belonging to class 0 or 1 were found.

In Choplin et al. (2016), we aimed at investigating quantitatively the effect of the back-and-forth mixing process using a one-zone (or box) nucleosynthesis code I developed. This code allows the injection of chemical species in the box while nucleosynthesis is calculated. It mimics the effect of rotational mixing at work in complete rotating stellar models. In the paper, I used the one-zone code to mimic the hydrogen burning shell of a massive rotating star in which ^{12}C , ^{16}O , ^{22}Ne , and ^{26}Mg are injected (these species are supposed to come from the He-burning core of the rotating massive star). We studied the nucleosynthesis of the CNO cycle and the Ne-Na Mg-Al chains at different temperatures, densities, and with different nuclear reaction rates while injecting chemical species.

Initial setup

For the initial composition of the box, a rotating $60 M_{\odot}$ model is used, with $Z = 10^{-5}$ (corresponding to $[\text{Fe}/\text{H}] = -3.8$) and computed with an α -enhanced mixture. The initial abundances in the box are taken from the H-burning shell of this stellar model, when it starts the core He-burning stage (central ^4He mass fraction equals to 0.98). The corresponding initial $[\text{X}/\text{Fe}]$ ratios in the box are shown in Fig. 4.4 by the patterns with squares. The initial composition of the box is different than the initial composition of the stellar model since some nuclear burning has already operated in the stellar model during the H-burning phase. In particular, CNO burning has operated (that mainly transforms C and O into N) explaining the high initial $[\text{N}/\text{Fe}]$ and lower $[\text{C}/\text{Fe}]$ and $[\text{O}/\text{Fe}]$ in the box. The nuclear reaction rates of the CNO cycle are from Angulo et al. (1999)

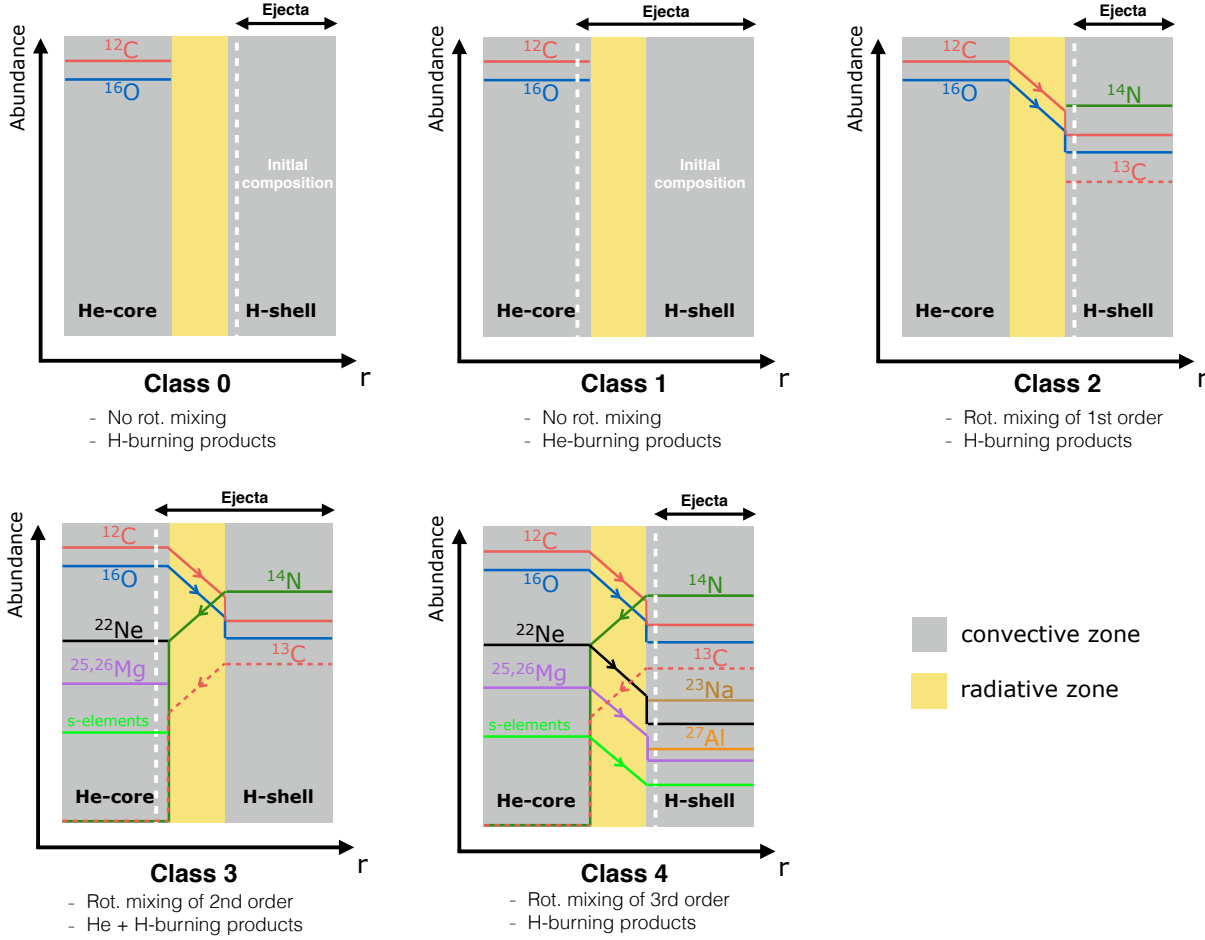


Figure 4.3: Five different possible chemical compositions of the CEMP-no source star at the end of the core He-burning phase. Each diagram corresponds to a different degree of mixing (top left: no mixing, bottom right: highest degree of mixing). The corresponding classes of CEMP-no stars are indicated, following the classification (simplified) of Maeder & Meynet (2015). *Ejecta* denotes the material that should be used to form the CEMP-no star.

except for $^{14}\text{N}(p, \gamma)^{15}\text{O}$ which is from Mukhamedzhanov et al. (2003) if $T \leq 0.1$ GK and Angulo et al. (1999) otherwise. The rates related to the Ne-Na and Mg-Al chains are from Iliadis et al. (2001). Only $^{20}\text{Ne}(p, \gamma)^{21}\text{Na}$ and $^{22}\text{Ne}(p, \gamma)^{23}\text{Na}$ are taken from Angulo et al. (1999) and Hale et al. (2002), respectively. For 20 – 60 M_{\odot} stellar models at such metallicity, $T \sim 50$ MK and $\rho \sim 1$ g cm^{-3} in the H-burning shell. There are the default temperature and density taken in the box. The box simulations are stopped either at H-exhaustion (^1H mass fraction is below 10^{-8}) or when the time exceeds 10 Myr.

Four separate injection experiments were carried out: (1) no injection, (2) injection of ^{12}C and ^{16}O , (3) injection of ^{12}C , ^{16}O and ^{22}Ne and (4) injection of ^{12}C , ^{16}O , ^{22}Ne and ^{26}Mg . The species are injected at a constant rate. During a time Δt , a mass $\Delta m_i = R_i \Delta t$ under the form of the isotope i is injected in the burning box. R_i is the injection rate of the isotope i expressed in $M_{\odot} \text{yr}^{-1}$. R_i was calibrated using results from complete stellar models. Details on this calibration are now given (see also the appendix of Choplin et al. 2016, page 176 of this thesis).

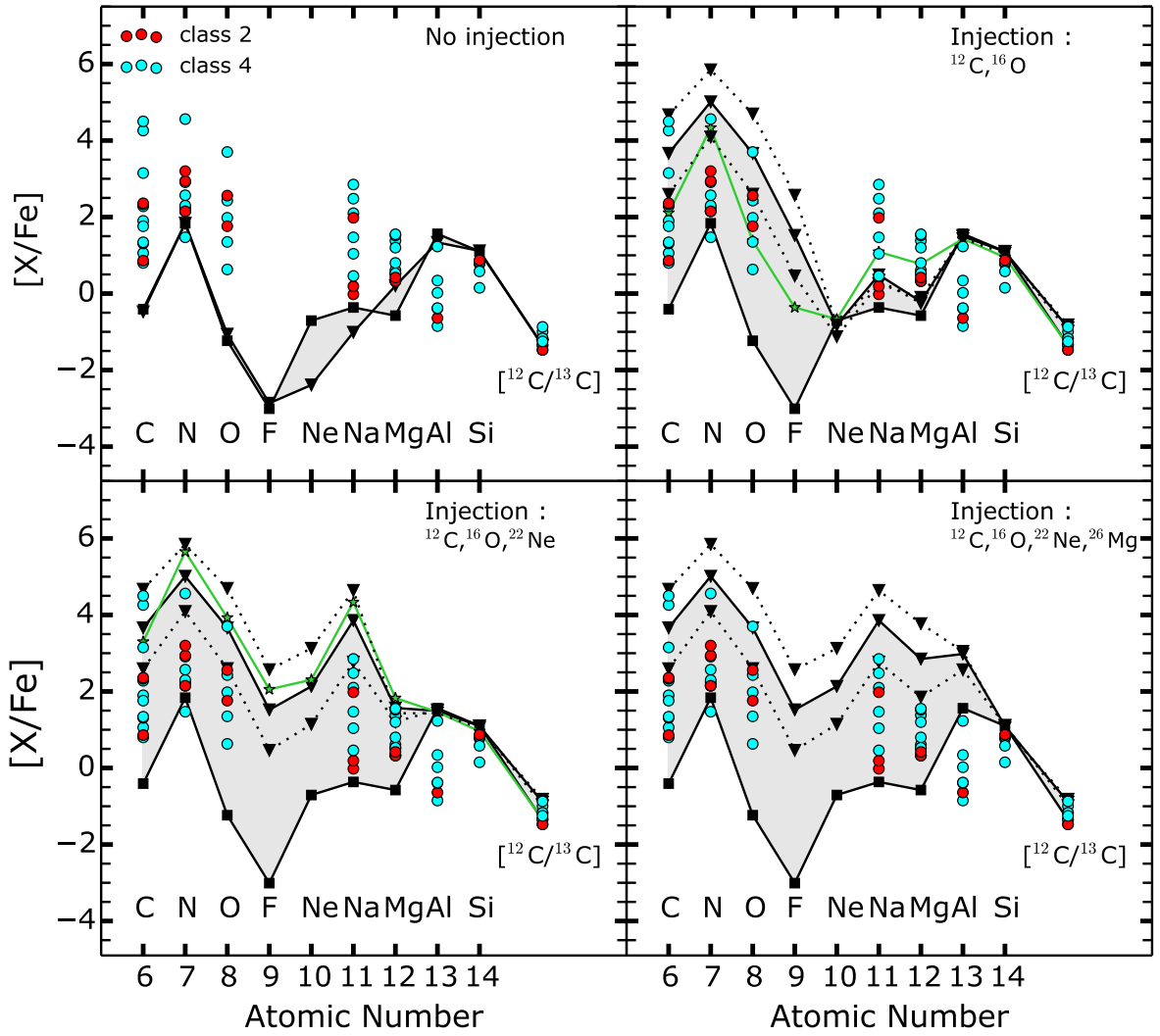


Figure 4.4: Composition of the box at H-exhaustion (or when the time t exceeds 10 Myr) for four injection cases. The density and temperature are $\rho = 1 \text{ g cm}^{-3}$ and $T_6 = 50 \text{ MK}$. The initial (final) composition is represented by black lines with squares (triangles). The lower (upper) black dotted lines represent the final composition when the rates of injection are divided (multiplied) by 100. The green pattern on the top right panel shows the composition in the H-burning shell at the end of the core He-burning phase of a $20 M_{\odot}$ stellar model with $v_{\text{ini}}/v_{\text{crit}} = 30 \%$. The green pattern on the bottom left panel shows the same stellar model but with $v_{\text{ini}}/v_{\text{crit}} = 70 \%$. The circles show observed CEMP-no stars of classes 2 and 4 (upper limits are excluded and the typical uncertainty is ± 0.3 dex).

Injection of chemical species

The rate $R_{12\text{C}}$ at which ^{12}C is injected in the box was calibrated by quantifying $M_{14\text{N}}^{\text{prim}}$ which is the mass of primary ^{14}N formed during the core helium burning phase of a rotating massive star. Primary ^{14}N during the core helium burning phase of rotating stars is formed because of the arrival of ^{12}C and ^{16}O from the helium core (cf. Sect. 4.1). $M_{14\text{N}}^{\text{prim}}$ can be expressed as the total amount of ^{14}N in the star at core helium exhaustion minus the amount of ^{14}N that can be formed

with the initial CNO content (the secondary ^{14}N):

$$M_{^{14}\text{N}}^{\text{prim}} = \left(\int_0^M X_{^{14}\text{N}}(M_r) dM_r \right)_{Y_c=0} - M (X_{\text{C,ini}} + X_{\text{N,ini}} + X_{\text{O,ini}}) \quad (4.1)$$

where Y_c is the central ^4He mass fraction, $X_{^{14}\text{N}}(M_r)$ the mass fraction of ^{14}N at coordinate M_r , $X_{\text{C,ini}}$, $X_{\text{N,ini}}$, $X_{\text{O,ini}}$ the initial mass fractions of the CNO elements in the stellar model, and M the total mass of the star at the end of the core helium burning phase. Let us suppose that all the ^{12}C and ^{16}O diffusing from the helium core to the hydrogen shell are transformed into ^{14}N . In this case, an average injection rate $R_{^{12}\text{C}+^{16}\text{O}}$ of $^{12}\text{C} + ^{16}\text{O}$ can be defined

$$R_{^{12}\text{C}+^{16}\text{O}} = \frac{M_{^{14}\text{N}}^{\text{prim}}}{\tau_{\text{HeB}}} \quad (4.2)$$

where τ_{HeB} is the duration of the core helium burning phase. It gives the average rate at which $^{12}\text{C} + ^{16}\text{O}$ should be injected in the H-burning shell so as to obtain $M_{^{14}\text{N}}^{\text{prim}}$ in the model at the end of core helium burning. For a $60 M_{\odot}$ model at $Z = 10^{-5}$ and with¹ $v_{\text{ini}}/v_{\text{crit}} = 0.7$, $R_{^{12}\text{C}+^{16}\text{O}}$ is equal to $5 \cdot 10^{-8} M_{\odot} \text{ yr}^{-1}$.

Of course, the amount of primary nitrogen synthesized, hence the value of $R_{^{12}\text{C}+^{16}\text{O}}$, can change significantly depending on the rotation, the mass of the stellar model, or the prescription for the rotational mixing for instance. The $R_{^{12}\text{C}+^{16}\text{O}}$ rate estimated above gives an idea of possible values but other injection rates around this value are possible. Here I set $R_{^{12}\text{C}} = R_{^{16}\text{O}} = 10^{-8} M_{\odot} \text{ yr}^{-1}$. The two rates are taken equal since there is roughly as much ^{12}C as ^{16}O in the helium core so that roughly as much ^{12}C as ^{16}O will enter in the H-burning shell. Finally, $R_{^{22}\text{Ne}} = R_{^{26}\text{Mg}} = R_{^{12}\text{C}}/100 = 10^{-10} M_{\odot} \text{ yr}^{-1}$. The factor 100 between the two rates accounts for the fact that ^{22}Ne and ^{26}Mg are about 100 times less abundant than ^{12}C and ^{16}O in the helium burning core so that about 100 times less ^{22}Ne and ^{26}Mg will enter by rotational mixing into the H-burning shell. Injection rates divided and multiplied by 100 were also investigated: 10^{-10} and $10^{-6} M_{\odot} \text{ yr}^{-1}$ for $R_{^{12}\text{C}}$ and $R_{^{16}\text{O}}$ and therefore 10^{-12} and $10^{-8} M_{\odot} \text{ yr}^{-1}$ for $R_{^{22}\text{Ne}}$ and $R_{^{26}\text{Mg}}$.

Results

As shown in Fig. 4.4, C, N, O and F are boosted by ~ 4 dex when injecting ^{12}C , ^{16}O because of the injection and the effect of CNO cycle. Injection of ^{22}Ne gives Ne, Na and Mg with Na being the main product. With the nuclear rates considered, the $^{23}\text{Na}(p, \alpha)^{20}\text{Ne}$ reaction is just 1.6 stronger than the $^{23}\text{Na}(p, \gamma)^{24}\text{Mg}$ reaction. It means that ^{23}Na goes almost 50–50 to ^{20}Ne and ^{24}Mg . It allows a significant production of ^{24}Mg . No Al is produced because the $^{24}\text{Mg}(p, \alpha)^{25}\text{Al}$ reaction, activating the Mg-Al cycle, is too slow at the considered temperature. Injection of ^{26}Mg boosts Mg and Al. The $[^{12}\text{C}/^{13}\text{C}]$ ratio² stays always around -1.5 (equivalent to $^{12}\text{C}/^{13}\text{C} \sim 3$), which is the CNO-equilibrium value. At $T = 50$ MK, the timescale for the $^{12}\text{C}/^{13}\text{C}$ ratio to reach CNO-equilibrium is about 10 yr, i.e. reached almost instantaneously.

This simple one-zone model gives a good estimation of what happens in complete stellar models: green patterns in Fig. 4.4 are from complete $20 M_{\odot}$ stellar models with $v_{\text{ini}}/v_{\text{crit}} = 30\%$ and 70% , at the end of the core He-burning phase. The abundances are taken in the stellar shell where the energy released by hydrogen burning is the highest. These patterns are close enough to the results obtained with the box model.

¹The critical velocity v_{crit} is reached when the gravitational acceleration is counterbalanced by the centrifugal force.

It is expressed as $v_{\text{crit}} = \sqrt{\frac{2}{3} \frac{GM}{R_{\text{p,c}}}}$ with $R_{\text{p,c}}$ the polar radius at the critical limit.

² $[^{12}\text{C}/^{13}\text{C}] = \log(^{12}\text{C}/^{13}\text{C})_{\star} - \log(^{12}\text{C}/^{13}\text{C})_{\odot}$. In the Sun, $(^{12}\text{C}/^{13}\text{C})_{\odot} = 89$, i.e. $\log(^{12}\text{C}/^{13}\text{C})_{\odot} = 1.95$.

Comparison with CEMP-no stars of classes 2 and 4

From the classification done in Maeder & Meynet (2015), the classes 2 and 4 CEMP-no stars were selected (13 stars). These classes of stars are made of a material that was processed by H-burning, with various degree of enrichment (Fig. 4.3). I considered only stars having a $[\text{Fe}/\text{H}]$ ratio close to the $[\text{Fe}/\text{H}] = -3.8$ of the box. HE 0057-5959 was classified as a class 2+Na star since it shows the characteristics of a class 2 star, except for Na, which is overabundant ($[\text{Na}/\text{Fe}] = 1.98$).

The best match between models and observations is when ^{12}C and ^{16}O are injected for the class 2 and when ^{12}C , ^{16}O and ^{22}Ne are injected for the class 4. Injecting only ^{12}C and ^{16}O does not allow to reproduce the stars of class 4, which are generally Na- and Mg-rich. Injecting additional ^{26}Mg raises the $[\text{Al}/\text{Fe}]$ ratio and leads to a larger discrepancy between models and observations. In any case, the models overestimate the $[\text{Al}/\text{Fe}]$ ratios. Below are discussed the uncertainties on the observed and predicted $[\text{Al}/\text{Fe}]$ ratios.

Uncertainties on the aluminum abundance of CEMP-no stars. The first point is that the CEMP sample is not homogeneous³. The abundance data considered comes from several sources. Ideally, an homogeneous sample is needed because a mixture of abundances from various authors sometimes adds an undesirable scatter that makes harder the use of the sample to constrain the models. However very metal-poor stars are very rare and no large homogeneous sample exists yet. The second point is that in the sample considered, most of the abundances are derived based on 1D LTE atmosphere models. For turnoff stars at $[\text{Fe}/\text{H}] \simeq -3$, Andrievsky et al. (2008) derived a correction $\Delta[\text{Al}/\text{Fe}] = [\text{Al}/\text{Fe}]_{\text{NLTE}} - [\text{Al}/\text{Fe}]_{\text{LTE}} \simeq 0.6$ dex. In addition to NLTE, 3D effects can add another correction factor. Nordlander & Lind (2017) have shown that the difference between 3D NLTE and 1D LTE for Al in metal-poor stars can amount $+0.5$ dex. In the stars plotted in Fig. 4.4, there is for instance CS 22949-037 with $[\text{Al}/\text{Fe}] = 0.02$. This ratio was derived based on 1D LTE model-atmosphere analyses (Norris et al. 2013). According to the previous discussion, NLTE/3D effects could rise $[\text{Al}/\text{Fe}]$ up to ~ 0.6 dex. This is still ~ 1 dex below the values predicted by the models.

Uncertainties on the aluminum abundance predicted by the models. As mentioned, the initial $[\text{Al}/\text{Fe}] \simeq 1.5$ in the box comes from the H-burning shell of a complete stellar model at core He-ignition. The initial $[\text{Al}/\text{Fe}]$ of this stellar model is 0 (i.e. solar). The nucleosynthesis during the main sequence and very beginning of core He-burning has synthesized some Al (especially through the Mg-Al chain), up to $[\text{Al}/\text{Fe}] \simeq 1.5$. I have investigated how the Al production is affected (considering both the stellar model and the box model) when varying some specific nuclear reaction rates. Several literature sources provide nuclear reaction rates for the three major reactions involving ^{27}Al in H-burning zones: $^{26}\text{Mg}(p, \gamma)^{27}\text{Al}$, $^{27}\text{Al}(p, \gamma)^{28}\text{Si}$ and $^{27}\text{Al}(p, \alpha)^{24}\text{Mg}$. For instance, there are six sources for $^{27}\text{Al}(p, \gamma)^{28}\text{Si}$ spanning ~ 4 order of magnitude at $T \sim 50$ MK (according to the JINA reaclib⁴). Using the rates in the literature that favor the destruction (or smallest production) of ^{27}Al leads to a final $[\text{Al}/\text{Fe}]$ in the box of about 0, i.e. ~ 1.5 dex below the $[\text{Al}/\text{Fe}]$ ratio shown in Fig. 4.4. It would match better the observations. Finally, because of important uncertainties existing on some nuclear rates, caution is required when interpreting the nucleosynthetic predictions of some elements like Al.

The $^{12}\text{C}/^{13}\text{C}$ ratio. The CEMP-no stars in Fig. 4.4 have low $^{12}\text{C}/^{13}\text{C}$ ratios compared to the Sun: $-1.5 \lesssim [^{12}\text{C}/^{13}\text{C}] \lesssim -1$, which is equivalent to $3 \lesssim ^{12}\text{C}/^{13}\text{C} \lesssim 9$ (in the solar system, the carbon isotopic ratio is about 90, Lodders 2003). Some CEMP-no stars are giants and may therefore have experienced mixing events like the first dredge-up. In this case, the observed $^{12}\text{C}/^{13}\text{C}$ may have

³A sample is homogeneous if the same procedure is used to obtain all observations and abundances.

⁴<http://jinaweb.org/reaclib/db/>.

changed since the formation of the CEMP-no star. If so, the link between the CEMP-no star and its source star is more difficult to establish (further discussions in Sect. 4.4.2, cf. also Sect. 2.4). By contrast, the surface composition of unevolved CEMP-no stars reflects more directly the composition of the cloud in which they formed, hence the composition of the material ejected by the previous source star. Some CEMP-no stars in the considered sample are still rather unevolved: CS 22958-042 for instance, has $T_{\text{eff}} = 6250$ K, $\log g = 3.5$ and $^{12}\text{C}/^{13}\text{C} = 9$. Such a $^{12}\text{C}/^{13}\text{C}$ ratio is consistent with a material processed only by H-burning in the previous massive source star. In He-burning regions of massive stars, ^{13}C is destroyed so that $^{12}\text{C}/^{13}\text{C} \sim \infty$. Consequently, it is unlikely that this CEMP-no star formed from a source star material processed by He-burning. This will be discussed in more details while considering yields from complete source star models (Sect. 4.3 and 4.4).

Conclusion

The conclusion from this box experiment is that the range of abundances of class 2 and 4 CEMP-no stars is overall well reproduced by a material processed by H-burning at a temperature and density characteristic of $20 - 60 M_{\odot}$ source stars. During its burning, the material was enriched in He-burning products: ^{12}C , ^{16}O for class 2, ^{12}C , ^{16}O and ^{22}Ne for class 4. This is consistent with the scenario of Maeder & Meynet (2015) proposing that CEMP-no stars are made of a material ejected from a massive star having experienced various degree of rotational mixing.

4.3 Massive source stars with rotation

As a next step, complete stellar models with various initial rotation rates are considered. It allows to give more realistic abundance predictions than with a one-zone model. Other source star parameters such as mass and metallicity are also investigated.

4.3.1 Physical ingredients

I computed $20 M_{\odot}$ models at a metallicity $Z = 10^{-5}$ with⁵ $v_{\text{ini}}/v_{\text{crit}} = 0, 0.1, 0.2, 0.3, 0.4, 0.5$ and 0.7 . I also computed a 40 and a $60 M_{\odot}$ model at $Z = 10^{-5}$ and with $v_{\text{ini}}/v_{\text{crit}} = 0.4$ to explore different initial masses. Finally, a $20 M_{\odot}$ at $Z = 0$ and with $v_{\text{ini}}/v_{\text{crit}} = 0.4$ was computed to evaluate the effect of metallicity. The nuclear reaction rates are the same than for the box model. The evolution is stopped at the end of core carbon burning. The very last burning stages (also explosive nucleosynthesis, cf. Sect. 3.1.3) significantly modify only the abundances of the most inner layers. The yields of the models presented here provide good predictions, provided the most inner layers of the star are not ejected and considered in the yields. More details on the other physical ingredients (shear mixing, mass loss, initial composition...) can be found in Sect. 3.3.

4.3.2 Evolution with rotation

This section discusses the effects of rotation by focusing on the $20 M_{\odot}$ models with various initial rotation rates.

The effective gravity of the stellar core is decreased by rotation because of the effect of the centrifugal force. It decreases the temperature in the convective core and tends to make it smaller. On the other hand, rotation tends to produce bigger cores because of the rotational mixing that provides additional fuel to the core. Overall, in the models presented here, rotation produces bigger cores at the end of the evolution (Fig. 4.5). For instance the size of the carbon-oxygen

⁵The critical velocity v_{crit} is reached when the gravitational acceleration is counterbalanced by the centrifugal force. It is expressed as $v_{\text{crit}} = \sqrt{\frac{2}{3} \frac{GM}{R_{\text{p,c}}}}$ with $R_{\text{p,c}}$ the polar radius at the critical limit.

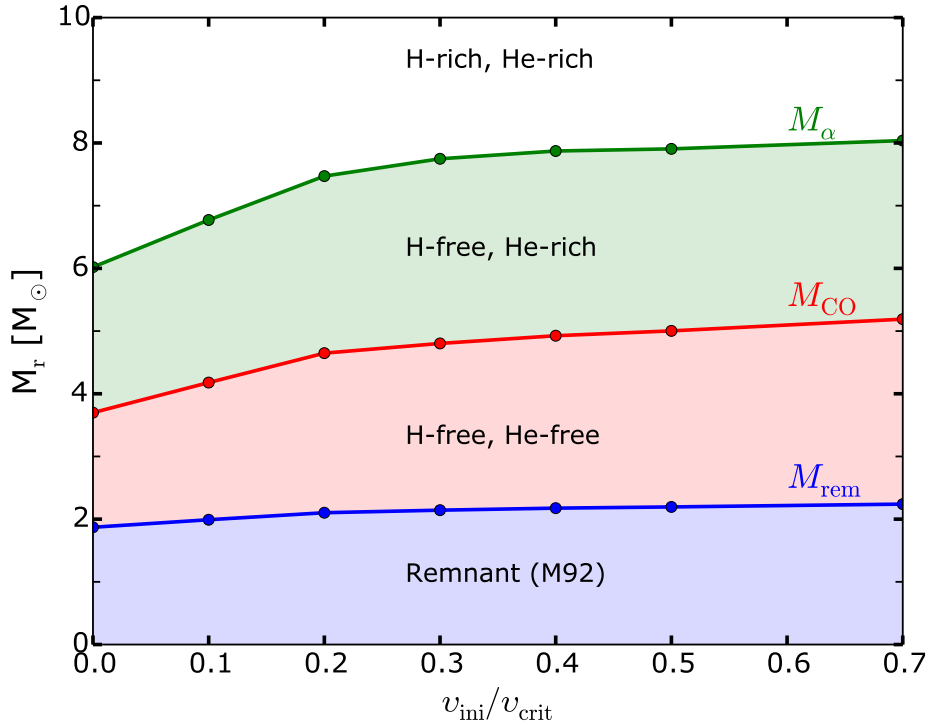


Figure 4.5: Masses of the various cores as a function of initial velocity for $20 M_{\odot}$ models with $Z = 10^{-5}$, at the end of the core carbon burning phase. M_{α} denotes the α -core (defined where the mass fraction of ^1H drops below 10^{-3}), M_{CO} the CO-core (defined where the mass fraction of ^4He drops below 10^{-3}) and M_{rem} shows the remnant mass (from the relation of Maeder 1992, that links the mass of the CO-core with the mass of the remnant).

core (CO-core, defined where the ^4He mass fraction drops below 10^{-3}) increases by about $1.5 M_{\odot}$ from the non rotating model to the fast rotating one. A consequence is that the base of the H-rich envelope and the He-rich region are shifted towards higher mass coordinates when initial rotation increases (Fig. 4.6, top panels).

As the initial rotation increases, the He-burning products (e.g. ^{12}C , ^{16}O , ^{22}Ne) transit quicker and in greater amount to the H-burning shell so that more ^{13}C , ^{14}N , ^{19}F , ^{23}Na are synthesized (Fig. 4.6 and 4.7). Around the mass coordinate $7 M_{\odot}$, ^{13}C and ^{14}N are boosted by ~ 4 dex from $v_{\text{ini}}/v_{\text{crit}} = 0$ to 0.7 . Rotation increases the production of ^{19}F , ^{22}Ne , ^{23}Na , $^{24,25,26}\text{Mg}$ and ^{27}Al in the He-burning core (cf. Sect. 4.1). Near the end of the core He-burning phase, ^{19}F is also destroyed in the central regions (below $5 M_{\odot}$) by $^{19}\text{F}(\alpha, p)^{22}\text{Ne}$. While the Ne-Na chain is boosted in the H-burning shell of rotating models (see the peak of ^{23}Na at $\sim 8 M_{\odot}$), the Mg-Al chain is not efficiently activated (no similar peak in the H-burning shell). This is mainly because the temperature in the H-burning shell is too low ($T \lesssim 45$ MK). Another reason is that the synthesis of extra Al in the H-burning shell needs extra Mg, which is only built in the He-core when $T \gtrsim 220$ MK (through an α -capture on ^{22}Ne). In a $20 M_{\odot}$ model, this temperature corresponds to the end of core He-burning phase. The extra Mg created in the core has then little time to be transported to the H-burning shell and boosts the Mg-Al chain. ^{28}Si is the only isotope that is barely affected by rotation (bottom right panel of Fig. 4.7).

As initial rotation increases, the surface is enriched in H-burning products. This is because of the rotational mixing that transports these elements from H-burning layers up to the surface. We indeed see that (1) the surface ^4He is increased in the faster rotating model, (2) the effect of CNO burning appears at the surface (less ^{12}C and ^{16}O , more ^{14}N) and (3) the products of the Ne-Na and Mg-Al cycles are more abundant (mostly ^{23}Na , ^{24}Mg and ^{27}Al). The surface abundances change

4.3. Massive source stars with rotation

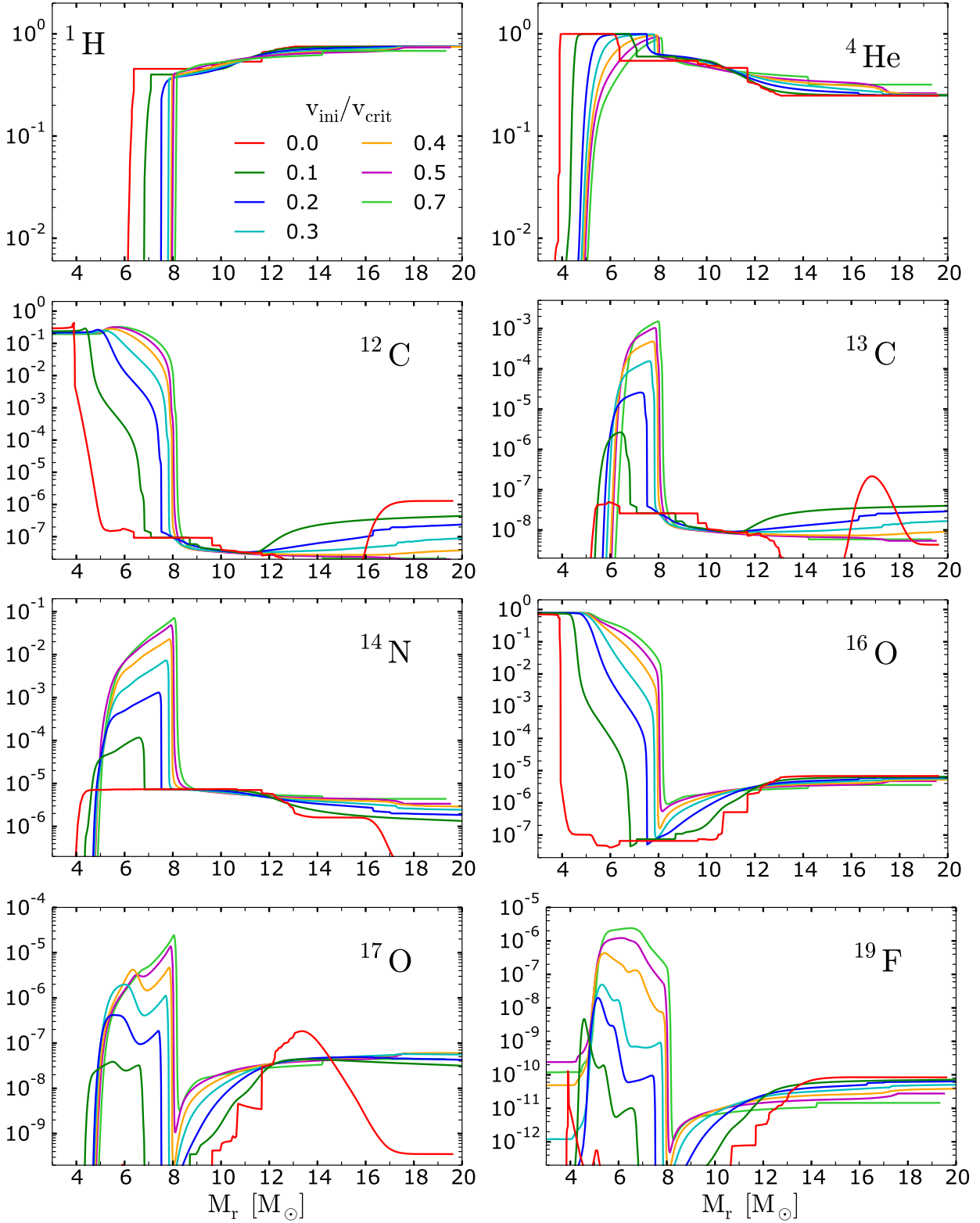


Figure 4.6: Internal abundance profiles in mass fraction of $20 M_{\odot}$ models at $Z = 10^{-5}$ with various initial rotation rates, at the end of the core helium burning phase, between $M_r = 3$ and $20 M_{\odot}$.

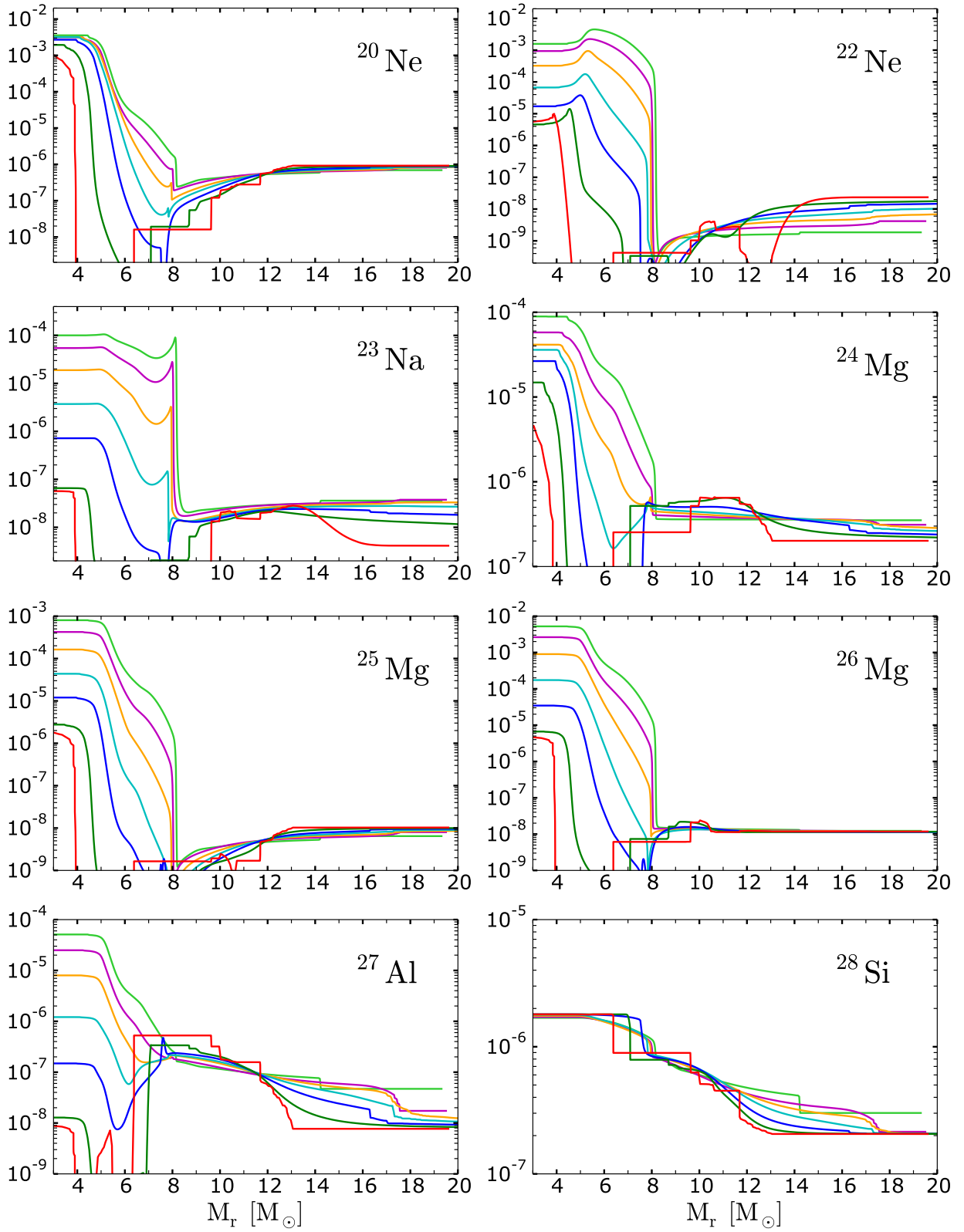


Figure 4.7: Same as Fig. 4.6 for other isotopes.

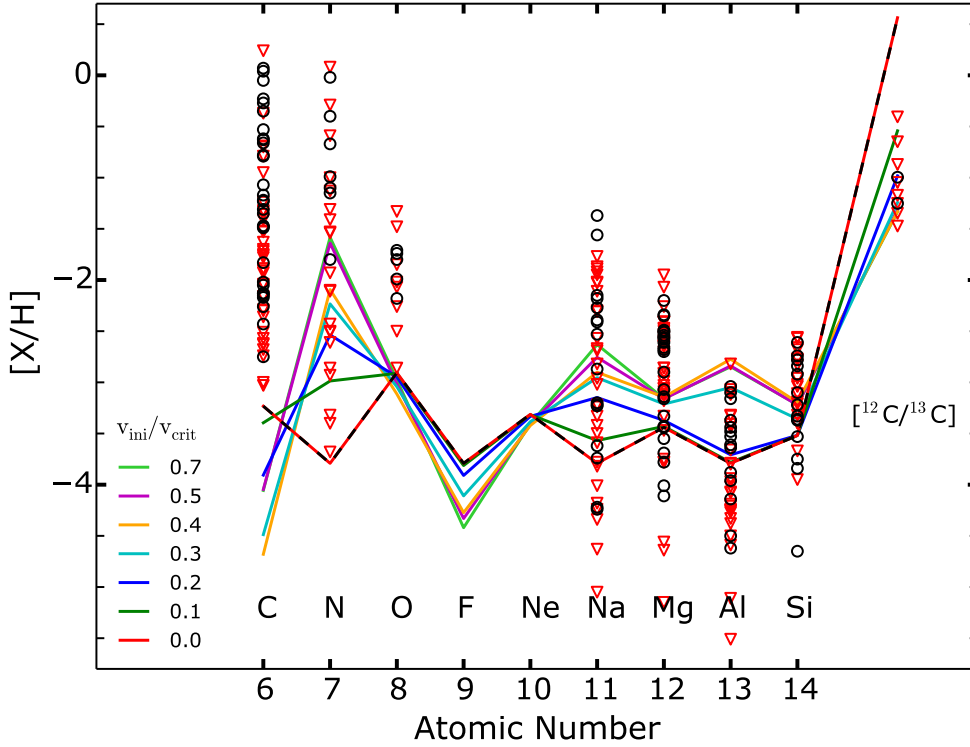


Figure 4.8: Composition of the wind of $20 M_{\odot}$ models at $Z = 10^{-5}$ with various initial rotation rates. The dashed black pattern (superimposed with the red pattern) shows the composition of the ISM. Black circles and red triangles show main-sequence and giant CEMP stars respectively, with $[\text{Fe}/\text{H}] < -3$ (Table 4.2). Recognized CEMP-r, -s and -r/s are excluded. Abundances with upper/lower limits are not plotted. The typical uncertainty is ± 0.3 dex.

mostly during the main sequence phase because of its longer duration (the chemical species have more time to be transported). When reaching the stellar surface, chemical species are potentially expelled through winds. In these models however, the mass loss metallicity relation ($M \propto Z^{0.85}$, cf. Sect. 3.3.5) plays a major role and thus prevents significant radiative mass loss episodes. Also the mechanical mass loss (cf. Sect. 3.3.5) stays small for these models. The $20 M_{\odot}$ model with $v_{\text{ini}}/v_{\text{crit}} = 0.7$ loses about $0.12 M_{\odot}$ through mechanic mass loss and $0.6 M_{\odot}$ through radiative mass loss. The total mass lost through winds is $< 1 M_{\odot}$ for all the $20 M_{\odot}$ models. We note that the mass loss may be strongly enhanced for higher mass stars.

4.3.3 Composition of the ejecta

The effect of varying the initial rotation, mass cut, dilution, efficiency of rotational mixing, mass and metallicity on the chemical composition of the source star ejecta is considered.

Initial rotation

Composition of the wind. Fig. 4.8 shows the $[X/H]$ ratios in the wind of the models. For all models, the wind contribution is less than $1 M_{\odot}$ and comes from the H-rich region. The non-rotating model (red) is superimposed with the ISM pattern since the ejected material has kept exactly the same composition as the ISM. As rotation increases, the wind is overall more and more enriched in a material processed by the CNO cycle, Ne-Na and Mg-Al chains (cf. Sect. 4.3.2). For the faster rotators, the $^{12}\text{C}/^{13}\text{C}$ ratio is equal to the CNO equilibrium value of ~ 4 (equivalent to $[\text{C}^{12}/\text{C}^{13}] = -1.35$).

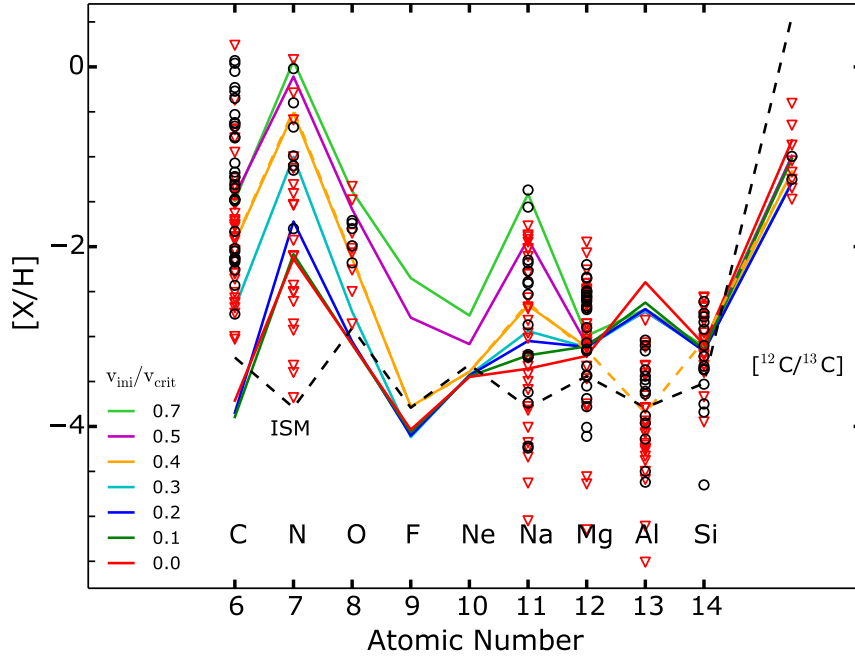


Figure 4.9: Same as Fig. 4.8 but for the composition of all the H-rich material. This material includes the wind material plus the material from a supernova with a mass cut set at M_{α} . M_{α} corresponds to the bottom of the H-envelope (the bottom of the H-envelope is defined where the ^1H mass fraction drops below 10^{-3}). The dashed orange line shows the $v_{\text{ini}}/v_{\text{crit}} = 0.4$ model with the rate of the $^{27}\text{Al}(p, \gamma)^{28}\text{Si}$ reaction from Cyburt et al. (2010) instead of Iliadis et al. (2001).

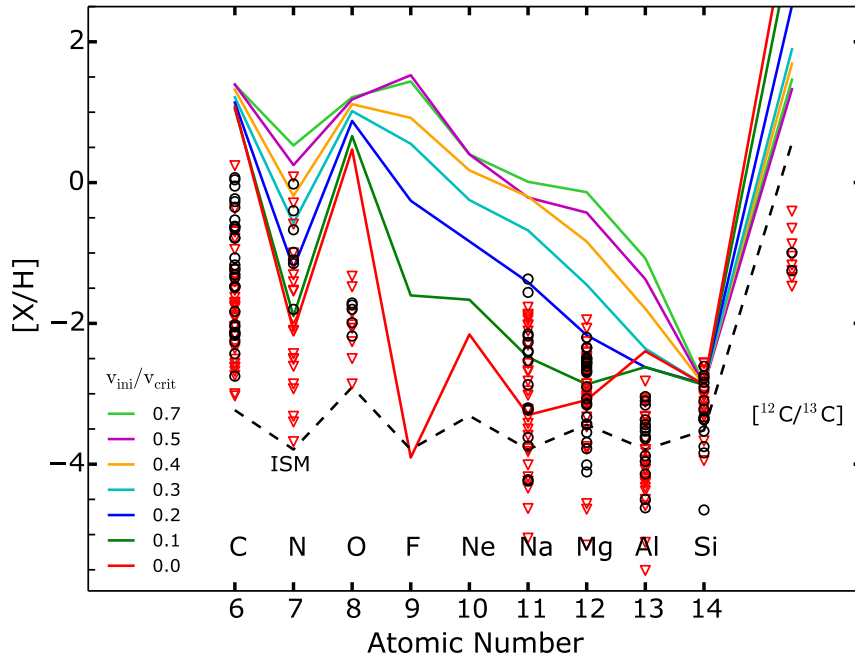


Figure 4.10: Same as Fig. 4.9 but for the composition of all the H-rich + He-rich material. This material includes the wind material plus the material from a supernova with a mass cut set at M_{CO} . M_{CO} corresponds to the bottom of the He-shell (the bottom of the He-shell is defined where the ^4He mass fraction drops below 10^{-3}). M_{CO} also corresponds to the top of the CO-core.

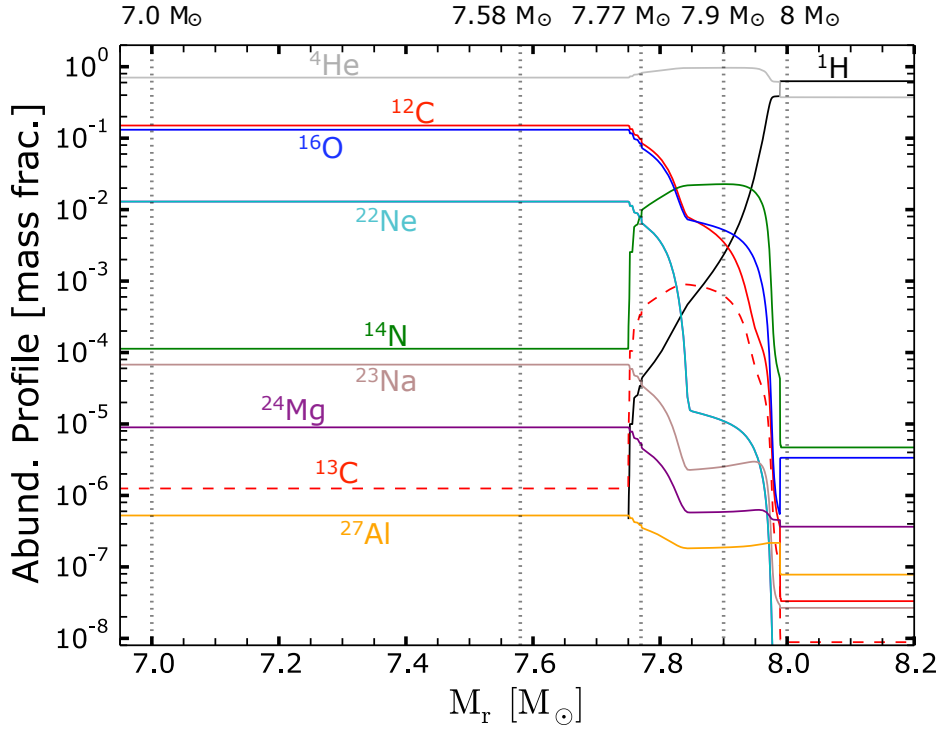


Figure 4.11: Abundance profile of the $20 M_{\odot}$ model with $Z = 10^{-5}$ and $v_{\text{ini}}/v_{\text{crit}} = 0.4$ at the pre-SN stage. Dashed vertical lines corresponds to the mass cuts of Fig. 4.12.

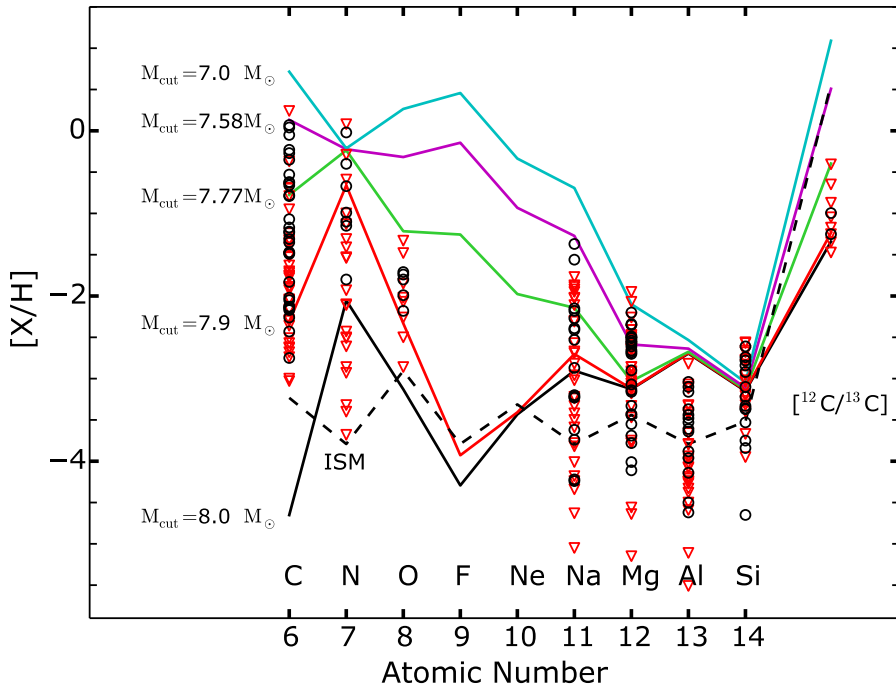


Figure 4.12: Composition of the ejecta of a $20 M_{\odot}$ model with $Z = 10^{-5}$ and $v_{\text{ini}}/v_{\text{crit}} = 0.4$ for various mass cuts taken in between the H-shell and He-shell. These mass cuts are also represented in Fig. 4.11.

Composition of the H-rich material. Fig. 4.9 shows the chemical composition of the ejecta when considering the wind plus all the material above the bottom of the H-rich region. In this case, $M_{\text{cut}} = M_{\alpha}$, where M_{α} is the mass of the helium core set where the mass fraction of ^1H drops below 10^{-3} . From the top left panel of Fig. 4.6 we see that it corresponds to a total ejected mass of $\sim 12 - 14 M_{\odot}$, depending on the model. The typical CNO pattern appears for all the models (more N, less C and O) but the sum of CNO elements increases with rotation, as a result of ^{12}C and ^{16}O having diffused to the H-burning shell. $[\text{Na}/\text{H}]$ spans ~ 2 dex while $[\text{Mg}/\text{H}]$, $[\text{Al}/\text{H}]$ and $[\text{Si}/\text{H}]$ do not vary more than 0.5 dex. Mg and Al are overproduced with rotation (Fig. 4.7) but only in the He-rich region, which is not considered in the yields of Fig. 4.9. $^{12}\text{C}/^{13}\text{C}$ is very close to the CNO equilibrium value.

Composition of the H-rich + He-rich material. Fig. 4.10 is similar as Fig. 4.9 but it considers the wind plus all the material above the bottom of the He-rich region. In this case, $M_{\text{cut}} = M_{\text{CO}}$. The total ejected mass is about $15 - 16 M_{\odot}$, depending on the model (Fig. 4.5). Compared to the previous case, the additional $\sim 2 M_{\odot}$ ejected are H-free, so that it raises a bit the $[X/\text{H}]$ ratios (by < 0.5 dex). The CNO pattern is reversed compared to Fig. 4.9 because in He-burning regions, ^{14}N is depleted while ^{12}C and ^{16}O are abundant (Fig. 4.6). No or very little additional ^{14}N is added to the ejecta compared to Fig. 4.9. The ratios containing He-burning products ($[\text{Ne}/\text{H}]$, $[\text{Na}/\text{H}]$, $[\text{Mg}/\text{H}]$ and $[\text{Al}/\text{H}]$) are largely boosted compared to Fig. 4.9. They also greatly increase with initial rotation as a result of the back-and-forth mixing process. In He-burning regions, ^{13}C is destroyed by $^{13}\text{C}(\alpha, n)^{16}\text{O}$ so that the $^{12}\text{C}/^{13}\text{C}$ ratio is largely enhanced compared to the case where only H-rich ejecta is considered. Considering deeper mass cuts raise again C/H, O/H, Ne/H, Mg/H, and $^{12}\text{C}/^{13}\text{C}$ but, overall, it does not change significantly the trends of Fig. 4.10.

Mass cut in the intershell region

Fig. 4.12 shows the chemical composition of the wind plus an ejecta defined with various mass cuts, for the $v_{\text{ini}}/v_{\text{crit}} = 0.4$ model. The 5 considered mass cuts are represented in Fig. 4.11 which shows the abundance profile of the $20 M_{\odot}$ model with $v_{\text{ini}}/v_{\text{crit}} = 0.4$ at the pre-SN stage. The zone between $7.8 \lesssim M_r \lesssim 8 M_{\odot}$ corresponds to the intershell region, in between the H- and He-burning shells. As M_{cut} decreases, deeper layers are ejected and we move progressively from the H-rich only ejecta to a mixed H+He ejecta. Varying the mass cut from 7 to $8 M_{\odot}$ leads to a quick increase of the $[X/\text{H}]$ ratios, up to ~ 5 dex for $[\text{C}/\text{H}]$. It illustrates the high sensitivity of the yields on the mass cut when varying it around the intershell region.

Dilution of the source star ejecta with ISM

The material ejected from the star can be mixed with the material in the ISM. The effect of the dilution depends on the composition of the ISM, which is not known at low metallicity (a choice has nevertheless to be made when computing low metallicity models, as done in this work). Generally, in the case of the scenario proposing that CEMP-no stars were formed from one or very few source stars, we can probably just guess that the ISM is either metal-free or very metal-poor. Table 4.1 reports how are affected the different abundance ratios in the source star ejecta while considering either a dilution with a metal-poor ISM or a metal-free ISM. A dilution with a metal-free ISM adds some H so that the $[X/\text{H}]$ ratios are affected (where X refers to metals). On the other hand, such an ISM does not modify the $[X/\text{Fe}]$ (where X refers to metals) or the isotopic ratios. In almost all the cases, when the $[X/\text{H}]$ or $[X/\text{Fe}]$ ratios are affected by dilution with ISM, they are reduced (cf. Fig. 4.13 and next paragraph). This is because in the source star ejecta, the H and Fe abundances are similar to the H and Fe abundances in the ISM while light metals (C to Al) are generally strongly overproduced by the source star compared to what is present in the ISM.

4.3. Massive source stars with rotation

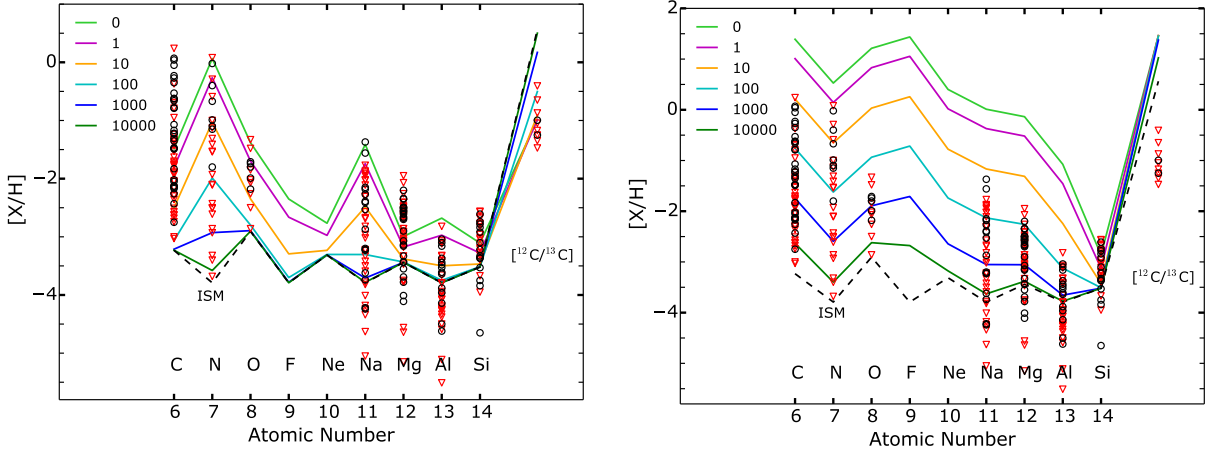


Figure 4.13: *Left panel:* composition of the H-rich ejecta of the $20 M_{\odot}$ model with $v_{\text{ini}}/v_{\text{crit}} = 0.7$ for various dilution factors D . The $D = 0$ pattern corresponds to the green pattern in Fig. 4.9. *Right panel:* same as left panel but for H-rich + He-rich ejecta. The $D = 0$ pattern corresponds to the green pattern in Fig. 4.10.

Table 4.1: Effect of diluting the source star ejecta with two different kinds of ISM: metal-poor and metal-free. Different kinds of abundance ratios are considered. X refers to metals.

	[X/H]	[X/Fe]	isotopic ratios
Metal-poor ISM	towards ISM value	towards ISM value	towards ISM value
Metal-free ISM	towards ISM value	unchanged	unchanged

In this work, when diluting the source star ejecta with ISM, I consider that the ISM material is the same than the ISM material used to form the source star (α -enhanced ISM, cf. Sect. 3.3.4 for details on the initial composition). To be more quantitative, a dilution factor D can be defined as

$$D = \frac{M_{\text{ISM}}}{M_{\text{ej}}} \quad (4.3)$$

with M_{ej} the total mass ejected by the source star and M_{ISM} the mass of initial ISM added to the massive star ejecta. The left panel of Fig. 4.13 shows the chemical composition of the wind plus the H-rich ejecta for the $v_{\text{ini}}/v_{\text{crit}} = 0.7$ model. Different dilution factors are considered. $D = 100$ means that there is $100 M_{\odot}$ of ISM for $1 M_{\odot}$ of source star ejecta. As D increases, the composition is shifted towards the ISM composition. The right panel of Fig. 4.13 is similar but for the H-rich + He-rich ejecta (like in Fig. 4.10). In this case, the amount of light elements is more important in the source star ejecta so that higher D values are needed to reach back the ISM pattern. The ISM considered here is α -enhanced, which explains why the $[\text{C}/\text{H}]$, $[\text{O}/\text{H}]$... ratios are enhanced compared to the $[\text{N}/\text{H}]$, $[\text{F}/\text{H}]$... ratios. Also, in this ISM, $^{12}\text{C}/^{13}\text{C} \simeq 0.5$, which corresponds to $^{12}\text{C}/^{13}\text{C} = 300$ (cf. Sect. 3.3.4). A more extended discussion about the $^{12}\text{C}/^{13}\text{C}$ ratio can be found in Sect. 4.4.

At the present day, the dilution factor cannot be strongly constrained. The point explosion or Sedov-Taylor explosion can be used as an approximation to estimate how fast will a shock wave travel and what would be left behind it. For a standard explosion energy of $E_{51} = 1$ (E_{51} is the SN energy in units of 10^{51} ergs) and typical ISM densities, the ejecta will be mixed with about $M_{\text{ISM}} = 10^4 M_{\odot}$ of ISM (Cioffi et al. 1988; Ryan et al. 1996; Wehmeyer et al. 2015). For the models of Fig. 4.13, the total mass ejected is between ~ 12 and $\sim 16 M_{\odot}$. Taking $10^4 M_{\odot}$ of ISM leads to a dilution factor of $10^4/16 < D < 10^4/12$, which gives $600 \lesssim D \lesssim 800$ (in between the cyan and blue patterns in Fig. 4.13). This would be for standard explosions energies. In the case of a

low-energetic supernova with $E_{51} = 0.1$ for instance, $60 \lesssim D \lesssim 80$ (i.e. D is divided by 10, this is because $D \sim M_{\text{ISM}} \sim E_{51}^{0.95}$, Ryan et al. 1996, their Sect. 5.6.1).

Another way to constrain the dilution factor may be the surface Li abundance of the CEMP-no stars. We can assume that Li is completely destroyed in massive stars so that $X(\text{Li})_{\text{ej}}$, the Li mass fraction in the source star ejecta is 0. The Li mass fraction $X(\text{Li})_{\text{CEMP}}$ in the CEMP-no star natal cloud (possibly different than the value observed today) is then

$$X(\text{Li})_{\text{CEMP}} = \frac{M_{\text{ej}}X(\text{Li})_{\text{ej}} + M_{\text{ISM}}X(\text{Li})_{\text{ISM}}}{M_{\text{ej}} + M_{\text{ISM}}} = \frac{M_{\text{ISM}}X(\text{Li})_{\text{ISM}}}{M_{\text{ej}} + M_{\text{ISM}}} \quad (4.4)$$

where M_{ej} is the mass ejected by the source star, and $X(\text{Li})_{\text{ISM}}$ the Li abundance in the ISM. The dilution factor can then be expressed as

$$D = \frac{M_{\text{ISM}}}{M_{\text{ej}}} = \frac{X(\text{Li})_{\text{CEMP}}}{X(\text{Li})_{\text{ISM}} - X(\text{Li})_{\text{CEMP}}}. \quad (4.5)$$

We can suppose that the Li abundance in the initial ISM is equal to the WMAP value of $A(\text{Li})_{\text{ISM}} = 2.72$ (Cyburt et al. 2008). If, as a first guess, we consider that in situ processes changing the Li abundance did not occur during the CEMP-no star life, we can take $X(\text{Li})_{\text{CEMP}}$ equal to the observed Li abundance. If the CEMP-no star has no Li at its surface, $D = 0$ and the CEMP-no star is made of pure source star ejecta. If the Li abundance is high, more ISM is needed to form the CEMP-no star. The maximal detected $A(\text{Li})$ for CEMP-no stars is about 2.1 (i.e. around the Spite Plateau value Spite & Spite 1982). It leads to a maximal dilution factor of $D_{\text{max}} \sim 0.3$, i.e. all CEMP-no stars would be made of almost pure source star ejecta, even the most Li-rich.

This estimation of D stays correct as long as (1) in situ processes changing the Li abundance did not occur in CEMP stars and (2) the Li ISM abundance is indeed $A(\text{Li})_{\text{ISM}} = 2.72$ (value from WMAP). If instead, $A(\text{Li})_{\text{ISM}} = 2.2$ for instance, $D_{\text{max}} \sim 4$, i.e. the source star ejecta may still largely dominate compared to the ISM (see Fig. 4.13). The main uncertainty in this method are the possible internal processes changing the surface Li abundance of the CEMP-no stars. Korn et al. (2009) have used models including atomic diffusion to estimate by how much the surface Li abundance of the dwarf CEMP-no star HE 1327-2326 was depleted since its birth. At maximum, Li was depleted by 1.2 dex. It would correspond to an initial Li of $A(\text{Li})_{\text{ini}} < 1.82$ for HE 1327-2326 and lead to a small D value. Overall, this method of guessing D is uncertain so precaution is required. It nevertheless suggests very small dilution factors. This is inconsistent with the high D values guessed from the Sedov-Taylor theory assuming standard explosions energies. It might nevertheless be more consistent with low energetic SNe ($E_{51} < 1$), that give smaller D values (for $E_{51} = 0.1$ however, there is still 1 order of magnitude of difference at least).

Efficiency of the rotational mixing

The f_{energ} parameter in the D_{shear} expression (Eq. 3.10) was taken equal to 4 in these models. It is consistent with the surface N/H enrichments of observed $10 - 20 M_{\odot}$ rotating stars (cf. Sect. 3.3.1). $f_{\text{energ}} = 4$ corresponds to a critical Richardson number⁶ $Ri_c = 2$. $f_{\text{energ}} = 1$ ($Ri_c = 0.5$) is also a reasonable choice, likely consistent with the observations (cf. Sect. 3.3.1).

Fig. 4.14 shows the effect of changing f_{energ} from 1 to 4. The 2 top panels show the H-rich (left) and H-rich + He-rich ejecta (right) of the $20 M_{\odot}$ models with $v_{\text{ini}}/v_{\text{crit}} = 0.2$ and with various f_{energ} . The yields are barely affected when changing f_{energ} . The same plots for the $20 M_{\odot}$ model with $v_{\text{ini}}/v_{\text{crit}} = 0.7$ are shown below. In this case, the effect is much larger and leads to differences of 1 – 1.5 dex at maximum. The $f_{\text{energ}} = 1$ model with $v_{\text{ini}}/v_{\text{crit}} = 0.7$ has similar yields than the $f_{\text{energ}} = 4$ model with $v_{\text{ini}}/v_{\text{crit}} = 0.3$. Changing f_{energ} does not change the general trends but shifts the yields upward or downward, for a given initial rotation. To obtain similar yields as the

⁶Physical values of Ri_c are likely between 0.25 and 2, cf. Sect 3.3.1.

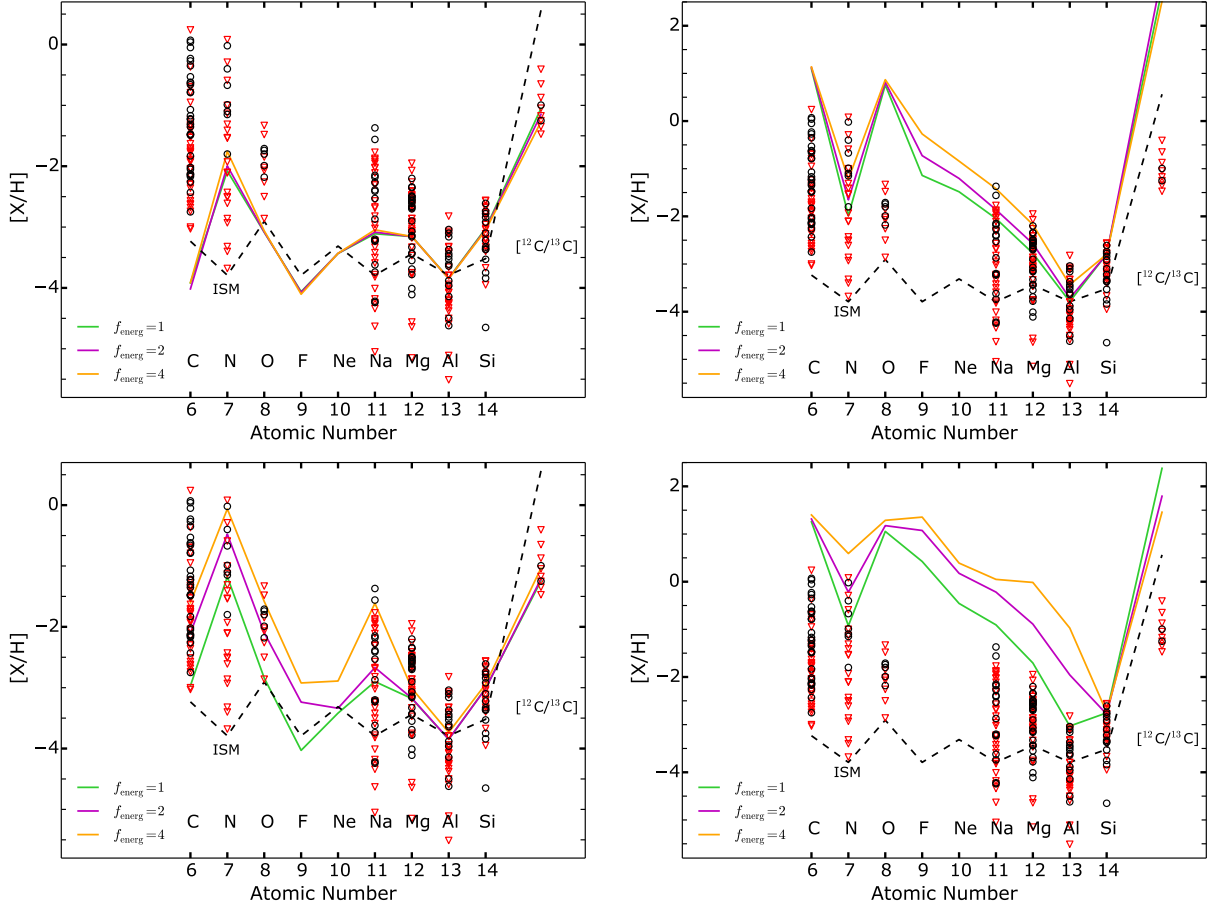


Figure 4.14: Effect of varying the efficiency of rotational mixing (f_{energ}) on the yields. The top panels show the $20 M_{\odot}$ models with $v_{\text{ini}}/v_{\text{crit}} = 0.2$. The bottom panels show the $20 M_{\odot}$ models with $v_{\text{ini}}/v_{\text{crit}} = 0.7$. The left panels show the H-rich ejecta. The right panels show the H-rich + He-rich ejecta.

$v_{\text{ini}}/v_{\text{crit}} = 0.7$, $f_{\text{energ}} = 4$ model while setting $f_{\text{energ}} = 1$, it is probably needed to raise $v_{\text{ini}}/v_{\text{crit}}$ up to about 1. The $f_{\text{energ}} \sim Ri_c$ parameter is important, especially for fast rotators, but its accurate value is not known.

Mass

Figure 4.15 shows the yields of 20, 40 and $60 M_{\odot}$ models with $v_{\text{ini}}/v_{\text{crit}} = 0.4$ at $Z = 10^{-5}$. The final yields are rather similar. The $60 M_{\odot}$ produces more N because its H-shell is more active than in lower mass models. In the H-rich layers, more Na is produced in the $20 M_{\odot}$ models because the back-and-forth mixing process (Fig. 4.1) is more efficient in lower masses. It is mainly because the process has more time to operate due to the longer duration of the core helium burning stage. Also, Al and Si are overproduced in the H-rich layers of the 40 and $60 M_{\odot}$ because of the higher H-burning temperature, increasing the efficiency of the Mg-Al-Si chain. The yields of the $60 M_{\odot}$ in the H-rich + He-rich layers show significant differences compared to the other models (right panel). It is explained by the fact that the He-burning shell becomes convective in the 20 and $40 M_{\odot}$ models while it does not for the $60 M_{\odot}$ model. In the $60 M_{\odot}$ model, the H-burning shell is very active and therefore limits the activation of the He-burning shell. In the 20 and $40 M_{\odot}$ models, while becoming convective, the He-shell engulfs some ^{14}N from the H-rich region. It boosts the production of F and Na through the chains $^{14}\text{N}(n, \gamma)^{15}\text{N}(\alpha, \gamma)^{19}\text{F}$ and

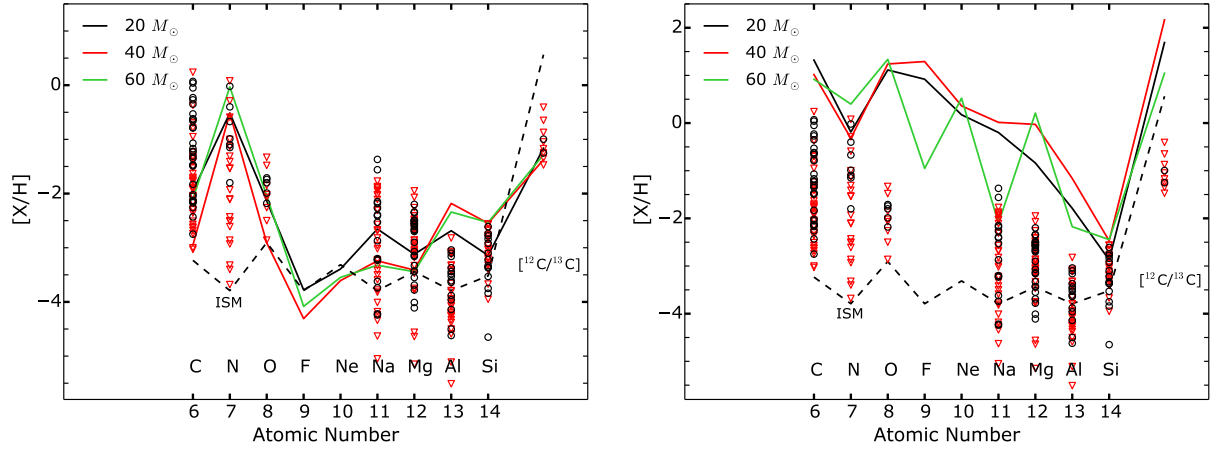


Figure 4.15: Composition of the H-rich (*left panel*, same as Fig. 4.9) and H-rich + He-rich (*right panel*, same as Fig. 4.10) ejecta of $Z = 10^{-5}$, $v_{\text{ini}}/v_{\text{crit}} = 0.4$ models with different initial masses.

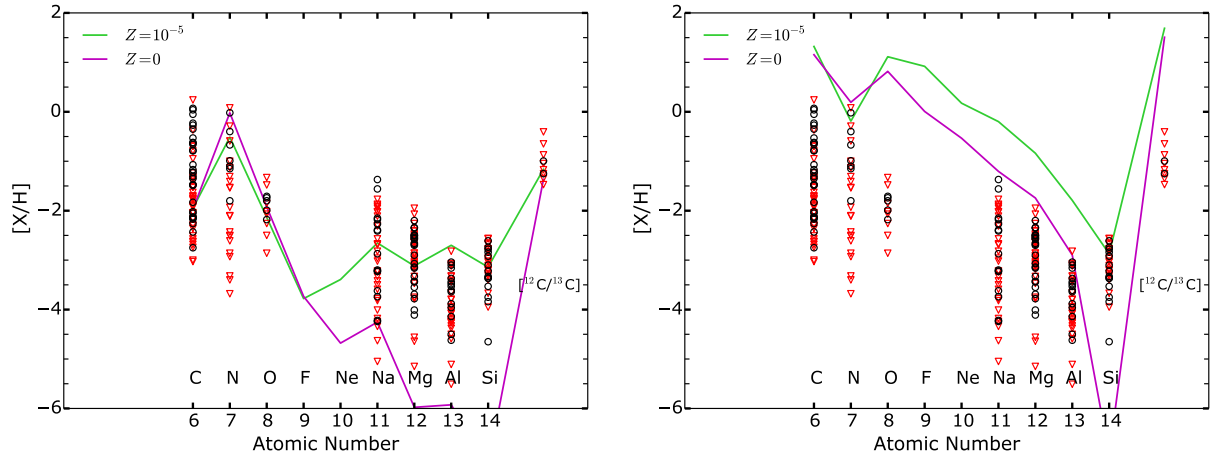


Figure 4.16: Same as Fig. 4.15 but for $20 M_{\odot}$ models with $v_{\text{ini}}/v_{\text{crit}} = 0.4$ and with two different initial metallicities.

$^{14}\text{N}(\alpha, \gamma)^{18}\text{F}(e^+ \nu_e)^{18}\text{O}(\alpha, \gamma)^{22}\text{Ne}(n, \gamma)^{23}\text{Ne}(e^- \bar{\nu}_e)^{23}\text{Na}$. The neutrons required to activate this chain come from $^{22}\text{Ne}(\alpha, n)$.

Metallicity

Figure 4.16 shows the yields (H-rich: left panel, H-rich + He-rich: right panel) of the $20 M_{\odot}$ models with $v_{\text{ini}}/v_{\text{crit}} = 0.4$ at $Z = 10^{-5}$ (green pattern) and $Z = 0$ (magenta). The two models are computed with the same physics. The $[\text{C}/\text{H}]$, $[\text{N}/\text{H}]$ and $[\text{O}/\text{H}]$ ratios do not change by more than 0.5 dex from the $Z = 10^{-5}$ the $Z = 0$ model. The reason is that the transport by rotation of ^{12}C and ^{16}O from the convective He-burning core to the convective H-burning shell operates at a similar efficiency in the $Z = 0$ model. In the H-rich ejecta (left panel), the elements from Ne to Si are much less abundant in the $Z = 0$ model compared to the $Z = 10^{-5}$ model. Considering also the He-rich ejecta raises considerably the abundances of these elements in both models. The exception is for the $[\text{Si}/\text{H}]$ ratio in the $Z = 0$ model, which stays several dex below the $[\text{Si}/\text{H}]$ ratio of the $Z = 10^{-5}$ model. The differences are mainly due to the fact that the H-burning shell of the $Z = 0$ model is more active, which limits the growth of the convective He-burning core (at the middle of the core He-burning phase, the size of the convective He-cores are $3.9 M_{\odot}$ and $2.7 M_{\odot}$ in

the $Z = 10^{-5}$ and $Z = 0$ models, respectively). The consequence is that less H-burning products (e.g. ^{14}N) let in between the He-core and the H-shell are engulfed by the convective He-core of the $Z = 0$ model. Globally, it has the effect of reducing the efficiency of the exchanges of material between the He-core and the H-shell. Finally, the nucleosynthesis is less rich and varied in the $Z = 0$ model. Also, Si is barely affected in the models considered (see also Fig. 4.7) so that the $[\text{Si}/\text{H}]$ ratio in the ejecta mostly reflects the initial $[\text{Si}/\text{H}]$ ratio. In the $Z = 0$ model, the initial Si abundance is zero so that $[\text{Si}/\text{H}] \sim \log(\text{Si}/\text{H}) \sim -\infty$ in the ejecta.

4.4 Comparison with CEMP-no stars

It is now discussed whether the abundances of observed metal-poor stars can be reproduced by the massive stellar models discussed previously. Particular attention is paid to the constraints provided by the $^{12}\text{C}/^{13}\text{C}$ ratio.

For the observations, I consider CEMP stars with $[\text{Fe}/\text{H}] < -3$ and $[\text{C}/\text{Fe}] > 1.0$. Recognized CEMP-r, -s and -r/s stars are excluded (according to the criteria of Table 2.2). I took into account the $\Delta[\text{C}/\text{Fe}]$ of Placco et al. (2014c) which allows to correct the effect of the first dredge-up of evolved stars and recover the initial C abundance. For the considered stars, $0 < \Delta[\text{C}/\text{Fe}] < 0.74$. With this correction, 12 stars become CEMP and are then added to the sample. It gives the 69 stars of Table 4.2. Stars with $T_{\text{eff}} \geq 5500$ K and $\log g \geq 3.25$ are classified as main-sequence stars and the other as giants stars⁷.

4.4.1 A global comparison

Let us first mention that $Z = 0$ source star models may face more difficulties in reproducing the abundance patterns of CEMP-no stars than very low metallicity source star models: the $20 M_{\odot}$ Pop III model in Fig. 4.16 either produces enough C, N, O but not enough Na, Mg, Al (left panel) or it produces enough Na, Mg, Al but then C, O and $^{12}\text{C}/^{13}\text{C}$ are overestimated (right panel). Also $[\text{Si}/\text{H}]$ is underestimated by several dex.

Considering all the other source star models discussed in Sect. 4.3.3, we see that a global match can be found with the abundances of CEMP-no stars. Source star ejecta with various initial rotation rates, mass cuts and dilution factors allow to reproduce all or nearly all the range of CEMP-no star abundances. However, a global match does not mean that individual CEMP-no stars can be well reproduced. The next step is to compare source star models with individual CEMP-no stars. As it will be discussed thereafter (especially in Sect. 4.4.2), a more in-depth comparison reveals some difficulties for models to reproduce some of the abundances of individual CEMP-no stars.

Interestingly, we also note that the CNO pattern of the material ejected by the source star has generally either a \wedge -shape (H-rich ejecta, Fig. 4.9) or a \vee -shape (H-rich + He-rich ejecta, Fig. 4.10). It is nevertheless not always the case (e.g. Fig. 4.12). In Table 4.2, very few stars have C, N and O abundances available together, without upper limits. CS 29498-043 has C, N and O abundances available and it has a clear \vee -shape. By contrast, HE 1327-2326 has a clear \wedge -shape. Another example is the CNO pattern of HE 0107-5240, which has a different shape (it has as much N as O). When considering the entire sample of Table 4.2, about 70 % is compatible with a \wedge -shape for the CNO pattern. Similarly, about 70 % is compatible with a \vee -shape. About the same fraction (70 %) of the sample is compatible with an almost flat CNO pattern. Detailed comparisons between source star models and CEMP stars are likely required to obtain more informations on the CEMP source stars (Sect. 4.5 and 4.6).

⁷With the exception of G77-61, with $T_{\text{eff}} = 4000$ K and $\log g = 5.05$ that is considered as a main-sequence star, following Plez & Cohen (2005) and Beers et al. (2007).

Table 4.2: Stars with $[\text{Fe}/\text{H}] < -3$ and $[\text{C}/\text{Fe}] > 1$. $[\text{C}/\text{Fe}]$ is corrected from $\Delta[\text{C}/\text{Fe}]$ (also reported in the table), that accounts for the effect of the first dredge-up (Placco et al. 2014c). Recognized CEMP-s, r/s and -r stars are excluded. Abundance data is from the SAGA database (Suda et al. 2008). When multiple abundances exist for a star, the abundance from the most recent literature source is selected.

Star	T_{eff}	$\log g$	$[\text{Fe}/\text{H}]$	$A(\text{Li})$	$[\text{C}/\text{Fe}]$	$[\text{N}/\text{Fe}]$	$[\text{O}/\text{Fe}]$	$[\text{Na}/\text{Fe}]$	$[\text{Mg}/\text{Fe}]$	$[\text{Al}/\text{Fe}]$	$[\text{Si}/\text{Fe}]$	$^{12}\text{C}/^{13}\text{C}$	$\Delta[\text{C}/\text{Fe}]$	Ref
BD+44 493	5430	3.4	-3.8	0.64	1.23	<2.2	1.54	0.3	0.89	-0.44	0.48	>15.0	0.0	1,2,3
CS22877-001	4790	1.45	-3.24	0.66	1.54	-0.08	1.22	-	0.38	-0.73	-	35.0	0.44	2
CS22891-200	4490	0.5	-3.88	<0.13	1.26	1.38	<1.67	0.29	0.82	-0.37	1.05	>6.0	0.73	2,4
CS22897-008	4550	0.7	-3.73	0.77	1.05	0.05	<1.86	-0.05	0.6	-0.77	0.46	>20.0	0.45	5,6,7
CS22949-037	4630	0.95	-4.2	<0.13	1.9	2.67	<2.39	1.89	1.56	0.26	1.52	>4.0	0.74	5,8,2
CS22950-046	4380	0.5	-3.64	<-0.05	1.13	1.13	<2.39	-0.18	0.58	-0.63	1.08	-	0.52	5,4
CS22953-037	6150	3.7	-3.05	1.97	1.0	<2.18	<0.5	-	0.55	-0.56	0.21	-	0.0	5
CS22957-027	5220	2.65	-3.0	<0.86	2.63	1.69	<1.2	0.98	0.08	-0.12	-	6.0	0.02	2
CS22960-053	4860	1.65	-3.33	<0.55	1.42	3.41	-	-	0.77	0.51	-	-	0.02	5
CS29498-043	4440	0.5	-3.85	<-0.05	3.06	1.74	2.37	1.03	1.78	0.75	1.08	8.0	0.31	2
CS29502-092	4820	1.5	-3.2	<0.45	1.45	1.1	1.13	-0.02	0.5	-0.6	-	12.0	0.39	2
CS29527-015	6240	4.0	-3.55	2.091	1.29	-	-	-0.19	0.41	0.07	0.18	-	0.0	9,10,11,12,13,14
CS29528-041	6170	4.0	-3.06	1.71	1.57	3.04	<1.38	0.67	0.38	-0.38	-0.16	-	0.0	12,15
G77-61	4000	5.1	-4.0	<3.31	3.21	2.2	1.82	0.77	0.56	-	-	5.0	0.0	16,17
HE0015+0048	4600	0.9	-3.07	<0.92	1.29	-	-	-	0.66	-0.37	0.5	-	0.67	18
HE0017-4346	6198	3.8	-3.07	-	3.11	-	-	1.51	0.87	0.03	-	-	0.0	8
HE0102-0633	6012	3.7	-3.1	-	1.08	-	-	<1.06	0.44	-0.27	0.32	-	0.0	8
HE0107-5240	5100	2.2	-5.4	<1.12	3.88	2.54	2.54	1.06	0.25	<-0.08	<0.48	>50.0	0.06	19,20
HE0134-1519	5500	3.2	-4.0	1.27	1.0	<1.0	<2.9	-0.24	0.25	-0.38	0.05	>4.0	0.0	21,22
HE0146-1548	4636	1.7	-3.46	-	1.57	-	-	1.16	0.87	0.14	0.5	-	0.73	23,24
HE0233-0343	6100	3.4	-4.7	1.77	3.48	<2.8	<4.0	<0.5	0.59	<0.03	0.05	>5.0	0.0	21
HE0251-3216	5750	3.7	-3.15	-	2.53	-	-	0.97	0.61	0.05	-0.6	-	0.0	8
HE0450-4902	6300	4.5	-3.1	<1.98	2.03	2.0	<3.5	0.23	0.53	-0.78	0.0	-	0.0	21
HE0557-4840	4900	2.2	-4.8	<0.7	1.77	<0.96	2.3	-0.25	0.16	-0.71	-	-	0.01	25,26
HE1005-1439	5000	1.9	-3.2	-	2.51	1.79	-	1.17	0.59	-	-	-	0.02	27
HE1012-1540	5230	2.65	-3.76	<0.75	2.4	1.15	<2.18	1.65	1.81	0.69	0.65	>30.0	0.0	2,8
HE1029-0546	6650	4.3	-3.3	<2.0	2.64	2.9	<3.7	-	-0.03	<-0.42	-0.03	9.0	-	21
HE1150-0428	5200	2.5	-3.21	-	2.51	2.62	-	1.44	0.35	-	-	-	0.02	8
HE1201-1512	5725	4.2	-3.89	-	1.14	<1.23	-	-0.35	0.2	-0.73	-	-	0.0	23,24
HE1249-3121	5373	3.4	-3.23	-	1.91	-	-	-	0.24	-0.79	-	-	0.0	28,29
HE1300+0157	5550	3.3	-3.49	1.06	1.34	<0.8	1.78	-0.13	0.33	-0.15	0.57	-	0.0	8,30
HE1300-0641	5308	2.96	-3.14	-	1.25	-	-	-	0.02	-1.19	-	-	0.01	28,29
HE1305-0331	6081	4.22	-3.26	-	1.09	-	-	-	-	-0.7	-	-	0.0	31,28
HE1310-0536	5000	1.9	-4.2	<0.8	2.44	3.2	<2.8	0.19	0.42	-0.39	0.8	3.0	0.08	21
HE1327-2326	6180	3.7	-5.66	<0.7	4.18	4.67	3.86	2.46	1.65	1.16	-	>5.0	0.0	32,33
HE1338-0052	5856	3.7	-3.0	-	1.53	-	-	-	0.44	-0.16	0.39	-	0.0	8
HE1351-1049	5204	2.85	-3.46	-	1.74	-	-	-	0.28	-0.75	-	-	0.01	28,29

4.4. Comparison with CEMP-no stars

Table 4.2 – continued

Star	T_{eff}	$\log g$	[Fe/H]	A(Li)	[C/Fe]	[N/Fe]	[O/Fe]	[Na/Fe]	[Mg/Fe]	[Al/Fe]	[Si/Fe]	$^{12}\text{C}/^{13}\text{C}$	$\Delta[\text{C}/\text{Fe}]$	Ref
HE1410-0004	5605	3.5	-3.02	<1.32	2.24	-	1.28	0.61	0.53	-	-	-	0.04	8,34
HE1413-1954	6302	3.8	-3.5	2.035	1.67	-	-	-	-	-	-	-	0.0	10,29
HE1456+0230	5664	2.2	-3.32	-	2.37	3.03	-	0.3	0.29	-0.09	0.54	-	0.02	8
HE1506-0113	5016	2.4	-3.54	-	1.49	0.61	-	1.65	0.89	-0.53	0.5	-	0.02	23,24
HE2123-0329	4725	1.15	-3.22	<0.58	1.06	-	-	-	0.58	-0.57	0.56	-	0.66	18
HE2139-5432	5416	2.2	-4.02	-	2.61	2.09	-	2.15	1.61	0.36	1.0	-	0.01	23,24
HE2318-1621	4846	1.4	-3.67	-	1.04	1.24	-	0.71	0.2	-0.58	-	-	0.5	35
HE2331-7155	4900	1.5	-3.7	<0.37	1.34	2.57	<1.7	0.46	1.2	-0.38	<0.25	5.0	-	21
LAMOSTJ125346.09	6030	3.65	-4.02	1.8	1.59	-	-	-0.2	0.24	-	-	-	-	36
LAMOSTJ131331.18	4750	1.6	-4.12	<0.68	1.83	-	-	-0.06	0.34	-	0.45	-	-	36
LAMOSTJ1626+1721	5930	3.6	-3.2	-	1.07	-	-	-0.02	0.5	-0.33	0.46	-	-	37
LAMOSTJ1709+1616	5780	3.5	-3.71	-	1.58	-	-	-	0.28	-	0.18	-	-	37
SDSSJ0002+2928	6150	4.0	-3.26	-	2.63	-	-	0.99	0.36	-	-	-	-	38
SDSSJ0126+0607	6900	4.0	-3.01	<2.2	3.08	-	-	0.86	0.66	-	-	-	-	38,39
SDSSJ0212+0137	6333	4.0	-3.59	2.04	2.28	<2.66	1.6	-	0.52	-0.55	0.23	-	-	40
SDSSJ0351+1026	5450	3.6	-3.18	-	1.55	-	-	-0.15	0.71	-	-	-	-	38
SDSSJ0723+3637	5150	2.2	-3.32	-	1.79	-	-	-0.1	0.23	-	-	-	-	38
SDSSJ1035+0641	6262	4.0	<-5.07	<1.1	3.54	-	-	-	<-0.06	-	-	-	-	40
SDSSJ1114+1828	6200	4.0	-3.35	-	3.3	2.2	-	-	-	-	-	>60.0	-	41
SDSSJ1143+2020	6240	4.0	-3.15	-	2.8	2.48	-	-	-	-	-	20.0	-	41
SDSSJ1245-0738	6110	2.5	-3.21	-	3.45	-	-	1.29	0.68	-0.12	0.02	-	-	40
SDSSJ131326.89	5200	2.6	-5.0	<0.8	2.96	3.46	-	0.37	0.44	-0.11	<0.21	-	-	42
SDSSJ1349-0229	6200	4.0	-3.24	-	3.01	-	-	1.87	0.73	-	-	>30.0	-	38,43
SDSSJ1422+0031	5200	2.2	-3.03	-	1.7	-	-	0.36	0.77	-	-	-	-	38
SDSSJ1613+5309	5350	2.1	-3.33	-	2.09	-	-	0.76	0.92	-	-	-	-	38
SDSSJ161956+170539	6191	4.0	-3.57	-	2.34	-	-	-	0.02	-	-0.27	-	-	44
SDSSJ1646+2824	6100	4.0	-3.05	-	2.52	-	-	-	0.71	-	-	-	-	38
SDSSJ1742+2531	6345	4.0	-4.8	-	3.63	-	<3.03	<0.7	<0.27	-	<0.34	-	-	40
SDSSJ1746+2455	5350	2.6	-3.17	-	1.24	-	-	0.48	0.69	-	-	-	-	38
SDSSJ2209-0028	6440	4.0	-3.96	-	2.61	-	-	-	-	-	-	-	-	41
SMSSJ005953.98	5413	2.95	-3.94	2.0	1.2	-	-	1.99	0.61	-0.25	0.73	-	-	45
SMSSJ031300.36	5125	2.3	<-7.3	0.7	4.9	<3.8	<5.0	<1.8	3.0	<1.1	<3.0	-	-	46

References. 1 - Placco et al. (2014a); 2 - Roederer et al. (2014a); 3 - Ito et al. (2013); 4 - Venn et al. (2004); 5 - Roederer et al. (2014b); 6 - Cayrel et al. (2004); 7 - Spite et al. (2006); 8 - Cohen et al. (2013); 9 - Spite et al. (2012); 10 - Sbordone et al. (2010); 11 - Bonifacio et al. (2009); 12 - Andrievsky et al. (2007); 13 - Andrievsky et al. (2010); 14 - Andrievsky et al. (2008); 15 - Sivarani et al. (2006); 16 - Beers et al. (2007); 17 - Plez & Cohen (2005); 18 - Hollek et al. (2011); 19 - Bessell et al. (2004); 20 - Christlieb et al. (2004); 21 - Hansen et al. (2015a); 22 - Hansen et al. (2014); 23 - Norris et al. (2013); 24 - Yong et al. (2013); 25 - Norris et al. (2012); 26 - Norris et al. (2007); 27 - Aoki et al. (2007); 28 - Barklem et al. (2005); 29 - Zhang et al. (2011); 30 - Frebel et al. (2007b); 31 - Ren et al. (2012); 32 - Frebel et al. (2008); 33 - Aoki et al. (2006); 34 - Cohen et al. (2006); 35 - Placco et al. (2014b); 36 - Li et al. (2015); 37 - Li et al. (2015); 38 - Aoki et al. (2013); 39 - Aoki et al. (2008); 40 - Bonifacio et al. (2015); 41 - Spite et al. (2015); 42 - Frebel & Norris (2015); 43 - Behara et al. (2010); 44 - Caffau et al. (2013); 45 - Jacobson et al. (2015); 46 - Keller et al. (2014)

Constraints from the $^{12}\text{C}/^{13}\text{C}$ ratio

The CEMP-no stars with a measured $^{12}\text{C}/^{13}\text{C}$ ratio have $3 < ^{12}\text{C}/^{13}\text{C} < 35$. Two stars are still dwarfs, with $^{12}\text{C}/^{13}\text{C} \sim 6$. As mentioned previously (Sect. 4.2), the $^{12}\text{C}/^{13}\text{C}$ ratio at the surface of an unevolved CEMP-no star is probably similar to the $^{12}\text{C}/^{13}\text{C}$ ratio in the cloud in which the star formed, hence similar to the $^{12}\text{C}/^{13}\text{C}$ ratio in the source star ejecta.

The $^{12}\text{C}/^{13}\text{C}$ ratios of the CEMP-no star sample are well reproduced by the H-rich ejecta of the source star models (Fig. 4.9). By contrast, they are largely overestimated by the H-rich + He-rich ejecta (Fig. 4.10, cf. also Choplin et al. 2016, Sect. 5.1, page 176 of this thesis). Of course one could imagine to dilute the H-rich + He-rich ejecta, having a high $^{12}\text{C}/^{13}\text{C}$, with an ISM having a very low $^{12}\text{C}/^{13}\text{C}$ (as discussed in Sect. 3.3.4, here I take $^{12}\text{C}/^{13}\text{C} = 300$ in the ISM but a lower value may also be chosen). The final mixture may present a low $^{12}\text{C}/^{13}\text{C}$ ratio, consistent with observations. In this case however, it just pushes back the problem: the need for a source producing a large amount of ^{13}C in the early Universe remains and has to be explained by some mechanism.

It is worth mentioning here that Galactic evolution models predict that a standard population of very low metallicity massive source stars will lead to a $^{12}\text{C}/^{13}\text{C}$ ratio of 4500 – 31000 in the (almost) primordial ISM (Chiappini et al. 2008). If instead, this population is dominated by massive fast rotators, Galactic evolution models predict $30 < ^{12}\text{C}/^{13}\text{C} < 300$. Rotation in massive stars is indeed a way to produce large amounts of ^{13}C (e.g. Fig. 4.6). The fact that it exists CEMP-no stars (especially unevolved stars) with a $^{12}\text{C}/^{13}\text{C}$ ratio even lower than 30 suggests that a very special material is required to form them, maybe coming from the relatively external layers of one specific rotating massive source star.

As a remark, let us mention that the fact that there is no CEMP star with a $^{12}\text{C}/^{13}\text{C}$ ratio below the CNO-equilibrium value (which is about 4) suggests that the dominant source of ^{13}C in the early Universe comes from CNO burning. If there was another important source of ^{13}C , we should observe CEMP-no stars with lower $^{12}\text{C}/^{13}\text{C}$ ratios. Moreover if such stars exist, they should be observable since low $^{12}\text{C}/^{13}\text{C}$ ratios are easier to detect: if the ratio is low, ^{13}C is abundant and then ^{13}C lines are stronger. This last point also shows that it can exist a bias towards low $^{12}\text{C}/^{13}\text{C}$. Some CEMP-no stars have a lower limit for $^{12}\text{C}/^{13}\text{C}$ (e.g. HE 1201-1512 and HE 1327-2326 with $^{12}\text{C}/^{13}\text{C} > 20$ and > 5 respectively, Aoki et al. 2006; Norris et al. 2013). Future observations may reveal a population of stars with higher $^{12}\text{C}/^{13}\text{C}$ ratios.

Can the H-rich material of massive source stars explain the abundances of CEMP-no stars?

In the previous discussion and in Sect. 4.2, it was proposed that CEMP-no stars could have formed with only the H-rich material of the source star. However, if considering only the H-rich source star ejecta, several issues arise (see Fig. 4.9):

1. The ranges of Mg/H, Al/H and Si/H ratios are not covered by source star models (also N and Na to a smaller extent).
2. The predicted [Al/H] ratios are too high (also true if considering the H- + He-rich ejecta, Fig. 4.10).
3. Such an ejecta shows a clear CNO processed signature with a very characteristic CNO pattern (\wedge -shape), while some CEMP-no stars are not compatible with this pattern.
4. The most C-rich CEMP-no stars, with $[\text{C}/\text{H}] \gtrsim -1.5$ cannot be explained.

First, some scatter in the CEMP star abundances is probably induced by the fact that the abundance data is not homogeneous, together with the possible 3D/NLTE corrections on abundances (cf. Sect. 2.2.2 and 4.2). This could alleviate the issue 1.

Second, some nuclear reaction rates of the Ne-Na and Mg-Al chains are uncertain (cf. Sect. 4.2). Changing these rates will change the predicted Na/H, Mg/H, Al/H ratios but in a similar way

for all the models, i.e. the predicted scatter will not change. I computed again the $v_{\text{ini}}/v_{\text{crit}} = 0.4$ model with the nuclear rate of $^{27}\text{Al}(p, \gamma)^{28}\text{Si}$ from Cyburt et al. (2010) instead of Iliadis et al. (2001). This is an extreme case, favoring Al destruction, since the rate of Cyburt et al. (2010) is the highest one below 100 MK. At $T = 50$ MK, the Cyburt et al. (2010) rate is ~ 100 times larger than the Iliadis et al. (2001) rate. The orange dashed line in Fig. 4.9 shows that the $[\text{Al}/\text{H}]$ ratio in the ejecta of the model with the Cyburt et al. (2010) decreases by ~ 1 dex compared to the standard case. We note that the $[\text{Si}/\text{H}]$ is barely modified. Nuclear rate uncertainties can lead to significant differences in the predicted yields and make the $[\text{Al}/\text{H}]$ consistent with the bulk of observed abundances. This helps with the issue 2.

The issues 3 and 4 can be solved if considering the H-rich + He-rich ejecta (Fig. 4.10), which gives much more carbon and reverses the CNO pattern. Some dilution with the ISM might provide abundance patterns able to reproduce the observations (right panel of Fig. 4.13). However, in this case, the predicted $^{12}\text{C}/^{13}\text{C}$ is too high. The difficulty here is to get a high enough C/N ratio together with a low $^{12}\text{C}/^{13}\text{C}$ ratio, as it is observed on many CEMP-no stars (Fig. 4.17). This issue is discussed in the next section.

4.4.2 The C/N – $^{12}\text{C}/^{13}\text{C}$ puzzle

Standard source star models

In source star models, either both C/N and $^{12}\text{C}/^{13}\text{C}$ ratios are low (H-rich ejecta), or both ratios are high (H-rich + He-rich ejecta). The crosses in Fig. 4.17 show the ratios in the total wind of some source star models discussed in the previous section. The tracks show the variation of the ratios in the ejecta with M_{cut} let as a free parameter. A specific M_{cut} value gives one point in such a track. Here, for a given source star model, all possible mass cuts are considered: in Eq. 3.15, M_{cut} is varied between 0 and M_{fin} . It gives a collection of points, which can be seen as a line.

We see that whatever the source star ejecta considered, none can match the bulk of observed stars (the tracks are nevertheless consistent with some lower limit $^{12}\text{C}/^{13}\text{C}$ ratios). All models show a similar behavior. CNO processed material gives $\log(^{12}\text{C}/^{13}\text{C}) \sim 0.6$ and $[\text{C}/\text{N}] \sim 2$ and He-processed material $\log(^{12}\text{C}/^{13}\text{C}) \gg 1$ and $[\text{C}/\text{N}] \gg 1$. A mix of CNO and He-processed material gives something in between, but not in the region where most of the CEMP-no stars lie.

Effect of the first dredge-up in CEMP-no stars

Some CEMP-no stars in Fig. 4.17 are giants (big grey circles) and have likely experienced the first dredge-up. This process can change the location of the stars in the C/N – $^{12}\text{C}/^{13}\text{C}$ diagram. Below is investigated by how much and in which direction the first dredge-up can move a CEMP-no star in this diagram.

First, I started from a reference $0.8 M_{\odot}$ model having the composition of the star CS 22958-042 at the Zero-Age Main-Sequence (ZAMS). CS 22958-042 is a subgiant with $[\text{Fe}/\text{H}] = -2.99$, $[\text{C}/\text{Fe}] = 2.15$, $[\text{N}/\text{Fe}] = 2.25$ and $^{12}\text{C}/^{13}\text{C} = 7$ (Roederer et al. 2014a). Then, 9 other $0.8 M_{\odot}$ models were computed with different initial $[\text{C}/\text{N}]$ and $^{12}\text{C}/^{13}\text{C}$ ratios. Table 4.3 gives the initial ratios of the 10 models. The standard model, having the composition of CS 22958-042, initially has $\log(^{12}\text{C}/^{13}\text{C}) = 0.85$ and $[\text{C}/\text{N}] = -0.1$.

The evolution is stopped after the first dredge-up. The thermohaline mixing is not considered. The surface $\log(^{12}\text{C}/^{13}\text{C})$ and $[\text{C}/\text{N}]$ ratios after the first dredge-up are reported in Table 4.3. The effect of the first dredge-up on the surface $[\text{C}/\text{N}]$ and $\log(^{12}\text{C}/^{13}\text{C})$ ratios of these models is also shown in Fig. 4.17 by the orange arrows. In all the cases, the surface abundance ratios are decreased. The decrease ranges from 0 to 0.63 dex. The lower the initial $^{12}\text{C}/^{13}\text{C}$ and C/N ratios, the smaller the effect of the dredge-up. This is because if starting with $^{12}\text{C}/^{13}\text{C}$ and C/N ratios already close to CN equilibrium in the stellar envelope, then, adding some material at CN equilib-

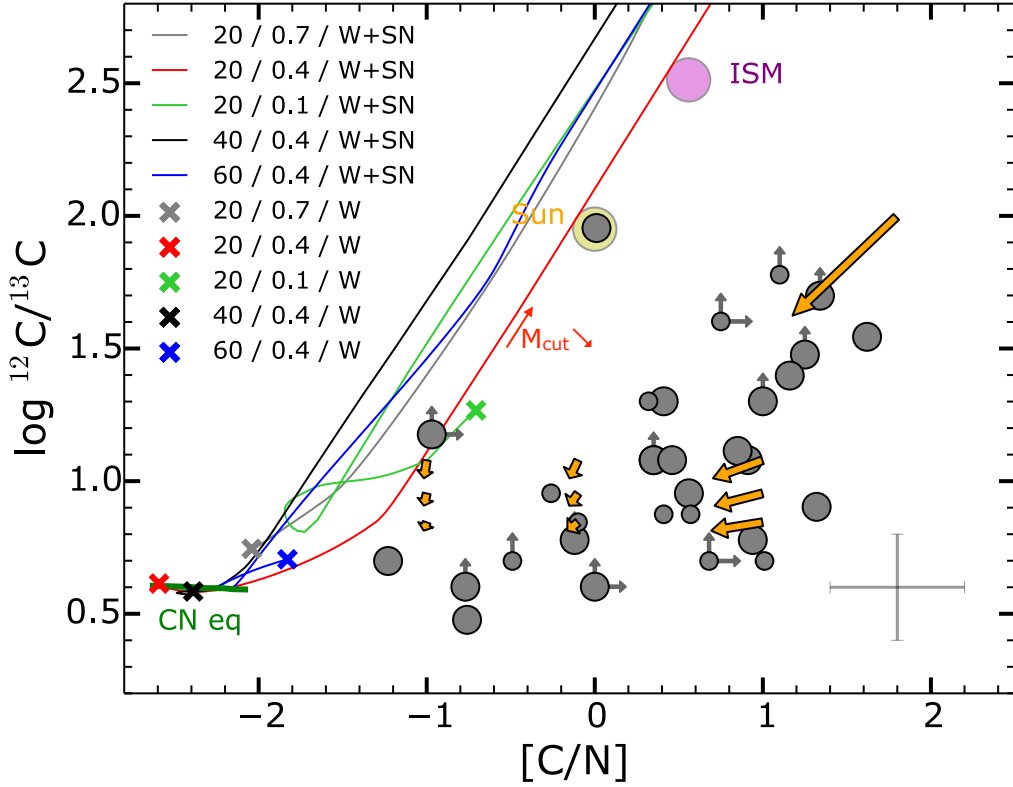


Figure 4.17: Grey circles are observed main sequence (small circles) and giants (big circles) CEMP stars with $[\text{Fe}/\text{H}] < -2.5$ (a few stars were added compared to Table 4.2). Recognized CEMP-r, -s and -r/s are excluded. The grey arrows indicate that only limits are deduced from spectroscopy. The typical uncertainty is shown. The orange arrows show the effect of the first dredge-up on the surface composition of low metallicity $0.8 M_{\odot}$ models with various initial C/N and $^{12}\text{C}/^{13}\text{C}$ ratios. The yellow and purple circles show the solar ratios and the ratio in the α -enhanced ISM considered here, respectively. The crosses show the ratios in the wind (W) at the end of core carbon burning. The tracks represent the integrated ratios as more and more layers of the final structure are ejected and added to the wind (W+SN). The red arrow shows in which direction the tracks are going when decreasing the mass cut (i.e. ejecting deeper layers). In the legend, the first and second numbers refer to initial masses and rotation rates, respectively. The thick green line labelled *CN eq* represents the ratios obtained in a one-zone model at CN-equilibrium for $30 < T < 80$ MK.

Table 4.3: Initial and final (after the first dredge-up) surface $\log(^{12}\text{C}/^{13}\text{C})$ and $[\text{C}/\text{N}]$ ratios for the ten $0.8 M_{\odot}$ models computed.

$\log(^{12}\text{C}/^{13}\text{C})_{\text{ini}}$	0.85	0.85	0.85	0.95	0.95	0.95	1.08	1.08	1.08	2
$\log(^{12}\text{C}/^{13}\text{C})_{\text{1DUP}}$	0.81	0.81	0.81	0.91	0.91	0.91	1.01	1.01	1.01	1.17
$[\text{C}/\text{N}]_{\text{ini}}$	-1	-0.1	1	-1	-0.1	1	-1	-0.1	1	1.8
$[\text{C}/\text{N}]_{\text{1DUP}}$	-1.02	-0.16	-0.69	-1.02	-0.15	0.71	-1.02	-0.15	0.70	1.62

rium barely affects the ratios. On the opposite, if the initial $^{12}\text{C}/^{13}\text{C}$ and C/N ratios are far from equilibrium, adding a bit of CN-processed material in the envelope has a stronger impact on the ratios. These results suggest a rather modest effect of the first dredge-up, except for the CEMP stars that were formed from a material in which the C/N and $^{12}\text{C}/^{13}\text{C}$ ratios were very far from CN equilibrium (see the biggest orange arrow in Fig. 4.17).

Other mixing processes in CEMP-no stars

In Fig. 4.17, some observed evolved CEMP-no stars may also have experienced other mixing processes like thermohaline (cf. Sect. 2.4). As discussed, however, a significant fraction of CEMP-no stars may not have experienced too much mixing, except the most evolved stars (cf. Fig. 2.6). Also, it has to be noted that unevolved CEMP-no stars lie globally at similar positions than evolved CEMP-no stars in Fig. 4.17. If the internal mixing processes had a strong impact on the surface C/N and $^{12}\text{C}/^{13}\text{C}$ ratios, we should probably see distinct groups of CEMP-no stars: the bulk of evolved CEMP-no stars on the one hand, the bulk of unevolved CEMP-no stars on the other hand. The fact that it is not the case may finally indicate that the composition of the evolved CEMP-no stars shown in Fig. 4.17 reflects quite well the composition of the cloud in which they formed.

4.5 The late mixing process in the source star

A solution to the C/N – $^{12}\text{C}/^{13}\text{C}$ puzzle is to introduce a *late mixing process* in the source star, occurring between the H- and He-burning shell, about 200 yr before the end of the evolution. Below I give more details on this process and discuss how it can naturally produce a material with a high C/N ratio and a low $^{12}\text{C}/^{13}\text{C}$ ratio, able to improve the fit between models and observations. In Sect. 4.8, I investigate whether other models available in the literature can provide a solution. This mixing process was investigated in Choplin et al. (2017b, page 159 of this thesis). The main points of the paper are summarized in this section.

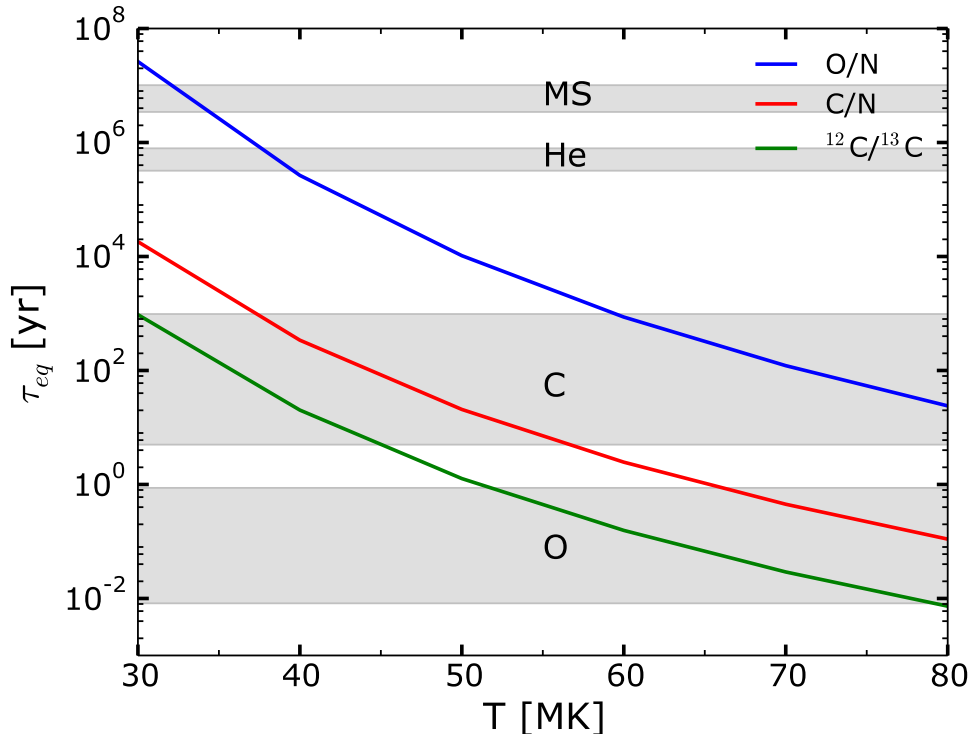


Figure 4.18: CNO equilibrium timescales of the O/N, C/N, and $^{12}\text{C}/^{13}\text{C}$ ratios as a function of the temperature. A one-zone model at density $\rho = 1 \text{ g cm}^{-3}$ is used. The shaded areas show the ranges of duration for the various burning stages (main sequence, He-, C-, and O-burning) of the models presented in Table 4.4.

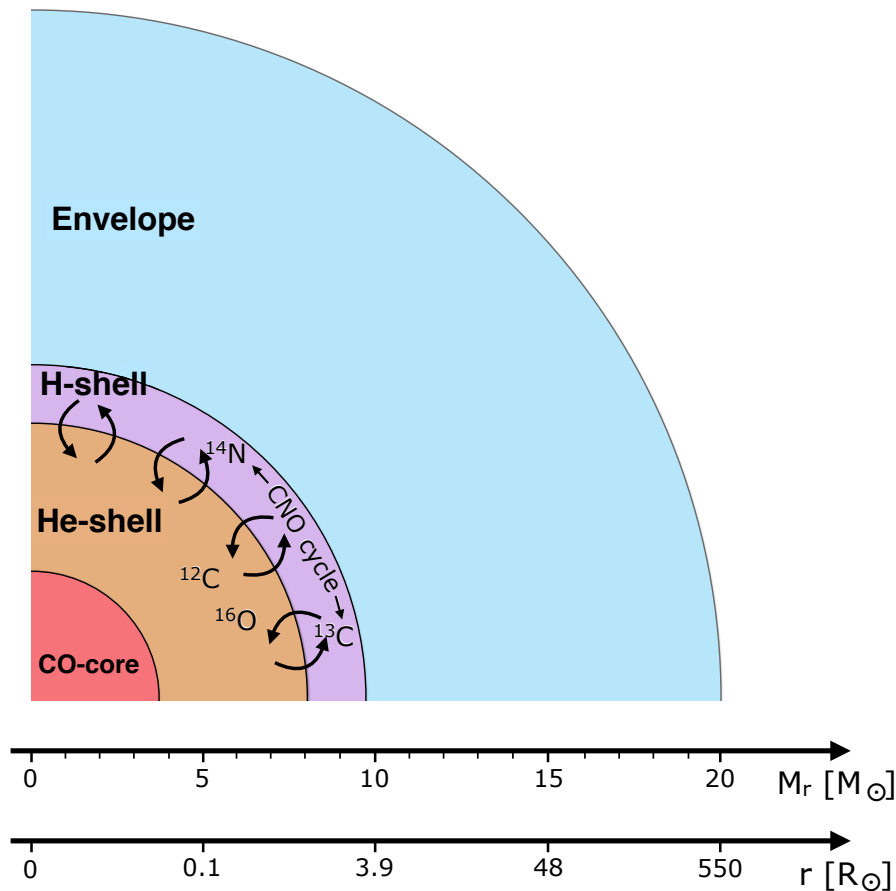


Figure 4.19: Schematic view of the late mixing process at work in the source star. The mixing starts during the core carbon burning phase. The curved black arrows show the region where it operates. The scheme is at scale in mass. Corresponding radii are indicated.

4.5.1 General idea

Figure 4.18 shows the time it takes for the C/N , O/N and $^{12}C/^{13}C$ ratios to reach their CNO equilibrium value in a H-burning zone at $30 < T < 80$ MK. Results are obtained using the one-zone model described in Sect. 4.2. Equilibrium values are reached quicker when the temperature increases. Whatever the temperature, $^{12}C/^{13}C$ reaches equilibrium ~ 10 times faster than C/N , and C/N reaches equilibrium 100 – 1000 times faster than O/N . In the H-burning shell of a complete stellar model, there is a gradient of temperature and the temperature $30 \lesssim T \lesssim 80$ MK. The global equilibrium timescale of the shell cannot be deduced directly from Fig. 4.18. However, the relative difference between the different timescale stays the same.

Let us now assume that some ^{12}C is injected in a single burning zone at $T = 30$ MK which is at CNO equilibrium. The extra ^{12}C disturbs the CNO equilibrium. Fig. 4.18 tells us that after 2000 yr, $^{12}C/^{13}C$ will have reached back its equilibrium value while C/N and O/N will not. It means that if the H-burning shell of the massive star is burning at 30 MK and some ^{12}C is injected 2000 yr before the end of the evolution, then, at the pre-SN stage, the H-shell will have C/N above equilibrium and $^{12}C/^{13}C$ at equilibrium. The average temperature in the H-burning shell of a massive source star is about 40 MK. Then, to obtain a partially processed CN material, with C/N above equilibrium and $^{12}C/^{13}C$ at equilibrium, some ^{12}C has to be injected in the H-burning shell $\sim 100 - 200$ yr before the end of the evolution. At this time, the source star burns carbon in its core. For 20 – 60 M_{\odot} models, the core carbon burning stage lasts for 10 – 1000 yr (grey area in Fig. 4.18).

4.5. The late mixing process in the source star

Table 4.4: Properties of the source star models: model label (column 1) initial mass (column 2), $v_{\text{ini}}/v_{\text{crit}}$ (column 3), initial equatorial velocity (column 4), total lifetime (column 5), duration of the main sequence, helium, carbon, neon, oxygen, and silicon-burning phases (column 6 – 11), mass of the model at the end of the evolution (column 12), remnant mass according to the relation of Maeder (1992, column 13).

Model	M_{ini} [M_{\odot}]	$v_{\text{ini}}/v_{\text{crit}}$	v_{ini} [km/s]	τ_{life} [Myr]	τ_{MS} [Myr]	τ_{He} [Myr]	τ_{C} [yr]	τ_{Ne} [day]	τ_{O} [day]	τ_{Si} [day]	M_{final} [M_{\odot}]	M_{rem} [M_{\odot}]
No rotation												
20s0	20	0	0	8.93	8.02	0.79	978	168	318	3.1	19.98	1.88
32s0	32	0	0	5.78	5.24	0.48	124	22	47	0.6	31.94	2.98
60s0	60	0	0	3.81	3.44	0.33	15	7	7	0.5	59.80	6.35
Rotation												
20s7	20	0.7	610	11.0	10.1	0.76	400	277	128	1.4	19.50	2.20
32s7	32	0.7	680	7.14	6.61	0.47	45	7	15	0.6	30.71	3.69
60s7	60	0.7	770	4.69	4.33	0.32	5	1	3	0.2	47.65	8.88
No rotation, late mix												
20s0mix	20	0	0	8.93	8.02	0.79	993	-	-	-	19.98	1.88
32s0mix	32	0	0	5.78	5.24	0.48	157	-	-	-	31.94	2.98
60s0mix	60	0	0	3.81	3.44	0.33	18	-	-	-	59.80	6.35
Rotation, late mix												
20s7mix	20	0.7	610	11.0	10.1	0.76	412	-	-	-	19.50	2.20
32s7mix	32	0.7	680	7.14	6.61	0.47	51	-	-	-	30.70	3.69
60s7mix	60	0.7	770	4.69	4.33	0.32	5	-	-	-	47.64	8.73

4.5.2 Implementation in source star models

This mixing process was investigated for a grid of six models whose characteristics are given in Table 4.4. Small differences exist between the input parameters of these models and the models of the previous section. First, when $\log(T_{\text{eff}}) \geq 3.95$, the mass-loss rates are from Kudritzki & Puls (2000), instead of Vink et al. (2001). Radiative winds are generally small at low metallicity so that no big impact is expected. Second, following the study on Al discussed in Sect. 4.2, the nuclear rates from the literature that minimize the production of Al are selected: Angulo et al. (1999) for $^{26}\text{Mg}(p, \gamma)^{27}\text{Al}$, Cyburt et al. (2010) for $^{27}\text{Al}(p, \gamma)^{28}\text{Si}$ and $^{27}\text{Al}(p, \alpha)^{24}\text{Mg}$. Third, f_{energ} in the expression of D_{shear} (Eq. 3.10) was taken equal to 1 instead of 4.

First, the models were computed normally (without late mixing) until the end of the central silicon-burning phase. The computation is stepped when the mass fraction of ^{28}Si in the core is less than 10^{-8} . For rotating models, the effects of rotation were taken into account until the end of the carbon burning phase. Last stages were computed without rotation. It saves a lot of computational time and leads to only very small differences in the abundance profiles since the duration of the last stages is short ($\sim 1 - 300$ days, cf. Table 4.4) compared to the rotational mixing timescale. In a second step, I have computed again the end of the evolution for the six models while triggering the late mixing process ~ 200 yr before the end of the evolution (Fig. 4.19 for a schematic view). For these models, the evolution was stopped at the end of core carbon burning. Last stages are very short and change only the composition of the most inner layers. It gives four categories of models: (1) no rotation, no late mixing, (2) no rotation, late mixing, (3) fast rotation, no late mixing and (4) fast rotation, late mixing.

To model the late mixing process in rotating models, the shear diffusion coefficient D_{shear} is multiplied by a factor of 100 in between the H- and He-shell. In non-rotating models, an artificial and constant diffusion coefficient $D_{\text{no rot}} = 10^9 \text{ cm s}^{-1}$ is set in the mixing zone. This is a typical value of the diffusion coefficient found in rotating models including late mixing. Although modeled through the shear diffusion coefficient, it is not assumed that the physical origin of the late mixing process is linked to the shear. Its possible physical origin is discussed in Sect. 4.5.4.

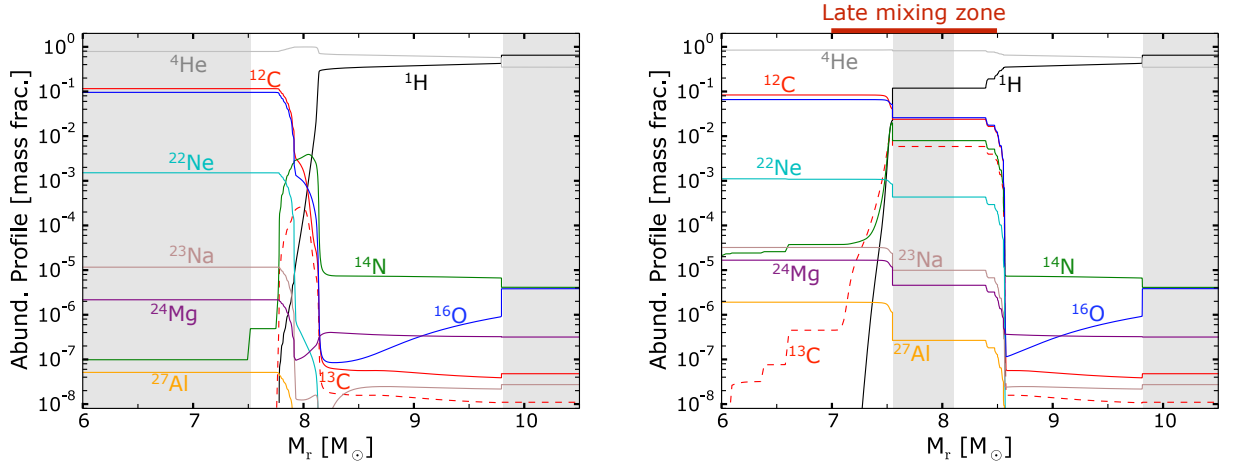


Figure 4.20: Abundance profiles of the $20 M_{\odot}$ models with $v_{\text{ini}}/v_{\text{crit}} = 0.7$ at the end of the core carbon-burning phase with no late mixing (left) and with late mixing (right). Shaded areas show the convective zones. The zone where the late mixing process occurs is indicated on the top.

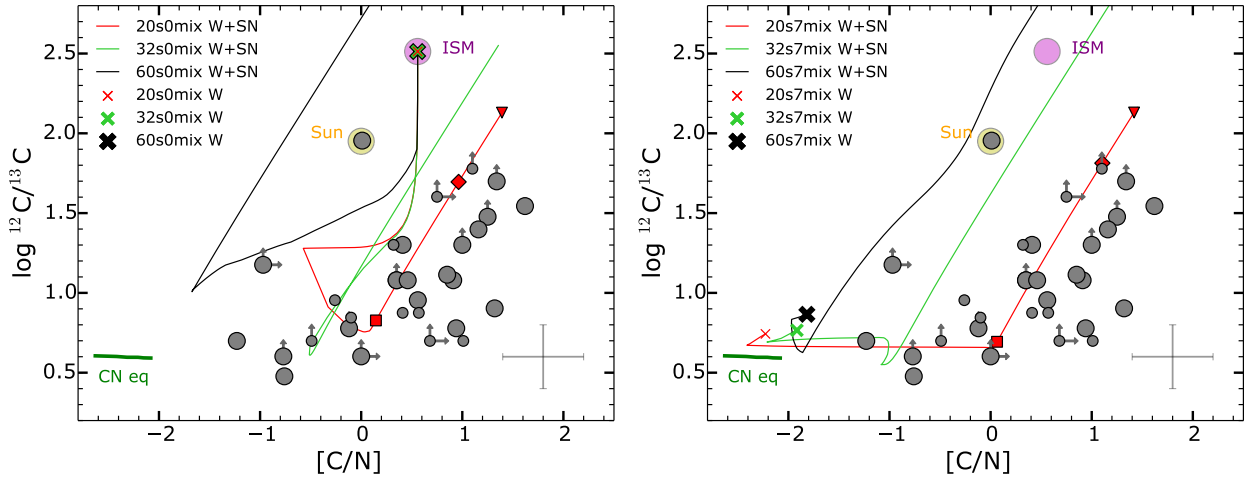


Figure 4.21: Same as Fig. 4.17 but for the 20, 32 and $60 M_{\odot}$ models of Table 4.4 including the late mixing process and with $v_{\text{ini}}/v_{\text{crit}} = 0$ (left) and 0.7 (right). The red square, diamond and triangle show the composition of the ejecta of the $20 M_{\odot}$ model when the mass cut is equal to M_{α} , M_{CO} , and M_{rem} , respectively.

4.5.3 Comparison with CEMP-no stars

When the late mixing process is included, additional ^{12}C and ^{16}O enter into the H-shell, boosting the CNO cycle and then releasing more energy. The H-shell becomes convective, extends in mass so that more He-burning products are engulfed. The fresh ^{12}C starts to be transformed into ^{13}C and ^{14}N in the H-shell. However, the time remaining before the end of the evolution being short, the $[\text{C}/\text{N}]$ equilibrium value of ~ -2.3 is not reached. The right panel of Fig. 4.20 shows the abundance profile of the rotating $20 M_{\odot}$ model with late mixing, at the end of core carbon burning. We see that the convective H-shell contains a lot of CNO elements, and has $X(\text{C})/X(\text{N}) > 1$ while $X(^{12}\text{C})/X(^{13}\text{C})$ is at equilibrium, around 4. This process builds a zone which is, at the end of evolution, partially processed by the CN cycle in the source star, where C/N is high and $^{12}\text{C}/^{13}\text{C}$ at equilibrium.

Fig. 4.21 shows the ejecta of the non-rotating (left panel) and rotating (right panel) 20, 32 and $60 M_{\odot}$ models including the late mixing process. With increasing mass, the tracks in Fig. 4.21 are

shifted to the left, away from observations. This is mainly due to the fact that higher-mass models have a higher temperature in the H-burning shell. This implies that the CN cycle operates faster. In this case, the injected ^{12}C is transformed more rapidly into ^{14}N . Then, the [C/N] ratio in the H-burning shell is closer to the equilibrium value (~ -2) at the end of evolution. It finally implies that the ejecta of higher-mass models cannot reach high [C/N] ratios together with low $^{12}\text{C}/^{13}\text{C}$ ratios. There are several reasons that may make the late mixing process more likely to occur in $\sim 20 M_{\odot}$ source stars than in $\sim 60 M_{\odot}$ source stars:

- In a $60 M_{\odot}$ model, the late mixing process should occur very late in the evolution, so as to end up with a high C/N (see above). If it occurs too early, C/N has enough time to reach back equilibrium. It means that the time window for the late mixing to operate is shorter in a $60 M_{\odot}$ model than in a $20 M_{\odot}$ model.
- In more massive stars, the mixing process should be extremely strong so as to compensate for the short time available.
- In more massive stars, the distance between the H- and He-burning shells is greater, so that the connection between the two shells might be less likely.

Overall, $\sim 20 M_{\odot}$ source stars might be better candidates for the late mixing process, hence for reproducing the observations.

Fig. 4.21 shows that both the non-rotating and rotating $20 M_{\odot}$ models can reproduce the bulk of observations. These two kind of models show however important differences regarding other elements. In fact, the late mixing process changes the distribution of chemical species in the source star (Fig. 4.20) but in the models presented here, it implies further nucleosynthesis almost only for the elements⁸ ^{12}C , ^{13}C and ^{14}N . This is because the burning timescales for the other species considered in the network (e.g. O, Ne, Na, Mg, Al) are longer compared to the remaining time before the end of the evolution. For instance, there is little time for the Ne-Na cycle to operate and produce additional ^{23}Na in models including late mixing. Instead, a progressive mixing, achieved by rotation during the core helium burning stage can form extra ^{23}Na (Sect. 4.3.2 and Fig. 4.7). This is an important difference between non-rotating (little Na) and rotating models (high Na) including late mixing. Many CEMP-no stars are enriched in Na. It may suggest that, at least for a part of the CEMP-no star sample, two kind of mixing are needed: rotational mixing (for Na) and the late mixing process (for a high C/N with a low $^{12}\text{C}/^{13}\text{C}$).

4.5.4 Physical origin

In the present work, the late mixing process is triggered artificially. It has to be noted that in some cases, similar events occur naturally. Indeed, various authors reported sudden ingestion events of H-burning material into the He-burning core or shell in low or zero metallicity massive stellar models (with or without rotation, Hirschi 2007; Ekström et al. 2008; Heger & Woosley 2010; Limongi & Chieffi 2012, see also Sect. 4.8). Although observed in some stellar models, the occurrence conditions and physical process(es) responsible for such events remain unknown. No specific behaviour is observed with any stellar parameter.

The treatment of the convection in stellar evolution codes may impact the shell/shell interaction or the core/shell interaction and thus the occurrence of the late mixing event. In GENEC, the convective boundaries are determined using the Schwarzschild criterion. The boundaries of the convective zones are sharp (step functions). During the main sequence and core He-burning phase, the convective core is extended using a penetrative overshoot. The overshoot is applied neither for the more advanced phases of stellar evolution, nor for the intermediate convective shells. This prescription probably does not capture the whole physics of convection (Arnett et al.

⁸This process may also form heavy elements through neutron captures, see Sect. 4.8.

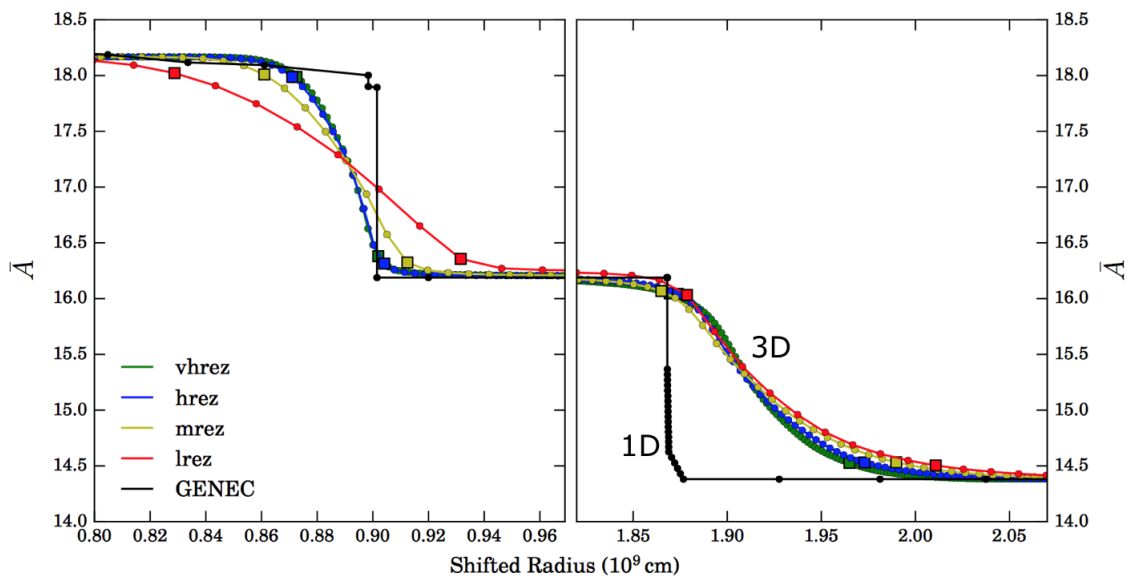


Figure 4.22: Radial profile of the averaged atomic weight \bar{A} at the lower (left) and upper (right) convective boundary regions of the C-burning shell of a $15 M_{\odot}$ model. The radius of each profile is shifted such that the boundary position coincides with the boundary position of the *vhrez* model. The symbols denote the mesh points. The black profile is from GENEC while the other profiles are from 3D hydrodynamic simulations of various resolutions. The range of radius shown corresponds approximately to the range of mass coordinates $1.2 - 1.8 M_{\odot}$ (figure from Cristini et al. 2017).

2015). Multi-dimension hydrodynamics numerical simulations of convection in deep stellar interior show that the chemical composition of each side of the convective boundary makes a smooth transition and is not a step function. (Herwig et al. 2006; Meakin & Arnett 2007; Arnett & Meakin 2011; Cristini et al. 2017). Fig. 4.22 shows a comparison between 1D code (GENEC) and 3D simulations, for the carbon burning shell. We see that in 3D, the carbon shell extends further in mass compared to 1D models. Multi-D simulations of H/He burning-zones during earlier stages (e.g. core He-burning stage) do not exist since they are computationally too expansive, mainly because the burning timescales are long.

It might be that improving the way convection is treated in classical 1D codes to follow more closely the behavior observed in multi-dimensional simulations strengthens the exchanges between the H- and He-burning shells. This could naturally induce the creation of the late mixing zone. If so, the late mixing invoked in this work would result from an overly poor description of the convective boundaries in 1D stellar evolution models.

4.6 A systematic study of the CEMP-no source star population

I now investigate what is the best source star model for each individual CEMP-no star. All the 69 CEMP stars of Table 4.2 are considered. To fit the abundance pattern of each CEMP star, I consider the 12 source star models of Table 4.4 and vary the dilution factor and mass cut for each models. The final structure of the source star is taken at the end of the core carbon burning stage for all the 12 models since ultimate stages were not computed for the 6 models including late mixing. Four dilution factors are considered : $D = 0, 10, 100$ and 1000 . It gives $12 \times 4 = 48$ combinations. For each of these 48 cases, the mass cut of the given source star model is varied between its final mass (i.e. only winds) and M_{rem} (cf. Table 4.4). The mass cut is chosen so as to minimize the sum of the residuals (in absolute value):

4.6. A systematic study of the CEMP-no source star population

Table 4.5: Parameters of the best source star models (column 2) for the considered CEMP-no stars (column 1). f_{H} , f_{He} and f_{CO} correspond to the ejected fraction of the H-envelope (above M_{α}), He-shell (between M_{α} and M_{CO}) and CO-core (below M_{CO}), respectively. D is the dilution factor, $X(\text{He})$ is the mass fraction of helium predicted for the CEMP-no star, ξ the error on the fit and N the number of abundances used to make the fit.

Star	Best model	$M_{\text{cut}} [M_{\odot}]$	f_{H}	f_{He}	f_{CO}	D	$X(\text{He})$	ξ	N
BD+44_493	60s7mix	29.88	1	0.72	0	1000	0.25	0.46	4
CS22877-001	20s7mix	5.07	1	0.97	0	1000	0.25	1.32	5
CS22891-200	20s7mix	8.5	0.92	0	0	10	0.26	0.62	4
CS22897-008	60s0	22.7	1	0.47	0	1000	0.25	0.31	4
CS22949-037	20s7mix	8.54	0.92	0	0	0	0.38	1.38	4
CS22950-046	20s7mix	8.53	0.92	0	0	10	0.26	0.21	4
CS22957-027	20s7mix	7.4	1	0.03	0	10	0.26	1.03	5
CS22960-053	20s7	7.97	1	0.02	0	0	0.39	1.11	3
CS29502-092	20s7mix	7.32	1	0.07	0	100	0.25	1.19	6
CS29527-015	60s7mix	28.04	1	1	0	1000	0.25	0.1	3
CS29528-041	32s7mix	19.05	0.75	0	0	0	0.42	0.99	4
G77-61	20s0mix	12.78	0.5	0	0	0	0.27	1.28	6
HE0017-4346	20s7mix	7.77	0.98	0	0	0	0.4	0.28	3
HE0134-1519	60s0mix	24.21	1	0.1	0	10	0.27	0.71	3
HE0146-1548	20s7mix	8.51	0.92	0	0	0	0.38	1.05	3
HE0251-3216	20s7mix	7.09	1	0.16	0	10	0.26	0.34	3
HE0450-4902	20s7mix	8.43	0.92	0	0	0	0.38	0.94	4
HE1005-1439	20s7mix	6.86	1	0.25	0	10	0.27	0.66	4
HE1029-0546	20s0mix	11.58	0.58	0	0	0	0.31	0.55	4
HE1150-0428	20s7mix	8.31	0.93	0	0	0	0.38	0.45	4
HE1201-1512	60s0	24.29	1	0.13	0	10	0.27	0.63	3
HE1300+0157	60s7	28.22	1	1	0.01	1000	0.25	0.27	4
HE1310-0536	32s0mix	14.99	0.79	0	0	10	0.27	0.89	5
HE1327-2326	60s7	33.51	1	0.21	0	0	0.62	1.08	5
HE1410-0004	20s7mix	8.43	0.92	0	0	0	0.38	1.04	4
HE1456+0230	20s7	7.86	1	0.06	0	0	0.4	0.96	4
HE2318-1621	20s0mix	13.63	0.44	0	0	0	0.25	0.73	4
HE2331-7155	20s7	7.99	1	0.02	0	0	0.39	1.14	5
LAMOSTJ125346.09	60s0mix	24.22	1	0.1	0	0	0.53	0.5	3
LAMOSTJ131331.18	60s0	24.33	1	0.12	0	0	0.53	0.42	3
LAMOSTJ1626+1721	20s0	5.8	1	0.16	0	0	0.38	0.7	3
SDSSJ0002+2928	20s7mix	7.18	1	0.12	0	10	0.26	0.16	3
SDSSJ0126+0607	32s7mix	10.73	1	1	0.03	10	0.27	0.18	3
SDSSJ0212+0137	20s7	7.89	1	0.05	0	0	0.4	0.21	3
SDSSJ0351+1026	60s7mix	8.84	1	1	0.68	1000	0.25	0.51	3
SDSSJ0723+3637	20s0	5.78	1	0.16	0	0	0.38	0.23	3
SDSSJ1143+2020	20s7mix	6.48	1	0.41	0	10	0.27	0.51	3
SDSSJ1245-0738	20s7	3.72	1	1	0.26	10	0.26	0.23	3
SDSSJ1349-0229	20s7mix	5.78	1	0.69	0	10	0.27	0.48	3
SDSSJ1422+0031	20s7mix	3.03	1	1	0.4	100	0.25	0.67	3
SDSSJ1613+5309	20s7mix	3.3	1	1	0.34	100	0.25	0.68	3
SDSSJ1746+2455	20s7mix	8.51	0.92	0	0	0	0.38	0.79	3
SMSSJ005953.98	20s7mix	8.55	0.92	0	0	0	0.38	1.13	3

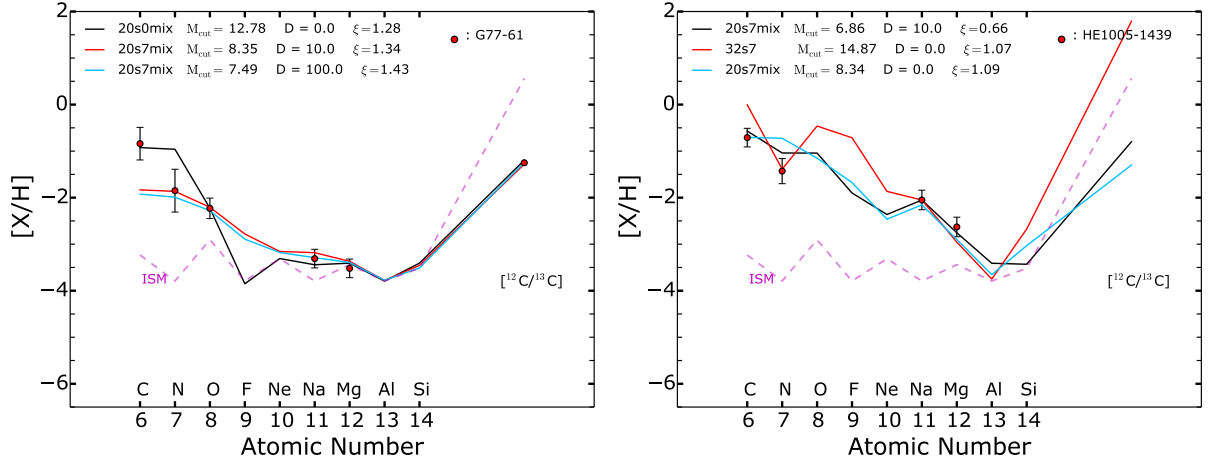


Figure 4.23: Best abundance fits of G77-61 (left) and HE 1005-1439 (right) with the source star models of Table 4.4, when considering the dilution factor and the mass cut as free parameters. The three best models, with the lowest ξ , are shown (black, red and green patterns sorted by increasing ξ). Uncertainties and limits on CEMP abundances are shown by vertical bars and arrows, respectively.

$$\xi = \sum_i | A_i^{\text{obs}} - A_i^{\text{mod}} | . \quad (4.6)$$

A_i^{obs} are the [C/H], [N/H], [O/H], [Na/H], [Mg/H] and $\log(^{12}\text{C}/^{13}\text{C})$ ratios of the CEMP-no star to fit⁹. A_i^{mod} are the same ratios but in the source star ejecta, after the eventual dilution with ISM. ξ is then evaluated using 1 to 6 abundance ratios. When no abundance or just an upper limit is available for a CEMP star, the abundance is not considered to estimate ξ . For rotating and non-rotating source star models, the number of possible mass cuts is about 1000 and 500 respectively (it depends on the resolution, which is higher in rotating models). In total, there are about 35000 possible ejecta compositions.

For each of the 48 cases, the ejecta composition with the mass cut that minimizes ξ is saved. Among these 48 ejecta, the 3 best ones (the 3 lowest ξ), are shown in Fig. 4.23 for two CEMP stars. This procedure was applied for the 69 CEMP stars (all the plots are shown in Appendix B). In this sample, I selected the cases where ξ was estimated with at least 3 abundances. Fits using only 1 or 2 abundances can lead to a high degree of degeneracy (many source star models provide a good solution). After this selection, it gives a subsample of 50 CEMP-no stars (19 stars excluded). In this new sample, the CEMP-no stars for which no satisfactory fit was found were excluded: fits with $\xi \geq 1.5$ are excluded. It finally gives 43 stars. The parameters of the best source star models for these 43 CEMP-no stars are reported in Table 4.5.

Figures 4.24, 4.25 and 4.26 show the results. $20 M_{\odot}$ source stars are preferred in 70 % of the cases, before the $60 M_{\odot}$ (23 %) and $32 M_{\odot}$ (7 %) source stars. Rotation gives the best fit for 74 % of the sample. The late mixing process appears in 72 % of the best models. $D \leq 10$ in 79 % of the cases. Figure 4.25 shows that rotation + late mixing gives the best fit in 58 % of the cases. The histogram of Fig. 4.26 shows the distribution of the sum $f_{\text{H}} + f_{\text{He}} + f_{\text{CO}}$ (i.e. the sum of the ejected fraction of the H-rich envelope, He-shell and CO-core, cf. Table 4.5) for the best source star models. This sum varies between 0 (no material ejected from the source star) and 3 (all the material is ejected). A value of 1.5, for instance, means that 100 % of the H-rich envelope plus 50 % of the He-shell of the source star was ejected. The sum $f_{\text{H}} + f_{\text{He}} + f_{\text{CO}}$ can also be seen as a mass cut value normalized to 3. Figure 4.26 shows that in most of the cases (about 70 %), $f_{\text{H}} + f_{\text{He}} + f_{\text{CO}}$ is about 1 or just

⁹Table 4.2 reports the [X/Fe] ratios. For the present analysis, I used the [X/H] ratios (taken from the SAGA database).

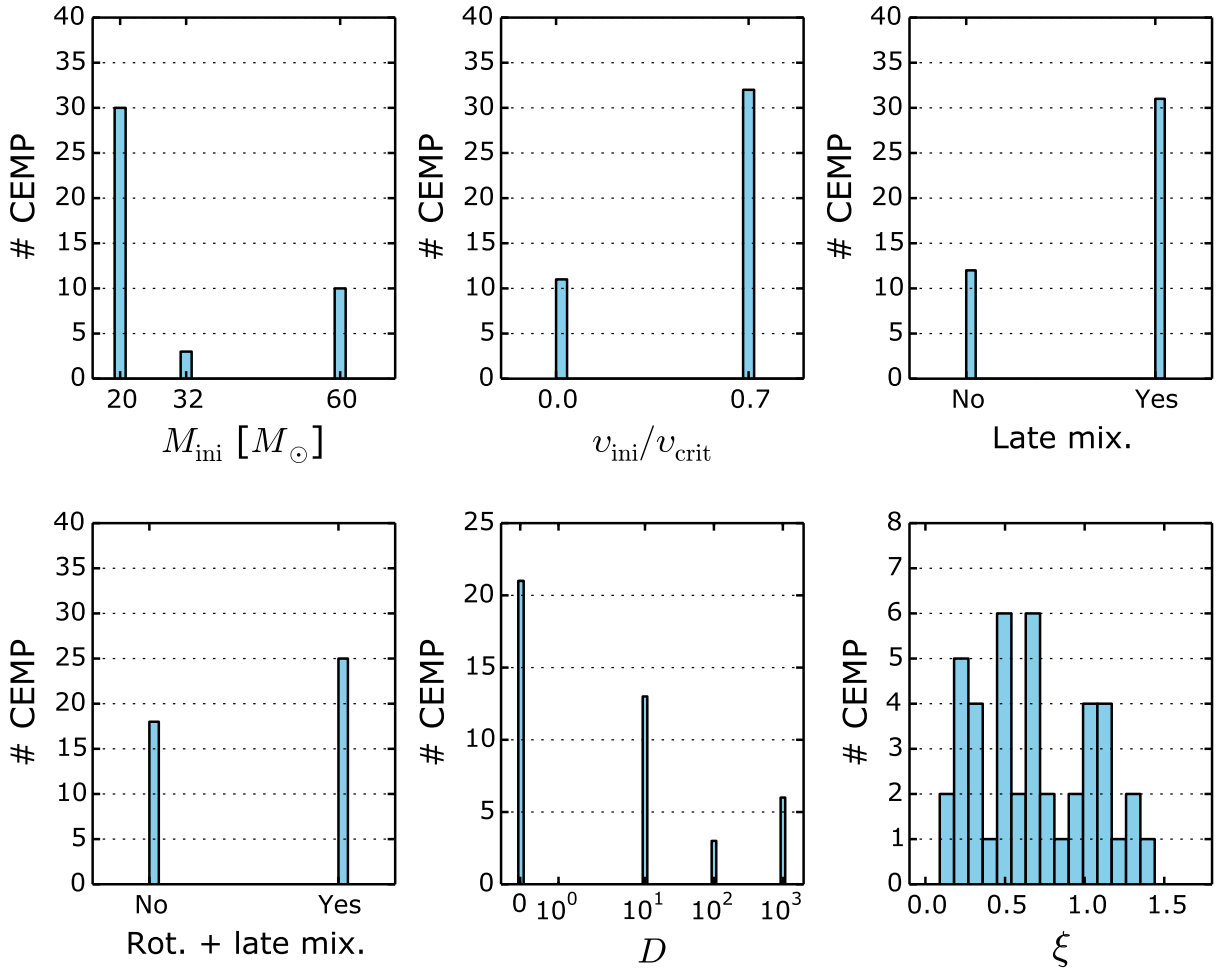


Figure 4.24: Occurrence of various parameters for the best source star models (with the lowest ξ) of the 43 CEMP-no stars of Table 4.5. Shown are the initial mass of the source star, initial velocity, if the model includes late mixing, if it includes late mixing and rotation, the dilution factor and the error on the fit ξ .

above 1. It means that the CEMP-no stars mostly formed with the H-rich envelope of the source star plus possibly a small part of the He-shell. In other other words, a mass cut located around the bottom of the H-rich region of the source star is preferred. It corresponds to $M_{\text{cut}} = M_{\alpha}$. In 15 – 20 % of the cases, $f_{\text{H}} + f_{\text{He}} + f_{\text{CO}} \geq 2$. In this case, it suggests a deeper mass cut in the source star, located around the top or in the CO core.

The results suggest that the CEMP-no source stars are preferentially rotating $20 M_{\odot}$ models experiencing the late mixing process. In most cases, only the outer layer of the source star should be expelled. Also, the results suggest a modest dilution with ISM. In Choplin et al. (2017b), we investigated the individual abundances of only six CEMP-no stars in details but reached similar conclusions.

It is worth noting that the late mixing process, developed to explain the abundances of a small sample of CEMP-no stars in the C/N vs. $^{12}\text{C}/^{13}\text{C}$ diagram (cf. Sect. 4.5), is still favored when considering a larger sample of CEMP stars that often do not have a measured $^{12}\text{C}/^{13}\text{C}$ ratio and/or the N abundance available. One reason is that standard models with or without rotation tend to give either much more N than C or much more C than N while numerous CEMP-no stars have roughly as much C as N. The late mixing process allows to get as much C as N in the ejecta. Also to note is that, even if both non-rotating and rotating models including late mixing can provide a

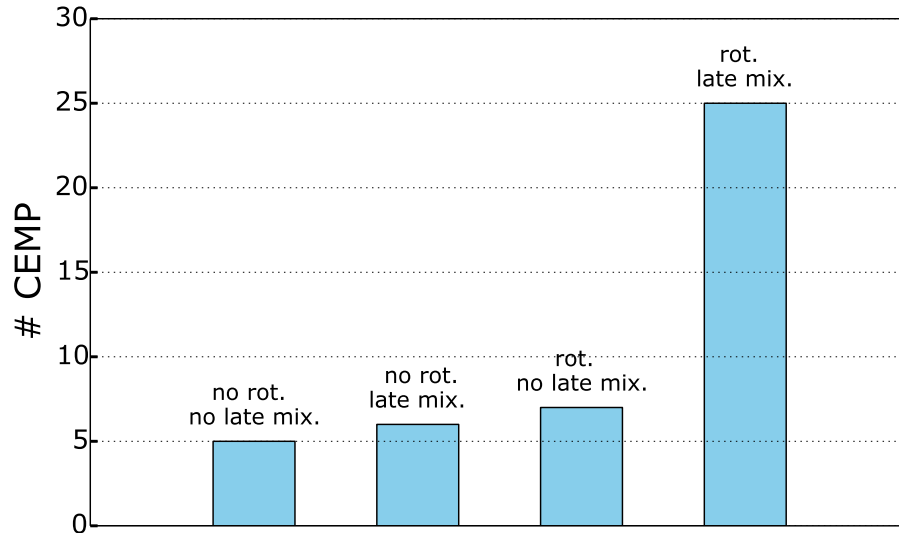


Figure 4.25: Occurrence of the four categories of the best source star models (with the lowest ξ) of the 43 CEMP-no stars of Table 4.5.

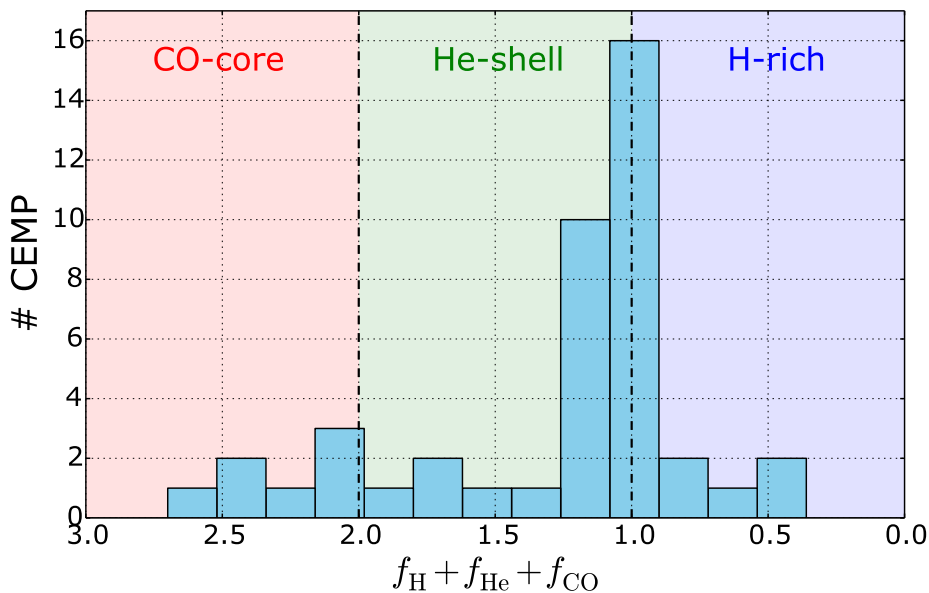


Figure 4.26: Distribution of $f_H + f_{He} + f_{CO}$ (cf. Table 4.5) for the best source star models of Table 4.5. This sum corresponds to the ejected fraction of the H-rich envelope, He-shell and CO-core (see text for details). The purple, green and red shaded area delimitate these three different regions (the extension of each region is normalized to 1).

solution in the C/N vs. $^{12}\text{C}/^{13}\text{C}$ diagram (cf. Fig. 4.21), rotating source stars models are preferred. One reason is that rotation can provide the additional Na and Mg needed to reproduce some CEMP-no stars while the late mixing process cannot.

Possible improvements

This analysis can be improved in different ways. Only the best source star models were considered here. The second best models could also be considered with smaller weights than the best models. It can also be done for the third best models, etc... This would allow to also include the

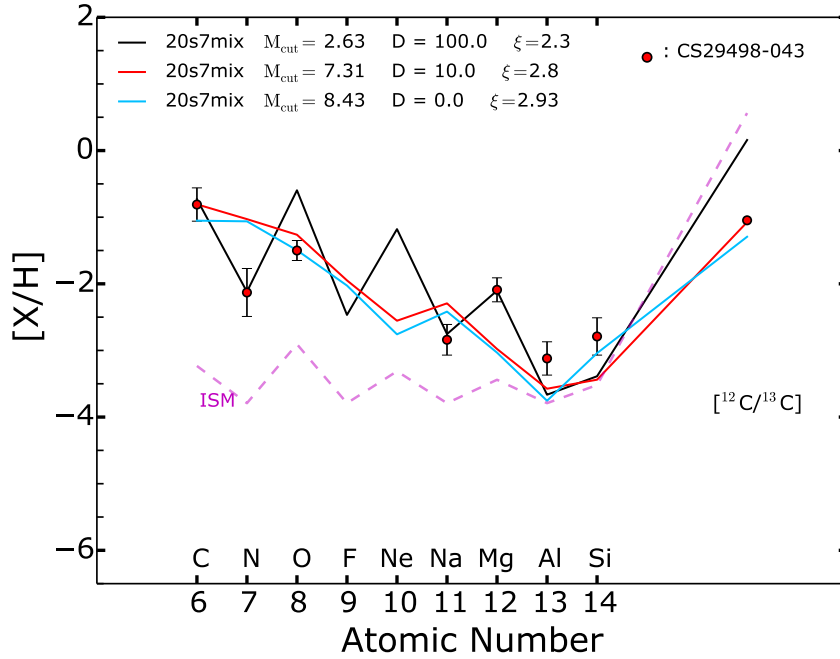


Figure 4.27: Same as Fig. 4.23 but for CS 29498-043.

good (but not best) models. It may increase the statistics of the results. An other improvement could be to attribute weights to the different abundances used to perform the fit. For instance, the abundances that are strongly affected by NLTE/3D effects should have a lower weight. The abundances that are the most affected by nuclear rate uncertainties in stellar models should also have a lower weight.

In the future, it would be interesting to do the same analysis while considering larger grids of source star models with more initial masses and rotation rates, and with different initial metallicities. This could allow to derive a initial mass or velocity function for the early generations of massive stars. However, the sample of CEMP-no stars may still be quite small. Larger (and homogeneous) samples are required so as to obtain meaningful statistic results.

Finally, let us mention that among the 50 stars fitted (69 in total but 19 were excluded because of a too small abundance data) 7 stars could not be fitted correctly.

- 3 out of these 7 stars (HE 0107-5240, HE 0557-4840 and SDSS J131326.89) have very low $[\text{Na}/\text{H}]$ and $[\text{Mg}/\text{H}]$ ratios, at least 1 dex below the ISM values considered here. No solution can give such low values. Zero metallicity source star models may provide a better solution. As discussed at the end of Sect. 4.3.3, zero metallicity source stars may produce as much CNO as low metallicity source stars but less Na, Mg, Al and Si. This remains to be tested.
- 3 other stars (HE 1506-0113, HE 1012-1540 and HE 2139-5432) have high $[\text{Na}/\text{H}]$ together with low $[\text{N}/\text{H}]$ ratios. This is difficult to explain with the present source star models, where N and Na are rather well correlated. In particular, both are produced in rotating models.
- The last star (CS 29498-043) has a CNO pattern very typical of an He-burning material but a very low $^{12}\text{C}/^{13}\text{C}$ ratio, typical of an H-burning material (see Fig. 4.27). Although the models with extra mixing can approach the solution closer than standard models, no satisfactory fit can be found.

Overall, these seven stars may require different kinds of progenitors. In any case, these stars will require further attention. This is among the next steps of this analysis.

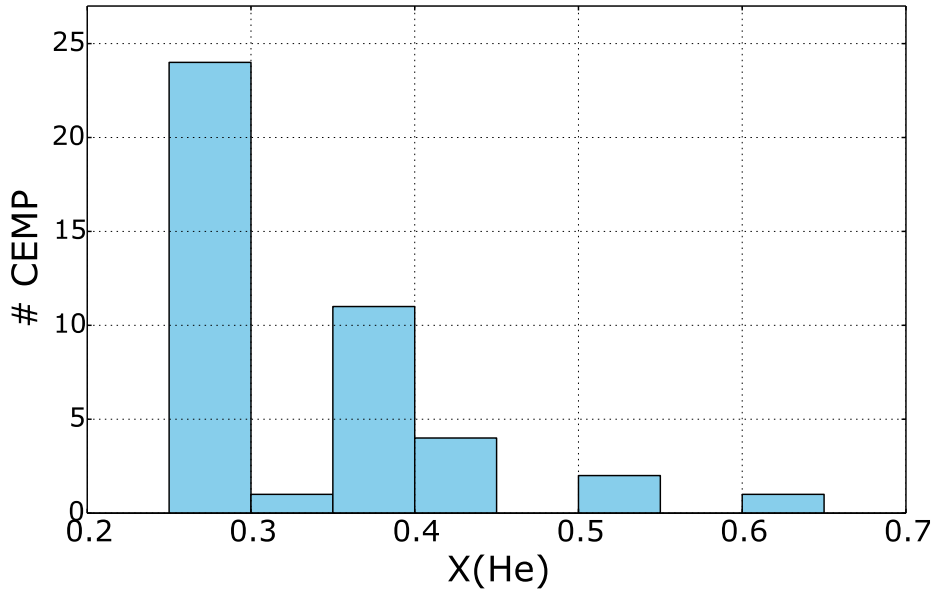


Figure 4.28: Distribution of the helium mass fraction in the ejecta of the best source star models (Table 4.5). It corresponds to the helium mass fraction in the source star ejecta, mixed with some ISM material if $D \neq 0$. This distribution shows the helium mass fraction predicted for the 43 CEMP-no stars of Table 4.5.

4.7 Are CEMP-no stars helium-rich?

A signature of the operation of the CNO cycle is an enrichment in helium. Thus, the CEMP-no stars that formed with almost only the envelope of massive source stars (i.e. $D \simeq 0$) should be He-rich (Meynet et al. 2010). If instead the source star ejecta was significantly mixed with ISM, the mass fraction of helium $X(\text{He})$ in the CEMP-no star should be around the primordial value of 0.248 (Cyburt et al. 2003).

Table 4.5 reports the predicted helium mass fraction in the ejecta (after dilution) of the best source star models. It shows for instance that the star CS 22960-053 should have formed with 0.39 of helium in mass fraction. Fig. 4.28 shows the distribution of helium mass fractions. While $\sim 60\%$ of the CEMP star sample is predicted to have formed with rather normal helium mass fractions ($X(\text{He}) \leq 0.3$), about 40% should have formed with $X(\text{He}) > 0.3$. I discuss below what are the effects on the evolution of CEMP stars if changing the initial He. The specific case of the He-rich candidate CS 22949-037, with $X(\text{He}) = 0.38$, is then investigated.

Low-mass metal-poor models enriched in helium

Chantereau et al. (2015) have investigated the evolution of $0.3 - 1 M_{\odot}$ stars at $[\text{Fe}/\text{H}] = -1.75$ with an initial He mass fraction Y_{ini} between 0.248 and 0.8. As Y_{ini} increases, the opacity in the stellar interior is reduced, making the star more compact. This shifts the evolutionary tracks towards higher T_{eff} . The higher compactness of the star makes the central temperature higher, increasing the rate at which hydrogen is burnt. This, together with the fact that there is less hydrogen fuel in helium rich stars, lead to shorter main sequence lifetimes for the helium rich models. Their $0.8 M_{\odot}$ models with $Y_{\text{ini}} = 0.248$ (standard), 0.4 and 0.8 spend 12.9, 4.62 and 0.16 Gyr on the main sequence, respectively.

To investigate the specific case of the CEMP-no star CS 22949-037, I computed non-rotating 0.5, 0.6, 0.7, 0.8 and 0.9 M_{\odot} stellar models starting with the chemical composition of CS 22949-037. For each mass, different initial helium mass fractions are tested: 0.25, 0.3, 0.4 and 0.5. What is

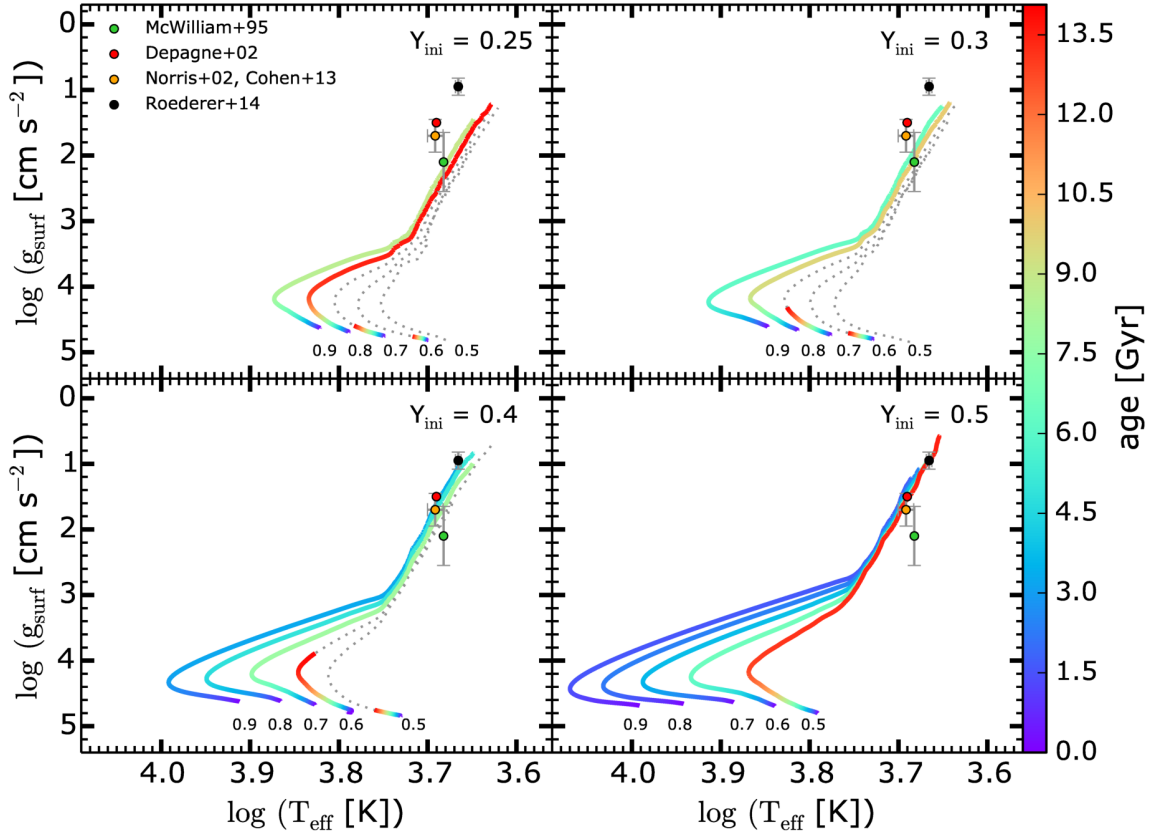


Figure 4.29: Surface gravity as a function of effective temperature. Lines represent stellar models between 0.5 and 0.9 M_{\odot} . The age of the models in Gyr is given by the color. Each panel corresponds to a different initial helium mass fraction. When the lifetime of the model exceeds 14 Gyr (age of the Universe), the rest of the track is represented by a dotted line. Squares are observations of CS 22949-037 (from McWilliam et al. 1995; Depagne et al. 2002; Norris et al. 2002; Cohen et al. 2013; Roederer et al. 2014b, uncertainties are indicated if available).

added to the initial helium mass fraction is removed from the initial hydrogen mass fraction. The OPAL tool was used to compute new opacity tables accordingly to the particular composition of CS 22949-037. For the other input parameters, I followed Ekström et al. (2012).

Fig. 4.29 shows the tracks of these models. The observations of CS 22949-037 are better reproduced by the tracks having $Y_{\text{ini}} = 0.4$ and 0.5. This is consistent with the analysis of Sect. 4.6 which predict $Y_{\text{ini}} = 0.38$ for CS 22949-037. However, because of uncertainties on both the modeling and observational sides, it is difficult to make meaningful comparisons between the observations and the tracks of Fig. 4.29.

Considerations on the age of CS 22949-037 can give additional hints. The color of the track shows the age of the model. To match the observables, the tracks of Fig. 4.29 have to reach the $\log g$ and T_{eff} of CS 22949-037 at the age of CS 22949-037. For instance, while the 0.9 M_{\odot} model with $Y_{\text{ini}} = 0.4$ seems a good candidate, it reaches the $\log g$ and T_{eff} of CS 22949-037 after only ~ 4 Gyr. It is unlikely that CS 22949-037 is only 4 Gyr old. On the other hand, the 0.5 M_{\odot} model (still with $Y_{\text{ini}} = 0.4$) is not a solution since it would still be unevolved today, with a much higher $\log g$ than CS 22949-037. We can see that if CS 22949-037 has $Y_{\text{ini}} = 0.4$, it should be between 0.6 and 0.7 M_{\odot} .

We see here that the scenario investigated in this work to explain CEMP-no stars predicts that some of the CEMP-no stars (the ones that are He-rich) will have rather small masses, due to their He-richness. Both the determination of the helium abundance and the mass of the CEMP-no stars may provide further clues on their origin.

Measuring the helium abundance and the mass of CEMP-no stars

Helium is challenging to detect and direct measurements are rare. One possibility is to focus on the HeI line at $1.08 \mu\text{m}$ that forms in the upper chromosphere of cool stars. In doing so, Pasquini et al. (2011) managed to measure the difference in helium abundance for two giant stars ($[\text{Fe}/\text{H}] = -1.22$ and -1.08) in the globular cluster NGC 2808. With their chromospheric model, they found a difference of 0.17 in helium mass fraction, meaning that if one of the two stars has a solar He abundance, the other would have $Y \sim 0.42$. Also, Dupree & Avrett (2013) reported an helium abundance of $Y < 0.22$ and $0.39 < Y < 0.44$ in two other giant stars ($[\text{Fe}/\text{H}] = -1.86$ and -1.79) belonging to the globular cluster ω Centauri. In CEMP-no stars and generally in very iron-poor stars, no helium measurements have been performed yet.

Let us mention that asteroseismology may provide the mass of giant CEMP-no stars. The asteroseismic information (hence the mass) of cool giant stars with $1.9 < \log g < 3.2$ may be obtained with the Kepler K2 mission (e.g. Stello et al. 2015). Another way to have a direct estimation of the mass is if the CEMP-no star is in an eclipsing binary system: since the inclination of an eclipsing system is known, masses of the two stars can be determined from the Kepler's laws. Tracks of stellar models computed with the right masses and with various helium abundances may allow to get an estimation of the helium abundance of these observed stars.

Proxies for the helium abundance

Some abundances of other elements may give a proxy for the helium abundance. A high helium abundance requires a small dilution factor otherwise the helium abundance goes back towards the ISM value of ~ 0.25 . A small dilution factor might be related to a low Li abundance (Sect. 4.3.3, paragraph about dilution), meaning that He-rich CEMP stars could also be Li-poor (caution is required since Li is a fragile element that can be heavily affected by various processes in the CEMP star itself). Interestingly, the He-rich candidate CS 22949-037 has a very low Li abundance ($A(\text{Li}) < 0.13$). Two other He-rich candidates, CS 22960-053 ($X(\text{He}) = 0.39$) and HE 2331-7155 ($X(\text{He}) = 0.39$), have $A(\text{Li}) < 0.55$ and $A(\text{Li}) < 0.37$, respectively. He-rich candidates are nevertheless not always Li-poor (e.g. CS 22960-053 with a predicted helium abundance of $X(\text{He}) = 0.42$ and a Li abundance, deduced from observations, of $A(\text{Li}) = 1.71$).

It is also worth noting that the He-rich CEMP stars should probably not be searched among the CEMP stars having a \vee -shape CNO pattern (cf. Sect. 4.4.1). It may be surprising since it is a pattern characteristic of a material processed by He-burning, hence potentially He-rich. However, when a CEMP star is predicted to be formed with the He-processed material of the source star, a high dilution factor is generally also predicted (often $D = 1000$, see Table 4.5) so that the final helium abundance (the one of the CEMP) is close to the ISM value of 0.25. Instead, it is predicted here that many He-rich CEMP stars should have a \wedge -shape CNO pattern. This pattern is characteristic of an ejecta processed by H-burning. Such an ejecta is also enriched in helium (provided the dilution with ISM is small).

4.8 Other CEMP-no source star models

4.8.1 An energetic H-ingestion event in the source star

Let us first mention the recent work of Clarkson et al. (2018), that investigated the origin of the 3 most iron-poor stars with a non-rotating $45 M_{\odot}$ source star model experiencing an energetic H-ingestion event during shell He burning. It is interesting in the frame of the present work since the ingestion process they consider is similar to the late mixing process described in Sect. 4.5. In their work, nucleosynthesis was calculated in post-processing, using a one-zone model. They found

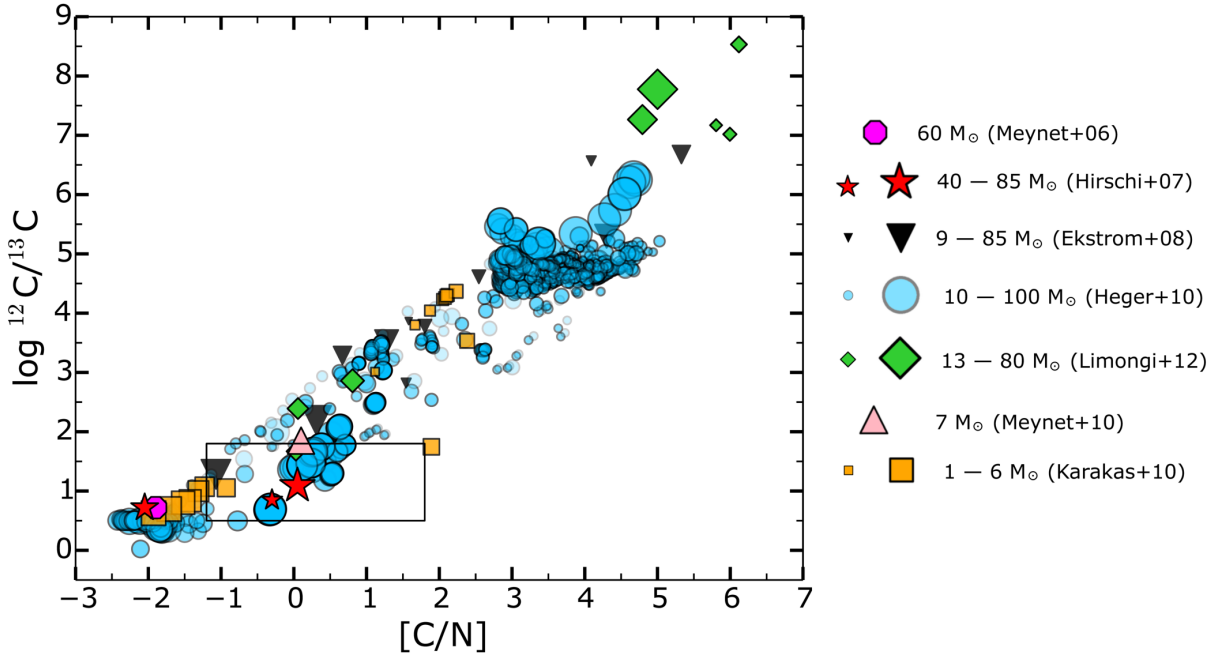


Figure 4.30: Composition of the ejecta of massive and AGB star models from various authors. The symbol size scales with the initial mass (see the legend on the right). The black frame shows where observed CEMP-no stars lie. Symbols show the composition of the ejecta of rotating $60 M_{\odot}$, $Z = 10^{-5}$ (Meynet et al. 2006); rotating 40, 60 and $85 M_{\odot}$, $Z = 10^{-8}$ (Hirschi 2007); non-rotating and rotating $9 - 85 M_{\odot}$, $Z = 0$ (Ekström et al. 2008); rotating $7 M_{\odot}$ early AGB, $Z = 10^{-5}$ (Meynet et al. 2010); non-rotating $1 - 6 M_{\odot}$ AGB, $Z = 10^{-4}$ (Karakas 2010); non-rotating $10 - 100 M_{\odot}$, $Z = 0$ (Heger & Woosley 2010); and non-rotating $13 - 80 M_{\odot}$, $Z = 0$ (Limongi & Chieffi 2012).

that after the H-ingestion event, neutron densities of 10^{-13} cm^{-3} are reached (typical of the i-process), leading to neutron captures on light seeds. These neutron captures allow the synthesis of small amounts of heavier elements like Ca (not much heavier elements than Ca are synthesized). Globally they found a reasonable agreement for 2 out of the 3 iron-poor stars considered. One difficulty is that neutron captures in the source star model do not produce enough Fe so that an additional enrichment process is required. Also, one of the stars they reproduce (HE 1327-2326) has $[\text{Sr}/\text{Fe}] = 1.08$. It is not mentioned if their models can account for it. The origin of Sr in HE 1327-2326 is investigated in the Sect. 5.4.2 of this work.

4.8.2 Other source star models in the $\text{C}/\text{N} - {}^{12}\text{C}/{}^{13}\text{C}$ diagram

It is now investigated whether various massive source star models from different authors can provide a solution in the $\text{C}/\text{N} - {}^{12}\text{C}/{}^{13}\text{C}$ diagram. Low or zero metallicity massive star models with available yields are considered. Some intermediate mass models are also included (see the legend of Fig. 4.30 for the complete list of models). In the non-rotating $10 - 100 M_{\odot}$ Pop III models of Heger & Woosley (2010), explosive nucleosynthesis is calculated and various assumptions for the mixing (in the sense of the mixing & fallback process of Umeda & Nomoto 2002) and the explosion energy are considered. Explosive nucleosynthesis is also calculated in the non-rotating $13 - 80$ Pop III stars of Limongi & Chieffi (2012).

The composition of the ejecta of all the considered models is shown in Fig. 4.30. The observations lie in a very small zone (black frame) compared to the region occupied by the source star models. Worth to remind is that some CEMP-no stars have an upper limit for N and/or a lower

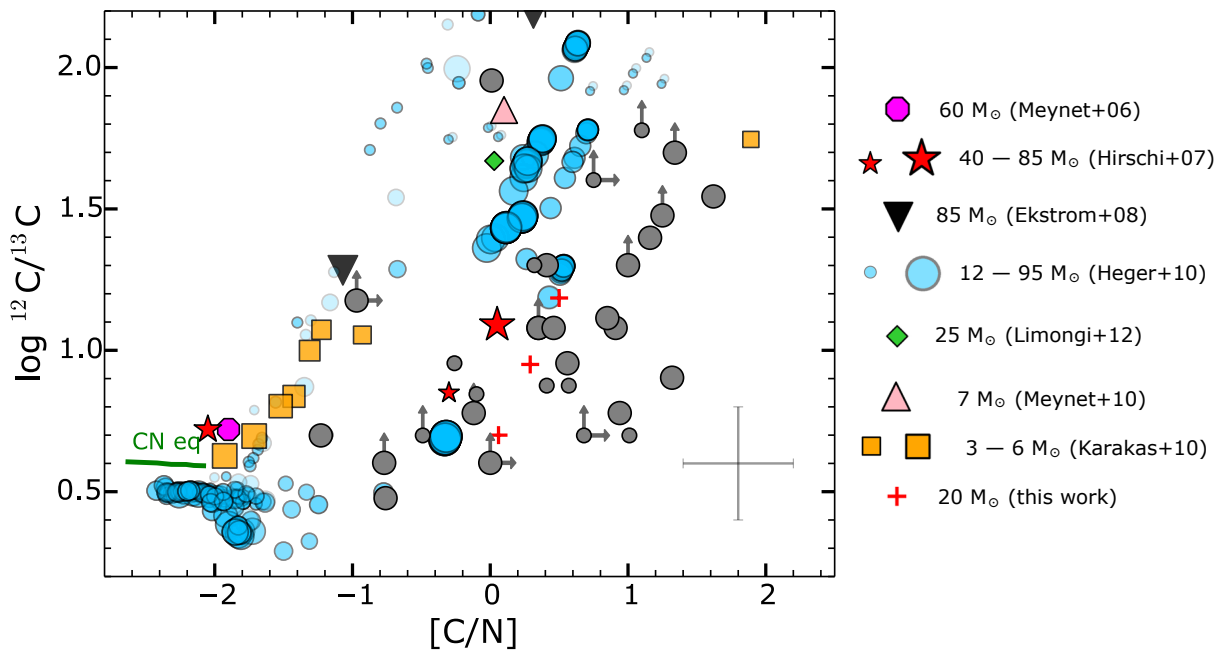


Figure 4.31: Same as Fig. 4.30 but in the region where the observations lie (grey circles). Red crosses show models from the present work ($20 M_{\odot}$ with $v_{\text{ini}}/v_{\text{crit}} = 0.7$, $Z = 10^{-5}$ and with the late mixing process). The 3 crosses correspond to 3 different mass cuts.

limit for $^{12}\text{C}/^{13}\text{C}$. It means that it might exist an unseen population of stars with higher $^{12}\text{C}/^{13}\text{C}$ and C/N ratios. For what regards the observations without upper/lower limits, only a small fraction of the source star models could possibly account for them.

Fig. 4.31 shows a zoom in the region where observations lie. Models of Limongi & Chieffi (2012) consider standard core collapse supernovae, with $E_{51} \sim 1$ and deep mass cuts. As they say (see also Fig. 4.30 and 4.31), this assumption likely cannot account for the majority of the most metal-poor stars. It is similar for the models of Ekström et al. (2008) where a deep mass cut is considered, following the relation of Maeder (1992). Higher mass cut values (closer to the stellar surface) in the models of Limongi & Chieffi (2012) and Ekström et al. (2008) may improve the fit between models and observations. AGB models may account for some observations but there are generally away from the majority of CEMP-no stars. Models approaching the most the bulk of observed stars are (1) some non-rotating $50 - 100 M_{\odot}$ Pop III models from Heger & Woosley (2010), represented by big blue circles, and (2) fast-rotating 40 and $85 M_{\odot}$ models with $Z = 10^{-8}$ from Hirschi (2007).

A fast rotating massive source star with extreme mass loss

Let us first summarize the peculiar evolution of the fast rotating $85 M_{\odot}$ model of Hirschi (2007), that leads to $[\text{C}/\text{N}] \simeq 0$ and $\log(^{12}\text{C}/^{13}\text{C}) \simeq 1.1$ in the ejecta (big red star in Fig. 4.31). From the beginning of the core helium burning stage, ^{12}C and ^{16}O diffuse progressively to the radiative H-shell. At the middle of the core helium burning phase, the helium convective core encroaches the H-shell so that the CNO cycle is suddenly boosted in the H-shell and a copious amount of ^{14}N and ^{13}C is quickly formed. The energy released makes the H-shell convective. This CNO-rich convective zone quickly reaches the stellar surface so that the surface metallicity is enhanced and dramatic mass loss occurs, removing about $60 M_{\odot}$ from the star. The material ejected is only partially processed by the CNO cycle because the convective zone extends very quickly in cold

regions where the CNO cycle operates slowly or does not operate at all. In addition, the strong mass loss episode occurs also quickly after the encroaching of the H-shell, saving definitely the material from further processing. From the instant of the encroaching of the H-shell to the instant where strong mass loss stops, only ~ 0.03 Myr have past. Finally, the model (which is now about $25 M_{\odot}$) finishes to burn helium in its core (and then subsequent burning stages occur normally). The big red star in Fig. 4.31 shows the chemical composition in the wind of this model, which is indeed partially CNO processed.

H/He interaction in non-rotating massive source stars

Some $50 - 100 M_{\odot}$ models of Heger & Woosley (2010, blue circles) experience a similar encroaching (cf. previous paragraph) of the He-core with the H-shell, as they mention in their paper. Also, as they note, in some models, the encroaching occurs during the core carbon burning stage, between the He- and H-burning shells (like for the late mixing process, cf. Sect. 4.5). In both cases, it produces a lot of ^{13}C and ^{14}N . Mass loss was taken equal to zero in their models so that no material is ejected through winds. However, some material is likely saved in cold regions from further CNO processing until the end of the source star evolution. It leads to a partially processed CNO material in the ejecta as shown by some of the blue points in Fig. 4.31 that approach the bulk of observed CEMP-no stars.

A strong H/He interaction: a characteristic shared by the best source star models?

All the models able to fit the observations in the $[\text{C}/\text{N}] - ^{12}\text{C}/^{13}\text{C}$ diagram (including the models of this work discussed in Sect. 4.5) likely share a common feature: a strong interaction between the H- and He-region occurred in the source star, boosting the CNO cycle, but right after, the material was saved from further CNO processing (either by being ejected quickly, or by being saved in cold regions of the source star until a supernova expels these layers). The fact that this interaction occurs also in non-rotating models (e.g. Heger & Woosley 2010) may indicate that the origin of the phenomena is not entirely due to rotation. Rotation may facilitate such interactions. As discussed in Sect. 4.5.4, the main ingredient might be convection. Convection constitutes a major uncertainty that should be better constrained in the future thanks to multi-D simulations.

This said, the present work suggests that this strong interaction between the H- and He-regions is required but not sufficient to explain the CEMP-no stars. The special nucleosynthesis induced by the progressive rotational mixing at work in the source star also appears to be needed to account for the abundances of CEMP-no stars (e.g. Sect. 4.6).

The mass of the source stars

Models of Hirschi (2007) and Heger & Woosley (2010) in Fig. 4.31 suggest that the CEMP-no source stars could have initial masses of $50 - 100 M_{\odot}$ while this work suggest lower masses, about $20 M_{\odot}$ (e.g. Fig. 4.24). Heger & Woosley (2010) investigated the origin of the CEMP stars HE 0107-5240 and HE 1327-2326 with their Pop III massive models. In both cases, the best fits are given by their $10.5 - 25 M_{\odot}$ source star models. Similarly to Umeda & Nomoto (2003), an artificial mixing episode is included in their models at the time of the supernova in order to mix a little bit of iron in upper stellar layers. The iron is then expelled and the little iron content of HE 0107-5240 and HE 1327-2326 can be reproduced. Placco et al. (2016) have used the models of Heger & Woosley (2010) to investigate the origin of 12 stars with $[\text{Fe}/\text{H}] < -4$. They found that the best fits are given by $12.6 - 41 M_{\odot}$ models (in both studies, the $^{12}\text{C}/^{13}\text{C}$ ratio is not considered). Also, in these works, comparisons are made through the $[\text{X}/\text{H}]$ ratios but no dilution with primordial ISM was considered. It likely means that the yields of the source stars models considered should be seen as

upper limits since any dilution with primordial ISM will decrease the $[X/H]$ ratios. Some caution is therefore required.

From Fig. 4.30 and 4.31, we see that the $10 - 40 M_{\odot}$ of Heger & Woosley (2010) are not reproducing the bulk of observations. Fig. 4.31 rather suggests that their models with $M > 40 M_{\odot}$ may be better source stars. In the present section, since the comparison is made using only few abundances (C and N), it is not possible to conclude further. It suggests that tensions probably exist and that the preferred masses of the CEMP-no source stars may require further investigations.

4.9 Summary

This chapter has investigated the origin of the CEMP stars with $[Fe/H] < -3$ and not significantly enriched in s- and/or r-elements (CEMP-no stars). The main results are summarized below.

The high abundance scatter (especially for C, N, O, Na, Mg and Al) of these stars was suggested to originate from a material ejected by previous massive source stars that experienced various degree of rotational mixing. A part of the CEMP-no star sample is thought to have formed mainly with the H-burning shell of the massive source star. During the core He-burning phase of rotating source stars, He-burning products are transported to the H-burning shell by the operation of the rotational mixing. Once into the H-shell, these products are further processed by H-burning and transported back to the He-burning core, etc. I developed a one-zone nucleosynthesis model that mimics the H-burning shell of a rotating massive star. The effect of rotation was modeled by progressively injecting He-burning products (^{12}C , ^{16}O , ^{22}Ne and ^{26}Mg) in the burning zone. The ranges of abundances of the considered CEMP-no stars were found to be overall well reproduced by a material processed by H-burning at a temperature and density characteristic of $20 - 60 M_{\odot}$ source stars. To reproduce the observations, this material should be enriched, while burning, in ^{12}C , ^{16}O and occasionally ^{22}Ne . This suggests that the CEMP-no source stars experienced mid to strong rotational mixing.

Source stars models with various initial masses, rotation rates and metallicities were computed. As the result of the rotation induced mixing during the core He-burning phase, the yields of elements from C to Al scale with initial rotation. In the fastest rotating model, the $[X/H]$ ratios in the ejecta can be boosted by ~ 2 to ~ 5 dex compared to the non-rotating model. The mass cut and the dilution of the source star ejecta with ISM are important and weakly constrained parameters, that strongly affect the source star yields. Overall, a global match between the abundances of CEMP-no stars and very low metallicity $20 M_{\odot}$ source star models with various initial rotation rates can be found. The low $^{12}\text{C}/^{13}\text{C}$ ratio (especially on unevolved CEMP-no stars) requires that no or little material processed by He-burning was expelled from the source star. In this case however, $[C/N] \sim -2$, which does not account for the bulk of CEMP-no stars, that generally have higher $[C/N]$ ratios. The source star ejecta either have low $^{12}\text{C}/^{13}\text{C}$ ratios together with low $[C/N]$ ratios or high $^{12}\text{C}/^{13}\text{C}$ ratios together with high $[C/N]$ ratios. It cannot fit the bulk of CEMP-no stars.

A solution to improve the fit is to include a *late mixing process* in the massive source star, operating in between the H-burning and the He-burning shell, about 200 yr before the end of the source star evolution. It may occur preferentially in $\sim 20 M_{\odot}$ source stars (both rotating and non-rotating). This additional process was studied by computing new source star models with initial masses of 20, 32 and $60 M_{\odot}$, without and with fast rotation, without and with the late mixing process (12 models). Using the yields of these 12 source star models, an automatic abundance fitting procedure was applied to the CEMP-no stars with $[Fe/H] < -3$. I found that the best CEMP-no source stars are preferentially rotating $20 M_{\odot}$ models that experienced the late mixing process, that ejected the layers above or just below the interface between the H-rich and He-rich region and whose ejecta underwent a modest dilution with the ISM.

4.9. Summary

Finally, to avoid confusion, I recall the three different kinds of mixing that may arise in the source star:

- The mixing induced by rotation that occurs progressively and everywhere, during the entire life of the source star.
- The late mixing process (Sect. 4.5) arising between the H-burning shell and He-burning shell, shortly before the end of the evolution¹⁰.
- The mixing in the sense of Umeda & Nomoto (2002) that occurs between two limiting shells, at the time of the supernova.

¹⁰It may also occur earlier in the evolution, between the H-burning shell and He-burning core, cf. Sect. 4.8.

The s-process in CEMP source stars

The previous chapter focused on light elements, from C to Si. These elements are of particular interest for studying the origin of the most iron poor stars (with $[\text{Fe}/\text{H}] < -3$) that are mostly CEMP-no stars. The reason is that these stars are often strongly enriched in such elements while, by definition, they are generally little enriched in heavier elements.

Many CEMP stars show overabundances in s-elements, especially at higher metallicities ($-3 \lesssim [\text{Fe}/\text{H}] \lesssim -2$), but also sometimes at very low metallicity (e.g. HE 1327-2326 with $[\text{Fe}/\text{H}] < -5$ and $[\text{Sr}/\text{Fe}] = 1.08$). The weak s-process is expected to occur in massive stars (provided the metallicity is not zero). As mentioned in Sect. 3.1.2 (also Fig. 4.1), the effect of rotation in massive stars can alter the production of s-elements. At very low/zero metallicity, the amount of seed (especially iron) is very low so that little s-elements can be produced. At higher metallicities, there are more seeds, hence possibly more s-elements.

The main purpose of this chapter is to extend the study to heavier elements that can be formed in the source stars through the s-process. The s-process is studied in a new grid of massive source stars at $[\text{Fe}/\text{H}] \sim -2$ together within lower metallicity source star models. Then, I investigate whether the nucleosynthetic signatures of these massive stars can be recognized in observed metal-poor stars. A very recent paper (in Sect. 5.2) and a letter (in Sect. 5.3) are directly included in this chapter. Additional results and discussions are included, particularly in Sect. 5.4.

5.1 The weak s-process in a box

Before investigating complete stellar models, the s-process in a single burning zone is discussed. Using a similar code as in Sect. 4.2 but that now mimics the He-burning core of massive stars (this is mostly where the s-process operates, cf. Sect. 3.1.2), the s-process in massive stars can be studied qualitatively. The single burning zone considered burns at $T = 300$ MK and $\rho = 500$ g cm⁻³, as characteristic values of the He-burning core of massive stars. The initial mass fractions in the zone are ~ 0.4 for ⁴He, ~ 0.3 for ¹⁶O, ~ 0.3 for ¹²C and 10^{-7} for ⁵⁶Fe (in mass fraction). The initial mass fraction of ²²Ne is varied from 10^{-4} to 0.05. The calculation is stopped when all the ⁴He is burnt. The final chemical patterns in the burning zone are shown in Fig. 5.1.

When increasing the initial ²²Ne, heavier s-elements are produced at the expense of lighter s-elements. If little ²²Ne is available, the neutron flux is small and only light s-elements are produced. When the initial ²²Ne mass fraction is 0.05, the pattern becomes flatter. It shows the effect of changing the source (²²Ne) over seed (⁵⁶Fe) ratio. If this ratio increases (provided some reasonable amount of seed is present) the hs (heavy s-elements) over ls (light s-elements) ratio increases.

Fig. 5.2 illustrates the poisoning effect of ¹⁶O by changing the initial ¹⁶O mass fraction. For higher initial ¹⁶O mass fractions, the production of s-elements is reduced. This is because if ¹⁶O is

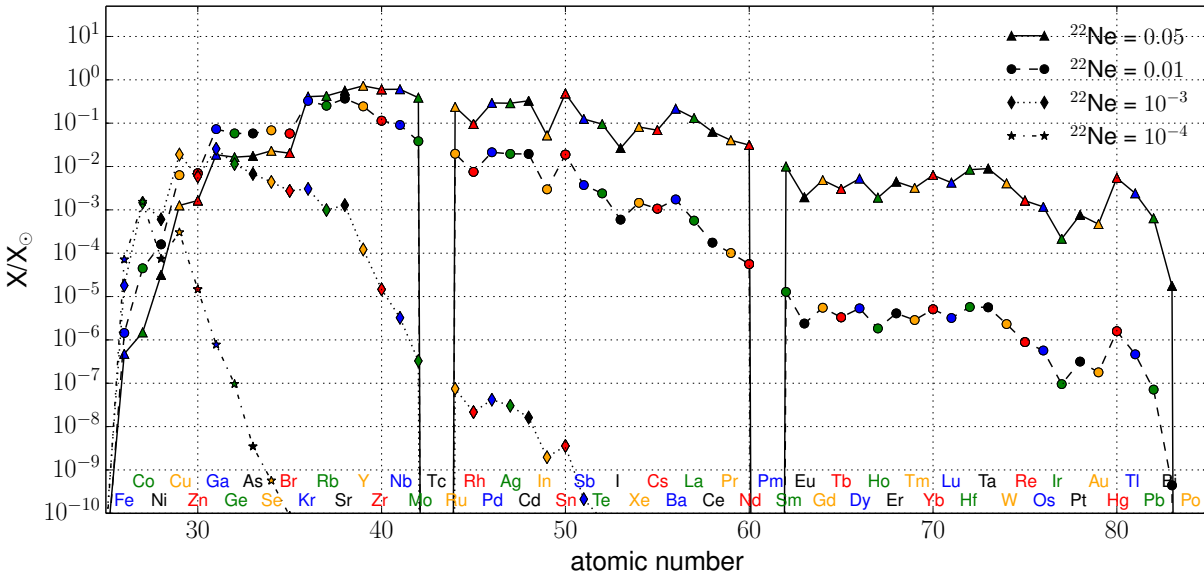


Figure 5.1: Final mass fraction X (normalized to solar) of heavy elements in a single burning zone at $T = 300$ MK and $\rho = 500$ g cm $^{-3}$. The initial mass fraction of ^{56}Fe is 10^{-7} . The initial mass fraction of ^{22}Ne is varied from 10^{-4} to 0.05.

more abundant, the $^{16}\text{O}(n, \gamma)^{17}\text{O}(\alpha, \gamma)^{21}\text{Ne}$ chain is boosted, so that less neutrons are available for heavy elements.

5.2 A new grid of massive stars with rotation and s-process

Grids of massive stellar models including rotation and full s-process network are needed in order to investigate the role of such stars in the chemical enrichment of the Universe. To date, only Frischknecht et al. (2016) and very recently Limongi & Chieffi (2018) have provided such grids. An important part of my work was to compute a new grid of massive rotating star with full s-process, so as to extend the study of Frischknecht et al. (2016). The final goal being to gain knowledge on the nature of such massive stars by comparing their yields to the abundances of observed low-mass metal-poor stars enriched in s-elements.

In Choplin et al. (2018) we computed a new grid of massive stars with initial masses between 10 and $150 M_{\odot}$, at a metallicity $Z = 0.001$ in mass fraction (corresponding to $[\text{Fe}/\text{H}] = -1.8$). The models were computed either without rotation or with $v_{\text{ini}}/v_{\text{crit}} = 0.4$. We considered only one metallicity but significantly extended the range of mass compared to the study of Frischknecht et al. (2016), that focused on $15 - 40 M_{\odot}$ models. We also investigated the impact of a faster initial rotation and a different $^{17}\text{O}(\alpha, \gamma)^{21}\text{Ne}$ reaction rate. Most of the physical ingredients of this grid are the same than for the models discussed previously. The main change is the size of the nuclear network that now comprises 737 species, from ^1H to ^{212}Po instead of 31 species (cf. Sect 3.3.3).

The paper describing the models is directly included in the thesis (in the present section). It was very recently accepted in A&A and I have therefore almost no discussion to add yet. Before the paper itself, I discuss several aspects that were not published: several additional physical ingredients and some obstacles I had to overcome. In Appendix A.5, additional parameters, allowing to quantify the efficiency of the s-process, are defined and tabulated for the new grid of models. The table was not published in the paper but it may be useful to have these quantities for future comparisons with other models.

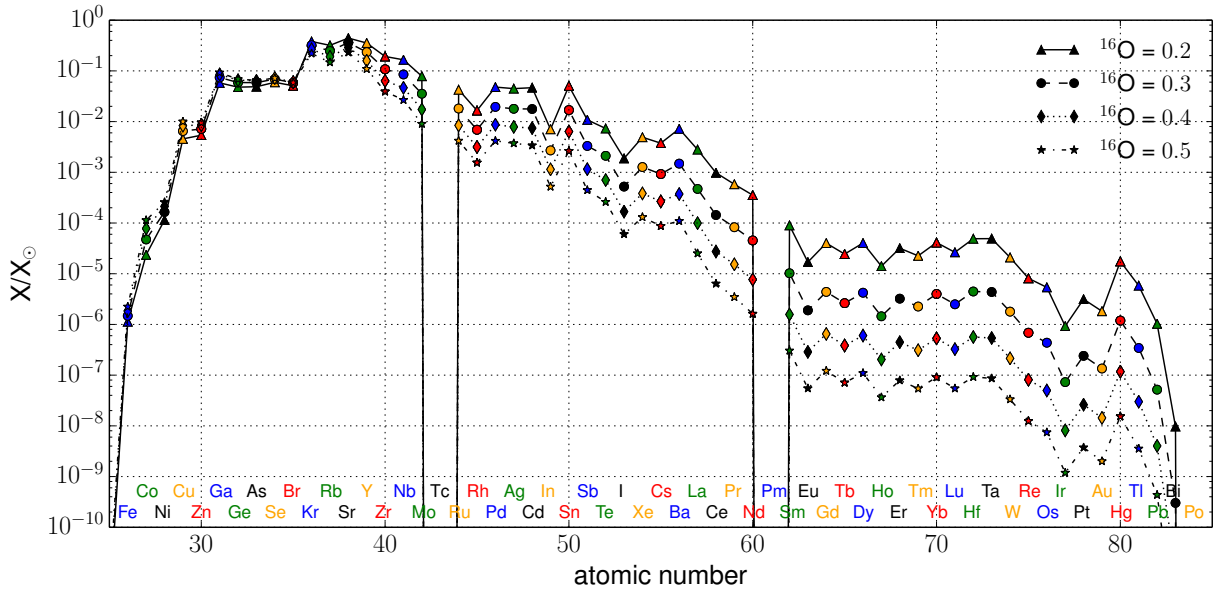


Figure 5.2: Same as Fig. 5.1 but when varying the initial mass fraction of ^{16}O from 0.2 (solid pattern) to 0.5 (dot-dashed pattern).

5.2.1 Nuclear network and reaction rates

As shown in Table 2 of the paper below, 8 important nuclear reaction rates were updated compared to the study of Frischknecht et al. (2016). Originally, the reaction rate format in stellar evolution codes is the following: one table for each reaction rate with two columns, one for the temperature, one for the associated rate. Then, interpolations are done in these tables to evaluate the rates at the desired temperatures. With large networks, it is convenient to use analytical reaction rates such as in the REACLIB format (Cyburt et al. 2010) in order to save computational time. Such a format allows to express a reaction rate with n sets of 7 parameters a_0, \dots, a_6 . For 2-body reactions, it yields

$$\langle\sigma v\rangle N_A = \sum_{k=1}^n e^{[a_0(k)+a_1(k)T_9^{-1}+a_2(k)T_9^{-1/3}+a_3(k)T_9^{1/3}+a_4(k)T_9+a_5(k)T_9^{5/3}+a_6(k)\log(T_9)]} \quad (5.1)$$

with $T_9 = 10^{-9} T$ and N_A the Avogadro number. For 1- and 3-body reactions, the left side of Eq. 5.1 is respectively equal to $\langle\sigma v\rangle N_A^2$ and λ , where λ represents the photodisintegration or β -decay rate. If just the standard tabulated rate exists, one has to find the a parameters that allow to fit correctly the rate. A leastsquare method is used to estimate these parameters from a temperature-rate table. $n > 1$ is often required to reach a reasonable accuracy. Finding the a parameters can sometime be challenging, mainly because of the large range of temperature to be covered (several orders of magnitude, it depends on the reactions). Once the a parameters are determined for the forward reaction, the a_{rev} parameters for the reverse reaction can be easily calculated (Rauscher & Thielemann 2000).

Best et al. (2013) provided, in the tabular form, new rate measurements for the $^{17}\text{O}(\alpha, n)^{20}\text{Ne}$ and the $^{17}\text{O}(\alpha, \gamma)^{21}\text{Ne}$ reactions, that are of crucial importance for the s-process in massive stars. I used the fitting method described in Rauscher & Thielemann (2000, also nucastro.org) to convert these tabulated rates into the REACLIB format. For the two fits, I found that $n = 3$ provides satisfactory results: the final deviation is less than 5 % (Fig. 5.3, only one of the two fit is shown).

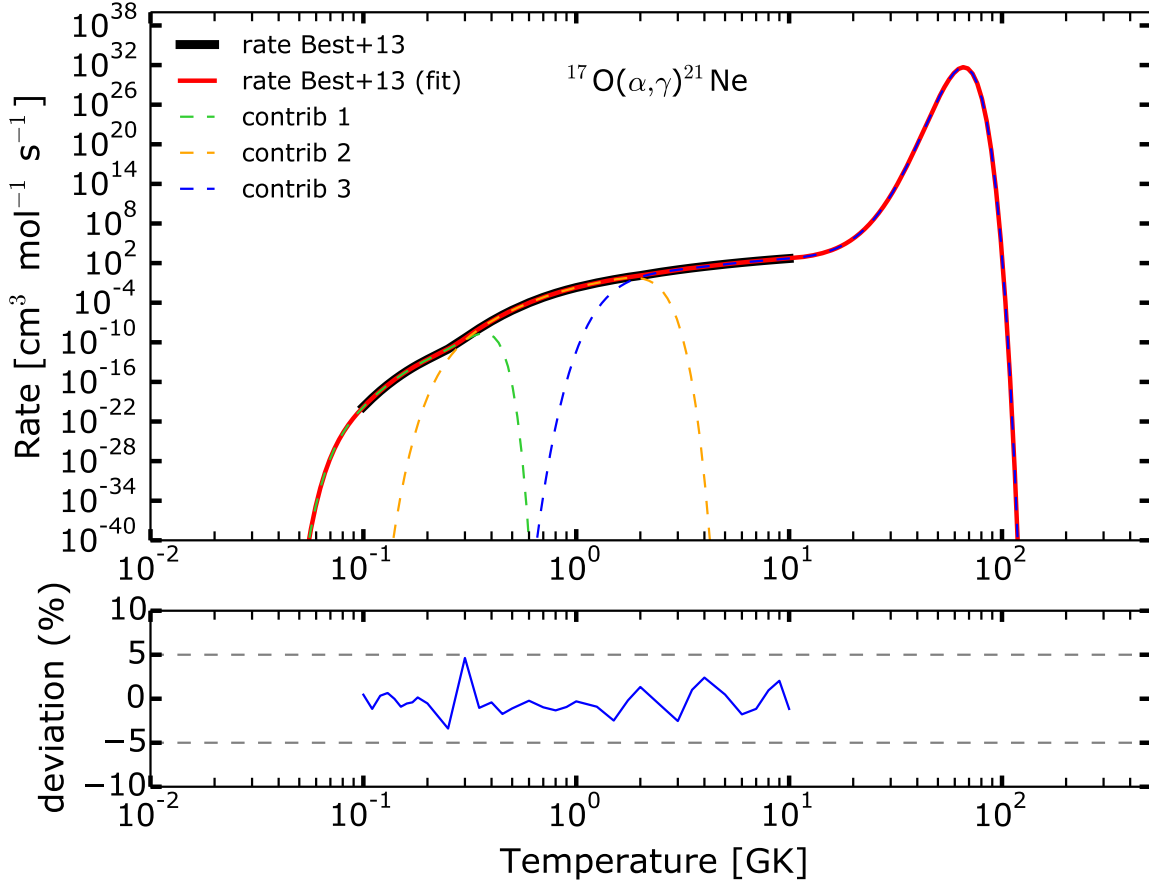


Figure 5.3: Rate of the $^{17}\text{O}(\alpha, \gamma)^{21}\text{Ne}$ reaction. The thick black line corresponds to the recommended values tabulated in Best et al. (2013). Dashed lines show the different contributions, which were fitted according to the method described in Rauscher & Thielemann (2000, also nucastro.org). Three different contributions ($n = 3$, see Eq. 5.1) were found to provide an acceptable fit. The thin red line shows the sum of the 3 contributions. The deviation from the original tabulated rate (Best et al. 2013) is shown in the bottom panel.

5.2.2 The μ and Ω profiles

When first trying to reproduce the results of Frischknecht et al. (2016), I found significantly different results: many s-elements were underproduced by a factor of 100 in the new models. It was caused by strong oscillations of the D_{shear} coefficient in between the H- and He-burning zones, during the core He-burning stage. The green profile in the left panel of Fig. 5.4 shows such oscillations. The low values of D_{shear} at $M_r \simeq 7.5$ strongly reduces the exchanges of material between the He-core and the H-shell, leading to a smaller synthesis of primary ^{14}N and ^{22}Ne (Fig. 5.4, right panel, green line). Such D_{shear} oscillations are likely not physical since their shape change or disappear when changing the model resolution. An example is shown by the blue profiles in Fig. 5.4: the resolution of this model (*res-* model in Fig. 5.4) is reduced compared to the green model (*res+* model) but it is still enough to see the eventual D_{shear} oscillations. In this case, the D_{shear} does not oscillate so that the mixing is not cut and more ^{14}N and ^{22}Ne are synthesized compared to the green model (Fig. 5.4, right panel). While the changes induced by the presence or the absence of oscillations are not huge for ^{14}N and ^{22}Ne (factor of about 5), they are much more significant for s-elements (factor of about 100 at maximum, as shown in Fig. 5.5). Models of

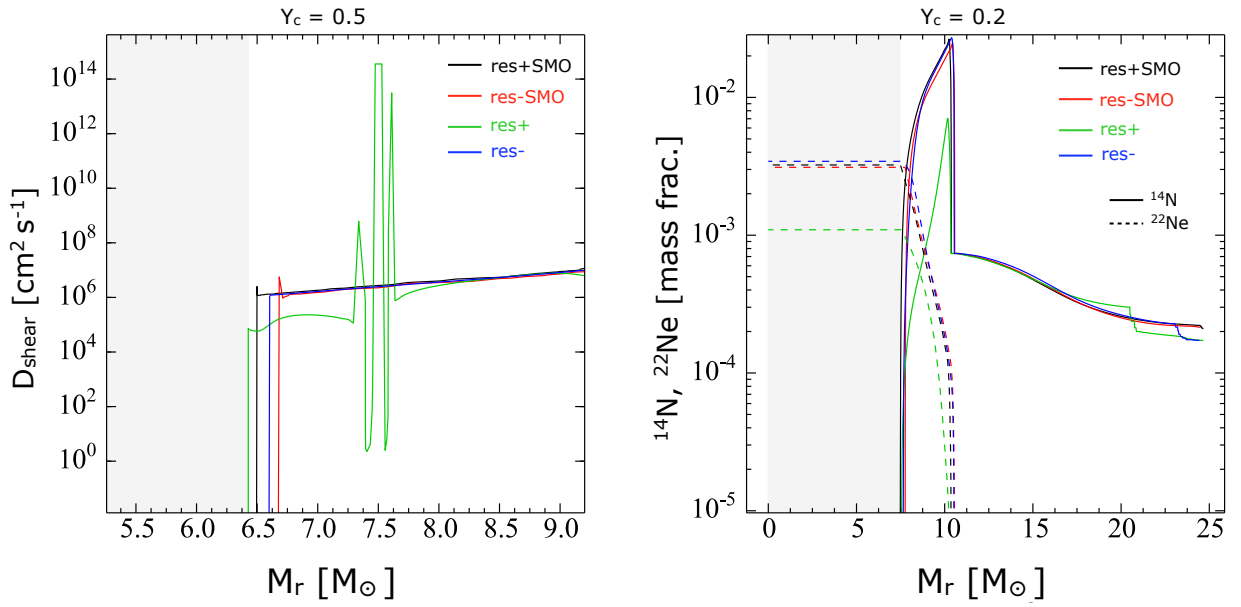


Figure 5.4: *Left panel:* D_{shear} coefficient between the He-core and H-shell. *Right panel:* internal mass fraction of ^{14}N and ^{22}Ne . Models shown are rotating $25 M_\odot$ at $Z = 10^{-3}$, during the core helium burning phase (the central mass fraction of ^4He is 0.5 on the left panel and 0.2 on the right panel). Shaded area show convective zones. *res+* models (black and green) are computed with high resolution (about twice more shells than *res-* models). *SMO* models (black and red) include the smoothing technique (see text and Appendix A.4).

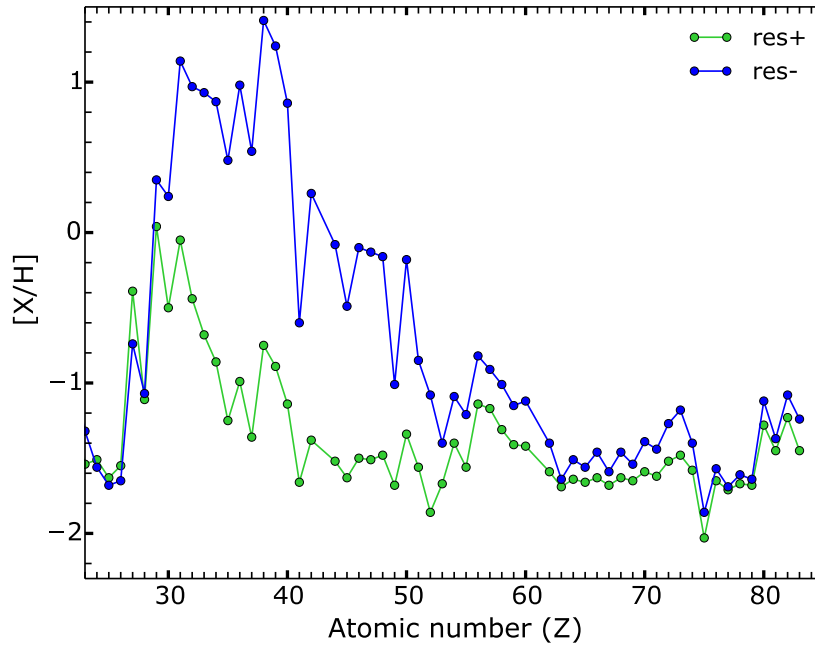


Figure 5.5: $[X/H]$ ratios in the ejecta of the green (high resolution) and blue (low resolution) models of Fig. 5.4.

Frischknecht et al. (2016) are similar to the blue lines in Fig. 5.4 and 5.5 while new models to the green lines.

To improve the stability of the code and find similar results when changing the mesh number, I improved the way of calculating D_{shear} (Eq. 3.10), by trying to better evaluate the derivative of μ and Ω , that appeared to be responsible for the oscillation of the D_{shear} coefficient. The oscillation problem is solved if properly smoothing the μ and Ω profiles when calculating their derivatives (see Appendix A.4 for more details). If applied, this technique gives similar results when changing the mesh number (see Fig. 5.4, black and red profiles). It also gives similar s-process yields compared to the models of Frischknecht et al. (2016).

Non-standard s-process in massive rotating stars

Yields of 10–150 M_{\odot} models at $Z = 10^{-3}$ *

Arthur Choplin¹, Raphael Hirschi^{2,3,4}, Georges Meynet¹, Sylvia Ekström¹, Cristina Chiappini⁵, and Alison Laird^{4,6}

¹ Geneva Observatory, University of Geneva, Maillettes 51, 1290 Sauverny, Switzerland
 e-mail: arthur.choplin@unige.ch

² Astrophysics Group, Lennard-Jones Labs 2.09, Keele University, ST5 5BG, Staffordshire, UK

³ Kavli Institute for the Physics and Mathematics of the Universe (WPI), University of Tokyo, 5-1-5 Kashiwanoha, 277-8583 Kashiwa, Japan

⁴ UK Network for Bridging the Disciplines of Galactic Chemical Evolution (BRIDGCE), UK

⁵ Leibniz-Institut für Astrophysik Potsdam, An der Sternwarte 16, 14482 Potsdam, Germany

⁶ Department of Physics, University of York, YO10 5DD York, UK

Received 23 April 2018 / Accepted 18 July 2018

ABSTRACT

Context. Recent studies show that rotation significantly affects the *s*-process in massive stars.

Aims. We provide tables of yields for non-rotating and rotating massive stars between 10 and 150 M_{\odot} at $Z = 10^{-3}$ ($[\text{Fe}/\text{H}] = -1.8$). Tables for different mass cuts are provided. The complete *s*-process is followed during the whole evolution with a network of 737 isotopes, from hydrogen to polonium.

Methods. A grid of stellar models with initial masses of 10, 15, 20, 25, 40, 60, 85, 120, and 150 M_{\odot} and with an initial rotation rate of both 0% or 40% of the critical velocity was computed. Three extra models were computed in order to investigate the effect of faster rotation (70% of the critical velocity) and of a lower $^{17}\text{O}(\alpha, \gamma)$ reaction rate.

Results. At the considered metallicity, rotation has a strong impact on the production of *s*-elements for initial masses between 20 and 60 M_{\odot} . In this range, the first *s*-process peak is boosted by 2–3 dex if rotation is included. Above 60 M_{\odot} , *s*-element yields of rotating and non-rotating models are similar. Increasing the initial rotation from 40% to 70% of the critical velocity enhances the production of $40 \leq Z \leq 60$ elements by ~ 0.5 –1 dex. Adopting a reasonably lower $^{17}\text{O}(\alpha, \gamma)$ rate in the fast-rotating model (70% of the critical velocity) boosts again the yields of *s*-elements with $55 \leq Z \leq 82$ by about 1 dex. In particular, a modest amount of Pb is produced. Together with *s*-elements, some light elements (particularly fluorine) are strongly overproduced in rotating models.

Key words. stars: massive – stars: rotation – stars: interiors – stars: abundances – stars: chemically peculiar – nuclear reactions, nucleosynthesis, abundances

1. Introduction

The standard view of the *s*-process in massive stars is that it occurs in He- and C-burning regions and contributes to the production of elements up to about $A = 90$, hence giving only *s*-elements up to the first peak, at $N = 50$, where N is the number of neutrons (e.g. Peters 1968; Couch et al. 1974; Lamb et al. 1977; Langer et al. 1989; Raiteri et al. 1991a,b, 1993; Käppeler et al. 2011, and references therein). In standard models of massive stars, both the neutron source (mainly ^{22}Ne) and the seed (mainly ^{56}Fe) decrease with initial metallicity, while the main neutron poison (^{16}O) remains similar whatever the metallicity, leading to a threshold of about $Z/Z_{\odot} = 10^{-2}$ below which the *s*-process becomes negligible (Prantzos et al. 1990).

Meynet et al. (2006) and Hirschi (2007) suggested that this picture would be modified in rotating stars because of the rotational mixing operating between the H-shell and He-core during the core helium burning phase. The abundant ^{12}C and ^{16}O isotopes in the convective He-burning core are mixed within the H-shell, boosting the CNO cycle and forming primary

^{14}N (e.g. Meynet & Maeder 2002b; Ekström et al. 2008). The ^{14}N is mixed back into the convective He-burning core and allows the synthesis of extra ^{22}Ne , via the reaction chain $^{14}\text{N}(\alpha, \gamma)^{18}\text{F}(e^+ \nu_e)^{18}\text{O}(\alpha, \gamma)^{22}\text{Ne}$. The growth of the convective He-burning core also helps to reach layers that had been previously enriched in ^{14}N . Neutrons are finally released by the $^{22}\text{Ne}(\alpha, n)^{25}\text{Mg}$ reaction. The production of ^{22}Ne in rotating stars is extensively discussed in Frischknecht et al. (2016; Sect. 3.1, their Figs. 2–5; see also Fig. 1 of Choplin et al. 2016, for a schematic view of this mixing process). By investigating the effect of rotation in a 25 M_{\odot} model, Pignatari et al. (2008) have shown that rotational mixing would allow the production of *s*-elements up to $A \approx 140$. Since then, a few studies (e.g. Frischknecht et al. 2012, 2016, F12 and F16 hereafter) have started to build a picture of the *s*-process in massive rotating stars by computing models of different masses ($15 < M < 40 M_{\odot}$) and metallicities ($10^{-7} < Z < Z_{\odot}$) while following the complete *s*-process during evolution. So far, the most complete *s*-process study from rotating massive star models was carried out in F16. They computed 29 non-rotating and rotating models of 15, 20, 25, and 40 M_{\odot} , with metallicities of $Z = 0.014, 10^{-3}, 10^{-5}$, and 10^{-7} and with a nuclear network of 613 or 737 isotopes, depending on the burning phase.

* Table 4 (yields) is only available at the CDS via anonymous ftp to cdsarc.u-strasbg.fr (130.79.128.5) or via <http://cdsarc.u-strasbg.fr/viz-bin/qcat?J/A+A/618/A133>

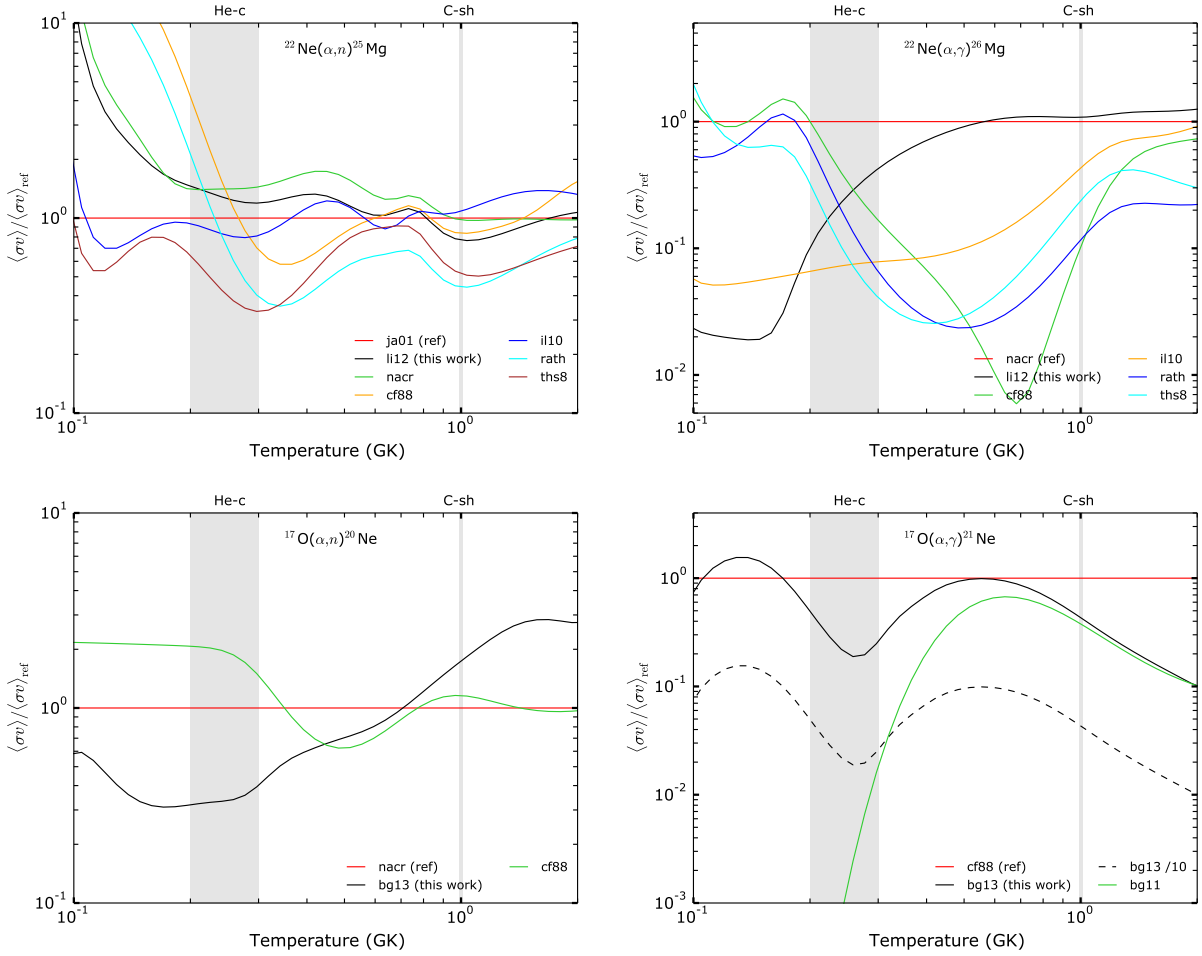


Fig. 1. Comparison between different sources of the important reaction rates for the *s*-process in massive stars as a function of the temperature. “ja01”: Jaeger et al. (2001), “nacr”: Angulo et al. (1999), “li12”: Longland et al. (2012), “cf88”: Caughlan & Fowler (1988), “il10”: Iliadis et al. (2010), “rath”: Rauscher & Thielemann (2000), “ths8”: Cyburt et al. (2010), “bg11”: Best et al. (2011), “bg13”: Best et al. (2013). We note that the Best et al. (2011) rate is an experimental lower limit. The shaded bands indicate the approximate ranges of temperature of interest for the *s*-process in massive stars: the first area named “He–c” is associated to the *s*-process during the core helium burning phase and the second area (“C–sh”) during carbon shell burning.

Several observational signatures tend to support the view of an enhanced *s*-process in massive rotating stars. The first one is that of globular cluster NGC 6522, located in the Galactic bulge and possibly being about 12.5 Gyr old (Kerber et al. 2018). It contains eight stars whose pattern is enriched in *s*-elements (Barbuy et al. 2009) and consistent with the yields of massive rotating models (Chiappini et al. 2011).

The second signature regards the iron-poor low-mass stars enriched in *s*-elements in the halo of the Milky Way. Using an inhomogeneous Galactic chemical evolution model, Cescutti et al. (2013) have shown that the observed scatter in the [Sr/Ba] ratio of normal (i.e. not enriched in carbon, see next discussion) halo stars with [Fe/H] < −2.5 can be reproduced if yields from fast-rotating massive stars are included.

The third one regards some of the [Fe/H] ≲ −4 stars enriched in *s*-elements. At such a low metallicity, asymptotic giant branch (AGB) stars might not have contributed yet to the chemical enrichment. HE 1327-2326 (Aoki et al. 2006; Frebel et al. 2006, 2008) has [Fe/H] = −5.7, [Sr/Fe] = 1.08, [Ba/Fe] < 1.39 and

is enriched in light elements (C, N, O, Na, Mg, Al) relative to Fe. As discussed in the Sect. 7.2 of Maeder et al. (2015), this is consistent with the ejecta of a fast-rotating, low-metallicity massive star, where a strong mixing between H- and He-burning zones occurred, triggering the synthesis of a variety of elements, including Sr and Ba.

A fourth signature concerns the CEMP-*s* stars, which are Carbon-Enhanced Metal-Poor stars enriched in *s*-elements (Beers & Christlieb 2005). CEMP-*s* stars are mostly found at [Fe/H] > −3 (e.g. Yong et al. 2013; Norris et al. 2013). Some significantly *s*-rich stars also exist at [Fe/H] < −3, like HE 1029-0546 or SDSSJ1036+1212 with [Fe/H] around −3.3 (Behara et al. 2010; Aoki et al. 2013; Hansen et al. 2015). The peculiar chemical pattern of such stars is generally considered as acquired from an AGB star companion during a mass-transfer (or wind-mass-transfer) episode (Stancliffe & Glebbeek 2008; Lau et al. 2009; Bisterzo et al. 2010, 2012; Lugaro et al. 2012; Abate et al. 2013, 2015a,b; Hollek et al. 2015). A consequence of such a scenario is that CEMP-*s* stars should mostly be in

A. Choplin et al.: Non-standard s -process in massive rotating stars

binary systems, which seems to be the case for most CEMP- s since they show radial velocity variations (Lucatello et al. 2005; Starkenburg et al. 2014; Hansen et al. 2016). Nevertheless, some CEMP- s stars are very likely single stars (four out of 22 in the sample of Hansen et al. 2016), challenging the AGB scenario. The yields of a fast-rotating $25 M_{\odot}$ model can reproduce the pattern of three out of the four apparently single CEMP- s stars (Choplin et al. 2017b). Furthermore, we cannot exclude the possibility that some CEMP- s stars in binary systems show the nucleosynthetic signature of massive rotating stars since massive rotating stars could have enriched the cloud in which the binary system formed. On the other hand, single CEMP- s stars may be explained by the AGB scenario anyway since (1) single CEMP- s stars might have lost their companion, or (2) they might be in a binary system with very long period, explaining the non-detection of radial velocity variation.

Extensive and homogeneous grids of massive stellar models including rotation and full s -process network are needed to further investigate the role of such stars in the chemical enrichment of the universe. In this work, we study the impact of rotation on the s -element production at a metallicity $Z = 10^{-3}$ in mass fraction and in the range 10 – $150 M_{\odot}$. We focus on one metallicity but extend significantly the range of mass compared to the study of F16. It allows us to draw a more complete picture of the s -process in massive stars at the considered metallicity. We investigate also the impact of a faster initial rotation and a lower $^{17}\text{O}(\alpha, \gamma)^{21}\text{Ne}$ reaction rate. Section 2 describes the physical ingredients used throughout this work. Results are presented in Sect. 3. In Sect. 4 we investigate the effect of the mass cut and describe the table of yields. Section 5 presents the conclusions and additional discussions.

2. Physical ingredients

2.1. Input parameters

We used the Geneva stellar evolution code (Eggenberger et al. 2008). The models were computed at $Z = 10^{-3}$ ($[\text{Fe}/\text{H}] = -1.8$) with initial masses of 10, 15, 20, 25, 40, 60, 85, 120, and $150 M_{\odot}$. The initial rotation rate on the zero-age main-sequence (ZAMS), $v_{\text{ini}}/v_{\text{crit}}^1$ is 0, 0.4 or 0.7. Only the $25 M_{\odot}$ was computed with $v_{\text{ini}}/v_{\text{crit}} = 0.7$. As in Ekström et al. (2012) and Georgy et al. (2013), we use $v_{\text{ini}}/v_{\text{crit}} = 0.4$ for the grid. It corresponds well to the peak of the velocity distribution of the sample of 220 young main-sequence B-type stars of Huang et al. (2010, their Fig. 6). At lower metallicities, stars are more compact and the mass loss by line-driven winds is weaker so that the removal of angular momentum during evolution is smaller. Consequently, for a given $v_{\text{ini}}/v_{\text{crit}}$ ratio, lower metallicity stars have higher surface rotational values during the main-sequence (MS) phase (Maeder & Meynet 2001).

At the metallicity considered here, F16 computed (with the same stellar evolution code) non-rotating 15, 20, and $25 M_{\odot}$ and 15, 20, 25, and $40 M_{\odot}$ models with $v_{\text{ini}}/v_{\text{crit}} = 0.4$. These models were computed again in the present work with the latest version of the code and with updated nuclear reaction rates (see below, the present section). A comparison of the yields is done in Sect. 3.2. Our models are generally stopped at the end of the neon photo-disintegration phase. Only the $10 M_{\odot}$

¹ The initial equatorial velocity is v_{ini} and v_{crit} is the initial equatorial velocity at which the gravitational acceleration is balanced by the centrifugal force. It is defined as $v_{\text{crit}} = \sqrt{\frac{2GM}{3R_{\text{pb}}}}$, where R_{pb} is the polar radius at the break-up velocity (see Maeder & Meynet 2000).

Table 1. Main characteristics of the models.

M_{ini} (M_{\odot})	Model	$v_{\text{ini}}/v_{\text{crit}}$	$\langle v \rangle_{\text{MS}}$ (km s^{-1})	Phase	τ (Myr)	M_{fin} (M_{\odot})
10	10s0	0.0	0	end C	23.4	9.9
10	10s4	0.4	214	end C	27.1	9.8
15	15s0	0.0	0	end Ne	13.0	14.8
15	15s4	0.4	234	end Ne	15.4	14.3
20	20s0	0.0	0	end Ne	9.32	19.9
20	20s4	0.4	260	end Ne	10.9	17.4
25	25s0	0.0	0	end Ne	7.61	24.7
25	25s4	0.4	281	end Ne	8.81	16.7
25	25s7	0.7	490	end Ne	9.20	16.2
25	25s7B ^a	0.7	490	end Ne	9.20	16.0
40	40s0	0.0	0	end Ne	5.24	34.1
40	40s4	0.4	332	end Ne	5.97	24.6
60	60s0	0.0	0	end Ne	4.11	44.2
60	60s4	0.4	375	end Ne	4.62	40.8
85	85s0	0.0	0	end Ne	3.49	59.3
85	85s4	0.4	403	end Ne	3.88	58.3
120	120s0	0.0	0	end Ne	3.06	82.4
120	120s0B ^a	0.0	0	end Ne	3.06	83.2
120	120s4	0.4	423	end He	3.36	85.8
150	150s0	0.0	0	end Ne	2.85	100.3
150	150s4	0.4	432	end Ne	3.14	99.6

Notes. Initial mass (Col. 1), model label (Col. 2), initial ratio of surface velocity to critical velocity (Col. 3), time-averaged surface velocity during the main-sequence phase (Col. 4), final nuclear phase computed (Col. 5), total lifetime (Col. 6), and final mass (Col. 7). ^(a) Models computed with the rate of $^{17}\text{O}(\alpha, \gamma)$ divided by 10.

models are stopped at the end of C-burning and the rotating $120 M_{\odot}$ is stopped at the end of He-burning. Computing the advanced stages is important since the s -process occurs in the C-burning shell (also in the He-burning shell to a smaller extent, see The et al. 2007). However, the contribution from He-core burning dominates both in non-rotating and rotating models, and the C-shell contribution decreases quickly with initial metallicity (F16, especially their Fig. 13). Table 1 shows the initial properties of the models computed in this work as well as the final nuclear phase computed, the total lifetimes, and the final masses.

The nuclear network is fully coupled to the evolution and used throughout all of it. It comprises 737 isotopes, from hydrogen to polonium ($Z = 84$). The size of the network is similar to the network used in The et al. (2000), F12, and F16, and allows us to follow the complete s -process. At the end of evolution, before computing stellar yields, unstable isotopes are decayed to stable ones. The initial composition of metals (elements heavier than helium²) is α -enhanced (we refer to Sect. 2.1 of F16 where more details are given).

Opacity tables are computed with the OPAL tool³. At low temperature, the opacities from Ferguson et al. (2005) are used to complement the OPAL tables. Radiative mass-loss rates are from Vink et al. (2001) when $\log T_{\text{eff}} \geq 3.9$ and if $M_{\text{ini}} > 15 M_{\odot}$. Otherwise, they are from de Jager et al. (1988). For rotating models, the radiative mass-loss rates are corrected with the factor

² The initial helium mass fraction Y is calculated according to the relation $Y = Y_{\text{p}} + \Delta Y/\Delta Z \times Z$, where Z is the metallicity, Y_{p} the primordial helium abundance, and $\Delta Y/\Delta Z = (Y_{\odot} - Y_{\text{p}})/Z_{\odot}$ the average slope of the helium-to-metal enrichment law. We set $Y_{\text{p}} = 0.248$, according to Cyburt et al. (2003). We use $Z_{\odot} = 0.014$ and $Y_{\odot} = 0.266$ as in Ekström et al. (2012), derived from Asplund et al. (2005). The initial mass fraction of hydrogen is deduced from $1 - Y - Z = 0.752$.

³ <http://opalopacity.llnl.gov>

described in [Maeder & Meynet \(2000\)](#). Following [Ekström et al. \(2012\)](#), the mass-loss rate is increased by a factor of three when the luminosity of any layer in the stellar envelope becomes higher than five times the Eddington luminosity.

The Schwarzschild criterion is used for convection. During the H- and He-burning phases, overshoot is considered: the size of the convective core is extended by $d_{\text{over}} = \alpha H_p$, where H_p is the pressure scale height and $\alpha = 0.1$. α was calibrated so as to reproduce the observed MS width of stars with $1.35 < M < 9 M_\odot$ ([Ekström et al. 2012](#)). Rotation is included according to the shellular theory of rotation ([Zahn 1992](#)). The angular momentum is transported according to an advection-diffusion equation ([Chaboyer & Zahn 1992](#)), which is fully solved during the main sequence. Only the diffusive part of the equation is solved after the main sequence. For chemical species, the combination of meridional circulation and horizontal turbulence can be described as a pure diffusive process ([Chaboyer & Zahn 1992](#)). The associated diffusion coefficient is

$$D_{\text{eff}} = \frac{1}{30} \frac{|rU(r)|^2}{D_h}, \quad (1)$$

with $U(r)$ the amplitude of the radial component of the meridional velocity ([Maeder & Zahn 1998](#)) and D_h the horizontal shear diffusion coefficient from [Zahn \(1992\)](#). The equation for the transport of chemical elements is therefore purely diffusive with a total diffusion coefficient $D_{\text{tot}} = D + D_{\text{eff}}$, where D is the sum of the various instabilities (convection, shear). After the main sequence, the advective effects are not considered so that $D_{\text{eff}} = 0$. The secular shear diffusion coefficient is from [Talon & Zahn \(1997\)](#). It is expressed as

$$D_{\text{shear}} = f_{\text{energ}} \frac{H_p}{g\delta} \frac{K + D_h}{(\nabla_{\text{ad}} - \nabla_{\text{rad}}) + \frac{\mu}{\delta} \nabla_\mu \left(\frac{K}{D_h} + 1 \right)} \left(\frac{9\pi}{32} \Omega \frac{d \ln \Omega}{d \ln r} \right)^2. \quad (2)$$

The efficiency of the shear is calibrated with the f_{energ} parameter. We set $f_{\text{energ}} = 4$, which is the value needed for a $15 M_\odot$ model at solar metallicity and with $v_{\text{ini}} = 300 \text{ km s}^{-1}$ to obtain an enhancement of the surface N abundance by a factor of three at core H depletion (a similar calibration is done in e.g. [Heger et al. 2000](#); [Chieffi & Limongi 2013](#)). Such a surface enrichment agrees qualitatively with observations of 10–20 M_\odot rotating stars (e.g. [Gies & Lambert 1992](#); [Villamariz & Herrero 2005](#); [Hunter et al. 2009](#)).

Except for some nuclear rates, we used the same inputs as those used in F16 so that the interested reader can refer to this work for further details. Table 2 lists the rates important for the *s*-process that were updated in the present work. In the stellar evolution code, the rates in their analytical form ([Rauscher & Thielemann 2000](#)) are used. The new rates of $^{17}\text{O}(\alpha, \gamma)$ and $^{17}\text{O}(\alpha, n)$ from [Best et al. \(2013\)](#), used in stellar evolution models for the first time, are only tabulated. As a consequence, we derived the analytical form of these rates⁴. We checked that the difference between the fit and the tabulated rate was less than 5%. The rates of $^{17}\text{O}(\alpha, \gamma)$, $^{17}\text{O}(\alpha, n)$, $^{22}\text{Ne}(\alpha, \gamma)$, and $^{22}\text{Ne}(\alpha, n)$ are still uncertain in the range of temperature of interest for the *s*-process in massive stars (e.g. [Best et al. 2011](#); [Nishimura et al. 2014](#)). Figure 1 compares the different available rates in the literature for these four reactions. In the range of tem-

Table 2. Updated reactions important for the *s*-process.

Reaction	F12, F16	This work
$^{12}\text{C}(\alpha, \gamma)^{16}\text{O}$	Kunz et al. (2002)	Xu et al. (2013)
$^{13}\text{C}(\alpha, n)^{16}\text{O}$	Angulo et al. (1999)	Guo et al. (2012)
$^{14}\text{N}(\alpha, \gamma)^{18}\text{F}$	Angulo et al. (1999)	Iliadis et al. (2010)
$^{18}\text{O}(\alpha, \gamma)^{22}\text{Ne}$	Angulo et al. (1999)	Iliadis et al. (2010)
$^{17}\text{O}(\alpha, \gamma)^{21}\text{Ne}$	Caughlan & Fowler (1988)	Best et al. (2013)
$^{17}\text{O}(\alpha, n)^{20}\text{Ne}$	Angulo et al. (1999)	Best et al. (2013)
$^{22}\text{Ne}(\alpha, \gamma)^{26}\text{Mg}$	Angulo et al. (1999)	Longland et al. (2012)
$^{22}\text{Ne}(\alpha, n)^{25}\text{Mg}$	Jaeger et al. (2001)	Longland et al. (2012)

Notes. Rates used in F12 and F16 (Col. 1), rates used in the present work (Col. 2).

perature of interest for us (mainly 0.2–0.3 GK, corresponding to the temperature of the helium burning core), the most uncertain rate is $^{17}\text{O}(\alpha, \gamma)$. It varies by about 3 dex from the rate of [Caughlan & Fowler \(1988\)](#) to the rate of [Best et al. \(2011\)](#); see the bottom right panel of Fig. 1). This motivated us to test the impact of a lower $^{17}\text{O}(\alpha, \gamma)$ rate in some models. We tried a rate divided by ten (dotted line in Fig. 1) for the fast-rotating 25 M_\odot and non-rotating 120 M_\odot models.

2.2. Yields and production factors

The yields provided contain a contribution from the wind and a contribution from the supernova. The yields from the supernova depend on the mass cut⁵ M_{cut} . Explosive nucleosynthesis, which is not considered here, will mostly affect the iron-group elements in the innermost layers of the star ([Woosley & Weaver 1995](#); [Thielemann et al. 1996](#); [Limongi & Chieffi 2003](#); [Nomoto et al. 2006](#); [Heger & Woosley 2010](#)) and is not expected to strongly modify the yields of *s*-elements ([Rauscher et al. 2002](#); [Tur et al. 2009](#)). Our results hence provide good predictions for the yields of light nuclei and *s*-process nuclei. The yield of an isotope *i* is calculated according to the relation

$$m_i = \int_{M_{\text{cut}}}^{M_{\text{fin}}} (X_i(M_r) - X_{i,0}) dM_r + \int_0^\tau \dot{M}(t) (X_{i,s}(t) - X_{i,0}) dt, \quad (3)$$

where M_{fin} and τ are the mass at the end of the evolution and the total lifetime of the model, respectively (both given in Table 1), $X_i(M_r)$ is the mass fraction of isotope *i* at coordinate M_r , at the end of the calculation, $X_{i,0}$ is the initial mass fraction, and $X_{i,s}(t)$ and $\dot{M}(t)$ are the surface mass fraction and the mass-loss rate at time *t* respectively. As a first step, M_{cut} is estimated using the relation of [Maeder \(1992\)](#), which links the mass of the CO-core to the mass of the remnant. Such remnant masses are defined as M_{rem} and are given in the last column of Table 3 for our models⁶. The impact of different assumptions on the mass cut, and hence on the remnant mass, are discussed in Sect. 4.1.

In addition to the yields, we use in this work the production factors. For an isotope *i*, the production factor is defined as

$$f_i = \frac{M_{\text{ej}} X_i}{M_{\text{ini}} X_{i,0}}, \quad (4)$$

⁵ At the time of the supernova, the mass cut delimits the part of the star that is expelled from the part that is locked into the remnant. The mass cut is equal to the mass of the remnant.

⁶ In [Maeder \(1992\)](#), the relation between the mass of the CO core and the mass of the remnant is applied for $M_{\text{ini}} \leq 120 M_\odot$. For our 150 M_\odot model, we have extrapolated the relation linearly.

⁴ More details can be found at <http://nucastro.org/forum/viewtopic.php?id=22>

A. Choplin et al.: Non-standard s -process in massive rotating stars

Table 3. Initial and final masses, mass lost through winds and size of the cores of the models computed in the present work.

Model	M_{ini} (M_{\odot})	M_{fin} (M_{\odot})	$M_{\text{ej,wind}}$ (M_{\odot})	M_{He} (M_{\odot})	M_{CO} (M_{\odot})	M_{rem} (M_{\odot})
10s0	10	9.93	0.07	2.91	1.58	1.28
10s4	10	9.78	0.22	3.35	1.86	1.36
15s0	15	14.78	0.22	4.67	2.62	1.56
15s4	15	14.34	0.66	5.74	3.36	1.75
20s0	20	19.87	0.13	6.46	4.04	1.92
20s4	20	17.36	2.64	8.21	5.31	2.24
25s0	25	24.68	0.32	8.65	5.88	2.39
25s4	25	16.68	8.32	10.85	7.53	2.80
25s7	25	16.21	8.79	10.91	7.56	2.81
25s7B ^a	25	16.01	8.99	10.96	7.62	2.82
40s0	40	34.10	5.90	15.29	11.75	3.80
40s4	40	24.60	15.40	19.10	14.66	4.54
60s0	60	44.17	15.83	25.36	20.94	6.44
60s4	60	40.81	19.19	30.77	25.35	7.77
85s0	85	59.33	25.67	37.86	32.86	9.90
85s4	85	58.27	26.73	45.57	39.30	11.73
120s0	120	82.45	37.55	54.30	50.01	14.69
120s0B ^a	120	83.18	36.82	54.46	49.35	14.51
120s4	120	85.81	34.19	65.28	61.78	17.95
150s0	150	100.26	49.74	70.77	65.34	18.94
150s4	150	99.59	50.41	83.83	80.04	23.04

Notes. Model label (Col. 1), initial mass (Col. 2), final mass (Col. 3), mass ejected through winds (Col. 4), mass of the H-free region (mass coordinate where the mass fraction of hydrogen $X(\text{H})$ drops below 0.01, Col. 5), mass of the CO core (mass coordinate where the ^4He mass fraction $X(^4\text{He})$ drops below 0.01, Col. 6), remnant mass M_{rem} using the relation of Maeder (1992, Col. 7). ^(a) Models computed with the rate of $^{17}\text{O}(\alpha, \gamma)$ divided by 10.

with M_{ej} the total mass ejected by the star, M_{ini} the initial mass, and X_i the mass fraction of isotope i in the ejecta. It expresses the ratio of what is given back by the star divided by what was present initially in the whole star.

3. Massive stars with rotation and s -process

3.1. Non-rotating models

The central temperature at the beginning of the helium-burning stage (when the central helium mass fraction $Y_c = 0.95$) is 182, 210, and 220 MK for the 25, 85, and 150 M_{\odot} models, respectively. Above 220 MK, the $^{22}\text{Ne}(\alpha, n)^{25}\text{Mg}$ and $^{22}\text{Ne}(\alpha, \gamma)^{26}\text{Ne}$ reactions start to be active and provide the main source of neutrons. Below 220 MK, the neutrons are provided by other (α, n) reactions from elements between C and Ne (especially $^{13}\text{C}(\alpha, n)^{16}\text{O}$). The top panels of Fig. 2 show the neutron profile (black dashed lines) in the 25 and 150 M_{\odot} models at the beginning of the core helium burning phase. The central neutron peak is bigger for the 150 M_{\odot} because of the higher central temperature that activates more efficiently the (α, n) reactions between N and Ne. At this early stage of core He-burning, the s -process is not activated significantly (see the flat ^{88}Sr and ^{138}Ba profiles in the top panels of Fig. 2) and leads only to slight overabundances of light s -elements like ^{63}Cu (dashed magenta line).

At the end of core helium burning (bottom panels), the temperature is $T > 220$ MK in the core so that the main neutron source in the He-burning core is ^{22}Ne for both models. Also, in both models and during all the core He-burning phase, the

second neutron peak (at higher mass coordinates) is mainly due to $^{13}\text{C}(\alpha, n)$. The s -process is not efficient in this region (see the ^{63}Cu , ^{88}Sr , and ^{138}Ba profiles) because of the high ^{14}N abundance, acting as a strong neutron poison.

In more massive models, the temperature required for the efficient activation of the $^{22}\text{Ne}(\alpha, n)$ reaction (220 MK) is reached earlier during the core helium burning phase: while the 150 M_{\odot} model reaches a central temperature $T_c = 220$ MK at the very start of core He-burning, the 25 M_{\odot} model reaches this temperature only close to the end of He-burning, when $Y_c \sim 0.2$. The duration of the stage where the central temperature is $T_c > 220$ MK is 0.16, 0.22, and 0.25 Myr for the 25, 85, and 150 M_{\odot} models, respectively. The amount of burnt ^{22}Ne during core He-burning therefore increases with initial mass (dashed line in the left panel of Fig. 3). As the initial mass increases, it converges toward a plateau whose value is almost equal to the sum of the initial CNO mass fraction $X(\text{CNO})_{\text{ini}}$ (horizontal blue line in the left panel of Fig. 3). Indeed, during the main sequence, the CNO cycle mainly transforms ^{12}C and ^{16}O into ^{14}N . Consequently, at the end of the main sequence, $X(\text{CNO})_{\text{ini}} \approx X(^{14}\text{N})$ in the core. When the core helium burning phase starts, ^{14}N is transformed into ^{22}Ne by successive α captures. Hence, at core He depletion, the maximum amount of burnt ^{22}Ne is about $X(\text{CNO})_{\text{ini}}$.

Since more ^{22}Ne is burnt in more massive stars, less is left at core He depletion (e.g. Fig. 4 and the dashed line in the right panel of Fig. 3). For stars with $M_{\text{ini}} > 40 M_{\odot}$, almost all the available ^{22}Ne burns during the core helium burning phase so that the contribution of the C-shell burning in producing s -element is in general negligible. Additional contributions from $^{13}\text{C}(\alpha, n)^7$ or $^{12}\text{C}(\alpha, n)^{23}\text{Mg}$ are in principle possible during carbon burning (see Bennett et al. 2012; Pignatari et al. 2013, for more details) but these contributions generally remain much smaller than the ^{22}Ne contribution during He-burning for very massive stars.

A higher temperature also favours the production of s -elements because the ratio of the rate of $^{17}\text{O}(\alpha, n)^{20}\text{Ne}$ over the rate of $^{17}\text{O}(\alpha, \gamma)^{21}\text{Ne}$ increases with increasing temperature. It means that for higher temperatures, the poisoning effect of ^{16}O is reduced since neutrons are more efficiently recycled⁸ by ^{17}O . The mean central temperatures of the 25 and 150 M_{\odot} models during He-burning are 207 and 233 MK, respectively. At 233 MK, the ratio $(\alpha, n) / (\alpha, \gamma)$ is roughly twice that at 207 MK.

Finally, s -elements are also overproduced in more massive stars because these stars have larger He-burning cores. The mass of the He-burning core corresponds roughly to the mass of the CO-core at the end of the evolution, which increases with initial mass (Col. 6 in Table 3) and also represents a larger fraction of the final stellar mass.

The effects discussed above lead to an increasing production of s -elements with initial stellar mass (Fig. 5), as has been found before (Langer et al. 1989; Prantzos et al. 1990; Käppeler 1999; The et al. 2007). In our models, the production factors of the s -elements for the 150 M_{\odot} model exceed the factors of the 25 M_{\odot} model by about two orders of magnitude at maximum (e.g. for Sr, see Fig. 5). Whatever the mass, the production factors of elements with $Z \gtrsim 50$ stay very small. Considering a lower $^{17}\text{O}(\alpha, \gamma)^{21}\text{Ne}$ rate mostly affects the range $30 \lesssim Z \lesssim 50$ (see red dashed line on Fig. 5). Even if the production factors of

⁷ Starting from $^{12}\text{C}(p, \gamma)$, with the protons coming from $^{12}\text{C}(^{12}\text{C}, p)^{23}\text{Na}$.

⁸ The isotope ^{16}O is an abundant poison that absorbs neutrons in the He-core and limits the production of s -elements. With the chain $^{16}\text{O}(n, \gamma)^{17}\text{O}(\alpha, \gamma)^{21}\text{Ne}$, the neutron captured by ^{16}O is definitely lost. With the chain $^{16}\text{O}(n, \gamma)^{17}\text{O}(\alpha, n)^{20}\text{Ne}$, the neutron is captured by ^{16}O and then recycled.

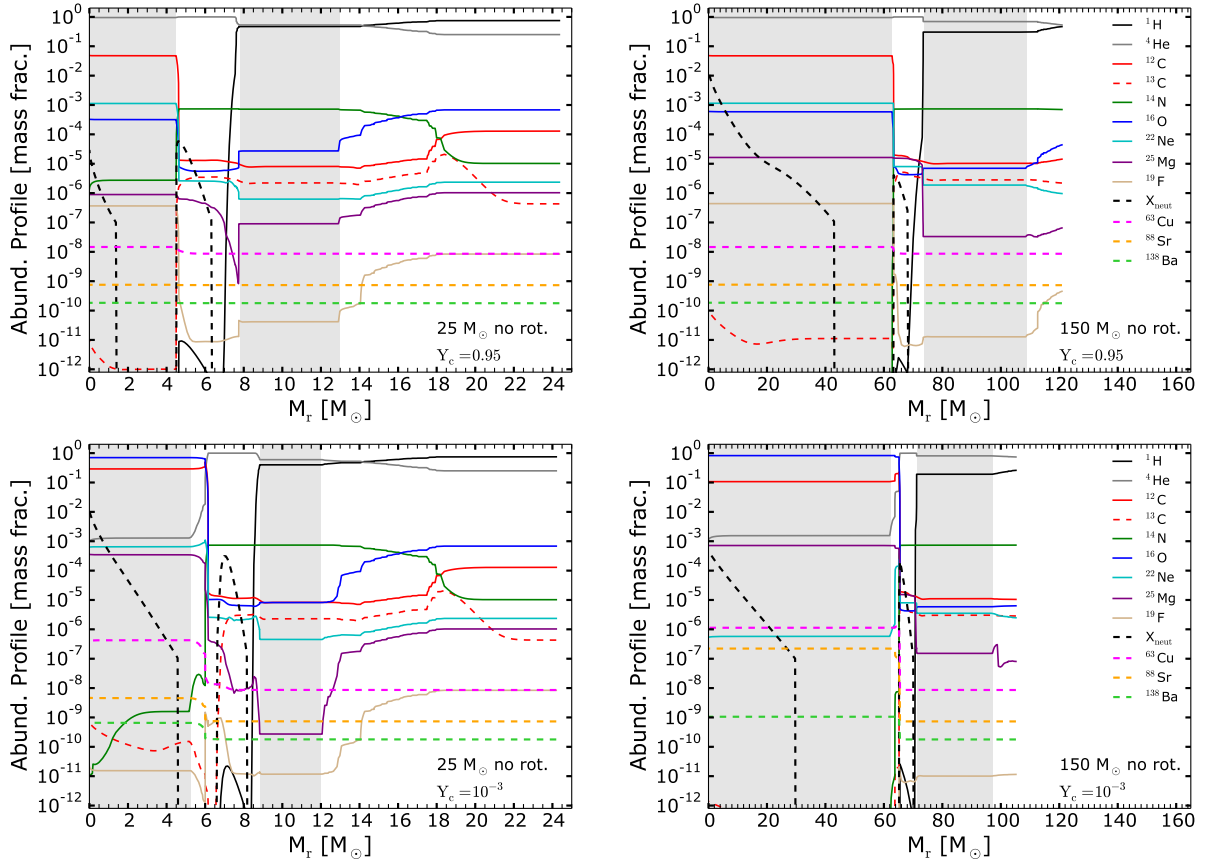


Fig. 2. Abundance profile of the non-rotating $25 M_{\odot}$ (left panels) and $150 M_{\odot}$ (right panels) models at the beginning (top panels) and at the end (bottom panels) of central helium burning phase. Grey areas show the convective zones. The neutron profile is scaled up by a factor of 10^{18} .

heavy *s*-elements like Pb do not vary much (a factor of ~ 2) in the considered mass range, the Pb yield in M_{\odot} (Eq. (3)) is about 3 dex higher in the $150 M_{\odot}$ compared to the $10 M_{\odot}$, because much more mass (hence Pb) is ejected in the case of the $150 M_{\odot}$.

3.2. Rotating models

The boost in the production of *s*-elements due to rotation is the highest between 20 and $60 M_{\odot}$. Figure 6 shows indeed that the production factors first increase from 10 to $40 M_{\odot}$ and decrease for $M > 40 M_{\odot}$. As shown in Fig. 6, the 60 , 85 , 120 , and $150 M_{\odot}$ models with rotation have similar patterns. Figure 7 shows that our models agree well with the 15 , 20 , 25 , and $40 M_{\odot}$ of F16 (green pattern). It means that overall, the new rates used in the present work (cf. Table 2) do not affect much the yields compared to the yields published in F16. Figure 7 also shows that rotation only significantly affects the yields if $M_{\text{ini}} < 60 M_{\odot}$. For $10 < M_{\text{ini}} < 40 M_{\odot}$, the ^{88}Sr , ^{138}Ba , and ^{208}Pb yields are boosted by ~ 2 – 3 , ~ 1 , and ~ 1 dex, respectively (see Fig. 7). There are two main reasons for that:

- First, close to the convective helium burning core, the D_{shear} coefficient (Eq. (2)) is generally smaller in more massive models (Fig. 8, red line between the two convective zones) and hence transports less efficiently the He-burning products to the H-shell. It ultimately leads to a smaller amount of extra ^{22}Ne , hence less neutrons. The smaller D_{shear} is explained by

the fact that (1) more massive stars have higher K/D_{h} ratios just above the convective core (dashed line in Fig. 8, this point was already discussed in F16, Sect. 3.1), and (2) Ω and its gradient are smaller in this same region (magenta line). Also, for the $25 M_{\odot}$ (left panel of Fig. 8), the D_{shear} drops just below the convective H-shell. This is because the convective H-shell migrates upward and leaves behind an almost flat Ω profile (at $M_r \sim 10 M_{\odot}$), which strongly reduces the D_{shear} (see also F16, Sect. 3.1). However, the bottom of the H-envelope extends down to about $9 M_{\odot}$ so that the He-products reach the H-rich region anyway and extra ^{14}N can be synthesized.

- The second reason is that the most massive stars have a more active H-burning shell. The shell remains convective during the whole He-burning stage and contributes well to the total stellar luminosity. This limits the growth of the He-core of the most massive stars. The growth of the convective He-burning core contributes to form extra ^{22}Ne by engulfing ^{14}N . Since the He-core of the most massive stars does not grow as much as the core of less massive stars, less primary ^{14}N is engulfed in the He-core, leading to a smaller production of *s*-elements. A word of caution is here required: the previous statement may be affected by the current uncertainties in convective boundaries and the mixing across these boundaries. For example, using Ledoux criterion instead of Schwarzschild criterion may limit the

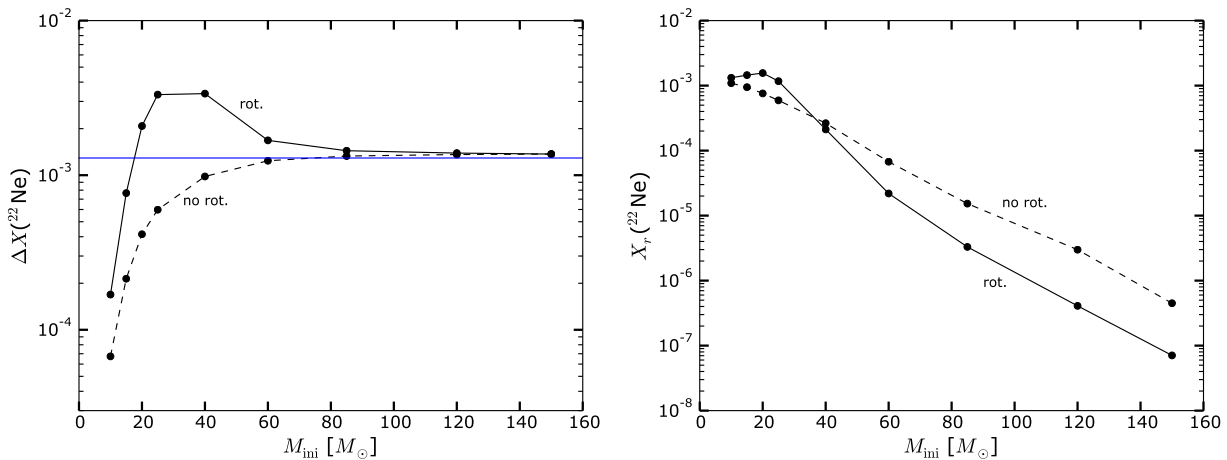
A. Choplin et al.: Non-standard *s*-process in massive rotating stars


Fig. 3. Mass fraction of burnt (left panel) and remaining (right panel) ^{22}Ne at the end of core helium burning as a function of initial mass. The blue line on the left panel shows the sum of the initial mass fraction of CNO isotopes.

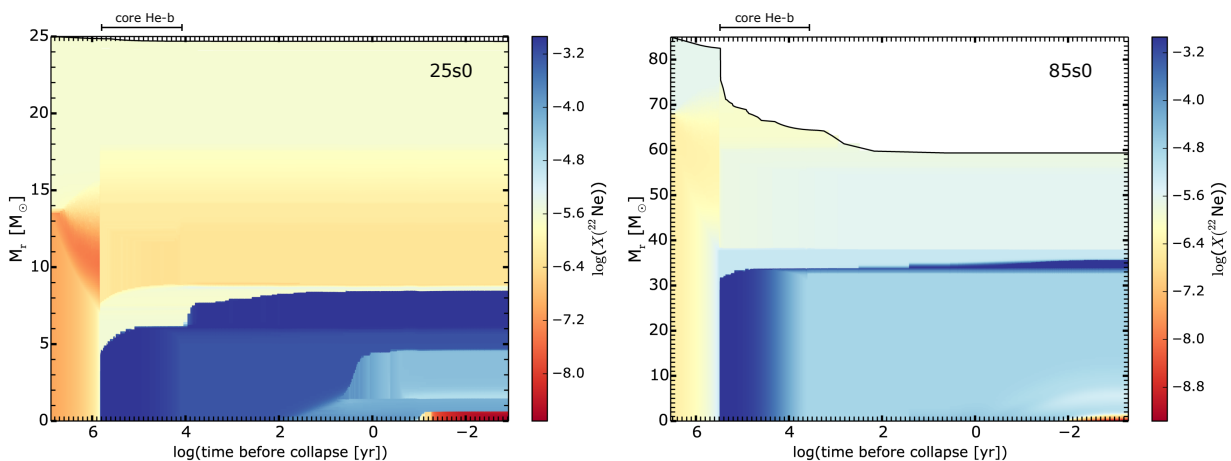


Fig. 4. Kippenhahn diagrams of the non-rotating $25 M_{\odot}$ (left panel) and $85 M_{\odot}$ (right panel) models. The colour map shows the mass fraction of ^{22}Ne (the initial ^{22}Ne mass fraction is $\log(X(^{22}\text{Ne}))_{\text{ini}} = -5.6$). The duration of the core helium burning phase is indicated at the top of the panels.

extent and growth of both the convective H-burning shell and He-burning core. These uncertainties can be tackled with multi-dimensional hydrodynamic simulations and asteroseismology (e.g. Arnett et al. 2015; Arnett & Moravvej 2017; Cristini et al. 2017).

For these reasons, more extra ^{22}Ne is available and burnt in $M_{\text{ini}} < 60 M_{\odot}$ models, as shown by the bump between 20 and $60 M_{\odot}$ in Fig. 3 (solid line, both panels). The bottom panels of Fig. 9 show the abundance profiles at the end of the core He-burning phase for the rotating $25 M_{\odot}$ (left) and $150 M_{\odot}$ (right) models. We see indeed that less primary ^{14}N is synthesized in the $150 M_{\odot}$ model (compare the ^{14}N bumps at $M_r \sim 9$ and $80 M_{\odot}$ for the 25 and $150 M_{\odot}$ models, respectively).

Another important product of rotation is ^{19}F , which is synthesized after the core He-burning phase, in the He-burning shell. Figure 10 shows the convective He-burning shell (between ~ 8 and $\sim 10.5 M_{\odot}$) of the rotating $25 M_{\odot}$ model. The abundance of ^{19}F is about 10^{-4} in the He-shell (it is only about 10^{-7} in the non-rotating $25 M_{\odot}$ model). Fluorine comes from the $^{14}\text{N}(\alpha, \gamma)^{18}\text{F}(\beta^+)^{18}\text{O}(p, \alpha)^{15}\text{N}(\alpha, \gamma)^{19}\text{F}$ chain (Goriely et al. 1989). The protons mainly come from the $^{14}\text{N}(n, p)^{14}\text{C}$ reaction.

The neutrons needed for the previous reactions are released by (α, n) reactions, especially $^{13}\text{C}(\alpha, n)$ and $^{22}\text{Ne}(\alpha, n)$. Figure 10 shows the abundances of the species involved in the synthesis of ^{19}F . The additional ^{13}C , ^{14}N , and ^{22}Ne synthesized in rotating models largely contributes to boost the sequence described above and consequently the ^{19}F production.

In general, rotating models lose more mass during their evolution. It occurs mainly for three reasons:

- rotation increases the mass losses by line-driven winds,
- rotation changes the distribution of the chemical species in the stellar interior. It can modify the tracks in the HR diagram and therefore the mass loss experienced by the star,
- rotation can also induce mechanical mass losses when the stellar surface reaches the critical velocity.

The surfaces of the 25 , 40 , and $60 M_{\odot}$ models reach critical velocity at the end of the main sequence so that mechanical mass loss occurs. The mass lost due to that effect remains modest (less than $0.1 M_{\odot}$). For the models of this work, the most important effect comes from the second reason mentioned above. After the main sequence, rotating models have higher luminosities than non-rotating models (Fig. 11). This is due to internal

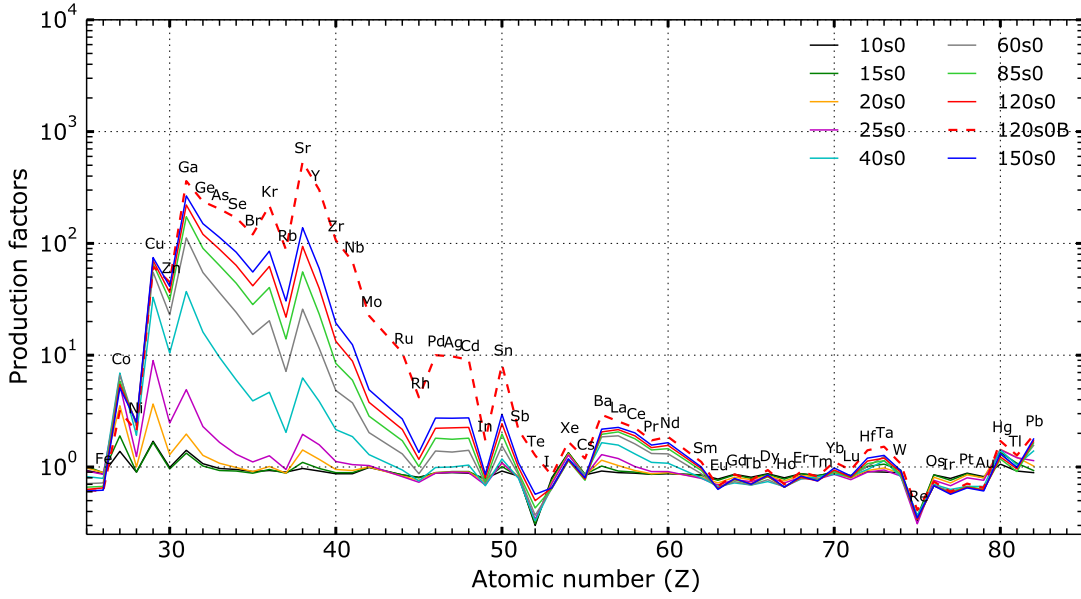


Fig. 5. Production factors (Eq. (4)) of non-rotating models. The mass cut is set according to the relation of [Maeder \(1992\)](#).

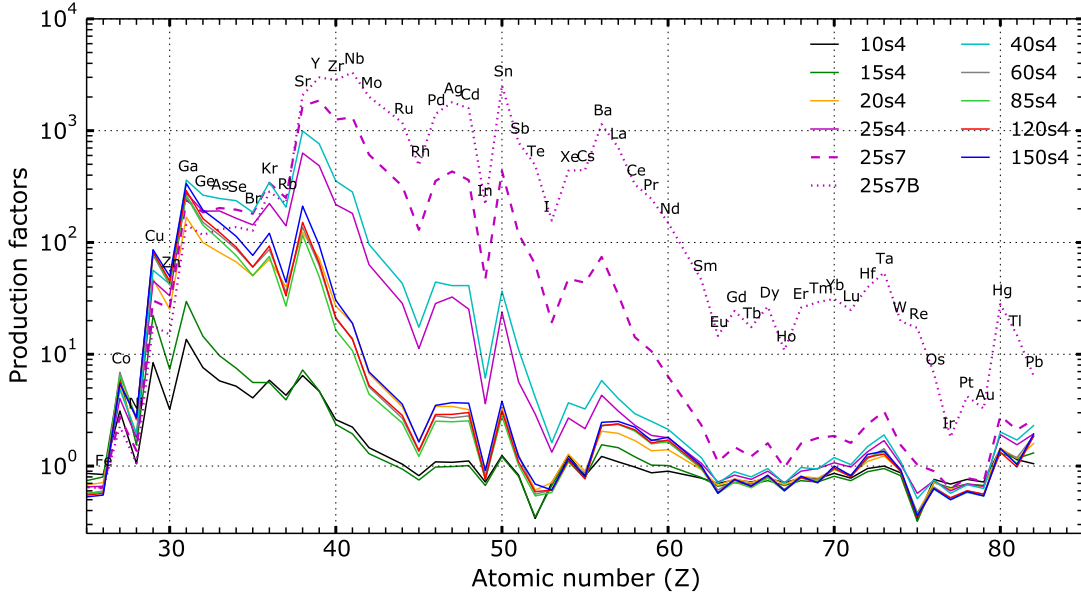


Fig. 6. Same as Fig. 5 but for rotating models.

mixing, which tends to produce larger helium burning cores. The higher luminosity (1) increases directly the mass-loss rate, and (2) makes the model more likely to enter the supra-Eddington regime. In this regime, additional mass loss occurs (cf. Sect. 2.1). The rotating $25 M_{\odot}$ model becomes supra-Eddington close to the end of the core helium burning stage, while its non-rotating counterpart never enters this regime. In the end, the rotating $25 M_{\odot}$ model loses eight more solar masses compared to the non-rotating model (Table 1, last column). Quickly after core He ignition, the rotating $60 M_{\odot}$ model reaches $\log T_{\text{eff}} \sim 3.8$ and experiences a supra-Eddington stage that removes $\sim 8 M_{\odot}$. The stellar surface is then enriched in helium and makes the star

go back to the blue (Fig. 11). The non-rotating $60 M_{\odot}$ enters the supra-Eddington regime only at the very end of core He-burning. Its surface is not very enriched in helium so that it stays red.

3.3. Integrated production factors

The integrated production factor $f_{i,\text{int}}$ for an isotope i is

$$f_{i,\text{int}} = \frac{\int_{M_{\text{min}}}^{M_{\text{max}}} f_i(M_{\text{ini}}) \phi(M_{\text{ini}}) dM_{\text{ini}}}{\int_{M_{\text{min}}}^{M_{\text{max}}} \phi(M_{\text{ini}}) dM_{\text{ini}}}, \quad (5)$$

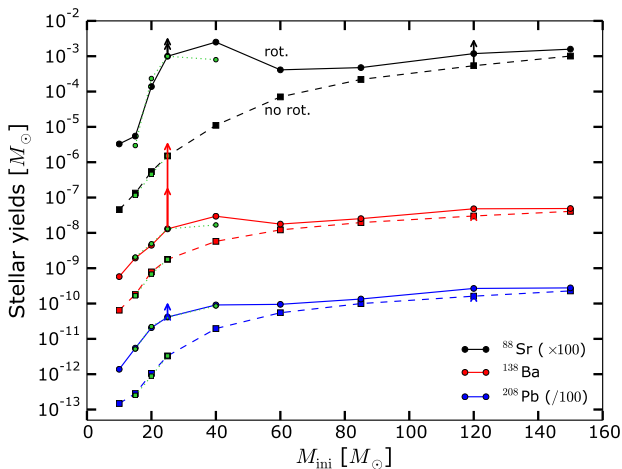
A. Choplin et al.: Non-standard s -process in massive rotating stars


Fig. 7. Stellar yields in M_{\odot} (Eq. (3)) as a function of the initial mass M_{ini} for the non-rotating (dashed lines) and rotating (solid lines) models. The mass cut is set using the relation of [Maeder \(1992\)](#). Isotopes ^{88}Sr , ^{138}Ba , and ^{208}Pb are shown. Green patterns between 15 and 40 M_{\odot} are the yields of the F16 models. The small and big red arrows at $M_{\text{ini}} = 25 M_{\odot}$ indicate the yields of ^{138}Ba for the fast-rotating 25 M_{\odot} model and the fast-rotating 25 M_{\odot} models with a lower $^{17}\text{O}(\alpha, \gamma)$ rate respectively. The same arrows are plotted for ^{88}Sr and ^{208}Pb . Arrows at $M_{\text{ini}} = 120 M_{\odot}$ represent the 120 M_{\odot} model with a lower $^{17}\text{O}(\alpha, \gamma)$ rate. We note that some arrows are not visible because there are too small.

where $M_{\text{min}} = 10 M_{\odot}$, $M_{\text{max}} = 150 M_{\odot}$, and $\phi(M_{\text{ini}})$ is the initial mass function. Here we take the initial mass function of [Chabrier \(2003\)](#) defined as $\phi(M_{\text{ini}}) = AM_{\text{ini}}^{-\alpha}$ with $A = 7.1 \cdot 10^{-5}$ and $\alpha = 2.3$. The $f_{i,\text{int}}$ factors were computed for the non-rotating and rotating (40% of critical velocity) models (black and red lines in Fig. 12).

Because of the low weight associated with very massive stars (cf. Eq. (5)), the contribution of such stars to the integrated pattern is small. The final pattern resembles that of an $\sim 20 M_{\odot}$ model. Strong differences between the rotating and non-rotating pattern occur between $30 < Z < 50$, especially around $Z = 38$ (strontium). Also of interest is the fluorine, which is overproduced by more than 2 dex by the rotating population (cf. Sect. 3.2).

3.4. Faster rotation

Increasing the initial rotation rate from 40% to 70% of the critical velocity for the 25 M_{\odot} model allows the production of s -elements up to $Z \sim 60$ (dashed purple line in Fig. 6). Compared to the 25 M_{\odot} model with slower rotation, Sr and Ba are overproduced by ~ 0.2 and 1 dex respectively. This is shown by the small blue and red arrows in Fig. 7. Fast rotation boosts more the second than the first s -process peak with respect to the 40% case. This is because faster rotation gives more ^{22}Ne , hence more neutrons, and a higher source (neutrons) over seed (heavy elements) ratio shifts the production of s -elements towards higher masses ([Gallino et al. 1998](#)).

3.5. Lower $^{17}\text{O}(\alpha, \gamma)$ rate

When the $^{17}\text{O}(\alpha, \gamma)$ rate is reduced in the fast-rotating 25 M_{\odot} model, the source over seed ratio is also increased since more neutrons are recycled. This allows the production of even more massive elements, up to Pb (dotted line in Fig. 6). The largest

difference between the two fast-rotating models with different reaction rates occurs for $Z > 55$. In particular, Ba and Hg are overproduced by more than 1 dex. Reducing the rate of $^{17}\text{O}(\alpha, \gamma)$ in the non-rotating 120 M_{\odot} model boosts the production of light s -elements by ~ 0.5 dex but does not allow the significant production of elements heavier than $Z \sim 50$. A better knowledge of the $^{17}\text{O}(\alpha, \gamma)$ rate is crucial to better constrain the production of the s -elements, especially from the second peak, which are greatly affected when changing this nuclear rate.

4. Effect of the mass cut and table of yields

4.1. Effect of the mass cut

In the previous section, we discussed the yields assuming a specific mass cut (following [Maeder 1992](#)). However, how massive stars explode is still poorly constrained, and even less if rotation is included. It is generally difficult to state definitively which part of the star is expelled and contributes to the chemical enrichment of the interstellar medium (ISM). In what follows, we discuss the effect of varying the mass cut. In the table of yields provided with this work, the mass cut is let as a free parameter.

Figures 13 and 14 show the dependence of the yields on the mass cut for the 25 and 150 M_{\odot} models. They show how elements are produced (positive yield, red colour) or destroyed (negative yield, blue colour) when varying the mass cut between the final mass M_{fin} and the remnant mass M_{rem} of the model. The gaps at $Z = 43$ and 61 in every panel correspond to the elements Tc and Pm, which have no stable isotope and are consequently neither produced nor destroyed in the final yields. Considering the fast-rotating 25 M_{\odot} model with lower $^{17}\text{O}(\alpha, \gamma)$ (Fig. 13, bottom right panel), we see that a mass cut below $\sim 10.5 M_{\odot}$ is needed to expel s -elements with $27 < Z < 60$ and a mass cut below $\sim 7.5 M_{\odot}$ (corresponding to the bottom of the He-burning shell) to expel s -elements with $Z > 60$. Interestingly, elements with $60 < Z < 70$ (among them Eu) are exclusively produced in the inner regions of the two fast-rotating 25 M_{\odot} models (bottom panels of Fig. 13). Also, out of these two models, only the one with a lower $^{17}\text{O}(\alpha, \gamma)$ is able to produce elements with $75 < Z < 80$.

Models including rotation generally lose more mass during their evolution (cf. Sect. 3.2) and have larger helium cores so that s -elements are located closer to the stellar surface at the end of the evolution. A large mass cut (i.e. close to the surface) will then already eject some s -elements in the case of the rotating models. Without rotation, s -elements are located deeper inside the star so that a smaller mass cut (i.e. deeper inside the star) is required to eject these elements. As an example, $M_{\text{cut}} = 70 M_{\odot}$ will eject some s -elements for the rotating 150 M_{\odot} model while it will not for the non-rotating 150 M_{\odot} model (Fig. 14). Ejecting deeper layers likely requires a more powerful explosion. Consequently, rotation in massive stars not only boosts the production of s -elements but might also make it easier to expel these elements. This could be viewed as an indirect effect of the rotation providing more s -elements to the ISM.

4.2. Table of yields

Yields is available online⁹. In this table, the mass cut M_{cut} is varied between the final mass of the considered stellar model and the remnant mass M_{rem} from [Maeder \(1992\)](#). One hundred values of M_{cut} are considered for each model, equally spaced

⁹ See <https://www.unige.ch/sciences/astro/evolution/en/database/> or the CDS database at cdsarc.u-strasbg.fr

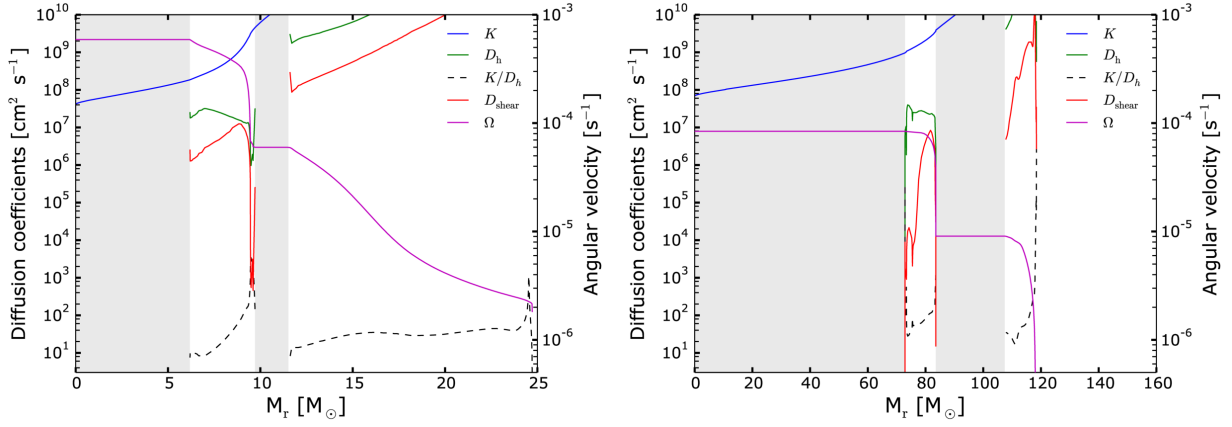


Fig. 8. Internal Ω profile, D_{shear} coefficient, and other diffusion coefficients in Eq. (2) for the rotating 25 (left panel) and $150 M_\odot$ models (right panel) during the core He-burning phase ($Y_c = 0.66$). Grey areas represent the convective zones and the dashed lines show the K/D_h ratio.

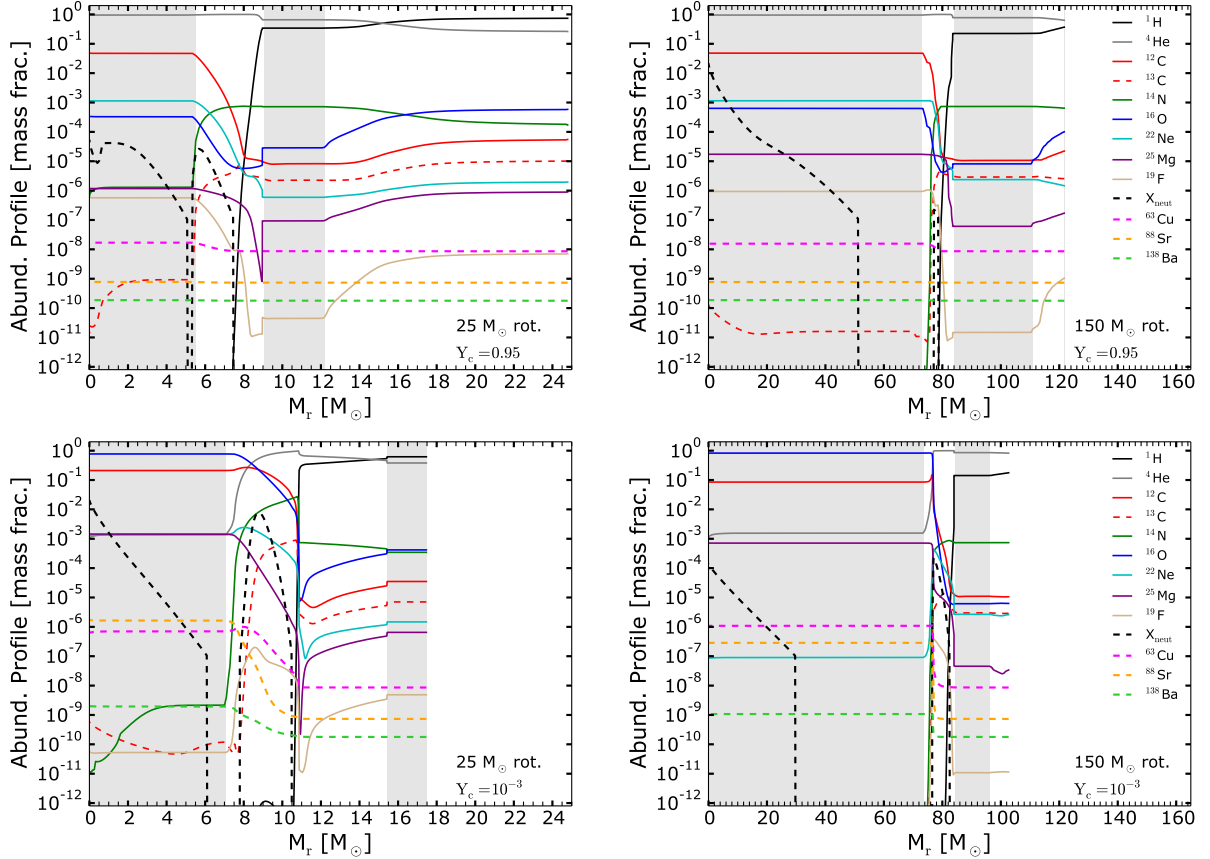


Fig. 9. Abundance profile of the rotating $25 M_\odot$ (left panels) and $150 M_\odot$ (right panels) models at the beginning (top panels) and at the end (bottom panels) of central helium burning phase. Grey areas show the convective zones. The neutron profile is scaled up by a factor of 10^{18} .

between M_{rem} and M_{fin} . The entire table therefore contains 21 stellar models times $100 M_{\text{cut}}$, which means 2100 different ejecta compositions. For each model, the first value of M_{cut} is equal to the final mass of the model M_{fin} (given in Table 3). It corresponds to the case where only the mass lost through stellar wind is taken into account (also given in Table 3). In all the other cases, the

yield of an isotope is the sum of the yields in the wind plus the yields in the material ejected by a supernova of the indicated mass cut. The last value of M_{cut} corresponds to the case where all the material above $M_{\text{cut}} = M_{\text{rem}}$ is ejected (also the stellar wind is taken into account). Yields below $10^{-15} M_\odot$ in absolute value are set to zero.

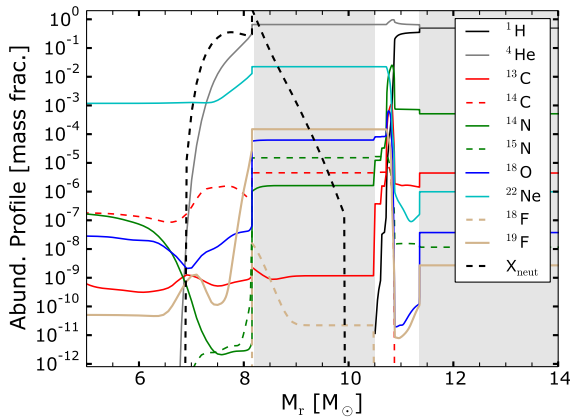
A. Choplin et al.: Non-standard *s*-process in massive rotating stars


Fig. 10. Abundance profile of the rotating $25 M_{\odot}$ during the shell He-burning phase. Grey areas show the convective zones (the convective He-burning shell is in-between ~ 8 and $\sim 10.5 M_{\odot}$). The neutron profile is scaled up by a factor of 10^{18} .

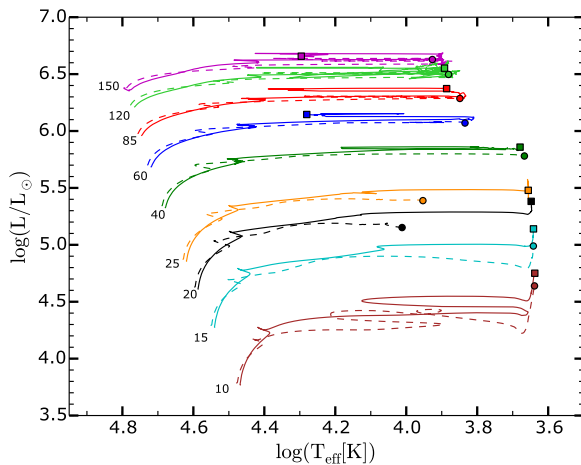


Fig. 11. Tracks of the models in the Hertzsprung–Russell diagram. Dashed and solid lines show non-rotating and rotating models respectively. Circles and squares denote the endpoint of the evolution for the non-rotating and rotating models, respectively.

5. Summary and discussions

We computed a grid of 21 models with and without rotation, at $Z = 10^{-3}$ and with initial masses between 10 and $150 M_{\odot}$. Rotating models were computed with an initial rotation of 40% of the critical velocity. One model was computed with 70% of the critical velocity and two models with the rate of $^{17}\text{O}(\alpha, \gamma)$ divided by 10. With this paper, we provide a table of yields including the effect of varying the mass cut.

The main result of this work is that rotation has the strongest impact on *s*-element production for $20 < M_{\text{ini}} < 60 M_{\odot}$. The first *s*-process peak is the most affected by rotation. In the $25 M_{\odot}$ rotating model, the yield of ^{88}Sr is increased by ~ 3 dex (Fig. 7). Although to a smaller extent, the second and third peaks are also affected: ^{138}Ba and ^{208}Pb are overproduced by ~ 1 dex. Faster rotation boosts even more the *s*-element production in the range $40 < Z < 60$. Taking a reasonably lower $^{17}\text{O}(\alpha, \gamma)$ reaction rate in the fast-rotating model overproduces the *s*-elements with

$Z > 55$ (among them Pb) by about 1 dex compared to the standard fast-rotating model.

5.1. Initial rotation of the models

The boost of *s*-process element production in massive stars is obtained here through rotational mixing. The importance of the boost depends, amongst other parameters, on the initial angular momentum content of the star, here determined by the choice of the surface rotation velocity on the ZAMS where the star is supposed to rotate as a solid body. The present results have been obtained for only one initial rotation for each initial mass and of course, to obtain a broader view of the impact of rotation, families of models with different initial rotation rates should be computed for each initial mass. Here, to limit the computational time (which is significant when following the changes in the abundances of such a large number of isotopes), we focused on a particular choice (40% of the critical velocity at the ZAMS). We adopted this value for the following reasons: first, at solar metallicity, this choice is consistent with the peak of the velocity distribution of young main-sequence B-type stars (cf. Sect. 2.1). Second, we wanted to use the same initial rotations as those used in F12 and F16 in order to check what some changes brought to the code since these computations may have affected the results. Since there are no observational constraints concerning the velocity distributions at the metallicity considered here, it is difficult to know whether such a choice is representative or not. At the moment, in the absence of such a confirmation, we can see the present computations as an exploration of how the boost of the *s*-process due to rotation varies as a function of the initial masses over a large range of initial masses. The reader has to keep in mind that the absolute values of the yields depend here on the choice of the initial rotation.

5.2. Model uncertainties

One has also to keep in mind that the yields of stellar models are affected by several sources of uncertainty. By changing the rate of $^{17}\text{O}(\alpha, \gamma)$, we provided an example of how current nuclear rate uncertainties can affect the yields. The three other key reactions for *s*-process in massive stars (shown in Fig. 1), which are still not completely constrained, add another source of uncertainty in the yields. Uncertainties on neutron-capture and β -decay rates also affect the *s*-process yields by a factor of two at maximum, in general (Nishimura et al. 2017, 2018).

Also, even if we know that stars rotate, important uncertainties remain on the effects of rotation in the stellar interiors, and hence on the *s*-process yields of rotating stars. The production of *s*-elements is highly sensitive to the amount of ^{22}Ne available, which in turn depends on stellar evolution inputs such as the way rotational mixing (also convection) is treated in the code. Different recipes exist in the literature for the horizontal diffusion (Zahn 1992; Maeder 2003; Mathis et al. 2004) and the shear diffusion coefficients (Talon & Zahn 1997; Maeder 1997; Maeder et al. 2013) that govern the transport of chemical elements (see Meynet et al. 2013, for a review). Different combinations of these coefficients will lead to a higher or lower production of extra ^{22}Ne , hence a possibly different production of *s*-elements. Such uncertainties might be at the origin of the differences between this work and the recent work of Prantzos et al. (2018). They used a chemical evolution model to discuss the abundance evolution of elements up to uranium in the Milky Way. They included yields of rotating massive stars from Chieffi

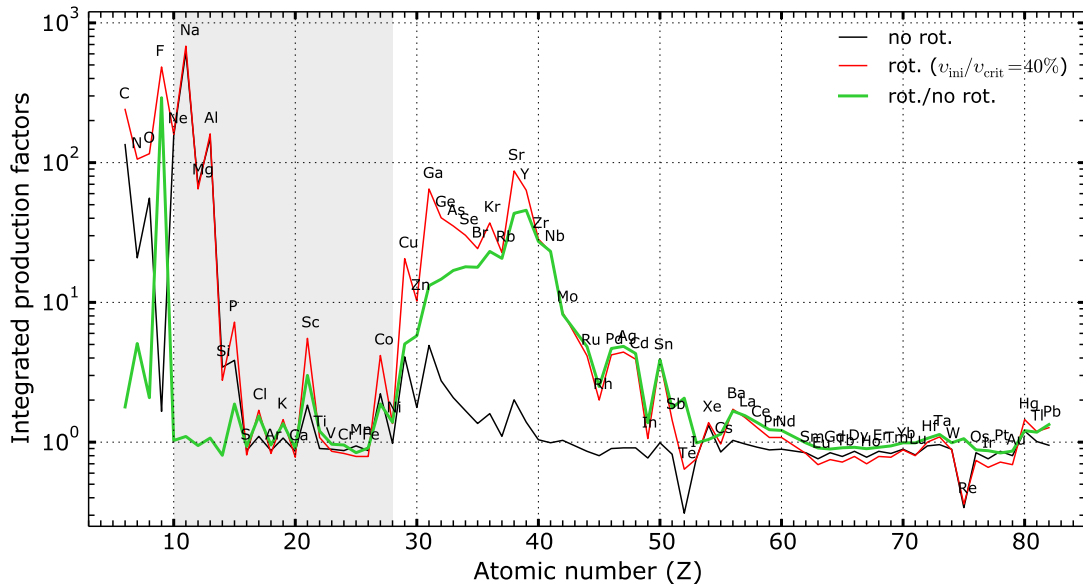


Fig. 12. Integrated production factors $f_{i,\text{int}}$ (Eq. 5) for the population of non-rotating and rotating models. The mass function of Chabrier (2003) is used. The green line shows the ratio between the two curves. The mass cut is set using the relation of Maeder (1992). The grey area highlights the elements that are likely affected by explosive nucleosynthesis.

& Limongi. Elements from Ba to Pb are generally overproduced compared to our models. Since these stellar models are not published yet, we do not know the detailed physics ingredients and cannot do extensive comparisons.

5.3. Fluorine and *s*-elements

From discussions in Sect. 3.3 and Fig. 12, we note that the production of *s*-elements in massive rotating stars should be correlated with the production of several light elements, particularly fluorine. This correlation might be found in the next generation of low-mass halo field stars. Importantly, AGB stars are also believed to contribute to the production of both fluorine and *s*-elements (e.g. Jorissen et al. 1992; Lugaro et al. 2004, 2008; Abia et al. 2010; Karakas 2010; Bisterzo et al. 2010; Gallino et al. 2010), leaving open the possibility for AGB and massive stars to be responsible for such abundance patterns. In addition to AGB and massive rotators, the ν -process in core-collapse supernovae is also generally expected to contribute to fluorine production (Woosley 1977; Woosley et al. 1990; Kobayashi et al. 2011; Izutani et al. 2012). Recent studies suggest, however, that both the ν -process in supernovae (Jönsson et al. 2017) and AGB stars (Abia et al. 2015) might be insufficient to explain the observed evolution of fluorine in the solar neighbourhood. This potentially makes rotating massive stars interesting complementary fluorine sources that might improve the agreement between Galactic chemical evolution models and observations (Meynet & Arnould 2000; Palacios et al. 2005).

Around the metallicity considered in this work ($[\text{Fe}/\text{H}] \sim -2$), the few iron-poor halo field stars whose fluorine abundance was determined are generally F-rich (Otsuka et al. 2008; Lucatello et al. 2011; Li et al. 2013; Schuler et al. 2007). One star (HD 5223) with $[\text{Fe}/\text{H}] \sim -2$ has both fluorine and heavy element abundances available. It is enriched in F, Sr, Ba, and Pb (Goswami et al. 2006; Lucatello et al. 2011) and shows

radial velocity variations (McClure & Woodworth 1990). The enhancement in Pb may not be reproduced by the massive stellar models of the present work. A mass transfer episode from an AGB star's companion may be the main process for explaining the abundances of HD 5223. Further determinations of fluorine and *s*-elements abundances in metal-poor stars should help to test stellar model predictions.

5.4. Rotation from solar to very low metallicity

As a final note, we would like to emphasize here that the impact of rotation on the evolution of stars (in particular on the stellar yields) allows us to unify in the same theoretical framework the properties of stars observed, for instance, in the solar neighbourhood to the properties of stars and their impact on nucleosynthesis at very low metallicities (see e.g. Maeder et al. 2015; Chiappini 2013).

Let us first recall that rotational mixing was first included in stellar models to account for surface enrichments observed at the surface of main-sequence B-type stars in the solar neighbourhood (see e.g. Maeder & Meynet 2012, and references therein). In general, rotating models need to be calibrated in order to constrain the efficiency of rotation-induced mixing (cf. Sect. 2.1). In the present work, the value of f_{energ} (Eq. (2)) is chosen in order for solar metallicity models with initial masses around $15 M_{\odot}$ to fit the averaged observed chemical enrichments of Galactic B-type stars rotating with an average surface velocity. Although the calibration can be done using different observations (Brott et al. 2011, for instance, used a sample of B-type stars in the Large Magellanic Cloud), at very low metallicities there are no observations allowing us to check whether a different value of f_{energ} is needed. At the moment the most reasonable choice is to keep this quantity constant. Once the calibration is done, the physics describing the transport processes of both chemical elements and angular momentum due to rotation is not changed. As a consequence, the results of the stellar models for other

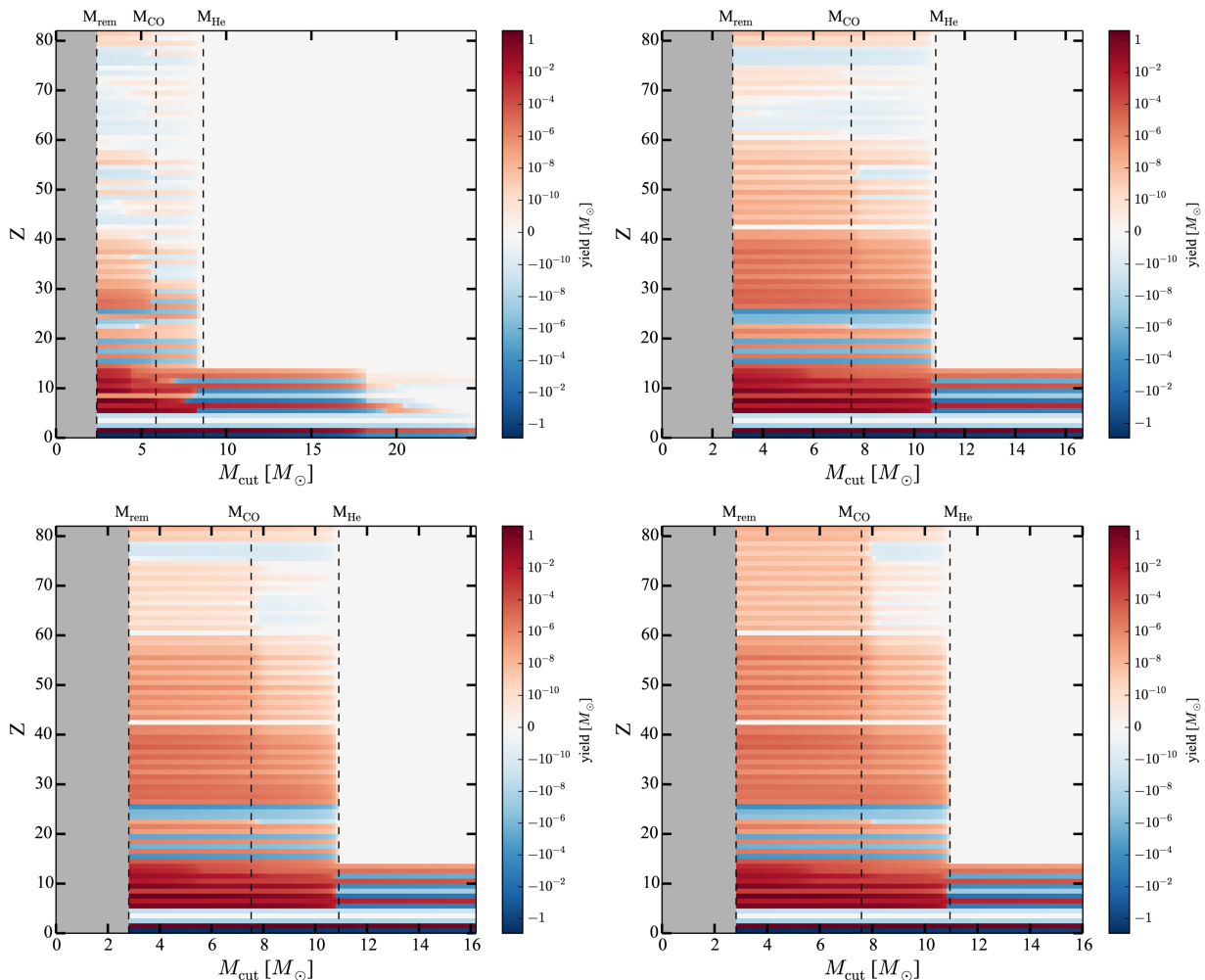
A. Choplin et al.: Non-standard s -process in massive rotating stars


Fig. 13. Yields of elements (characterized here by the atomic number Z) for different values of the mass cut. The colour map shows the yields for the non-rotating $25 M_{\odot}$ (top left panel), rotating $25 M_{\odot}$ (top right), fast-rotating $25 M_{\odot}$ (bottom left panel), and fast-rotating $25 M_{\odot}$ with lower $^{17}\text{O}(\alpha, \gamma)$ (bottom right panel). The ticks labelled M_{rem} show the location of the remnant mass using the relation of [Maeder \(1992\)](#); last column of Table 3). “CO” and “He” denote the location of the top of the CO and He core, respectively (fifth and sixth columns of Table 3).

initial masses and metallicities can be seen as stellar model predictions. Interestingly, when this physics is used for low metallicity rotating stars of both intermediate and high masses, the rotational mixing produces, without any artificial tuning, primary nitrogen production ([Meynet & Maeder 2002a](#)). Rotating massive star models have been invoked to explain the N/O plateau shown by metal-poor halo stars, the C/O upturn ([Chiappini et al. 2006](#)), and have provided predictions concerning the $^{12}\text{C}/^{13}\text{C}$ ratio ([Chiappini et al. 2008](#)).

Rotation is also interesting to explain the CEMP stars with $[\text{Fe}/\text{H}] < -3$ that are not highly enriched in s - and/or r -elements ([Meynet et al. 2006, 2010](#); [Hirschi 2007](#); [Joggerst et al. 2010](#); [Takahashi et al. 2014](#); [Maeder et al. 2015](#); [Maeder & Meynet 2015](#); [Choplin et al. 2016, 2017a](#)). It was reported by [Placco et al. \(2014\)](#) that 43% of stars with $[\text{Fe}/\text{H}] < -3$ are CEMP (with $[\text{C}/\text{Fe}] > 0.7$ and excluding the stars showing clear overabundances of neutron-capture elements). A major difference between CEMP stars and normal metal-poor halo stars is likely due to the degree of mixing of the cloud of

interstellar material from which these two types of stars formed. CEMP stars likely formed from pockets of the ISM that have been enriched by the ejecta of a few objects, maybe only one, while normal halo stars are likely formed from a much better mixed reservoir in which the ejecta of many more sources have accumulated. In both cases (normal halo stars and at least some CEMP stars), rotational mixing provides a very interesting mechanism for explaining the surface abundances of many of these objects, while still being able to account for observed features of massive stars at solar metallicity. Of course alternative explanations exist (e.g. [Umeda & Nomoto 2003](#); [Limongi et al. 2003](#); [Iwamoto et al. 2005](#); [Tominaga et al. 2014](#); [Clarkson et al. 2018](#)) and in the future some specific signatures will hopefully allow us to decide which of these models or combination of models are the most probable. A comparison between the different models for explaining the most iron-poor stars is beyond the scope of this work, which focuses on higher metallicities. We plan to compute similar models as done in the present paper but with a lower metallicity ($[\text{Fe}/\text{H}] \sim -4$).

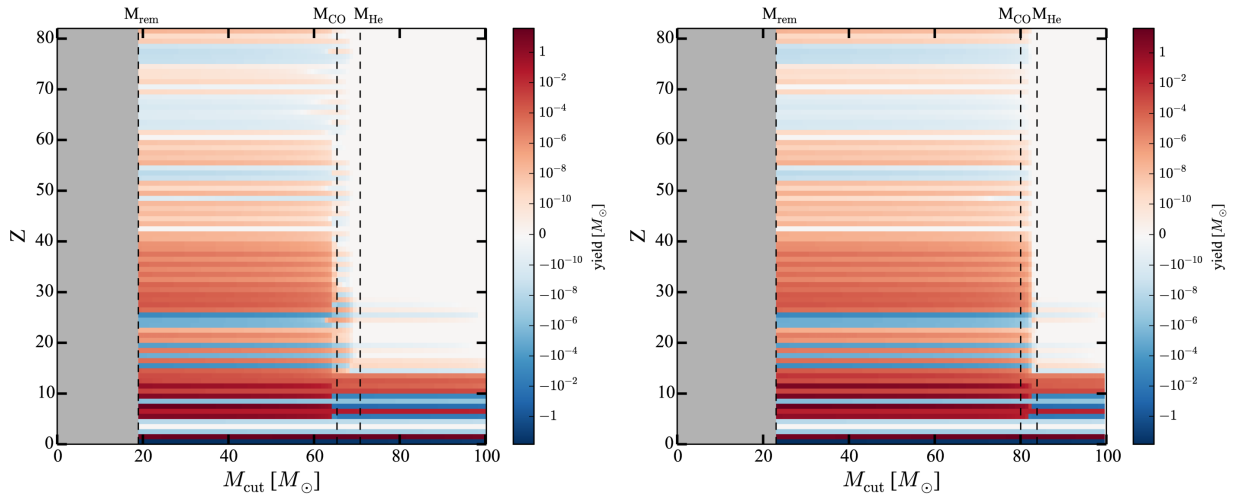


Fig. 14. Same as Fig. 13 but for the non-rotating $150 M_{\odot}$ (left panel) and rotating $150 M_{\odot}$ (right panel).

Acknowledgements. This work was supported by the SNF project number 200020-172505. The authors acknowledge support from the “ChETEC” COST Action (CA16117), supported by COST (European Cooperation in Science and Technology). RH acknowledges the European Research Council under the European Union’s Seventh Framework Programme (FP/2007-2013)/ERC Grant Agreement no. 306901. RH acknowledges support from the World Premier International Research Center Initiative (WPI Initiative), MEXT, Japan. CC acknowledges support from DFG Grant CH1188/2-1.

References

- Abate, C., Pols, O. R., Izzard, R. G., Mohamed, S. S., & de Mink, S. E. 2013, *A&A*, **552**, A26
- Abate, C., Pols, O. R., Izzard, R. G., & Karakas, A. I. 2015a, *A&A*, **581**, A22
- Abate, C., Pols, O. R., Karakas, A. I., & Izzard, R. G. 2015b, *A&A*, **576**, A118
- Abia, C., Cunha, K., Cristallo, S., et al. 2010, *ApJ*, **715**, L94
- Abia, C., Cunha, K., Cristallo, S., & de Laverny, P. 2015, *A&A*, **581**, A88
- Angulo, C., Arnould, M., Rayet, M., et al. 1999, *Nucl. Phys. A*, **656**, 3
- Aoki, W., Frebel, A., Christlieb, N., et al. 2006, *ApJ*, **639**, 897
- Aoki, W., Beers, T. C., Lee, Y. S., et al. 2013, *AJ*, **145**, 13
- Arnett, W. D., & Moravveji, E. 2017, *ApJ*, **836**, L19
- Arnett, W. D., Meakin, C., Viallet, M., et al. 2015, *ApJ*, **809**, 30
- Asplund, M., Grevesse, N., & Sauval, A. J. 2005, in *Cosmic Abundances as Records of Stellar Evolution and Nucleosynthesis*, eds. T. G. Barnes, & F. N. Bash, *ASP Conf. Ser.*, **336**, 25
- Barbuy, B., Zoccali, M., Ortolani, S., et al. 2009, *A&A*, **507**, 405
- Beers, T. C., & Christlieb, N. 2005, *ARA&A*, **43**, 531
- Behara, N. T., Bonifacio, P., Ludwig, H.-G., et al. 2010, *A&A*, **513**, A72
- Bennett, M. E., Hirschi, R., Pignatari, M., et al. 2012, *MNRAS*, **420**, 3047
- Best, A., Görres, J., Couder, M., et al. 2011, *Phys. Rev. C*, **83**, 052802
- Best, A., Beard, M., Görres, J., et al. 2013, *Phys. Rev. C*, **87**, 045805
- Bisterzo, S., Gallino, R., Straniero, O., Cristallo, S., & Käppeler, F. 2010, *MNRAS*, **404**, 1529
- Bisterzo, S., Gallino, R., Straniero, O., Cristallo, S., & Käppeler, F. 2012, *MNRAS*, **422**, 849
- Brott, I., de Mink, S. E., Cantiello, M., et al. 2011, *A&A*, **530**, A115
- Caughlan, G. R., & Fowler, W. A. 1988, *At. Data Nucl. Data Tables*, **40**, 283
- Cescutti, G., Chiappini, C., Hirschi, R., Meynet, G., & Frischknecht, U. 2013, *A&A*, **553**, A51
- Chaboyer, B., & Zahn, J.-P. 1992, *A&A*, **253**, 173
- Chabrier, G. 2003, *PASP*, **115**, 763
- Chiappini, C. 2013, *Astron. Nachr.*, **334**, 595
- Chiappini, C., Hirschi, R., Meynet, G., et al. 2006, *A&A*, **449**, L27
- Chiappini, C., Ekström, S., Meynet, G., et al. 2008, *A&A*, **479**, L9
- Chiappini, C., Frischknecht, U., Meynet, G., et al. 2011, *Nature*, **472**, 454
- Chieffi, A., & Limongi, M. 2013, *ApJ*, **764**, 21
- Choplin, A., Maeder, A., Meynet, G., & Chiappini, C. 2016, *A&A*, **593**, A36
- Choplin, A., Ekström, S., Meynet, G., et al. 2017a, *A&A*, **605**, A63
- Choplin, A., Hirschi, R., Meynet, G., & Ekström, S. 2017b, *A&A*, **607**, L3
- Clarkson, O., Herwig, F., & Pignatari, M. 2018, *MNRAS*, **474**, L37

- Couch, R. G., Schmiedekamp, A. B., & Arnett, W. D. 1974, *ApJ*, **190**, 95
- Cristini, A., Meakin, C., Hirschi, R., et al. 2017, *MNRAS*, **471**, 279
- Cybur, R. H., Fields, B. D., & Olive, K. A. 2003, *Phys. Lett. B*, **567**, 227
- Cybur, R. H., Amthor, A. M., Ferguson, R., et al. 2010, *ApJS*, **189**, 240
- de Jager, C., Nieuwenhuijzen, H., & van der Hucht, K. A. 1988, *A&AS*, **72**, 259
- Eggenberger, P., Meynet, G., Maeder, A., et al. 2008, *Ap&SS*, **316**, 43
- Ekström, S., Meynet, G., Chiappini, C., Hirschi, R., & Maeder, A. 2008, *A&A*, **489**, 685
- Ekström, S., Georgy, C., Eggenberger, P., et al. 2012, *A&A*, **537**, A146
- Ferguson, J. W., Alexander, D. R., Allard, F., et al. 2005, *ApJ*, **623**, 585
- Frebel, A., Christlieb, N., Norris, J. E., Aoki, W., & Asplund, M. 2006, *ApJ*, **638**, L17
- Frebel, A., Collet, R., Eriksson, K., Christlieb, N., & Aoki, W. 2008, *ApJ*, **684**, 588
- Frischknecht, U., Hirschi, R., & Thielemann, F.-K. 2012, *A&A*, **538**, L2
- Frischknecht, U., Hirschi, R., Pignatari, M., et al. 2016, *MNRAS*, **456**, 1803
- Gallino, R., Arlandini, C., Busso, M., et al. 1998, *ApJ*, **497**, 388
- Gallino, R., Bisterzo, S., Cristallo, S., & Straniero, O. 2010, *Mem. Soc. Astron. It.*, **81**, 998
- Georgy, C., Ekström, S., Eggenberger, P., et al. 2013, *A&A*, **558**, A103
- Gies, D. R., & Lambert, D. L. 1992, *ApJ*, **387**, 673
- Gorieli, S., Jorissen, A., & Arnould, M. 1989, in *Proc. 5th Workshop on Nuclear Astrophysics*, eds. W. Hillebrandt, & E. Müller, *Max Planck Inst. für Astrophys. Rep.*, **60**
- Goswami, A., Aoki, W., Beers, T. C., et al. 2006, *MNRAS*, **372**, 343
- Guo, B., Li, Z. H., Lugaro, M., et al. 2012, *ApJ*, **756**, 193
- Hansen, T., Hansen, C. J., Christlieb, N., et al. 2015, *ApJ*, **807**, 173
- Hansen, T. T., Andersen, J., Nordström, B., et al. 2016, *A&A*, **588**, A3
- Heger, A., & Woosley, S. E. 2010, *ApJ*, **724**, 341
- Heger, A., Langer, N., & Woosley, S. E. 2000, *ApJ*, **528**, 368
- Hirschi, R. 2007, *A&A*, **461**, 571
- Hollek, J. K., Frebel, A., Placco, V. M., et al. 2015, *ApJ*, **814**, 121
- Huang, W., Gies, D. R., & McSwain, M. V. 2010, *ApJ*, **722**, 605
- Hunter, I., Brott, I., Langer, N., et al. 2009, *A&A*, **496**, 841
- Iliadis, C., Longland, R., Champagne, A. E., Coc, A., & Fitzgerald, R. 2010, *Nucl. Phys. A*, **841**, 31
- Iwamoto, N., Umeda, H., Tominaga, N., Nomoto, K., & Maeda, K. 2005, *Science*, **309**, 451
- Izutani, N., Umeda, H., & Yoshida, A. J. 2012, in *Death of Massive Stars: Supernovae and Gamma-Ray Bursts*, eds. P. Roming, N. Kawai, & E. Pian, *IAU Symp.*, **279**, 339
- Jaeger, M., Kunz, R., Mayer, A., et al. 2001, *Phys. Rev. Lett.*, **87**, 202501
- Joggerst, C. C., Almgren, A., Bell, J., et al. 2010, *ApJ*, **709**, 11
- Jönsson, H., Ryde, N., Spitoni, E., et al. 2017, *ApJ*, **835**, 50
- Jorissen, A., Smith, V. V., & Lambert, D. L. 1992, *A&A*, **261**, 164
- Käppeler, F. 1999, *Prog. Part. Nucl. Phys.*, **43**, 419
- Käppeler, F., Gallino, R., Bisterzo, S., & Aoki, W. 2011, *Rev. Mod. Phys.*, **83**, 157
- Karakas, A. I. 2010, *MNRAS*, **403**, 1413
- Kerber, L. O., Nardiello, D., Ortolani, S., et al. 2018, *ApJ*, **853**, 15
- Kobayashi, C., Izutani, N., Karakas, A. I., et al. 2011, *ApJ*, **739**, L57

A. Choplin et al.: Non-standard s-process in massive rotating stars

- Kunz, R., Fey, M., Jaeger, M., et al. 2002, *ApJ*, 567, 643
- Lamb, S. A., Howard, W. M., Truran, J. W., & Iben, I., Jr. 1977, *ApJ*, 217, 213
- Langer, N., Arcoragi, J.-P., & Arnould, M. 1989, *A&A*, 210, 187
- Lau, H. H. B., Stancliffe, R. J., & Tout, C. A. 2009, *MNRAS*, 396, 1046
- Li, H. N., Ludwig, H.-G., Caffau, E., Christlieb, N., & Zhao, G. 2013, *ApJ*, 765, 51
- Limongi, M., & Chieffi, A. 2003, *ApJ*, 592, 404
- Limongi, M., Chieffi, A., & Bonifacio, P. 2003, *ApJ*, 594, L123
- Longland, R., Iliadis, C., & Karakas, A. I. 2012, *Phys. Rev. C*, 85, 065809
- Lucatello, S., Tsangarides, S., Beers, T. C., et al. 2005, *ApJ*, 625, 825
- Lucatello, S., Masseron, T., Johnson, J. A., Pignatari, M., & Herwig, F. 2011, *ApJ*, 729, 40
- Lugaro, M., Ugalde, C., Karakas, A. I., et al. 2004, *ApJ*, 615, 934
- Lugaro, M., de Mink, S. E., Izzard, R. G., et al. 2008, *A&A*, 484, L27
- Lugaro, M., Karakas, A. I., Stancliffe, R. J., & Rijs, C. 2012, *ApJ*, 747, 2
- Maeder, A. 1992, *A&A*, 264, 105
- Maeder, A. 1997, *A&A*, 321, 134
- Maeder, A. 2003, *A&A*, 399, 263
- Maeder, A., & Meynet, G. 2000, *A&A*, 361, 159
- Maeder, A., & Meynet, G. 2001, *A&A*, 373, 555
- Maeder, A., & Meynet, G. 2012, *Rev. Mod. Phys.*, 84, 25
- Maeder, A., & Meynet, G. 2015, *A&A*, 580, A32
- Maeder, A., & Zahn, J.-P. 1998, *A&A*, 334, 1000
- Maeder, A., Meynet, G., Lagarde, N., & Charbonnel, C. 2013, *A&A*, 553, A1
- Maeder, A., Meynet, G., & Chiappini, C. 2015, *A&A*, 576, A56
- Mathis, S., Palacios, A., & Zahn, J.-P. 2004, *A&A*, 425, 243
- McClure, R. D., & Woodsworth, A. W. 1990, *ApJ*, 352, 709
- Meynet, G., & Arnould, M. 2000, *A&A*, 355, 176
- Meynet, G., & Maeder, A. 2002a, *A&A*, 390, 561
- Meynet, G., & Maeder, A. 2002b, *A&A*, 381, L25
- Meynet, G., Ekström, S., & Maeder, A. 2006, *A&A*, 447, 623
- Meynet, G., Hirschi, R., Ekstrom, S., et al. 2010, *A&A*, 521, A30
- Meynet, G., Ekstrom, S., Maeder, A., et al. 2013, in *Lect. Notes Phys.*, eds. M. Goupil, K. Belkacem, C. Neiner, F. Lignières, & J. J. Green (Berlin: Springer Verlag), 865, 3
- Nishimura, N., Hirschi, R., Pignatari, M., et al. 2014, *Am. Inst. Phys. Conf. Ser.*, 1594, 146
- Nishimura, N., Hirschi, R., Rauscher, T., Murphy, A. S. J., & Cescutti, G. 2017, *MNRAS*, 469, 1752
- Nishimura, N., Hirschi, R., & Rauscher, T. 2018, *J. Phys. Conf. Ser.*, 940, 012051
- Nomoto, K., Tominaga, N., Umeda, H., Kobayashi, C., & Maeda, K. 2006, *Nucl. Phys. A*, 777, 424
- Norris, J. E., Yong, D., Bessell, M. S., et al. 2013, *ApJ*, 762, 28
- Otsuka, M., Izumiura, H., Tajitsu, A., & Hyung, S. 2008, *ApJ*, 682, L105
- Palacios, A., Arnould, M., & Meynet, G. 2005, *A&A*, 443, 243
- Peters, J. G. 1968, *ApJ*, 154, 225
- Pignatari, M., Gallino, R., Meynet, G., et al. 2008, *ApJ*, 687, L95
- Pignatari, M., Wiescher, M., Timmes, F. X., et al. 2013, *ApJ*, 767, L22
- Placco, V. M., Frebel, A., Beers, T. C., & Stancliffe, R. J. 2014, *ApJ*, 797, 21
- Prantzos, N., Hashimoto, M., & Nomoto, K. 1990, *A&A*, 234, 211
- Prantzos, N., Abia, C., Limongi, M., Chieffi, A., & Cristallo, S. 2018, *MNRAS*, 476, 3432
- Raiteri, C. M., Busso, M., Gallino, R., Picchio, G., & Pulone, L. 1991a, *ApJ*, 367, 228
- Raiteri, C. M., Busso, M., Picchio, G., & Gallino, R. 1991b, *ApJ*, 371, 665
- Raiteri, C. M., Gallino, R., Busso, M., Neuberger, D., & Kaeppler, F. 1993, *ApJ*, 419, 207
- Rauscher, T., Heger, A., Hoffman, R. D., & Woosley, S. E. 2002, *ApJ*, 576, 323
- Rauscher, T., & Thielemann, F.-K. 2000, *At. Data Nucl. Data Tables*, 75, 1
- Schuler, S. C., Cunha, K., Smith, V. V., et al. 2007, *ApJ*, 667, L81
- Stancliffe, R. J., & Glebbeek, E. 2008, *MNRAS*, 389, 1828
- Starkenbourg, E., Shetrone, M. D., McConnachie, A. W., & Venn, K. A. 2014, *MNRAS*, 441, 1217
- Takahashi, K., Umeda, H., & Yoshida, T. 2014, *ApJ*, 794, 40
- Talon, S., & Zahn, J.-P. 1997, *A&A*, 317, 749
- The, L.-S., El Eid, M. F., & Meyer, B. S. 2000, *ApJ*, 533, 998
- The, L.-S., El Eid, M. F., & Meyer, B. S. 2007, *ApJ*, 655, 1058
- Thielemann, F.-K., Nomoto, K., & Hashimoto, M.-A. 1996, *ApJ*, 460, 408
- Tominaga, N., Iwamoto, N., & Nomoto, K. 2014, *ApJ*, 785, 98
- Tur, C., Heger, A., & Austin, S. M. 2009, *ApJ*, 702, 1068
- Umeda, H., & Nomoto, K. 2003, *Nature*, 422, 871
- Villamariz, M. R., & Herrero, A. 2005, *A&A*, 442, 263
- Vink, J. S., de Koter, A., & Lamers, H. J. G. L. M. 2001, *A&A*, 369, 574
- Woosley, S. E. 1977, *Nature*, 269, 42
- Woosley, S. E., Hartmann, D. H., Hoffman, R. D., & Haxton, W. C. 1990, *ApJ*, 356, 272
- Woosley, S. E., & Weaver, T. A. 1995, *ApJS*, 101, 181
- Xu, Y., Takahashi, K., Goriely, S., et al. 2013, *Nucl. Phys. A*, 918, 61
- Yong, D., Norris, J. E., Bessell, M. S., et al. 2013, *ApJ*, 762, 26
- Zahn, J.-P. 1992, *A&A*, 265, 115

5.3 The origin of the single CEMP-s stars

As discussed in Sect. 2.5, CEMP-s stars are generally explained with the AGB binary scenario. This scenario predicts that the CEMP-s should have a white dwarf companion (cf. Fig. 2.7). The CEMP-s stars that appear to be single (Hansen et al. 2016b) may challenge the AGB scenario.

5.3.1 Massive source stars

In Choplin et al. (2017c, see letter in the next section), we have investigated the origin of the four apparently single CEMP-s stars in light of the new grid of massive stars including rotation and s-process presented in the previous paper. The abundances of the apparently single CEMP-s stars are reported in Table 5.1. We found that 3 out of the 4 CEMP-s stars can be well reproduced by the yields of the fast rotating ($v_{\text{ini}}/v_{\text{crit}} = 0.7$) $25 M_{\odot}$ model that was computed with the rate of the $^{17}\text{O}(\alpha, \gamma)$ reaction divided by 10. The dilution factors D are between 4 and 20 and in all the cases, the mass cut $M_{\text{cut}} = M_{\text{CO}}$. In general, the other models of the grid do not provide enough s-elements. If deep layers are expelled some models may nevertheless provide enough s-elements but in this case, Na, Mg and Al are overestimated by several order of magnitudes compared to the observations. These results show that some s-rich metal-poor ($[\text{Fe}/\text{H}] \sim -2$) halo stars may have formed with a material that was enriched by the ejecta of a previous fast rotating massive source star. It gives support to the spinstar scenario at higher metallicities (compared to the lower metallicities considered in Chapter 4).

The late mixing process introduced in Sect. 4.5 is not considered in these new CEMP source star models. This process will mostly affect the C and N abundances. It may nevertheless also synthesize heavier elements through neutron captures (Clarkson et al. 2018, cf. also Sect. 4.8). Including the late mixing process in the models with an extended network is among the possible next steps of this work. However, it is not excluded that the late mixing process occurs only at very low metallicity (maybe $[\text{Fe}/\text{H}] \lesssim -4$), and not in these new source star models, with $[\text{Fe}/\text{H}] = -1.8$. The reason is that at very low metallicity, source stars are more compact so that the H- and He-burning shells are closer from each other. It might imply an easier interaction of these two shells. This is however speculative and deserves more investigation.

Table 5.1: Apparently single CEMP-s stars (abundances taken from the SAGA database, Suda et al. 2008).

Star	HE 0206-1916	HE 1045+0226	HE 2330-0555	CS 30301-015
[Fe/H]	-2.09	-2.20	-2.78	-2.64
T_{eff}	5200	5077 (100)	4900	4750
$\log g$	2.7	2.2 (0.25)	1.7	0.8
[C/Fe]	2.11 (0.19)	1.18	2.09 (0.19)	1.72 (0.28)
[N/Fe]	1.61 (0.33)	-	0.99 (0.42)	1.84
[Na/Fe]	0.72 (0.14)	0.96 (0.05)	0.95 (0.12)	-
[Mg/Fe]	0.50 (0.15)	0.27 (0.09)	0.64 (0.17)	0.84 (0.22)
[Al/Fe]	-	-	-	0.17
[Si/Fe]	-	0.45 (0.17)	-	-
[K/Fe]	-	0.51	-	-
[Ca/Fe]	0.13 (0.13)	0.22 (0.16)	0.44 (0.19)	0.79 (0.16)
[Sc/Fe]	-	0.09 (0.05)	0.20 (0.08)	-
[Ti I/Fe]	0.41 (0.14)	0.34 (0.1)	0.31 (0.11)	0.30 (0.13)
[Ti II/Fe]	0.59 (0.19)	0.43 (0.13)	0.38 (0.23)	0.45 (0.24)
[Cr/Fe]	0.05 (0.13)	-0.05 (0.01)	-0.05 (0.10)	-
[Mn/Fe]	-	-0.23 (0.28)	-	-
[Ni/Fe]	-	0.17 (0.16)	-	-
[Zn/Fe]	-	-	-	0.37
[Sr/Fe]	-	-	-	0.37 (0.23)
[Y/Fe]	-	1.29 (0.25)	-	0.31 (0.20)
[Zr/Fe]	-	1.52	-	-
[Ba/Fe]	2.01 (0.16)	1.24 (0.1)	1.25 (0.25)	1.49 (0.16)
[La/Fe]	-	0.92 (0.17)	-	0.96 (0.25)
[Ce/Fe]	-	-	-	1.21 (0.15)
[Pr/Fe]	-	1.14	-	-
[Nd/Fe]	-	0.85 (0.32)	-	0.80 (0.17)
[Sm/Fe]	-	-	-	0.87 (0.20)
[Eu/Fe]	-	0.27	-	0.22 (0.18)
[Dy/Fe]	-	-	-	0.64 (0.20)
[Pb/Fe]	-	-	-	1.70 (0.24)
Source	1	2	1	3, 4

References. 1 - Aoki et al. (2007); 2 - Cohen et al. (2013); 3 - Aoki et al. (2002a); 4 - Aoki et al. (2002b)

LETTER TO THE EDITOR

Are some CEMP-*s* stars the daughters of spinstars?

Arthur Choplin¹, Raphael Hirschi^{2,3,4}, Georges Meynet¹, and Sylvia Ekström¹¹ Geneva Observatory, University of Geneva, Maillettes 51, 1290 Sauverny, Switzerland
e-mail: arthur.choplin@unige.ch² Astrophysics Group, Lennard-Jones Labs 2.09, Keele University, ST5 5BG, Staffordshire, UK³ Kavli Institute for the Physics and Mathematics of the Universe (WPI), University of Tokyo, 5-1-5 Kashiwanoha, Kashiwa 277-8583, Japan⁴ UK Network for Bridging the Disciplines of Galactic Chemical Evolution (BRIDGCE), UK

Received 14 September 2017 / Accepted 16 October 2017

ABSTRACT

Carbon-enhanced metal-poor (CEMP)-*s* stars are long-lived low-mass stars with a very low iron content as well as overabundances of carbon and *s*-elements. Their peculiar chemical pattern is often explained by pollution from an asymptotic giant branch (AGB) star companion. Recent observations have shown that most CEMP-*s* stars are in binary systems, providing support to the AGB companion scenario. A few CEMP-*s* stars, however, appear to be single. We inspect four apparently single CEMP-*s* stars and discuss the possibility that they formed from the ejecta of a previous-generation massive star, referred to as the “source” star. In order to investigate this scenario, we computed low-metallicity massive-star models with and without rotation and including complete *s*-process nucleosynthesis. We find that non-rotating source stars cannot explain the observed abundance of any of the four CEMP-*s* stars. Three out of the four CEMP-*s* stars can be explained by a 25 M_{\odot} source star with $v_{\text{ini}} \sim 500 \text{ km s}^{-1}$ (spinstar). The fourth CEMP-*s* star has a high Pb abundance that cannot be explained by any of the models we computed. Since spinstars and AGB predict different ranges of [O/Fe] and [ls/hs], these ratios could be an interesting way to further test these two scenarios.

Key words. nuclear reactions, nucleosynthesis, abundances – stars: interiors – stars: chemically peculiar – stars: abundances – stars: massive

1. Introduction

Carbon-enhanced metal-poor (CEMP) stars are iron-deficient stars with an excess of carbon compared to normal metal-poor stars. Some of these stars with very little iron, for example, SMSS J031300.36-670839.3, with $[\text{Fe}/\text{H}] < -7$ (Keller et al. 2014), should have formed from a material ejected by the first massive stars in the Universe. Nowadays, CEMP stars are generally considered as the best window into examining these very first stars.

CEMP stars are divided into several subclasses depending on their enrichment in *s*- and *r*-elements: CEMP-*s*, CEMP-*r*, CEMP-*r/s* (or CEMP-*i*, Hampel et al. 2016) and CEMP-no (little enriched in *s*- or *r*-elements). Most CEMP-*s* stars have $-3 < [\text{Fe}/\text{H}] < -2$ (Norris et al. 2013). Different scenarios are needed to explain CEMP stars (even in CEMP subclasses, different classes of progenitors seem to be needed, e.g. for the CEMP-no category, Placco et al. 2016; Yoon et al. 2016; Choplin et al. 2017). For CEMP-*s* stars, the main formation scenario is the asymptotic giant branch (AGB) scenario, suggesting that a more massive AGB companion has fed the secondary in carbon and *s*-elements during a mass transfer (or wind mass transfer) episode (Stancliffe & Glebbeek 2008; Lau et al. 2009; Bisterzo et al. 2010; Lugaro et al. 2012; Abate et al. 2013, 2015b,a; Hollek et al. 2015). Interestingly, it has been shown by Matrozis & Stancliffe (2017) that rotational mixing in the CEMP-*s* stars can severely inhibit atomic diffusion. If not counteracted, atomic diffusion would make the *s*-elements sink quickly into the star after the accretion episode. By considering a sample of CEMP-*s* stars, Lucatello et al. (2005) and Starkenburg et al. (2014) have shown that the whole sample is consistent with the hypothesis of them all existing in binary

systems. Hansen et al. (2016) have monitored the radial velocity of 22 CEMP-*s* stars over several years. They have found clear orbital motion for 18 stars, giving support to the AGB scenario. Four stars appear to be single. It is very unlikely that these apparently single stars are in fact face-on systems¹. These apparently single stars might have a companion with a long orbital period (about 10^3 – 10^4 days or even longer). Nevertheless, since some CEMP-*s* stars are apparently single, it is worth exploring scenarios which could explain their abundances under the assumption that they are indeed single.

It has been shown that rotation at low metallicity can considerably boost the *s*-process in massive stars (Meynet et al. 2006; Hirschi 2007). This is because of the rotational mixing operating between the He-core and H-shell during the core helium burning phase: ^{12}C and ^{16}O diffuse from the He-core to the H-shell, boosting the CNO cycle and forming primary ^{14}N . When growing, the He-core engulfs the extra ^{14}N , allowing the synthesis of extra ^{22}Ne (via $^{14}\text{N}(\alpha, \gamma)^{18}\text{F}(e^+ \nu_e)^{18}\text{O}(\alpha, \gamma)^{22}\text{Ne}$). Neutrons are then released by the reaction $^{22}\text{Ne}(\alpha, n)$. Pignatari et al. (2008) did the first study of the effect of rotational mixing on the *s*-process at low metallicity by studying a 25 M_{\odot} model with a post-processing code. Frischknecht et al. (2012, 2016) computed massive rotating models, following the *s*-process during the calculation. They confirmed that rotation at low metallicity (down to $[\text{Fe}/\text{H}] \sim -3.5$) greatly enhances *s*-element production in massive stars.

In this letter, we investigate whether or not the four apparently single CEMP-*s* stars might have formed from the material ejected by a massive star (source star) that lived before the birth

¹ The probability of finding one face-on orbit in their sample is $\sim 0.01\%$.

A&A 607, L3 (2017)

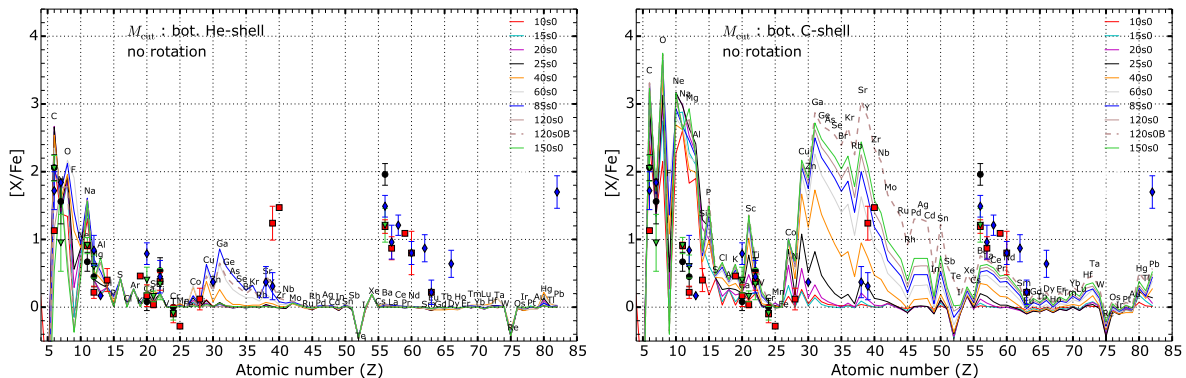


Fig. 1. Comparison of the material ejected by non-rotating source-star models with the chemical composition of four apparently single CEMP-*s* stars (Hansen et al. 2016). Different mass cuts M_{cut} are considered in the two panels: M_{cut} at the bottom of the He-shell (left panel), at the bottom of the C-shell (right panel). The models are labelled as follow: the first number is the initial mass in M_{\odot} , “s0” means no rotation and “B” means that the model was computed with a lower $^{17}\text{O}(\alpha, \gamma)$ rate. The four single CEMP-*s* stars are shown. HE 0206-1916: black circles, HE 1045+0226: red squares, HE 2330-0555: green triangles, CS 10301-015: blue diamonds.

of the CEMP-*s* star. The main difference with the AGB scenario is that the abundances of the CEMP-*s* stars would come from the natal cloud in which they formed. In the AGB scenario, only a relatively small mass fraction at the surface (received from the AGB companion) has the specific chemical composition making the star appear as a CEMP-*s* star. We computed 14 low-metallicity massive source-star models with and without rotation. The *s*-process is followed consistently during the evolution (no post-processing). Models from Frischknecht et al. (2016; F16 hereafter) are also considered in the analysis. Here we discuss the models in the framework of the four apparently single CEMP-*s* stars. A future work will discuss in detail the grid of massive stellar models with *s*-process and rotation. Only a few aspects of this grid are discussed here. In Sects. 2 and 3, we describe the computed models and compare their ejecta to the four CEMP-*s* stars. Conclusions are given in Sect. 4.

2. Source-star models

We use the Geneva stellar evolution code (GENEC). GENEC is described in detail by Eggenberger et al. (2008) and Ekström et al. (2012). We computed 14 rotating and non-rotating models at $Z = 10^{-3}$ ($[\text{Fe}/\text{H}] = -1.8$). The initial rotation rate, $v_{\text{ini}}/v_{\text{crit}}^2$ is 0, 0.4 or 0.7. Initial masses are 10, 25, 40, 60, 85, 120 and 150 M_{\odot} . The nuclear network, used throughout the evolution, comprises 737 isotopes, from hydrogen to polonium ($Z = 84$). The size of the network is similar to the network of, for example, The et al. (2000), Frischknecht et al. (2012, 2016) and follows the complete *s*-process. The initial composition of metals (elements heavier than helium) is α -enhanced (see Sect. 2.1 of F16 for more details). Radiative mass-loss rates are from Vink et al. (2001) when $\log T_{\text{eff}} \geq 3.9$ and when $M_{\text{ini}} > 15 M_{\odot}$. They are from de Jager et al. (1988) if these conditions are not met. The horizontal diffusion coefficient is from Zahn (1992) and the shear diffusion coefficient is from Talon & Zahn (1997). The models are generally stopped at the end of the Ne-photodisintegration phase. In any case, the end of the C-burning phase is reached. The *s*-process in massive stars mainly occurs during the core He-burning phase, in the He-core. There is also a contribution from the He- and C-burning shells but that generally stays low ($\leq 10\%$, F16). We used the same physical ingredients as the ones used in F16, except for some nuclear rates, which were

updated. For instance, F16 used the rates of Jaeger et al. (2001) and Angulo et al. (1999) for $^{22}\text{Ne}(\alpha, n)$ and $^{22}\text{Ne}(\alpha, \gamma)$ respectively, while we used the rates of Longland et al. (2012). Also, we used the new rates of Best et al. (2013) for $^{17}\text{O}(\alpha, n)$ and $^{17}\text{O}(\alpha, \gamma)$. We noticed that globally, these changes have very limited effects and thus the F16 models can be consistently used together with our models. We investigate the impact of a $^{17}\text{O}(\alpha, \gamma)$ rate divided by ten in two models (a 25 M_{\odot} with $v_{\text{ini}}/v_{\text{crit}} = 0.7$ and a 120 M_{\odot} without rotation). A lower $^{17}\text{O}(\alpha, \gamma)$ rate favours the reaction $^{17}\text{O}(\alpha, n)$ that releases the neutrons previously captured by ^{16}O . Thus, *s*-element production is increased. We tested this because the rate of $^{17}\text{O}(\alpha, \gamma)$ is still uncertain at relevant temperatures for the *s*-process (Best et al. 2011) and very recent measurements tend to show that this rate is lower than expected (Laird, priv. comm.). Other rates like $^{22}\text{Ne}(\alpha, n)$ are also uncertain and can affect the results (Nishimura et al. 2014). They will be studied in a future work.

3. Comparison to single CEMP-*s* stars

We compare the chemical composition of the material ejected by the source-star models with the chemical composition observed at the surface of the four apparently single CEMP-*s* stars. These CEMP-*s* stars are HE 0206-1916 (Aoki et al. 2007), HE 1045+0226 (Cohen et al. 2013), HE 2330-0555 (Aoki et al. 2007) and CS 10301-015 (Aoki et al. 2002a,b).

Non-rotating models cannot explain the considered CEMP-*s* stars. They underproduce elements with $Z > 55$ (see Fig. 1, the two panels correspond to different mass cuts³ M_{cut}). This is due to the secondary nature of the weak *s*-process in non-rotating models (Prantzos et al. 1990). Considering different mass cuts does not solve the problem. When expelling deep layers (Fig. 1, right panel), more *s*-elements are released but Na ($Z = 11$) and Mg ($Z = 12$) are overproduced by about 2 dex compared to the observations. Diluting the source-star ejecta with the ISM will shift down the Na and Mg abundances, but also the abundances of heavier elements, with $Z > 55$, which would contradict the observations.

Rotating models, especially models in the range 20–40 M_{\odot} , produce significantly more *s*-elements than their non-rotating counterparts (see Fig. 2) due to the rotational mixing, as explained in Sect. 1. As for non-rotating models, rotating models

² v_{crit} is the velocity at the equator at which the gravitational acceleration is exactly compensated by the centrifugal force.

³ The mass cut delimits the part of the star which is expelled from the part which is locked into the remnant.

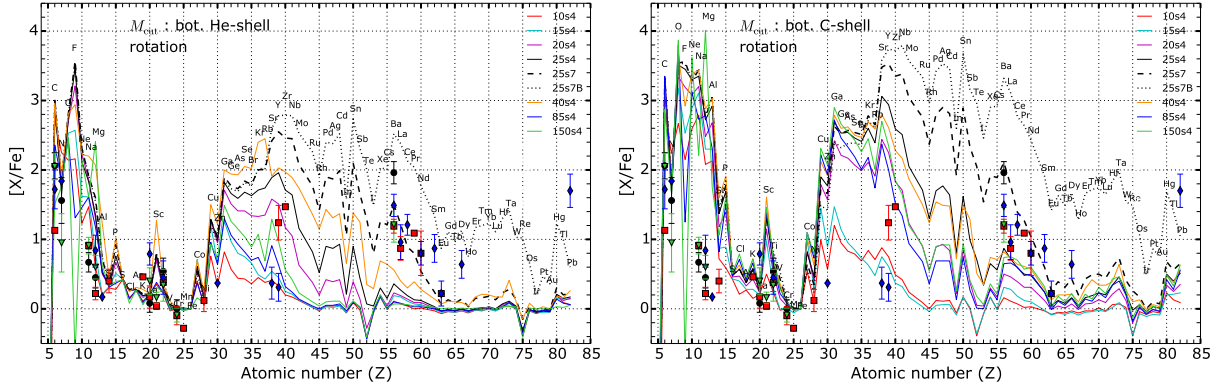


Fig. 2. Same as Fig. 1 but for rotating models. In the model labels, “s4” and “s7” means rotation ($v_{\text{ini}}/v_{\text{crit}} = 0.4$ or 0.7).

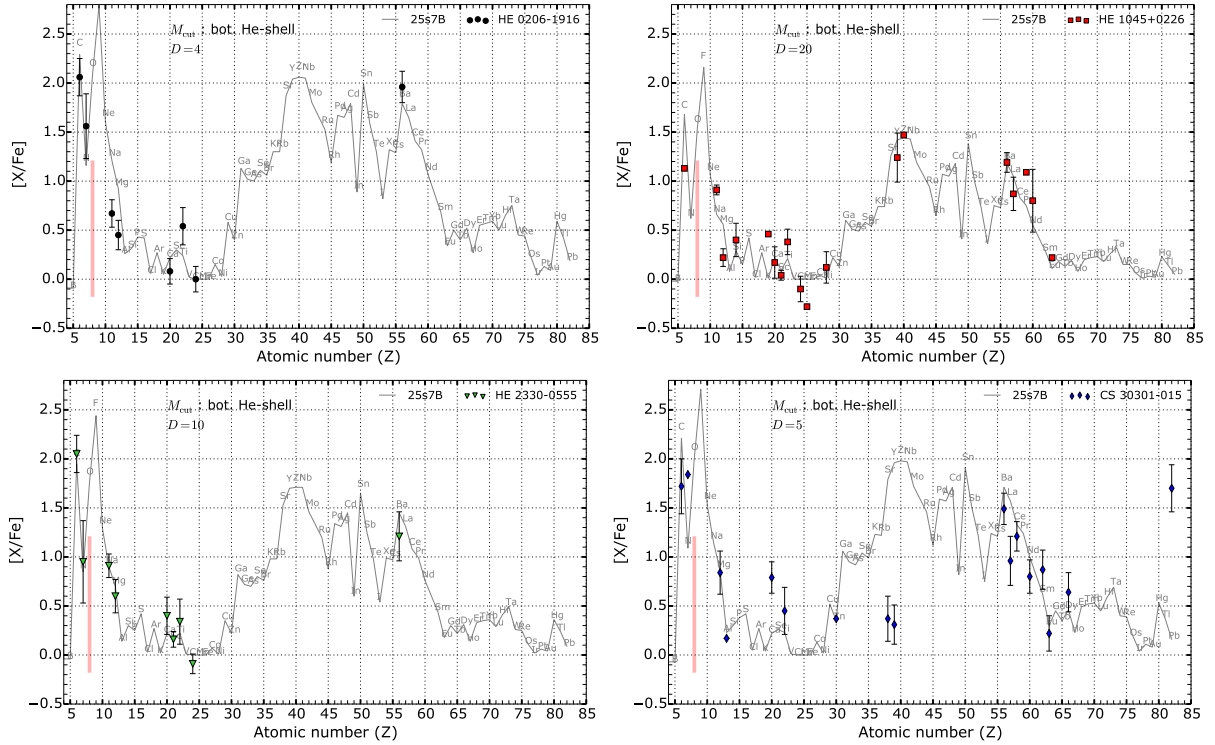


Fig. 3. Comparison of the material ejected by the 25s7B source star model (solid patterns) with the chemical composition of four apparently single CEMP-s stars (Hansen et al. 2016). The ejecta of the source star is made of wind plus supernova with a mass cut set at the bottom of the He-shell. The dilution factor $D = M_{\text{ISM}}/M_{\text{ej}}$ is indicated. The red band at $Z = 8$ shows the range of $[\text{O}/\text{Fe}]$ ratios predicted by the AGB models of Karakas (2010). These models have $1 < M_{\text{ini}} < 6 M_{\odot}$ and metallicities of $Z = 0.004$ and $Z = 0.0001$.

with a deep mass cut (Fig. 2, right panel) are excluded because they overproduce Na and Mg. When considering a larger mass cut (Fig. 2, left panel), we see that only the two $25 M_{\odot}$ models with $v_{\text{ini}}/v_{\text{crit}} = 0.7$ are able to produce enough elements with $Z > 55$.

The chemical composition of HE 0206-1916, HE 1045+0226 and HE 2330-0555 can be reproduced by the $25 M_{\odot}$ model with $v_{\text{ini}}/v_{\text{crit}} = 0.7$ and the rate of $^{17}\text{O}(\alpha, \gamma)$ divided by ten (model “25s7B” in Fig. 3). The mass cut is set at the bottom of the He-shell and different dilution factors are considered (see

Fig. 3). There are a few discrepancies: for HE 0206-1916, Na and Mg are overestimated by ~ 0.5 dex, for HE 1045+0226, Na and Mg are respectively underestimated and overestimated by ~ 0.3 dex and C is overestimated by ~ 0.5 dex. It is nevertheless interesting that a single-source star model with a given mass cut is able to reproduce the pattern of three CEMP-s stars. Only the dilution factor is changing.

For the last star, CS 10301-015, the trend between Ba and Dy ($56 < A < 66$) can be reproduced by the 25s7B model (see Fig. 3, bottom right panel). However, the high Pb abundance ($[\text{Pb}/\text{Fe}] = 1.7$) cannot be explained by our models, even

³ The dilution factor D can be written as $D = M_{\text{ISM}}/M_{\text{ej}}$ with M_{ISM} the mass of initial ISM mixed together with M_{ej} , the total mass ejected by

the source-star model (wind + supernova). For each star, D was chosen in order to fit the overall observed abundance pattern as well as possible.

if considering the 25s7B model with a deep mass cut (see Fig. 2, right panel). Reducing the rate of the $^{17}\text{O}(\alpha, \gamma)$ reaction could give enough Pb, but then, Sr ($Z = 38$) and Y ($Z = 39$) would be even more overestimated. It might be that this CEMP- s star acquired its peculiar abundances owing to several sources, especially AGB stars, that are able to produce a significant amount of Pb. Further monitoring of its radial velocity might reveal a companion with a long orbital period. If not, it would mean that this CEMP- s star formed with the material ejected by one (or more) source star(s) able to synthesise enough Pb while keeping Sr ($Z = 38$), Y ($Z = 39$) and Eu ($Z = 63$) low (Fig. 3, bottom right panel).

4. Discussion and conclusions

We investigated the possibility of explaining the abundances of four apparently single CEMP- s stars with the material ejected by rotating and non-rotating 10–150 M_{\odot} massive stars (source stars) that would have lived before the birth of the CEMP- s stars. First, we find that only layers above the bottom of the He-shell of the source star should be expelled, otherwise Na and Mg abundances in the ejecta of the source stars are well above the values observed at the surface of the CEMP- s stars. Dilution with the ISM is not a solution: it will shift down the Na and Mg abundances but also the abundances of the s -elements, that would therefore be underproduced compared to the observations. The fact that only relatively shallow layers should be expelled would be in line either with an enrichment through stellar winds only (Meynet et al. 2006; Hirschi 2007) and/or with a faint supernova event ending the source stellar lifetime (Umeda & Nomoto 2005; Tominaga et al. 2014).

We find that non-rotating source-star models do not provide enough s -elements with $Z > 55$. The most favoured mass range for producing the s -process elements observed at the surface of the considered CEMP- s stars is between 20 and 40 M_{\odot} . An initial rotation of $v_{\text{ini}}/v_{\text{crit}} = 40\%$ underproduces elements with $A > 55$ compared to the observations (20–40 M_{\odot} models included). A very fast rotating 25 M_{\odot} source star ($v_{\text{ini}}/v_{\text{crit}} = 70\%$ or $v_{\text{ini}} \sim 500 \text{ km s}^{-1}$) gives a material able to fit the pattern of three out of the four apparently single CEMP- s stars. It is not excluded that source stars of different masses with such a high initial rotation rate could also reproduce the observed patterns. The fourth CEMP- s star, CS 10301-015, has $[\text{Pb}/\text{Fe}] = 1.7$. Such a high Pb abundance cannot be explained by our models.

Our models predict that the CEMP- s stars should have a $[\text{O}/\text{Fe}]$ ratio of about 1.5–2 (see Fig. 3). Interestingly, the AGB models of Karakas (2010) predict $-0.2 < [\text{O}/\text{Fe}] < 1.2$ (see the red bands in Fig. 3). $[\text{O}/\text{Fe}] = 1.2$ is a maximum since no dilution is assumed to obtain these values. Observing the oxygen abundance of the CEMP- s stars might therefore be a way to decide between the spinstar or the AGB scenario. Another way to distinguish between these scenarios would be the ls/hs ratio (ratio of light to heavy s -elements, e.g. Y/Ba). While our models predict $[\text{ls}/\text{hs}] \geq 0$ (see Figs. 1–3; also Chiappini et al. 2011; Cescutti et al. 2013), AGB models predict $[\text{ls}/\text{hs}] < 0$ (e.g. Abate et al. 2015a).

Also, our spinstar models predict $\log(^{12}\text{C}/^{13}\text{C}) \sim 3$. HE 0206-1916 has $\log(^{12}\text{C}/^{13}\text{C}) = 1.2$ (Aoki et al. 2007). This discrepancy might come from the fact that HE 0206-1916 is a giant that has experienced the first dredge-up: this process reduces the surface $^{12}\text{C}/^{13}\text{C}$ ratio by bringing CNO products (mainly ^{13}C and ^{14}N) up to the surface. Likely, the initial surface $^{12}\text{C}/^{13}\text{C}$ was higher. Also, a late mixing event occurring in the source star can change the CNO abundance just before the end of its evolution

(for details, see Choplin et al. 2017, we did not consider this process in the present letter).

Our results suggest that fast rotating massive stars could have played a role in forming some of the CEMP- s stars. In general, our results suggest that fast rotation might have been a common phenomenon in the early universe, as already suggested by Chiappini et al. (2006, 2008) for instance.

Acknowledgements. We thank the anonymous referee who helped to improve this letter through constructive remarks. This work was sponsored by the Swiss National Science Foundation (project Interacting Stars, number 200020-172505). R.H. acknowledges support from the World Premier International Research Center Initiative (WPI Initiative), MEXT, Japan and from the ChETEC COST Action (CA16117), supported by COST (European Cooperation in Science and Technology). The research leading to these results has received funding from the European Research Council under the European Union's Seventh Framework Programme (FP/2007-2013)/ERC Grant Agreement No. 306901.

References

- Abate, C., Pols, O. R., Izzard, R. G., Mohamed, S. S., & de Mink, S. E. 2013, *A&A*, 552, A26
- Abate, C., Pols, O. R., Izzard, R. G., & Karakas, A. I. 2015a, *A&A*, 581, A22
- Abate, C., Pols, O. R., Karakas, A. I., & Izzard, R. G. 2015b, *A&A*, 576, A118
- Angulo, C., Arnould, M., Rayet, M., et al. 1999, *Nucl. Phys. A*, 656, 3
- Aoki, W., Norris, J. E., Ryan, S. G., Beers, T. C., & Ando, H. 2002a, *PASJ*, 54, 933
- Aoki, W., Ryan, S. G., Norris, J. E., et al. 2002b, *ApJ*, 580, 1149
- Aoki, W., Beers, T. C., Christlieb, N., et al. 2007, *ApJ*, 655, 492
- Best, A., Görres, J., Couder, M., et al. 2011, *Phys. Rev. C*, 83, 052802
- Best, A., Beard, M., Görres, J., et al. 2013, *Phys. Rev. C*, 87, 045805
- Bisterzo, S., Gallino, R., Straniero, O., Cristallo, S., & Käppeler, F. 2010, *MNRAS*, 404, 1529
- Cescutti, G., Chiappini, C., Hirschi, R., Meynet, G., & Frischknecht, U. 2013, *A&A*, 553, A51
- Chiappini, C., Hirschi, R., Meynet, G., et al. 2006, *A&A*, 449, L27
- Chiappini, C., Ekström, S., Meynet, G., et al. 2008, *A&A*, 479, L9
- Chiappini, C., Frischknecht, U., Meynet, G., et al. 2011, *Nature*, 472, 454
- Choplin, A., Ekström, S., Meynet, G., et al. 2017, *A&A*, 605, A63
- Cohen, J. G., Christlieb, N., Thompson, I., et al. 2013, *ApJ*, 778, 56
- de Jager, C., Nieuwenhuijzen, H., & van der Hucht, K. A. 1988, *A&AS*, 72, 259
- Eggenberger, P., Meynet, G., Maeder, A., et al. 2008, *Ap&SS*, 316, 43
- Ekström, S., Georgy, C., Eggenberger, P., et al. 2012, *A&A*, 537, A146
- Frischknecht, U., Hirschi, R., & Thielemann, F.-K. 2012, *A&A*, 538, L2
- Frischknecht, U., Hirschi, R., Pignatari, M., et al. 2016, *MNRAS*, 456, 1803
- Hampel, M., Stancliffe, R. J., Lugaro, M., & Meyer, B. S. 2016, *ApJ*, 831, 171
- Hansen, T. T., Andersen, J., Nordström, B., et al. 2016, *A&A*, 588, A3
- Hirschi, R. 2007, *A&A*, 461, 571
- Hollek, J. K., Frebel, A., Placco, V. M., et al. 2015, *ApJ*, 814, 121
- Jaeger, M., Kunz, R., Mayer, A., et al. 2001, *Phys. Rev. Lett.*, 87, 202501
- Karakas, A. I. 2010, *MNRAS*, 403, 1413
- Keller, S. C., Bessell, M. S., Frebel, A., et al. 2014, *Nature*, 506, 463
- Lau, H. H. B., Stancliffe, R. J., & Tout, C. A. 2009, *MNRAS*, 396, 1046
- Longland, R., Iliadis, C., & Karakas, A. I. 2012, *Phys. Rev. C*, 85, 065809
- Lucatello, S., Tsangarides, S., Beers, T. C., et al. 2005, *ApJ*, 625, 825
- Lugaro, M., Karakas, A. I., Stancliffe, R. J., & Rijs, K. 2012, *ApJ*, 747, 2
- Matrozis, E., & Stancliffe, R. J. 2017, *A&A*, 606, A55
- Meynet, G., Ekström, S., & Maeder, A. 2006, *A&A*, 447, 623
- Nishimura, N., Hirschi, R., Pignatari, M., et al. 2014, in *AIP Conf. Ser.*, 1594, eds. S. Jeong, N. Imai, H. Miyatake, & T. Kajino, 146
- Norris, J. E., Yong, D., Bessell, M. S., et al. 2013, *ApJ*, 762, 28
- Pignatari, M., Gallino, R., Meynet, G., et al. 2008, *ApJ*, 687, L95
- Placco, V. M., Frebel, A., Beers, T. C., et al. 2016, *ApJ*, 833, 21
- Prantzos, N., Hashimoto, M., & Nomoto, K. 1990, *A&A*, 234, 211
- Stancliffe, R. J., & Glebbeek, E. 2008, *MNRAS*, 389, 1828
- Starkenbourg, E., Shetrone, M. D., McConnachie, A. W., & Venn, K. A. 2014, *MNRAS*, 441, 1217
- Talon, S., & Zahn, J.-P. 1997, *A&A*, 317, 749
- The, L.-S., El Eid, M. F., & Meyer, B. S. 2000, *ApJ*, 533, 998
- Tominaga, N., Iwamoto, N., & Nomoto, K. 2014, *ApJ*, 785, 98
- Umeda, H., & Nomoto, K. 2005, *ApJ*, 619, 427
- Vink, J. S., de Koter, A., & Lamers, H. J. G. L. M. 2001, *A&A*, 369, 574
- Yoon, J., Beers, T. C., Placco, V. M., et al. 2016, *ApJ*, 833, 20
- Zahn, J.-P. 1992, *A&A*, 265, 115

5.3. The origin of the single CEMP-s stars

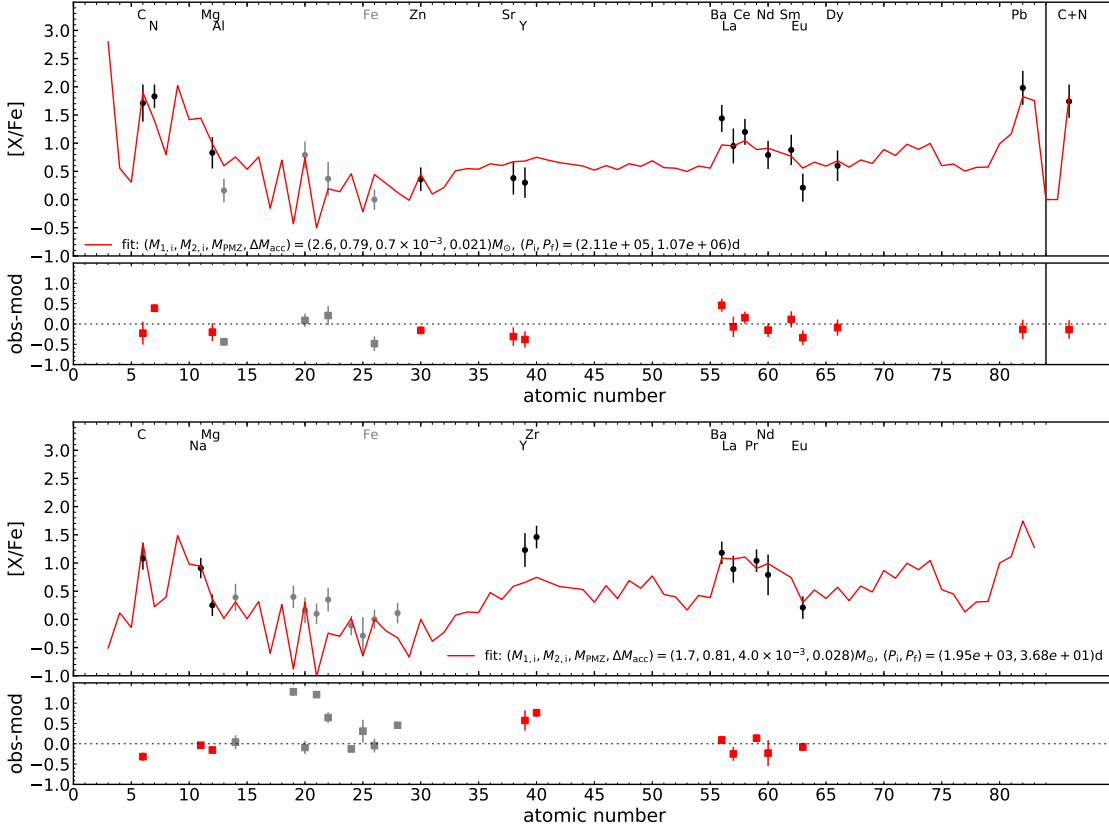


Figure 5.6: Comparison of AGB models (red patterns) with the chemical composition of the apparently single CEMP-s stars CS 30301-015 (top panel) and HE 1045+0226 (bottom panel, Carlo Abate, priv. com.).

5.3.2 The AGB scenario

Below is discussed some aspects of the AGB binary scenario for the four stars of the previous letter. Abate et al. (2015a,b) have used a binary evolution and population synthesis code to predict the orbital properties of the system (CEMP-s + AGB). The chemical composition in the AGB intershell region, from AGB models of Lugaro et al. (2012), is used. The abundances are function of 3 quantities: the mass of the AGB star at the first thermal pulse, the thermal pulse number and the mass of the partial mixing zone (cf. Sect. 3.2). The procedure is discussed in details in Abate et al. (2015a,b).

Because of its high Pb abundance, the apparently single CEMP-s star CS 30301-015 discussed in the previous letter likely cannot be reproduced if considering only the massive stars ejecta computed in this work. The best AGB fit for this CEMP-s star (shown in Fig. 5.6, top panel) is a $2.6 M_{\odot}$ AGB star with a period (at the present day) of about 10^6 days. Although not perfect, the fit is improved compared to what can be done with massive stars. In particular, Pb can be reproduced. Also, the long predicted period provides a simple explanation to why this CEMP-s star appears to be single: its orbits is so wide that no radial-velocity variations can be detected. It is consistent with the statement of Hansen et al. (2016b) that reported that any undiscovered binaries among their four apparently single CEMP-s stars would have periods of at least $10^3 - 10^4$ days.

For HE 1045+0226 (bottom panel in Fig. 5.6), AGB star models predict too low Y and Zr. Also, the predicted period for HE 1045+0226 is about 40 days, which is too short to explain the non-detection of radial velocity variations. For this star, a massive rotating source stars provides a better solution (cf. previous letter). For the two other CEMP-s stars, only the Ba abundance is

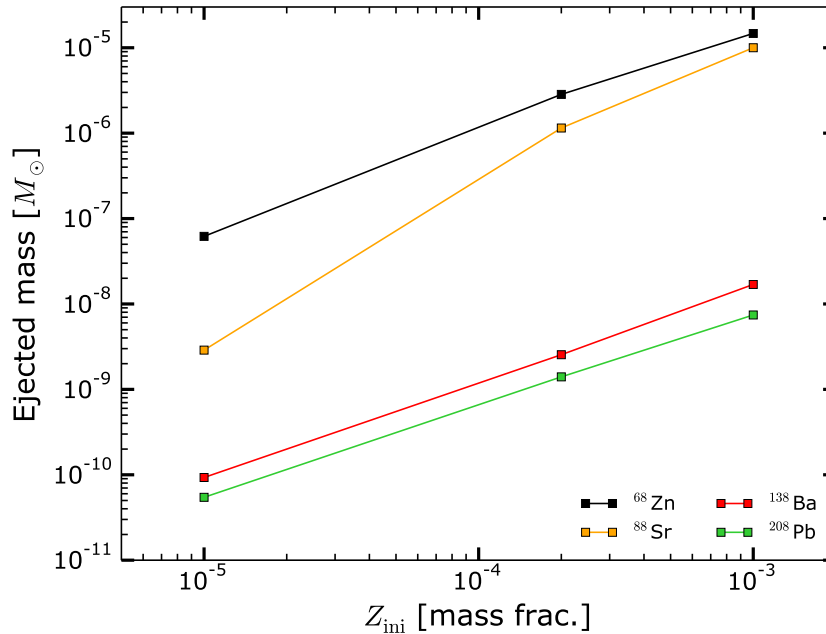


Figure 5.7: Ejected mass (Eq. 3.15) of 4 isotopes as a function of the initial metallicity for $25 M_{\odot}$ models with $v_{\text{ini}}/v_{\text{crit}} = 0.4$. The mass cut is set according to Maeder (1992).

available among the heavy elements so that both massive stars and AGB star models can provide a reasonable solution.

Generally speaking, massive stars tend to produce larger light s-element (e.g. Sr) over heavy s-element (e.g. Ba, Pb) ratios than AGB stars. Another difference, as discussed in the previous letter, is the oxygen, that can be higher by 1 – 2 dex in massive stars compared to AGB stars. Some CEMP-s stars are O-rich, a characteristic that AGB models may not be able to account for. For instance CS 31080-095 has $[\text{O}/\text{Fe}] = 2.35 \pm 0.12$ (Sivarani et al. 2006), LP625-44 has $[\text{O}/\text{Fe}] = 1.8$ (Aoki et al. 2002a), HE 2258-6358 has $[\text{O}/\text{Fe}] = 1.8 \pm 0.1$ (Placco et al. 2013). Such high ratios do not exclude a contribution from an AGB companion but may indicate a contribution of one (or more) additional source (i.e. previous massive stars). By detailed comparisons between AGB and massive star models, it would probably be interesting to try to spot the elements like oxygen that could help probing the nature of the additional source(s).

5.4 The weak s-process at lower metallicities

With decreasing metallicity, less seed is available so that less s-elements are produced. In non-rotating models, the production of s-nuclei in massive stars becomes negligible below about $Z = 10^{-4}$ (Prantzos et al. 1990). In rotating models, this metallicity threshold may be around $Z = 10^{-7}$: Frischknecht et al. (2016) have shown that at $Z = 10^{-7}$, rotation in a $25 M_{\odot}$ model has a modest effect on the abundances of s-elements. At very low metallicity, the lack of iron seed implies that even if the neutron source is boosted by rotation, there is no significant s-process boost. Also, it is worth mentioning that above an given metallicity threshold, the s-process boost induced by rotation becomes very small: at $Z = Z_{\odot}$, Frischknecht et al. (2016) have shown that the abundance patterns of rotating and non-rotating models are almost identical. This is because rotation does not provide much additional ^{22}Ne (neutron source) at this metallicity, as a result of the less efficient back-and-forth mixing process (Sect. 4.1). Indeed, at higher metallicity the distance between the He-core and the H-shell increases and the gradient of Ω is smaller so that the shear mixing between the He-core and the H-shell is less strong.

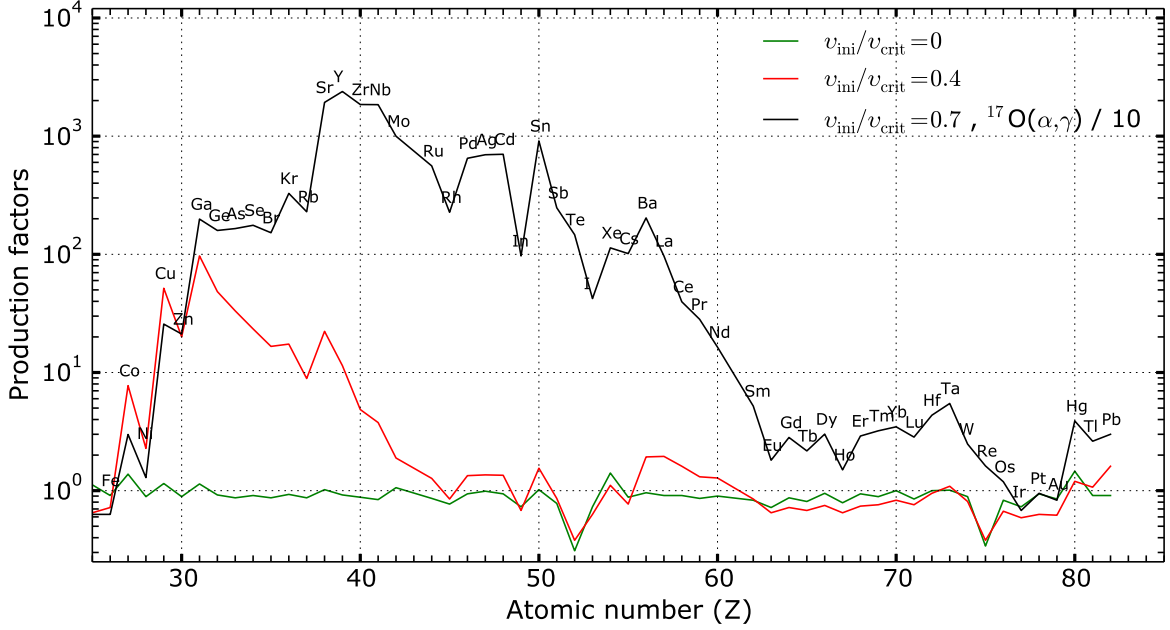


Figure 5.8: Production factors (Eq. 3.17) of $25 M_{\odot}$ models with $Z = 10^{-5}$ and with various initial rotation rates. For the fast rotating model, the rate of $^{17}\text{O}(\alpha, \gamma)$ was divided by 10. The mass cut is set according to Maeder (1992).

5.4.1 A rotating $25 M_{\odot}$ model with various initial metallicities

The computation of grids of massive star models at lower metallicities (including s-process) is a work in progress. Only $25 M_{\odot}$ models are presented here. Fig. 5.7 shows the ejected mass (Eq. 3.15) of four isotopes for rotating $25 M_{\odot}$ models with $Z = 10^{-3}$, 2×10^{-4} and 10^{-5} . As the metallicity decreases by 2 dex, the ejected mass of the considered isotopes decreases by 2 – 4 dex, depending on the chemical specie. The green and red patterns in Fig. 5.8 show the production factors (Eq. 3.17) of a non-rotating and a rotating $25 M_{\odot}$ model at $Z = 10^{-5}$, respectively. Compared to their initial abundances, elements between Cu and Y are overproduced by 1 – 2 dex in the rotating model. The black pattern shows an extreme case, with fast rotation and a lower $^{17}\text{O}(\alpha, \gamma)$ reaction rate ($/10$). In this case, the production of elements between Fe and Eu are enhanced by 1 up to about 3 dex compared to their initial abundances. Overall, it shows that at very low metallicity, although the absolute yields are low (Fig. 5.7), rotation can strongly affect the distribution of heavy elements that are initially present in the star (Fig. 5.8). If rotation is not considered, the initial distribution of heavy elements is barely modified at this metallicity.

5.4.2 The origin of HE 1327-2326

The star HE 1327-2326 (Frebel et al. 2005a) is one of the most iron-poor star with $[\text{Fe}/\text{H}] = -5.7$ and an excess of Sr compared to Fe. Red circles in Fig. 5.9 show its surface composition, according to a recent re-analysis (Ezzedine, priv. comm.). In particular, an overabundance of Zn was found ($[\text{Zn}/\text{Fe}] = 0.84 \pm 30$).

All possible chemical compositions one can obtain with the non-rotating $25 M_{\odot}$ model at $Z = 10^{-5}$ are shown by the purple area. This area shows the range of $[X/\text{Fe}]$ ratios one can obtain when varying the mass cut from the final mass of the model $M_{\text{fin}} = 24.5 M_{\odot}$ (in this case only the material in the stellar winds is considered) to the remnant mass $M_{\text{rem}} = 2.31 M_{\odot}$ (according to the relation of Maeder 1992). We see that whatever the mass cut, N is underproduced by more than 2

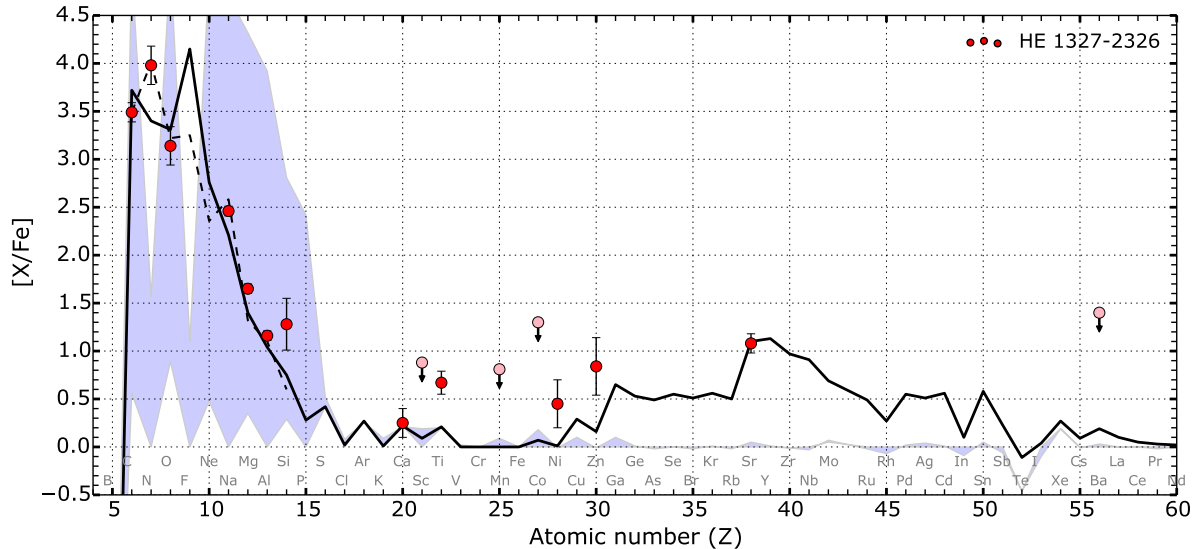


Figure 5.9: $[X/Fe]$ ratios of the $25 M_{\odot}$ model with $Z = 10^{-5}$ and $v_{\text{ini}}/v_{\text{crit}} = 0.7$ (thick black pattern). The mass cut is set to $M_{\text{cut}} = 10.5 M_{\odot}$ (it corresponds to the bottom of the H-envelope). The purple shaded area stands for the same model without rotation. This area shows the range of yields one can obtain when varying the mass cut from the final mass of the model (only winds) to M_{rem} (see text for details). The dashed pattern shows the yields of the $20 M_{\odot}$ model with $Z = 10^{-5}$ and $v_{\text{ini}}/v_{\text{crit}} = 0.7$ presented in Sect. 4.3 (computed with a smaller network). In this case, $M_{\text{cut}} = 7.9 M_{\odot}$. $D = 0$ in all the cases (i.e. no dilution with ISM). Symbols show the abundances of the star HE 1327-2326 (light red symbols denote upper limits, as shown by arrows).

dex and Sr by more than 1 dex.

The thick black pattern shows the $[X/Fe]$ ratios of the fast rotating $25 M_{\odot}$ model ($v_{\text{ini}}/v_{\text{crit}} = 0.7$). The mass cut is set to $10.5 M_{\odot}$, which is just below the H-rich envelope. No dilution with ISM was considered. In this case, the $[Sr/Fe]$ ratio of HE 1327-2326 can be reproduced. The fit for light elements is also satisfactory. In particular, N is much closer to the observed value. It is however still underproduced by 0.5 dex. The dashed pattern, shows the yields of a model with same metallicity and rotation but with an initial mass of $20 M_{\odot}$ and a small network (model of Sect. 4.3). This model can produce enough N, suggesting that a source star with a bit different initial mass may provide a better fit (at least for the light elements).

In Sect. 4.6, the source star model that best reproduced the abundance pattern (for light elements, C to Si) of HE 1327-2326 was a fast rotating $60 M_{\odot}$ model without late mixing, without dilution with ISM and with a mass cut close to the bottom of the H-envelope (cf. Table 4.5). All these characteristics are consistent with the new results obtained here, except for the initial mass of the source star ($20 - 25 M_{\odot}$ here vs. $60 M_{\odot}$ before). The high $[Sr/Fe]$ might favor rotating $\sim 25 M_{\odot}$ instead of $\sim 60 M_{\odot}$ source stars because the s-process boost induced by rotation peaks around $20 - 40 M_{\odot}$ (Choplin et al. 2018). A rotating $60 M_{\odot}$ source star may not produce enough Sr. In the future, the computation of additional source star models at this low metallicity but with different initial masses may help to further address this point.

The source star models presented here underproduce Ti, Ni and Zn by ~ 0.5 dex. Such elements can be affected by explosive nucleosynthesis. Interestingly, it was shown that Ti and Zn are overproduced in jet-induced SNe (Tominaga 2009). This kind of asymmetric SN may be produced by fast rotation of the massive stellar core at the time of the explosion (Woosley 1993). Fast rotation of the core at the time of explosion may be due to fast rotation of the progenitor. The fact that HE 1327-2326 is enriched in both the product of rotation (e.g. N, Sr) and of jet-induced SNe (e.g. Zn) may indicate that its source star was a massive rotating star that experienced a jet-induced SN.

In general, the determination of the abundances of both rotation products and jet-induced SNe products in very metal-poor stars might give clues on the impact of rotation on the explosion. An interesting perspective is to study these two families of elements in very metal-poor stars. However, for some interesting elements like Zn, almost only upper limits are available at the moment since they are very challenging to detect.

5.5 Summary

By increasing the amount of available neutrons, rotation boosts the s-process in massive stars. A new grid of non-rotating and rotating ($v_{\text{ini}}/v_{\text{crit}} = 0.4$) stellar models at $[\text{Fe}/\text{H}] = -1.8$ with initial masses of 10, 15, 20, 25, 40, 60, 85, 120 and $150 M_{\odot}$ was computed. Stellar yields are publicly available. Rotation has a strong impact on the production of s-elements (especially the first peak, e.g. Sr) for initial masses between about 20 and $60 M_{\odot}$. Two additional $25 M_{\odot}$ models were computed: one with faster rotation ($v_{\text{ini}}/v_{\text{crit}} = 0.7$) and another with faster rotation ($v_{\text{ini}}/v_{\text{crit}} = 0.7$) and lower $^{17}\text{O}(\alpha, \gamma)$ rate (divided by 10, it reduces the poisoning effect of ^{16}O). In these two models, the production of s-elements is boosted again. The fast rotating model with a lower $^{17}\text{O}(\alpha, \gamma)$ rate is the model where the s-process boost is the strongest. In particular, a modest amount of heavy s-elements (e.g. Pb) is synthesized. In stellar models with initial masses $M \gtrsim 60 M_{\odot}$, the back-and-forth mixing is less efficient so that the production of s-elements is similar whether or not rotation is considered.

Some CEMP-s stars appear to be single stars, which may challenge the AGB binary scenario (for these specific stars). The yields of the fast rotating $25 M_{\odot}$ model of the computed grid provide a material able to fit the abundance patterns of 3 out of the 4 apparently single CEMP-s stars.

The s-process boost induced by rotation still exists in lower metallicity massive stellar models (probably down to about $Z \sim 10^{-7}$). HE 1327-2326, one of the most iron-poor star known, has $[\text{Sr}/\text{Fe}] = 1.08$. Its abundance pattern can be reproduced by a fast rotating very low metallicity $20 - 25 M_{\odot}$ source star. The fact that this CEMP star is also enriched in Zn, which is a product of jet-induced SNe, is consistent with a scenario proposing that its source star was a fast rotator that experienced a jet-induced SN.

Conclusions and perspectives

6.1 Conclusions

This work mainly aimed at better understanding the nature of the early generations of massive stars. They are crucial objects to figure out the origin of the elements in the Universe. Although long-dead, indirect clues on these stars can be obtained from the surface chemical composition of still alive and observable low-mass metal-poor stars, formed early in the Universe. Some of these low-mass metal-poor stars, very little enriched in iron and showing highly non solar-like abundance patterns (CEMP stars, especially CEMP-no) are thought to have formed from the ejecta of only one or a few previous zero or very low-metallicity massive stars (the source stars). To gain knowledge on the characteristics of the early massive stars, I computed models of massive source stars under various assumptions so as to determine what are the source star ingredients required to reproduce the abundances of CEMP stars.

Below are listed the main concrete works carried out during this PhD, followed by the main results.

- I developed a nucleosynthetic one-zone code mimicking the effect of rotation on nucleosynthesis in stellar interiors and made comparisons with abundances of CEMP stars (Sect. 4.2 and Choplin et al. 2016).
- I computed pre-supernovae massive source star models under various assumptions (initial mass, rotation, extra mixing...) and made comparisons with abundances of CEMP stars (Sect. 4.3, 4.4, 4.6 and Choplin et al. 2017b).
- I developed a small module in GENEC allowing to generate extra mixing events in a specific zone of a stellar model (Sect. 4.5 and Choplin et al. 2017b).
- I computed a new grid of massive stars from 10 to 150 M_{\odot} , at $Z = 10^{-3}$, with and without rotation and including full nucleosynthesis so as to follow the s-process (Sect. 5.2 and Choplin et al. 2018). Stellar yields are available online¹. Then, comparisons with CEMP stars enriched in s-elements were done (Sect. 5.3, 5.4 and Choplin et al. 2017c).
- During a short term scientific mission with Prof. Jose Groh, I produced CMFGEN spectra for a population of main-sequence massive stars at $Z = 10^{-5}$ and started to investigate the effect of fast rotation in the spectral features of such stars (see Sect. 6.2.1 for more details).
- I included the effects of axion losses in GENEC and computed a grid of non rotating Pop III stars with and without axion losses (Sect. 3.4, Appendix A.1 and Choplin et al. 2017a).

¹See <https://www.unige.ch/sciences/astro/evolution/en/database/> or the CDS database at cdsarc.u-strasbg.fr.

- I included in GENEC the new diffusion coefficient of Maeder et al. (2013) that describes the interaction between various instabilities arising in rotating stars (Appendix A.2). I carried out several tests models to compare this prescription with other prescriptions (Sect. 3.3.1).
- I included in GENEC the new mass loss recipe of Moriya & Langer (2015) that considers the mass loss induced by pulsations in the late evolution of very massive metal-free stars (Appendix A.3).
- I improved the way of treating the rotational mixing in GENEC by upgrading the calculation techniques of the D_{shear} coefficient (Appendix A.4).
- I transformed the tabulated reaction rates of Best et al. (2013, $^{17}\text{O}(\alpha, \gamma)$ and $^{17}\text{O}(\alpha, n)$) into the REACLIB format (Sect. 5.2.1).

The main results of these works, presented in the chapters 4 and 5, can be summarized as follow:

- Using the one-zone nucleosynthetic code, I found that a significant fraction of the CEMP stars with $[\text{Fe}/\text{H}] < -3$ can be overall well reproduced by a material processed by H-burning at a temperature and density characteristic of $20 - 60 M_{\odot}$ source stars. While burning, this material has to be enriched in ^{12}C , ^{16}O and occasionally in ^{22}Ne . It suggests that the source stars experienced mid to strong rotational mixing.
- Complete source star models with various initial parameters (especially rotation) were computed. The efficient rotational mixing operating at low metallicity triggers exchanges of material between the He-burning core and the H-burning shell. It leads to a rich and varied nucleosynthesis, able to cover the ranges of abundances of light elements for the CEMP stars with $[\text{Fe}/\text{H}] < -3$.
- Comparisons between source star models and observations in the $[\text{C}/\text{N}]$ vs. $^{12}\text{C}/^{13}\text{C}$ diagram revealed some discrepancies that can be alleviated if a late mixing process is included in the source stars. The mixing operates in between the H-burning shell and the He-burning shell, about 200 yr before the end of the source star evolution. The mixing may also operate before, provided the material in the H-burning shell (at least some of it) is saved from further processing shortly after the mixing event (e.g. it is expelled through stellar winds).
- The abundance fitting (for light elements, C to Si) of 69 CEMP stars with $[\text{Fe}/\text{H}] < -3$ and not significantly enriched in s- and r-elements was performed with ~ 35000 ejecta composition of source star models. The best source stars are preferentially fast rotators (74 % of the cases), have initial masses of $20 M_{\odot}$ (70 %) and experienced the late mixing process (72 %). In most of the cases (~ 70 %), only the outer layers of the source stars (above or just below the interface between the H-rich and He-rich region) have to be expelled. Finally, the best abundance fits are mostly obtained with a modest dilution of the ejecta with the interstellar medium ($\sim 0 - 10$ times more interstellar material than source star ejecta).
- A new grid of massive source stars at $[\text{Fe}/\text{H}] = -1.8$ was computed with an extended nuclear network, able to follow the full s-process during the evolution. Rotation was found to strongly boost the first s-process peak (e.g. Sr) for stars with initial masses between 20 and $60 M_{\odot}$. If the initial rotation is high enough, models predict a significant synthesis of s-elements from the second peak (e.g. Ba). Elements from the third peak (e.g. Pb) were found to be little impacted by rotation.
- CEMP-s stars, which often have $-3 < [\text{Fe}/\text{H}] < -2$, are generally associated with the AGB binary scenario. Four CEMP-s stars were recently found to be single stars, a characteristic

that may challenge this scenario. The fast rotating $25 M_{\odot}$ model of the new grid of model including s-process provides a material able to fit the abundance pattern of 3 out of the 4 apparently single CEMP-s stars.

- The abundances of HE 1327-2326, one of the most iron-poor star, were examined in detail with the yields of new very low metallicity source star models including the s-process. Both the excess in light elements and Sr can be explained with the ejecta of a fast rotating 20 – 25 M_{\odot} source star model. Interestingly, the fact that HE 1327-2326 is enriched in both the products of rotation (e.g. N, Sr) and of jet-induced supernovae (e.g. Zn), is consistent with a scenario proposing that its source star was a fast rotator that experienced a jet-induced supernova.

The results of this work suggest that rotation in the source star is a crucial ingredient, which is able to provide a solution for the abundances of light elements (C to Si) and s-elements of many CEMP stars. It supports the idea that rotation was a dominant effect in the early generations of massive stars. The results propose that in most of the cases, a strong and late mixing event operated in between the H-burning and He-burning shell of early massive stars. It was also shown that CEMP stars should be formed with only the relatively outer layers of the source stars (generally only the H-envelope or the H-envelope plus a small part of the He-rich region). This suggests that early massive stars expelled only their envelope and experienced strong fallback. The present work does not offer a specific mechanism for the ejection of the source star envelope. Although stellar wind is a good candidate for the reasons mentioned in Sect. 3.3.5, the wind material of the source star models presented here is generally not sufficiently enriched in light and heavy elements for reproducing the CEMP star abundances. An additional (generally modest) supernova contribution is required. In any case, the fact that just the envelope of the source star should be expelled is consistent with the mixing & fallback scenario that could finally co-exist with the fast rotating massive star scenario.

6.2 Perspectives

The nature of the first stars is a topic where we are still scratching the surface and where to move on, modelers and observers should go hands in hands. Below are important possible future steps or projects (mainly on the modeling side) linked to the present work.

- The modeling of grids of source star models including s-process has to be continued, especially at very low metallicity. The aim is to get a more complete picture of the nucleosynthesis in rotating massive stars and perform extended comparisons with observations, with as much abundances as possible.
- The new scenario for the origin of HE 1327-2326 raises the interest for studying the outputs of rotating massive stars experiencing a jet-induced supernova. A consistent prediction of the nucleosynthetic yields of a rotating massive star ending its life as a jet SN could be an interesting project. In the future, the comparison of such models with observations might give clues on how the explosion of early massive stars can be affected by rotation.
- Although generally operating in very central regions, which may be finally locked into the remnant, the SN-shock may lead to further neutron capture nucleosynthesis in the He-shell. It could be included in source star models.
- The late mixing process could be studied using multi dimension models. Also, when available, constraints from such multi dimension models (especially on the convective boundaries of the H- and He-burning shells) should be included in 1D stellar evolution codes so as to further test the hypothesis of the late mixing process in the source stars.

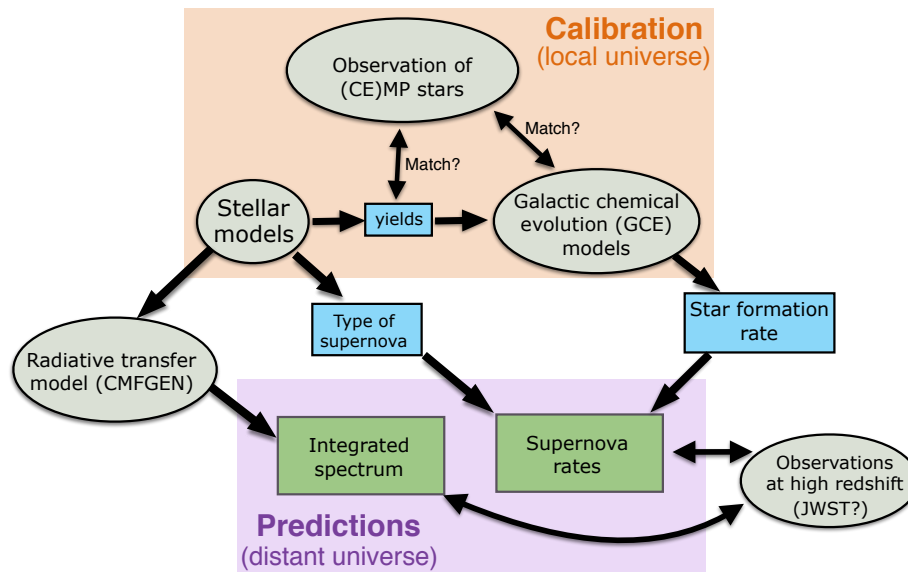


Figure 6.1: The cartoon shows how the old and local Universe (i.e. metal-poor stars) could be used so as to make predictions in the very high redshift Universe. Individual stellar models and Galactic chemical evolution (GCE) models are used to determine the best massive source stars, able to reproduce the abundances of metal-poor stars. The appearance (integrated spectrum and supernova rates), in the very distant Universe, of this calibrated massive source star population may be predicted and confronted to (future) observations. Grey ovale shapes show the modeling tools and data that should be used. Blue boxes show, in this context, the important inputs/outputs from stellar and GCE models.

- An important project would be to recover the initial surface composition of evolved CEMP stars by computing grids of CEMP star models including various mixing processes. To date, such a work on a large CEMP star sample has been done only for correcting effect of the first dredge-up on the C abundance (Placco et al. 2014c). Knowing well the initial surface composition of CEMP stars (especially for the most evolved CEMP stars) is crucial to connect them more consistently to their source stars.

There are also different observational perspectives. One may be to try determining the abundances of both rotation and jet-induced SN products on the most metal poor stars (cf. point 2 just above). Isotopic ratios (especially $^{12}\text{C}/^{13}\text{C}$) are very constraining (especially on rather unevolved stars) and can provide strong clues on nucleosynthetic processes at work in source stars. Also, the oxygen is likely overproduced in massive stars compared to AGB stars (Choplin et al. 2017c) and might help to further assess the relative contribution of these sources (particularly in the case of the apparently single CEMP-s stars, cf. Sect. 5.3). As first proposed in Meynet et al. (2010), this work predicts that some CEMP stars are enriched in helium (Sect. 4.7). Detecting helium in CEMP stars is probably very challenging but it may be mentioned here as a possible observational perspective. Generally, an observation campaign able to determine rather complete abundance patterns (as for HE 1045+0226 and CS 30301-015, cf. Sect. 5.3) will help very much in choosing between the different existing models. Also, although probably tedious and challenging, radial velocity measurements of more CEMP stars over a long period of time would be very interesting (Hansen et al. 2016a,b, did such measurements for 22 CEMP-s and 24 CEMP-no stars) and would help better understanding their origin.

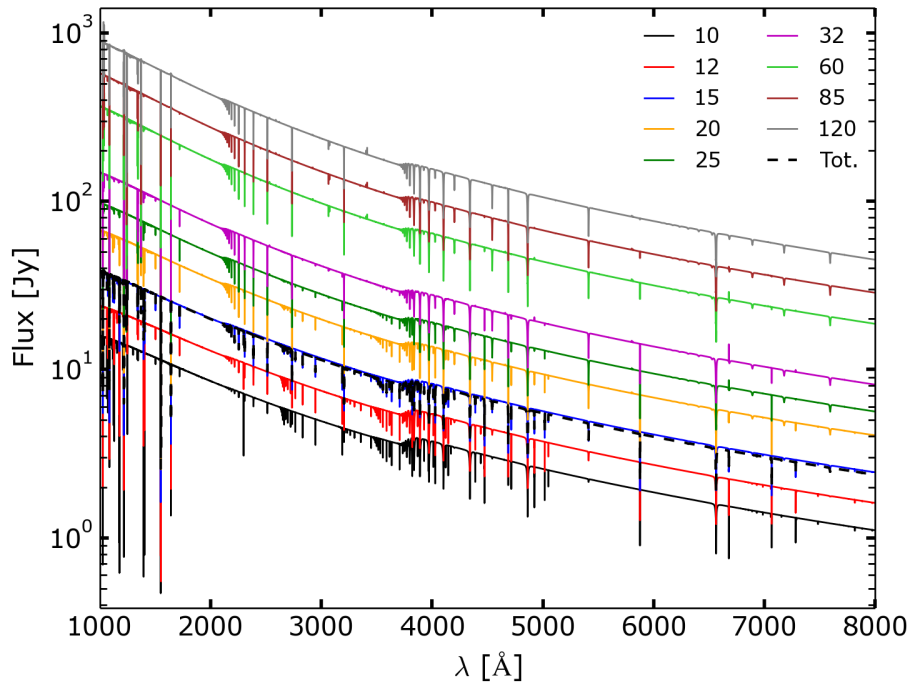


Figure 6.2: Emergent flux in Janskys (a distance of 1 kpc is assumed) as a function of the wavelength for non-rotating 10 – 120 M_{\odot} models at the middle of the main sequence (H in the core is half burnt). The dashed line shows the integrated spectrum, where a constant star formation rate was assumed and where the mass function of Chabrier (2003) was used (for a star of a mass m , $\phi(m) = Am^{-\alpha}$ with $A = 7.1 \cdot 10^{-5}$ and $\alpha = 2.3$).

6.2.1 Linking the old and local with the old and distant Universe

To gain knowledge on the first generation of massive stars, the present work focused on their signatures in the local Universe. As mentioned in the introduction (Sect. 1.4), an alternative way is to observe the distant Universe: either individual explosive/transient events or the integrated light of high redshift galaxies. An interesting project would be to predict the specific signatures in the high redshift Universe of the CEMP massive source stars. It will establish a connection between the old and local Universe with the old and distant Universe. A schematic view of such a project is shown in Fig. 6.1: the source star population that best account for observations of metal-poor stars is determined using stellar models (the aim of the present thesis, for CEMP stars) and also Galactic chemical evolution (GCE) models. GCE models are suitable to investigate the origin of *normal* metal-poor stars, which probably formed from a reservoir well enriched by different previous sources and not just ~ 1 source star. Type of supernovae, supernova rates, and emergent spectrum of this massive source star population may be estimated combining the outputs of stellar evolution modeling, GCE modeling and the predictions from a radiative transfer code. Such predictions could be compared to high redshift observations, especially observations from JWST, that may be able to catch the explosion of the first generations of massive stars (Whalen et al. 2013a,b,c).

During a Short Term Scientific Mission² of two weeks with Pr. Jose Groh (Trinity college, Dublin), we started to work on one aspect of this project. As a very first step, I tried to see what would be the emergent spectrum of a population of main sequence fast rotating massive source stars compared to a population of main sequence non-rotating massive source stars. I extended the small grid of massive stars presented in Sect. 4.5. In addition to the 20, 32 and 60 M_{\odot} models, I

²STSM, in the frame of the COST action ChETEC (<http://www.chetec.eu/>).

computed 10, 12, 15, 25, 85 and 120 M_{\odot} models. The initial rotation is either 0 or 70 % of the critical velocity. Only the main sequence was computed. To compute the output spectra of the models, the atmospheric radiative transfer code CMFGEN (Hillier & Miller 1998) is used. CMFGEN is a spherically-symmetric code that computes line and continuum formation in non-local thermodynamical equilibrium. Fig 6.2 shows the emergent spectra of the non-rotating models at the middle of the main sequence (H in the core is half burnt). Also the integrated spectrum is shown by the dashed line. After normalizing the spectra with their continuum, comparisons can be done with the rotating population. A detailed comparison of specific lines (e.g. HeI $\lambda 6680$ or HeII $\lambda 4687$) between the different models remains to be done.

In the future, after the analysis of these first results, it would be worth computing a more realistic emergent integrated spectrum by calculating more CMFGEN spectra (at different stages of the main sequence but also after the main sequence), by considering a non-constant star formation rate (e.g. a burst of star formation), by maybe considering additional rotational velocities, by introducing some noise and convolving the spectra with a Gaussian (corresponding to a given spectral resolution) so as to predict which kind of observing facility may be able to detect a given spectral feature predicted by the models.

Numerical aspects

A.1 Axion cooling

The energy loss by axions can be written as

$$\epsilon_{\text{ax}} = K g_{10}^2 T_8^7 \rho_3^{-1} Z(\xi^2) C \quad (\text{A.1})$$

where K and g_{10} are constants, $T_8 = 10^{-8} T$, $\rho_3^{-1} = 10^{-3} \rho$ and $Z(\xi^2) = A(\xi^2) \ln(B(\xi^2))$ with

$$A(\xi^2) = \frac{1.037\xi^2}{1.01 + \xi^2/5.4} + \frac{1.037\xi^2}{44 + 0.628\xi^2} \quad \text{and} \quad B(\xi^2) = 3.85 + \frac{3.99}{\xi^2} \quad (\text{A.2})$$

and where

$$\xi \equiv \frac{\hbar c k_S}{2k_B T}. \quad (\text{A.3})$$

\hbar is the reduced planck constant, c the speed of light and k_B the Boltzmann constant. The Debye–Hückel screening wavenumber k_S , is given by Raffelt (2008) as

$$k_S^2 \equiv 4\pi\alpha \left(\frac{\hbar c}{k_B T} \right) \sum_{i=e,\text{ions}} n_i Z_i^2 \quad (\text{A.4})$$

where α is the fine structure constant, Z_i the atomic number and n_i the ions/electron number densities. The term C in Eq. A.1 is equal to $C = \exp(-(\hbar\omega_0)/(k_B T))$ with ω_0 the plasma frequency defined as

$$\omega_0 \equiv \left[4\pi\alpha \left(\frac{\hbar c}{m_e c^2} \right) n_e \right]^{\frac{1}{2}} c. \quad (\text{A.5})$$

In GENEC, I have included the energy loss by axions ϵ_{ax} by adding it to ϵ_ν , the energy loss by neutrino. Axion losses are considered if the parameter `iaxions=1`. When solving the stellar structure equations with the Henyey method, the derivatives of ϵ_ν and ϵ_{ax} as a function of P and T are required for convergence. Most of the time, $\epsilon_{\text{ax}} \ll \epsilon_\nu$, so that ϵ_{ax} can be neglected. At the end of He-burning however, axion losses become the dominant source of energy loss and must be included in the energy derivatives. In the case of GENEC, the following terms have to be evaluated:

$$\left(\frac{\partial \ln \epsilon}{\partial \ln P} \right)_T \quad \text{and} \quad \left(\frac{\partial \ln \epsilon}{\partial \ln T} \right)_P \quad (\text{A.6})$$

where $\epsilon = \epsilon_\nu + \epsilon_{\text{ax}}$. The term on the left in A.6 can be written as

$$\left(\frac{\partial \ln(\epsilon_\nu + \epsilon_{\text{ax}})}{\partial \ln P} \right)_T = \frac{\epsilon_\nu}{\epsilon_\nu + \epsilon_{\text{ax}}} \left(\frac{\partial \ln \epsilon_\nu}{\partial \ln P} \right)_T + \frac{\epsilon_{\text{ax}}}{\epsilon_\nu + \epsilon_{\text{ax}}} \left(\frac{\partial \ln \epsilon_{\text{ax}}}{\partial \ln P} \right)_T. \quad (\text{A.7})$$

The derivative of ϵ_{ax} as a function of P is equal to

$$\left(\frac{\partial \ln \epsilon_{\text{ax}}}{\partial \ln P}\right)_T = \left(\frac{\partial \ln \epsilon_{\text{ax}}}{\partial \ln \rho}\right)_T \left(\frac{\partial \ln \rho}{\partial \ln P}\right)_T = \left[\frac{\rho}{Z(\xi^2)} \left(\frac{\partial Z(\xi^2)}{\partial \rho}\right)_T + \frac{\rho}{C} \left(\frac{\partial C}{\partial \rho}\right)_T - 1\right] \left(\frac{\partial \ln \rho}{\partial \ln P}\right)_T \quad (\text{A.8})$$

At this point, the derivatives of $Z(\xi^2)$ and C have to be calculated:

$$\left(\frac{\partial Z(\xi^2)}{\partial \rho}\right)_T = \left(\frac{\partial A(\xi^2)}{\partial \rho}\right)_T \ln(B(\xi^2)) + \left[A(\xi^2) \frac{1}{B(\xi^2)} \left(\frac{\partial B(\xi^2)}{\partial \rho}\right)_T\right]. \quad (\text{A.9})$$

The derivatives of A and B as a function of ρ are

$$\left(\frac{\partial A(\xi^2)}{\partial \rho}\right)_T = 1.037 \left(\frac{\partial \xi^2}{\partial \rho}\right)_T \left[\frac{1.01}{(1.01 + \xi^2/5.4)^2} + \frac{44}{(44 + 0.628\xi^2)^2}\right] \quad (\text{A.10})$$

and

$$\left(\frac{\partial B(\xi^2)}{\partial \rho}\right)_T = -\frac{3.99}{\xi^4} \left(\frac{\partial \xi^2}{\partial \rho}\right)_T \quad (\text{A.11})$$

with

$$\left(\frac{\partial \xi^2}{\partial \rho}\right)_T = \frac{\xi^2}{\rho} \quad (\text{A.12})$$

since $\xi^2 \propto k_S^2 \propto n \propto \rho$. The derivative of C in Eq. A.8 is non-zero because $C \propto \omega_0 \propto n_e \propto \rho$. It yields

$$\left(\frac{\partial C}{\partial \rho}\right)_T = -C \frac{\hbar\omega_0}{2\rho k_B T}. \quad (\text{A.13})$$

A similar derivation has to be done for the second term of A.6. Then, ϵ_{ax} has to be derived as a function of T (with P constant but not ρ , so that ρ has to be derived as a function of T). It yields

$$\left(\frac{\partial \ln \epsilon_{\text{ax}}}{\partial \ln T}\right)_P = 7 + \frac{T}{Z(\xi^2)} \left(\frac{\partial Z(\xi^2)}{\partial T}\right)_P + \frac{T}{C} \left(\frac{\partial C}{\partial T}\right)_P - \left(\frac{\partial \ln \rho}{\partial \ln T}\right)_P. \quad (\text{A.14})$$

The derivative of $Z(\xi^2)$ as a function of T is evaluated similarly to Eq. A.9, A.10 and A.11. Then, as in Eq. A.12, one needs the derivative of ξ but this time as a function of T :

$$\left(\frac{\partial \xi^2}{\partial T}\right)_P = \frac{\xi^2}{\rho} \left(\frac{\partial \rho}{\partial T}\right)_P - \frac{3\xi^2}{T} = \frac{\xi^2}{T} \left[\left(\frac{\partial \ln \rho}{\partial \ln T}\right)_P - 3\right]. \quad (\text{A.15})$$

Finally, the derivative of C as a function of T is

$$\left(\frac{\partial C}{\partial T}\right)_P = -C \frac{\hbar\omega_0}{2\rho k_B T^2} \left[\frac{1}{2} \left(\frac{\partial \ln \rho}{\partial \ln T}\right)_P - 1\right]. \quad (\text{A.16})$$

From this point, all quantities are defined or available in the code so that Eq. A.8 and A.14 can be calculated and the two quantities in A.6 evaluated.

A.2 Secular shear mixing

The D_{shear} used in this work is the one of Talon & Zahn (1997, Eq. 3.10). The other D_{shear} coefficient from Maeder (1997) can be written as

$$D_{\text{shear}}^{\text{M97}} = f_{\text{energ}} \frac{H_p}{g\delta} \frac{K}{(\nabla_{\text{ad}} - \nabla) + \frac{\xi}{\delta} \nabla_\mu} \left(\frac{9\pi}{32} \Omega \frac{d \ln \Omega}{d \ln r}\right)^2. \quad (\text{A.17})$$

with f_{energ} the fraction of the excess energy in the shear that contributes to mixing. It is generally calibrated on observations (cf. Sect. 3.3.1).

It also exists other instabilities (e.g. thermohaline instability...) that, when included in 1D stellar evolution codes, are generally translated as individual diffusion coefficients. The global diffusion coefficient is then expressed as the sum of the coefficients of the various effects considered independently. However, it can exist physical interactions between the different instabilities, possibly leading to amplification or damping effects. Maeder et al. (2013) have proposed a global stability criterion, taking into account different instabilities together (thermohaline instability, shear instability, Rayleigh-Taylor instability, semiconvective instability, the instability characterized by the Solberg-Høiland criterion and the baroclinic instability). From the stability criterium, I have derived the global diffusion coefficient and included it GENEC. The global stability criterium is written as

$$Ax^2 + Bx + C > 0 \quad (\text{A.18})$$

with

$$\begin{aligned} A &= N_{ad}^2 + N_{\mu}^2 + N_{\Omega-\delta v}^2 \\ B &= N_{ad}^2 D_h + N_{\mu}^2 (K + D_h) + N_{\Omega-\delta v}^2 (K + 2D_h) \\ C &= N_{\Omega-\delta v}^2 (D_h K + D_h^2) \end{aligned}$$

and where

$$\begin{aligned} N_{ad}^2 &= \frac{g\delta}{H_p} (\nabla_{ad} - \nabla) \\ N_{\mu}^2 &= \frac{g\varphi}{H_p} \nabla_{\mu} \\ N_{\Omega-\delta v}^2 &= \frac{1}{\bar{\omega}^3} \frac{d(\Omega^2 \bar{\omega}^4)}{d\bar{\omega}} \sin \theta - Ri_c \left(\frac{dU}{dr} \right)^2 \end{aligned}$$

with $\bar{\omega}$ the distance to the rotational axis. It can be written $\bar{\omega} = r \sin \theta$ where θ is the colatitude. U can be expressed as $U = r\Omega \sin \theta$. Let us express the first term of $N_{\Omega-\delta v}^2$:

$$\begin{aligned} \frac{1}{\bar{\omega}^3} \frac{d(\Omega^2 \bar{\omega}^4)}{d\bar{\omega}} \sin \theta &= \frac{1}{r^3 \sin^3 \theta} \frac{d(\Omega^2 r^4 \sin^4 \theta)}{dr} \frac{dr}{d\bar{\omega}} \sin \theta \\ &= 2\Omega \sin \theta \left(r \frac{d\Omega}{dr} + 2\Omega \right). \end{aligned} \quad (\text{A.19})$$

It yields

$$N_{\Omega-\delta v}^2 = 2\Omega \sin \theta \left(r \frac{d\Omega}{dr} + 2\Omega \right) - Ri_c r^2 \sin^2 \theta \left(\frac{d\Omega}{dr} \right)^2. \quad (\text{A.20})$$

In numerical calculations, one has to average $N_{\Omega-\delta v}^2$ over an isobar. We obtain

$$\begin{aligned} \overline{N_{\Omega-\delta v}^2} &= \frac{\int_0^{\pi} N_{\Omega-\delta v}^2 \sin^3 \theta d\theta}{\int_0^{\pi} \sin^3 \theta d\theta} \\ &= 2\Omega \left(r \frac{d\Omega}{dr} + 2\Omega \right) \frac{\int_0^{\pi} \sin^4 \theta d\theta}{\int_0^{\pi} \sin^3 \theta d\theta} - Ri_c r^2 \left(\frac{d\Omega}{dr} \right)^2 \frac{\int_0^{\pi} \sin^5 \theta d\theta}{\int_0^{\pi} \sin^3 \theta d\theta} \\ &= \frac{9\pi}{16} \Omega^2 \left(\frac{d \ln \Omega}{d \ln r} + 2 \right) - \frac{4}{5} Ri_c \Omega^2 \left(\frac{d \ln \Omega}{d \ln r} \right)^2. \end{aligned} \quad (\text{A.21})$$

The diffusion coefficient is $D_{\text{global}}^{\text{M13}} = (1/3)|v|l = 2|x|$ where x are the two solutions of Eq. A.18. Test models were computed with both solutions. The first solution leads to convergence issues while the second does not. The second one also gives plausible results (Fig. 3.5). In GENEC, the second solution was implemented as a standard choice.

A.3 Mass loss recipes

The pulsationally induced mass-loss rate derived by Moriya & Langer (2015) are

$$\log_{10} \dot{M} = \begin{cases} (10.38 \pm 1.58)\eta - (3.94 \pm 0.21) & \text{for } \epsilon = 0.1 \\ (15.51 \pm 2.92)\eta - (4.77 \pm 0.33) & \text{for } \epsilon = 0.3 \\ (12.55 \pm 2.88)\eta - (4.69 \pm 0.39) & \text{for } \epsilon = 0.5 \\ (5.08 \pm 2.87)\eta - (4.14 \pm 0.33) & \text{for } \epsilon = 0.8 \end{cases} \quad (\text{A.22})$$

where \dot{M} is expressed in $M_{\odot} \text{ yr}^{-1}$ and with $\eta = (-8.30 \pm 0.59) \times 10^{-4} T_{\text{eff}} + (4.15 \pm 0.29)$. In GENEC, this mass loss is considered and added to other kinds of mass losses (mechanical, radiative) if the parameter `ipuls=1` and if $\log(T_{\text{eff}}) < 3.698$ (it corresponds to $T_{\text{eff}} = 4992 \text{ K}$). This is the temperature below which the stellar envelope becomes pulsationally unstable (Moriya & Langer 2015). The parameter η is a free parameter that has to be chosen between the 4 possible values (0.1, 0.3, 0.5 or 0.8, parameter `epsil` in the code).

A small change was also done in the mass loss recipe of de Jager et al. (1988, `imloss=1`) in order to correct a bug happening for very luminous stars. In the expression of \dot{M} , there is a term

$$T_j \left[\frac{\log(L/L_{\odot}) - 4.6}{2.1} \right] \quad (\text{A.23})$$

where T_j is a function defined as $T_j(x) = \cos(j \arccos x)$. This definition implies that the term in brackets in Eq. A.23 must be ≤ 1 or equivalently, $\log(L/L_{\odot}) \leq 6.7$. In extreme cases (e.g. very massive stars), it happens that this condition is not verified, leading to convergence issues. To solve this issue, I just took the minimum between 1 and the bracket value in Eq. A.23.

A.4 Locally weighted scatterplot smoothing

In GENEC, a locally weighted scatterplot smoothing technique can be used for smoothing the profile of a quantity (e.g. μ or Ω) when calculating its derivative. It is used at least during the main sequence of rotating models to smooth the Ω , μ and U (vertical component of the meridional circulation) profiles. Without it, the code may experience convergence issues.

Fig. A.1 illustrates the technique. Let us consider N data points with given coordinates x_i and y_i (black crosses in Fig. A.1, upper panels). Let us focus on the point at $x_i \simeq 9$ in the upper left panel of Fig. A.1. A window of $n = 2W + 1$ points around that point is selected. W is a parameter to chose. In this example, $W = 2$ so that $n = 5$. A linear fit with these $n = 5$ points is then performed and the derivative is taken equal to the slope of the fit. Fig. A.1 (lower left) shows y' , the derivative of the data when considering just the two neighborhood values (black line) and the derivative if smoothing is done (red line). The smoothed data being more regular, the red profile is less sharp.

The size of the window W used to smooth the profile plays an important role. The upper right panel of Fig. A.1 shows the same data as well as the three smoothed profiles for $W = 1$ (blue), $W = 2$ and $W = 4$ (green). The larger the size of the window, the more damped the irregularity of the raw profile, because the fit is done using more points. It leads to smoother derivatives (Fig. A.1, lower right panel). This smoothing technique can be seen as a filter that damps the irregularity of

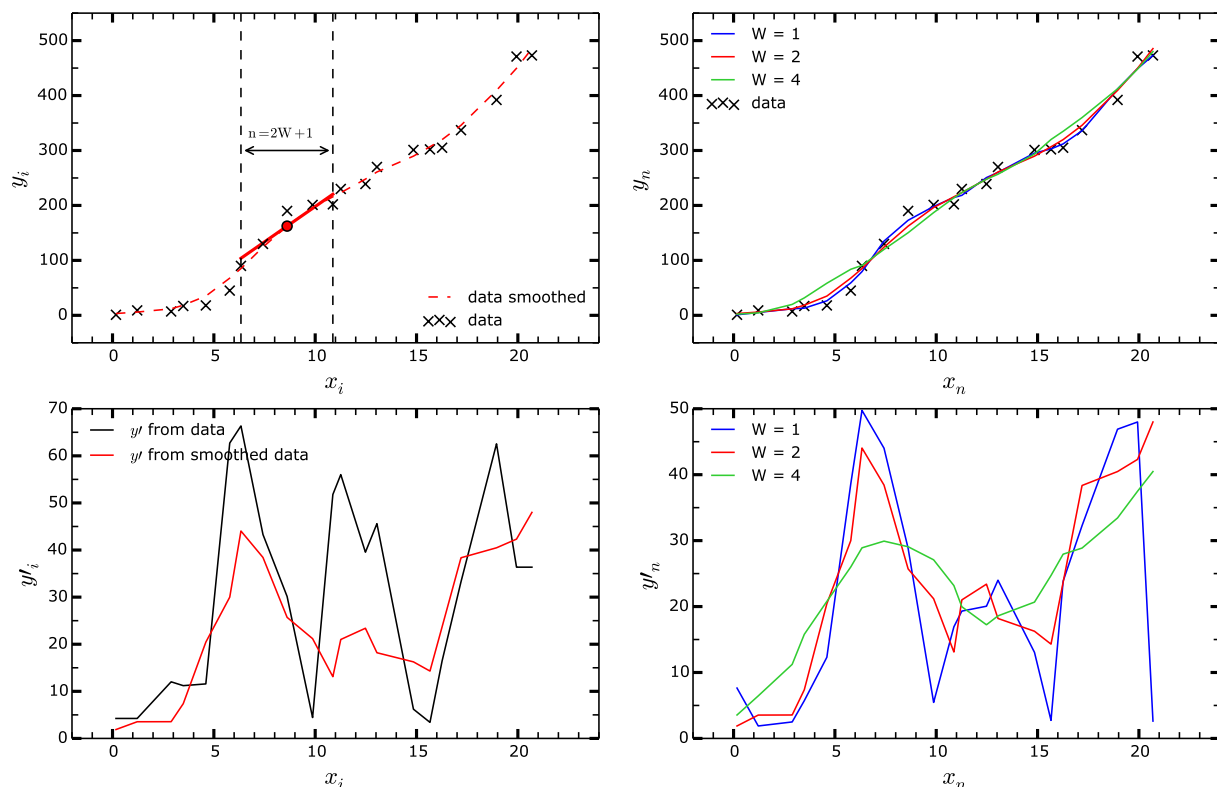


Figure A.1: *Upper left:* crosses represent the raw data. The red line shows the linear fit done around the $x_i \simeq 9$ point, considering the points between $i - W$ and $i + W$, where $W = 2$. The red dashed line show the resulting curve after the smoothing procedure done on each point. *Lower left:* derivative of the raw data using the two neighborhood values (black) and of the smoothed data (red). *Upper and lower right:* effect of varying the size of the fitting window W .

the y_i profile. If W is small, the smoothing is weak (i.e. close to the raw data), if W is large, some important (physical) features in the profile can be lost.

The effect of varying W in a complete stellar model is shown in Fig. A.2. The μ -gradient calculated from just the two neighborhood values (pink line) presents strong oscillations which are likely not physical. The smoothing procedure described previously damps these features (other lines).

In GENEC, I introduced a mesh-adaptative W parameter, defined as $W = m/a$ with m the mesh number and $a = 120$, a constant selected after carrying numerical tests with various values of a .

A.5 S-process parameters

I remind here some quantities that can be used to quantify the efficiency of the s-process. These quantities are tabulated in Table A.1 for the grid of models published in Choplin et al. (2018). These quantities may be useful for future comparisons with other models.

The central neutron exposure during core He-burning τ_c is defined as

$$\tau_c = \int_{t_{\text{ini-He}}}^{t_{\text{end-He}}} v_{\text{T}} n_{\text{n}} dt, \quad (\text{A.24})$$

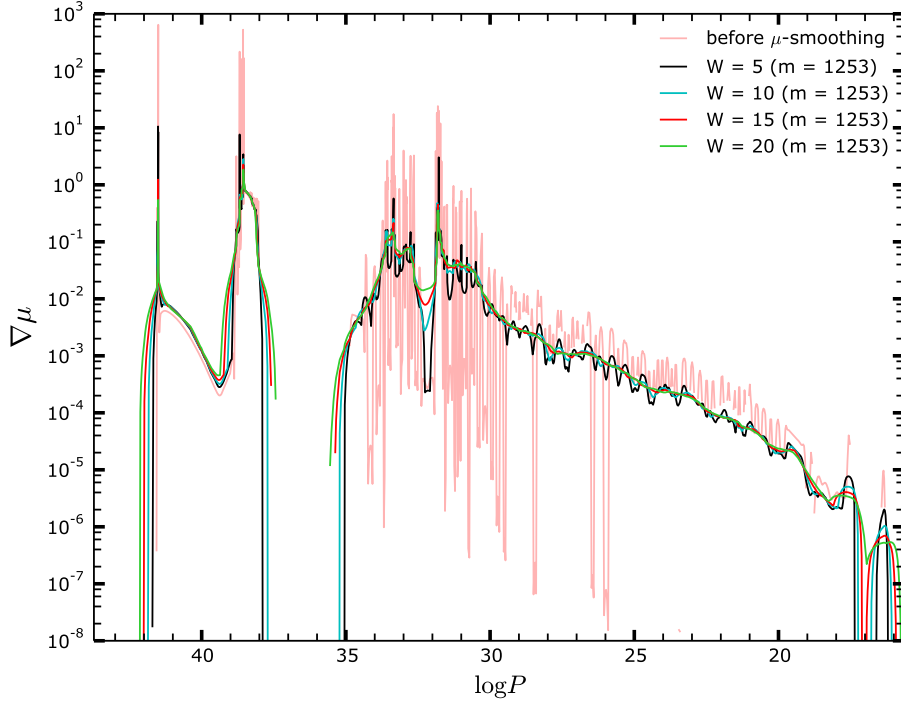


Figure A.2: $\nabla\mu$ as a function of $\log P$ in a rotating $25 M_{\odot}$ model at $Z = 0.001$ during the He-burning stage. The pink curve shows $\nabla\mu$ calculated with the raw μ profile. The other lines show $\nabla\mu$ calculated with the smoothing of μ , with different W values (see text for details). m is the mesh number of the model.

where $t_{\text{ini-He}}$ and $t_{\text{end-He}}$ are the age of the model at the beginning and the end of the core He-burning phase, respectively, n_n the neutron density and $v_T = \sqrt{2kT/m_n}$ the thermal velocity (with $kT = 30$ keV as a typical value in the helium burning core). Because the neutron density n_n varies with time and mass coordinate in the model, it is interesting to define the neutron exposure averaged over the He-core and over the He-burning lifetime:

$$\langle \tau \rangle = \int_{t_{\text{ini-He}}}^{t_{\text{end-He}}} \langle n_n(t) \rangle v_T dt. \quad (\text{A.25})$$

$\langle n_n(t) \rangle$ is the neutron density at time t averaged over the He-core. It is defined as

$$\langle n_n(t) \rangle = \frac{1}{M_{\text{He}}(t)} \int_0^{M_{\text{He}}(t)} n_n(M_r) dM_r \quad (\text{A.26})$$

where $M_{\text{He}}(t)$ is the mass of the helium core at time t and $n_n(M_r)$ the neutron density at coordinate M_r . Finally, the average number of neutron captures per iron seed n_c is defined as (Käppeler et al. 1990)

$$n_c = \frac{\sum_{A=56}^{209} (A - 56)(Y(A) - Y_0(A))}{Y_0(^{56}\text{Fe})} \quad (\text{A.27})$$

with $Y(A)$ and $Y_0(A)$ the final and initial number abundance of a nucleus with nuclear mass number A and $Y_0(^{56}\text{Fe})$ the initial number abundance of ^{56}Fe .

Table A.1: s-process parameters at the end of the core helium burning phase for the models in Choplin et al. (2018): model label (column 1), central neutron exposure (column 2, Eq. A.24), neutron exposure averaged over He-core (column 3, Eq. A.25), number of neutron capture per seed (Eq. A.27) averaged over the He-core mass (column 4), maximum of the central neutron density (column 5), ^{22}Ne burnt (column 6) and left (column 7).

Model	τ_c [mb^{-1}]	$\langle\tau\rangle$ [10^{-1}mb^{-1}]	n_c	$n_{n,c,max}$ [cm^{-3}]	$\Delta X(^{22}\text{Ne})$	$X_r(^{22}\text{Ne})$
10s0	0.23	0.13	0.13	8.01(5)	6.73(-5)	1.09(-3)
10s4	0.68	0.38	0.61	2.44(6)	1.69(-4)	1.32(-3)
15s0	0.93	0.45	0.62	5.07(6)	2.14(-4)	9.46(-4)
15s4	3.53	1.82	3.36	1.43(7)	7.66(-4)	1.45(-3)
20s0	2.10	0.88	1.45	1.15(7)	4.15(-4)	7.58(-4)
20s4	8.51	3.72	9.18	2.66(7)	2.08(-3)	1.56(-3)
25s0	3.29	1.29	2.32	1.71(7)	5.98(-4)	5.93(-4)
25s4	12.47	4.92	14.42	3.16(7)	3.32(-3)	1.17(-3)
25s7	16.56	6.52	22.54	7.11(7)	5.43(-3)	1.87(-3)
25s7B ^a	21.54	8.57	33.19	4.21(7)	5.08(-3)	1.83(-3)
40s0	6.16	2.14	4.47	2.23(7)	9.81(-4)	2.64(-4)
40s4	14.8	5.11	15.38	2.89(7)	3.37(-3)	2.12(-4)
60s0	8.57	2.70	6.26	2.04(7)	1.24(-3)	6.75(-5)
60s4	11.06	3.43	8.56	2.15(7)	1.68(-3)	2.19(-5)
85s0	10.05	2.98	7.27	1.99(7)	1.33(-3)	1.53(-5)
85s4	11.12	3.28	8.08	1.96(7)	1.44(-3)	3.30(-6)
120s0	11.08	3.19	8.08	1.94(7)	1.36(-3)	2.99(-6)
120s0B ^a	14.20	4.23	12.49	2.30(7)	1.30(-3)	2.33(-6)
120s4	11.87	3.37	8.52	2.66(8)	1.39(-3)	4.09(-7)
150s0	11.95	3.38	8.66	1.99(7)	1.37(-3)	4.49(-7)
150s4	12.68	3.52	9.04	1.94(8)	1.37(-3)	7.07(-8)

^a Models computed with the rate of $^{17}\text{O}(\alpha, \gamma)$ divided by 10.

Appendix B

Abundance fits

This appendix contains the abundance fits of the 69 CEMP stars of Table 4.2 with the source star models presented in Sect. 4.5 and 4.6.

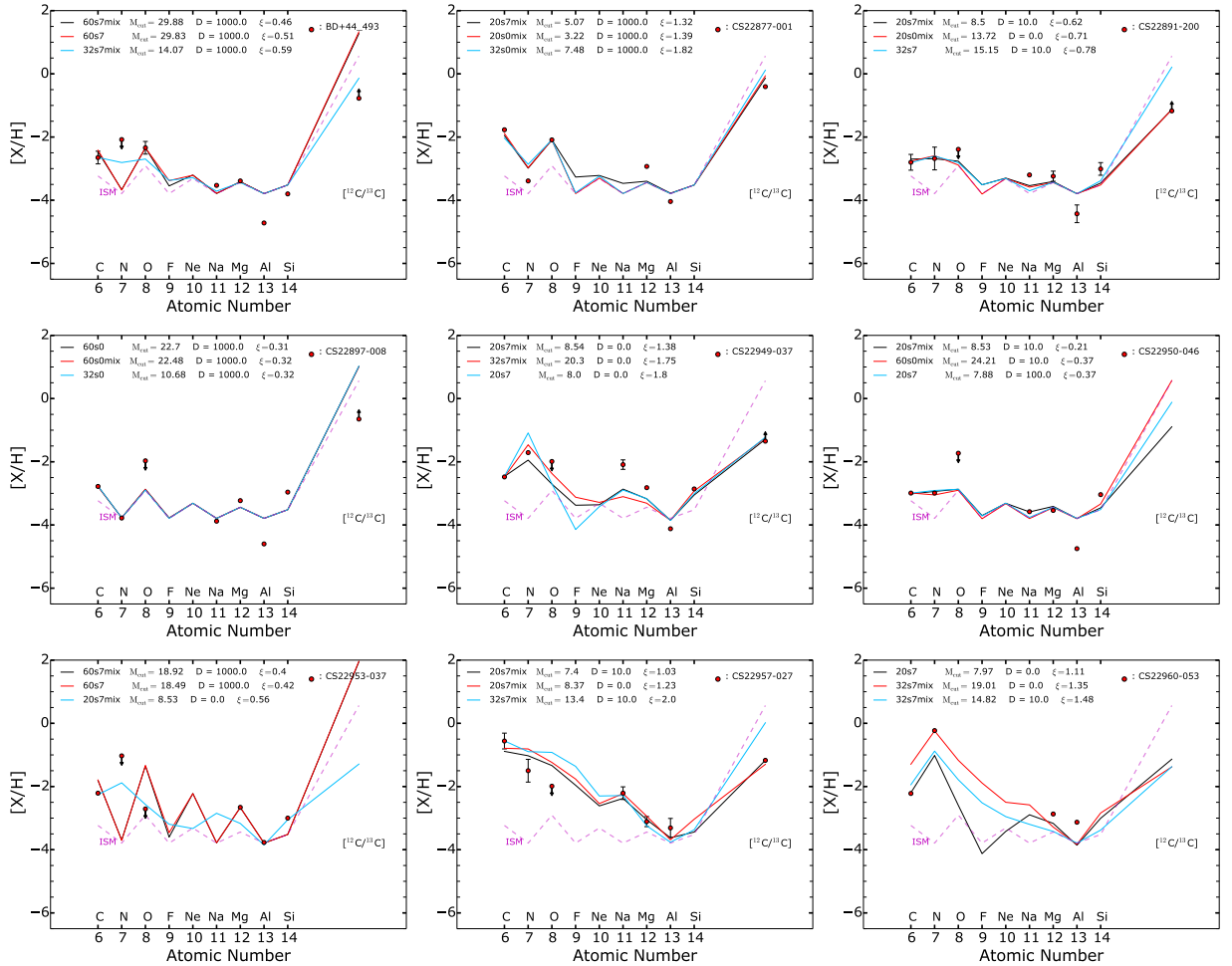


Figure B.1: Best fits of the 69 CEMP stars of Table 4.2 with the source star models of Table 4.4, when considering the dilution factor and the mass cut as free parameters. The three best models, with the lowest ξ , are shown (black, red and green patterns sorted by increasing ξ). Uncertainties and limits on abundances are shown by vertical bars and arrows, respectively (cf. Sect. 4.6 for details).

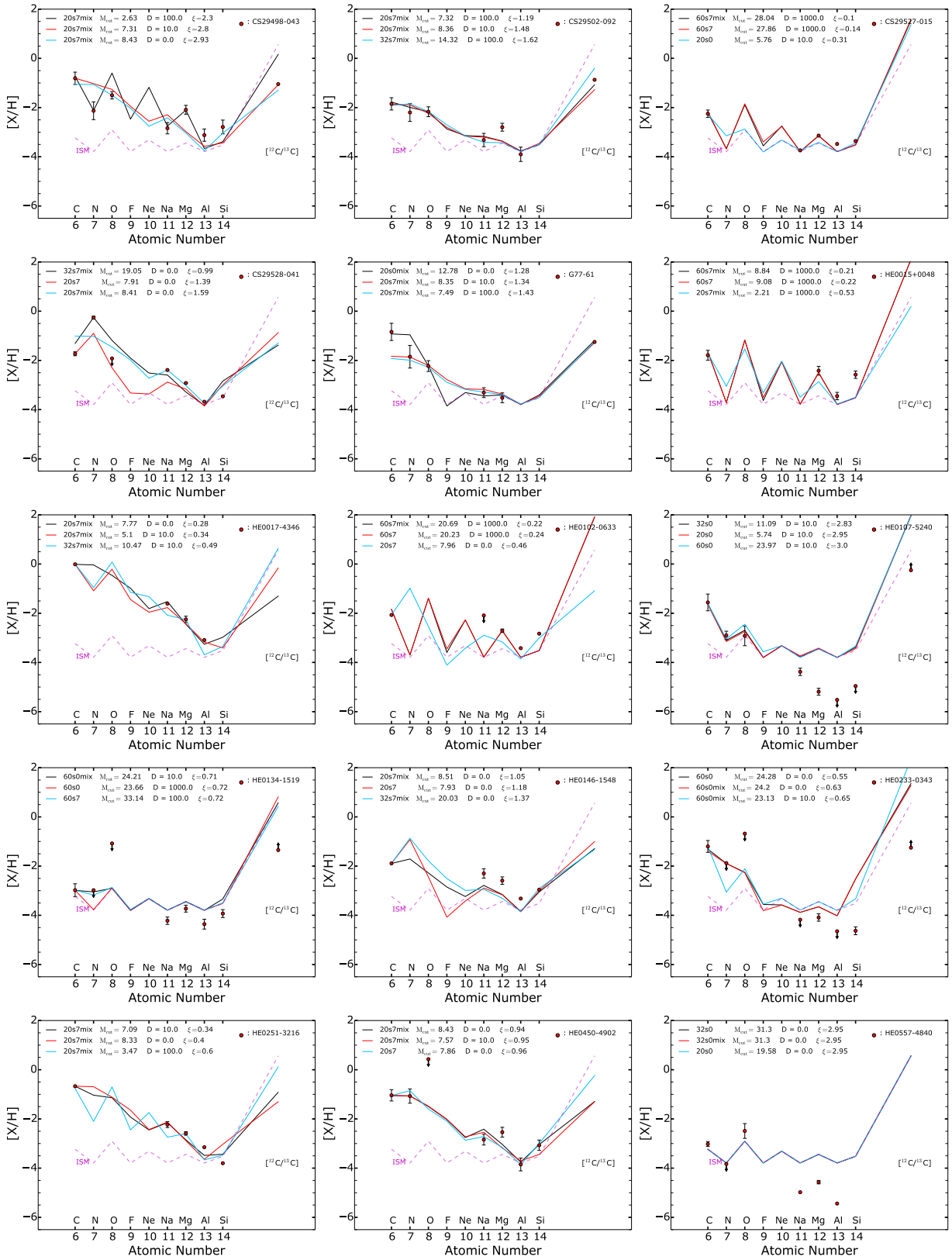


Figure B.2: continued

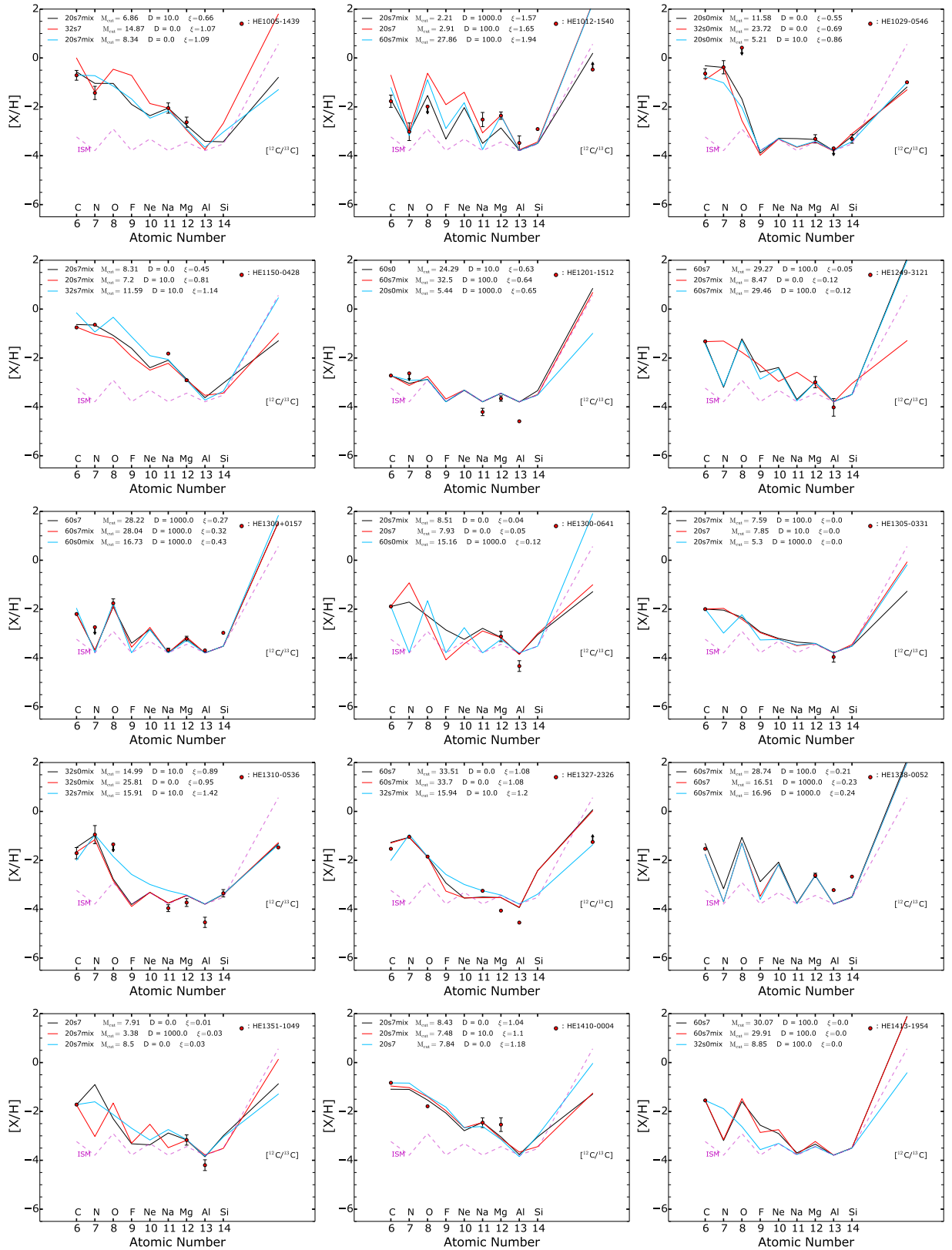


Figure B.3: continued

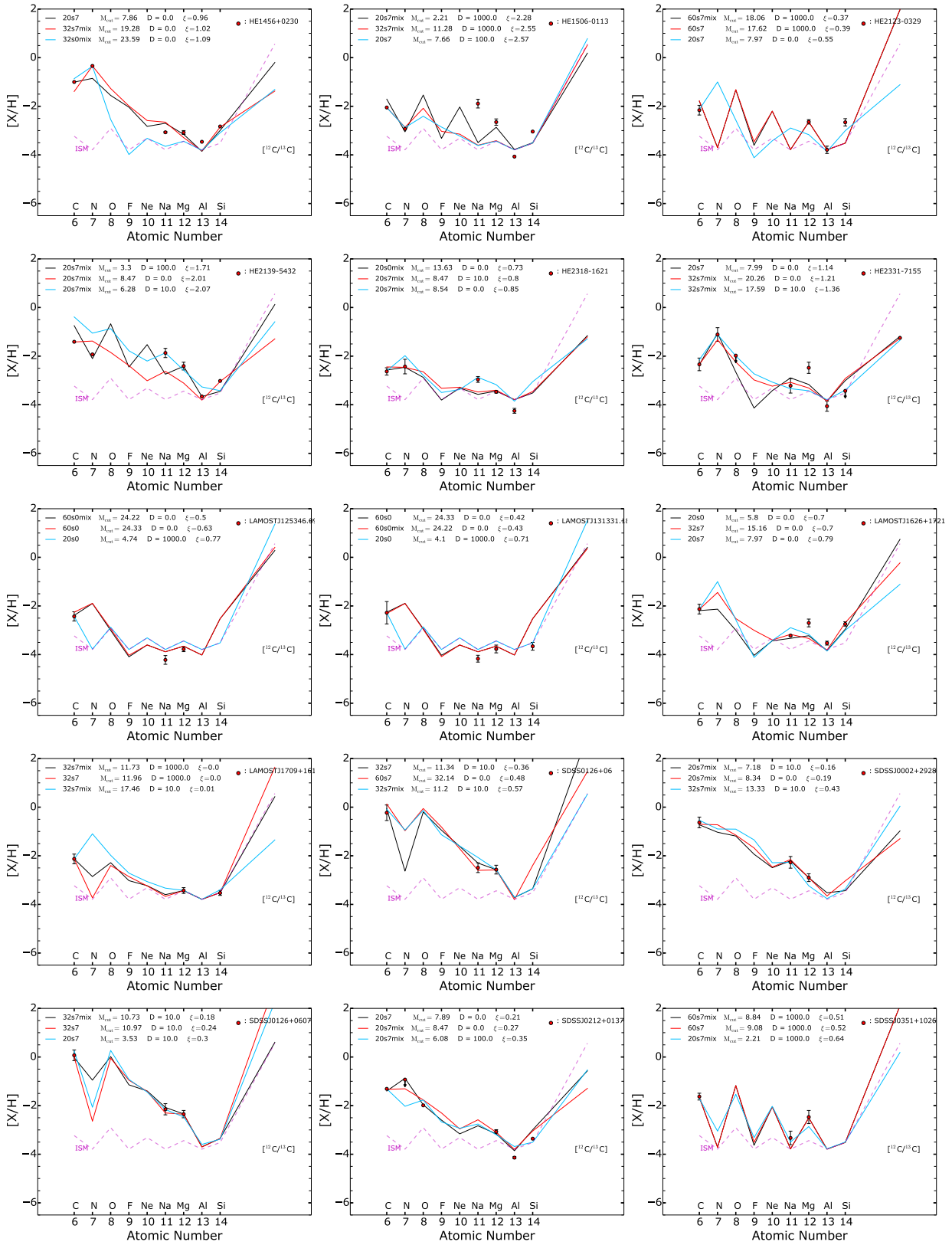


Figure B.4: continued

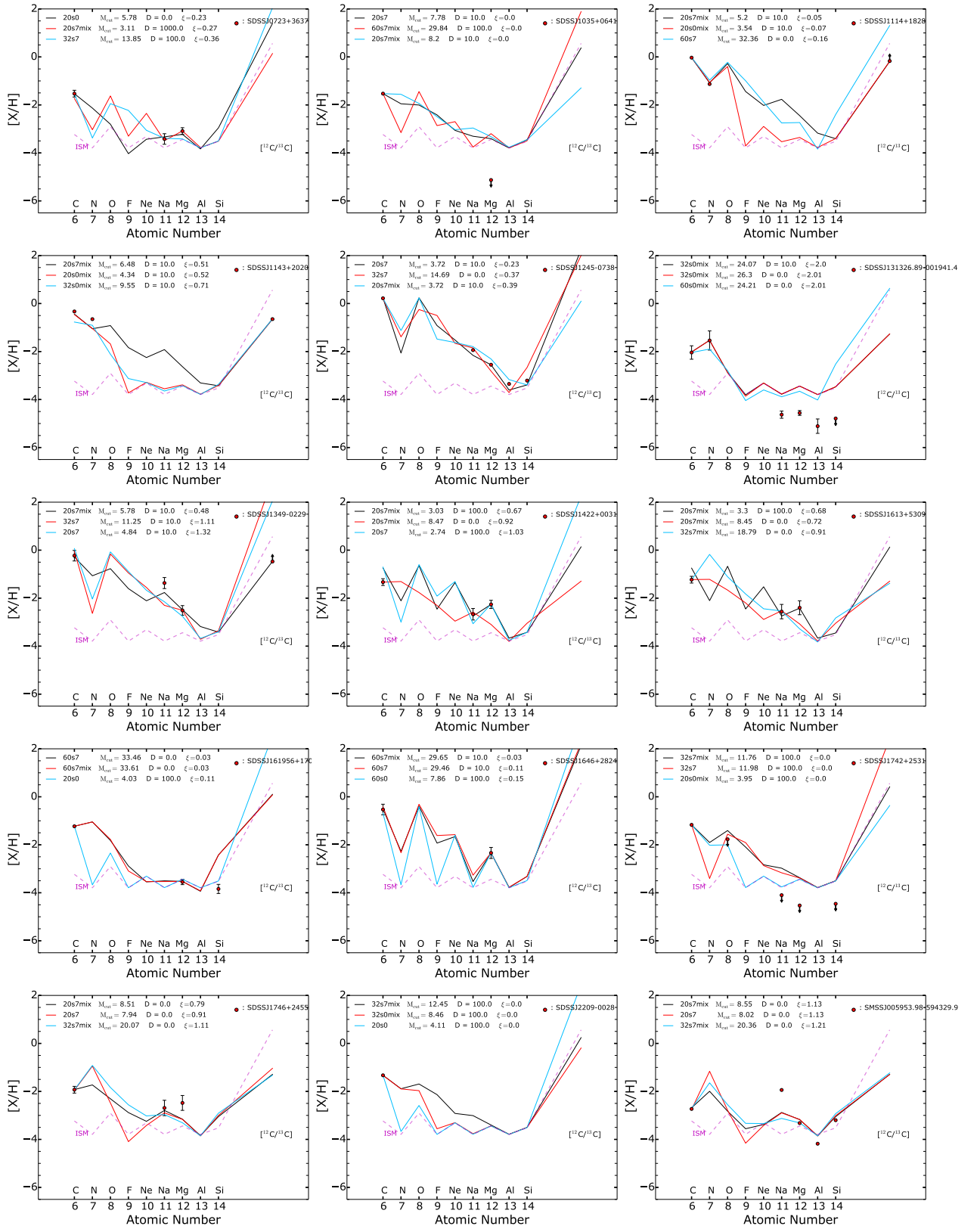


Figure B.5: continued



Publications

This section contains the list of publication. After the list are the 3 refereed papers (page 149, 159 and 176) that are not directly included in the thesis. The 2 others papers can be found page 101 and 118 of this thesis.

Refereed articles

- *Non standard s-process in massive rotating stars. Yields of 10 – 150 M_{\odot} models at $Z = 10^{-3}$*
Choplin, A., Hirschi R., Meynet G., Ekström S., Chiappini C. & Laird A.
2018, A&A, 618, A133
- *Are some CEMP-s stars the daughters of spinstars?*
Choplin, A., Hirschi R., Meynet G. & Ekström S.
2017, A&A, 607, L3
- *Effects of axions on Population III stars*
Choplin, A., Coc A., Meynet G., Olive K. A., Uzan J.-P. & Vangioni E.
2017, A&A, 605, A106
- *Pre-supernova mixing in CEMP-no source stars*
Choplin, A., Ekström S., Meynet G., Maeder A., Georgy C. & Hirschi R.
2017, A&A, 605, A63
- *Constraints on CEMP-no progenitors from nuclear astrophysics*
Choplin, A., Maeder A., Meynet G. & Chiappini C.
2016, A&A, 593, A36

Publications in conference proceedings

- *Toward the first stars*
Choplin, A.
Annual meeting of the French Society of Astronomy and Astrophysics, July 2017
- *Massive stars: stellar models and stellar yields, impact on Galactic Archaeology*
Meynet, G., **Choplin, A.**, Ekström, S. & Georgy, C.
IAU Symposium 334, Rediscovering our Galaxy 2017
- *Evolution and Nucleosynthesis of Massive Stars*
Meynet, G., Maeder, A., **Choplin, A.**, Takahashi, K., Ekström, S., Hirschi, R., Chiappini, C. &

Eggenberger, P.

14th International Symposium on Nuclei in the Cosmos (NIC2016), id.010401, 8 pp, 2017

- *Impact of rotation on stellar models*
Meynet, G., Maeder, A., Eggenberger, P., Ekstrom, S., Georgy, C., Chiappini, C., Privitera, G. & **Choplin, A.**
Astronomische Nachrichten, Vol.337, Issue 8-9, p.827 2016
- *Nucleosynthesis in the first massive stars*
Choplin, A., Meynet, G., Maeder, A., Hirschi, R. & Chiappini, C.
Nuclear in Astrophysics Conference, 2016
- *Clues about the first stars from CEMP-no stars*
Choplin, A., Meynet, G. & Maeder, A.
Annual meeting of the French Society of Astronomy and Astrophysics, June 2015

Poster proceedings

- *Insights on the First Stars from CEMP-no Stars*
Choplin, A., Meynet, G., Maeder, A., Hirschi, R., Ekström, S. & Chiappini, C.
International Symposium on Nuclei in the Cosmos, 2017
- *Clues on the first stars from CEMP-no stars*
Choplin, A., Meynet, G., Maeder, A., Hirschi, R., Ekström, S. & Chiappini, C.
IAU Symposium, Hawaii, USA, August 2016
- *Clues about the first stars from CEMP-no stars*
Meynet, G., Maeder, A., **Choplin, A.**, Hirschi, R., Ekström, S. & Chiappini, C.
IAU General Assembly, 2015

Other oral contributions (no proceeding)

- *Nucleosynthesis in Rotating massive stars and Abundances of metal-poor stars.* (Invited talk)
Choplin, A.
the JINA-CEE Frontiers in Nuclear Astrophysics Meeting, South Bend IN, US, May 2018
- *Shedding light on the first stars with CEMP-no stars.* (Invited talk)
Choplin, A., Meynet, G., Ekström, S., Hirschi, R., Maeder, A., Chiappini, C. & Georgy, C.
A Celebration of CEMP and Gala of GALAH, Melbourne, Australia, November 2017

Effects of axions on Population III stars

Arthur Choplin¹, Alain Coc², Georges Meynet¹, Keith A. Olive³, Jean-Philippe Uzan⁴, and Elisabeth Vangioni⁴

¹ Geneva Observatory, University of Geneva, Maillettes 51, 1290 Sauverny, Switzerland
 e-mail: arthur.choplin@unige.ch

² Centre de Sciences Nucléaires et de Sciences de la Matière (CSNSM), CNRS/IN2P3, Univ. Paris-Sud, Université Paris-Saclay, Bâtiment 104, 91405 Orsay Campus, France

³ William I. Fine Theoretical Physics Institute, School of Physics and Astronomy, University of Minnesota, Minneapolis, MN 55455, USA

⁴ Institut d'Astrophysique de Paris, UMR-7095 du CNRS, Université Pierre et Marie Curie; Sorbonne Universités, Institut Lagrange de Paris, 98bis bd Arago, 75014 Paris, France

Received 25 April 2017 / Accepted 3 July 2017

ABSTRACT

Aims. Following the renewed interest in axions as a dark matter component, we revisit the effects of energy loss by axion emission on the evolution of the first generation of stars. These stars with zero metallicity are assumed to be massive, more compact, and hotter than subsequent generations. It is hence important to extend previous studies, which were restricted to solar metallicity stars.

Methods. Our analysis first compares the evolution of solar metallicity 8, 10, and 12 M_{\odot} stars to previous work. We then calculate the evolution of 8 zero-metallicity stars with and without axion losses and with masses ranging from 20 to 150 M_{\odot} .

Results. For the solar metallicity models, we confirm the disappearance of the blue-loop phase for a value of the axion-photon coupling of $g_{ay} = 10^{-10} \text{ GeV}^{-1}$. We show that for $g_{ay} = 10^{-10} \text{ GeV}^{-1}$, the evolution of Population III stars is not much affected by axion losses, except within the range of masses 80–130 M_{\odot} . Such stars show significant differences in both their tracks within the T_c – ρ_c diagram and their central composition (in particular ^{20}Ne and ^{24}Mg). We discuss the origin of these modifications from the stellar physics point of view, and also their potential observational signatures.

Key words. elementary particles – stars: evolution – stars: Population III – stars: massive

1. Introduction

Two well studied particles that may be components of the dark matter are the lightest supersymmetric particle (Goldberg 1983; Ellis et al. 1984) and the axion (Preskill et al. 1983; Abbott & Sikivie 1983; Dine & Fischler 1983). While the former is intensely debated because of null searches for supersymmetry at the Large Hadron Collider (Bagnaschi et al. 2015), axions remain a viable dark matter candidate. Axions were originally proposed as a possible solution to the strong Charge Parity (CP) problem (Peccei & Quinn 1977a,b; Weinberg 1978; Wilczek 1978). In strong interactions, there is no reason for CP-violating effects to be small, and these interactions would disagree violently with experiments unless the coefficient of the CP-violating term, called θ , is tuned to be very small ($<10^{-10}$). However, the spontaneous breaking of a global U(1) (Peccei-Quinn (PQ) symmetry) allows for the possibility of a dynamical cancellation of the CP-violating phase in QCD. If the scale associated with the symmetry breaking, f_a , is large, interactions between the axion and matter become very weak, rendering the axion nearly invisible (Kim 1979; Shifman et al. 1980; Zhitnitskii 1980; Dine et al. 1981). Because the PQ symmetry is also explicitly broken (the CP-violating θ term is not PQ invariant), the axion picks up a low mass similar to a pion picking up a mass when chiral symmetry is broken. Roughly, $m_a \sim m_{\pi} f_{\pi} / f_a$ where $f_{\pi} \approx 92 \text{ MeV}$, is the pion decay constant, so that

$$m_a \approx (6 \times 10^6 \text{ GeV} / f_a) \text{ eV}. \quad (1)$$

As dark matter candidates, axions act as cold dark matter despite their low mass (if $f_a \gg f_{\pi}$) because the cosmological energy density in axions consists of their coherent scalar field oscillations. The energy density stored in the oscillations exceeds the critical density (Preskill et al. 1983; Abbott & Sikivie 1983; Dine & Fischler 1983) unless $f_a \lesssim 10^{12} \text{ GeV}$ or $m_a \gtrsim 6 \times 10^{-6} \text{ eV}$.

Although model dependent, the axion has couplings to photons and matter fermions. As a result, they may also be emitted by stars and supernovae (Raffelt 1990). In supernovae (SNe), axions are produced via nucleon-nucleon bremsstrahlung with a coupling $g_{AN} \propto m_N / f_a$. SN 1987A enables us to place an upper limit (Ellis & Olive 1987; Mayle et al. 1988, 1989; Raffelt & Seckel 1988, 1991; Burrows et al. 1990; Keil et al. 1997) on the axion mass of

$$m_a \lesssim (0.5\text{--}6) \times 10^{-3} \text{ eV}. \quad (2)$$

Axion emission from red giants implies (Dearborn et al. 1986; Raffelt & Weiss 1995) $m_a \lesssim 0.02 \text{ eV}$ (although this limit depends on the model-dependent axion-electron coupling). From Eq. (1), the limit in Eq. (2) translates into a limit $f_a \gtrsim (1\text{--}12) \times 10^9$, implying that only a narrow window exists for axion masses.

In most models, the axion will also couple electromagnetically to photons through the interaction term $\mathcal{L} = -g_{ay} \phi_a \mathbf{E} \cdot \mathbf{B}$, where ϕ_a is the axion field (Raffelt 1990). While not competitive in terms of axion mass limits, the axion-photon coupling, g_{ay} , can be constrained through several different stellar processes. While axion emission occurs throughout the lifetime of low-mass stars, emission at high temperatures can greatly reduce

the lifetime of the helium-burning phase, resulting in an upper limit of $g_{10} \equiv g_{a\gamma}/(10^{-10} \text{ GeV}^{-1}) < 0.66$ (Raffelt & Dearborn 1987; Ayala et al. 2014). A similar limit of $g_{10} < 0.8$ was derived from the evolution of more massive stars (in the range of 8–12 M_{\odot}) as energy losses in the helium-burning core would overly shorten the blue-loop phase of stellar evolution in these stars (Friedland et al. 2013). For recent reviews, see Kawasaki & Nakayama (2013) and Marsh (2016).

Here we consider the effect of axion emission in more massive but metal-free stars associated with Population III (Pop. III). In such stars we can expect enhanced axions losses compared to solar metallicity stars for at least two reasons. First, we expect higher initial masses for Pop. III stars. The lack of heavy elements prevents dust from forming, and dust is a key agent at solar metallicity to fragment proto-stellar clouds into small pieces of low mass. This is the reason why very few low-mass long-lived stars are believed to be formed in metal-free environments. Only massive or even very massive stars are expected to form (see for instance the review of Bromm 2013). The second reason is that the absence of heavy elements implies that stars of a given initial mass are more compact and thus reach higher central temperatures (see the discussion in Ekström et al. 2008a, for instance).

After describing the process of energy loss by axions in Sect. 2, we use the Geneva code of stellar evolution to confirm in Sect. 3 that axion emission from solar metallicity stars might be constrained by the disappearance of the blue-loop phase. Our goal, however, is to study the axion energy losses for massive Pop. III stars, which is described extensively in Sect. 4. Our conclusions are given in Sect. 5.

2. Energy loss by axions

For a given coupling of axions to photons, Primakoff emission (Primakoff 1951) of axions from photon-nucleus scattering will occur, mediated by the virtual photons from the electrostatic potential of the nucleus (Fig. 1). The screening of this potential by the freely moving electric charges (Debye-Hückel effect) needs to be taken into account, however (Raffelt 1986). The volume emissivity for this process as a function of temperature (for temperatures much greater than the plasma frequency) was computed in Raffelt (1986, 1990).

Dividing this emissivity by the mass density, ρ , we obtain an energy-loss rate per unit mass,

$$\epsilon_{\text{ax}} = \frac{g_{a\gamma}^2 T^7}{4\pi^2 \rho} \xi^2 f(\xi^2), \quad (3)$$

where the function f is defined in Eq. (4.79) of Raffelt (1990) and ξ is given by

$$\xi \equiv \frac{\hbar c k_S}{2k_B T}, \quad (4)$$

with \hbar the reduced Planck constant, c the speed of light, and k_B the Boltzmann constant (see the appendix for an explanation of the units). The Debye-Hückel screening wavenumber, k_S , is given by Raffelt (2008) as

$$k_S^2 \equiv 4\pi\alpha \left(\frac{\hbar c}{k_B T} \right) \sum_{i=\text{e,ions}} n_i Z_i^2, \quad (5)$$

where α is the fine-structure constant, Z_i is the atomic number, and n_i is the ion or electron number density, given by

$$n_{\text{ions}} = \rho \frac{X_i}{A_i} N_A \text{ and } n_e = \sum_{i=\text{ions}} n_i Z_i, \quad (6)$$

A106, page 2 of 10

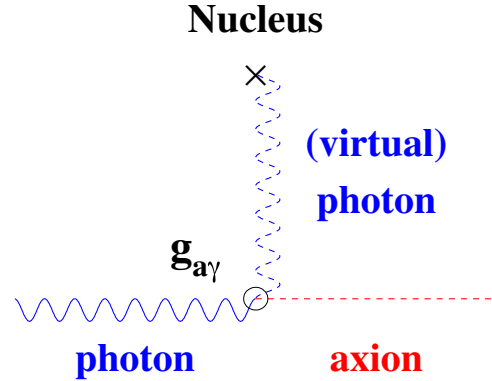


Fig. 1. Primakoff effect: a real photon from the thermal bath is converted into an axion by the electric field of a nucleus.

(because of charge neutrality), with N_A the Avogadro number. The energy-loss rate (Eq. (3)) can be rewritten as

$$\epsilon_{\text{ax}} = 283.16 \times g_{10}^2 T_8^7 \rho_3^{-1} \xi^2 f(\xi^2) \text{ erg/g/s}, \quad (7)$$

where $T_8 \equiv T/(10^8 \text{ K})$ and $\rho_3 \equiv \rho/(10^3 \text{ g/cm}^3)$. We note that the numerical constant differs from the constant in Eq. (3) of Friedland et al. (2013) by one order of magnitude (see the appendix for more details).

We correct Eq. (3) by the damping factor introduced by Aoyama & Suzuki (2015), namely, $\exp(-\hbar\omega_0/k_B T)$, where ω_0 is the plasma frequency in MeV:

$$\hbar\omega_0 = \left[4\pi\alpha \left(\frac{\hbar c}{m_e c^2} \right) n_e \right]^{\frac{1}{2}} \hbar c. \quad (8)$$

However, the damping factor always remains of the order of unity in our models.

During the main sequence (MS), most of the energy in massive stars is transported by radiation and convection so that the axions have little effect. Axion cooling is believed to have a significant effect during the core helium-burning phase, when the central temperature and density are about 10^8 K and 10^3 g cm^{-3} (see e.g. Friedland et al. 2013). In the next stages (core carbon burning, oxygen, etc.), the cooling by axions would be more pronounced because of the higher temperature and density. At these late stages, however, the axion cooling competes with neutrino losses. Whether axion losses in Pop. III stars are significant or not compared to other sinks of energy, like neutrino losses, is a point investigated in this paper.

3. Massive stars with solar metallicity

It was shown that at solar metallicity the energy losses by axions from the helium-burning core can eliminate the blue-loop phase (Friedland et al. 2013). Limits on the axion photon coupling were derived from studies of 8–12 M_{\odot} models. To check whether we find similar results, we have computed models at similar mass and metallicity.

3.1. Physical ingredients

We computed six models of 8, 10, and 12 M_{\odot} at solar metallicity, with and without energy losses by axions using the Geneva code.

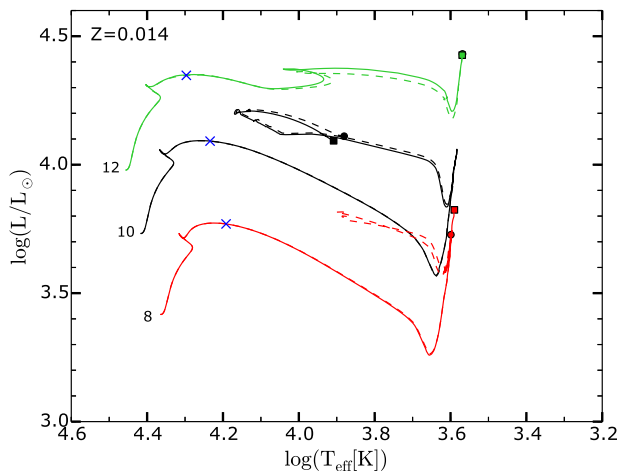


Fig. 2. Hertzsprung-Russell diagram for the six models computed at solar metallicity. Dashed lines show models without axion losses. Solid lines show models with axion losses. Circles (without axion losses) and squares (with axion losses) show the location of the models at the end of core He-burning. Blue crosses show the location of the tracks at core helium-burning ignition ($\epsilon(3\alpha) > 0$).

Similar input parameters as those used in Ekström et al. (2012) were considered for these computations. The initial abundance of H, He, and metals in mass fractions are $X = 0.72$, $Y = 0.266$, and $Z = 0.014$, respectively. The mixture of heavy elements was determined according to Asplund et al. (2005) except for Ne, whose abundance was taken from Cunha et al. (2006). The isotopic ratios are from Lodders (2003). The core-overshoot parameter $d_{\text{over}}/H_p = 0.1$, where H_p is the pressure scale height determined at the Schwarzschild convective core boundary. It extends the radius of the convective core by an amount of $0.1 H_p$. The outer layers, if convective, were treated using the mixing-length theory. The mixing-length parameter α_{MLT} was set to 1.6. This value allow to reproduce the solar radius at the age of the Sun as well as the positions of the red giants and supergiants in the HR diagram (Ekström et al. 2012).

To compute the energy-loss rate per unit mass due to axions, we took $g_{10} = g_{\text{ay}}/(10^{-10} \text{ GeV}^{-1}) = 1$ in all our models. The simulations were stopped at the end of the core helium-burning phase. The models are labelled “10g1” for instance, where “10” refers to the initial mass in solar masses and “g1” means $g_{10} = 1$.

3.2. Evolution in the Hertzsprung Russell diagram

Figure 2 depicts the evolutionary tracks in the HR diagram. For the $8 M_{\odot}$ models (red lines), the blue loop disappears when the energy loss by axions is included (solid red line). To understand this behaviour, we recall that a blue loop appears when the stellar envelope contracts, causing the star to leave the red supergiant branch and to evolve blueward in the HR diagram. During the core He-burning phase, the envelope contracts because the core expands. This is due to the mirror effect. The expansion of the core comes from the fact that when the abundance of helium decreases in the central regions, the central temperature increases. One effect of the increase in central temperature is the increase in nuclear energy generation by reactions such as $^{12}\text{C}(\alpha, \gamma)^{16}\text{O}$ (we note here that the rate of this reaction is still highly uncertain). The excess of nuclear energy is used to expand the core.

The appearance or disappearance of the blue loops is very sensitive to many inputs of the stellar models, and small changes can have important effects, such as changes in mesh resolution, the way to account for convection, and the mixing in the radiative zones (see e.g. Kippenhahn & Weigert 1990; Maeder & Meynet 2001; Walmswell et al. 2015).

When energy losses by axions are included, the energy produced by the nuclear reactions in the core is more efficiently removed from the helium-burning core (the energy removed by axions is $\lesssim 3 \times 10^4 \text{ erg g}^{-1} \text{ s}^{-1}$ for the models of this section). This limits the expansion of the helium core, which in turn limits the contraction of the envelope. This finally tends to reduce or even prevent the formation of a blue loop. This change in behaviour is restricted to the $8 M_{\odot}$ star in the three models with different initial masses considered here.

3.3. Duration of burning phases

Interestingly, for our $8 M_{\odot}$ model, the duration of the helium-burning phase is reduced by $\sim 13\%$ when axions are considered. For the 10 and $12 M_{\odot}$ models, the reduction is $\sim 8\%$ and $\sim 11\%$, respectively. Thus we see that the largest effects on the lifetimes are found for the $8 M_{\odot}$ case. This does appear somewhat consistent with the fact that the blue loop is affected in this model. The lifetimes are shorter when axions are considered because they add a new channel that is very efficient in removing energy from the core.

Friedland et al. (2013) found a decrease in duration of the helium burning by $\sim 23\%$ (cf. their Fig. 3 and discussion) for a $9.5 M_{\odot}$ with $g_{10} = 0.8$, which exceeds the lifetime decreases that we have obtained here. This might appear surprising in view of their value for g_{10} that is lower than the value adopted here. Instead, we would have expected that the lifetime decreases reported by Friedland and coauthors would be smaller than those obtained here with a $g_{10} = 1$. In all likelihood, our stellar models differ by some other physical ingredients, such as the overshoot parameter. These differences are difficult to trace back, however, because of the lack of details given in Friedland et al. (2013). More importantly, we find similar qualitative trends. Using a different stellar evolution code, we find as in Friedland et al. (2013) that axions suppress the blue loops for some masses and decrease the core He-burning lifetime.

In contrast to the helium-burning phase, the duration of the MS is very little affected by axions because the relevant temperature for axion cooling to be efficient is not reached in the core of massive MS stars. The duration of this phase is reduced by less than $\sim 0.1\%$ for our models. The reason is that the losses by axions are very small during this phase.

4. Pop. III stars

4.1. Physical ingredients

With the same physical ingredients used for solar metallicity models as in the previous section, we calculated Pop. III models of 20, 25, 32, 40, 60, 85, 120, and $150 M_{\odot}$ with and without axion losses. The evolution was stopped at the end of core C-burning. We used the mass-loss recipe of Vink et al. (2001). \dot{M} depends on $(Z/Z_{\odot})^{0.85}$ so that \dot{M} should be 0 for our Pop. III models. However, we used $Z = 10^{-4} Z_{\odot}$ as a threshold value for the mass-loss rate. This was done previously in Marigo et al. (2003) and Ekström et al. (2008a). We note that our models were computed

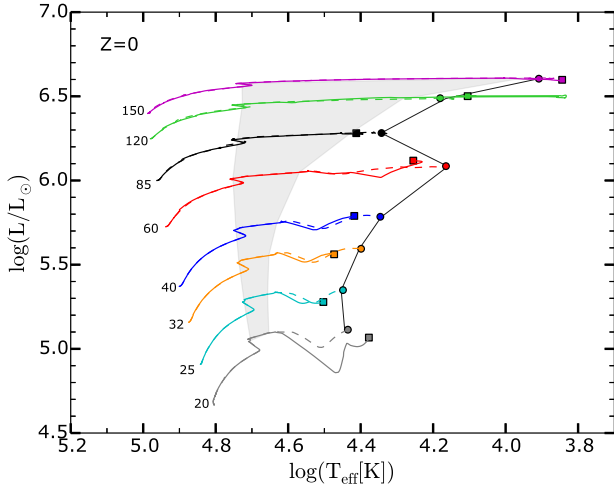


Fig. 3. Same as Fig. 2, but for the 16 Pop. III models. The shaded area shows the zone of the diagram where helium burns in the core of the models without axion losses. The thin black line shows the location of the models without axion losses when the carbon starts to burn into the core. The shaded area and the black line are similar for models with axion losses. Circles (without axion losses) and squares (with axion losses) show the location of the models at the end of core C-burning.

at $Z = 0$, but we adopted the mass-loss rates for these models that are given by a metallicity $Z = 10^{-4} Z_{\odot}$. In some models, the opacity peak produced by the variation in the ionisation level of hydrogen decreases the Eddington luminosity $L_{\text{Edd}} = 4\pi cGM/\kappa$ below the actual luminosity of the star. As a consequence, the external layers of such models exceed the Eddington luminosity. This unstable phase cannot be solved with our hydrostatic approach. It is accounted for by increasing the mass-loss rate by a factor of 3 whenever the luminosity of any of the layers of the stellar envelope is higher than $5L_{\text{Edd}}$ (Ekström et al. 2012).

4.2. Evolutionary tracks in the HR diagram and lifetimes

The tracks in the HR diagram (Fig. 3) are little affected by axion losses. The main differences between the two families of tracks arise close to the end of the evolution, when axion losses are higher than other sources of energy loss. We see that in general, models with axions remain bluer in the HR diagram than the models without axions. Since axions add a new channel for evacuating the energy from the central regions, it removes energy that otherwise might be used to inflate the envelope and push the track in the HR diagram redward. In the previous section, we saw that axions could suppress a blue loop, thus causing a contraction of the envelope. Here we see that axions may reduce the expansion of the envelope. This difference arises here because we considered the impact of axions at a different stages of the evolution. In the previous section, we discussed the case of a core He-burning star at the red supergiant stage. Here we consider stars after the core He-burning phase that still cross the HR gap. In both cases axions remove energy. In the first case, this decreases the ability of the core to extend and hence the envelope to contract. In the second case, it removes energy released by contraction of the core that otherwise is used to expand the envelope. This is what occurs for initial masses below $\sim 85 M_{\odot}$. The 120g1 model loses $\sim 20 M_{\odot}$ at the end of the core helium-burning phase.

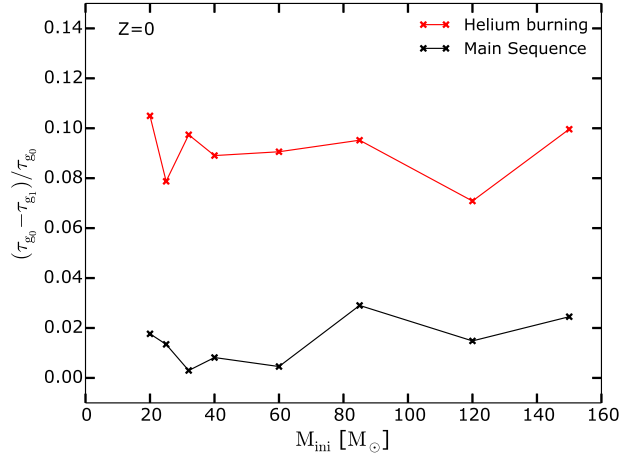


Fig. 4. Relative difference of the duration of MS and core helium-burning phases between Pop. III models with ($g_{10} = 1$, noted as g_1) and without ($g_{10} = 0$, noted as g_0) axion losses.

Before mass ejection, $\log T_{\text{eff}} \sim 3.8$ (solid green line in Fig. 3). While losing mass, $\log T_{\text{eff}}$ then decreases until it reaches a value of about 4.1. This model loses more mass than the 120g0 model ($120 M_{\odot}$ without axion) because it remains in a domain of the HR diagram where the luminosity becomes supra-Eddington for a longer time in some outer layers of the star.

The differences between the tracks in the HR diagram remain very modest. We computed different 85g1 models using different time-steps near the end of the evolution. This leads to slightly different final T_{eff} . The scatter is of the order of the difference in T_{eff} between the 85g0 and 85g1 models shown in Fig. 3. In any case, differences like this cannot be used to constrain the presence of axions. This is true for at least two reasons. (1) Pop. III stars cannot be directly observed and thus they cannot be placed into a HR diagram. With the James Webb Telescope, it will be possible, on the other hand, to detect supernovae from Pop. III stars. From the evolution of their early light curves (during the rise time), it might be possible to obtain some indications on the radius of the core-collapse supernova progenitors (see e.g. Nakar & Sari 2010; Bersten et al. 2012; Dessart et al. 2013; Morozova et al. 2016). However, this radius does not depend only on the presence of the axions. It also depends on convection, mixing in radiative layers, opacities, and mass losses, and thus there is little hope at the moment to use this channel to constrain the physics of axions. (2) Axions may change the lifetimes of stars somewhat. This may indirectly have an impact on the ionizing power of Pop. III stars. Changing the MS lifetime, for instance, will change the duration of the phase when UV photons are emitted by the star. The impact of axions on lifetimes is shown in Fig. 4. We see that axions shorten the MS lifetime by less than 3% and reduce the core helium burning lifetimes by 7–10%. As already mentioned above, this simply reflects the fact that the effects of axions are the most marked when temperature increases, i.e. in the more advanced phases of the evolution. Again, here the effects are very modest and of the same order of magnitude as changes that are due to other uncertain physical ingredients of the models. A consequence of a shorter helium lifetime is that the $^{12}\text{C}(\alpha, \gamma)^{16}\text{O}$ reaction has less time to operate during core helium burning so that the $^{12}\text{C}/^{16}\text{O}$ ratio at the end of central helium burning is slightly higher ($\leq 5\%$) for models with shorter helium lifetimes, hence with axion losses.

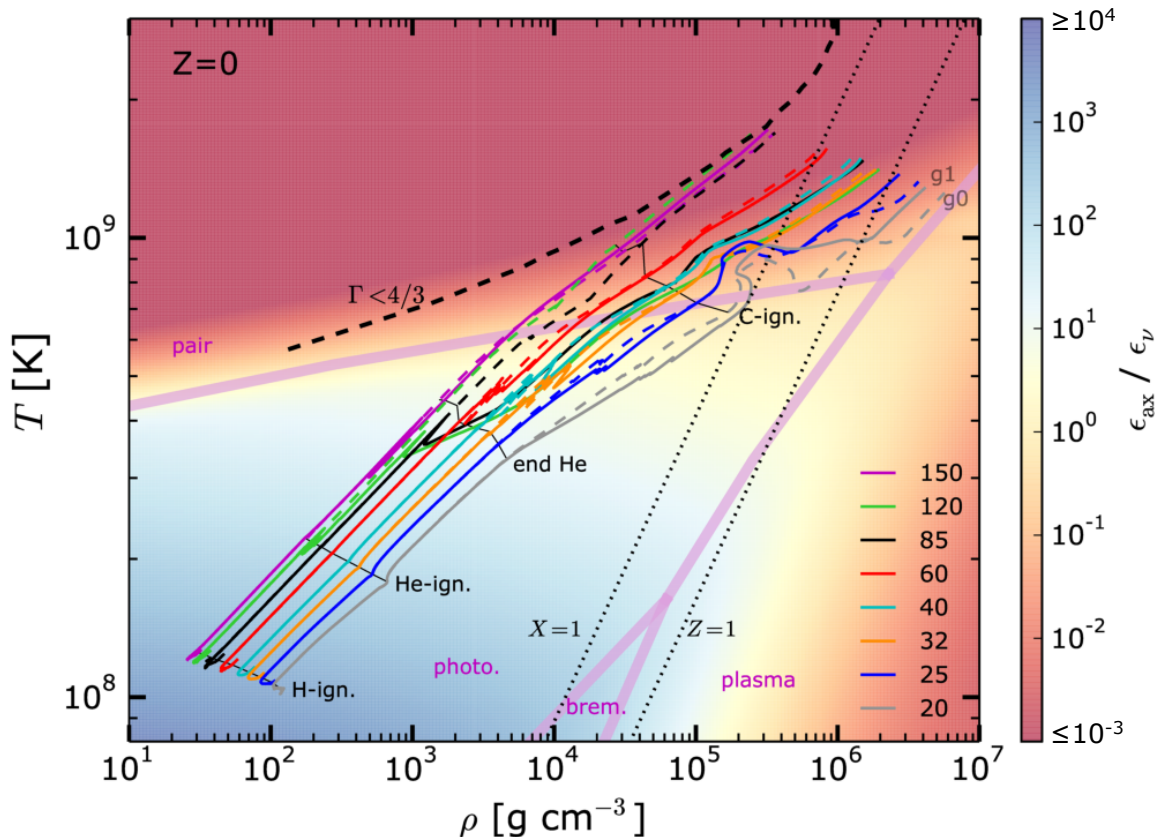


Fig. 5. Coloured lines show the tracks for the computed Pop. III models in the central temperature vs. central density plane. Dashed lines show models without axion losses, while solid lines show models with axion losses. The ignition of the different burning stages and the end of central helium burning are given for the models without axion losses. The broad dashed $\Gamma < 4/3$ line indicates the zone of the diagram where electron-positron pair creations lower the adiabatic index below $4/3$. The $X = 1$ and $Z = 1$ lines show the limit between the perfect gas and the completely degenerate non-relativistic gas for pure hydrogen and pure metal mixtures. Light purple lines delimitate the different regions where a given neutrino source (pair, photon, bremsstrahlung, and plasma) dominates. The colour map shows the ratio $\epsilon_{\text{ax}}/\epsilon_{\nu}$, where ϵ_{ν} is the sum of the four types of neutrino losses mentioned above, computed according to Itoh et al. (1989, 1996).

4.3. Central conditions

The coloured lines of Figs. 5 and 6 show the evolution in the $(\log T_c, \log \rho_c)$ diagram where T_c and ρ_c are the central temperature and density, respectively. The colour map shows the ratio $\epsilon_{\text{ax}}/\epsilon_{\nu}$ between axion and neutrino energy losses. It shows that axions remove more energy than neutrinos from the central regions before the beginning of the core C-burning phase. After C-ignition in the centre, neutrinos dominate. Thus, we can expect that axions will have their most important effects before the core C-burning phase. However, for axions to have a strong impact on the models, it is not sufficient that energy losses by axions are more important than neutrinos, energy losses due to axions must also be important with respect to the energy released either by nuclear reactions or gravitational contraction.

During the core H-burning phase, the energy is mainly transported by radiation and convection. Axion cooling has little effect. The same is also true, although to a smaller extent, during the core He-burning phase. The only phase where strong differences may appear due to axions is during the transition between the end of the core He-burning phase and the beginning of the core C-burning phase. During this phase, energy in the central part is produced by core contraction (see the green line in Fig. 7).

After the end of the core He-burning phase, the energy released by the contraction of the core is taken away by axions (between the abscissa 4 and 2.5 in Fig. 7). This is the phase during which axions may induce some significant changes in the models.

For most of the models, axions do not have a strong effect. There is an exception, however, in the cases of the 85 and 120 M_{\odot} models. As can be better seen in Fig. 6, the central density and temperature of the 85g1 (solid black line) and 120g1 (solid green line) models significantly deviates from the models without axions. After the core He-burning phase, the tracks with axions join the tracks of the 40 (cyan tracks) and 32 (yellow tracks) M_{\odot} models (see Fig. 5), respectively, and follow these tracks until the end of their evolution. In other words, they follow the evolution of stars with lower initial masses.

In these models, larger amounts of energy can be evacuated from the central regions than in models with only neutrinos. This decreases the content of entropy in the core and thus will make the central region more sensitive to degeneracy effects. This explains why the tracks with axions more rapidly approach the line separating the non-degenerate from the degenerate region (see the lines labelled $X, Z = 1$ in Fig. 6).

Surprisingly, this behaviour disappears above and below the range 85–120 M_{\odot} . Outside this specific mass range, axions no

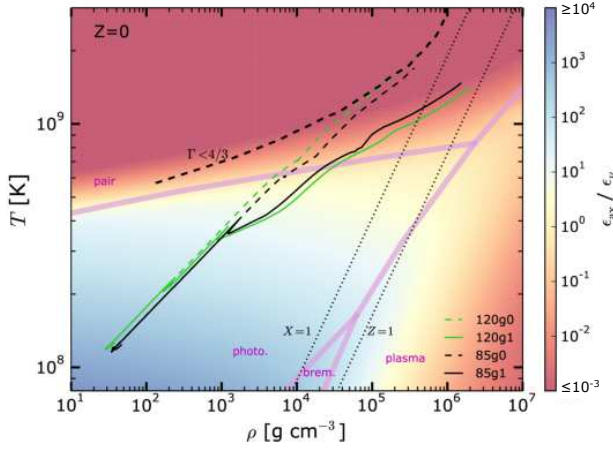


Fig. 6. Same as Fig. 5, but for the 85 and 120 M_{\odot} models.

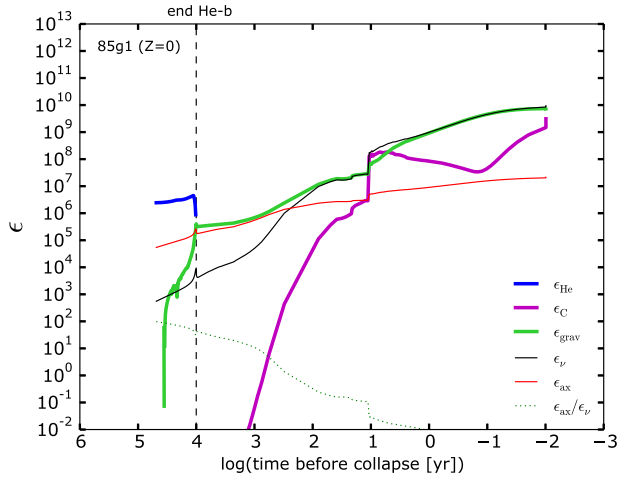


Fig. 7. Energy generated by helium burning (ϵ_{He}), carbon burning (ϵ_{C}), gravitational energy (ϵ_{grav}), energy of the neutrinos (ϵ_{ν}), and of the axions (ϵ_{ax}). Thick lines represent sources of energy, and thin lines represent sinks of energy. The dotted line shows the ratio $\epsilon_{\text{ax}}/\epsilon_{\nu}$. The vertical dashed line denotes the end of the core helium-burning phase.

longer have important effects, and the tracks are only slightly changed when axions are considered. To understand why this situation arises, we note the following:

- As indicated above, axions dominate the process of energy removal from the central regions just after the core He-burning phase, until neutrinos become dominant. The durations of this phase, obtained in the different initial mass models computed with axions, are shown in Fig. 8. We see that the longest axion-dominated phases occur for the 85 and 120 M_{\odot} models. This is consistent with the fact that axions have the strongest impact in these models. The 20 M_{\odot} model also has a rather long axion-dominated phase. A careful examination of Fig. 5 indicates that the track is more strongly shifted than the other towards lower densities at a given temperature. This shift disappears after C-ignition in the core, however.
- The duration of the axion-dominated phase can be estimated to first order as $GM_{\text{core}}^2/(R_{\text{core}}L_{\text{axion}})$, where M_{core} , R_{core} are the mass and the radius of the core at the end of the

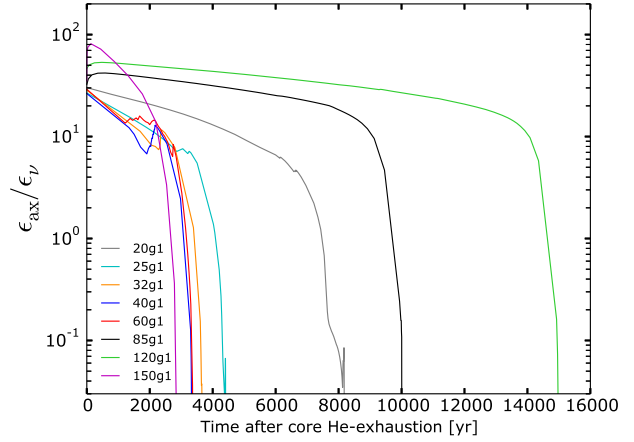


Fig. 8. $\epsilon_{\text{ax}}/\epsilon_{\nu}$ ratio in the core of Pop. III models as a function of the time after the end of central helium burning.

core He-burning phase, respectively, and L_{axion} is the axion luminosity. This equation expresses the fact that during this phase, the energy source is mainly the gravitational energy, i.e. $GM_{\text{core}}^2/R_{\text{core}}$. The gravitational energy increases with the mass. The axion luminosity increases rapidly with the temperature, and the temperature also increases with the mass. Therefore both the numerator and the denominator increase with the mass. This prevents an easy prediction of how the ratio will vary as a function of mass. Current numerical models tell us that for most of the initial masses, this ratio keeps a nearly constant value. For a few initial masses, this ratio is higher, however.

4.4. Internal structure of the 85 and 120 M_{\odot} models

The structure evolution of the of the 85g1 and 120g1 models shows striking differences compared to the 85g0 and 120g0 models. This is illustrated in Fig. 9, which compares the evolution as a function of time of the convective regions (grey areas) in the 85g0 and 85g1 models. We see that the core hydrogen- and helium-burning phases are very similar in both models. Differences appear after the core He-burning phase. In the model without axions, we have two convective burning shells during the whole post-He-burning phase. The outer shell is the convective H-burning shell, and the inner shell is the convective He-burning shell. In the models with axions, before C-ignition, there is only one convective burning shell, the He-burning shell. We also see that during this phase, the convective He-burning shell in the model with axions is more extended than in the model without axions. This is because in models with axion losses, more energy is removed from the He-shell and below. As a consequence, the star contracts more strongly in this region. This tends to make this region warmer, which in turn boosts the He-burning energy generation in the region where helium is still present. As a consequence, this convective region extends farther.

Because of the additional energy removed by axions, the cores of the 85g1 and 120g1 models contract more strongly than the cores of the 85g0 and 120g0 models. This leads to a high central density that makes the cores of the 120g1 and 85g1 models partially degenerate. In this case, the energy released by contraction is in part used to push some electrons to occupy higher energy quantum levels. This energy is not used to increase the thermal energy. This implies that the 85g1 and 120g1 models end

A. Choplin et al.: Effects of axions on Population III stellar evolution

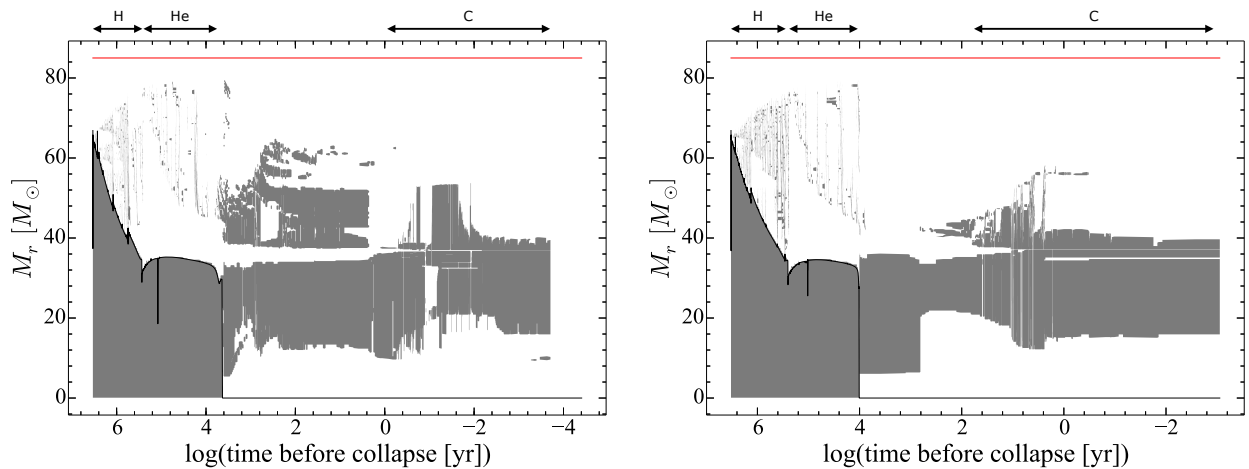


Fig. 9. Kippenhahn diagram of the 85g0 (*left*) and 85g1 (*right*) models. Grey areas represent the convective zones. The red line at the top shows the total mass. The core hydrogen-, helium-, and carbon-burning phases are indicated at the top of the panels.

Table 1. Masses of the helium and carbon-oxygen cores at the end of the core C-burning phase.

$M_{\text{ini}} [M_\odot]$	20	25	32	40	60	85	120	150
	$g_{10} = 0$							
$M_\alpha [M_\odot]$	3.93	5.37	8.45	12.08	21.94	36.94	54.82	67.81
$M_{\text{CO}} [M_\odot]$	3.42	5.36	8.35	12.08	21.90	36.86	54.82	67.70
	$g_{10} = 1$							
$M_\alpha [M_\odot]$	3.35	5.47	8.25	12.07	22.14	37.06	51.53	67.95
$M_{\text{CO}} [M_\odot]$	3.35	5.42	8.24	11.98	22.14	37.02	50.15	67.92

their evolution with a lower central temperature than the 85g0 and 120g0 models (see Fig. 6). We recall that on the other hand, the 85g1 and 120g1 models end their evolution with a higher temperature in the He-shell than the 85g0 and 120g0 models (cf. the discussion in this section).

The structure of these models during this stage (in between helium and carbon burning) is nevertheless sensitive to other parameters, like the resolution (number of shells). We again computed the 85g1 model with a different resolution, and the convective pattern from abscissa ~ 4 in Fig. 9 (right panel) is different. This illustrates once again that other parameters can impact the structure of the models during specific phases. It remains, nevertheless, that the effect of the axions is the strongest during that stage (cf. Fig. 8 and discussion). This is to say, during this stage, the axions are most likely to have an impact on the evolution or structure of the star.

In addition, the structure changes mentioned above are present only for a period of time. They appear as a transitory reaction of the model to the increased loss of energy in the central regions. In the end, the models converge towards structures that are again very similar (compare the two structures shown in Fig. 9 at the very end of the evolution). The final masses of the helium and carbon-oxygen cores are little affected by the effect of axions (see Table 1).

It is interesting to note that although the 85 and 120 M_\odot stars with axions would have very similar masses for the He and CO cores compared to their siblings without axions, they nevertheless show central conditions that are very different. As seen in Fig. 6, they show much higher densities at a given temperature,

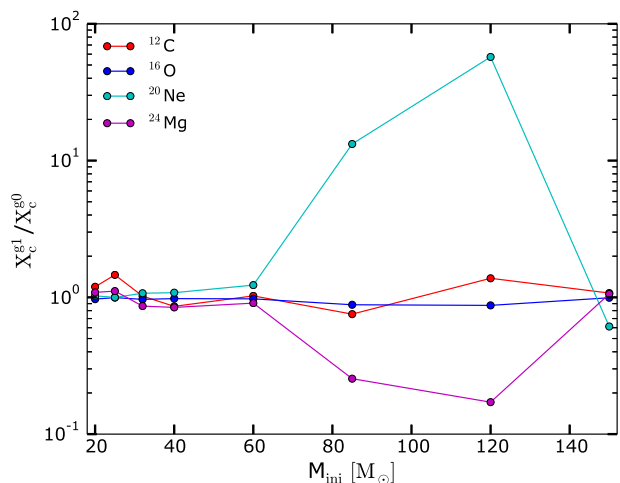


Fig. 10. Ratio of central abundances at the end of core C-burning between models with axion losses (X_c^{g1}) and models without axion losses (X_c^{g0}).

thus, as already underlined above, the models with axions are much more sensitive to degeneracy effects. Whether this produce some flashes or even an explosion in the presupernova phases remains to be explored.

Recently, [Woosley \(2017\)](#) has investigated the final evolution of 70–140 M_\odot stars. He found that such stars should experience pulsational pair-instability supernovae (PPISN). PPISN would occur if the final helium core is more massive than 30 M_\odot . For helium cores above 62 M_\odot , the star is disrupted as a single pulse (pair-instability supernovae). Our 85, 120, and 150 M_\odot models have helium cores of between ~ 37 and 68 M_\odot (see Table 1). They might experience PPISN (or PISN for helium cores above 62 M_\odot). However, the axion cooling might prevent our 85 and 120 M_\odot models from entering in the unstable regime (see Figs. 5 and 6). If so, such stars could produce black holes in the mass range where no black hole is usually expected, between 64 and 133 M_\odot ([Heger & Woosley 2002](#)). This could induce a potential signature in gravitational waves. Although still far from being able to use stellar models to verify the existence of axions, this possible axion signature has to be kept in mind for the future.

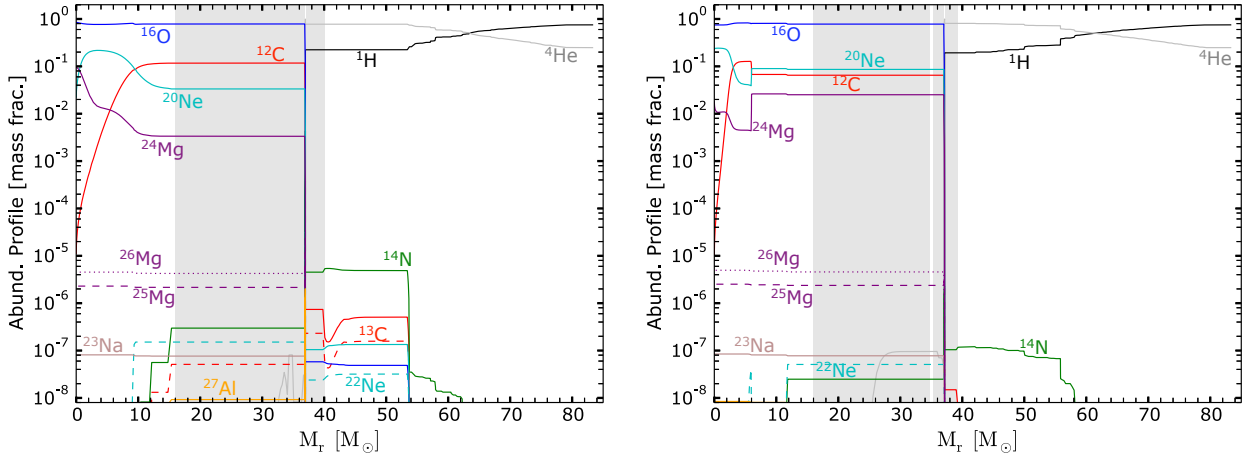


Fig. 11. Abundance profiles of the 85g0 (*left*) and 85g1 (*right*) models at the end of core carbon burning (central mass fraction of ^{12}C below 10^{-5}). The shaded area shows the convective zones.

4.5. Impact of the axion cooling on nucleosynthesis

Population III stars lose very little mass through stellar winds (although fast rotation may change this picture, see [Ekström et al. 2008a,b](#)). The only way they can contribute to nucleosynthesis would therefore be through supernova ejecta. As discussed above, the two masses for which the impact of axions are strongest are the 85 and $120 M_{\odot}$. If these two stars would end their life producing a black hole with very little or no mass ejecta, then their contribution in enriching the interstellar medium would likely be null. However, a successful explosion is also a possible scenario (e.g. [Ertl et al. 2016](#); [Sukhbold et al. 2016](#)). The discussion below investigates the possible impact of axions when some material is ejected.

Figure 10 shows central abundance ratios at the end of core C-burning for models with and without axion losses. The most abundant species are shown. The central abundances of 20–60 M_{\odot} models are little affected by axion losses. Over the whole range of masses considered, ^{12}C and ^{16}O are little affected. ^{20}Ne and ^{24}Mg are affected in the range 80–140 M_{\odot} . The central ^{20}Ne (^{24}Mg) abundance is ~ 60 times higher (~ 5 times lower) in the 120g1 model than in the 120g0 model. This is due to the higher central temperature in the 85g0 (120g0) compared to the 85g1 (120g1) model (cf. discussion in Sect. 4.3). In the case of the 85g0 and 120g0 models, the central temperature reaches values > 1.4 GK, where the $^{20}\text{Ne}(\alpha, \gamma)^{24}\text{Mg}$ channel becomes stronger than the $^{16}\text{O}(\alpha, \gamma)^{20}\text{Ne}$ channel, so that significantly more ^{24}Mg is synthesized, to the detriment of ^{20}Ne . However, the central abundances are not sufficient to determine the yield of an element. The complete chemical structure should be inspected.

Figure 11 shows the complete chemical structure obtained in the two 85 M_{\odot} models with and without axions. These structures are also representative of the 120 M_{\odot} models. For the other models, the axions do not lead to significant differences in the final abundance profiles, and we do not discuss them further. We see in Fig. 11 that the distribution of oxygen is very similar in both models, and we therefore do not expect important effects on the stellar yield of this element. For ^{12}C , we see some differences: the zone where carbon is depleted is smaller for the 85g1 model. This is because the cooling due to axion emission is more efficient before the core carbon-burning phase. This implies that a smaller fraction of the core reaches the conditions needed for

carbon burning to occur. The ^{14}N profiles are slightly different, but the mass fraction stays very small, below 10^{-5} in any case. This difference is not significant.

In the He-burning shell, the abundances of ^{20}Ne and ^{24}Mg are larger in the model with axions. These differences reflect the higher temperatures reached in the He-burning shell in the model with axions (cf. discussion in Sect. 4.3). On the whole, we see that when these layers that are associated with the He-burning shell are ejected, this may boost the yield by a factor 10 with respect to the yield of these two isotopes obtained in the corresponding models without axions. However, this will occur in a relatively short mass range, and the global effect on the yields integrated over an initial mass function where these massive stars are far out-numbered by lower mass stars will therefore remain quite modest.

5. Conclusions

We have explored the impact of axions in massive stars at solar metallicity and in Pop. III stars. In solar metallicity stars, we have confirmed that the axion coupling to photons might be constrained by the disappearance of the blue-loop phase in stars with masses between 8 and 12 M_{\odot} . However, caution is required because blue loops are very sensitive to many other uncertain physical processes (e.g. core convection and its efficiency and boundary mixing), which can also remove the blue loops from a stellar evolutionary track without need for axion cooling. In Pop. III stars, we have shown that the effects of axions on stellar evolution are very modest and are hardly observable, mainly because uncertainties in other parameters of stellar models produce effects at least as strong.

The most spectacular effect of axions explored in the present work is on the physical conditions obtained at the end of the evolution for Pop. III stars with masses between about 80 and 130 M_{\odot} . These stars present cores with some level of degeneracy, and the final fate of these objects is not clear. [Sukhbold et al. \(2016\)](#) have investigated the final fate of 9–120 M_{\odot} solar metallicity models. Above 30 M_{\odot} , most of the models do not explode and form black holes. The effect of axions might change this picture. This clearly needs further investigation, especially as we approach the era of observations with the James Webb Telescope, which might detect supernovae in the entire observable Universe. Such stars might give rise to a type of explosive event

with a clear non-ambiguous signature inherited from the particular structure of their progenitors.

In a broader perspective, this work shows that we are still far from a situation where Pop. III stellar models can be used as a physics laboratory to verify the presence of axions, and even farther from the situation where stars might constrain their properties. This shows the importance of continuing our efforts in stellar physics, making stellar models still more precise and reliable so that real stars can be used as physics laboratories, which will open new windows on questions at the frontier of physics, in the domain of temperatures and densities that are not reachable in a laboratory.

Acknowledgements. We would like to thank Jordi Isern for useful discussions during the early stage of this project. The work of K.A.O. was supported in part by DOE grant DE-SC0011842 at the University of Minnesota. The work of E.V. has been carried out at the ILPLABEX (under the reference ANR-10-LABX-63) supported by French state funds managed by the ANR within the Investissements d’Avenir programme under reference ANR-11-IDEX-0004-02.

References

- Abbott, L. F., & Sikivie, P. 1983, *Phys.Lett. B*, **120**, 133
- Aoyama, S., & Suzuki, T. K. 2015, *Phys. Rev. D*, **92**, 063016
- Asplund, M., Grevesse, N., & Sauval, A. J. 2005, in *Cosmic Abundances as Records of Stellar Evolution and Nucleosynthesis*, eds. T. G. Barnes, III, & F. N. Bash, *ASP Conf. Ser.*, **336**, 25
- Ayala, A., Domínguez, I., Giannotti, M., Mirizzi, A., & Straniero, O. 2014, *Phys. Rev. Lett.*, **113**, 191302
- Bagnaschi, E. A., Buchmueller, O., Cavanaugh, R., et al. 2015, *Eur. Phys. J C*, **75**, 500
- Bersten, M. C., Benvenuto, O. G., Nomoto, K., et al. 2012, *ApJ*, **757**, 31
- Bromm, V. 2013, *Rep. Prog. Phys.*, **76**, 112901
- Burrows, A., Ressel, M. T., & Turner, M. S. 1990, *Phys. Rev. D*, **42**, 3297
- Cunha, K., Hubeny, I., & Lanz, T. 2006, *ApJ*, **647**, L143
- Dearborn, D. S. P., Schramm, D. N., & Steigman, G. 1986, *Phys. Rev. Lett.*, **56**, 26
- Dessart, L., Hillier, D. J., Waldman, R., & Livne, E. 2013, *MNRAS*, **433**, 1745
- Dine, M., & Fischler, W. 1983, *Phys. Lett. B*, **120**, 137
- Dine, M., Fischler, W., & Srednicki, M. 1981, *Phys. Lett. B*, **104**, 199
- Ekström, S., Meynet, G., Chiappini, C., Hirschi, R., & Maeder, A. 2008a, *A&A*, **489**, 685
- Ekström, S., Meynet, G., & Maeder, A. 2008b, in *Massive Stars as Cosmic Engines*, eds. F. Bresolin, P. A. Crowther, & J. Puls, *IAU Symp.*, **250**, 209
- Ekström, S., Georgy, C., Eggenberger, P., et al. 2012, *A&A*, **537**, A146
- Ellis, J., & Olive, K. A. 1987, *Phys. Lett. B*, **193**, 525
- Ellis, J., Hagelin, J. S., Nanopoulos, D. V., Olive, K., & Srednicki, M. 1984, *Nucl. Phys. B*, **238**, 453
- Ertl, T., Janka, H.-T., Woosley, S. E., Sukhbold, T., & Ugliano, M. 2016, *ApJ*, **818**, 124
- Friedland, A., Giannotti, M., & Wise, M. 2013, *Phys. Rev. Lett.*, **110**, 061101
- Goldberg, H. 1983, *Phys. Rev. Lett.*, **50**, 1419
- Heger, A., & Woosley, S. E. 2002, *ApJ*, **567**, 532
- Keil, W., Janka, H.-T., Schramm, D. N., et al. 1997, *Phys. Rev. D*, **56**, 2419
- Itoh, N., Adachi, T., Nakagawa, M., Kohyama, Y., & Munakata, H. 1989, *ApJ*, **339**, 354
- Itoh, N., Hayashi, H., Nishikawa, A., & Kohyama, Y. 1996, *ApJS*, **102**, 411
- Kawasaki, M., & Nakayama, K. 2013, *Ann. Rev. Nucl. Part. Sci.*, **63**, 69
- Kim, J. E. 1979, *Phys. Rev. Lett.*, **43**, 103
- Kippenhahn, R., & Weigert, A. 1990, *Stellar Structure and Evolution* (Springer-Verlag)
- Lodders, K. 2003, *ApJ*, **591**, 1220
- Maeder, A., & Meynet, G. 2001, *A&A*, **373**, 555
- Marigo, P., Chiosi, C., & Kudritzki, R.-P. 2003, *A&A*, **399**, 617
- Marsh, D. J. E. 2016, *Phys. Rep.*, **643**, 1
- Mayle, R., Wilson, J. R., Ellis, J., et al. 1988, *Phys. Lett. B*, **203**, 188
- Mayle, R., Wilson, J. R., Ellis, J., et al. 1989, *Phys. Lett. B*, **219**, 515
- Morozova, V., Piro, A. L., Renzo, M., & Ott, C. D. 2016, *ApJ*, **829**, 109
- Nakar, E., & Sari, R. 2010, *ApJ*, **725**, 904
- Peccei, R. D., & Quinn, H. R. 1977a, *Phys. Rev. D*, **16**, 1791
- Peccei, R. D., & Quinn, H. R. 1977b, *Phys. Rev. Lett.*, **38**, 1440
- Preskill, J., Wise, M. B., & Wilczek, F. 1983, *Phys. Lett. B*, **120**, 127
- Primakoff, H. 1951, *Phys. Rev.*, **81**, 899
- Raffelt, G. G. 1986, *Phys. Rev. D*, **33**, 897
- Raffelt, G. G. 1990, *Phys. Rep.*, **198**, 1
- Raffelt, G. G. 2008, in *Axions, Lecture Notes in Physics* (Berlin: Springer Verlag), eds. M. Kuster, G. Raffelt, & B. Beltrán, **51**, 741
- Raffelt, G. G., & Dearborn, D. S. P. 1987, *Phys. Rev. D*, **36**, 2211
- Raffelt, G., & Seckel, D. 1988, *Phys. Rev. Lett.*, **60**, 1793
- Raffelt, G., & Seckel, D. 1991, *Phys. Rev. Lett.*, **67**, 2605
- Raffelt, G., & Weiss, A. 1995, *Phys. Rev. D*, **51**, 1495
- Shifman, M. A., Vainshtein, A. I., & Zakharov, V. I. 1980, *Nucl. Phys. B*, **166**, 493
- Sukhbold, T., Ertl, T., Woosley, S. E., Brown, J. M., & Janka, H.-T. 2016, *ApJ*, **821**, 38
- Vink, J. S., de Koter, A., & Lamers, H. J. G. L. M. 2001, *A&A*, **369**, 574
- Walmswell, J. J., Tout, C. A., & Eldridge, J. J. 2015, *MNRAS*, **447**, 2951
- Weinberg, S. 1978, *Phys. Rev. Lett.*, **40**, 223
- Wilczek, F. 1978, *Phys. Rev. Lett.*, **40**, 279
- Woosley, S. E. 2017, *ApJ*, **836**, 244
- Zhitnitskii, A. P. 1980, *Sov. J. Nucl. Phys.*, **31**, 260

Appendix A

The energy loss rate is given by Eq. (3) of Friedland et al. (2013) and has the form

$$\epsilon_{\text{ax}} = K g_{10}^2 T_8^7 \rho_3^{-1} Z(\xi^2), \quad (\text{A.1})$$

where the function $Z(\xi^2)$ is identical to $\xi^2 f(\xi^2)$ in Eq. (3). However, the numerical value of the constant K was found to be incorrect ($K \neq 27.2$) in Friedland et al. (2013). Indeed, starting from Eq. (3) and inserting the correct constants to obtain the proper dimensions, we obtain

$$\epsilon_{\text{ax}} = c \frac{g_{\text{ay}}^2 (k_B T)^7}{(\hbar c)^4 4\pi^2 \rho} \xi^2 f(\xi^2). \quad (\text{A.2})$$

For $g_{\text{ay}} = 10^{-10} \text{ GeV}^{-1}$, $T = 10^8 \text{ K}$, $\rho = 10^3 \text{ g/cm}^3$, and using $k_B = 8.617343 \times 10^{-14} \text{ GeV/K}$, $\hbar c = 197.326968 \times 10^{-16} \text{ GeV cm}$, $c = 299792458 \times 10^2 \text{ cm/s}$ and $1 \text{ GeV} = 1.60217653 \times 10^{-3} \text{ erg}$, we obtain the correct value, namely $K = 283.16 \text{ erg/g/s}$. It is a factor of 10 higher than in Aoyama & Suzuki (2015) and Friedland et al. (2013) because of a propagated typo. We confirmed that calculations by Aoyama & Suzuki (2015) were made with the incorrect value and need to be re-calculated. Our value is also consistent with Fig. 8.6 in Raffelt's review (Raffelt 1990).

Nevertheless, since Friedland et al. (2013) provided the energy loss (neutrinos plus axions) subroutine used in their MESA calculations, we analysed their modified MESA subroutine¹ to check whether they used the correct formula. Combining Eqs. (4) and (5), we obtain for ξ^2 (axioncsi in their code)

$$\xi^2 = \pi \alpha \left(\frac{\hbar c}{k_B T} \right)^3 N_A \rho \sum_i Y_i Z_i^2, \quad (\text{A.3})$$

where Y_i are the molar fractions $Y = X/A$ (mole/g). If T and ρ are in K and g/cm^3 , this leads to

$$\xi^2 = 1.65769 \times 10^{20} \frac{\rho}{T^3} \sum_i Y_i Z_i^2, \quad (\text{A.4})$$

with the numerical factor in agreement with Friedland's code,

$$\text{axioncsi} = 1.658d20 * \text{axionz2ye} * \text{Rho} / T^{**3}.$$

Combining Eq. (A.2) and (A.3), we obtain

$$\epsilon_{\text{ax}} = \alpha \frac{g_{\text{ay}}^2 (k_B T)^4}{4\pi \hbar} N_A f(\xi^2) \sum_i Y_i Z_i^2. \quad (\text{A.5})$$

This is equivalent to Eq. (3), without the artificial ρ dependence, now only present in $f(\xi^2)$. With T in K, it gives

$$\epsilon_a = 4.694 \times 10^{-31} f(\xi^2) g_{10}^2 T^4 \sum_i Y_i Z_i^2 (\text{erg/g/s}), \quad (\text{A.6})$$

again with a numerical factor in agreement with Friedland's code,

$$4.66d-31 * \text{axionz2ye} * \text{faxioncsi} * \text{axion_g10}^{**2} * T^{**4}.$$

For a homogeneous composition ($\frac{d}{Z}X$), the sum appearing in these equations $\sum_i Y_i Z_i^2$ is just equal to $Z/A + Z^2/A$, where the first and second term corresponds to the electron and ion contribution, respectively. This gives a factor of e.g. 2 for pure ^1H or $3/2$ for pure ^4He . However, Friedland et al. (2013) used for this sum

$$\begin{aligned} \text{ye} &= \text{zbar} * \text{abari} \\ \text{axionz2ye} &= \text{z2bar} + \text{ye}, \end{aligned}$$

which translates into $\bar{Z}^2 + \bar{Z}/\bar{A}$ (Mads Soerensen priv. comm.). The sum would then be calculated incorrectly, e.g. $4+2/4$ instead of $6/4$ for pure ^4He , i.e. a factor of 3 difference, which will increase during subsequent burning phases.

¹ <http://alexfriedland.com/papers/axion/>

Pre-supernova mixing in CEMP-no source stars

Arthur Choplin¹, Sylvia Ekström¹, Georges Meynet¹, André Maeder¹, Cyril Georgy¹, and Raphael Hirschi^{2,3,4}

¹ Geneva Observatory, University of Geneva, Maillettes 51, 1290 Sauverny, Switzerland

e-mail: arthur.choplin@unige.ch

² Astrophysics Group, Lennard-Jones Labs 2.09, Keele University, ST5 5BG, Staffordshire, UK

³ Kavli Institute for the Physics and Mathematics of the Universe (WPI), University of Tokyo, 5-1-5 Kashiwanoha, 277-8583 Kashiwa, Japan

⁴ UK Network for Bridging the Disciplines of Galactic Chemical Evolution (BRIDGCE), UK

Received 2 December 2016 / Accepted 26 May 2017

ABSTRACT

Context. CEMP-no stars are long-lived low-mass stars with a very low iron content, overabundances of carbon and no or minor signs for the presence of s- or r-elements. Although their origin is still a matter of debate, they are often considered as being made of a material ejected by a previous stellar generation (source stars).

Aims. We place constraints on the source stars from the observed abundance data of CEMP-no stars.

Methods. We computed source star models of 20, 32, and 60 M_{\odot} at $Z = 10^{-5}$ with and without fast rotation. For each model we also computed a case with a late mixing event occurring between the hydrogen and helium-burning shell ~ 200 yr before the end of the evolution. This creates a partially CNO-processed zone in the source star. We use the $^{12}\text{C}/^{13}\text{C}$ and C/N ratios observed on CEMP-no stars to put constraints on the possible source stars (mass, late mixing or not). Then, we inspect more closely the abundance data of six CEMP-no stars and select their preferred source star(s).

Results. Four out of the six CEMP-no stars studied cannot be explained without the late mixing process in the source star. Two of them show nucleosynthetic signatures of a progressive mixing (due e.g. to rotation) in the source star. We also show that a 20 M_{\odot} source star is preferred compared to one of 60 M_{\odot} and that likely only the outer layers of the source stars were expelled to reproduce the observed $^{12}\text{C}/^{13}\text{C}$.

Conclusions. The results suggest that (1) a late mixing process could operate in some source stars; (2) a progressive mixing, possibly achieved by fast rotation, is at work in several source stars; (3) $\sim 20 M_{\odot}$ source stars are preferred compared to $\sim 60 M_{\odot}$ ones; and (4) the source star might have preferentially experienced a low energetic supernova with large fallback.

Key words. stars: abundances – stars: massive – stars: chemically peculiar – nuclear reactions, nucleosynthesis, abundances – stars: interiors

1. Introduction

Carbon-enhanced metal-poor (CEMP) stars belong to the class of iron-deficient stars, and present an excess of carbon compared to the classical metal-poor stars (we refer to [Frebel & Norris 2015](#), for a recent review of metal-poor stars). The CEMP frequency rises as $[\text{Fe}/\text{H}]$ decreases, with increasing distance from the Galactic plane and when moving from the inner to outer halo ([Frebel et al. 2006](#); [Carollo et al. 2012](#); [Lee et al. 2013](#)). The two criteria defining a CEMP star are $[\text{Fe}/\text{H}] < -1.0$ and $[\text{C}/\text{Fe}] > 0.7$ ([Aoki et al. 2007](#)). Based on the amounts in s- and r-elements, a division of the CEMP class in four categories was made by [Beers & Christlieb \(2005\)](#). CEMP-s stars have their surface enriched in s-elements synthesised thanks to the slow neutron-capture process. The main scenario explaining the peculiar abundances observed at the surface of the CEMP-s stars is the binary mass transfer scenario ([Bisterzo et al. 2010](#); [Lugaro et al. 2012](#); [Abate et al. 2015](#)), supported by radial velocity detection of a companion for most of these objects ([Lucatello et al. 2005](#); [Starkenburg et al. 2014](#)). However, the binary frequency of the CEMP-s stars does not seem to reach 100% ([Hansen et al. 2016](#)) so another process

could be responsible for the formation of some CEMP-s stars. The second and third classes are the CEMP-r/s and CEMP-r (e.g. [McWilliam et al. 1995](#); [Snedden et al. 2003](#); [Goswami et al. 2006](#); [Roederer et al. 2014a](#)). Due to the correlation between the observed abundances in -s and -r/s stars, [Allen et al. \(2012\)](#) argued that the binary mass transfer scenario is also valid for CEMP-r/s stars, the r-elements being explained by a pre-existing source that polluted the molecular cloud, such as one or several Type II supernovae. The origin of the r-element-enrichment is however still largely debated. The fourth category, so-called CEMP-no (“no” for the absence of s- or r- elements), is of particular interest since it dominates at $[\text{Fe}/\text{H}] \lesssim -3$ ([Aoki 2010](#); [Norris et al. 2013](#)), allowing us to approach the primordial universe even closer. Their formation process likely differs from the one of the CEMP-s stars. Indeed, [Starkenburg et al. \(2014\)](#), using Monte Carlo simulations to constrain the binary fraction and binary period, concluded that the complete CEMP-no data set is inconsistent with the binary properties of the CEMP-s class. The formation scenarios for the CEMP-no stars generally assume that these stars formed from a cloud that was enriched by a previous generation of stars hereafter referred to as source stars. An assumption often made is that one CEMP-no star comes from one source star. If the CEMP-no star has not experienced mixing from its birth to now, the observed abundances at the surface are

¹ $[\text{X}/\text{Y}] = \log_{10}(N_{\text{X}}/N_{\text{Y}}) - \log_{10}(N_{\text{X}\odot}/N_{\text{Y}\odot})$ with $N_{\text{X},\text{Y}}$ the number density of elements X and Y.

the same as the ones in the cloud that formed the star. There are three broad categories of models proposed to explain the CEMP-no stars.

In the “mixing and fallback” scenario (Umeda & Nomoto 2002, 2005; Tominaga et al. 2014) the sources of the peculiar abundances shown by the CEMP-no stars are faint supernovae from Population III (Pop. III) stars. The supernova is faint because part of the envelope falls back on the remnant black-hole. Some mixing in internal regions of the source star is assumed, allowing part of the inner chemical species, such as iron, to be nevertheless ejected in small quantities. The mass cut² and the mixed region are free parameters, adjusted for each CEMP-no star to reproduce the observed abundance pattern.

The “spinstar” scenario (Meynet et al. 2006, 2010; Hirschi 2007; Chiappini 2013; Maeder & Meynet 2014) states that the material constituting a CEMP-no star comes from a massive source star experiencing mass-loss and strong internal mixing, owing to an average-to-high rotation rate. In this scenario, the light elements (C to Si) come directly from the source star. The small amounts of heavier elements (e.g. Ca, Ti, Ni) have either been produced by a generation of stars preceding the source stars, or by the source star. In the latter case, a very small amount of heavy elements should be ejected. This can be achieved through the models of fall back and mixing invoked by Umeda & Nomoto (2002). In those models, small amounts of heavy elements made their path through the ejected material thanks to a mixing process assumed to occur at the time of the supernova explosion. Interestingly, the spinstar scenario, using the yields of such fast-rotating stars in the context of a chemical evolution model for the halo can reproduce many observed characteristics of the chemical composition of normal halo stars (Chiappini 2013). Thus, CEMP-no and normal halo stars might be due to the same type of stars but from different reservoirs. In the case of the CEMP-no star, the reservoir of matter from which the star forms is a pocket of matter enriched by the ejecta of one or perhaps two fast-rotating massive stars. The normal halo stars, on the other hand, would be formed from a well mixed reservoir enriched by many more stars of different generations.

The “two supernovae model” (Limongi et al. 2003) assumes that the peculiar composition of one of the CEMP-no stars, HE 0107-5240, can be explained by the concurrent pollution of two supernova events; for instance a supernova of quite low mass (about $15 M_{\odot}$) that underwent a normal explosion and a supernova of a massive enough star (about $35 M_{\odot}$) that experienced a strong fallback that locked all the carbon-oxygen core in a compact remnant.

Presently, there is no strong argument favouring one scenario over another. In this paper, we propose to further investigate the spinstar scenario. We show that if the mass-loss rates that are used in our models accurately describe reality, the chemical composition of some CEMP-no stars needs to be explained by some mixing occurring very late in the course of the evolution of the source stars, typically a few hundred years before the core collapse. This mixing would take place at the interface between the hydrogen and helium-burning shells, and is considered here in a parametric form and thus cannot be attributed to a particular physical phenomenon (convection, rotation, etc.). However, we discuss evidence for its presence on the basis of nuclear processes. An additional transport process has already been invoked in Eggenberger et al. (2016) for instance, in order to reproduce the low degree of radial differential rotation of the red

giants, revealed by asteroseismic measurements. We study here the distinct nucleosynthetic signature of four categories of models: (1) no rotation, no late mixing; (2) no rotation, late mixing; (3) rotation, no late mixing; and (4) rotation, late mixing. Then, we try to see whether or not the nucleosynthetic signatures of these models are found at the surface of the CEMP-no stars.

The physical ingredients are presented in Sect. 2. Section 3 discusses the “[C/N] – $^{12}\text{C}/^{13}\text{C}$ puzzle” that presents itself when confronting source-star models with observed CEMP-no stars. Section 4 focuses on the late mixing process as a possible solution to the problem. A parametric study of this mixing is done in Sect. 5. Section 6 highlights nucleosynthetic signatures of the different source-star models. CEMP-no stars are inspected individually in Sect. 7. A discussion and the conclusions are given in Sects. 8 and 9, respectively.

2. Ingredients of the models

We first explore six rotating and non-rotating source-star models of 20, 32, and $60 M_{\odot}$. The metallicity is set to $Z = 10^{-5}$ ($[\text{Fe}/\text{H}] = -3.8$) and the initial rotation rate, V/V_{crit}^3 , is either 0 or 0.7.

The initial composition of metals (elements heavier than helium⁴) is α -enhanced. In this case, ^{12}C , ^{16}O , ^{20}Ne and ^{24}Mg are enhanced relative to iron (for more details, we refer to Sect. 2.1 of Frischknecht et al. 2016). The initial mixture at such a very low metallicity is poorly known. We take here an α -enhanced mixture for all the models, as taken for the low metallicity models of Meynet et al. (2006), Hirschi (2007) or Frischknecht et al. (2016) for example. Other initial mixtures cannot be excluded: The chemical heterogeneity of the interstellar medium (ISM) at very low metallicity may lead to different metal mixtures for the source stars. However, for most of the elements considered in this work, the abundances in the ejecta of the source-star models are so different from the initial ones that they depend very weakly on the initial composition.

The opacity tables were computed with the OPAL tool⁵. They are complemented at low temperatures by the opacities from Ferguson et al. (2005). The mass-loss rates are from Kudritzki & Puls (2000) when $\log T_{\text{eff}} \geq 3.95$ and from de Jager et al. (1988) when $\log T_{\text{eff}} < 3.95$.

Among the physical ingredients needed to describe a star in differential rotation, the D_{shear} coefficient is of major importance. This diffusion coefficient intervenes in the diffusion equation for the transport of chemical elements in the differentially rotating layers. The D_{shear} coefficient used in the present models is from Talon & Zahn (1997). It is expressed as:

$$D_{\text{shear}} = f_{\text{energy}} \frac{H_p}{g\delta} \frac{K + D_h}{\left[\frac{\varphi}{\delta} \nabla_{\mu} \left(1 + \frac{K}{D_h} \right) + \nabla_{\text{ad}} - \nabla_{\text{rad}} \right]} \left(\frac{9\pi}{32} \Omega \frac{d \ln \Omega}{d \ln r} \right)^2, \quad (1)$$

³ V_{crit} is the velocity at the equator at which the gravitational acceleration is exactly compensated by the centrifugal force (see Maeder & Meynet 2000).

⁴ The initial helium mass fraction Y is calculated according to the relation $Y = Y_p + \Delta Y/\Delta Z \times Z$ where Z is the metallicity, Y_p the primordial helium abundance and $\Delta Y/\Delta Z = (Y_{\odot} - Y_p)/Z_{\odot}$ the average slope of the helium-to-metal enrichment law. We set $Y_p = 0.248$, according to Cyburt et al. (2003). We use $Z_{\odot} = 0.014$ and $Y_{\odot} = 0.266$ as in Ekström et al. (2012), derived from Asplund et al. (2005). The initial helium mass fraction calculated, the initial mass fraction of hydrogen is then deduced from $1 - Y - Z = 0.752$.

⁵ <http://opalopacity.llnl.gov>

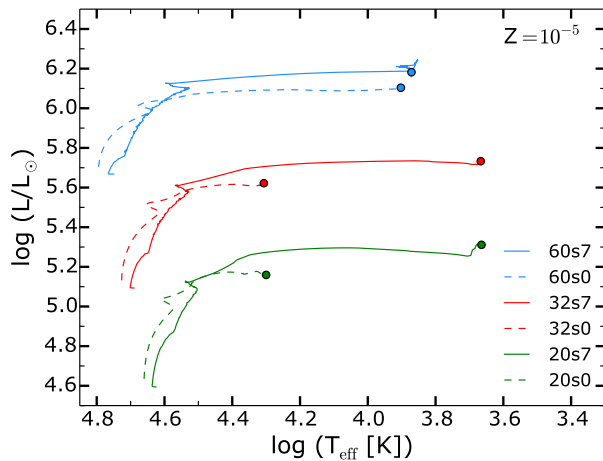
² The mass cut delimits the part of the star that is expelled from the part that is locked into the remnant.

A. Choplin et al.: Pre-supernova mixing in CEMP-no source stars

Table 1. Properties of source-star models.

Model	M_{ini} [M_{\odot}]	$V_{\text{ini}}/V_{\text{crit}}$	$\Omega_{\text{ini}}/\Omega_{\text{crit}}$	$V_{\text{eq,ini}}$ [km s^{-1}]	Initial composition	τ_{life} [Myr]	τ_{MS} [Myr]	τ_{He} [Myr]	τ_{C} [yr]	τ_{Ne} [day]	τ_{O} [day]	τ_{Si} [day]	M_{MS} [M_{\odot}]	M_{He} [M_{\odot}]	M_{final} [M_{\odot}]
No rotation															
20s0	20	0	0	0	α -enhanced	8.93	8.02	0.79	978	168	318	3.1	19.99	19.98	19.98
32s0	32	0	0	0	α -enhanced	5.78	5.24	0.48	124	22	47	0.6	31.97	31.94	31.94
60s0	60	0	0	0	α -enhanced	3.81	3.44	0.33	15	7	7	0.5	59.87	59.81	59.80
Rotation															
20s7	20	0.7	0.88	610	α -enhanced	11.0	10.1	0.76	400	277	128	1.4	19.84	19.84	19.50
32s7	32	0.7	0.88	680	α -enhanced	7.14	6.61	0.47	45	7	15	0.6	31.48	31.42	30.71
60s7	60	0.7	0.88	770	α -enhanced	4.69	4.33	0.32	5	1	3	0.2	58.47	47.97	47.65

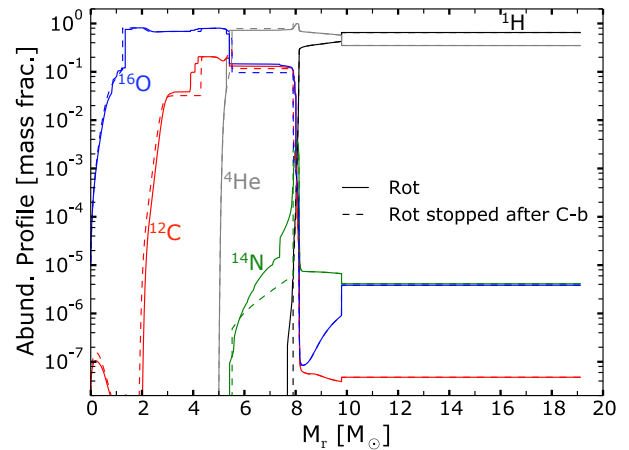
Notes. The table includes: model name (Col. 1) initial mass (Col. 2), $V_{\text{ini}}/V_{\text{crit}}$ (Col. 3), $\Omega_{\text{ini}}/\Omega_{\text{crit}}$ (Col. 4), initial equatorial velocity (Col. 5), initial composition (Col. 6), total lifetime of the MS, helium, carbon, neon, oxygen, and silicon-burning phases (Cols. 7–13), mass of the model at the end of MS, helium-burning phase, and at the end of evolution (Cols. 14–16).

**Fig. 1.** Tracks of the models of Table 1 in the Hertzsprung-Russell diagram.

where $K = \frac{4ac}{3k} \frac{T^4 \nabla_{\text{ad}}}{\rho P \delta}$ is the thermal diffusivity, D_h the diffusion coefficient for horizontal turbulence taken from Zahn (1992), and f_{energy} the fraction of the excess energy in the shear that contributes to mixing (taken equal to 1).

We took the nuclear rates used in the Geneva grids (see e.g. Ekström et al. 2012; Georgy et al. 2013). For the CNO cycle, they are mainly from Angulo et al. (1999). Almost all the rates related to the Ne-Na Mg-Al chains are from Hale et al. (2002). Only $^{20}\text{Ne}(p, \gamma)^{21}\text{Na}$ and $^{21}\text{Ne}(p, \gamma)^{22}\text{Na}$ are taken from Angulo et al. (1999) and Iliadis et al. (2001), respectively. We have also taken into account our previous study where it is shown that the aluminum range observed in CEMP-no stars is either rather well reproduced or overestimated, depending on the nuclear rates used for the reactions involving ^{27}Al (Choplin et al. 2016). Following this study, we took the rate of Angulo et al. (1999) for $^{26}\text{Mg}(p, \gamma)^{27}\text{Al}$ and the rates of Cyburt et al. (2010) for $^{27}\text{Al}(p, \gamma)^{28}\text{Si}$ and $^{27}\text{Al}(p, \alpha)^{24}\text{Mg}$. Those rates favour a low synthesis of ^{27}Al in the hydrogen-burning shell, that is likely needed to reproduce the observed aluminium distribution.

The evolutionary tracks of the six models of Table 1 are shown in Fig. 1. They are computed until the end of the central silicon-burning phase, when the mass fraction of ^{28}Si in the

**Fig. 2.** Abundance profiles of the 20s7 model at the end of the oxygen-burning phase when the rotation is taken into account until the end (solid line) and when the rotation is stopped at the end of the carbon-burning phase (dashed lines).

core is less than 10^{-8} . We need a realistic pre-supernova structure of the star in order to obtain a reliable chemical composition of the supernova ejecta. As a consequence, reaching advanced stages of the evolution is an important point for the models presented in this work. The effects of rotation are taken into account in the rotating models only until the end of the carbon-burning phase, which saves a lot of computational time and leads to only very small differences in the abundance profiles (Fig. 2). This is mainly due to the fact that the duration of the last stages is short (~ 1 – 300 days, cf. Table 1) compared to the timescale of rotational mixing. Also, for most of the elements considered here, the explosive nucleosynthesis will have little impact. In that case, the final structures of the present models give a reasonable view of the chemical composition of the supernova ejecta.

2.1. The chemical composition of the ejecta

The source-star ejecta can be decomposed into wind- and supernova ejecta. The section below explains how these two types of ejecta are computed and combined together.

2.1.1. The chemical composition of the wind

As an example, let us consider the isotope ^{12}C . First, we express the total ejected mass of ^{12}C in the wind as a function of time t :

$$M_{12\text{C}}^{\text{W}}(t) = \int_0^t \dot{M}(t') X_{12\text{C}}(t') dt', \quad (2)$$

where $\dot{M}(t')$ is the mass-loss rate computed at time t' and $X_{12\text{C}}(t')$ the surface mass fraction of ^{12}C at time t' . The integrated mass fraction of ^{12}C in the wind as a function of time t is then

$$X_{12\text{C}}^{\text{W}}(t) = \frac{M_{12\text{C}}^{\text{W}}(t)}{M^{\text{W}}(t)}, \quad (3)$$

with $M^{\text{W}}(t)$ the total mass of wind ejected after a time t . It is important to note that $X_{12\text{C}}^{\text{W}}(t)$ is the mass fraction of ^{12}C in the whole wind ejected from the ZAMS ($t = 0$) to the time t . We have supposed here that the wind is homogeneously mixed.

2.1.2. The chemical composition of the supernova

The ejected mass of ^{12}C in the supernova as a function of the mass cut, M_{cut} , is

$$M_{12\text{C}}^{\text{SN}}(M_{\text{cut}}) = \int_{M_{\text{cut}}}^{M_{\text{fin}}} X_{12\text{C}}(M_r) dM_r, \quad (4)$$

with M_{fin} the mass of the star at the end of the evolution (see Table 1) and $X_{12\text{C}}^{\text{SN}}(M_r)$ the mass fraction of ^{12}C , at the lagrangian coordinate M_r , at the end of evolution. $M_{12\text{C}}^{\text{SN}}(M_{\text{cut}})$ corresponds to the mass of ^{12}C in the part of the star that is expelled (layers between M_{cut} and M_{fin}).

2.1.3. The chemical composition in the wind and supernova combined

To obtain the chemical composition in the wind and supernova ejecta combined, we add the material ejected through the wind to the material ejected through the supernova. The mass fraction of ^{12}C in the ejected material as a function of M_{cut} is finally:

$$X_{12\text{C}}^{\text{W+SN}}(M_{\text{cut}}) = \frac{M_{12\text{C}}^{\text{W}}(\tau_{\text{life}}) + M_{12\text{C}}^{\text{SN}}(M_{\text{cut}})}{M^{\text{W}}(\tau_{\text{life}}) + M^{\text{SN}}(M_{\text{cut}})}, \quad (5)$$

where $M_{12\text{C}}^{\text{W}}(\tau_{\text{life}})$ is computed according to Eq. (2), τ_{life} is the lifetime of the star (see Table 1), and $M^{\text{W}}(\tau_{\text{life}}) + M^{\text{SN}}(M_{\text{cut}})$ represents the total ejected mass.

3. The [C/N] – $^{12}\text{C}/^{13}\text{C}$ puzzle

In the present section, the models of Table 1 are discussed. We mainly focus on the [C/N] and $^{12}\text{C}/^{13}\text{C}$ ratios, that provide interesting constraints on the possible CEMP-no source stars.

3.1. Non-rotating models

Figure 3 shows the evolution in the [C/N] versus $\log(^{12}\text{C}/^{13}\text{C})$ diagram of the non-rotating models. Since there is no rotational mixing operating inside these models, the surface is not enriched in ^{13}C and ^{14}N , so the ratios in the material ejected at the end of the evolution (crosses) are the same as the ratios in the initial ISM. The three crosses are thus superimposed, so that only the

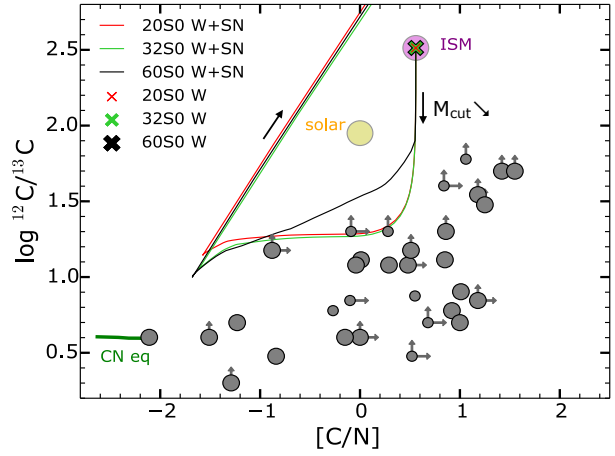


Fig. 3. [C/N] vs. $\log(^{12}\text{C}/^{13}\text{C})$ diagram. Grey circles are ratios observed at the surface of CEMP-no stars with $[\text{Fe}/\text{H}] < -2.5$, $[\text{C}/\text{Fe}] > 0.7$ and $[\text{Ba}/\text{Fe}] < 1$ (Christlieb et al. 2004; Beers et al. 2007; Johnson et al. 2007; Lai et al. 2008; Masseron et al. 2010; Allen et al. 2012; Norris et al. 2013; Spite et al. 2013; Yong et al. 2013; Cohen et al. 2013; Roederer et al. 2014c; Hansen et al. 2015). Small circles are MS stars or subgiants while large circles are bright giants. The arrows indicate that only lower limits are deduced from spectroscopy. The yellow and purple circles represent the solar ratios and the ratio in an α -enhanced ISM, respectively. The tracks represent the integrated ratios as more and more layers of the final structure are ejected and added to the wind (W+SN, effect of the mass cut, see Eq. (5)) for the 20, 32, and $60 M_{\odot}$ non-rotating models. The crosses show the ratios in the wind (W) at the end of silicon-burning (the crosses are superimposed). The thick green lines labelled “CN eq” represent the ratios obtained in a single zone at CN-equilibrium for $30 < T < 80$ MK.

black one is visible. The red, green, and black lines show the effect of the mass cut (see Eq. (5)). When varying M_{cut} inward, we reach hotter and hotter regions where the CN cycle has operated so that [C/N] and $^{12}\text{C}/^{13}\text{C}$ in the ejecta get closer to the CN equilibrium line. We note that even when the whole H-burning shell has been expelled, the ejecta is a mix between the initial ISM and the CN-processed material, so the CN equilibrium ratios are never reached. Expelling then deeper layers (where He has burnt and ^{13}C and ^{14}N have been completely depleted) strongly raises the two ratios (steep rise of the lines in Fig. 3).

3.2. Rotating models

The left panel of Fig. 4 shows the final abundance profile of the 20s7 model. The convective zone below $M_r \sim 7.5 M_{\odot}$ corresponds to the He-burning shell. During the core He-burning phase and after, the products of He-burning (mainly ^{12}C and ^{16}O) diffuse from the He-burning region to the H-burning shell. This boosts the CNO cycle in the shell and creates primary ^{13}C and ^{14}N (hence the bump around mass coordinate $8 M_{\odot}$).

Figure 5 shows that at the end of the evolution, the [C/N] and $\log(^{12}\text{C}/^{13}\text{C})$ ratios in the wind (crosses) are very close to characteristic CNO-equilibrium values (green line labelled “CN eq”). This is because during the evolution, the surface of the star is enriched in products of the CNO cycle brought from inner regions to the surface thanks to rotational mixing. This modified composition is then expelled in the wind. This point is also well illustrated by the left panel of Fig. 6, which focuses on the 20s7 model. It shows [C/N] and $\log(^{12}\text{C}/^{13}\text{C})$ ratios in the ejecta as

A. Choplin et al.: Pre-supernova mixing in CEMP-no source stars

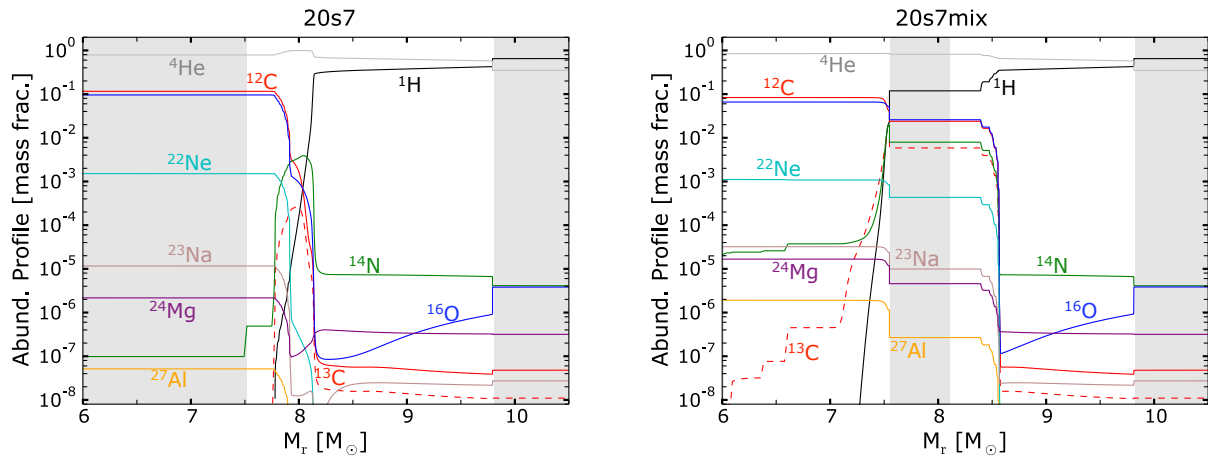


Fig. 4. Abundance profiles inside the 20s7 model at the end of the carbon-burning with no late mixing between the H- and He-burning shells (*left*) and with late mixing (*right*). Shaded areas show the convective zones.

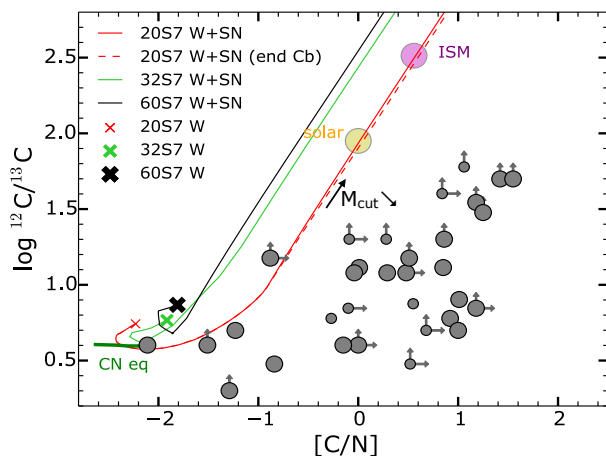


Fig. 5. Same as Fig. 3 but for rotating models. The red dashed line corresponds to the case where the evolution is stopped at the end of carbon burning instead of silicon burning for the 20s7 model. The chemical composition of the wind at the end of carbon burning and at the end of silicon burning is the same (red cross).

a function of the ejected mass. The yellow area represents the wind. The thick lines are the integrated ratios in the wind as evolution proceeds, computed according to Eq. (2). $[C/N]$ and $\log(^{12}C/^{13}C)$ decrease in the wind, reaching -2.2 and 0.7 at the end of evolution.

The thin lines in Fig. 6 show the effect of the mass cut. When only the outer layers are expelled, $[C/N]$ and $^{12}C/^{13}C$ do not change because only the hydrogen-rich envelope is ejected in this case; this is a CN-processed region, having a similar composition to the wind. As we dig deeper into the source star, we reach a region processed by He-burning (at $M_{ej} \sim 12 M_{\odot}$) so that $[C/N]$ and $^{12}C/^{13}C$ increase dramatically in the ejecta. As a complement, the red line in Fig. 5 shows how $[C/N]$ and $^{12}C/^{13}C$ are linked together when varying the mass cut for the 20s7 model. The 32s7 and 60s7 models are also shown and behave similarly to the 20s7 model.

3.3. Can a low $^{12}C/^{13}C$ with a high $[C/N]$ be reproduced by models?

The middle and right panels of Fig. 6 show the observed $^{12}C/^{13}C$ and $[C/N]$ distribution of CEMP stars with $^{6}Fe/H < -2.5$, $[C/Fe] > 0.7$ and $[Ba/Fe] < 1$. The condition on $[Ba/Fe]$ rules out the CEMP stars significantly enriched in barium, generally classified as CEMP-s, -r/s or -r stars. While the distribution of observed $\log(^{12}C/^{13}C)$ peaks close to the CN-equilibrium value of ~ 0.6 , the distribution of $[C/N]$ spans a wide range, extending largely above the CN-equilibrium value of ~ 2.3 . To reproduce the whole $[C/N]$ range, one needs to consider material coming from layers belonging both to the outer layers of the source stars and from deeper layers, having been processed by He-burning. In contrast, to reproduce the observed variations of $\log(^{12}C/^{13}C)$, no layers that have been processed by He-burning should be involved. We note that although some stars have a measured $^{12}C/^{13}C$ close to CN-equilibrium (e.g. CS22945-017 and HE0007-1832, which are MS CEMP-no with $\log(^{12}C/^{13}C) = 0.8$ and 0.9 respectively Masseron et al. 2010; Cohen et al. 2004), some others have only a lower limit, requiring some caution regarding the previous statements. Arrows mark these limits in Figs. 3 and 5. The tracks on these two figures clearly show that the ejecta of the six source-star models are unable to provide a solution matching the observed bulk of CEMP-no stars. We remark however that although globally out of the observed range, these models might explain some CEMP-no stars. This is discussed in more detail in Sects. 6 and 7.

An important point here is that, in any case, only the outer layers of the source stars should be ejected, otherwise the $^{12}C/^{13}C$ ratio in the ejecta is largely above the bulk of observed values. This being said, the difficulty remains of having a high C/N at the same time in the ejecta.

At this point, we think that two important points need to be addressed regarding $^{12}C/^{13}C$: (1) can the source star ejecta be diluted with the ISM in such a way that the $^{12}C/^{13}C$ ratio is reduced? (2) Can the CEMP-no stars themselves have modified their surface composition?

⁶ In this plot, some CEMP-no stars have a different $[Fe/H]$ than the one of the models (about -3.8). We think that this is not a problem since we are looking at isotope ratios; the CNO equilibrium value of $^{12}C/^{13}C$ does not vary with metallicity for instance.

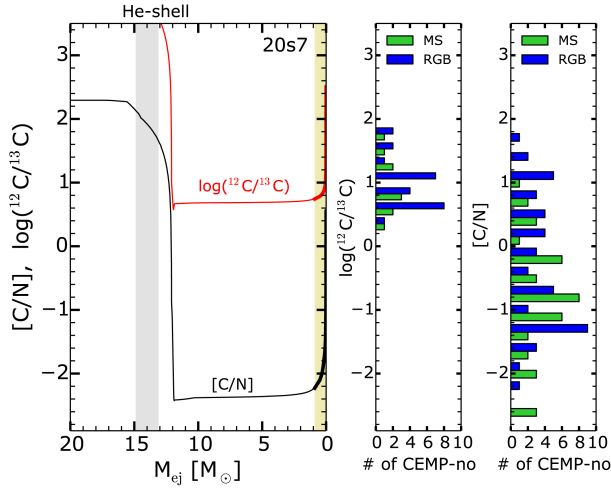


Fig. 6. *Left:* $[C/N]$ and $\log(^{12}C/^{13}C)$ in the ejecta as a function of the ejected mass for the 20s7 model. The thick lines in the yellow zone represent the integrated ratios in the wind (Eq. (2)) as a function of $M_{\text{ej}}^W = \int_0^t \dot{M}(t') dt'$. The thin lines show the integrated ratios in the ejecta (Eq. (5)) as a function of $M_{\text{ej}}^{W+SN} = M_{\text{ini}} - M_{\text{cut}}$. The grey shaded area shows the location of the He-burning shell (where the energy produced by He-burning $\epsilon_{\text{He}} > 10^3 \text{ erg g}^{-1} \text{ s}^{-1}$) at the end of the evolution. *Middle and right:* distribution of observed $\log(^{12}C/^{13}C)$ and $[C/N]$ for the CEMP-no stars with $[\text{Fe}/\text{H}] < -2.5$, $[\text{C}/\text{Fe}] > 0.7$ and $[\text{Ba}/\text{Fe}] < 1$ (Cohen et al. 2004, 2013; Honda et al. 2004; Christlieb et al. 2004; Sivarani et al. 2006; Beers et al. 2007; Johnson et al. 2007; Lai et al. 2008; Masseron et al. 2010; Caffau et al. 2011; Allen et al. 2012; Norris et al. 2012, 2013; Yong et al. 2013; Spite et al. 2013; Placco et al. 2014a; Roederer et al. 2014b,c; Hansen et al. 2014, 2015). The green histogram represents the MS stars or subgiants close to the turnoff with $T_{\text{eff}} > 5500 \text{ K}$ and $\log g \geq 3.25$, as by Norris et al. (2013). The blue histogram shows the other stars.

3.4. Dilution with the interstellar medium

Let us consider that the source star could have expelled a material with a high $^{12}C/^{13}C$ ratio that would afterwards be diluted with the ISM, having a lower $^{12}C/^{13}C$ ratio. The values of the $\log(^{12}C/^{13}C)$ ratio for a solar and α -enhanced ISM are about 2.5 and 2 respectively (see purple and yellow circles in Fig. 5). The dilution of a material with a high $^{12}C/^{13}C$ ratio coming from the source star with the ISM can lead to $\log(^{12}C/^{13}C)$ values of 2.5 and 2 at best, respectively. Relying on such an ISM, the dilution cannot likely be a solution. Of course, the composition of the ISM at such low metallicity is barely known and might be different. With chemical evolution models, Chiappini et al. (2008) have shown that if fast rotators were dominant in the early universe, the $\log(^{12}C/^{13}C)$ ratio would lay between 1.5 and 2.5 in the ISM. This is still above the bulk of the $\log(^{12}C/^{13}C)$ distribution of CEMP-no stars. Considering an even lower $^{12}C/^{13}C$ ratio in the ISM might be a solution. However, in that case, we think that this would simply push the problem further: where do such low $^{12}C/^{13}C$ ratios come from?

3.5. In situ modification of CEMP-no stars

The CEMP-no stars could have changed their surface abundances because of internal processes. In that case, the comparison between their surface abundances and the material ejected by

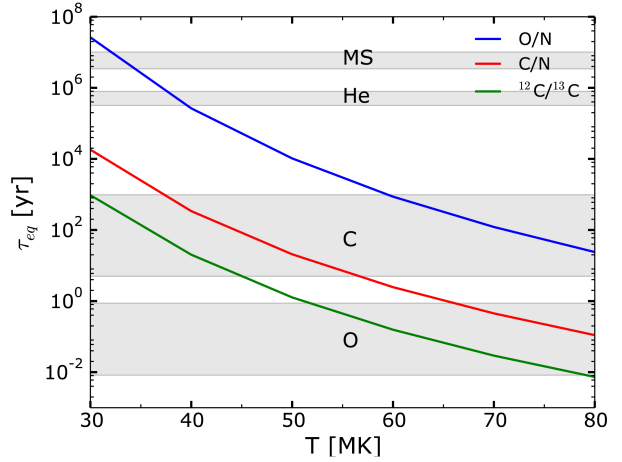


Fig. 7. Equilibrium timescales of O/N, C/N, and $^{12}C/^{13}C$ as a function of the temperature. We used a one zone model at density $\rho = 1 \text{ g cm}^{-3}$. The shaded areas show the ranges of duration for the various burning stages (main sequence, He-, C-, and O-burning) of the models presented in Table 1.

the source star is more difficult. The two main processes known are (1) atomic diffusion and (2) the first dredge up. The atomic diffusion comprises different processes like gravitational settling and radiative acceleration. Since CEMP-no stars are old, these processes may have had time to change their surface composition. However, the $^{12}C/^{13}C$ ratio is barely affected by gravitational settling or by radiative acceleration since the two isotopes have similar weights and electronic transitions. Atomic diffusion in a more general context is discussed in Sect. 7.

The first dredge up, occurring after the main sequence, brings internal material up to the surface of the CEMP-no star. As this material comes from hotter regions, where the CN cycle is likely operating, it is enriched in ^{14}N and ^{13}C and depleted in ^{12}C . As a consequence, the dredge up is expected to decrease the surface $[C/N]$ and $^{12}C/^{13}C$ ratios. We note that the ON branch is likely not activated because of the overly low temperature in these low-mass stars. It is particularly interesting to compare the $[C/N]$ and $^{12}C/^{13}C$ ratios of the MS sample with the RGB sample. A possible guess based on the previous discussion is that the RGB stars should present lower $[C/N]$ and $^{12}C/^{13}C$ ratios than MS stars due to the effect of the first dredge up. The green histograms in Fig. 6 show MS stars or subgiants close to the turnoff. The blue histograms show the other stars, classified as RGB. We see that for both $[C/N]$ and $^{12}C/^{13}C$, the MS sample covers the same range of values as the RGB sample. This shows that the effect of the first dredge up is probably small compared to the effect of the observed dispersion of the $[C/N]$ and $^{12}C/^{13}C$ ratios. Should it be a strong effect, we would see a clear separation between MS and RGB stars.

This discussion shows that most likely the abundances that are observed at the surface of CEMP-no stars do not result from in situ processes but reflect indeed the composition of the cloud from which they formed.

3.6. A partially CN-processed material?

We have seen above that the present source star models cannot reproduce the CEMP-no stars showing simultaneously values of the $^{12}C/^{13}C$ ratio typical of the CNO equilibrium and C/N ratios

A. Choplin et al.: Pre-supernova mixing in CEMP-no source stars

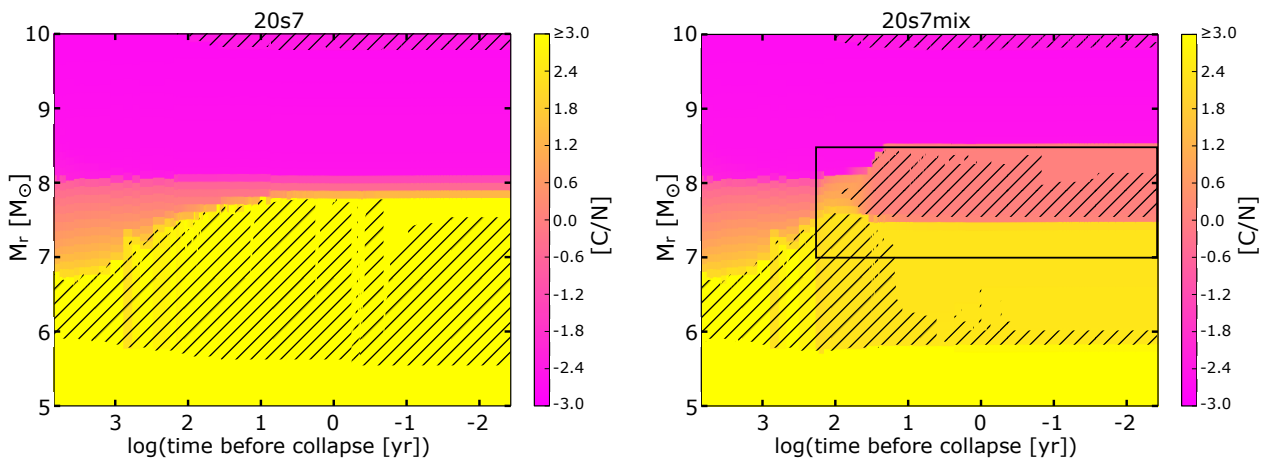


Fig. 8. Evolution of the structure as a function of the time left until the core collapse (Kippenhahn diagram) for the 20s7 model without (*left*) and with (*right*) late mixing. The colour-scale shows the value of $[C/N]$ inside the star. Hatched areas represent the convective zones. The black frame on the *right panel* indicates where and when the mixing is enhanced.

above the CNO equilibrium value. We propose here a possible solution to the $C/N - {}^{12}C/{}^{13}C$ puzzle.

Figure 7 shows the equilibrium timescales of the C/N (red) and ${}^{12}C/{}^{13}C$ (green) ratios as a function of the temperature. O/N is also shown for comparison. We used a one-zone model at constant temperature and density. We considered temperatures ranging from 30 to 80 MK. The timescales are taken when the ratios in the zone are equal to 99% of their equilibrium value. When the temperature increases, the ratios reach the equilibrium value more quickly. From 30 to 80 MK, the timescales decrease by ~ 4 – 5 orders of magnitude. Also, whatever the temperature, ${}^{12}C/{}^{13}C$ reaches the equilibrium approximately ten times faster than C/N , and C/N reaches the equilibrium approximately 100–1000 times faster than O/N .

In a massive and low-metallicity source-star model, the zone where the H is burning (core or shell) can be convective. In that case, the material is assumed to be mixed instantaneously. Each mesh point in this H-burning zone has a different temperature (between ~ 30 and ~ 80 MK), hence a different equilibrium timescale. However, since the equilibrium timescales change monotonically with the temperature, the global equilibrium timescales in the convective H-burning zone are bound between the timescales at 30 and 80 MK. Also, the relative difference between these three global equilibrium timescales remains the same as the difference shown in Fig. 7.

Let us now consider that some ${}^{12}C$ is injected into the convective H-burning shell which is initially at CNO equilibrium. We consider that the global equilibrium timescales of this shell correspond to the timescales at 40 MK (~ 30 yr for ${}^{12}C/{}^{13}C$, ~ 300 yr for C/N , see Fig. 7). After a length of time of between ~ 30 and ~ 300 yr, the ${}^{12}C/{}^{13}C$ will be at equilibrium while the C/N will not. Thus we see that if the injection of ${}^{12}C$ occurs less than ~ 300 yr before the core collapse, we would have some part of the star with a chemical composition potentially resolving the $C/N - {}^{12}C/{}^{13}C$ puzzle. From Fig. 7, we can deduce that this injection should occur after the core He-burning phase, during the C or O-burning phase (in our models, C burning lasts for 10–1000 yr for instance). The injection of ${}^{12}C$ can occur if a mixing event happens between the H- and He-burning regions. The mixing event should be strong enough so that sufficient ${}^{12}C$ is injected. If not, the CNO cycle quickly returns to equilibrium.

Mixing naturally happens in our rotating models but remains mild enough so that C/N and ${}^{12}C/{}^{13}C$ in the hydrogen shell are at CNO equilibrium at the end of evolution. A stronger injection of ${}^{12}C$ in the hydrogen shell is needed to boost the CNO cycle more and leave an excess of ${}^{12}C$ with respect to ${}^{14}N$ at the end of evolution. We have explored the consequences of this idea by considering such late mixing episodes in our stellar models.

4. A late and strong mixing process in source stars

4.1. The recipe

For the six models of Table 1, we have triggered a late mixing event ~ 200 yr before the end of the core C burning phase. The end of this phase is defined such that $X({}^{12}C)_c$, the central mass fraction of ${}^{12}C$ is equal to 10^{-5} . From Table 1, we know that the duration of core C burning can be shorter than 200 yr. In such cases, the late mixing begins before the C starts to burn but still after the core He-burning phase. Late mixing is only operating in radiative zones and is triggered around the bottom of the H-burning shell. To model this late mixing process in rotating models, we multiply the D_{shear} coefficient (Eq. (1)) by a factor of 100. Non-rotating models are also studied to see whether or not the effect of the late mixing alone might be sufficient to explain the abundances observed at the surface of CEMP-no stars. In those models, we set $D_{\text{shear}} = 10^9 \text{ cm s}^{-1}$ in the late mixing zone, a characteristic value found in rotating models with late mixing. These new models⁷ are identified with “mix” (20s0mix, 32s0mix...). Although modelled with a shear diffusion coefficient, we do not assume that the physical origin of the late mixing process is linked to the shear. Its possible physical origin is discussed in Sect. 8.2. Also, a parametric study of this late mixing is done in Sect. 5.

4.2. Late mixing in the 20s7 model

Figure 8 shows a Kippenhahn diagram of the 20s7 (left panel) and 20s7mix (right panel) models. Only the post core

⁷ These new models do not appear in Table 1. They have the same properties as the models without late mixing, shown in Table 1. Only the duration of the C-burning phase changes slightly.

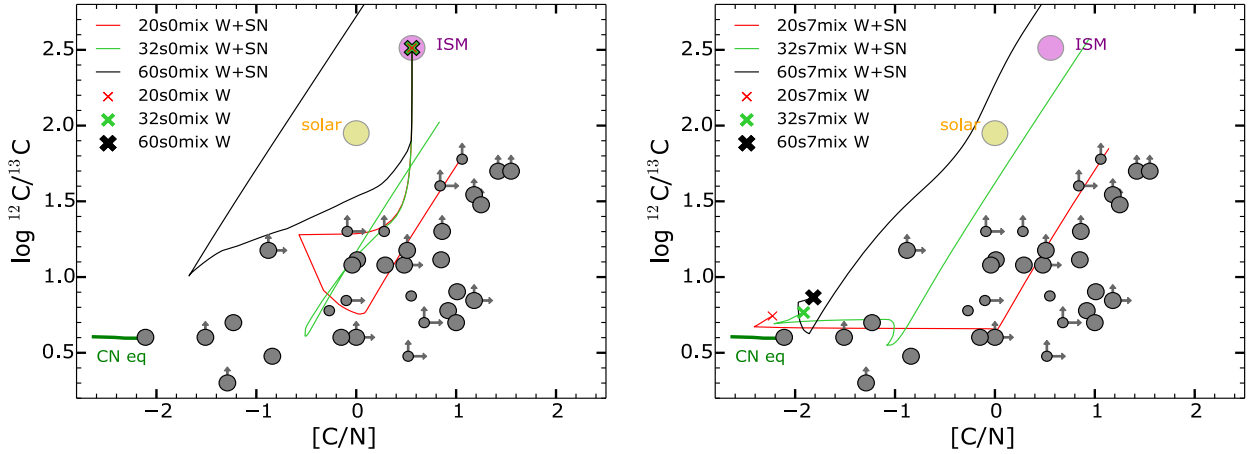


Fig. 9. As in Figs. 3 and 5 but for the models with late mixing (see Sect. 4.1 for explanation). The endpoint of the lines correspond to a mass cut located at the bottom of the He-burning shell. *Left panel:* non-rotating models; *right panel:* rotating models.

He-burning stage is shown, where there is both a He-burning and a H-burning shell. On the left panel, the convective zone between ~ 6 and $8 M_{\odot}$ (hatched area) corresponds to the He shell. On the right panel, the lower convective zone corresponds to the He shell and the upper one, appearing at the abscissa ~ 1.6 , corresponds to the H shell. The black frame shows the region in space and time where the mixing is enhanced.

Without late mixing, the mixing is mild enough so that not too much ^{12}C diffuses from the He-burning shell to the H-burning shell. As a consequence, the CNO cycle is not very active and at the end of the evolution, we distinguish (1) a zone with a high $[\text{C}/\text{N}]$ where He-burning has destroyed ^{14}N (yellow zone) and (2) a zone with $[\text{C}/\text{N}]$ at CNO-equilibrium (magenta zone).

With late mixing, more ^{12}C enters the H shell, boosting the CNO cycle. The H shell becomes convective and more He-burning products are engulfed. The fresh C starts to be transformed into ^{13}C and ^{14}N in the H shell. However, the time remaining before the end of the evolution being short, the $[\text{C}/\text{N}]$ equilibrium value of ~ 2.3 is not reached. The right panel of Fig. 4 shows the abundance profile of the 20s7mix model at the end of core C-burning. We clearly see the convective H shell with a lot of CNO elements, and where $X(\text{C})/X(\text{N}) > 1$ while $X(^{12}\text{C})/X(^{13}\text{C})$ is at equilibrium, around 5. The right panel of Fig. 8 shows this intermediate zone where $[\text{C}/\text{N}]$ is about 0 at the end of evolution. The late mixing process is then able, for the rotating $20 M_{\odot}$ model, to build a zone partially processed by the CNO cycle in the source star, where C/N is high and $^{12}\text{C}/^{13}\text{C}$ at equilibrium.

Figure 9 shows the same results as Figs. 3 and 5 but for the models with late mixing. The 20s7mix model is represented on the right panel by the red track. Because of the partially CN-processed zone, there now exists a solution able to better reproduce the observed $\text{C}/\text{N} - ^{12}\text{C}/^{13}\text{C}$ feature. The partially CN-processed zone for this model is characterised by $\log(^{12}\text{C}/^{13}\text{C}) \sim 0.6$ and $[\text{C}/\text{N}] \sim 0$, explaining the plateau going from $[\text{C}/\text{N}] \sim -2.5$ to ~ 0 . For the models with late mixing, we stopped the evolution at the end of the core C-burning phase. We did not compute the very end of the evolution but this would lead to only very small changes in the abundance profiles of the outer layers, above the C-burning shell (see the red solid and dashed lines in Fig. 5).

4.3. Late mixing in the other models

The right panel of Fig. 9 shows that the 32s7mix (green) and 60s7mix (black) source-star models do not behave like the 20s7mix model. This is mainly because higher-mass models have a higher temperature in the convective H shell meaning that the CN cycle is faster. In this case, ^{12}C is transformed more rapidly into ^{14}N . The $[\text{C}/\text{N}]$ ratio in the H-burning shell is then closer to the equilibrium value at the end of evolution. This explains the different lengths of the plateau in the tracks shown on the right panel of Fig. 9. The longest plateau is for the 20s7mix model (red track) that has the lowest temperature in the H-burning shell. A low temperature implies that the CN cycle has not significantly operated. This gives a high $[\text{C}/\text{N}]$ ratio at the end of the evolution. The 32s7mix plateau reaches lower $[\text{C}/\text{N}]$ ratios (about -1) because of the higher rate of the CN cycle. In the 60s7mix model, there is no plateau; the zone is at CN equilibrium at the end of the evolution because of the even higher temperature in the H-burning shell.

Triggering a late mixing in the non-rotating models also leads to this partially CNO-processed zone for the 20s0mix and 32s0mix models. For the 60s0mix model, the distance between the two shells is too large; the He-products (^{12}C and ^{16}O) do not reach the H-burning shell. The left panel of Fig. 9 shows that the 20s0mix and 32s0mix models might also yield a material able to better reproduce the observed distribution. Sect. 6 investigates how the “s0mix” and “s7mix” models can be discriminated by considering other chemical species.

An important point here is that the late mixing is more efficient in building a zone with a high C/N in the $20 M_{\odot}$ source star than in more massive models, mainly because the temperature in the H-burning shell is lower in a $20 M_{\odot}$ model, implying a slower pace of the CN cycle. The time window in which the late mixing process would give a partially CNO-processed material at the end of evolution is much longer for the $20 M_{\odot}$ source star. This makes the $20 M_{\odot}$ source stars better candidates for the late mixing scenario. We note, nevertheless, that if the late mixing occurs sufficiently late (later than ~ 200 yr before the end of the evolution), the material might be partially processed even in a $60 M_{\odot}$ source star, where the CN cycle is faster. In this case however, the mixing event should be extremely strong so as to compensate for the short time available.

A. Choplin et al.: Pre-supernova mixing in CEMP-no source stars

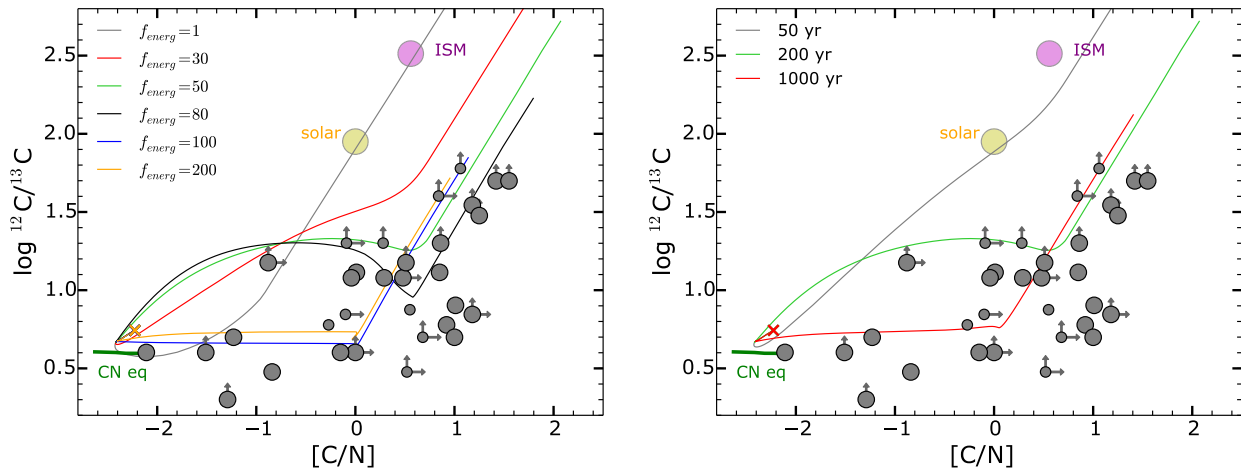


Fig. 10. As in Fig. 9 but when varying the f_{energ} parameter (see Eq. (1)) for the 20s7mix model (*left panel*) and when triggering the late mixing at different times ($\sim 50, 200$ and 1000 yr before the end of C-burning), with $f_{\text{energ}} = 50$ (*right panel*). The endpoint of the lines corresponds to a mass cut located at the bottom of the He-burning shell.

5. Varying the parameters of the late mixing event

Since the late mixing is artificially triggered, it is natural to wonder what happens if we vary the intensity of this process for instance, or if we trigger the late mixing at different times close to the end of the evolution. Changing the spatial extension of the late mixing zone is not investigated. We focus here on a rather small zone in the star, near the bottom of the hydrogen burning shell.

5.1. Intensity of the late mixing

Figure 10 (*left panel*) shows the effect of varying the intensity of the late mixing in the 20s7 model by changing the value for f_{energ} (see Eq. (1)). The late mixing is triggered ~ 200 yr before the end of evolution, using $f_{\text{energ}} = 1$ (standard case), 30, 50, 80, 100 (case discussed in the previous section), and 200. As f_{energ} increases, more and more ^{12}C enters into the H-burning shell. We see that the stronger the mixing (higher f_{energ}) the easier we reach regions of low $^{12}\text{C}/^{13}\text{C}$ and non-equilibrium C/N ratios.

Let's focus on the shape of the $f_{\text{energ}} = 80$ curve (black); it shows that four zones exist in this source-star model:

1. A CN processed zone (external layers, represented by the orange cross). This zone is similar to the region above $M_r \sim 8.6 M_{\odot}$ in the right panel of Fig. 4⁸.
2. A zone where ^{12}C is overabundant with respect to ^{13}C and ^{14}N (the curve rises).
3. A partially CN processed zone where $^{12}\text{C}/^{13}\text{C}$ decreases towards equilibrium (or closeby) and C/N is high. This zone is similar to the region between ~ 7.5 and $\sim 8.5 M_{\odot}$ in the right panel of Fig. 4.
4. A region processed by He-burning that makes the curve rise dramatically (similar to the region below $M_r \sim 7.5 M_{\odot}$ in the right panel of Fig. 4).

The bump of the black curve in this diagram is explained when we understand what happens in zones 2 and 3. Zone 2 is formed

⁸ Figure 4 actually corresponds to the $f_{\text{energ}} = 100$ model while we discuss here the $f_{\text{energ}} = 80$ model. Although slightly different, the abundance profiles of these two models show many similarities.

because some ^{12}C diffuses into regions where $T_6 \lesssim 30$ MK. At such a temperature, C/N and $^{12}\text{C}/^{13}\text{C}$ reach CNO equilibrium after $\sim 10^4$ and $\sim 10^3$ yr, respectively (see Fig. 7). This is more than the remaining time before the end of evolution so that there is a carbon excess at the end. Zone 3 corresponds to deeper (and hotter) layers that have become convective once a sufficient amount of carbon has diffused and boosted the CNO cycle. In this zone, the CNO cycle is closer to equilibrium at the end of the evolution because of the higher temperature compared to zone 2.

For the $f_{\text{energ}} = 100$ and 200 models (blue and orange curves), the zone 2 does not exist. Indeed, the convective zone that forms because of the energy released by the CNO cycle expands further out and grows in time, engulfing the zone 2. In the end, this induces sharp transitions between the CNO processed zone (orange cross), the partially CNO processed zone (around coordinates (0, 0.6) for the orange curve) and the He-processed zone (dramatic rise of the curve).

5.2. Time of the late mixing

Figure 10 (*right panel*) shows the effect of varying the time at which the mixing is triggered. For this study we set $f_{\text{energ}} = 50$. For a given f_{energ} , if the mixing is triggered too late, not enough ^{12}C diffuses into the H shell and it does not create the partially CNO processed zone (see the grey line). If it is triggered ~ 1000 yr before the end, the partially CNO processed zone is created. We see that this model (red curve) is behaving like the models with a higher f_{energ} in the left panel (blue and orange lines), illustrating that a stronger intensity for the mixing or a longer time for it to occur can have similar results.

To summarise what precedes:

- the late mixing process has to occur sufficiently late in the evolution otherwise [C/N] have enough time to go back to CN equilibrium (cf. Fig. 7);
- the partially-processed zone is more likely built in a $20 M_{\odot}$ source star than in a $60 M_{\odot}$;
- if the mixing event is triggered in a $20 M_{\odot}$ source star ~ 200 yr before the end of the evolution, the mixing has to

- be enhanced by at least a factor of 50 for the partially CNO-processed zone to be created;
- if the mixing event is triggered earlier, the same behaviour is found provided the mixing has been reduced. This would be the opposite if the mixing event was triggered later (e.g. during O-burning); the mixing has to be increased to compensate for the shorter available time before evolution ends.

For what follows, we select the cases (for each model) where the late mixing is triggered ~ 200 yr before evolution ends and with $f_{\text{energ}} = 100$.

6. Nucleosynthetic signatures of the source-star models

In this section, we highlight nucleosynthetic differences between the four categories of model computed: non rotating, rotating, non rotating with late mixing, and rotating with late mixing. Other chemical elements, such as Na, are discussed. The goal is to find a distinct nucleosynthetic signature for each category of model. It should allow to attribute a preferred source star to an observed CEMP-no star and then further test the possible scenarios (especially the late mixing scenario).

We mainly study $[X/H]$ ratios (where X is C, N, O, or Na etc.) and then use them to go further in the comparison between models and observations (cf. Sect. 8). $[X/H]$ ratios likely give the absolute amount of elements since the abundance variation of H is modest.

6.1. Non rotating models without late mixing

The outer layers of the non-rotating models without late mixing have a $[X/H]$ pattern generally close to the initial ISM pattern. They do not synthesise primary ^{13}C and ^{14}N . A low $[N/H]$ is then a signature of this class of models. Also a high $^{12}\text{C}/^{13}\text{C}$ ratio might be a signature, although this ratio can nevertheless be low in the layers of the stars where the CNO cycle has operated (see Fig. 3). Globally, however, a high $^{12}\text{C}/^{13}\text{C}$ is favoured since no primary ^{13}C is synthesised.

6.2. Rotating models without late mixing

Because of the rotational mixing that allows some exchanges of material between the H- and He-burning regions, rotating models synthesise a variety of isotopes (see e.g. Maeder & Meynet 2015; Choplin et al. 2016). Among them ^{13}C and ^{14}N are created because ^{12}C and ^{16}O diffuse from the He core to the H shell. Some primary ^{14}N is then engulfed by the He-burning region. The chain $^{14}\text{N}(\alpha, \gamma)^{18}\text{F}(\text{e}^+\nu_e)^{18}\text{O}(\alpha, \gamma)^{22}\text{Ne}$ boosts the ^{22}Ne abundance in the He core compared to the non rotating case. When rotation is sufficiently fast, some ^{22}Ne can diffuse back to the H-burning shell so that the Ne-Na cycle is boosted and some extra ^{23}Na is synthesised. We call it the *first channel* of ^{23}Na production. To a lesser extent, the Mg-Al cycle is also enhanced. Close to the end of the core He-burning phase, some ^{22}Ne in the He-burning core is transformed into ^{25}Mg and ^{26}Mg through $^{22}\text{Ne}(\alpha, n)^{25}\text{Mg}$ and $^{22}\text{Ne}(\alpha, \gamma)^{26}\text{Mg}$. At this point, only a short time is left until the end of the evolution but some Mg can still diffuse in the H shell, boosting the Mg-Al cycle so that more Al can be created. The neutrons released by $^{22}\text{Ne}(\alpha, n)^{25}\text{Mg}$ can be captured by ^{22}Ne to form ^{23}Na through $^{22}\text{Ne}(n, \gamma)^{23}\text{Ne}(\beta^-\bar{\nu}_e)^{23}\text{Na}$. We call this the *second channel* of ^{23}Na production. The ^{23}Na synthesised in this way cannot be

ejected without being accompanied by He-burning products, which would drastically increase the $^{12}\text{C}/^{13}\text{C}$ ratio, in contrast with what is observed. Also the *s*-process is boosted in the He core compared to non-rotating models. Indeed, more neutrons are released since the abundance of ^{22}Ne is higher. The s-elements could be an interesting complementary nucleosynthetic signature, likely differing between the categories of models. Although the present work focuses on lighter elements, we plan to investigate the *s*-process in the frame of the CEMP stars in a future work. To summarise, the main signatures of this category of model would be a relatively high $[N/H]$ and $[Na/H]$. In addition, a lower $^{12}\text{C}/^{13}\text{C}$ is expected compared to non-rotating models because of the synthesis of primary ^{13}C .

6.3. Non-rotating models with late mixing

These models synthesise a lot of primary ^{13}C and ^{14}N . The late mixing boosts the CNO cycle so that C, N, and O are strongly processed in the H shell but the equilibrium is not necessarily reached. The amount of primary ^{13}C and ^{14}N produced by the late mixing event is higher than the amount produced with pure rotational mixing. The other elements (especially Na, see explanation in the previous and following paragraphs) remain at lower abundances than in rotating models. The characteristic $[X/H]$ pattern for these models would be a high CNO enhancement but with few other light elements and a higher $[C/N]$ ratio than non-rotating and rotating models.

6.4. Rotating models with late mixing

As in the previous category, the CNO cycle is boosted a lot in these models. Because of the late mixing, some ^{23}Na , synthesised through the *second channel* (cf. previous discussion about rotating models), is transferred from the He-burning to the H-burning shell, so $[Na/H]$ is enhanced in the H shell. $^{12}\text{C}/^{13}\text{C}$ is low because of the late mixing that synthesises a lot of primary ^{13}C (cf. the previous category). To summarise, these models would present the same signature as the previous category but with a lot more Na.

An interesting point is that a high Na abundance can only be achieved with a progressive mixing at work during the whole evolution of the source star. This is because the source of ^{23}Na in both the H (*first channel*) and He shell (*second channel*) is ^{22}Ne , which is largely boosted if the progressive mixing operates. A natural candidate for the progressive mixing is the rotational mixing.

7. Connecting the CEMP-no with their source star(s)

Here we discuss the case of some CEMP-no stars and make an attempt to select their most likely source star(s). We investigate 20 stars having $[C/Fe] > 0.7$, $[Ba/Fe] < 1$, and $[Fe/H] = -3.8 \pm 0.3$ (see Table 2). We have selected the CEMP-no stars having a narrow range of $[Fe/H]$ so that the source-star models can be computed with only one metallicity. Since the observed $^{12}\text{C}/^{13}\text{C}$ ratios imply that only the outer regions of the source-star models should be expelled (the inner regions, and thus all the iron produced, being locked into the remnant), we use the same $[Fe/H]$ for the source stars as for the CEMP stars.

A. Choplin et al.: Pre-supernova mixing in CEMP-no source stars

Table 2. CEMP-no stars with $-3.5 < [\text{Fe}/\text{H}] < -4.1$, $[\text{C}/\text{Fe}] > 0.7$ and $[\text{Ba}/\text{Fe}] < 1$.

Star	Type	[Fe/H]	A(Li)	[C/H]	[N/H]	[O/H]	[Na/H]	[Mg/H]	[Al/H]	[Si/H]	$^{12}\text{C}/^{13}\text{C}$	Ref.
CS29498-043	RGB	-3.85	<-0.05	-1.13	-2.14	-1.48	-2.82	-2.07	-3.1	-2.77	8.0	1, 2
CS29527-015	MS	-3.55	2.07	-2.37	-	-	-3.75	-3.12	-3.5	-3.4	-	3, 4, 5, 6, 7, 8
G77-61	RGB	-4.0	<1.16	-0.8	-1.8	-2.2	-3.4	-3.51	-	-	5.0	9, 10
HE0134-1519	RGB	-3.98	1.27	-2.98	<-2.98	<-1.08	-4.22	-3.73	-4.36	-3.93	>4.0	11
HE1012-1540	RGB	-3.76	<0.75	-1.77	-3.02	<-1.76	-2.11	-1.96	-3.07	-3.2	>30.0	1, 2, 12
HE2331-7155	RGB	-3.68	<0.37	-2.34	-1.11	<-1.98	-3.22	-2.48	-4.06	-	5.0	11
HE0049-3948	RGB	-3.68	-	<-1.87	<-1.28	-	-3.76	-3.39	-	-3.69	-	13
HE0057-5959	RGB	-4.08	-	-3.22	-1.93	-	-2.1	-3.57	-	-	>2.0	13, 14
HE0228-4047	MS	-3.75	-	<-1.87	-	-	-	-3.49	-	-3.4	-	13
HE0945-1435	MS	-3.78	-	<-2.08	-	-	-	-3.88	-	<-1.78	-	13
HE1201-1512	MS	-3.92	-	-2.78	<-2.69	-	-4.27	-3.72	-4.65	-	>20.0	13, 14
HE1346-0427	MS	-3.58	-	<-2.48	-	-	-3.73	-3.33	-3.65	<-1.78	-	12, 13
HE1506-0113	RGB	-3.54	-	-2.07	-2.93	-	-1.89	-2.65	-4.07	-3.04	>20.0	13, 14
HE2032-5633	MS	-3.63	-	<-1.27	<-1.03	-	-3.72	-3.34	-4.14	-3.3	-	13
HE2139-5432	RGB	-4.02	-	-1.43	-1.94	-	-1.87	-2.41	-3.66	-3.02	>15.0	13, 14
HE2318-1621	RGB	-3.67	-	-2.63	-2.43	-	-2.96	-3.47	-4.25	-	-	15
SDSSJ161956+170539	MS	-3.57	-	-1.35	-	-	-	-3.53	-	-3.88	-	16
SDSSJ2209-0028	MS	-3.96	-	-1.4	-	-	-	-	-	-	-	17
53327-2044-515 ^a	-	-4.05	-	-2.7	-	<-1.24	-3.91	-3.65	-4.22	-	>2.0	13, 14
Segue1-7	RGB	-3.52	-	-1.22	-2.77	<-1.31	-2.99	-2.58	-3.29	-2.72	>50.0	14

Notes. Taken mainly from the SAGA database, Suda et al. (2008). The stars are classified as MS if $T_{\text{eff}} > 5500$ K and $\log g \geq 3.25$ and as RGB otherwise. ^(a) The evolutionary status of 53327-2044-515 is uncertain so that the average abundances of dwarf and subgiant solutions are taken, as done in Norris et al. (2013).

References. 1. Roederer et al. (2014c); 2. Roederer et al. (2014b); 3. Spite et al. (2012); 4. Bonifacio et al. (2007); 5. Bonifacio et al. (2009); 6. Andrievsky et al. (2007); 7. Andrievsky et al. (2010); 8. Andrievsky et al. (2008); 9. Beers et al. (2007); 10. Plez & Cohen (2005); 11. Hansen et al. (2015); 12. Cohen et al. (2013); 13. Yong et al. (2013); 14. Norris et al. (2013); 15. Placco et al. (2014a); 16. Caffau et al. (2013); 17. Spite et al. (2013).

7.1. Correcting for the effect of the first dredge up in CEMP-no stars

To compare the predicted and observed $[\text{X}/\text{H}]$ ratios, we need to know the initial $[\text{X}/\text{H}]$ surface ratios of the CEMP-no stars, the ones that likely reflect the abundances of their natal cloud, hence the ratios in the material ejected by the source star (we note that the dilution of the source star ejecta with the ISM can be important; it is discussed in Sect. 7.3). Non-evolved CEMP-no stars have a surface composition that is probably very close to the initial one. In more-evolved stars, the first dredge up can have occurred, likely reducing the surface carbon abundance. When available for the considered CEMP-no star, we have taken into account the correction on $[\text{C}/\text{Fe}]$ predicted by Placco et al. (2014b). For 505 metal-poor stars, they have determined the correction to apply to this ratio in order to recover the initial ratio. This correction, generally lower than 1 dex, remains small compared to the dispersion of observed $[\text{C}/\text{Fe}]$.

7.2. The atomic diffusion

In addition to the dredge up, the atomic diffusion adds another source of uncertainty when one wishes to link a CEMP-no with its possible source star. The effect of atomic diffusion (gravitational settling, thermal diffusion, and radiative acceleration) in low-mass metal-poor stars has been studied by Richard et al. (2002), for example. They predict changes ranging between ~ 0.1 and 1 dex, depending on the chemical species considered, T_{eff}

and on the evolutionary status of the model (cf. their Figs. 13 and 14). Richer et al. (2000) have shown that an additional turbulence seems to be required to explain the chemical anomalies of AmFm stars. When such an additional turbulence is considered in the metal-poor models of Richard et al. (2002), the effect of the atomic diffusion on the surface abundances is significantly reduced; around ~ 0.1 dex in many cases, when the turbulence is strong enough. The effect of atomic diffusion on the surface abundances of CEMP-no stars cannot be very well predicted but there are hints suggesting that it is modest.

7.3. Dilution of the ejecta with the ISM

A third aspect to take into account before comparing the source-star ejecta with the CEMP stars is that the ejecta could have been diluted in the ISM. In that case, the CEMP-no star would be made of a mixture of ejecta plus initial ISM⁹. We need to ascertain the degree of dilution. As discussed in Meynet et al. (2010), we use the Li abundance for this purpose: Li is a fragile element, so it is completely destroyed in the ejecta of the source star. When Li is observed at the surface of the CEMP-no stars, it must come from the dilution with the initial ISM. Here we suppose that the Li abundance in the initial ISM is equal to the WMAP value of 2.72 (Cyburt et al. 2008). Knowing how much mass is ejected from the source star, one can find the mass of

⁹ By initial ISM we mean here the ISM in which the source star formed.

initial ISM M_{ISM} to add to the ejected mass M_{ej} in order to reproduce the Li abundance observed at the surface of the CEMP-no star. The dilution factor D is then expressed as

$$D = \frac{M_{\text{ISM}}}{M_{\text{ej}}} = \frac{X(\text{Li})_{\text{CEMP}}}{X(\text{Li})_{\text{ISM}} - X(\text{Li})_{\text{CEMP}}}, \quad (6)$$

where $X(\text{Li})_{\text{CEMP}}$ and $X(\text{Li})_{\text{ISM}}$ are the mass fraction of Li at the surface of the CEMP-no star and in the initial ISM, respectively. A simple example is if the CEMP-no star has no Li. In this case, $D = 0$ and it would be made of pure source star ejecta. If the Li abundance is instead very close to the WMAP value, much more initial ISM would be needed to form this CEMP-no star. When the considered CEMP-no star has a measured Li abundance, we apply this method and dilute the source-star ejecta with the corresponding mass of initial ISM. If no Li data is available, we assume $D = 0$ by default. We also discuss the impact of having $D > 0$ in some cases, even without Li measurement. We do not pretend to give the right value of D for the CEMP-no stars but rather try to discuss the impact of dilution.

We have assumed that the surface Li abundance has not changed since the birth of the CEMP-no star. If in situ processes have occurred and destroyed some Li, it would mean that $X(\text{Li})_{\text{CEMP}}$ should be corrected to recover the initial Li content. This point is discussed for the star HE2331-7155.

7.4. Condition on the mass cut, weak explosion

The source-star ejecta is composed of the wind ejected during the evolution plus a supernova with a M_{cut} defined such that

$$\left| \log \left({}^{12}\text{C}/{}^{13}\text{C} \right)_{\text{obs}} - \log \left({}^{12}\text{C}/{}^{13}\text{C} \right)_{\text{mod}} \right| + |[C/H]_{\text{obs}} - [C/H]_{\text{mod}}| \quad (7)$$

is minimal. In this expression, “obs” refers to the observed value and “mod” to the value coming from the models. ${}^{12}\text{C}/{}^{13}\text{C}$ generally gives tight constraints on the mass cut because this ratio varies considerably between the different burning zones of the source star; it goes from ~ 5 to $\sim \infty$ when going from the H- to the He-burning shell. The $[C/H]$ ratio is also taken into account in the above criterion because sometimes there is no ${}^{12}\text{C}/{}^{13}\text{C}$ value available and also because relying on ${}^{12}\text{C}/{}^{13}\text{C}$ only can give multiple mass cut possibilities. This parametrisation and its consequences are discussed in Sect. 8.1.

We note that there is no degeneracy between the effect of the mass cut and the dilution. Expelling deep layers, where He has burnt, raises $[C/H]$. Increasing D allows one to reduce $[C/H]$. However, ${}^{12}\text{C}/{}^{13}\text{C}$ increases both when deep layers are expelled and when D increases meaning that a solution implying deep layers with significant dilution will always lead to a high ${}^{12}\text{C}/{}^{13}\text{C}$, likely out of the observed range.

7.5. Comparison of the source-star models with observed CEMP-no stars

We now more closely inspect six CEMP-no stars, the others being discussed together in Sect. 7.6. Each of the six panels of Fig. 11 is dedicated to one star (represented by the red starry shaped symbols) together with the composition of the source-star model ejecta.

We focus on light elements: C, N, O, Na, Mg, Al and Si. By definition, the CEMP-no stars are generally not enhanced in heavier elements (especially s- and r-elements). As we see below, in some stars, heavy elements, such as Sr or Ba for instance,

are present, and although they are only in small amounts, they should be explained (cf. discussion about 53327-2044-515).

7.5.1. HE0049-3948

This star (see the upper-left panel of Fig. 11) has only upper limits available for C and N so some caution is required regarding these elements. The low sodium abundance favours non-rotating models; $[\text{Na}/\text{H}]$ is indeed too high when considering the 20s7mix model (green pattern). The silicon abundance is also low. This can be achieved if only the outer layers of the source star are expelled, because in deeper layers, the temperature is higher and more silicon is synthesised through the Mg-Al-Si chain. We see, indeed, that the models expelling the largest amount of mass (see M_{W} and M_{SN} in Fig. 11), that is, the 20s0 (blue dashed line) and 20s7mix (green line) models, have an overly high $[\text{Si}/\text{H}]$. Constraining the mass of the source star could be done through a comparison between the predicted and observed C and N abundance and ${}^{12}\text{C}/{}^{13}\text{C}$ ratio (cf. Fig. 9 for instance). The determination of these abundances at the surface of this star would be required. We note that our models reproduce the upper limit of the $[C/H]$ ratio. Of course lower values can be obtained by varying the mass cut for instance.

The heavier elements observed in this star are little or not enhanced. For instance, $[\text{Sr}/\text{Fe}] = -0.85$ and $[\text{Ba}/\text{Fe}] < 0.14$ (Yong et al. 2013).

No Li data is available so D cannot be constrained. By default we have taken $D = 0$. The case $D = 50$ (it would imply $A(\text{Li}) = 2.71$) for the ejecta of the 20s0mix model is shown by the dotted blue line; it is shifted towards the ISM pattern (magenta line). The case of a large dilution factor cannot be discarded because of the upper limits on C and N and because although raised, ${}^{12}\text{C}/{}^{13}\text{C}$ remains within the observed range.

7.5.2. HE2331-7155

This star (upper-right panel in Fig. 11) has a high $[\text{N}/\text{H}]$ and $[\text{C}/\text{N}] = -1.23$. The high $[\text{N}/\text{H}]$ clearly shows the need for a mixing event (progressive or brutal) between the H and He-burning regions of the source star. The low $[\text{C}/\text{N}]$ discards the models with late mixing. At the same time, the low ${}^{12}\text{C}/{}^{13}\text{C}$ favours models with mixing (rotational or late), where primary ${}^{13}\text{C}$ is formed. These points, together with the relatively high Na and high Mg point towards models with a progressive mixing, achieved here by rotation. The best source star for HE2331-7155 is the 20s7 model (represented by the solid blue curve). This model provides enough N together with a low ${}^{12}\text{C}/{}^{13}\text{C}$. The 32s7 and 60s7 models (green and orange solid lines) do not provide enough primary N and have a higher ${}^{12}\text{C}/{}^{13}\text{C}$ ratio. The Na, Al and ${}^{12}\text{C}/{}^{13}\text{C}$ are also rather well explained by the 20s7 model. Only the Mg is underproduced by ~ 1 dex. However, the nuclear rates implying Mg at relevant temperature in the H-burning shell (30–80 MK) are not very well known. Changing these rates can lead to significant differences in the nucleosynthesis and thus in the composition of the ejecta (see e.g. Decressin et al. 2007; Choplin et al. 2016). Future laboratory measurements of these rates will allow a more accurate comparison of the observed Mg/H value with the value predicted by stellar models. $A(\text{Li}) < 0.37$ for that star. Taking 0.37 for $A(\text{Li})$ gives $D = 0.0045$, which is small and then barely changes the composition of the source-star ejecta. Let us suppose that this CEMP-no star has destroyed 2 dex of

A. Choplin et al.: Pre-supernova mixing in CEMP-no source stars

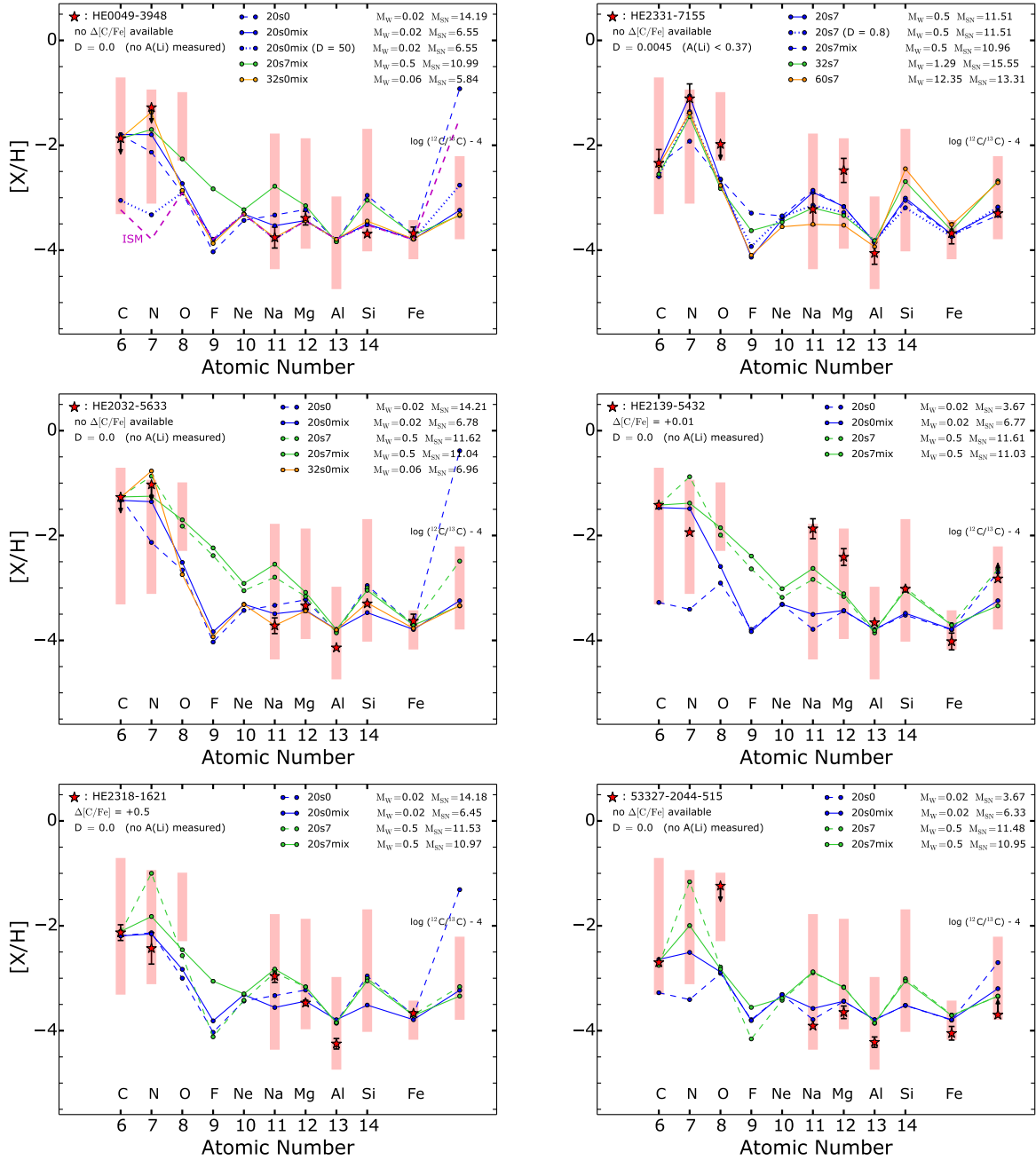


Fig. 11. $[X/H]$ as a function of the atomic number. Also $\log^{12}\text{C}/^{13}\text{C}$ is shown (shifted downwards by 4 dex for clarity). Each panel is dedicated to one observed CEMP-no star (red starry symbols). Arrows indicate upper/lower limits. If available, error bars are indicated. The correction $\Delta[\text{C}/\text{Fe}]$ of Placco et al. (2014b) applied on $[\text{C}/\text{Fe}]$ (if any) is taken into account and indicated in the upper-left corner. In each panel we show the composition of the ejecta of the indicated models (solid, dashed and dotted lines). The masses ejected by the winds (M_W) and the supernova (M_{SN}) are written in the upper-right corner of each panel. The composition of the ISM is shown in the *first panel*. The dilution coefficient D and $A(\text{Li})$ value (if available) are shown in the upper-left corner. The range of observed $[X/H]$ ratios and $\log(^{12}\text{C}/^{13}\text{C})$ ratios for the stars in Table 2 are shown by the red rectangles.

Li at its surface since its birth¹⁰ so that its initial $A(\text{Li})$ would be 2.37. In this case, $D = 0.8$. The 20s7 model with such a dilution

¹⁰ The models of Korn et al. (2009) predict a maximum Li depletion of 1.2 dex for the star HE1327-2326. Here 2 dex would likely correspond to an extreme case.

factor is shown by the blue dotted pattern. Whatever the species considered, it implies a shift of less than 0.5 dex compared to the $D = 0.0045$ case. This is because the initial ISM is much more metal poor than the material ejected from the source star; it shows the small effect of the dilution even if the initial Li content in the CEMP-no – hence D – was higher.

The heavier elements observed on this star are little or not enhanced. Especially, $[\text{Sr}/\text{Fe}] = -0.85$ and $[\text{Ba}/\text{Fe}] = -0.90$ (Hansen et al. 2015).

7.5.3. HE2032-5633

The upper limits on C and N together with the absence of $^{12}\text{C}/^{13}\text{C}$ measurement prevent any strong conclusion regarding this star (middle-left panel of Fig. 11). The $^{12}\text{C}/^{13}\text{C}$ ratio of the 20s0 model is ~ 2 dex above the observed range. The other standard non-rotating models behave in a similar way. However, as long as no $^{12}\text{C}/^{13}\text{C}$ ratio is observed at the surface of this star, we cannot discard these models.

Also, as we see by comparing the blue and green patterns, the low $[\text{Na}/\text{H}]$ ratio on HE2032-5633 would favour non-rotating models. Finally, the 20s0mix model is the best source star candidate for this CEMP-no star. The 32s0mix has an overly high $[\text{N}/\text{H}]$ ratio (see the orange pattern). However, we remain very cautious, since the mass cuts of the models are set to reproduce the observed $[\text{C}/\text{H}]$. Here, $[\text{C}/\text{H}]$ is only an upper limit. A lower measured $[\text{C}/\text{H}]$ ratio would imply a smaller amount of ejected mass (smaller M_{SN}) and would change the abundances in the material ejected by the source star models.

There are also few heavy elements at the surface of HE 2032-5633: $[\text{Sr}/\text{Fe}] < -0.68$ and $[\text{Ba}/\text{Fe}] < 0.31$ (Yong et al. 2013).

7.5.4. HE2139-5432

This star (middle-right panel of Fig. 11) has $[\text{C}/\text{N}] = 0.51$ meaning that the models with late mixing are favoured. The 20s7mix model has the highest $[\text{C}/\text{N}]$ (see Fig. 9), closer to the observed $[\text{C}/\text{N}]$ than the 32s7mix and 60s7mix models. $[\text{Na}/\text{H}]$ is the highest in the sample and $[\text{Mg}/\text{H}]$ is high as well. This cannot be explained at all by non-rotating models. The high Na, Mg, and $[\text{C}/\text{N}]$ clearly point towards the rotating models with late mixing. The 20s7mix model provides an interesting solution. We note however two discrepancies: (1) Na and Mg are underestimated by about ~ 1 dex and (2) $[\text{N}/\text{H}]$ is ~ 0.5 dex too high, while $^{12}\text{C}/^{13}\text{C}$ is too low by at least ~ 0.5 dex. A solution to the first discrepancy could be to consider a faster rotator, since more mixing would enhance Na and possibly Mg (cf. Sect. 6). A solution for the second discrepancy would be to have a material less processed by the CNO cycle in the partially processed zone. In this case, we would have less ^{14}N and $^{12}\text{C}/^{13}\text{C}$ might not have reached its CNO equilibrium value at the end of the evolution. This would be coherent with the $[\text{N}/\text{H}]$ and $^{12}\text{C}/^{13}\text{C}$ ratios of this CEMP-no star. Less CNO processing can be achieved in the source star if the late mixing event occurs closer to the end of evolution. Hence, to resolve (1) and (2) simultaneously, a possibility might be to consider a faster rotator that underwent a late mixing event very close to the end of its evolution. Even if the 20s7mix model does not perfectly match this CEMP-no star, rotational mixing with a late mixing process are likely to provide a solution.

This star is also poor in heavy elements: $[\text{Sr}/\text{Fe}] = -0.55$ and $[\text{Ba}/\text{Fe}] < -0.33$ (Yong et al. 2013).

7.5.5. HE2318-1621

Because of its low $\log g$ and T_{eff} , Placco et al. (2014b) have proposed a correction $\Delta[\text{C}/\text{Fe}] = 0.5$ dex for this star (lower-left panel of Fig. 11). This implies $[\text{C}/\text{H}] = -2.13$ and $[\text{C}/\text{N}] = 0.3$. The high $[\text{C}/\text{N}]$ points towards models with late mixing. As for

HE2139-5432, the 20s7mix model is preferred because of its high $[\text{C}/\text{N}]$ in the partially CNO-processed zone, closer to the observed value than the 32s7mix and 60s7mix models. Also, the relatively high $[\text{Na}/\text{H}]$ favours the rotating models. The 20s0mix model for instance provides a relatively good fit but underestimates $[\text{Na}/\text{H}]$. The 20s7mix provides the right amount of Na but slightly too much N. In any case, the $20 M_{\odot}$ models with late mixing, both rotating and non-rotating, provide the best solutions. Since deeper layers are expelled from the rotating model, $[\text{Si}/\text{H}]$ is higher in the ejecta by about 0.7 dex compared to the non-rotating model (compare the solid blue and green lines). Then, the silicon abundance of this star would be an interesting diagnostic to discriminate the two source stars and find the best one.

At the surface of this CEMP-no star, $[\text{Sr}/\text{Fe}] = -1$ and $[\text{Ba}/\text{Fe}] = -1.61$. Also, $[\text{Eu}/\text{Fe}] < 0.13$ (Placco et al. 2014a).

7.5.6. 53327-2044-515

The low $[\text{Na}/\text{H}]$ of this star disfavours the rotating models, as we see on the lower-right panel of Fig. 11. Since the 20s0 model cannot provide both a high $[\text{C}/\text{H}]$ and a low $^{12}\text{C}/^{13}\text{C}$, the 20s0mix model is preferred. We note however the lower limit for $^{12}\text{C}/^{13}\text{C}$. The O is largely underestimated (by about 2 dex) but since it is an upper limit, it is not incompatible with the low predicted $[\text{O}/\text{H}]$.

At the surface of this star, $[\text{Sr}/\text{Fe}] = 1.09$ or 0.53 , depending on whether it is considered as a dwarf or a subgiant (Yong et al. 2013; Norris et al. 2013). Similarly, $[\text{Ba}/\text{Fe}] < 0.34$ or < 0.04 . The modest enrichment in Sr (and eventually Ba) at the surface of this star might be explained by the weak *s*-process having operated in the source star. Rotation boosts the weak *s*-process because of the extra ^{14}N brought into the He core, transformed into ^{22}Ne that afterwards releases neutrons (Frischknecht et al. 2012, 2016). There is however a drawback: Rotating models are rather disfavoured because of the low observed $[\text{Na}/\text{H}]$. Source star models with an extended nucleosynthetic network are needed to make quantitative predictions. This will be done in the future.

7.5.7. General remarks

Table 3 summarises the above discussion on the six CEMP-no stars. We see that in most cases, the source stars with late mixing are preferred, even if there are some important uncertainties for some stars (see previous discussion). We found that four out of the six considered CEMP-no stars probably cannot be explained without the late mixing process in the source star. Two stars cannot be explained without a progressive mixing, that can be achieved by rotation. One star, HE2331-7155, probably cannot be explained through the late mixing. It is explained better by a $20 M_{\odot}$ rapidly rotating source star with no late mixing. Globally, the lower-mass source stars ($20 M_{\odot}$) are preferred compared to the higher mass ones ($60 M_{\odot}$).

7.6. Other CEMP-no stars

We have discussed in detail six out of the 20 stars in the sample (see Table 2). Here we discuss three points regarding the other stars:

1. Some of these stars have very little abundance data available (e.g. HE0945-1435, SDSSJ161956+170539 or SDSSJ2209-0028), meaning that different solutions could match the observations. More abundance data are needed to provide

A. Choplin et al.: Pre-supernova mixing in CEMP-no source stars

Table 3. Preferred source star(s) of the six CEMP-no stars discussed above.

Star	No Rot. models			Rot. models			No Rot. mix models			Rot. mix models		
	20s0	32s0	60s0	20s7	32s7	60s7	20s0mix	32s0mix	60s0mix	20s7mix	32s7mix	60s7mix
HE0049-3948	no	no	no	no	no	no	yes	yes	yes	no	no	no
HE2331-7155	no	no	no	yes	no	no	no	no	no	no	no	no
HE2032-5633	yes/no	yes/no	yes/no	yes/no	yes/no	yes/no	yes	yes/no	yes/no	yes/no	yes/no	yes/no
HE2139-5432	no	no	no	no	no	no	no	no	no	yes/no	no	no
HE2318-1621	no	no	no	no	no	no	yes	no	no	yes	no	no
53327-2044-515	no	no	no	no	no	no	yes/no	yes/no	yes/no	no	no	no

Notes. “yes” indicates that the source star is the (or among the) preferred one(s), “yes/no” indicates the possible candidates for which caution is needed or some additional observational data would be needed to reach stronger conclusions.

constraints and allow for a better estimation of the source star.

- Several stars have very low $[X/H]$ ratios, meaning that they might be formed with only a little amount of the source star ejecta and mainly with the ISM. For instance, HE10134-1519 and HE1201-1512 belong to the less enriched stars in the sample. HE10134-1519 is a RGB star with $A(\text{Li}) = 1.27$. As discussed, the presence of Li might indicate an important contribution of the ISM. However, the initial Li content might be higher since this star is a RGB, in which internal processes could have depleted this element at the surface. In that case, the dilution factor would be higher. Also CS29527-015 has generally low $[X/H]$ ratios. It is also the Li-richest star in the sample ($A(\text{Li}) = 2.07$), suggesting an important contribution of the ISM.
- Finally, some stars are difficult to explain with the models presented in this work; those having a low $[\text{N}/\text{H}]$, together with high $[\text{C}/\text{H}]$ and $[\text{O}/\text{H}]$. HE1012-1540 and Segue1-7 show such a trend and this cannot be explained correctly with our models. HE1012-1540 has the lowest $[\text{N}/\text{H}]$ of the sample and is highly enriched in Na and Mg (see Fig. 12). Our models cannot explain a very low $[\text{N}/\text{H}]$ together with a high $[\text{Na}/\text{H}]$ because Na is boosted thanks to rotation but rotation also synthesises primary N. None of our models can provide the right observed trend (see examples in Fig. 12).

The range of observed abundances is very large; up to ~ 3 dex for CEMP-no stars having roughly the same $[\text{Fe}/\text{H}]$ (red rectangles in Figs. 11 or 12). The observed abundance patterns can vary strongly from one CEMP-no star to another. We think that this variety might rule out by itself a single scenario that could account for the entire CEMP-no star class. In summary, although our approach cannot explain the whole considered sample, it might provide a solution for a significant part of it, or at least a clue on some ingredients (late mixing and progressive mixing) able to reproduce the observations. This gives some support to the idea that mixing (either progressive or late and brutal) has played an important role on the early and massive star generations.

8. Discussion

8.1. Low energetic supernova and winds

There are three constraints in favour of an ejection of just the outer layers of the source star.

First, as we saw, if overly deep layers are ejected, the $^{12}\text{C}/^{13}\text{C}$ ratio is too high compared to the observed values.

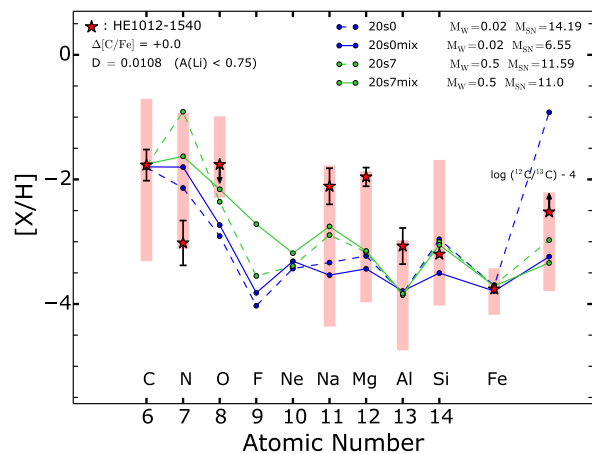


Fig. 12. As in Fig. 11 but for HE1012-1540. The mass cut is calibrated to reproduce $[\text{C}/\text{H}]$ only.

The second constraint is related to the s -process. At this metallicity ($Z = 10^{-5}$) and in non-rotating models, the content in ^{22}Ne (neutron source) and ^{56}Fe (neutron seed) is too low for the s -process to occur significantly. However, including rotation produces extra ^{22}Ne , which significantly boosts the s -process. (the production of Sr can be raised by several orders of magnitude; Frischknecht et al. 2016, especially their Fig. 8). The weak s -process mainly happens at the end of the core He-burning phase. At the end of evolution, most of the s -elements are located in the He-burning shell. If the He shell (plus eventually deeper layers) is ejected, the ISM will be enriched in s -elements, contradicting the fact that CEMP-no stars generally show no s -elements. For instance, we have seen that HE2331-7155 is best explained by the 20s7 model. This model will produce s -elements because of fast rotation. However, HE2331-7155 shows no enhancement in s -elements ($[\text{Sr}/\text{Fe}] = -0.85$ and $[\text{Ba}/\text{Fe}] = -0.90$). As a consequence, only the outer layers (above the He-shell) of the 20s7 model have to be ejected, otherwise some s -elements are released in the ISM.

Finally, in the late mixing region, a lot of protons are ingested by the He-burning shell. It produces extra energy and inflates the star in this region. This decreases the gravitational binding and makes the outer layers easier to eject.

In the present work, the outer layers of the models are expelled through a low energetic supernova. The CEMP-no stars form from that material. Our source star models lose almost no

material through winds. It might be, however, that the winds are underestimated. [Moriya & Langer \(2015\)](#) have shown that the envelope of massive Pop. III stars can become pulsationally unstable near the end of their evolution and then undergo extreme mass-loss events. This might be viewed as a fourth piece of evidence in favour of an ejection of only the outer layers of the source star. Source star models including this new wind prescription should be computed in the future. We can speculate that a wind occurring at the very end of the evolution will barely change the results presented here since at that time the composition of the outer layers does not change anymore.

If the winds were to occur earlier, the results discussed here would change for the following reasons: firstly, the chemical composition of these outer layers would be different from those they would have acquired if that matter were to have remained locked in the star until the end of evolution. Secondly, the importance and even the presence of the late mixing process invoked here might be disputed. This point would require some exploratory work with different mass-loss algorithms. This will be done in a future study.

8.2. Physical origin of the late mixing process and partially processed zone

We have seen how a late mixing event in the source star could provide a solution for some CEMP-no stars. In our models, this mixing is artificially triggered. Our conclusions would be of course strengthened if a known physical process were able to explain this mixing. Our main aim here was to see to what extent the CEMP-no sample could be reproduced by standard source-star models and if it could not, to try to find which ingredients are missing.

We note that the treatment of the convection can impact the shell interaction and thus the formation or not of the partially CNO-processed zone. In the Geneva code, the boundaries of the convective zones are determined using the Schwarzschild criterion, and the convection is assumed to be adiabatic¹¹. The boundaries of the convective zones are sharp (step functions). This prescription probably does not capture the whole physics of convection ([Arnett et al. 2015](#)). Indeed, multi-dimension hydrodynamics numerical simulations of convection in deep stellar interior show that the chemical composition of each side of the convective boundary makes a smooth transition and is not a step function. Moreover, the boundaries are not strict barriers for the chemical elements, and part of them can be mixed through the boundary ([Herwig et al. 2006](#); [Meakin & Arnett 2007](#); [Arnett & Meakin 2011](#); [Cristini et al. 2017](#); [Jones et al. 2017](#)), in contrast with the way convection is modelled in the present paper.

It might be that improving the way convection is treated in classical 1D codes to follow more closely the behaviour observed in multi-dimensional simulations strengthens the exchanges between the H- and He-burning shells (or even leads to shell mergers. We refer to e.g. [Rauscher et al. 2002](#); [Tur et al. 2010](#); [Pignatari et al. 2015](#), for discussions about shell mergers). This could induce the creation of the partially CNO-processed zone. If so, the late mixing invoked in our work would simply

mean that an overly poor description of the convective boundaries is used in present 1D stellar evolution models.

In any case, mixing between the H- and He-burning shells would be naturally favoured in low-metallicity stars compared to higher-metallicity ones because of the increasing compactness when metallicity decreases and because of the lack of CNO elements that leads to a weaker entropy barrier at the bottom of the H-burning shell.

9. Conclusions

We have investigated the origin of CEMP-no stars. The material forming a CEMP-no star could come from a previous massive star, referred to as a source star.

We have computed 20–60 M_{\odot} source stars with no and fast rotation. Through a comparison between observations and models in the $^{12}\text{C}/^{13}\text{C}$ versus C/N plane, we have shown that standard source-star models (rotating or not) have difficulty in providing a material with a high C/N together with a low $^{12}\text{C}/^{13}\text{C}$. Many CEMP-no stars present this trend. Source-star models tend to produce either a low C/N with a low $^{12}\text{C}/^{13}\text{C}$ due to the effect of the CN cycle, or a high C/N with a high $^{12}\text{C}/^{13}\text{C}$ because of He-burning that destroys ^{13}C and ^{14}N . Increasing the dilution of the ejected material with the ISM increases the $^{12}\text{C}/^{12}\text{C}$ ratio. Decreasing the mass cut – hence expelling deeper layers from the source star – also increases the $^{12}\text{C}/^{13}\text{C}$ ratio.

To explain the numerous cases of CEMP-no stars showing $^{12}\text{C}/^{13}\text{C}$ ratios near CNO equilibrium and C/N ratio above the CNO equilibrium value, we suggest that a late mixing, occurring just before ejection is needed. This is the main point of this paper. This conclusion remains robust against changes of the mass cut and dilution that would both increase the $^{12}\text{C}/^{13}\text{C}$ ratio much above the observed values. This trend, in our view, reflects a mixing process that is not yet properly accounted for in the stellar models.

The late mixing event should occur between the H- and He-burning shells, a few hundred years before the end of source star's life. This mixing brings extra ^{12}C from the He to the H shell, boosting the CN cycle in the H shell. The short time remaining before the end of evolution allows $^{12}\text{C}/^{13}\text{C}$ to reach its equilibrium value but not C/N. A second possibility to obtain such material would be to undergo a strong mixing event, as described in this work, but not necessarily occurring at the very end of evolution; the mixing would be quickly followed by a dredge up of the partially CNO-processed material up to the surface and then heavy mass loss would occur due to the sudden increase of the surface metallicity. This occurs in the rotating 85 M_{\odot} model at $Z = 10^{-8}$ of [Hirschi \(2007\)](#); see also, [Maeder et al. 2015](#). We plan to further investigate this second scenario in the future.

The generally low $^{12}\text{C}/^{13}\text{C}$ ratio observed in CEMP-no stars suggests that only the outer layers should have been expelled by the source star to obtain a ^{13}C -rich material. This could imply a weak supernova explosion at the end of the source star's life, together with a large amount of matter falling back on the central black hole. Strong winds occurring in late stages is also a possibility.

We have more closely inspected six CEMP-no stars through a comparison between observed and predicted [X/H] ratios. We found that four out of the six stars probably cannot be explained without a late mixing event in the source star, and that two stars probably cannot be explained without a progressive mixing, achieved by fast rotation of the source star in our models. This suggests the possibility of two kinds of mixing operating in CEMP-no source stars: a progressive mixing that could be

¹¹ During the main sequence and core He-burning phase, the core is extended using a penetrative overshoot, the length of which is proportional to a fraction of the pressure scale height at the edge of the core. This is applied neither for the more advanced phases of stellar evolution, nor for the intermediate convective shells, and is thus not relevant to the above discussion.

achieved by rotation, and a late mixing, possibly linked to shell mergers. The late mixing invoked in the present work could simply mean that an overly poor description of convective boundaries is used in current 1D stellar evolution codes. More generally, we have shown that Na-rich CEMP-no stars are difficult to explain without progressive mixing operating in the source star. Also, $20 M_{\odot}$ source stars are generally preferred compared to higher-mass source stars (32 or $60 M_{\odot}$) because of the lower temperature in the H-burning shell that induces a slower pace of the CN-cycle. A few CEMP-no stars could not be explained by either of our source-star models. The diversity of the abundances observed at the surface of these stars might suggest the need for multiple scenarios.

Acknowledgements. R.H. acknowledges support from the World Premier International Research Center Initiative (WPI Initiative), MEXT, Japan and from the ChETEC COST Action (CA16117), supported by COST (European Cooperation in Science and Technology). The research leading to these results has received funding from the European Research Council under the European Union's Seventh Framework Programme (FP/2007–2013)/ERC Grant Agreement No. 306901.

References

- Abate, C., Pols, O. R., Karakas, A. I., & Izzard, R. G. 2015, *A&A*, 576, A118
- Allen, D. M., Ryan, S. G., Rossi, S., Beers, T. C., & Tsangarides, S. A. 2012, *A&A*, 548, A34
- Andrievsky, S. M., Spite, M., Korotin, S. A., et al. 2007, *A&A*, 464, 1081
- Andrievsky, S. M., Spite, M., Korotin, S. A., et al. 2008, *A&A*, 481, 481
- Andrievsky, S. M., Spite, M., Korotin, S. A., et al. 2010, *A&A*, 509, A88
- Angulo, C., Arnould, M., Rayet, M., et al. 1999, *Nucl. Phys. A*, 656, 3
- Aoki, W. 2010, in IAU Symp., 265, eds. K. Cunha, M. Spite, & B. Barbuy, 111
- Aoki, W., Beers, T. C., Christlieb, N., et al. 2007, *ApJ*, 655, 492
- Arnett, W. D., & Meakin, C. 2011, *ApJ*, 733, 78
- Arnett, W. D., Meakin, C., Viallet, M., et al. 2015, *ApJ*, 809, 30
- Asplund, M., Grevesse, N., & Sauval, A. J. 2005, in *Cosmic Abundances as Records of Stellar Evolution and Nucleosynthesis*, eds. T. G. Barnes, III, & F. N. Bash, *ASP Conf. Ser.*, 336, 25
- Beers, T. C., & Christlieb, N. 2005, *ARA&A*, 43, 531
- Beers, T. C., Sivarani, T., Marsteller, B., et al. 2007, *AJ*, 133, 1193
- Bisterzo, S., Gallino, R., Straniero, O., Cristallo, S., & Käppeler, F. 2010, *MNRAS*, 404, 1529
- Bonifacio, P., Molaro, P., Sivarani, T., et al. 2007, *A&A*, 462, 851
- Bonifacio, P., Spite, M., Cayrel, R., et al. 2009, *A&A*, 501, 519
- Caffau, E., Bonifacio, P., François, P., et al. 2011, *Nature*, 477, 67
- Caffau, E., Bonifacio, P., François, P., et al. 2013, *A&A*, 560, A15
- Carollo, D., Beers, T. C., Bovy, J., et al. 2012, *ApJ*, 744, 195
- Chiappini, C. 2013, *Astron. Nachr.*, 334, 595
- Chiappini, C., Ekström, S., Meynet, G., et al. 2008, *A&A*, 479, L9
- Choplin, A., Maeder, A., Meynet, G., & Chiappini, C. 2016, *A&A*, 593, A36
- Christlieb, N., Gustafsson, B., Korn, A. J., et al. 2004, *ApJ*, 603, 708
- Cohen, J. G., Christlieb, N., McWilliam, A., et al. 2004, *ApJ*, 612, 1107
- Cohen, J. G., Christlieb, N., Thompson, I., et al. 2013, *ApJ*, 778, 56
- Cristini, A., Meakin, C., Hirschi, R., et al. 2017, *MNRAS*, 471, 279
- Cybur, R. H., Fields, B. D., & Olive, K. A. 2003, *Phys. Lett. B*, 567, 227
- Cybur, R. H., Fields, B. D., & Olive, K. A. 2008, *J. Cosmol. Astropart. Phys.*, 11, 012
- Cybur, R. H., Amthor, A. M., Ferguson, R., et al. 2010, *ApJS*, 189, 240
- Decressin, T., Meynet, G., Charbonnel, C., Prantzos, N., & Ekström, S. 2007, *A&A*, 464, 1029
- de Jager, C., Nieuwenhuijzen, H., & van der Hucht, K. A. 1988, *A&AS*, 72, 259
- Eggenberger, P., Lagarde, N., Miglio, A., et al. 2016, *Astron. Nachr.*, 337, 832
- Ekström, S., Georgy, C., Eggenberger, P., et al. 2012, *A&A*, 537, A146
- Ferguson, J. W., Alexander, D. R., Allard, F., et al. 2005, *ApJ*, 623, 585
- Frebel, A., & Norris, J. E. 2015, *ARA&A*, 53, 631
- Frebel, A., Christlieb, N., Norris, J. E., et al. 2006, *ApJ*, 652, 1585
- Frischknecht, U., Hirschi, R., & Thielemann, F.-K. 2012, *A&A*, 538, L2
- Frischknecht, U., Hirschi, R., Pignatari, M., et al. 2016, *MNRAS*, 456, 1803
- Georgy, C., Ekström, S., Eggenberger, P., et al. 2013, *A&A*, 558, A103
- Goswami, A., Aoki, W., Beers, T. C., et al. 2006, *MNRAS*, 372, 343
- Hale, S. E., Champagne, A. E., Iliadis, C., et al. 2002, *Phys. Rev. C*, 65, 015801
- Hansen, T., Hansen, C. J., Christlieb, N., et al. 2014, *ApJ*, 787, 162
- Hansen, T., Hansen, C. J., Christlieb, N., et al. 2015, *ApJ*, 807, 173
- Hansen, T. T., Andersen, J., Nordström, B., et al. 2016, *A&A*, 588, A3
- Herwig, F., Freytag, B., Hueckstaedt, R. M., & Timmes, F. X. 2006, *ApJ*, 642, 1057
- Hirschi, R. 2007, *A&A*, 461, 571
- Honda, S., Aoki, W., Kajino, T., et al. 2004, *ApJ*, 607, 474
- Iliadis, C., D'Auria, J. M., Starrfield, S., Thompson, W. J., & Wiescher, M. 2001, *ApJS*, 134, 151
- Johnson, J. A., Herwig, F., Beers, T. C., & Christlieb, N. 2007, *ApJ*, 658, 1203
- Jones, S., Andrassy, R., Sandalski, S., et al. 2017, *MNRAS*, 465, 2991
- Korn, A. J., Richard, O., Mashonkina, L., et al. 2009, *ApJ*, 698, 410
- Kudritzki, R.-P., & Puls, J. 2000, *ARA&A*, 38, 613
- Lai, D. K., Bolte, M., Johnson, J. A., et al. 2008, *ApJ*, 681, 1524
- Lee, Y. S., Beers, T. C., Masseron, T., et al. 2013, *AJ*, 146, 132
- Limongi, M., Chieffi, A., & Bonifacio, P. 2003, *ApJ*, 594, L123
- Lucatello, S., Tsangarides, S., Beers, T. C., et al. 2005, *ApJ*, 625, 825
- Lugaro, M., Karakas, A. I., Stancliffe, R. J., & Rijs, C. 2012, *ApJ*, 747, 2
- Maeder, A., & Meynet, G. 2000, *A&A*, 361, 159
- Maeder, A., & Meynet, G. 2014, *ApJ*, 793, 123
- Maeder, A., & Meynet, G. 2015, *A&A*, 580, A32
- Maeder, A., Meynet, G., & Chiappini, C. 2015, *A&A*, 576, A56
- Masseron, T., Johnson, J. A., Plez, B., et al. 2010, *A&A*, 509, A93
- McWilliam, A., Preston, G. W., Sneden, C., & Searle, L. 1995, *AJ*, 109, 2757
- Meakin, C. A., & Arnett, D. 2007, *ApJ*, 667, 448
- Meynet, G., Ekström, S., & Maeder, A. 2006, *A&A*, 447, 623
- Meynet, G., Hirschi, R., Ekström, S., et al. 2010, *A&A*, 521, A30
- Moriya, T. J., & Langer, N. 2015, *A&A*, 573, A18
- Norris, J. E., Christlieb, N., Bessell, M. S., et al. 2012, *ApJ*, 753, 150
- Norris, J. E., Yong, D., Bessell, M. S., et al. 2013, *ApJ*, 762, 28
- Pignatari, M., Zinner, E., Hoppe, P., et al. 2015, *ApJ*, 808, L43
- Placco, V. M., Frebel, A., Beers, T. C., et al. 2014a, *ApJ*, 781, 40
- Placco, V. M., Frebel, A., Beers, T. C., & Stancliffe, R. J. 2014b, *ApJ*, 797, 21
- Plez, B., & Cohen, J. G. 2005, *A&A*, 434, 1117
- Rauscher, T., Heger, A., Hoffman, R. D., & Woosley, S. E. 2002, *ApJ*, 576, 323
- Richard, O., Michaud, G., Richer, J., et al. 2002, *ApJ*, 568, 979
- Richer, J., Michaud, G., & Turcotte, S. 2000, *ApJ*, 529, 338
- Roederer, I. U., Cowan, J. J., Preston, G. W., et al. 2014a, *MNRAS*, 445, 2970
- Roederer, I. U., Preston, G. W., Thompson, I. B., Shectman, S. A., & Sneden, C. 2014b, *ApJ*, 784, 158
- Roederer, I. U., Preston, G. W., Thompson, I. B., et al. 2014c, *AJ*, 147, 136
- Sivarani, T., Beers, T. C., Bonifacio, P., et al. 2006, *A&A*, 459, 125
- Sneden, C., Cowan, J. J., Lawler, J. E., et al. 2003, *ApJ*, 591, 936
- Spite, M., Andrievsky, S. M., Spite, F., et al. 2012, *A&A*, 541, A143
- Spite, M., Caffau, E., Bonifacio, P., et al. 2013, *A&A*, 552, A107
- Starkenburg, E., Shetrone, M. D., McConnachie, A. W., & Venn, K. A. 2014, *MNRAS*, 441, 1217
- Suda, T., Katsuta, Y., Yamada, S., et al. 2008, *PASJ*, 60, 1159
- Talon, S., & Zahn, J.-P. 1997, *A&A*, 317, 749
- Tominaga, N., Iwamoto, N., & Nomoto, K. 2014, *ApJ*, 785, 98
- Tur, C., Heger, A., & Austin, S. M. 2010, *ApJ*, 718, 357
- Umeda, H., & Nomoto, K. 2002, *ApJ*, 565, 385
- Umeda, H., & Nomoto, K. 2005, *ApJ*, 619, 427
- Yong, D., Norris, J. E., Bessell, M. S., et al. 2013, *ApJ*, 762, 26
- Zahn, J.-P. 1992, *A&A*, 265, 115

Constraints on CEMP-no progenitors from nuclear astrophysics

Arthur Choplin¹, André Maeder¹, Georges Meynet¹, and Cristina Chiappini²

¹ Geneva Observatory, University of Geneva, Maillettes 51, 1290 Sauverny, Switzerland
 e-mail: arthur.choplin@unige.ch

² Leibniz-Institut für Astrophysik Potsdam, An der Sternwarte 16, 14482 Potsdam, Germany

Received 6 January 2016 / Accepted 7 June 2016

ABSTRACT

Context. The CEMP-no stars are long-lived small mass stars presenting a very low iron content and overabundances of carbon with no sign or only very weak signs of s- or r-elements. Although the origin of this abundance pattern is still a matter of debate, it was very likely inherited from a previous massive star, which we call the source star.

Aims. We rely on a recent classification of CEMP-no stars arguing that some of them are made of a material processed by hydrogen burning that was enriched in products of helium burning during the nuclear life of the source star. We examine the possibility of forming CEMP-no stars with this material.

Methods. We study the nucleosynthesis of the CNO cycle and the Ne-Na Mg-Al chains in a hydrogen burning single zone while injecting the helium burning products ^{12}C , ^{16}O , ^{22}Ne , and ^{26}Mg . We investigate the impact of changing density, temperature and the injection rate. The nuclear reaction rates involving the creation and destruction of ^{27}Al are also examined.

Results. ^{14}N , ^{23}Na , ^{24}Mg , and ^{27}Al are formed when injecting ^{12}C , ^{16}O , ^{22}Ne , and ^{26}Mg in the hydrogen burning zone. The $^{12}\text{C}/^{13}\text{C}$ ratio is constant under various conditions in the hydrogen burning zone. The predicted $[\text{Al}/\text{Fe}]$ ratio varies up to ~ 2 dex depending on the prescription used for the reaction rates involving ^{27}Al .

Conclusions. The experiments we carried out support the view that some CEMP-no stars are made of a material processed by hydrogen burning that comes from a massive star experiencing mild to strong rotational mixing. During its burning, this material was likely enriched in helium burning products. No material coming from the carbon-oxygen rich core of the source star should be added to form the daughter star, otherwise the $^{12}\text{C}/^{13}\text{C}$ ratio would be largely above the observed range of values.

Key words. nuclear reactions, nucleosynthesis, abundances – stars: chemically peculiar – stars: abundances

1. Introduction

The content of iron at the surface of a star is often used as an indication of the chemical enrichment of its environment. A very small amount of iron relative to the sun indicates a region similar to the early universe where only few nucleosynthetic events occurred. A way to obtain new clues on stars in the early universe is then to examine the most iron deficient objects. Carbon-enhanced metal-poor stars (CEMP) are a subclass of iron deficient stars that have an excess of carbon relative to the sun and also an excess of oxygen and nitrogen in general. Although it can vary a bit from one author to another, the two common criteria defining a CEMP are $[\text{Fe}/\text{H}] < -1.0$ and $[\text{C}/\text{Fe}] > 0.7$ (Aoki et al. 2007). The range of $[\text{C}/\text{Fe}]$ covers ~ 3.5 dex, from $[\text{C}/\text{Fe}] = 0.7$ to $[\text{C}/\text{Fe}] = 4.26$ for HE1327-2326 (Norris et al. 2013; Allen et al. 2012). The frequency of CEMP seems to rise toward lower $[\text{Fe}/\text{H}]$ (Lee et al. 2013), but also with increasing distance from the Galactic plane (Frebel et al. 2006) or moving from inner to outer halo (Carollo et al. 2012). The so-called CEMP-no subclass is characterized by its low content in s- or r-elements, contrary to the other subclasses of CEMP stars: CEMP-s, CEMP-r, and CEMP-r/s (Beers & Christlieb 2005). CEMP-no stars are of particular interest since they dominate at $[\text{Fe}/\text{H}] \lesssim -3$ (Aoki 2010; Norris et al. 2013).

Among the scenarios explored to explain CEMP-no stars, we note the “spinstar” scenario (Meynet et al. 2006, 2010; Hirschi 2007; Chiappini 2013; Maeder et al. 2015) and the

“mixing and fallback” scenario (Umeda & Nomoto 2002, 2005; Tominaga et al. 2014). The latter explains CEMP-no with a model of faint supernovae from Pop III stars with mixing and fallback. The mixing considered in these models occurs just before or during the explosion. The zone of mixing and the mass cut² are free parameters of the models adjusted differently in each star to reproduce observed abundance patterns of CEMP-no stars.

According to the spinstar scenario, CEMP-no form in a region previously enriched by material that comes from low metallicity, rotating massive stars. During their nuclear lifetimes, spinstars experience mass loss and strong mixing triggered by rotation. As developed in Maeder et al. (2015), although they are different, these two models appear more complementary than contradictory. Processes like strong internal mixing in the source star, winds, or faint supernova may all have happened. Recently, Takahashi et al. (2014) has presented results based on rotating models with strong fallback (but no mixing in the sense of the works by Umeda & Nomoto) and tried to deduce the initial rotation of the source stars from comparisons with observed abundance patterns from three CEMP-no stars.

Maeder et al. (2015) proposed the idea that the variety of observed ratios is likely due to material being processed back and forth by hydrogen and helium burning regions in the spinstar. In other words, these two burning regions are exchanging material between them. These exchanges are triggered by the rotational mixing. In a first step, the helium burning products diffuse

¹ $[\text{X}/\text{Y}] = \log_{10}(N_{\text{X}}/N_{\text{Y}}) - \log_{10}(N_{\text{X}\odot}/N_{\text{Y}\odot})$ where $N_{\text{X},\text{Y}}$ is the number density of elements X and Y, and \odot denotes the abundances in the sun.

² The mass cut delimits the part of the star expelled from the part which is kept in the remnant.

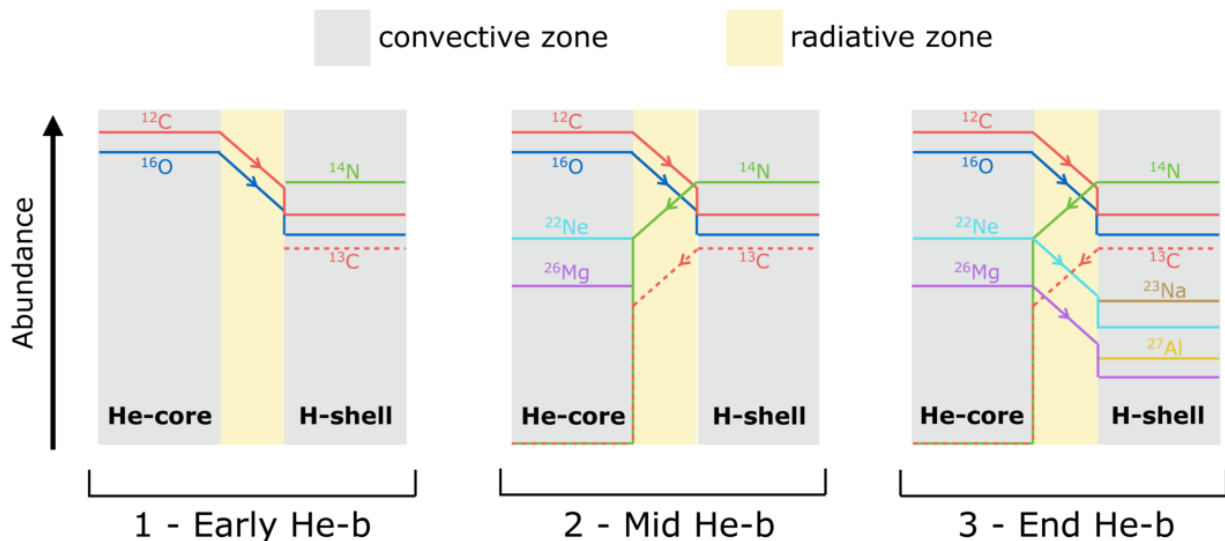


Fig. 1. Schematic view of the “back and forth” process at work in the spinstar. It occurs during the core helium burning phase and it is an exchange of chemical species between the helium burning core and the hydrogen burning shell.

into the hydrogen burning shell. More specifically, ^{12}C and ^{16}O synthesized in the helium core diffuse in the hydrogen burning shell, boosting the CNO cycle and creating primary ^{14}N and ^{13}C (see left panel of Fig. 1). In turn, the products of the hydrogen burning shell (among them ^{14}N) diffuse back into the helium core. The isotope ^{22}Ne is synthesized through the nuclear chain $^{14}\text{N}(\alpha, \gamma)^{18}\text{F}(e^+ \nu_e)^{18}\text{O}(\alpha, \gamma)^{22}\text{Ne}$. The isotope ^{26}Mg can also be synthesized thanks to the reaction $^{22}\text{Ne}(\alpha, \gamma)^{26}\text{Mg}$ (middle panel of Fig. 1). Some ^{25}Mg can also be created through the reaction $^{22}\text{Ne}(\alpha, n)^{25}\text{Mg}$. Neon and magnesium can enter the hydrogen burning shell again, boosting the Ne-Na and Mg-Al chains and therefore creating sodium and aluminium (right panel of Fig. 1). Through these back and forth exchanges between the hydrogen and helium burning regions, a series of isotopes can be formed. The abundances can vary a lot depending on the strength and number of these exchanges and thus such models can easily account for the variety of the abundance ratios observed at the surface of CEMP-no stars. For a given initial mass and rotation rate, the rotational mixing responsible for the exchanges described above is stronger at low metallicity. This effect is mainly due to the higher compactness of low metallicity stars (Maeder & Meynet 2001).

Putting aside the complexity of stellar models, we realize in this work simple nuclear experiments in order to illustrate the idea of Maeder et al. (2015) and to constrain the conditions needed in the source stars that would lead to the appropriate nucleosynthesis required to form CEMP-no stars. We study the impact of injecting ^{12}C , ^{16}O , ^{22}Ne , and ^{26}Mg in a hydrogen burning single zone at typical temperatures and densities of the hydrogen burning shell of a 20–60 M_{\odot} source star model at very low metallicity ($Z = 10^{-5}$). Different sets of nuclear rates are tested for the three main reactions involving ^{27}Al . We compare our results with a subsample of five CEMP-no stars which have a similar metallicity to that considered in our models and which are, according to Maeder & Meynet (2015), made of a material processed by hydrogen burning coming from the source star. We note that the active hydrogen burning shell in the source star can be enriched in products of helium burning, as explained

previously. Although limited, these numerical experiments, by focusing mainly on the nucleosynthesis of the problem, allow us to explore just what nuclear physics can do and how the results are sensitive to only some nuclear aspects of the problem. As we shall see, even these very simple numerical experiments allow us to obtain very interesting constraints on the sources of CEMP-no stars, constraints that are particularly strong since they are based on the most simple numerical experiments that we can imagine doing.

In Sect. 2, we recall briefly the classification of CEMP-no stars made by Maeder & Meynet (2015) and select the subsample of CEMP-no stars used in this work. The experiments we carried out are described in Sect. 3 and the results obtained in Sect. 4. Sections 5 and 6 are dedicated to a discussion about the $^{12}\text{C}/^{13}\text{C}$ ratio, the lithium and aluminium abundances. In Sect. 7, we discuss the possible astronomical origin of the CEMP-no stars considered. Conclusions are given in Sect. 8.

2. CEMP-no stars in classes 2 and 4

Maeder & Meynet (2015) provided a method for classifying the abundance patterns observed at the surface of CEMP-no stars based on two main ideas: the first is that some material can be exchanged between the hydrogen and helium burning regions inside the star. As noted in the previous section, the hydrogen burning reactions can transform the material enriched in helium burning products. This will boost the abundance of some isotopes, for instance ^{14}N . This ^{14}N can in turn diffuse into the helium burning region where it is transformed into ^{22}Ne , and ^{22}Ne can migrate into the hydrogen burning region, being transformed (at least in part) into ^{23}Na . Focusing on hydrogen burning regions, we speak of secular mixing of first order when the CNO cycle processes material enriched by the normal products of helium burning (typically C and O), and of second order when the nuclear reactions process material enriched in helium burning products resulting from material that was enriched in hydrogen burning products (typically ^{22}Ne , resulting from α -captures on ^{14}N). Similar definitions can be made for the helium burning

Table 1. Type (MS if $T_{\text{eff}} \geq 5500$ K and $\log g \geq 3.25$, RGB otherwise), class, and abundance data for the CEMP-no stars considered in this work.

Star	Type	Class	[Fe/H]	[C/Fe]	[N/Fe]	[O/Fe]	[Na/Fe]	[Mg/Fe]	[Al/Fe]	[Si/Fe]	[¹² C/ ¹³ C]	A(Li)	Ref.
CS 22945-017	MS	4++	-2.52	2.28	2.24	<2.36	-	0.61	-	-	-1.17	<1.51	4, 6, 9
CS 22949-037	RGB	4+	-3.97	1.06	2.16	1.98	2.10	1.38	0.02	0.77	-1.35	<0.13	7, 9
CS 22958-042	MS	4	-2.85	3.15	2.15	1.35	2.85	0.32	-0.85	0.15	-1.00	<1.33	4, 6, 9
CS 29498-043	RGB	4	-3.49	1.90	2.30	2.43	1.47	1.52	0.34	0.82	-1.17	<-0.05	7, 9
CS 30322-023	RGB	4++	-3.39	0.80	2.91	0.63	1.04	0.80	-	0.58	-1.35	<-0.3	1, 4, 5, 6
HE 0057-5959	RGB	2+Na	-4.08	0.86	2.15	<2.77	1.98	0.51	-	-	>-1.65	-	7
HE 1300+0157	MS	2	-3.75	1.31	<0.71	1.76	-0.02	0.33	-0.64	0.87	>-1.47	1.06	2, 6, 7
HE 1310-0536	RGB	2+	-4.15	2.36	3.20	<2.80	0.19	0.42	-0.39	<0.25	-1.47	<0.8	10, 11
HE 1327-2326	MS	4++	-5.76	4.26	4.56	3.70	2.48	1.55	1.23	-	>-1.25	<0.62	3, 6, 7
HE 1410+0213	RGB	2+	-2.52	2.33	2.94	2.56	-	0.33	-	-	-1.47	-	4, 6
HE 1419-1324	RGB	4++	-3.05	1.76	1.47	<1.19	-	0.53	-	-	-0.87	-	4, 6
HE 2331-7155	RGB	4	-3.68	1.34	2.57	<1.70	0.46	1.20	-0.38	-	-1.25	-	11
SMSS 0313-6708	MS	4++	<-7.1	>4.50	-	-	-	>3.3	-	-	-	0.7	8

References. 1 – Masseron et al. (2006); 2 – Frebel et al. (2007); 3 – Frebel et al. (2008); 4 – Masseron et al. (2010); 5 – Masseron et al. (2012); 6 – Allen et al. (2012); 7 – Norris et al. (2013); 8 – Keller et al. (2014); 9 – Roederer et al. (2014); 10 – Hansen et al. (2014); 11 – Hansen et al. (2015).

region. Different families of abundance patterns resulting from hydrogen and helium burning and secular mixing of various orders can result from these back and forth exchanges.

The second idea is that a second type of mixing can be envisaged; this one occurs between the stellar ejecta when the nuclear reactions have stopped. We call this type stellar ejecta mixing. Typically, some CEMP-no stars show signs of being made of material processed by hydrogen and helium burning and then mixed once ejected into the ISM. The material processed by hydrogen burning can result from secular mixing of various orders.

Using these lines of reasoning, Maeder & Meynet (2015) divided the CEMP-no class in five subclasses.

- Class 0: the CEMP-no is made of a material processed by hydrogen burning, but not enriched in helium burning products (no secular mixing, no mixing of the ejecta).
- Class 1: the CEMP-no is made of a material processed by helium burning, but not enriched in hydrogen burning products (no secular mixing, no mixing of the ejecta).
- Class 2: the CEMP-no is made of a material processed by hydrogen burning enriched in the normal products of helium burning (secular mixing of first order, no mixing of the ejecta).
- Class 3: the CEMP-no is made of a mixture of ejecta involving material processed by both hydrogen and helium burning. The material processed by hydrogen burning results from a secular mixing of first order, and the material processed by helium burning results from a secular mixing of second order (which means that the material processed by helium burning has been enriched by hydrogen burning products that have transformed helium burning products). For instance, large amounts of ¹⁴N and ¹³C coming from the transformation of ¹²C and ¹⁶O, enter the helium core by mixing. Then, successive α -captures on ¹⁴N create some ²²Ne and ^{25,26}Mg.
- Class 4: the CEMP-no is made of a material processed by hydrogen burning (no mixing of the ejecta) resulting from secular mixing of second order. This means that the hydrogen burning transforms material that was processed two times by helium burning. Typically, neon and magnesium enter the hydrogen shell again, boosting the Ne-Na and Mg-Al chains.

In each of the classes, refinements are made depending on how advanced the nuclear burning is. For instance, the Mg-Al chain may have acted to a greater or lesser degree in the source star

so that more or less aluminium has been created. A “+” after the class number indicates a material that is more processed. A material that is even more processed is indicated with “++” after the class number. We see that classes 1 and 3 are, at least partly, made of helium burning products while classes 0, 2, and 4 are made of hydrogen burning products. Maeder & Meynet (2015) attributed a class to 30 out of 46 CEMP-no stars: 4 belonging to class 2, 17 to class 3, and 9 to class 4.

In the present work, we focus on CEMP-no stars in classes 0, 2, and 4, i.e. made of a material processed by hydrogen burning that was eventually enriched in helium burning products. A characteristic shared by both stars in classes 2 and 4 (to date there are no observed CEMP-no in class 0) is a relatively low ¹²C/¹³C ratio, between 2 and 12 with a mean of 5.1. This value is characteristic of the CNO processing. The other CEMP-no stars generally have a higher ¹²C/¹³C (up to 50). Part of the helium burning region (¹²C-rich and ¹³C-poor) expelled by the source star is used to form classes 1 and 3, which explains the higher ¹²C/¹³C ratios for class 3 CEMP-no stars (there are no observed CEMP-no in class 1).

Our subsample is finally made of 13 CEMP-no stars in classes 2 and 4 with a mean [Fe/H] of -3.9. Table 1 gives the type, the class, and the abundance data for the sample of CEMP-no stars considered in this work. We note the class 2+Na for HE 0057-5959; “Na” stands because of the high [Na/Fe] ratio. The interpretation is the following: owing to a sufficiently high temperature, a significant amount of ²⁰Ne was synthesized in the helium burning core of the source star. Some of it diffused in the hydrogen burning shell, boosting the Ne-Na chain and therefore creating some ²³Na.

We note that among those 13 CEMP-no stars, 5 are dwarfs (MS, cf. Table 1) and 8 are giants (RGB, cf. Table 1) according to the following criteria: the stars with $T_{\text{eff}} \geq 5500$ K and $\log g \geq 3.25$ are dwarfs, the others are giants. The RGB CEMP may have undergone a dredge-up event, modifying their surface abundances. Such a dredge-up decreases the ¹²C surface abundances and increases the ¹³C and ¹⁴N surface abundance. The abundances of O, Ne, Na, Mg, and Al elements will not change since the temperature inside the hydrogen burning shell of such a low mass star is likely too low to activate the ON, Ne-Na, and Mg-Al cycles. If we look at the plots [C/Fe] and [N/Fe] versus $\log g$ for the observed CEMP-no stars (cf. Choplin et al. 2016, Fig. 1) we see that the dispersion of the carbon and nitrogen abundances with respect to iron are quite similar for MS and

RGB stars. This means that the effect of the first dredge-up does not change the abundance of carbon and nitrogen significantly with respect to the changes related to the dispersion of the initial abundances (about 4 dex). Based on stellar evolution models, [Placco et al. \(2014\)](#) have determined a correction

$$\Delta[\text{C}/\text{Fe}] = [\text{C}/\text{Fe}]_{\text{ini}} - [\text{C}/\text{Fe}]_{\text{after 1DU}} \quad (1)$$

to apply to the $[\text{C}/\text{Fe}]$ ratio of 505 metal-poor stars in order to recover their initial $[\text{C}/\text{Fe}]$. This correction corresponds to the effect of the first dredge-up (if any). Any dredge-up would decrease $[\text{C}/\text{Fe}]$ so that $\Delta[\text{C}/\text{Fe}] \geq 0$. We note that $\Delta[\text{C}/\text{Fe}] = 0$ for MS CEMP since they likely did not experience the first dredge-up. Five out of the eight RGB CEMP considered here belong to this sample; three have $\Delta[\text{C}/\text{Fe}] < 0.1$, one $\Delta[\text{C}/\text{Fe}] = 0.31$ (CS 29498-043), and one $\Delta[\text{C}/\text{Fe}] = 0.74$ (CS 22949-037). These corrections are small compared to the observed range of $[\text{C}/\text{Fe}]$ ratios.

In addition, because the CNO equilibrium value of $^{12}\text{C}/^{13}\text{C}$ is obtained at the surface of the MS stars, this implies that such low values, at least in these stars, cannot be due to a dredge-up event. Moreover, the highest $^{12}\text{C}/^{13}\text{C}$ belong to HE 1419-1324, a RGB CEMP, showing that the RGB feature is not necessarily associated with a low $^{12}\text{C}/^{13}\text{C}$ ratio, as expected by the effect of the dredge-up. Correcting the CNO abundances of the evolved CEMP-no stars is of course important in general, but in the framework of the present work we focus on the range of observed abundances rather than of individual stars, and hence these small corrections have no impact on our conclusions.

3. Presentation of the experiment

The conducted experiment consists in injecting products synthesized in the helium burning core of massive stars like ^{12}C , ^{16}O , ^{22}Ne , or ^{26}Mg in a hydrogen burning single zone of $1 M_{\odot}$ (hereafter H-box) with a constant temperature T and density ρ . The H-box schematically reproduces the convective hydrogen burning shell during the core helium burning phase of the source star.

To set the initial conditions in the H-box, we rely on a rotating $60 M_{\odot}$ model computed with the Geneva code. The initial metallicity is $Z = 10^{-5}$. It corresponds to $[\text{Fe}/\text{H}] = -3.8$ for the initial mixture we considered (α -enhanced). The initial abundances in the H-box are taken from the hydrogen burning shell of this model, at the beginning of the core helium burning phase, when the mass fraction of ^4He in the core $X_c(^4\text{He}) = 0.98$. Figure 2 shows the temperature and density profiles of this model during the core helium burning phase. The variable M_r is the mass coordinate and $X_c(^4\text{He})$ the central mass fraction of ^4He . We see from this figure that T and ρ in the convective hydrogen burning shell take values of 30–80 MK and 1–5 g cm^{-3} , respectively. For a $20 M_{\odot}$ model, the ranges of T and ρ are 30–60 MK and 1–10 g cm^{-3} . As a first step, we fix $T = 50$ MK and $\rho = 1 \text{ g cm}^{-3}$ in the H-box. Different temperatures and densities in the H-box are discussed later. The simulation is stopped either when the hydrogen in the box is exhausted (when the mass fraction of hydrogen in the H-box $X(^1\text{H}) < 10^{-8}$) or when the time t exceeds 10 Myr. We note that depending on the stellar model chosen for setting the initial abundances in the H-box, we can have a slightly different initial chemical composition in the H-box. This will depend on the chemical composition of the model in its hydrogen burning shell, at the core helium burning ignition ($X_c(^4\text{He}) = 0.98$). The CNO abundances in the hydrogen burning shell at the core helium burning ignition do not change significantly from a $20 M_{\odot}$ to a $60 M_{\odot}$ model. The abundances of neon, sodium, magnesium, and aluminium do vary a

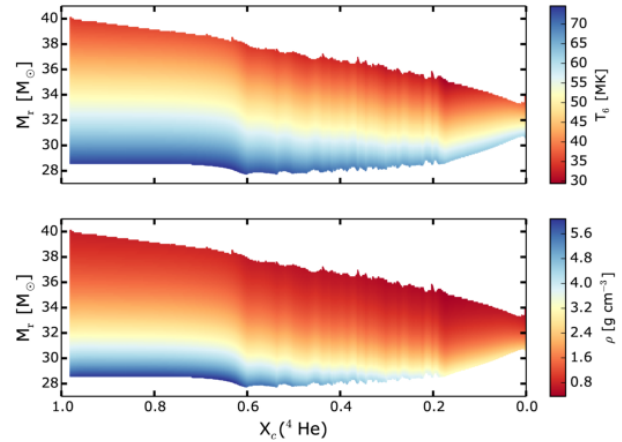


Fig. 2. M_r as a function of $X_c(^4\text{He})$, the central mass fraction of ^4He for a rotating $60 M_{\odot}$ model at a metallicity $Z = 10^{-5}$ (similar to a Kippenhahn diagram). Shown in color is the temperature T_6 in MK (upper panel) and the density ρ in g cm^{-3} (lower panel) in the convective hydrogen burning shell during the core helium burning phase from $X_c(^4\text{He}) = 0.98$ to $X_c(^4\text{He}) = 0$.

bit more owing to the difference in temperature that implies a slightly different nucleosynthesis in the hydrogen burning shell at the very beginning of the core helium burning phase.

Regarding the nuclear reaction rates, we took the ones used in the Geneva code (see [Ekström et al. 2012](#)). These rates are mainly from [Angulo et al. \(1999\)](#) for the CNO cycle, but almost all rates for Ne-Na Mg-Al chains are from [Hale et al. \(2002\)](#). Only $^{20}\text{Ne}(p, \gamma)^{21}\text{Na}$ and $^{21}\text{Ne}(p, \gamma)^{22}\text{Na}$ are taken from [Angulo et al. \(1999\)](#) and [Iliadis et al. \(2001\)](#), respectively. We note that the final abundance of ^{26}Al in the H-box is added to the one of ^{26}Mg since ^{26}Al is a radioactive isotope ($t_{1/2} = 7.17 \times 10^5$ yrs) decaying into ^{26}Mg .

In order to reproduce schematically the diffusion of ^{12}C , ^{16}O , ^{22}Ne , and ^{26}Mg from the helium core to the hydrogen shell, we inject a constant mass per year into the H-box, which comes from a reservoir composed only of the considered species (^{12}C , ^{16}O , ^{22}Ne , or ^{26}Mg). We consider injection rates of 10^{-10} , 10^{-8} , and $10^{-6} M_{\odot} \text{ yr}^{-1}$ for ^{12}C and ^{16}O and 10^{-12} , 10^{-10} , and $10^{-8} M_{\odot} \text{ yr}^{-1}$ for ^{22}Ne and ^{26}Mg . More details about the method for injecting the species and the justification of the adopted injection rates are given in the Appendix. Four cases are tested in the present experiment:

- no injection is made in the H-box;
- ^{12}C and ^{16}O are injected;
- ^{12}C , ^{16}O , and ^{22}Ne are injected;
- ^{12}C , ^{16}O , ^{22}Ne , and ^{26}Mg are injected.

We note that in a real star, the mass is conserved and thus any injection into the hydrogen burning shell implies that some matter has to diffuse away from that region. In complete stellar models, the elements that are more abundant in the hydrogen burning shell than in one of the two adjacent regions will diffuse into the region(s) where this element is less abundant. However to keep the model as simple as possible we do not consider that complication here. The present work can be seen as a numerical experiment and not as an attempt to model all the details of what happens in stars. Indeed, the most important gradients of abundances are those from the difference in the abundances between the helium core and the hydrogen burning shell. Diffusion from

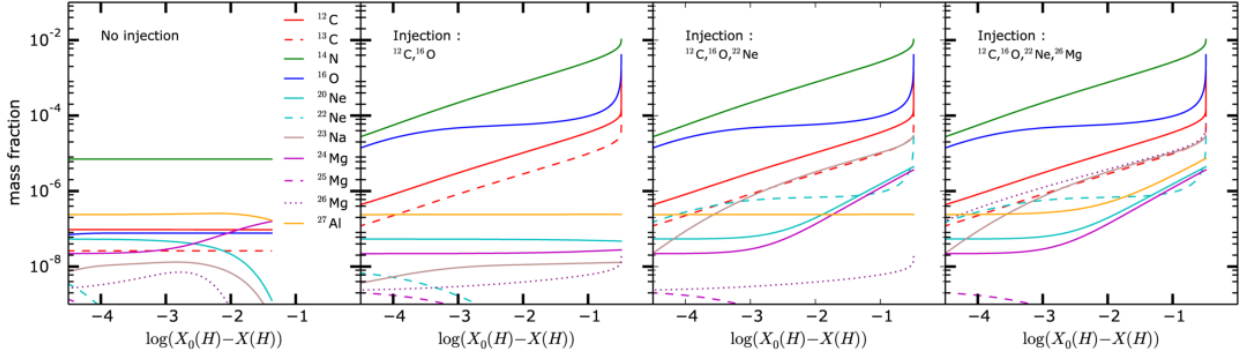


Fig. 3. Abundances in the H-box as a function of the logarithm of $X_0(\text{H}) - X(\text{H})$. The four panels (from left to right) correspond to the four considered cases: when no injection is made; when ^{12}C and ^{16}O are injected; when ^{12}C , ^{16}O , and ^{22}Ne are injected; and when ^{12}C , ^{16}O , ^{22}Ne , and ^{26}Mg are injected. Density and temperature in the box are $\rho = 1 \text{ g cm}^{-3}$ and $T_6 = 50 \text{ MK}$.

the helium core to the hydrogen burning shell is therefore clearly the dominant feature, blurring all the other diffusion processes. In complete stellar models, injection of nitrogen into the helium core occurs dominantly by convection when the helium core slightly grows in regions left over by the hydrogen burning shell, not by diffusion from the hydrogen to the helium burning region. Also, as we show, the results obtained from complete stellar models (that follow in a consistent way the mixing of the elements) are well reproduced by our simple box model. Thus we are quite confident that our simple approach grasps the essentials of the process.

We also note that the origin of the iron is not investigated in the present work. By choosing a non-zero metallicity, we assume that the small iron content observed at the surface of the CEMP-no stars is already present in the source star (and in the H-box). Our sample of class 2 and 4 CEMP-no stars is expected to be made of a material processed by hydrogen burning that comes from the source star, i.e. from the outer layers of this star. The iron abundance in those outer layers is likely not affected by the nucleosynthesis and remains equal to its initial value. As a consequence, a comparison of the models with the observed ratios like $[\text{C}/\text{Fe}]$ or $[\text{N}/\text{Fe}]$ can be made, provided that the iron content in the models (the $[\text{Fe}/\text{H}]$ ratio) is similar to the iron content of the CEMP-no stars. In our models, $[\text{Fe}/\text{H}] = -3.8$ so that the observed CEMP-no stars around this value can be consistently compared with the models.

4. Results of the experiment

Figure 3 shows the mass fraction of elements as a function of $\log(X_0(\text{H}) - X(\text{H}))$ (i.e. the logarithm of the initial mass fraction of hydrogen minus the current hydrogen mass fraction in the H-box) for the four cases presented in Sect. 3. The initial mass fraction of ^1H in the box is equal to 0.33, the temperature and density are set to $T = 50 \text{ MK}$ and $\rho = 1 \text{ g cm}^{-3}$, and the injection rates are $10^{-8} M_\odot \text{ yr}^{-1}$ for ^{12}C and ^{16}O and $10^{-10} M_\odot \text{ yr}^{-1}$ for ^{22}Ne and ^{26}Mg . We describe now the four panels in Fig. 3, from left to right:

1. When no injection is made only 4.28×10^{-2} of hydrogen (in mass fraction) is consumed at the end of the limited time, which we fixed at 10 Myr. No transient regime is seen for the CNO elements since the CNO cycle is already at equilibrium at $t = 0$. The initial increase of $X(^{23}\text{Na})$, the mass fraction of sodium, is due to the effect of the Ne-Na chain. It finally drops, like $X(^{20}\text{Ne})$, in favour of $X(^{24}\text{Mg})$ owing to the reaction $^{23}\text{Na}(p, \gamma)^{24}\text{Mg}$. At $T_6 = 50$, since the $^{24}\text{Mg}(p, \gamma)^{25}\text{Al}$ reaction is weak, it does not transform efficiently the ^{24}Mg synthesized so that the ^{24}Mg abundance increases. A small amount of ^{27}Al is destroyed when little ^1H remains in the shell and is transformed either into ^{28}Si through $^{27}\text{Al}(p, \gamma)^{28}\text{Si}$, or into ^{24}Mg through $^{27}\text{Al}(p, \alpha)^{24}\text{Mg}$, both channels being almost equal at this temperature.
2. When ^{12}C and ^{16}O are injected, the CNO cycle is boosted and primary ^{14}N and ^{13}C are created. The CNO elements are more and more abundant so that more and more hydrogen is burnt. It is finally exhausted after $\sim 0.8 \text{ Myr}$. The reactions in the CN cycle are fast so that an equilibrium is almost instantaneously reached for ^{12}C , ^{13}C , and ^{14}N . Since the reaction $^{16}\text{O}(p, \gamma)^{17}\text{F}$ is much slower, the injected ^{16}O accumulates before being transformed into ^{17}F . These two regimes can be seen in the second panel of Fig. 3: the curve showing ^{16}O first increases until $\log(X_0(\text{H}) - X(\text{H})) \sim -3$ (accumulation) and then becomes flatter for $-3 < \log(X_0(\text{H}) - X(\text{H})) < -1$ (^{16}O destruction becomes important). No permanent regime is attained for ^{16}O . At the end ^{12}C and ^{16}O rise dramatically because the hydrogen is almost exhausted: the CNO cycle works less and less, implying an accumulation of the injected ^{12}C and ^{16}O . Regarding the other elements, we see that ^{22}Ne decreases in favour of ^{23}Na , but the duration of the simulation is too short in this case for the Ne-Na and Mg-Al chains to operate significantly.
3. When the same experiment is performed and some ^{22}Ne is also injected, ^{23}Na and ^{24}Mg are synthesized through the reactions $^{22}\text{Ne}(p, \gamma)^{23}\text{Na}$ and $^{23}\text{Na}(p, \gamma)^{24}\text{Mg}$. Some ^{20}Ne is also created when the reaction $^{23}\text{Na}(p, \alpha)^{20}\text{Ne}$ occurs. At this temperature and for the selected rates, the (p, α) channel is 1.6 higher than the (p, γ) channel so that ^{23}Na is almost equally destroyed in ^{20}Ne and ^{24}Mg . The reaction $^{24}\text{Mg}(p, \alpha)^{25}\text{Al}$ is too slow to activate the Mg-Al chain. Since neon, sodium, and magnesium are much less abundant than the CNO elements, the hydrogen is not burnt significantly quicker than in case 2 when only ^{12}C and ^{16}O are injected.
4. When injecting ^{26}Mg as well there is a ~ 2 dex increase in ^{27}Al due to the direct transformation of ^{26}Mg into ^{27}Al thanks to a proton capture. For the temperature, density, and time of simulation considered, the ^{27}Al destruction through either the (p, α) or (p, γ) channels is not significant.

A&A 593, A36 (2016)

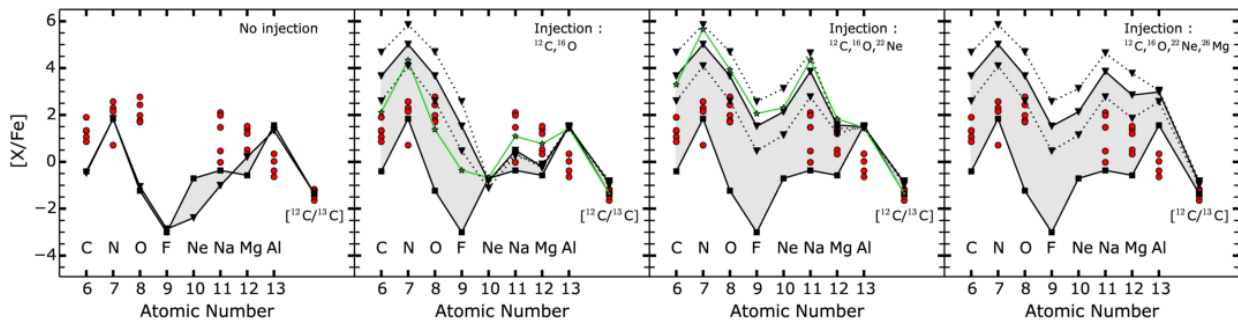


Fig. 4. $[X/Fe]$ ratios in the H-box for the four considered cases (from left to right). The $[^{12}C/^{13}C]$ ratio is also shown (i.e. $^{12}C/^{13}C$ ratio relative to the sun, in logarithm). The red points show the CEMP-no stars of Table 1 with $[Fe/H] = -3.8 \pm 0.3$. The abundance patterns in the box at $t = 0$ are represented by black lines with squares and the patterns at the end of the simulation by black lines with triangles. The lower and upper black dotted lines represent the final composition in the H-box when the rates of injection are divided and multiplied by 10^2 , respectively. The green pattern on the second (third) panel shows the composition in the hydrogen burning shell at the end of the core helium burning phase of a complete $20 M_{\odot}$ stellar model at 30% (70%) of the critical velocity on the ZAMS. Density and temperature in the box are $\rho = 1 \text{ g cm}^{-3}$ and $T_6 = 50 \text{ MK}$.

Figure 4 shows the $[X/Fe]$ ratios for the four cases presented in Fig. 3. The initial abundance pattern in the H-box (lines with squares) and the final pattern (lines with triangles) are plotted. The grey area corresponds to the range of values covered during the simulation. The dotted lines correspond to the final patterns in the H-box when the rates of injection are divided and multiplied by 100. The red points represent the observed ratios in CEMP-no stars of similar metallicities ($[Fe/H] = -3.8 \pm 0.3$) to the metallicity considered in our numerical experiment ($[Fe/H] = -3.8$). As mentioned in Sect. 3, it is important to focus on the CEMP-no stars that have similar metallicities to the one in the models since the iron abundance in our model is an initial condition that is not modified by the nuclear reactions occurring in the H-box. Any change in the initial iron abundance in the models will produce a shift of the $[X/Fe]$ ratios predicted by the models.

Without injection, the abundance pattern in the H-box does not change very much and all the $[X/Fe]$ ratios (except $[N/Fe]$ and $[Al/Fe]$) stay below the observed values. This is not surprising since the observed values correspond to classes 2 and 4, while the present experiment (no injection) would instead correspond to the CEMP-no stars in class 0. This class is made of a material processed only by hydrogen burning and where no mixing occurred between the hydrogen and helium burning regions. Injecting some ^{12}C and ^{16}O enhances the corresponding $[X/Fe]$ ratios and the $[N/Fe]$ (Fig. 4, second panel). Increasing or decreasing the rate of injection by a factor of 100 (dotted lines) changes the final pattern in the box, but not dramatically: from the lower to the upper dotted line, the rate of injection is multiplied by 4 dex while the difference in $[X/Fe]$ values does not exceed 2 dex (for C, N, and O) because when injecting more ^{12}C and ^{16}O in the H-box, the hydrogen is burnt more rapidly and hydrogen exhaustion occurs earlier. We have here a negative feedback process: increasing the rate of injection increases the amount of injected species, but at the same time reduces the available time for injecting those new chemical species in the H-box. This explains qualitatively why injecting ^{12}C and ^{16}O at a rate 10^4 higher does not lead to an increase of 4 dex in the final $[C/Fe]$, $[N/Fe]$, and $[O/Fe]$ ratios. The third case shows enhancements of $[Ne/Fe]$, $[Na/Fe]$, and $[Mg/Fe]$ ratios: protons captured on the injected ^{22}Ne create ^{23}Na and then ^{24}Mg . The final patterns of the fourth case present enhancements of $[Mg/Fe]$ and $[Al/Fe]$ ratios compared to case 3: owing to the injection of ^{26}Mg , the Mg-Al chain is boosted, hence creating some ^{27}Al .

Changing the temperature and the density in the H-box leads to the results presented in Fig. 5. We tested temperatures of $T_6 = 50, 60,$ and 80 MK at a constant density $\rho = 1 \text{ g cm}^{-3}$ (left panel) and densities of $\rho = 1, 10,$ and 100 g cm^{-3} at a constant temperature $T_6 = 50 \text{ MK}$ (right panel). For both cases, the injected species are ^{12}C , ^{16}O , ^{22}Ne , and ^{26}Mg and the injection rates are $10^{-8} M_{\odot} \text{ yr}^{-1}$ for ^{12}C and ^{16}O and $10^{-10} M_{\odot} \text{ yr}^{-1}$ for ^{22}Ne and ^{26}Mg . In addition to the other $[X/Fe]$ ratios, $[Si/Fe]$ is also shown. Increasing either the temperature or the density leads to lower $[X/Fe]$ ratios at hydrogen exhaustion (except for the $[Si/Fe]$ ratio at $T_6 = 80 \text{ MK}$). When raising the density for instance, the rates of the nuclear reactions increase allowing a quicker synthesis of the chemical species than at lower densities. At the same time, the hydrogen is burnt more rapidly so that hydrogen exhaustion occurs earlier, leaving less time to inject new species. Summing those two opposite effects finally leads to lower $[X/Fe]$ ratios at hydrogen exhaustion. For the same reasons, similar results are found when varying the temperature, although the dependence of the nuclear rates on temperature is much stronger than the dependence on the density. This is the reason why the various temperatures spanning a relatively small range of values (see Fig. 5) change the $[X/Fe]$ ratios much more significantly than the various densities, even though they cover a much larger range of values.

The initial $[Si/Fe]$ ratio in the box is about 1 and it is little affected by changes in temperature and density. However, increasing the temperature to $T_6 = 80 \text{ MK}$ leads to about 0.5 dex more silicon at the end. The first reason is that the nuclear rates associated with Mg, Al, and Si are generally 3–4 dex higher at $T_6 = 80 \text{ MK}$ than at $T_6 = 50 \text{ MK}$, allowing the synthesis of some ^{28}Si . The second reason is that the ^{27}Al is destroyed either to form ^{28}Si thanks to the $^{27}Al(p, \gamma)^{28}Si$ reaction or to form ^{24}Mg owing to the reaction $^{27}Al(p, \alpha)^{24}Mg$. When ^{27}Al transforms into ^{24}Mg , the Mg-Al chain operates and synthesizes ^{27}Al again. Instead, ^{27}Al is definitely destroyed when it is transformed into ^{28}Si . At $T_6 = 50$ and 60 MK , both channels are roughly equal. At $T_6 = 80 \text{ MK}$, the (p, γ) channel is ~ 40 times higher than the (p, α) channel. This tends to reduce Mg and Al and to increase Si.

Also shown in Figs. 4 and 5 is the $[^{12}C/^{13}C]$ ratio, i.e. $\log(^{12}C/^{13}C) - \log(^{12}C/^{13}C)_{\odot}$. The isotopic ratio in the Sun is taken from Lodders (2003). In all cases, the $[^{12}C/^{13}C]$ ratio does not vary more than 0.5 dex, always staying around -1.5 because

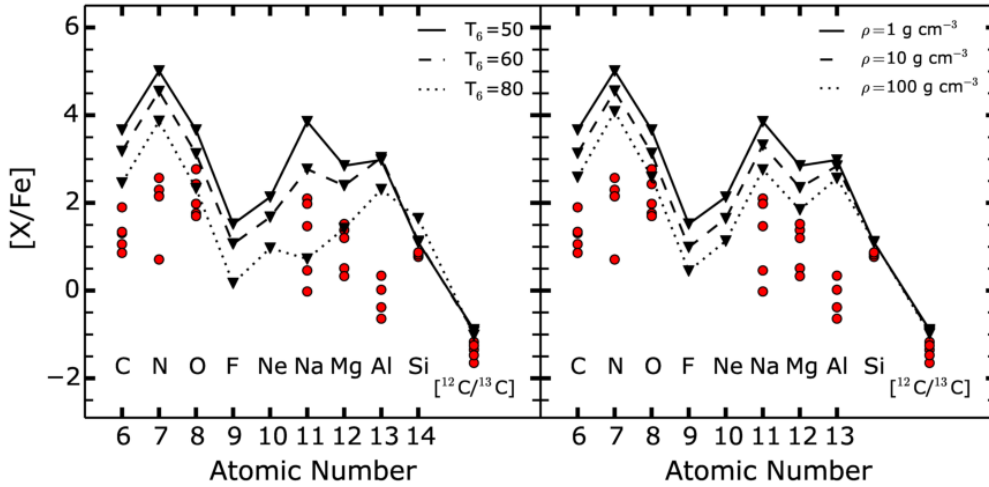


Fig. 5. *Left:* same as Fig. 4 but for three different temperatures in the H-box. The [Si/Fe] ratio is also shown. Only the final abundance patterns in the box are plotted. The injected species are ^{12}C , ^{16}O , ^{22}Ne , and ^{26}Mg . Density is unchanged (1 g cm^{-3}) and the injection rate is $10^{-8}\text{ }M_{\odot}\text{ yr}^{-1}$ for ^{12}C and ^{16}O and $10^{-10}\text{ }M_{\odot}\text{ yr}^{-1}$ for ^{22}Ne and ^{26}Mg . *Right:* same as the *left panel* but for three different densities in the H-box. The temperature is set to 50 MK.

the equilibrium value is quickly reached when the CNO cycle operates. After each injection of ^{12}C , the equilibrium ratio is reached again almost instantaneously compared to the current timestep. In particular, $[^{12}\text{C}/^{13}\text{C}]$ reaches similar final values under all the explored temperatures and densities. When the CNO cycle operates, the $[^{12}\text{C}/^{13}\text{C}]$ equilibrium ratio is indeed almost temperature and density independent.

We see that the observed $[X/\text{Fe}]$ ratios are best covered when injecting ^{12}C , ^{16}O , and ^{22}Ne (see the grey area in the third panel of Fig. 4). We note, however, that the models always give values that are too high for the $[\text{Al}/\text{Fe}]$ ratios (see Sect. 6). For all the other ratios, our very simple numerical experiment confirms the need for some mixing between the helium and hydrogen burning zones in the source star to explain the general pattern observed in CEMP-no stars in classes 2 and 4. The injection of ^{22}Ne seems to be needed, which supports the view that a strong mixing might be at work in the source star: ^{22}Ne can enter the hydrogen burning shell if ^{12}C and ^{16}O have first diffused in the hydrogen burning shell, but also if the created ^{14}N have entered in turn in the helium burning core. For most of the ratios, however, we note that the grey region is wider than the ranges covered by the observations. We do not think this is a very serious problem when considering that CEMP-no stars are not made of pure hydrogen shell material. To be used to form new stars, this matter needs to be ejected either by winds or at the time of the supernova. In this process, the region where the CNO cycle is active (hydrogen shell) is mixed with other layers of the star and eventually with some interstellar medium. For instance, any mixing with the outer layers of the star where the iron has the same abundance as in the hydrogen shell – but where the CNO abundances are smaller and close to their initial values ($\sim 10^{-5}$ for a model with $Z = 10^{-5}$) – will shift the nitrogen abundance downward. Therefore, in order to obtain the observed nitrogen abundances in CEMP-no stars, it is likely needed that much higher abundances are reached in the hydrogen burning shell. While our box experiments provide some interesting constraints on the nuclear processes that might be needed to reproduce the peculiar abundance patterns of CEMP-no stars, only the computation of complete stellar models that take into account the ejection

mechanism (both through winds and through the supernova explosion) and some possible mixing with the circumstellar material can provide abundances ratios that might be compared with the observed ratios in CEMP-no stars. This has to be kept in mind when interpreting the comparison shown in Fig. 4.

We note also that injecting some ^{26}Mg raises the $[\text{Al}/\text{Fe}]$ ratio far above the observed range. In stellar models, ^{26}Mg comes from the transformation of ^{22}Ne which occurs at the very end of the core helium burning phase. Thus, ^{26}Mg could be injected (if at all) only at the very end or after the core helium burning phase, leaving little time for nuclear burning to transform this ^{26}Mg into ^{27}Al in the hydrogen burning shell. In this respect, the present numerical experiments injecting ^{26}Mg regularly all along the burning of the hydrogen shell clearly overestimates what occurs in real stars. Thus, the hypothesis without ^{26}Mg injection is by far the most probable.

It is interesting to note that detailed stellar models are qualitatively well enough reproduced by this simple one-zone model. The two green patterns in Fig. 4 show the $[X/\text{Fe}]$ ratio in the hydrogen burning shell of a complete stellar model at the end of the core helium burning phase. The abundances are taken in the hydrogen shell where the energy released by hydrogen burning is the highest. The two stellar models are $20\text{ }M_{\odot}$, $Z = 10^{-5}$ stars computed at 30% (second panel) and 70% (third panel) of the critical velocity on the ZAMS, which correspond to an initial equatorial velocity of 280 and 610 km s^{-1} , respectively. Increasing the initial velocity can be modelled in the single-zone model by increasing the injection rate and injecting some ^{22}Ne in addition to the ^{12}C and ^{16}O . By comparing the two green patterns, it is also interesting to see the strong impact of the initial rotation on the $[X/\text{Fe}]$ ratios in the hydrogen burning shell at core helium exhaustion. This shows that the stellar rotation at low metallicity is likely a non-negligible process.

One point that deserves more discussion is the constant value found for the $^{12}\text{C}/^{13}\text{C}$ ratio under various conditions. What can be learnt from this ratio? How can it be used in stellar evolution models? The lithium content at the surface of the CEMP-no stars can give interesting constraints as well. A deeper investigation into the $[\text{Al}/\text{Fe}]$ ratio also seems worthwhile because of the

discrepancy we found between models and observations. Which conditions or assumptions will favour a lower $[Al/Fe]$ ratio, closer to the observed values?

5. Dilution with material processed by helium burning and with initial ISM

In the previous section we investigate the secular mixing between the hydrogen and helium burning regions during the nuclear life of the source star. We now discuss the mixing events that can happen outside the star when the nuclear reactions are no longer active. Different kinds of materials can be ejected by the source star into the ISM. We consider two of them here: (i) the material processed by hydrogen burning and (ii) the material processed by helium burning. Outside the star, these materials can be mixed together and/or with the ISM. We distinguish two kinds of dilutions:

1. the dilution between the material processed by hydrogen burning and the material processed by helium burning. This corresponds to a mixing between different parts of the star. By mixing we mean mixing of the ejecta (or stellar ejecta mixing, as defined in Sect. 2), hence outside of the star and without nuclear reactions.
2. the dilution between all the material ejected by the source star (processed by either hydrogen or helium burning) and the initial ISM, in which the source star formed. This is a mixing of the stellar ejecta with the initial ISM.

Based on considerations of the $^{12}C/^{13}C$ ratio and the lithium abundance, we investigate the possibility of constraining these two kinds of mixing events.

5.1. Using the $^{12}C/^{13}C$ ratio to constrain the amount of ejecta processed by helium burning

The $^{12}C/^{13}C$ ratio of the selected CEMP-no stars gives a strong constraint on the kind of material needed to form these stars. As we see in Fig. 4, this ratio is very close to the value found in a CNO processed material. We see from Figs. 4 and 5 that injecting some ^{12}C into a hydrogen burning region does not change the $^{12}C/^{13}C$ ratio under various densities, temperatures, and rates of injection. However, when the nuclear reactions are switched off (which is what happens when the material is ejected from the source star) and the CNO processed material is mixed with part of the region processed by helium burning, this ratio will no longer stay around the observed values.

This point can be illustrated with a simple experiment. It is possible to mix the two kinds of material ejected by the source star, the ejecta processed by hydrogen burning and by helium burning (hereafter H-ejecta and He-ejecta). It is interesting to follow the evolution of the $[^{12}C/^{13}C]$ ratio as adding more and more He-ejecta to the H-ejecta. The left panel of Fig. 6 shows $[^{12}C/^{13}C]$ as a function of f_{mix} defined as the fraction of He-ejecta added to the H-ejecta. For instance, $f_{mix} = 10^{-2}$ means 1% of He-ejecta with 99% of H-ejecta. We tested two compositions for the H-ejecta. The first has mass fraction of ^{12}C and ^{13}C equal to 1.11×10^{-7} and 3.10×10^{-8} . It is called *C-poor H-ejecta*. These mass fractions are the ones in the H-box at $t = 0$. The second mixture has a ^{12}C mass fraction of 2.01×10^{-4} and a ^{13}C mass fraction of 5.45×10^{-5} . We call it *C-rich H-ejecta*. These values correspond to the mass fractions of ^{12}C and ^{13}C in the H-box, a short time before hydrogen exhaustion when ^{12}C is injected.

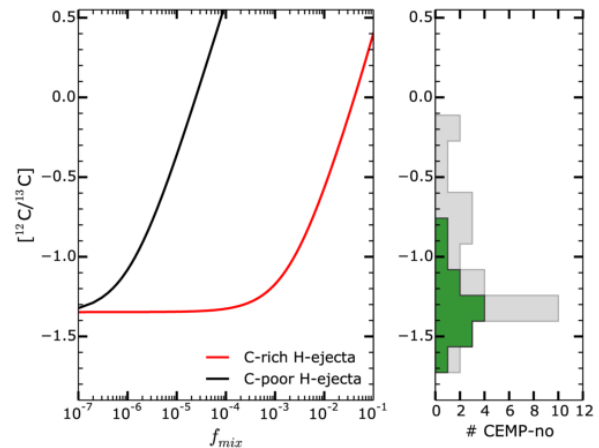


Fig. 6. Left: $[^{12}C/^{13}C]$ ratio as a function of the mixing factor f_{mix} , which represents the fraction of material processed by helium burning mixed with the material processed by hydrogen burning. Two compositions are tested for the material processed by hydrogen burning: a C-rich composition (red line) and a C-poor composition (black line). Right: green histogram showing the distribution of the CEMP-no stars used in this work. They belong to class 2 or 4. The grey histogram shows all known CEMP-no stars with a measured $^{12}C/^{13}C$ ratio.

- The *C-poor H-ejecta* corresponds to the low rotational mixing case. A small amount of ^{12}C has diffused from the helium core to the hydrogen shell so that the mass fractions of ^{12}C and ^{13}C in the hydrogen burning shell stay around their initial value, i.e. around 10^{-7} . When this part of the star is expelled, we get ejecta that is poor in carbon.
- The *C-rich H-ejecta* corresponds to the strong rotational mixing case. A lot of ^{12}C has diffused into the hydrogen burning shell, raising its abundance and that of ^{13}C far above their initial values. At the time of the ejection, this material is more enriched in carbon than in the previous case.

For the carbon abundances in the He-ejecta, we took the characteristic values in the helium burning core. We set $X_{Heb}(^{12}C) = 0.1$ and $X_{Heb}(^{13}C) = 0$ as a correct approximation.

We see in the left panel of Fig. 6 that mixing 1% (i.e. $f_{mix} = 10^{-2}$) of the He-ejecta with 99% of a C-rich H-ejecta leads to a $[^{12}C/^{13}C]$ of -0.6 , which lies above the range of observed values for the CEMP-no stars in classes 2 and 4 (see green histogram in left panel of Fig. 6 and Table 1). If no rotational mixing has occurred between the helium burning core and hydrogen burning shell of the source star, the H-ejecta is C-poor. In this case, mixing the same amount of He-ejecta as before with the H-ejecta material leads to a $[^{12}C/^{13}C]$ ratio of 2.6, far above the observed range. It seems that whatever the C-richness of the H-ejecta, hence whatever the amount of helium products that enter the hydrogen burning shell during the life of the source star, the final contribution of the material processed by helium burning coming from the source star should be null to form the CEMP-no stars in classes 2 and 4. This strongly supports the idea that the CEMP-no stars in classes 2 and 4 are only made of the hydrogen envelope of the source star. More generally, since $^{12}C/^{13}C$ is highly sensitive to the burning region considered (it is low for a hydrogen burning region and high for helium burning), this ratio could be used to constrain the mass cut of spinstar models at the time of the supernova: the mass cut could be chosen in

order to reproduce the observed $^{12}\text{C}/^{13}\text{C}$ ratio of the considered CEMP-no star.

The grey histogram in the right panel of Fig. 6 shows the distribution of all observed $^{12}\text{C}/^{13}\text{C}$ ratios at the surface of CEMP-no stars. It contains the 12 CEMP-no stars from Table 1 with a measured $^{12}\text{C}/^{13}\text{C}$ ratio plus 15 other CEMP-no stars. Some CEMP-no stars have higher $^{12}\text{C}/^{13}\text{C}$ ratios, suggesting the need for a small amount of material processed by helium burning to form them. We see, however, that the amount of material processed by helium burning needed should remain small in any case ($f_{\text{mix}} \lesssim 0.05$): mainly the hydrogen envelope of the progenitor should be used to form the CEMP-no stars. Nevertheless, we note that some CEMP-no stars only have a lower limit for the $^{12}\text{C}/^{13}\text{C}$ ratio (3 out of 12 in our subsample). An accurate determination of this ratio for those stars would be interesting in order to validate the previous statement regarding these stars.

5.2. $A(\text{Li})$ to constrain the dilution with the initial ISM

In the previous section, we discussed the mixing of the stellar ejecta: the regions processed by hydrogen and helium burning ejected by the source star can be mixed together when the nuclear burning has stopped. The following discussion is related to the mixing (or the dilution) of the whole stellar ejecta with the initial ISM in which the source star formed.

Lithium is an interesting element that can be used to obtain information on the amount of ISM that should be mixed with the source star ejecta to form the CEMP-no stars. The abundance of lithium $A(\text{Li})$ in the pristine ISM is equal to 2.72 according to Cyburt et al. (2008). It is totally destroyed in massive stars. As a consequence, as soon as the ejecta of the massive source star is mixed with the ISM, the abundance of lithium is raised (in the mixture made of initial ISM and source star ejecta). If we assume that the lithium content at the surface of the CEMP-no star reflects the lithium content in the cloud where it formed, then the higher the lithium content at the surface of the CEMP-no star, the more the source star ejecta was diluted with the ISM. The dilution factor for mixing the progenitor ejecta with the ISM can be chosen in order to obtain the observed $A(\text{Li})$ value of the considered CEMP-no star.

One difficulty is that the lithium at the surface of the CEMP-no star can be depleted by internal mixing processes in the CEMP-no star itself. However, such processes might not be able to explain the low content of lithium observed at the surface of some CEMP-no stars. Meynet et al. (2010) pointed out that the maximal depletion predicted by the models of Korn et al. (2009) (1.2 dex) is unable to account for the $A(\text{Li})$ value observed at the surface of HE 1327-2326 ($A(\text{Li}) < 0.62$, see Table 1). According to the models of Korn et al. (2009), we would indeed expect a minimum observed value of $A(\text{Li}) = 2.72 - 1.2 = 1.52$ i.e. the WMAP content minus the maximum predicted depletion factor. We see that the depletion mechanism cannot easily account for the lowest observed $A(\text{Li})$ values. The alternative for HE 1327-2326 is that it formed from Li-poor material.

The $A(\text{Li})$ values (or upper limits) for nine of the considered CEMP-no stars are shown in Table 1. The lower panel of Fig. 3 in Meynet et al. (2010) shows the dilution factor $M_{\text{ISM}}/M_{\text{eje}}$ vs. $A(\text{Li})$. According to this figure and if we consider that the lithium was not depleted by the CEMP-no stars themselves, the dilution factor should be less than ~ 0.1 for the stars considered in this work. The highest dilution factor being for CS 22945-017, which has $A(\text{Li}) < 1.51$. The final mass fraction of ^{12}C , ^{14}N , and ^{16}O

in the H-box when injecting ^{12}C and ^{16}O is at least 10^{-3} (see Fig. 3). The mass fraction of the CNO elements in a $Z = 10^{-5}$ ISM is about 10^{-6} . Using 90% of 10^{-3} with 10% of 10^{-6} gives $\sim 10^{-3}$; the dilution does not play a significant role in this case.

We now suppose that the lithium was depleted by the CEMP-no stars. We take the maximum depletion factor (1.2 dex) from Korn et al. (2009) and we add it to the observed $A(\text{Li})$ in order to get the initial $A(\text{Li})$ value before the depletion process. The two highest $A(\text{Li})$ belong to CS 22945-017 (< 2.71) and CS 22958-042 (< 2.53). Because $A(\text{Li})$ is close to the WMAP value for CS 22945-017, it would imply a high dilution factor. However, for CS 22958-042 and all the other considered CEMP-no stars, the dilution factor should be less than ~ 2 . There is still not enough ISM for the dilution to have a significant effect, except for CS 22945-017. Caution is needed when considering these simple statements about the dilution between ejecta and ISM, but in the framework of our simple model we see that the dilution with the initial ISM might only play a limited role because the metal abundances in the region processed by hydrogen burning are much higher than the values in the initial ISM and because the dilution factors derived from the lithium abundance are small in most of the cases.

6. Al and Si abundances

The experiments presented in Sect. 4 show that the $[\text{Al}/\text{Fe}]$ ratio in the H-box at hydrogen exhaustion always lies above the observed range of values. Even the initial $[\text{Al}/\text{Fe}]$ – taken from the hydrogen burning shell of a $60 M_{\odot}$ model at the beginning of the core helium burning phase – is just above the observed range (see lines with squares in Fig. 4). We investigate now three effects on the aluminium abundance: the injection (species and rate), the temperature, and the nuclear reaction rates.

6.1. Impact of injection on Al: species and rate

First of all, a lower final $[\text{Al}/\text{Fe}]$ ratio is expected if no ^{26}Mg is injected. If it is injected, some ^{27}Al is created through the reaction $^{26}\text{Mg}(p, \gamma)^{27}\text{Al}$. This is illustrated in the third and fourth panels of Fig. 4. We see indeed that injecting ^{26}Mg leads to a higher final $[\text{Al}/\text{Fe}]$ than if no ^{26}Mg is injected.

Figure 7 shows $[\text{Al}/\text{Fe}]$ as a function of $R_{^{22}\text{Ne}}$: the rate of injection of ^{22}Ne at $T_6 = 50$ MK (left panel) and $T_6 = 80$ MK (right panel). The injected species are ^{12}C , ^{16}O , and ^{22}Ne . The blue, black, and green lines are associated with three sets of nuclear reactions rates that we tested and that will be discussed in Sect. 6.3. We focus on case 2 (black lines), which corresponds to the nuclear rates used here so far. The horizontal black line shows the initial $[\text{Al}/\text{Fe}]$ ratio in the H-box and the black line with triangles shows the final values. We see that the final $[\text{Al}/\text{Fe}]$ ratio at $T_6 = 80$ MK (right panel of Fig. 7) is lower when less ^{22}Ne is injected. When the injection rate is low enough, overall there is more ^{27}Al destroyed than created. We see that some aluminium is created at the end if $R_{^{22}\text{Ne}} > 3 \times 10^{-11} M_{\odot} \text{ yr}^{-1}$ for the considered case. This aluminium comes mainly from the injected ^{22}Ne thanks to successive proton captures.

These two arguments suggest that a moderate amount of ^{22}Ne coming from the helium burning core to the hydrogen burning shell together with no ^{26}Mg would probably play in favour of a lower final $[\text{Al}/\text{Fe}]$ ratio.

6.2. Impact of temperature on Al

The final abundance of aluminium depends on the strength of the nuclear reactions rates that create and destroy it. The nuclear

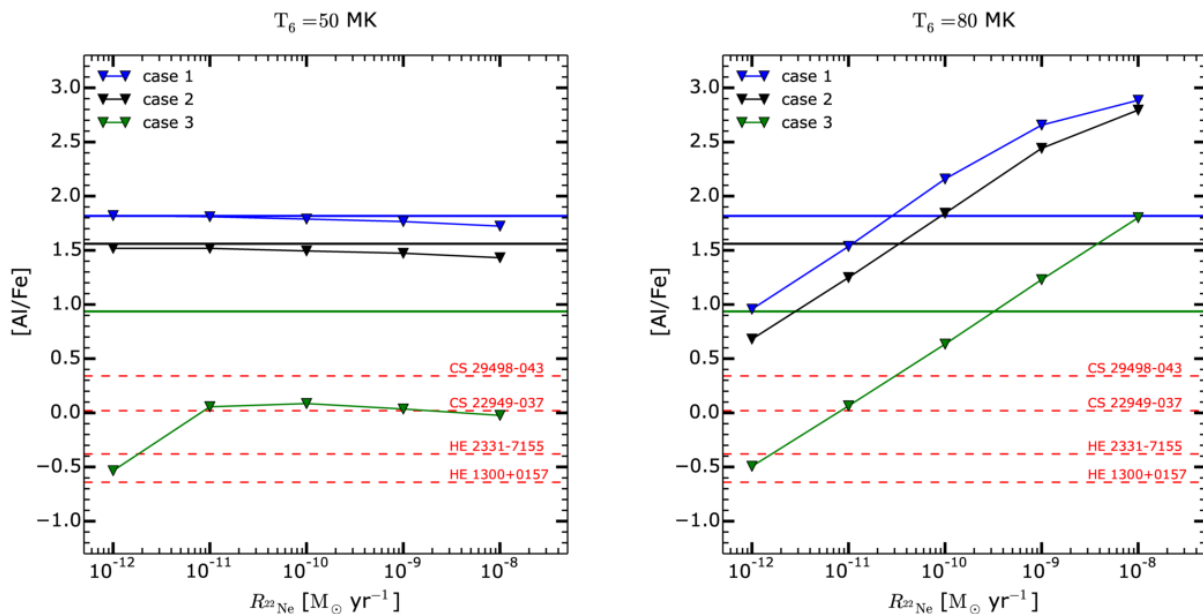


Fig. 7. [Al/Fe] ratios in the H-box as a function of $R_{22\text{Ne}}$, the rate of injection of ^{22}Ne (^{12}C and ^{16}O are also injected). The temperature is $T_6 = 50$ MK (left) and $T_6 = 80$ MK (right); the density $\rho = 1$ g cm $^{-3}$; and ^{12}C , ^{16}O , and ^{22}Ne are injected. The three lines with triangles show the final [Al/Fe] ratios in the H-box when considering three different sets of nuclear rates for the three principal reactions implying ^{27}Al (see text for explanations). The horizontal blue, black, and green lines correspond to the initial [Al/Fe] in the H-box for the three considered cases. Observed [Al/Fe] are shown by the red dashed lines for the CEMP-no stars that have $[\text{Fe}/\text{H}] = -3.8 \pm 0.3$.

rates for the Ne-Na and Mg-Al cycles are generally 3–4 dex higher at $T_6 = 80$ MK than at $T_6 = 50$ MK so that the synthesis of aluminium is slower at $T_6 = 50$ MK. Figure 7 shows that indeed the final [Al/Fe] ratios deviate very little from their initial values at $T_6 = 50$ MK (left panel), while the difference is much more significant at $T_6 = 80$ MK (right panel). We note however that the case 3 pattern at $T_6 = 50$ MK lies largely below its initial value (horizontal green line), but this is due to the ^{26}Al that has decayed into ^{26}Mg at the end of the simulation (this reduces [Al/Fe] by about 1 dex). The green triangle at the abscissa $10^{-12} M_{\odot} \text{yr}^{-1}$ also deviates from the others. The considered nuclear rates in this case disfavour the synthesis of ^{27}Al (see discussion in Sect. 6.3). This, together with the low injection rate that implies a longer time before hydrogen exhaustion, allows a larger depletion of ^{27}Al than at higher injection rates.

In addition, we saw in Sect. 4 (see also Fig. 5, left panel) that increasing the temperature leads to a lower final [Al/Fe] ratio (and a higher [Si/Fe]). This remains true as long as some ^{26}Mg is injected: if ^{22}Ne is injected but not ^{26}Mg (as in Fig. 7), [Al/Fe] can be higher when increasing the temperature. This can be seen by comparing the left and right panels of Fig. 7 at the abscissa $10^{-9} M_{\odot} \text{yr}^{-1}$ for instance. In this case, no ^{26}Mg is injected so that ^{27}Al comes mainly from the successive protons captured on the injected ^{22}Ne . The chain leading to ^{27}Al is longer when starting from ^{22}Ne than from ^{26}Mg . In that chain, the rate of $^{24}\text{Mg}(p, \gamma)^{25}\text{Al}$ at $T_6 = 50$ MK is very low compared to the other reaction rates. This reaction tends to stop the chain at $T_6 = 50$ MK so that the final content in ^{27}Al is generally close to the initial one, even with high injection rates of ^{22}Ne . Injecting some ^{26}Mg is a way to avoid this bottleneck reaction and synthesize some aluminium, even at $T_6 = 50$ MK (see the fourth panel of Fig. 4). The rate of $^{24}\text{Mg}(p, \gamma)^{25}\text{Al}$ strongly increases from $T_6 = 50$ to 80 MK (by about 7 dex) so that the chain leading to ^{27}Al (and ^{28}Si) is no longer blocked at $T_6 = 80$ MK.

A moderate temperature in the hydrogen shell (~ 50 MK) is likely more compatible with a lower [Al/Fe] under various amounts of ^{22}Ne coming from the helium core to the hydrogen shell. In the strong mixing case (high $R_{22\text{Ne}}$) and at high temperatures, this could lead to a very high [Al/Fe] ratio (Fig. 7, right panel).

6.3. Impact of changing the nuclear rates on Al

A point that deserves to be investigated is the uncertainties of the nuclear rates. In a hydrogen burning region, the two reactions destroying ^{27}Al are $^{27}\text{Al}(p, \gamma)^{28}\text{Si}$ and $^{27}\text{Al}(p, \alpha)^{24}\text{Mg}$. The reaction which creates ^{27}Al is $^{26}\text{Mg}(p, \gamma)^{27}\text{Al}$. The three nuclear rates associated with these reactions are very uncertain at the considered temperatures. To illustrate this point, we compared three sets of nuclear rates for the three reactions involving ^{27}Al . We used rates provided by the JINA REACLIB database (Cyburt et al. 2010).

- Case 1: the best scenario for the ^{27}Al synthesis. We took the maximum rate (at $T_6 = 80$) for $^{26}\text{Mg}(p, \gamma)^{27}\text{Al}$ (Cyburt et al. 2010). The minimum rate was taken for both $^{27}\text{Al}(p, \gamma)^{28}\text{Si}$ and $^{27}\text{Al}(p, \alpha)^{24}\text{Mg}$ (van Wormer et al. 1994).
- Case 2: we used the rates taken from this work (see Sect. 3).
- Case 3: the best scenario for ^{27}Al destruction. The minimum rate for $^{26}\text{Mg}(p, \gamma)^{27}\text{Al}$ is from Angulo et al. (1999) and the maximum rates for $^{27}\text{Al}(p, \gamma)^{28}\text{Si}$ and $^{27}\text{Al}(p, \alpha)^{24}\text{Mg}$ are from Cyburt et al. (2010).

To be consistent, we computed two other complete stellar models from the ZAMS to core helium burning ignition with the two new sets of nuclear rates (cases 1 and 3). Depending on the set of nuclear rates chosen, the initial abundances in the H-box are taken from the hydrogen burning shell of the corresponding stellar model. The three initial [Al/Fe] ratios taken in the H-box are

shown by the blue (case 1), black (case 2), and green (case 3) horizontal lines. We see that the scatter is significant. This occurs because the Mg-Al cycle is already operating in the core of the complete stellar model during the main sequence so that the aluminium abundance is affected if the nuclear rates are changed. Depending on the set of nuclear rates, it finally leads to a different aluminium content in the hydrogen shell at core helium burning ignition, hence in the H-box.

The lines with triangles correspond to the final [Al/Fe] ratios in the H-box for the three cases. We verify that the rates considered in this work (case 2) lead to a final [Al/Fe] ratios that is between the two extreme cases. Whatever the injection rate, at least 1.5 dex separates the blue pattern from the green; the green pattern gives lower [Al/Fe] since this is the case where ^{27}Al is the most destroyed and the least synthesized. A word of caution: for case 3, the abundance of ^{26}Al is higher than that of ^{27}Al during the burning, so that [Al/Fe] is significantly affected when ^{26}Al decays into ^{26}Mg . For cases 1 and 2, ^{27}Al is more abundant so that decaying ^{26}Al at the end reduces [Al/Fe] only a little.

Four out of five CEMP-no stars with $[\text{Fe}/\text{H}] = -3.8 \pm 0.3$ have an observed [Al/Fe]. These ratios are represented by the red dashed lines in Fig. 7. The scatter of the observed [Al/Fe] ratios is covered well enough by case 3 (green pattern) when relying on different values of $R_{22\text{Ne}}$, the injection rate of ^{22}Ne . If we select that set of rates, our model indicates that (i) the CEMP-no stars with $[\text{Al}/\text{Fe}] \geq 0$ could be made of a material processed by hydrogen burning at relatively high temperatures (about 80 MK) because $T \sim 50$ MK would not lead to a high enough aluminium content (see left panel of Fig. 7) and (ii) only a high enough injection rate of ^{22}Ne can account for Al-enhanced CEMP-no stars. The four stars considered here do not show such a high [Al/Fe] ratio (except a modest enhancement in CS 29498-043). This might tend to disfavour the progenitors where the mixing is very strong (very high initial velocity) and with a high temperature in the hydrogen shell ($\geq 60 M_{\odot}$ stars). The two remaining possibilities are either a high temperature (~ 80 MK) in the hydrogen shell but a weak mixing (a low $R_{22\text{Ne}}$), or a moderate temperature in the hydrogen shell (~ 50 MK) with a weak to strong mixing. A moderate temperature in the hydrogen shell is more likely achieved in $\sim 20 M_{\odot}$ progenitors (30–60 MK) rather than in $\sim 60 M_{\odot}$ ones (30–80 MK, see Fig. 2).

6.4. Sensitivity of the Si abundance

The silicon abundance is also affected when changing the injection, temperature, or nuclear reaction rates. In the explored range of parameters (temperature, injection rate, and nuclear reaction rates; see Fig. 7) and for the injected species considered (^{12}C , ^{16}O , and ^{22}Ne), the final [Si/Fe] ranges from 1 to 1.8.

At $T_6 = 50$ MK, the final [Si/Fe] ratio depends very weakly on the injection rate because the Ne-Si chain is stopped by the $^{24}\text{Mg}(p, \gamma)^{25}\text{Al}$ reaction (see Sect. 6.2). In this case, the final [Si/Fe] ratio is almost equal to the initial value, which ranges from 1 (case 1, lowest rate for $^{27}\text{Al}(p, \gamma)^{28}\text{Si}$) to 1.2 (case 3, highest rate for $^{27}\text{Al}(p, \gamma)^{28}\text{Si}$).

At $T_6 = 80$ MK, the final abundance of silicon is always enhanced compared to the initial level. The $^{24}\text{Mg}(p, \gamma)^{25}\text{Al}$ reaction no longer blocks the Ne-Si chain so that the injected ^{22}Ne synthesizes some ^{28}Si . The final [Si/Fe] ratios range between 1.2 and 1.8.

Three CEMP-no stars with $[\text{Fe}/\text{H}] = -3.8 \pm 0.3$ have a measured [Si/Fe]. The values are 0.77, 0.82, and 0.87. These values are closer to the results given by the model at $T_6 = 50$ MK ($1 < [\text{Si}/\text{Fe}] < 1.2$), which might indicate a moderate temperature

in hydrogen shell of the progenitor ($T_6 \simeq 50$ MK), consistent with the discussion in Sect. 6.3.

7. Possible astronomical sources of classes 2 and 4 CEMP-no stars

Through the present work, we suggest that the high observed abundances of C together with that of N, O, Na, and Mg at the surface of the CEMP-no stars are the signatures of a mixing between the helium and hydrogen burning regions of the source star during its nuclear life. What objects are able to experience such a mixing process? In the framework of our results, but also in a more global context, we speculate on the possible progenitors of classes 2 and 4 CEMP-no stars.

7.1. AGB stars

AGB stars are known contributors to s-process elements. They are generally believed to be responsible for the enrichment, by mass transfer, in s-elements observed at the surface of the CEMP-s stars. In addition to the abundances, the models have to reproduce the period of the binary system for instance, which can give tight constraints but also increase the difficulty of finding models matching the observations (see e.g. Abate et al. 2015).

In AGB stars, there is a mixing between the two shells. It could also, in principle, be enhanced by rotation or, at the very least, rotation may change the chemical structure of the star at the beginning of the AGB phase (see e.g. the $7 M_{\odot}$ model in Meynet et al. 2010).

It seems however that there are at least two difficulties in this scenario to explain the CEMP-no stars. First, the AGB stars are experiencing the s-process and by definition, the CEMP-no class is not enriched in s-elements (or is weakly enriched). This feature would be difficult to explain relying on AGB stars. Second, it seems difficult to account for the CEMP-no stars having $[\text{Fe}/\text{H}] \lesssim -4$ with the AGB stars: such a low iron content likely indicates that only the most massive objects, more massive than the AGB stars, have contributed.

7.2. Faint supernovae, mixing and fallback

Tominaga et al. (2014) discussed the scenario of faint supernovae from Pop III stars with mixing and fallback. In these models, only the outer layers are ejected from the progenitor. It is indeed needed to explain the observed CNO abundance patterns, as well as the low $^{12}\text{C}/^{13}\text{C}$ ratios. This is in line with the discussion about the mixing of the ejecta; we see in Sect. 5 that little or no material processed by helium burning coming from the source star should be mixed into the hydrogen rich envelope when the nuclear life of the star is finished. In other words, mainly the hydrogen rich envelope of the progenitor would be needed to form the future CEMP-no star.

On the other hand, these models are generally non-rotating, leading to some difficulties in explaining the high nitrogen abundance observed in some CEMP-no stars without invoking an extra mixing process in the progenitor. Rotating models were however considered in Takahashi et al. (2014), predicting higher N/Fe ratios in the ejecta, almost in line with the observed values at the surface of two out of the three CEMP-no stars they considered (HE 0107-5240 and HE 1327-2326).

7.3. Contribution of more than one source

Limongi et al. (2003) proposed a two-step scenario: a normal supernova from a $\sim 15 M_{\odot}$ progenitor responsible for the iron-peak

elements, followed by a fainter one experiencing strong fallback coming from a $\sim 35 M_{\odot}$ progenitor. The second more massive progenitor enriches the ISM in light elements: C, N, Na, and Mg. These elements are produced thanks to a partial mixing between hydrogen and helium burning shells that can occur in $Z = 0$ models, even in non-rotating models.

What seems to not match with the CEMP-no stars in classes 2 and 4 is the predicted $^{12}\text{C}/^{13}\text{C}$ ratio of 240 for this two-step model. The corresponding $[^{12}\text{C}/^{13}\text{C}]$ ratio is 0.4 and this is not compatible with the values of the CEMP-no stars considered here (see Fig. 6, right panel). We note, however, that 3 out of 12 have only a lower limit for the $^{12}\text{C}/^{13}\text{C}$ ratio (see Table 1) so that such a high predicted $^{12}\text{C}/^{13}\text{C}$ could be consistent with these CEMP-no stars.

7.4. Spinstars

Several signatures of fast rotation at low metallicity have been found over the past years. One strong signature is that the high nitrogen abundances and the low $^{12}\text{C}/^{13}\text{C}$ ratios observed in normal very metal-poor (VMP) stars are much better reproduced by low metallicity chemical evolution models when including fast rotators, also called spinstars (Chiappini et al. 2006, 2008). Because of the high rotation, the injection process we investigate here operates in the spinstar and it could be a way to obtain material enriched in C, N, O, Na, and Mg, together with a low $^{12}\text{C}/^{13}\text{C}$, that will ultimately form a CEMP-no star in class 2 or 4.

The spinstars and more generally the objects experiencing mixing between hydrogen and helium burning regions appear to be interesting progenitor candidates for class 2 and 4 CEMP-no stars.

8. Conclusions

We studied the possibility of forming CEMP-no stars with a material processed by hydrogen burning coming from the source star. We carried out nuclear experiments where the convective hydrogen burning shell of the source star was modelled by a hydrogen burning single zone (H-box). The mixing between the helium burning core and the hydrogen burning shell was mimicked by injecting the products of helium burning ^{12}C , ^{16}O , ^{22}Ne , and ^{26}Mg in the H-box. When injecting these species in the hydrogen burning zone ^{14}N , ^{23}Na , ^{24}Mg , and ^{27}Al are synthesized. The $^{12}\text{C}/^{13}\text{C}$ ratio is constant under various densities, temperatures in the H-box, and also under various injection rates. The $[\text{Al}/\text{Fe}]$ ratio in the hydrogen burning zone lies generally above the observations. Using different nuclear reaction rates found in the literature for the reactions involving ^{27}Al leads to a better coverage of the observed $[\text{Al}/\text{Fe}]$ scatter. The high observed $[\text{Al}/\text{Fe}]$ ratios are reproduced at sufficiently high hydrogen burning temperature (80 MK) and if the injection rate of ^{22}Ne is high enough. This might point toward a massive (high temperature) and fast rotating (high injection rate) progenitor.

Throughout this work, we suggest that the high observed abundances of light elements at the surface of the CEMP-no stars are the signatures of a mixing between the helium and hydrogen burning regions of the progenitor during its nuclear life. It supports the CEMP-no star formation scenario of Maeder & Meynet (2015) for classes 2 and 4. This scenario states that these stars are made of a material processed by hydrogen burning only, but were products of helium burning coming from the helium core of the source star diffused into the hydrogen burning shell thanks to the rotational mixing. This arrival of new elements boosts

the nucleosynthesis in the hydrogen burning shell. Considerations on the $^{12}\text{C}/^{13}\text{C}$ ratio confirmed that the CEMP-no stars in classes 2 and 4 are made of a material that was only processed by hydrogen burning in the source star. This corroborates the assumption that the CEMP-no stars formed mainly with the hydrogen-rich envelope of the source star. The $^{12}\text{C}/^{13}\text{C}$ ratio is highly sensitive to the burning region considered in the source star (hydrogen or helium burning region). It could be used to constrain the part expelled from the source star at the time of the supernova in order to reproduce the observed $^{12}\text{C}/^{13}\text{C}$ ratio at the surface of the CEMP-no stars.

The spinstars are interesting candidates for being the class 2 and 4 CEMP-no progenitors because of their rotation which induces exchanges of material between the hydrogen and helium burning regions. This gives some support to the idea that the rotation played an important role in the early chemical evolution of galaxies.

Acknowledgements. The authors thank the anonymous referee who helped to improve this paper through very constructive remarks. This work was supported by the Swiss National Science Foundation (project number 200020-160119).

References

- Abate, C., Pols, O. R., Karakas, A. I., & Izzard, R. G. 2015, *A&A*, 576, A118
- Allen, D. M., Ryan, S. G., Rossi, S., Beers, T. C., & Tsangarides, S. A. 2012, *A&A*, 548, A34
- Angulo, C., Arnould, M., Rayet, M., et al. 1999, *Nucl. Phys. A*, 656, 3
- Aoki, W. 2010, in IAU Symp. 265, eds. K. Cunha, M. Spite, & B. Barbuy, 111
- Aoki, W., Beers, T. C., Christlieb, N., et al. 2007, *ApJ*, 655, 492
- Beers, T. C., & Christlieb, N. 2005, *ARA&A*, 43, 531
- Carollo, D., Beers, T. C., Bovy, J., et al. 2012, *ApJ*, 744, 195
- Chiappini, C. 2013, *Astron. Nachr.*, 334, 595
- Chiappini, C., Hirschi, R., Meynet, G., et al. 2006, *A&A*, 449, L27
- Chiappini, C., Ekström, S., Meynet, G., et al. 2008, *A&A*, 479, L9
- Choplin, A., Meynet, G., Maeder, A., Hirschi, R., & Chiappini, C. 2016, ArXiv e-prints [arXiv:1602.04122]
- Cybur, R. H., Fields, B. D., & Olive, K. A. 2008, *J. Cosmol. Astropart. Phys.*, 11, 012
- Cybur, R. H., Amthor, A. M., Ferguson, R., et al. 2010, *ApJS*, 189, 240
- Ekström, S., Georgy, C., Eggenberger, P., et al. 2012, *A&A*, 537, A146
- Frebel, A., Christlieb, N., Norris, J. E., et al. 2006, *ApJ*, 652, 1585
- Frebel, A., Norris, J. E., Aoki, W., et al. 2007, *ApJ*, 658, 534
- Frebel, A., Collet, R., Eriksson, K., Christlieb, N., & Aoki, W. 2008, *ApJ*, 684, 588
- Hale, S. E., Champagne, A. E., Iliadis, C., et al. 2002, *Phys. Rev. C*, 65, 015801
- Hansen, T., Hansen, C. J., Christlieb, N., et al. 2014, *ApJ*, 787, 162
- Hansen, T., Hansen, C. J., Christlieb, N., et al. 2015, *ApJ*, 807, 173
- Hirschi, R. 2007, *A&A*, 461, 571
- Iliadis, C., D'Auria, J. M., Starrfield, S., Thompson, W. J., & Wiescher, M. 2001, *ApJS*, 134, 151
- Keller, S. C., Bessell, M. S., Frebel, A., et al. 2014, *Nature*, 506, 463
- Korn, A. J., Richard, O., Mashonkina, L., et al. 2009, *ApJ*, 698, 410
- Lee, Y. S., Beers, T. C., Masseron, T., et al. 2013, *AJ*, 146, 132
- Limongi, M., Chieffi, A., & Bonifacio, P. 2003, *ApJ*, 594, L123
- Lodders, K. 2003, *ApJ*, 591, 1220
- Maeder, A., & Meynet, G. 2001, *A&A*, 373, 555
- Maeder, A., & Meynet, G. 2015, *A&A*, 580, A32
- Maeder, A., Meynet, G., & Chiappini, C. 2015, *A&A*, 576, A56
- Masseron, T., van Eck, S., Famaey, B., et al. 2006, *A&A*, 455, 1059
- Masseron, T., Johnson, J. A., Plez, B., et al. 2010, *A&A*, 509, A93
- Masseron, T., Johnson, J. A., Lucatello, S., et al. 2012, *ApJ*, 751, 14
- Meynet, G., Ekström, S., & Maeder, A. 2006, *A&A*, 447, 623
- Meynet, G., Hirschi, R., Ekström, S., et al. 2010, *A&A*, 521, A30
- Norris, J. E., Yong, D., Bessell, M. S., et al. 2013, *ApJ*, 762, 28
- Ploc, V. M., Frebel, A., Beers, T. C., & Stancliffe, R. J. 2014, *ApJ*, 797, 21
- Roederer, I. U., Preston, G. W., Thompson, I. B., et al. 2014, *AJ*, 147, 136
- Takahashi, K., Umeda, H., & Yoshida, T. 2014, *ApJ*, 794, 40
- Tominaga, N., Iwamoto, N., & Nomoto, K. 2014, *ApJ*, 785, 98
- Umeda, H., & Nomoto, K. 2002, *ApJ*, 565, 385
- Umeda, H., & Nomoto, K. 2005, *ApJ*, 619, 427
- van Wormer, L., Görres, J., Iliadis, C., Wiescher, M., & Thielemann, F.-K. 1994, *ApJ*, 432, 326

Appendix A

Let us consider a box of initial mass $m = 1 M_{\odot}$, where X_i denotes the mass fraction of the element i . We also consider a reservoir composed only of the element e , so that its mass fraction X'_e in the reservoir is 1. During a time Δt , we inject a mass

$$\Delta m = R_e \Delta t \quad (\text{A.1})$$

from the reservoir into the box. R_e is the injection rate of the element e expressed in $M_{\odot} \text{ yr}^{-1}$. After the injection, the new mass fraction X_e^{new} of the injected element in the box is

$$X_e^{\text{new}} = \frac{X_e m + X'_e \Delta m}{m + \Delta m} = \frac{X_e m + R_e \Delta t}{m + R_e \Delta t}. \quad (\text{A.2})$$

The new mass fraction of the other elements in the box can be expressed as

$$X_{i \neq e}^{\text{new}} = \frac{X_i m}{m + R_e \Delta t}. \quad (\text{A.3})$$

We note that the H-box that was initially $1 M_{\odot}$ grows in mass as a result of the injection. Its final mass is generally similar to the initial one and never exceeds $\sim 1.3 M_{\odot}$ for the presented results, which stays relatively close to $1 M_{\odot}$.

The point is now to estimate R_e the injection rate. Let us consider the example of the carbon. In stellar models, the primary ^{14}N is synthesized through the diffusion of ^{12}C and ^{16}O from the helium core to the hydrogen burning shell. The secondary ^{14}N is formed with the initial CNO elements in the star. It is possible to roughly quantify $M_{^{14}\text{N}}^{\text{prim}}$ the mass fraction of primary ^{14}N formed during the core helium burning phase as

$$M_{^{14}\text{N}}^{\text{prim}} = \left(\int_0^M X_{^{14}\text{N}}(M_r) dM_r \right)_{Y_c=0} - (X_{\text{C,ini}} + X_{\text{N,ini}} + X_{\text{O,ini}})M, \quad (\text{A.4})$$

where Y_c is the central ^4He mass fraction; $X_{^{14}\text{N}}(M_r)$ the mass fraction of ^{14}N at coordinate M_r ; $X_{\text{C,ini}}$, $X_{\text{N,ini}}$, $X_{\text{O,ini}}$ the mass fractions of the CNO elements at the ZAMS; and M the total mass of the star at the end of the core helium burning phase. $M_{^{14}\text{N}}^{\text{prim}}$ is defined as the total amount of ^{14}N in the star at core helium exhaustion minus the amount of ^{14}N that can be formed with the initial CNO content (secondary ^{14}N). We suppose that all the ^{12}C and ^{16}O diffusing from the helium core to the hydrogen shell are transformed into ^{14}N . In this case, to get a mass $M_{^{14}\text{N}}^{\text{prim}}$ of primary nitrogen in the star at the end of core helium burning, an average injection rate of ($^{12}\text{C} + ^{16}\text{O}$) is needed in the hydrogen shell of

$$R_{^{12}\text{C}+^{16}\text{O}} = \frac{M_{^{14}\text{N}}^{\text{prim}}}{\tau_{\text{HeB}}}, \quad (\text{A.5})$$

where τ_{HeB} is the duration of the core helium burning phase. For a $60 M_{\odot}$ model at $Z = 10^{-5}$ and at 70% of the critical velocity at the ZAMS, we find $R_{^{12}\text{C}+^{16}\text{O}} = 5 \times 10^{-8} M_{\odot} \text{ yr}^{-1}$.

The amount of primary nitrogen synthesized (hence the value of $R_{^{12}\text{C}+^{16}\text{O}}$) can change significantly depending on the rotation, the mass of the model, or the prescription for the rotational mixing for instance. In the present work we consider $10^{-10} < R_{^{12}\text{C}} < 10^{-6} M_{\odot} \text{ yr}^{-1}$ (the chosen values are 10^{-10} , 10^{-8} , and $10^{-6} M_{\odot} \text{ yr}^{-1}$). In addition, we set $R_{^{12}\text{C}} = R_{^{16}\text{O}}$ and $R_{^{22}\text{Ne}} = R_{^{26}\text{Mg}} = R_{^{12}\text{C}}/100$. The factor 100 between the two rates accounts at first order for the fact that ^{22}Ne and ^{26}Mg are ~ 100 times less abundant than ^{12}C and ^{16}O in the helium burning core of a low metallicity massive stellar model, so that ~ 100 times less ^{22}Ne and ^{26}Mg will enter by rotational mixing into the hydrogen burning shell.

Bibliography

- Abate, C., Pols, O. R., Izzard, R. G., & Karakas, A. I. 2015a, *A&A*, 581, A22
- Abate, C., Pols, O. R., Karakas, A. I., & Izzard, R. G. 2015b, *A&A*, 576, A118
- Abazajian, K. N., Adelman-McCarthy, J. K., Agüeros, M. A., et al. 2009, *ApJS*, 182, 543
- Abbott, B. P., Abbott, R., Abbott, T. D., et al. 2016, *Physical Review Letters*, 116, 061102
- Abbott, B. P., Abbott, R., Abbott, T. D., et al. 2017, *Physical Review Letters*, 119, 161101
- Abbott, L. F. & Sikivie, P. 1983, *Physics Letters B*, 120, 133
- Abel, T., Bryan, G. L., & Norman, M. L. 2002, *Science*, 295, 93
- Abohalima, A. & Frebel, A. 2017, *ArXiv e-prints*
- Adelman-McCarthy, J. K., Agüeros, M. A., Allam, S. S., et al. 2008, *ApJS*, 175, 297
- Aguado, D. S., Allende Prieto, C., González Hernández, J. I., & Rebolo, R. 2018, *ApJL*, 854, L34
- Andrievsky, S. M., Spite, M., Korotin, S. A., et al. 2010, *A&A*, 509, A88
- Andrievsky, S. M., Spite, M., Korotin, S. A., et al. 2007, *A&A*, 464, 1081
- Andrievsky, S. M., Spite, M., Korotin, S. A., et al. 2008, *A&A*, 481, 481
- Angulo, C., Arnould, M., Rayet, M., et al. 1999, *Nuclear Physics A*, 656, 3
- Aoki, W., Barklem, P. S., Beers, T. C., et al. 2009, *ApJ*, 698, 1803
- Aoki, W., Beers, T. C., Christlieb, N., et al. 2007, *ApJ*, 655, 492
- Aoki, W., Beers, T. C., Lee, Y. S., et al. 2013, *AJ*, 145, 13
- Aoki, W., Beers, T. C., Sivarani, T., et al. 2008, *ApJ*, 678, 1351
- Aoki, W., Frebel, A., Christlieb, N., et al. 2006, *ApJ*, 639, 897
- Aoki, W., Norris, J. E., Ryan, S. G., Beers, T. C., & Ando, H. 2000, *ApJL*, 536, L97
- Aoki, W., Norris, J. E., Ryan, S. G., Beers, T. C., & Ando, H. 2002a, *PASJ*, 54, 933
- Aoki, W., Ryan, S. G., Norris, J. E., et al. 2002b, *ApJ*, 580, 1149
- Arcoragi, J.-P., Langer, N., & Arnould, M. 1991, *A&A*, 249, 134

- Argast, D., Samland, M., Thielemann, F.-K., & Qian, Y.-Z. 2004, *A&A*, 416, 997
- Arnett, W. D. & Meakin, C. 2011, *ApJ*, 733, 78
- Arnett, W. D., Meakin, C., Viallet, M., et al. 2015, *ApJ*, 809, 30
- Arnett, W. D. & Thielemann, F.-K. 1985, *ApJ*, 295, 589
- Asplund, M., Grevesse, N., & Sauval, A. J. 2005, in *Astronomical Society of the Pacific Conference Series*, Vol. 336, *Cosmic Abundances as Records of Stellar Evolution and Nucleosynthesis*, ed. T. G. Barnes, III & F. N. Bash, 25
- Asplund, M., Grevesse, N., Sauval, A. J., & Scott, P. 2009, *ARA&A*, 47, 481
- Baade, W. 1946, *PASP*, 58, 249
- Baraffe, I., El Eid, M. F., & Prantzos, N. 1992, *A&A*, 258, 357
- Barbuy, B., Zoccali, M., Ortolani, S., et al. 2009, *A&A*, 507, 405
- Barkana, R. 2018, *Nature*, 555, 71
- Barklem, P. S., Christlieb, N., Beers, T. C., et al. 2005, *A&A*, 439, 129
- Beers, T. C. & Christlieb, N. 2005, *ARA&A*, 43, 531
- Beers, T. C., Preston, G. W., & Shectman, S. A. 1985, *AJ*, 90, 2089
- Beers, T. C., Preston, G. W., & Shectman, S. A. 1992, *AJ*, 103, 1987
- Beers, T. C., Sivarani, T., Marsteller, B., et al. 2007, *AJ*, 133, 1193
- Behara, N. T., Bonifacio, P., Ludwig, H.-G., et al. 2010, *A&A*, 513, A72
- Bensby, T., Yee, J. C., Feltzing, S., et al. 2013, *A&A*, 549, A147
- Bessell, M. S., Christlieb, N., & Gustafsson, B. 2004, *ApJL*, 612, L61
- Best, A., Beard, M., Görres, J., et al. 2013, *Phys. Rev. C*, 87, 045805
- Bidelman, W. P. & MacConnell, D. J. 1973, *AJ*, 78, 687
- Bisterzo, S., Gallino, R., Straniero, O., Cristallo, S., & Käppeler, F. 2011, *MNRAS*, 418, 284
- Bisterzo, S., Gallino, R., Straniero, O., Cristallo, S., & Käppeler, F. 2012, *MNRAS*, 422, 849
- Bond, H. E. 1970, *ApJS*, 22, 117
- Bonifacio, P., Caffau, E., Spite, M., et al. 2015, *A&A*, 579, A28
- Bonifacio, P., Sbordone, L., Caffau, E., et al. 2012, *A&A*, 542, A87
- Bonifacio, P., Spite, M., Cayrel, R., et al. 2009, *A&A*, 501, 519
- Bouwens, R. J., Illingworth, G. D., Franx, M., et al. 2009, *ApJ*, 705, 936
- Bouwens, R. J., Illingworth, G. D., Franx, M., & Ford, H. 2007, *ApJ*, 670, 928
- Bowman, J. D., Rogers, A. E. E., Monsalve, R. A., Mozdzen, T. J., & Mahesh, N. 2018, *Nature*, 555, 67

- Bromm, V., Coppi, P. S., & Larson, R. B. 2002, *ApJ*, 564, 23
- Brüggen, M. & Hillebrandt, W. 2001, *MNRAS*, 320, 73
- Burbidge, E. M., Burbidge, G. R., Fowler, W. A., & Hoyle, F. 1957, *Reviews of Modern Physics*, 29, 547
- Burris, D. L., Pilachowski, C. A., Armandroff, T. E., et al. 2000, *ApJ*, 544, 302
- Busso, M., Gallino, R., & Wasserburg, G. J. 1999, *ARA&A*, 37, 239
- Caffau, E., Bonifacio, P., François, P., et al. 2011, *Nature*, 477, 67
- Caffau, E., Bonifacio, P., François, P., et al. 2013, *A&A*, 560, A15
- Cameron, A. G. W. 1960, *AJ*, 65, 485
- Campbell, S. W., Lugaro, M., & Karakas, A. I. 2010, *A&A*, 522, L6
- Canuto, V. M. 2002, *A&A*, 384, 1119
- Carbon, D. F., Barbuy, B., Kraft, R. P., Friel, E. D., & Suntzeff, N. B. 1987, *PASP*, 99, 335
- Carney, B. W. & Peterson, R. C. 1981, *ApJ*, 245, 238
- Carollo, D., Beers, T. C., Bovy, J., et al. 2012, *ApJ*, 744, 195
- Carollo, D., Beers, T. C., Lee, Y. S., et al. 2007, *Nature*, 450, 1020
- Carollo, D., Freeman, K., Beers, T. C., et al. 2014, *ApJ*, 788, 180
- Carretta, E., Gratton, R., Cohen, J. G., Beers, T. C., & Christlieb, N. 2002, *AJ*, 124, 481
- Caughlan, G. R. & Fowler, W. A. 1988, *Atomic Data and Nuclear Data Tables*, 40, 283
- Cayrel, R., Depagne, E., Spite, M., et al. 2004, *A&A*, 416, 1117
- Cescutti, G. & Chiappini, C. 2014, *A&A*, 565, A51
- Cescutti, G., Chiappini, C., Hirschi, R., Meynet, G., & Frischknecht, U. 2013, *A&A*, 553, A51
- Chaboyer, B. & Zahn, J.-P. 1992, *A&A*, 253, 173
- Chabrier, G. 2003, *PASP*, 115, 763
- Chamberlain, J. W. & Aller, L. H. 1951, *ApJ*, 114, 52
- Chantereau, W., Charbonnel, C., & Decressin, T. 2015, *A&A*, 578, A117
- Charbonnel, C. 1994, *A&A*, 282, 811
- Charbonnel, C. & Zahn, J.-P. 2007, *A&A*, 467, L15
- Chiappini, C., Ekström, S., Meynet, G., et al. 2008, *A&A*, 479, L9
- Chiappini, C., Frischknecht, U., Meynet, G., et al. 2011, *Nature*, 472, 454
- Chiappini, C., Hirschi, R., Meynet, G., et al. 2006, *A&A*, 449, L27
- Chieffi, A. & Limongi, M. 2003, *PASA*, 20, 324

- Chiti, A., Simon, J. D., Frebel, A., et al. 2018, *ApJ*, 856, 142
- Choplin, A., Coc, A., Meynet, G., et al. 2017a, *A&A*, 605, A106
- Choplin, A., Ekström, S., Meynet, G., et al. 2017b, *A&A*, 605, A63
- Choplin, A., Hirschi, R., Meynet, G., & Ekström, S. 2017c, *A&A*, 607, L3
- Choplin, A., Hirschi, R., Meynet, G., et al. 2018, *A&A*, 618, A133
- Choplin, A., Maeder, A., Meynet, G., & Chiappini, C. 2016, *A&A*, 593, A36
- Christlieb, N., Gustafsson, B., Korn, A. J., et al. 2004, *ApJ*, 603, 708
- Cioffi, D. F., McKee, C. F., & Bertschinger, E. 1988, *ApJ*, 334, 252
- Clark, P. C., Glover, S. C. O., Klessen, R. S., & Bromm, V. 2011, *ApJ*, 727, 110
- Clarkson, O., Herwig, F., & Pignatari, M. 2018, *MNRAS*, 474, L37
- Clayton, D. D., Fowler, W. A., Hull, T. E., & Zimmerman, B. A. 1961, *Annals of Physics*, 12, 331
- Coc, A., Goriely, S., Xu, Y., Saimpert, M., & Vangioni, E. 2012, *ApJ*, 744, 158
- Coc, A., Uzan, J.-P., & Vangioni, E. 2014, *J. Cosmol. Astropart. Phys.*, 10, 050
- Cohen, J. G., Christlieb, N., McWilliam, A., et al. 2008, *ApJ*, 672, 320
- Cohen, J. G., Christlieb, N., McWilliam, A., et al. 2004, *ApJ*, 612, 1107
- Cohen, J. G., Christlieb, N., Thompson, I., et al. 2013, *ApJ*, 778, 56
- Cohen, J. G., McWilliam, A., Sheckman, S., et al. 2006, *AJ*, 132, 137
- Cohen, J. G., Sheckman, S., Thompson, I., et al. 2005, *ApJL*, 633, L109
- Cooke, R. J., Pettini, M., & Steidel, C. C. 2017, *MNRAS*, 467, 802
- Couch, R. G., Schmiedekamp, A. B., & Arnett, W. D. 1974, *ApJ*, 190, 95
- Cowan, J. J. & Rose, W. K. 1977, *ApJ*, 212, 149
- Cristallo, S., Piersanti, L., Straniero, O., et al. 2011, *ApJS*, 197, 17
- Cristallo, S., Straniero, O., Piersanti, L., & Gobrecht, D. 2015, *ApJS*, 219, 40
- Cristini, A., Meakin, C., Hirschi, R., et al. 2017, *MNRAS*, 471, 279
- Cunha, K., Hubeny, I., & Lanz, T. 2006, *ApJL*, 647, L143
- Cyburt, R. H., Amthor, A. M., Ferguson, R., et al. 2010, *ApJS*, 189, 240
- Cyburt, R. H., Fields, B. D., & Olive, K. A. 2003, *Physics Letters B*, 567, 227
- Cyburt, R. H., Fields, B. D., & Olive, K. A. 2008, *J. Cosmol. Astropart. Phys.*, 11, 012
- de Jager, C., Nieuwenhuijzen, H., & van der Hucht, K. A. 1988, *A&AS*, 72, 259
- Decressin, T., Meynet, G., Charbonnel, C., Prantzos, N., & Ekström, S. 2007, *A&A*, 464, 1029
- Deng, L.-C., Newberg, H. J., Liu, C., et al. 2012, *Research in Astronomy and Astrophysics*, 12, 735

- Denissenkov, P. A., Herwig, F., Battino, U., et al. 2017, *ApJL*, 834, L10
- Denissenkov, P. A. & Pinsonneault, M. 2008, *ApJ*, 684, 626
- Depagne, E., Hill, V., Spite, M., et al. 2002, *A&A*, 390, 187
- Dine, M. & Fischler, W. 1983, *Physics Letters B*, 120, 137
- Doherty, C. L., Gil-Pons, P., Lau, H. H. B., Lattanzio, J. C., & Siess, L. 2014, *MNRAS*, 437, 195
- Domiciano de Souza, A., Kervella, P., Jankov, S., et al. 2003, *A&A*, 407, L47
- Dupree, A. K. & Avrett, E. H. 2013, *ApJL*, 773, L28
- Eggenberger, P., Meynet, G., Maeder, A., et al. 2008, *Ap&SS*, 316, 43
- Eggleton, P. P., Dearborn, D. S. P., & Lattanzio, J. C. 2008, *ApJ*, 677, 581
- Eisenstein, D. J., Weinberg, D. H., Agol, E., et al. 2011, *AJ*, 142, 72
- Ekström, S. 2008, PhD thesis, Geneva Observatory, University of Geneva
- Ekström, S., Georgy, C., Eggenberger, P., et al. 2012, *A&A*, 537, A146
- Ekström, S., Meynet, G., Chiappini, C., Hirschi, R., & Maeder, A. 2008, *A&A*, 489, 685
- Ezzeddine, R., Frebel, A., & Plez, B. 2017, *ApJ*, 847, 142
- Feltzing, S., Bensby, T., Bergemann, M., et al. 2017, *ArXiv e-prints*
- Ferguson, J. W., Alexander, D. R., Allard, F., et al. 2005, *ApJ*, 623, 585
- Frebel, A. 2010, *Astronomische Nachrichten*, 331, 474
- Frebel, A., Aoki, W., Christlieb, N., et al. 2005a, in *IAU Symposium*, Vol. 228, *From Lithium to Uranium: Elemental Tracers of Early Cosmic Evolution*, ed. V. Hill, P. Francois, & F. Primas, 207–212
- Frebel, A., Aoki, W., Christlieb, N., et al. 2005b, *Nature*, 434, 871
- Frebel, A., Christlieb, N., Norris, J. E., Aoki, W., & Asplund, M. 2006a, *ApJL*, 638, L17
- Frebel, A., Christlieb, N., Norris, J. E., et al. 2006b, *ApJ*, 652, 1585
- Frebel, A., Christlieb, N., Norris, J. E., et al. 2007a, *ApJL*, 660, L117
- Frebel, A., Collet, R., Eriksson, K., Christlieb, N., & Aoki, W. 2008, *ApJ*, 684, 588
- Frebel, A., Johnson, J. L., & Bromm, V. 2009, *MNRAS*, 392, L50
- Frebel, A. & Norris, J. E. 2015, *ARA&A*, 53, 631
- Frebel, A., Norris, J. E., Aoki, W., et al. 2007b, *ApJ*, 658, 534
- Freiburghaus, C., Rosswog, S., & Thielemann, F.-K. 1999, *ApJL*, 525, L121
- Friedland, A., Giannotti, M., & Wise, M. 2013, *Physical Review Letters*, 110, 061101
- Frischknecht, U., Hirschi, R., Pignatari, M., et al. 2016, *MNRAS*, 456, 1803
- Frischknecht, U., Hirschi, R., & Thielemann, F.-K. 2012, *A&A*, 538, L2

- Fujimoto, M. Y., Ikeda, Y., & Iben, Jr., I. 2000, *ApJL*, 529, L25
- Fukugita, M., Ichikawa, T., Gunn, J. E., et al. 1996, *AJ*, 111, 1748
- Fulbright, J. P., Wyse, R. F. G., Ruchti, G. R., et al. 2010, *ApJL*, 724, L104
- Fumagalli, M., O’Meara, J. M., & Prochaska, J. X. 2011, *Science*, 334, 1245
- Gallino, R., Arlandini, C., Busso, M., et al. 1998, *ApJ*, 497, 388
- Gallino, R., Busso, M., Picchio, G., Raiteri, C. M., & Renzini, A. 1988, *ApJL*, 334, L45
- Gehrels, N., Chincarini, G., Giommi, P., et al. 2004, *ApJ*, 611, 1005
- Gies, D. R. & Lambert, D. L. 1992, *ApJ*, 387, 673
- Girard, T. M., Platais, I., Kozhurina-Platais, V., van Altena, W. F., & López, C. E. 1998, *AJ*, 115, 855
- Goriely, S. & Clerbaux, B. 1999, *A&A*, 346, 798
- Gull, M., Frebel, A., Cain, M. G., et al. 2018, *ArXiv e-prints*
- Hale, S. E., Champagne, A. E., Iliadis, C., et al. 2002, *Phys. Rev. C*, 65, 015801
- Hambly, N. C., MacGillivray, H. T., Read, M. A., et al. 2001, *MNRAS*, 326, 1279
- Hampel, M., Stancliffe, R. J., Lugaro, M., & Meyer, B. S. 2016, *ApJ*, 831, 171
- Hansen, T., Hansen, C. J., Christlieb, N., et al. 2015a, *ApJ*, 807, 173
- Hansen, T., Hansen, C. J., Christlieb, N., et al. 2014, *ApJ*, 787, 162
- Hansen, T. T., Andersen, J., Nordström, B., et al. 2016a, *A&A*, 586, A160
- Hansen, T. T., Andersen, J., Nordström, B., et al. 2016b, *A&A*, 588, A3
- Hansen, T. T., Andersen, J., Nordström, B., et al. 2015b, *A&A*, 583, A49
- Hartwig, T., Volonteri, M., Bromm, V., et al. 2016, *MNRAS*, 460, L74
- Heger, A. & Langer, N. 2000, *ApJ*, 544, 1016
- Heger, A., Langer, N., & Woosley, S. E. 2000, *ApJ*, 528, 368
- Heger, A. & Woosley, S. E. 2010, *ApJ*, 724, 341
- Herwig, F. 2004, *ApJS*, 155, 651
- Herwig, F. 2005, *ARA&A*, 43, 435
- Herwig, F., Freytag, B., Hueckstaedt, R. M., & Timmes, F. X. 2006, *ApJ*, 642, 1057
- Herwig, F., Pignatari, M., Woodward, P. R., et al. 2011, *ApJ*, 727, 89
- Herwig, F., Woodward, P. R., Lin, P.-H., Knox, M., & Fryer, C. 2014, *ApJL*, 792, L3
- Hill, V., Plez, B., Cayrel, R., et al. 2002, *A&A*, 387, 560
- Hillier, D. J. & Miller, D. L. 1998, *ApJ*, 496, 407
- Hinshaw, G., Larson, D., Komatsu, E., et al. 2013, *ApJS*, 208, 19

- Hirano, S. & Bromm, V. 2018, MNRAS
- Hirano, S., Hosokawa, T., Yoshida, N., et al. 2014, ApJ, 781, 60
- Hirschi, R. 2007, A&A, 461, 571
- Hirschi, R. & Maeder, A. 2010, A&A, 519, A16
- Hirschi, R., Meynet, G., & Maeder, A. 2004, A&A, 425, 649
- Hollek, J. K., Frebel, A., Roederer, I. U., et al. 2011, ApJ, 742, 54
- Hollowell, D. & Iben, Jr., I. 1988, ApJL, 333, L25
- Hosokawa, T., Hirano, S., Kuiper, R., et al. 2016, ApJ, 824, 119
- Howes, L. M., Asplund, M., Casey, A. R., et al. 2014, MNRAS, 445, 4241
- Howes, L. M., Asplund, M., Keller, S. C., et al. 2016, MNRAS, 460, 884
- Howes, L. M., Casey, A. R., Asplund, M., et al. 2015, Nature, 527, 484
- Huang, W. & Gies, D. R. 2006, ApJ, 648, 580
- Hunter, I., Brott, I., Langer, N., et al. 2009, A&A, 496, 841
- Hunter, I., Lennon, D. J., Dufton, P. L., et al. 2008, A&A, 479, 541
- Iben, Jr., I. 1964, ApJ, 140, 1631
- Iben, Jr., I. & Renzini, A. 1983, ARA&A, 21, 271
- Iliadis, C., D'Auria, J. M., Starrfield, S., Thompson, W. J., & Wiescher, M. 2001, ApJS, 134, 151
- Iliadis, C., Longland, R., Champagne, A. E., & Coc, A. 2010, Nuclear Physics A, 841, 251
- Inayoshi, K., Kashiyama, K., Visbal, E., & Haiman, Z. 2016, MNRAS, 461, 2722
- Iocco, F., Mangano, G., Miele, G., Pisanti, O., & Serpico, P. D. 2007, Phys. Rev. D, 75, 087304
- Ishigaki, M. N., Tominaga, N., Kobayashi, C., & Nomoto, K. 2014, ApJL, 792, L32
- Ito, H., Aoki, W., Beers, T. C., et al. 2013, ApJ, 773, 33
- Iwamoto, N., Umeda, H., Tominaga, N., Nomoto, K., & Maeda, K. 2005, Science, 309, 451
- Jacobson, H. R., Keller, S., Frebel, A., et al. 2015, ApJ, 807, 171
- Joggerst, C. C., Almgren, A., Bell, J., et al. 2010, ApJ, 709, 11
- Johnson, J. L. & Bromm, V. 2006, MNRAS, 366, 247
- Johnson, J. L. & Khochfar, S. 2011, MNRAS, 413, 1184
- Jones, S., Ritter, C., Herwig, F., et al. 2016, MNRAS, 455, 3848
- Jonsell, K., Barklem, P. S., Gustafsson, B., et al. 2006, A&A, 451, 651
- Kappeler, F., Beer, H., & Wisshak, K. 1989, Reports on Progress in Physics, 52, 945
- Käppeler, F., Gallino, R., Bisterzo, S., & Aoki, W. 2011, Reviews of Modern Physics, 83, 157

- Käppeler, F., Gallino, R., Busso, M., Picchio, G., & Raiteri, C. M. 1990, *ApJ*, 354, 630
- Karakas, A. I. 2010, *MNRAS*, 403, 1413
- Karakas, A. I. & Lattanzio, J. C. 2014, *PASA*, 31, e030
- Kawai, N., Kosugi, G., Aoki, K., et al. 2006, *Nature*, 440, 184
- Keller, S. C., Bessell, M. S., Frebel, A., et al. 2014, *Nature*, 506, 463
- Keller, S. C., Schmidt, B. P., Bessell, M. S., et al. 2007, *PASA*, 24, 1
- Kerber, L. O., Nardiello, D., Ortolani, S., et al. 2018, *ApJ*, 853, 15
- Kinugawa, T., Inayoshi, K., Hotokezaka, K., Nakauchi, D., & Nakamura, T. 2014, *MNRAS*, 442, 2963
- Klemola, A. R., Jones, B. F., & Hanson, R. B. 1987, *AJ*, 94, 501
- Kogut, A., Spergel, D. N., Barnes, C., et al. 2003, *ApJS*, 148, 161
- Korn, A. J., Richard, O., Mashonkina, L., et al. 2009, *ApJ*, 698, 410
- Kudritzki, R.-P. & Puls, J. 2000, *ARA&A*, 38, 613
- Lagarde, N., Decressin, T., Charbonnel, C., et al. 2012, *A&A*, 543, A108
- Lai, D. K., Johnson, J. A., Bolte, M., & Lucatello, S. 2007, *ApJ*, 667, 1185
- Lamb, S. A., Howard, W. M., Truran, J. W., & Iben, Jr., I. 1977, *ApJ*, 217, 213
- Langer, N., Arcoragi, J.-P., & Arnould, M. 1989, *A&A*, 210, 187
- Lattanzio, J. C. & Lugaro, M. A. 2005, *Nuclear Physics A*, 758, 477
- Lau, H. H. B., Stancliffe, R. J., & Tout, C. A. 2009, *MNRAS*, 396, 1046
- Lee, Y. S., Beers, T. C., Masseron, T., et al. 2013, *AJ*, 146, 132
- Lehner, N., O'Meara, J. M., Howk, J. C., Prochaska, J. X., & Fumagalli, M. 2016, *ApJ*, 833, 283
- Li, H., Aoki, W., Zhao, G., et al. 2015, *PASJ*, 67, 84
- Limongi, M. & Chieffi, A. 2012, *ApJS*, 199, 38
- Limongi, M. & Chieffi, A. 2018, *ApJS*, 237, 13
- Limongi, M., Chieffi, A., & Bonifacio, P. 2003, *ApJL*, 594, L123
- Lind, K., Bergemann, M., & Asplund, M. 2012, *MNRAS*, 427, 50
- Lodders, K. 2003, *ApJ*, 591, 1220
- Loeb, A. 2010, *How Did the First Stars and Galaxies Form?*
- Lucatello, S., Beers, T. C., Christlieb, N., et al. 2006, *ApJL*, 652, L37
- Lucatello, S., Tsangarides, S., Beers, T. C., et al. 2005, *ApJ*, 625, 825
- Lugaro, M., Karakas, A. I., Stancliffe, R. J., & Rijs, C. 2012, *ApJ*, 747, 2

- Lugaro, M., Ugalde, C., Karakas, A. I., et al. 2004, *ApJ*, 615, 934
- Maeda, K. & Nomoto, K. 2003, *ApJ*, 598, 1163
- Maeder, A. 1987, *A&A*, 178, 159
- Maeder, A. 1992, *A&A*, 264, 105
- Maeder, A. 1997, *A&A*, 321, 134
- Maeder, A. 1999, *A&A*, 347, 185
- Maeder, A. 2009, *Physics, Formation and Evolution of Rotating Stars*
- Maeder, A., Grebel, E. K., & Mermilliod, J.-C. 1999, *A&A*, 346, 459
- Maeder, A. & Meynet, G. 2000, *ARA&A*, 38, 143
- Maeder, A. & Meynet, G. 2012, *Reviews of Modern Physics*, 84, 25
- Maeder, A. & Meynet, G. 2015, *A&A*, 580, A32
- Maeder, A., Meynet, G., & Chiappini, C. 2015, *A&A*, 576, A56
- Maeder, A., Meynet, G., Lagarde, N., & Charbonnel, C. 2013, *A&A*, 553, A1
- Maeder, A. & Zahn, J.-P. 1998, *A&A*, 334, 1000
- Marassi, S., Schneider, R., & Ferrari, V. 2009, *MNRAS*, 398, 293
- Marsteller, B., Beers, T. C., Rossi, S., et al. 2005, *Nuclear Physics A*, 758, 312
- Martayan, C., Frémat, Y., Hubert, A.-M., et al. 2007, *A&A*, 462, 683
- Martell, S. L. 2016, in *Astronomical Society of the Pacific Conference Series*, Vol. 507, *Multi-Object Spectroscopy in the Next Decade: Big Questions, Large Surveys, and Wide Fields*, ed. I. Skillen, M. Balcells, & S. Trager, 51
- Martins, F., Hervé, A., Bouret, J.-C., et al. 2015, *A&A*, 575, A34
- Matrozis, E., Abate, C., & Stancliffe, R. J. 2017, *A&A*, 606, A137
- Matrozis, E. & Stancliffe, R. J. 2017, *A&A*, 606, A55
- McLure, R. J., Dunlop, J. S., Cirasuolo, M., et al. 2010, *MNRAS*, 403, 960
- McWilliam, A., Preston, G. W., Sneden, C., & Searle, L. 1995, *AJ*, 109, 2757
- Meakin, C. A. & Arnett, D. 2007, *ApJ*, 667, 448
- Merrill, P. W. 1952, *ApJ*, 116, 21
- Meyer, B. S., Clayton, D. D., & The, L.-S. 2000, *ApJL*, 540, L49
- Meynet, G., Ekström, S., & Maeder, A. 2005, in *IAU Symposium*, Vol. 228, *From Lithium to Uranium: Elemental Tracers of Early Cosmic Evolution*, ed. V. Hill, P. Francois, & F. Primas, 141–150
- Meynet, G., Ekström, S., & Maeder, A. 2006, *A&A*, 447, 623
- Meynet, G., Hirschi, R., Ekstrom, S., et al. 2010, *A&A*, 521, A30

- Meynet, G. & Maeder, A. 1997, *A&A*, 321, 465
- Meynet, G. & Maeder, A. 2000, *A&A*, 361, 101
- Meynet, G. & Maeder, A. 2002, *A&A*, 390, 561
- Michaud, G., Alecian, G., & Richer, J. 2015, *Atomic Diffusion in Stars*
- Morales, M. F. & Wyithe, J. S. B. 2010, *ARA&A*, 48, 127
- Moriya, T. J. & Langer, N. 2015, *A&A*, 573, A18
- Mukhamedzhanov, A. M., Bém, P., Brown, B. A., et al. 2003, *Phys. Rev. C*, 67, 065804
- Ness, M., Freeman, K., Athanassoula, E., et al. 2013, *MNRAS*, 430, 836
- Nishimura, N., Takiwaki, T., & Thielemann, F.-K. 2015, *ApJ*, 810, 109
- Noguchi, K., Aoki, W., Kawanomoto, S., et al. 2002, *PASJ*, 54, 855
- Nomoto, K., Maeda, K., Umeda, H., et al. 2003, in *IAU Symposium, Vol. 212, A Massive Star Odyssey: From Main Sequence to Supernova*, ed. K. van der Hucht, A. Herrero, & C. Esteban, 395
- Nomoto, K., Tominaga, N., Umeda, H., Kobayashi, C., & Maeda, K. 2006, *Nuclear Physics A*, 777, 424
- Nordlander, T. & Lind, K. 2017, *A&A*, 607, A75
- Norris, J. E., Beers, T. C., & Ryan, S. G. 2000, *ApJ*, 540, 456
- Norris, J. E., Christlieb, N., Bessell, M. S., et al. 2012, *ApJ*, 753, 150
- Norris, J. E., Christlieb, N., Korn, A. J., et al. 2007, *ApJ*, 670, 774
- Norris, J. E., Ryan, S. G., & Beers, T. C. 1997, *ApJ*, 488, 350
- Norris, J. E., Ryan, S. G., Beers, T. C., Aoki, W., & Ando, H. 2002, *ApJL*, 569, L107
- Norris, J. E., Yong, D., Bessell, M. S., et al. 2013, *ApJ*, 762, 28
- Oesch, P. A., Bouwens, R. J., Illingworth, G. D., et al. 2010, *ApJL*, 709, L16
- Oesch, P. A., Brammer, G., van Dokkum, P. G., et al. 2016, *ApJ*, 819, 129
- Paczyński, B. 1965, *Acta Astron.*, 15, 89
- Pasquini, L., Mauas, P., Käufel, H. U., & Cacciari, C. 2011, *A&A*, 531, A35
- Pawlik, A. H., Milosavljević, M., & Bromm, V. 2011, *ApJ*, 731, 54
- Perryman, M. A. C., de Boer, K. S., Gilmore, G., et al. 2001, *A&A*, 369, 339
- Peters, J. G. 1968, *ApJ*, 154, 225
- Pettini, M. 2008, in *IAU Symposium, Vol. 250, Massive Stars as Cosmic Engines*, ed. F. Bresolin, P. A. Crowther, & J. Puls, 415–428
- Pettini, M. & Pagel, B. E. J. 2004, *MNRAS*, 348, L59
- Pian, E., D’Avanzo, P., Benetti, S., et al. 2017, *Nature*, 551, 67

- Pignatari, M., Gallino, R., Meynet, G., et al. 2008, *ApJL*, 687, L95
- Pignatari, M., Wiescher, M., Timmes, F. X., et al. 2013, *ApJL*, 767, L22
- Placco, V. M., Beers, T. C., Roederer, I. U., et al. 2014a, *ApJ*, 790, 34
- Placco, V. M., Frebel, A., Beers, T. C., et al. 2014b, *ApJ*, 781, 40
- Placco, V. M., Frebel, A., Beers, T. C., et al. 2013, *ApJ*, 770, 104
- Placco, V. M., Frebel, A., Beers, T. C., & Stancliffe, R. J. 2014c, *ApJ*, 797, 21
- Placco, V. M., Frebel, A., Beers, T. C., et al. 2016, *ApJ*, 833, 21
- Planck Collaboration, Adam, R., Aghanim, N., et al. 2016, *A&A*, 596, A108
- Plez, B. & Cohen, J. G. 2005, *A&A*, 434, 1117
- Prantzos, N., Hashimoto, M., & Nomoto, K. 1990, *A&A*, 234, 211
- Preskill, J., Wise, M. B., & Wilczek, F. 1983, *Physics Letters B*, 120, 127
- Pritchard, J. R. & Loeb, A. 2012, *Reports on Progress in Physics*, 75, 086901
- Raffelt, G. G. 2008, in *Lecture Notes in Physics*, Berlin Springer Verlag, Vol. 741, *Axions*, ed. M. Kuster, G. Raffelt, & B. Beltrán, 51
- Raiteri, C. M., Busso, M., Gallino, R., Picchio, G., & Pulone, L. 1991a, *ApJ*, 367, 228
- Raiteri, C. M., Busso, M., Picchio, G., & Gallino, R. 1991b, *ApJ*, 371, 665
- Rauscher, T., Heger, A., Hoffman, R. D., & Woosley, S. E. 2002, *ApJ*, 576, 323
- Rauscher, T. & Thielemann, F.-K. 2000, *Atomic Data and Nuclear Data Tables*, 75, 1
- Rayet, M. & Hashimoto, M.-a. 2000, *A&A*, 354, 740
- Reddy, B. E., Lambert, D. L., & Allende Prieto, C. 2006, *MNRAS*, 367, 1329
- Ren, J., Christlieb, N., & Zhao, G. 2012, *Research in Astronomy and Astrophysics*, 12, 1637
- Renzini, A. & Voli, M. 1981, *A&A*, 94, 175
- Rhee, J. 2001, *PASP*, 113, 1569
- Richard, O., Michaud, G., Richer, J., et al. 2002, *ApJ*, 568, 979
- Richer, J., Michaud, G., & Turcotte, S. 2000, *ApJ*, 529, 338
- Ricker, P. M. & Taam, R. E. 2008, *ApJL*, 672, L41
- Roederer, I. U., Karakas, A. I., Pignatari, M., & Herwig, F. 2016, *ApJ*, 821, 37
- Roederer, I. U., Preston, G. W., Thompson, I. B., Shectman, S. A., & Sneden, C. 2014a, *ApJ*, 784, 158
- Roederer, I. U., Preston, G. W., Thompson, I. B., et al. 2014b, *AJ*, 147, 136
- Roman, N. G. 1950, *ApJ*, 112, 554
- Rufus, W. C. 1916, *Publications of Michigan Observatory*, 2, 103

- Ryan, S. G. & Norris, J. E. 1991, *AJ*, 101, 1835
- Ryan, S. G., Norris, J. E., & Beers, T. C. 1996, *ApJ*, 471, 254
- Rydberg, C.-E., Zackrisson, E., Lundqvist, P., & Scott, P. 2013, *MNRAS*, 429, 3658
- Salvaterra, R. 2015, *Journal of High Energy Astrophysics*, 7, 35
- Salvaterra, R., Ferrara, A., & Dayal, P. 2011, *MNRAS*, 414, 847
- Sandick, P., Olive, K. A., Daigne, F., & Vangioni, E. 2006, *Phys. Rev. D*, 73, 104024
- Saslaw, W. C. & Zipoy, D. 1967, *Nature*, 216, 976
- Sbordone, L., Bonifacio, P., Caffau, E., et al. 2010, *A&A*, 522, A26
- Schaerer, D. 2002, *A&A*, 382, 28
- Schwarzschild, M. & Schwarzschild, B. 1950, *ApJ*, 112, 248
- Secchi, A. 1868, *MNRAS*, 28, 196
- Simcoe, R. A., Sullivan, P. W., Cooksey, K. L., et al. 2012, *Nature*, 492, 79
- Simmerer, J., Sneden, C., Cowan, J. J., et al. 2004, *ApJ*, 617, 1091
- Sivarani, T., Beers, T. C., Bonifacio, P., et al. 2006, *A&A*, 459, 125
- Sivarani, T., Bonifacio, P., Molaro, P., et al. 2004, *A&A*, 413, 1073
- Smartt, S. J., Chen, T.-W., Jerkstrand, A., et al. 2017, *Nature*, 551, 75
- Smith, V. V. & Lambert, D. L. 1990, *ApJS*, 72, 387
- Smith, V. V. & Wallerstein, G. 1983, *ApJ*, 273, 742
- Sneden, C., Cowan, J. J., & Gallino, R. 2008, *ARA&A*, 46, 241
- Sneden, C., Cowan, J. J., Lawler, J. E., et al. 2003, *ApJ*, 591, 936
- Sneden, C., McWilliam, A., Preston, G. W., et al. 1996, *ApJ*, 467, 819
- Spergel, D. N., Bean, R., Doré, O., et al. 2007, *ApJS*, 170, 377
- Spite, F. & Spite, M. 1982, *A&A*, 115, 357
- Spite, M., Andrievsky, S. M., Spite, F., et al. 2012, *A&A*, 541, A143
- Spite, M., Caffau, E., Bonifacio, P., et al. 2013, *A&A*, 552, A107
- Spite, M., Cayrel, R., Hill, V., et al. 2006, *A&A*, 455, 291
- Stacy, A., Bromm, V., & Lee, A. T. 2016, *MNRAS*, 462, 1307
- Stacy, A., Bromm, V., & Loeb, A. 2011, *MNRAS*, 413, 543
- Stancliffe, R. J. 2010, *MNRAS*, 403, 505
- Stancliffe, R. J., Church, R. P., Angelou, G. C., & Lattanzio, J. C. 2009, *MNRAS*, 396, 2313
- Stancliffe, R. J., Glebbeek, E., Izzard, R. G., & Pols, O. R. 2007, *A&A*, 464, L57

- Starkenburger, E., Martin, N., Youakim, K., et al. 2017, *MNRAS*, 471, 2587
- Starkenburger, E., Shetrone, M. D., McConnachie, A. W., & Venn, K. A. 2014, *MNRAS*, 441, 1217
- Steinmetz, M. 2003, in *Astronomical Society of the Pacific Conference Series*, Vol. 298, *GAIA Spectroscopy: Science and Technology*, ed. U. Munari, 381
- Stello, D., Huber, D., Sharma, S., et al. 2015, *ApJL*, 809, L3
- Straniero, O., Gallino, R., Busso, M., et al. 1995, *ApJL*, 440, L85
- Suda, T., Aikawa, M., Machida, M. N., Fujimoto, M. Y., & Iben, Jr., I. 2004, *ApJ*, 611, 476
- Suda, T. & Fujimoto, M. Y. 2010, *MNRAS*, 405, 177
- Suda, T., Katsuta, Y., Yamada, S., et al. 2008, *PASJ*, 60, 1159
- Suwa, Y., Takiwaki, T., Kotake, K., & Sato, K. 2007, *ApJL*, 665, L43
- Symbalisty, E. & Schramm, D. N. 1982, *ApL*, 22, 143
- Takahashi, K., Umeda, H., & Yoshida, T. 2014, *ApJ*, 794, 40
- Talon, S. & Zahn, J.-P. 1997, *A&A*, 317, 749
- Tanaka, M., Moriya, T. J., & Yoshida, N. 2013, *MNRAS*, 435, 2483
- The, L.-S., El Eid, M. F., & Meyer, B. S. 2007, *ApJ*, 655, 1058
- Thielemann, F.-K., Arcones, A., Käppeli, R., et al. 2011, *Progress in Particle and Nuclear Physics*, 66, 346
- Thielemann, F. K. & Arnett, W. D. 1985, *ApJ*, 295, 604
- Thielemann, F.-K., Eichler, M., Panov, I. V., & Wehmeyer, B. 2017, *Annual Review of Nuclear and Particle Science*, 67, 253
- Thielemann, F.-K., Hashimoto, M.-A., & Nomoto, K. 1990, *ApJ*, 349, 222
- Thielemann, F.-K., Nomoto, K., & Hashimoto, M.-A. 1996, *ApJ*, 460, 408
- Thöne, C. C., Fynbo, J. P. U., Goldoni, P., et al. 2013, *MNRAS*, 428, 3590
- Tominaga, N. 2009, *ApJ*, 690, 526
- Tominaga, N., Iwamoto, N., & Nomoto, K. 2014, *ApJ*, 785, 98
- Tominaga, N., Umeda, H., & Nomoto, K. 2007, *ApJ*, 660, 516
- Truran, J. W. & Iben, Jr., I. 1977, *ApJ*, 216, 797
- Tumlinson, J. 2010, *ApJ*, 708, 1398
- Tur, C., Heger, A., & Austin, S. M. 2009, *ApJ*, 702, 1068
- Umeda, H. & Nomoto, K. 2002, *ApJ*, 565, 385
- Umeda, H. & Nomoto, K. 2003, *Nature*, 422, 871
- Umeda, H. & Nomoto, K. 2005, *ApJ*, 619, 427

- Van Eck, S., Goriely, S., Jorissen, A., & Plez, B. 2001, *Nature*, 412, 793
- Venn, K. A., Irwin, M., Shetrone, M. D., et al. 2004, *AJ*, 128, 1177
- Venn, K. A. & Lambert, D. L. 2008, *ApJ*, 677, 572
- Venn, K. A., Puzia, T. H., Divell, M., et al. 2014, *ApJ*, 791, 98
- Villamariz, M. R. & Herrero, A. 2005, *A&A*, 442, 263
- Vink, J. S., de Koter, A., & Lamers, H. J. G. L. M. 2001, *A&A*, 369, 574
- von Zeipel, H. 1924, *MNRAS*, 84, 665
- Wallerstein, G. & Carlson, M. 1960, *ApJ*, 132, 276
- Wanajo, S., Sekiguchi, Y., Nishimura, N., et al. 2014, *ApJL*, 789, L39
- Wehmeyer, B., Pignatari, M., & Thielemann, F.-K. 2015, *MNRAS*, 452, 1970
- Whalen, D. J., Even, W., Frey, L. H., et al. 2013a, *ApJ*, 777, 110
- Whalen, D. J., Fryer, C. L., Holz, D. E., et al. 2013b, *ApJL*, 762, L6
- Whalen, D. J., Joggerst, C. C., Fryer, C. L., et al. 2013c, *ApJ*, 768, 95
- Wildey, R. L., Burbidge, E. M., Sandage, A. R., & Burbidge, G. R. 1962, *ApJ*, 135, 94
- Winteler, C., Käppeli, R., Perego, A., et al. 2012, *ApJL*, 750, L22
- Wisotzki, L., Koehler, T., Groote, D., & Reimers, D. 1996, *A&AS*, 115, 227
- Woosley, S. E. 1993, *ApJ*, 405, 273
- Woosley, S. E. 2017, *ApJ*, 836, 244
- Woosley, S. E., Heger, A., & Weaver, T. A. 2002, *Reviews of Modern Physics*, 74, 1015
- Woosley, S. E. & Weaver, T. A. 1995, *ApJS*, 101, 181
- Yanny, B., Rockosi, C., Newberg, H. J., et al. 2009, *AJ*, 137, 4377
- Yong, D., Norris, J. E., Bessell, M. S., et al. 2013, *ApJ*, 762, 26
- Yoon, J., Beers, T. C., Placco, V. M., et al. 2016, *ApJ*, 833, 20
- York, D. G., Adelman, J., Anderson, Jr., J. E., et al. 2000, *AJ*, 120, 1579
- Youakim, K., Starkenburg, E., Aguado, D. S., et al. 2017, *MNRAS*, 472, 2963
- Zahn, J.-P. 1992, *A&A*, 265, 115
- Zhang, L., Karlsson, T., Christlieb, N., et al. 2011, *A&A*, 528, A92